Development of Space-Time Finite Element Method for Seismic Analysis of Hydraulic Structures

2018

Vikas Sharma

Acknowledgement

This study presents the results of research conducted over a period of three years by the author who has been studying as doctoral student at the Graduate School of Agriculture at Kyoto University.

First and foremost, I would like to express my sincere gratitude to Professor Akira Murakami for his supervision and also for his enthusiastic guidance and encouragement. I also extend my great appreciation to Associate Professor Kazunori Fujisawa for sharing his knowledge about finite element method and computer programing. The discussions have proved very valuable in understanding the subject better.

I am indebt to the members of my Dissertation Committee, Professor Shigeto Kawashima, Professor Ryosuke Uzuoka, and Professor Masayuki Fujihara, for their valuable insights and constructive suggestions in reviewing the manuscript.

I am thankful to Professor D.N. Singh at IIT-Bombay for inspiring me to pursue the path of research. I am grateful to my labmates Haruka Tomobe and Nobuyuki Yamashita for their warm companionship in this foreign land. I also take the opportunity to thank my parents for everything. Lastly, I thank my partner Rachana Subba for the constant support.

Contents

List of Figures

List of Tables

1 Introduction

1.1 Motivation and Objectives

Mathematical (analytical or numerical) modeling of continuum mechanics problems is an integral part of engineering design, scientific research, and technological inventions. For example, in the field of geotechnical engineering, numerical methods are indispensable tool for designing and health monitoring of ground and soil-structures, such as embankments, bridges and pile foundations, and tunnels subjected to static and dynamic loading conditions. In recent years, techniques have been developed for handling the issues related to the erosion of soil structures, piping flows within natural slopes, and the stability of embankments subjected to tidal waves. Further, environmental impact and safety assessments of the ground vibrations generated by high-speed trains (Ditzel et al., 2001; Krylov, 1996; Takemiya, 2003) and road traffic (Chua et al., 1992; Clemente and Rinaldis, 1998; Clouteau et al., 2001; Maeda et al., 1998) close to the residential areas, hospitals, and high-tech industries are of paramount importance.

The finite element method is one of the most popular numerical methods for computing accurate solutions to partial differential equations (PDEs) that describe many engineering problems. The FEM originated from the structural mechanics discipline and has since been extended to other areas of solid mechanics as well as heat transfer, fluid dynamics, and electromagnetism. In dealing with PDEs, it is useful to differentiate between several types; elliptic, hyperbolic, and parabolic PDEs. For example, elliptic PDEs generally represent static problems in which only boundary conditions (viz., Dirichlet boundary condition and/or Neumann boundary condition) need to be prescribed. Hyperbolic and parabolic PDEs, on the other hand, represent a transient problem and require specification of both intial and boundary conditions. Clearly, both the theoretical and numerical treatment differ considerably for these three types of PDEs.

The most extending approach for solving a transient problem is based on a classical semi-discretized FEM formulation. In this approach, usually a generalized Galekin methods are first employed to construct the weak-form of governing PDEs. Such weak-forms are constructed in the spatial domain while assuming that the shape functions are independent of time. Furthermore, spatial nodal values of the trial

functions only depend upon the time while nodal values of the test functions remain independent of the time. The time-independece of the shape functions and time-dependence of nodal values of the solution create an uncoupled space-time domain. Consequently, one obtains a system of ordinary differential equations in time. Time-marching schemes based on the finite difference methods are then used to solve the resultant system of ODEs. In this way, the semi-discrete FEM treats the problem differently in the space and time domain; variation principles are used for the former domain, and finite difference techniques are used for latter domain. Further, it is well established that the finite differnce methods produce less accurate solutions than FEM. Therefore,careful selection of a finite difference scheme is required to achieve the desired level of accuracy. Here, let us mentioned that a poor selection of FDM may limit the overall accuracy of the semi-discrete FEM, or in some cases may even produce inconsistent results. Lastly, selection of the appropriate FDM mainly depend upon the type of problem, for example, the algorithms which works well for the heat-diffusion problem may not be suitable for the problem of elastodynamics.

In transient problems, one wishes to use a high-order accurate time integration scheme with a large time-step size in an attempt to reduce the computation cost. However, the use of large time-step size is only possible if the time-marching scheme is unconditionally stable; the stability of the time integration algorithm does not depend upon the time-step size. Unconditionally stable methods, such as the Newmark-beta method (Newmark, 1959), the HHT–α method (Hilber et al., 1977), the Houbolt method (Houbolt, 1950), and the Wilson–θ method (Bathe and Wilson, 1976), are the most often used dynamic solvers in semi-discrete FEM. However, these methods are only second-order accurate. Furthermore, Dahlquist's theorem says that a single-step unconditionally stable time-integration algorithm can be at most second-order accurate (Dahlquist, 1963). High-order accurate time-integration schemes based on the finite difference schemes can be employed. However, these schemes are generally conditionally stable and require very small time steps for stability (Hughes, 1983). The requirement of small time steps increases the overall computational cost of large-scale simulations. Therefore, there is still a need for dynamic solvers which are high-order accurate and unconditionally stable, such that large time steps can be used to reduce the computational cost while maintaining the accuracy of the solutions.

At present, time-discontinuous Galerkin approach have been well studied for the problems involving first order time derivatives. In the field of computational fluid dynamics, this approach have been used for problems involving the moving and free boundaries (**Bazilevs2013**). In TDG/ST/FEM, shape-functions are usually defined on the space-time domain. The weak form of the govering equations are formulated in a space-time slab, therefore, no additional time-marching schemes are required. Therefore, such method may provide a unified framework for using

the Lagrangian mesh, Eulerian mesh, and arbitrary moving mesh. In addition, for problems involving the second-order time derivatives TDG/ST/FEM facilitates the weak-enforcement of initial conditions through jump-discontinuity in time. In this way, TDG/ST/FEM provides a general framework for arbitrary high order accurate, unconditionally stable time integration algorithms. We believe that these characteristics of TDG/ST/FEM may have great potential for solving the problems of large-deformation dynamic problems.

The objective of this thesis is to develope an efficient space-time finite element method within time-discontinuous Galerkin framework. In this context, a velocity-based single-field ST/FEM is developed. Hereafter, the term v-ST/FEM will be used to denote the proposed method. In v-ST/FEM, velocity is the primary unknowns which is discontinuous in time and continuous in space. The displacement field is obtained by time integration of the velocity field in a post-processing step. The main advantage of v-ST/FEM is that it involves less number of unknowns–unlike other ST/FEM–which makes v-ST/FEM applicable to the large-scale practical problems at relatively low computation cost. In addition, the proposed scheme naturally allows the coupling of space-time domain, consequently, it can be used with Lagrangian mesh, Eulerian mesh, or arbitrary moving mesh framework. We believe that the proposed method can be developed further as an effective tool for simulating problems with moving and free boundaries.

This thesis includes the following chapters:

In **Chapter 2**, the working principles of the time-discontinuous Galerkin finite element method (TDG/FEM) are described by using a first order ordinary differential equation (ODE) and a second order ODE. Subsequently, a velocity-based time-discontinuous space-time finite element method (v-ST/FEM) for a multidimensional elastodynamics problem is developed. Several numerical tests are performed to demonstrate the efficiency and the applicability of the v-ST/FEM.

In **Chapter 3**, a concise presentation regarding the theory of wave propagation in an elastic solid is given. After briefly discussing the reflection and refraction of a plane harmonic waves it is shown that the problem of dynamic soil-structure interaction (SSI) can be viewed as a wave-scattering phenomenon, in which the free-field response of an elastic half-space is perturbed by the existing structure. The chapter presents some of the most popular boundary conditions for solving wave propagation problems in the unbounded domain. In addition, the viscous boundary conditions and modified viscous boundary conditions are derived.

In **Chapter 4**, v-ST/FEM method is used to solve the problem of dynamic soil-structure interaction. In this context, finite element modeling of the unbounded

soil domain is performed by placing modified viscous boundaries at some distance from the existing structure. A dynamic dam-soil interaction problem is considered to validate the formulation and computer implementation of v-ST/FEM. The results obtained by proposed scheme are validated by solving the same problem using the semi-discrete FEM with classical Newmark-β method. Results obtained by two methods are compared and found to be nearly identical.

In **Chapter 5**, v-ST/FEM is used to compute the seismic response of the dam-reservoir (DR) and dam-reservoir-soil (DRS) system while considering all types of dynamic interaction. Both dam and the underlying soil domain is assumed to be linearly elastic, and material damping is modeled by Rayleigh damping. The water in the reservoir is assumed to be inviscid, linearly compressible with a small amplitudes for the displacements and velocity. Thus, the hydrodynamic pressure in the reservoir is given by the pressure wave equation. In the finite element modeling, viscous boundary conditions are used to truncate the semi-infinite domain of reservoir and underlying soil-domain.

In **Chapter 6**, v-ST/FEM is employed for the problems involving dynamic response of solids and structures with nonlinear stress-strain relationships. The problem of dynamic interaction between the concrete gravity dam and reservoir is taken as a model problem, in which a generalized nonlinear stress-strain relationship is used to describe the material behavior of concrete in the dam. The foundation underneath the dam-reservoir (DR) system is assumed to be perfectly rigid. The governing equations describing the dynamic interaction between dam and reservoir constitute a system of linear-nonlinear coupled equations, in which linear equations govern the reservoir domain and nonlinear equations govern the solid domain. A block-iterative scheme is used to enforce the coupling between the solid and fluid domain. In each iteration of v-ST/FEM with the block-iterative scheme, the linearized equations of the solid domain are first solved to compute the increments in the velocity field. Subsequently, the total velocities are corrected and then used for computing the trial values of hydrodynamic pressures in the reservoir by solving the linear equation for the reservoir domain. In each iteration of the proposed scheme, therefore, linear equations for the solid and fluid domain are solved, separately, which significantly decreases the computation cost.

2 Time-Discontinuous Galerkin Methods for Elastodynamics Problem

2.1 Introduction

Numerical methods for computing the dynamic response of the ground and soil-structures, such as embankments, bridges and pile foundations, and tunnels, are an indispensable tool for designing and monitoring ground structures. The Finite Element Method (FEM) has been undoubtedly accepted as the most popular, reliable, and successful numerical tool for simulating soil dynamics problems (Anandarajah, 1993; Khoshnoudian and Shahrour, 2002; Kimura and Zhang, 2000; Kuwano et al., 1991; Li and Ugai, 1998; Murakami et al., 2010). Further, environmental impact and safety assessments of the ground vibrations generated by high-speed trains (Ditzel et al., 2001; Krylov, 1996; Takemiya, 2003) and road traffic (Chua et al., 1992; Clemente and Rinaldis, 1998; Clouteau et al., 2001; Maeda et al., 1998) close to the residential areas, hospitals, and high-tech industries are of paramount importance. FEM has also been extensively used for investigating the level of vibrations and schemes to reduce them (Hung et al., 2001; Ju, 2007; Ju, 2009; Ju et al., 2006; Ju and Lin, 2004). Moreover, in the field of transportation engineering, nondestructive deflection testing, with the Falling Weight Deflectometer (FWD), has become increasingly popular for monitoring the structural health of flexible pavement systems over time Chai et al., 2014; Elbagalati et al., 2018; Maina et al., 2000. In FWD testing, the recorded time histories of surface deflections are used to back-calculate the moduli of pavement layers by employing parameter-identification techniques (Goktepe et al., 2006). Recently, FEM has been employed extensively to simulate FWD testing under realistic conditions and to predict the response of pavement systems brought about by impulsive loading (Loizos and Scarpas, 2005; Nazarian and Boddapati, 1995; Picoux et al., 2009).

In the preceding discussion, the most extended approach for solving elastodynamics problems was based on a semi-discretized FEM formulation. In this approach, FEM is first applied to the spatial domain leading to a system of ordinary differential equations (ODE) in the time domain. Subsequently, direct time integration schemes, based on the finite difference method, are employed to solve the resulting system

of ODEs. In general, the errors in the finite element simulations of soil-dynamics problems are partially due to the space-time discretization and to the uncertainties involved in the material constitutive relationship and the material parameters. Numerical errors can be reduced by adopting high-order accurate time solvers within FEM framework. Unconditionally stable methods, such as the Newmark-beta method (Newmark, 1959), the HHT-α method (Hilber et al., 1977), the Houbolt method (Houbolt, 1950), and the Wilson-θ method (Bathe and Wilson, 1976), are the most often used dynamic solvers. However, these methods are only second-order accurate. Furthermore, Dahlquist's theorem says that a single-step unconditionally stable time-integration algorithm can be at most second-order accurate (Dahlquist, 1963). High-order accurate time-integration schemes based on finite difference schemes can be employed. However, these schemes are generally conditionally stable and require very small time steps for stability (Hughes, 1983). The requirement of small time steps increases the overall computational cost of large-scale simulations. Therefore, there is still a need for dynamic solvers which are high-order accurate and unconditionally stable, such that large time steps can be used to reduce the computational cost while maintaining the accuracy of the solutions. The aim of this thesis is to devise such a scheme.

To achieve high-order accuracy combined with stability, an alternative strategy called the Space-Time Finite Element Method (ST/FEM) was proposed in the past; it is still being actively researched. The concept of finite elements in the time domain was first exploited independently in Argyris and Scharpf, 1969 and Fried, 1969 using Hamilton's principle. Unfortunately, these formulations were found to be inconsistent, and even inaccurate in some cases, due to the vanishing variation in the displacement at the end points of the time interval. Soon after, Bailey, 1975; Bailey, 1980; Bailey, 1982 and Simkins, 1981 established that instead of Hamilton's principle, Hamilton's law of varying action, HLVA, should be used as the starting point for the time-finite element formulations, as it includes the initial conditions implicitly. However, for quite some time, researchers misinterpreted the so-called *trailing terms* of HLVA, and believed that both the displacement field and the velocity field should be continuous in time (M. Borri and Mantegazzat, 1985). Due to this misconception, many studies adopted Hermite cubic polynomials as the lowest order of interpolation functions for the displacement field (Baruch and Riff, 1982; Baruch and Riff, 1984; Gellert, 1978; Geradin, 1974; Howard and Penny, 1978; Riff and Baruch, 1984; Simkins, 1981; Sorek and Blech, 1982). Later, Borri and his colleagues (Borri, 1986; Borri et al., 1985; M. Borri and Mantegazzat, 1985) showed that the need to use Hermite polynomials can be avoided by employing Hamilton's weak principle (HWP) in which approximating functions should ensure the continuity of only the displacement field (i.e., $C0$ continuity in time), and not that of any of its time-derivatives. More recently, unconditionally stable time-finite element formulations have been derived using the two-field form of HWP instead of

the primal form (Aharoni and Bar-Yoseph, 1992; Borri et al., 1990; Borri et al., 1991; Borri and Bottasso, 1993; Mello et al., 1990; Ruge, 1996). For a comprehensive overview and recent advances in the time-finite element formulations based on Hamilton's law, readers are referred to Tamma et al., 2011.

Another approach towards development of the ST/FEM is by weighted residual techniques, such as the continuous Galerkin method (Bajer and Bohatier, 1995; Bajer, 1987), the discontinuous Galerkin method (Hughes and Hulbert, 1988), and the Petrov-Galerkin method (Fung and Leung, 1996; Fung, 1999), while working directly with the differential equations rather than a variational principle. Moreover, ST/FEM derived from the time-discontinuous Galerkin (TDG) method led to the unconditionally stable and high-order accurate ODE solvers (Delfour et al., 1981; Johnson and Pitkäranta, 1986; Lasaint and Raviart, 1974). The discontinuous Galerkin (DG) method was first developed for the neutron-transport equation Lasaint and Raviart, 1974; Reed and Hill, 1973. Soon after, the TDG method was introduced by Jamet (Bonnerot and Jamet, 1979; Jamet, 1978) for solving the parabolic differential equation with the time- dependent spatial domain. Almost a decade afterwards, Hughes and Hulbert presented the time-discontinuous Galerkin space-time FEM (TDG/ST/FEM) for the fields of elastodynamics and structural dynamics (Hughes and Hulbert, 1988). In this paper, two general formulations of TDG/ST/FEM were provided: (i) the single-field formulation, in which the displacement field is the primary unknown, and (ii) the two-field formulation, in which both the displacement field and the velocity field are treated as the primary unknowns. In a latter approach, the trial functions for both fields were continuous in space and discontinuous in time, whereas the test functions were continuous in both space and time. In the two-field formulation, the displacement-velocity compatibility condition and the continuity of both unknown fields in time were satisfied in a weak sense by using some inner products. This is the key element allowing for the generalization of TDG/ST/FEM developed for first order hyperbolic equations to the second order hyperbolic equations (Hughes and Hulbert, 1988). However, the main disadvantage of the two-field formulation is that it leads to larger systems of coupled equations than formulations derived from direct integration schemes. To overcome this difficulty, various efficient iterative predictor-multi-corrector algorithms have been suggested by Li and Wiberg, 1998; Mancuso and Ubertini, 2003; Chien and Wu, 2000; Mancuso and Ubertini, 2006, among others. Details on the numerical characteristics of two-field formulations, such as stability, the order of accuracy, and algorithmic damping, have been discussed elsewhere (Fan et al., 1997; Fung and Leung, 1996; Hulbert, 1992).

At present, time-discontinuous Galerkin approach have been well studied for the problems involving first order time derivatives. In the field of computational fluid dynamics, this approach have been used for problems involving the moving and free

boundaries (**Bazilevs2013**). In TDG/ST/FEM, shape-functions are usually defined on the space-time domain. Therefore, such method may provide a unified framework for using the Lagrangian mesh, Eulerian mesh, and Arbitrary moving mesh. In addition, for problems involving the second-order time derivatives TDG/ST/FEM facilitates the weak-enforcement of initial conditions through jump-discontinuity in time. In this way, TDG/ST/FEM provides a general framework for arbitrary high order accurate, unconditionally stable time integration algorithms. We believe that these characteristics of TDG/ST/FEM may have great potential for solving the problems of large-deformation dynamic problems.

Accordingly, in this chapter, a velocity-based single-field ST/FEM is developed within a TDG framework. Hereafter, the term v-ST/FEM will be used to denote the proposed method. In v-ST/FEM, velocity is the primary unknowns which is discontinuous in time and continuous in space. The displacement field is obtained by time integration of the velocity field in a post-processing step. The advantage of v-ST/FEM is that it involves less number of unknowns–unlike other ST/FEM–which makes v-ST/FEM applicable to the large-scale practical problems at relatively low computation cost.

The remainder of the paper is organized as follows. First, in Section 2.2, the concept of time-discontinuous Galerkin finite element method (TDG/FEM) is explained for the first order ordinary differential equation (ODE) in time. Subsequently, the numerical properties of the resultant algorithm are discussed. Section 2.3 extends these concepts to a second order ODE in time. In this section, three types of TDG/FEM formulations are presented; uv-TDG/FEM, u-TDG/FEM, and v-TDG/FEM. In uv-TDG/FEM, both displacement and velocity are approximated by using the time discontinuous trial functions, in addition, displacement-velocity compatibility condition is weakly enforced. In u-TDG/FEM, displacement is the primary unknown, and velocity is obtained by taking the time derivative of the displacement. Accordingly, the displacement-velocity relationship is strongly enforced. Lastly, in v-TDG/FEM velocity is the primary unknown, and displacement is obtained in a post-processing step by consistent time integration of the velocity field. Further, in Section 2.4 numerical properties of the TDG/FEM schemes for second order ODE are discussed. The continuum theory of elastodynamics and the initial-boundary value problem (IBVP) are summarized in Section 2.5. Section 2.6 describes the general theoretical development and formulation aspects of the v-ST/FEM approach. In this section the implementation details of the current methodology are also discussed. The applicability and the validity of v-ST/FEM are then demonstrated in Section 2.7 through different numerical examples.

2.2 TDG/FEM for the first order ODE

To understand the working principle of the time-discontinuous Galerkin finite element method (TDG/FEM) consider the following initial value problem [1] described by a first order ordinary differential equation equation (ODE).

$$\begin{aligned} \frac{du}{dt} + \lambda u - f(t) = 0 \quad t \in [0, T], \\ u(0) = u_0 \end{aligned} \tag{2.1}$$

where T is the total time, $u := u(t)$ is the primary unknown, $f(t)$ represents the excitation function, and u_0 is the initial condition. The analytical solution to this problems takes the form of

$$u(t) = u_0 e^{-\lambda t} + \int_0^t e^{-\lambda(t-\tau)} f(\tau)\, d\tau \tag{2.2}$$

Let us now consider a non-uniform subdivision for the time domain $[0, T]$,

$$0 = t_0 < t_1 < \cdots < t_N = T,$$

with

$$I_n = (t_n, t_n + 1), \qquad \Delta t_n = t_{n+1} - t_n, \qquad \Delta t = \max_{(0 \leqslant n \leqslant N-1)} (\Delta t_n).$$

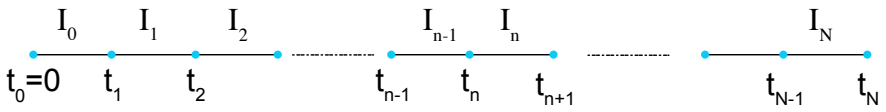

Fig. 2.1.: Discretization of time domain $[0, T]$ by using the time-finite elements.

In the finite element method (FEM), the time interval, I_n, denotes the interior of the one-dimensional time finite element, and $\partial I_n = \{t_n, t_{n+1}\}$ denotes the boundary of I_n [2]. Accordingly, the finite element discretization of the continuous time domain can be written as (see also Fig. 2.1),

$$I_h := \bigcup_{n=0}^{N-1} (I_n \cup \partial I_n)$$

[1] Eq. (2.1) characterizes the modal equations of a linear parabolic partial differential equation (e.g., heat diffusion equation)

[2] The boundary of a one-dimensional finite element comprises end-points only.

In TDG/FEM, the solutions to the problem, $u^h(t)$, are considered to be discontinuous at the boundary of the time-domain. The solutions, however, remain continuous inside the time-finite element I_n, and approximated by piecewise polynomials (e.g., Lagrange polynomials). Therefore, the discontinuity in $u^h(t)$ occurs at times that belong to the finite set $\{t_0, t_1, \cdots, t_N\}$. The jump discontinuity in time for u^h is given by

$$\left[\left[u^h\right]\right]_n = u_n^+ - u_n^- \tag{2.3}$$

where

$$u_n^+ = \lim_{\varepsilon \to 0} u^h\left(t+\varepsilon\right), \qquad u_n^- = \lim_{\varepsilon \to 0} u^h\left(t-\varepsilon\right) \tag{2.4}$$

are the discontinuous values of u^h at time $t = t_n$. **Fig. 2.2** illustrates the concept of time discontinuity.

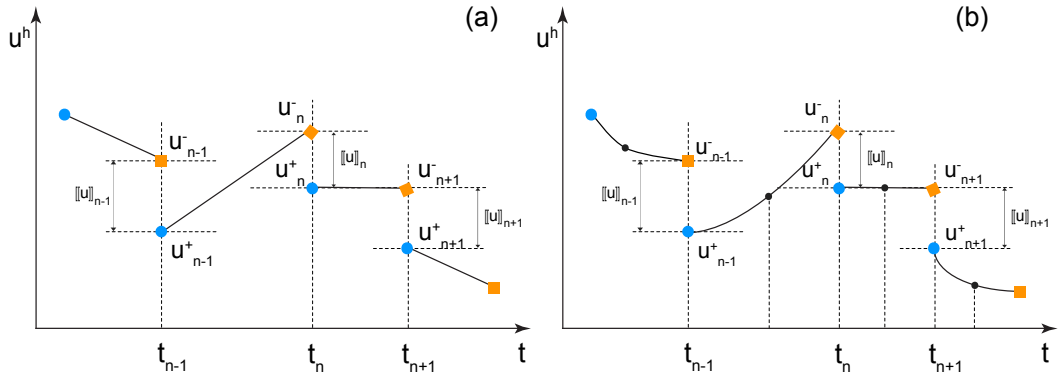

Fig. 2.2.: Schematic diagram of time discontinuous approximation: (a) piecewise linear interpolation, and (b) piecewise quadratic interpolation.

Let $C^0(\star)$ denote the space of piecewise continuous functions defined on domain $(\star)$. In addition, consider $\wp_l\left(I_n\right)$, the collection of all polynomials defined on I_n with a total degree of no more than l. Accordingly, the functional space required for the TDG/FEM is given by,

$$\Im_l^h := \left\{ u^h \middle| \, u^h \in C^0\left(\bigcup_{n=0}^{N-1} I_n\right), u^h\Big|_{I_n} \in \wp_l\left(I_n\right) \right\} \tag{2.5}$$

where, u^h, denotes the global solutions which can be discontinuous at time steps given by the end points of the interval I_n, and $u^h\Big|_{I_n}$ denotes the restriction of u_h to I_n.

2.2.1 Weak forms for the TDG/FEM

For any $\delta u^h, u^h \in \Im_l^h$ consider the following variational form corresponding to Eq. (2.1),

$$\delta\Pi_n := \int_{I_n} \delta u^h \left(\frac{du^h}{dt} + \lambda u^h - f\left(t\right) \right) dt \tag{2.6}$$

or

$$\delta\Pi_n = \int_{I_n} \delta u^h \frac{du^h}{dt} dt + \int_{I_n} \delta u^h \left[\lambda u^h - f\left(t\right) \right] dt \tag{2.7}$$

Here, once again note that the domain of integration is I_n, and u^h is discontinuous at times t_n and t_{n+1}.

Use of the integration by parts for the first term in Eq. (2.7) will result in the following variation form for the TDG/FEM,

$$\delta\Pi_n = -\int_{I_n} u^h \frac{d\delta u^h}{dt} dt + \left[\delta u^h \cdot u^* \right]_{t_n}^{t_{n+1}} + \int_{I_n} \delta u^h \left[\lambda u^h - f\left(t\right) \right] dt \tag{2.8}$$

where, u^* denotes the unique value of u^h to be used at the end-points of the interval I_n and obtained by computing the information from the neighboring time intervals. A detailed definition concerning its concrete value will be soon introduced in the following text.

Subsequent use of the integration by parts for the first term in Eq. (2.8) will yield another variation form for the TDG/FEM. This variation form is described below.

$$\delta\Pi_n = \int_{I_n} \delta u^h \frac{du^h}{dt} dt + \left[\delta u^h \left(u^* - u^h \right) \right]_{t_n}^{t_{n+1}} + \int_{I_n} \delta u^h \left[\lambda u^h - f\left(t\right) \right] dt \tag{2.9}$$

Mathematically, the formulations given in Eq. (2.8) and Eq. (2.9) are the TDG/FEM schemes for Eq. (2.1) in weak and strong form, respectively. In Eq. (2.8) due to the presence of first order time derivative of the test function δu^h, the test function should be continuous in time. In Eq. (2.9), however, the continuity of the test functions is not required since this form does not include the time derivative of δu^h.

In Eq. (2.8) and Eq. (2.9), recall that the solution (u^h) is not well defined at the $\partial I_n = \{t_n, t_{n+1}\}$ as it takes two values at each end-points of I_n. Hence, a unique representative value u^* has been adopted in the TDG formulation which should be specified only at time ∂I_n. The value of u^* at time t_n can be computed by using u_n^+

and u_n^- (see the footnote). [3] The most widely used definition for u^* is based on the upwind flux treatment in time (Eriksson et al., 1985; Chen et al., 2006; Cockburn, 2003; Hesthaven and Warburton, 2007) and given by,

$$u^* := \begin{cases} u_0 & \text{if} \quad n = 0 \\ u_n^- & \text{otherwise} \end{cases} \tag{2.10}$$

The choice of such a definition is inspired by the fact that in a transient problem the solutions at time t_n should be equal to the value of its immediate past $t_n - \varepsilon$. Therefore, it is natural to start the numerical procedure at $t = t_0$ with the prescribed initial condition $u^* = u_0$, and transport this idea to the subsequent time-slabs.

Incorporating the definition of u^* in Eq. (2.9),

$$\delta\Pi_n = \int_{I_n} \delta u^h \frac{du^h}{dt} dt + \delta u^h\left(t_n\right) \left[\!\left[u^h\right]\!\right]_n + \int_{I_n} \delta u^h \left[\lambda u^h - f\left(t\right)\right] dt \tag{2.11}$$

Let us now focus on the TDG/FEM weak form for the initial value problem (see Eq. 2.1). By multiplying the residual of Eq. (2.1) with the test function δu^h and then integrating in the time domain $[0, T]$ following weak form can be obtained.

$$\delta\Pi := \int_I \delta u \left[\frac{du}{dt} + \lambda u - f\left(t\right)\right] dt = \sum_{n=0}^{N-1} \delta\Pi_n = 0 \tag{2.12}$$

Due to the weakly prescribed initial condition, the weak form given above transforms into a local weak form defined on each time slab I_n.

$$\delta\Pi_n = \int_{I_n} \delta u^h \frac{du^h}{dt} dt + \delta u^h\left(t_n\right) \left[\!\left[u^h\right]\!\right]_n + \int_{I_n} \delta u^h \lambda u^h dt - \int_{I_n} \delta u^h f\left(t\right) dt = 0 \tag{2.13}$$

Rearranging the terms in Eq. (2.13) and using the expression for the jump discontinuity in time (see Eq. 2.3),

$$\int_{I_n} \delta u^h \frac{du^h}{dt} dt + \delta u_n u_n^+ + \int_{I_n} \delta u^h \lambda u^h dt = \delta u_n u_n^- + \int_{I_n} \delta u^h f\left(t\right) dt \tag{2.14}$$

in which the first term on right hand side depicts the initial condition for each time-slabs I_n. Here note that the information about u_n^- is already obtained from the computation in the previous time slab I_{n-1}. Further, in the beginning of the process (i.e., $n = 0$) the initial condition is incorporated in the computation according to the

[3] Informally speaking, the purpose of introducing the representative value u^* in TDG/FEM is to facilitate the weak enforcement of the initial condition in the time domain. Further, u^* connects the adjacent time-slabs by transferring the information about the solution from one time-slab to another time-slab. In TDG/FEM, this so-called connection between the time-slabs is weakly enforced which in turn allows the computation to be performed locally in an individual time-slab.

definition in Eq. (2.10). In this way, initial boundary condition becomes the part of the solution and need not to be specified in explicit terms.

2.2.2 Implementation of the TDG/FEM

One dimensional time-finite elements can be employed to discretize the TDG/FEM weak form presented in Eq. (2.11). In this process, the solutions are locally approximated by using the shape functions. These shape functions are generally given by the Lagrange polynomials, and determine the degree of accuracy. To construct a p-order Lagrange polynomial in time-domain, $p+1$ nodes should be selected inside the time slab I_n; two nodes are always located at the end-points t_n and t_{n+1}, and remaining $p-1$ nodes are distributed inside I_n (see Fig. 2.3). The internal nodes are generally located at equidistant points in I_n. [4]

Consider the parent time-domain $I_\theta := [-1, 1]$ on which the Lagrange polynomials $T_i^{(p)}(\theta)$ are defined. Here, p denotes the degree of polynomial, and $i = 1, \cdots, p+1$ corresponds to the $p+1$ locations

$$\{\theta_1, \theta_2, \cdots, \theta_{p+1}\}$$

in I_θ with $\theta_1 = -1$ and $\theta_2 = +1$. Let

$$\left\{t_1^{(n)}, t_2^{(n)}, \cdots, t_p^{(n)}, t_{p+1}^{(n)}\right\}$$

be the set of $p+1$ time-nodes in I_n with $t_1^{(n)} = t_n$, $t_2^{(n)} = t_n + 1$. The internal nodes are represented by $t_i^{(n)} = t_n$ for $i = 3, \cdots, p+1$ (see Fig. 2.3).

Further, the relationship between $t \in I_n$ and $\theta \in I_\theta$ is given by a linear mapping,

$$t(\theta) = \frac{(1-\theta)}{2} t_n + \frac{(1+\theta)}{2} t_{n+1}. \tag{2.15}$$

The expression for the Lagrange polynomial of degree p is described as follows:

$$T_i^{(p)} = \prod_{\substack{j=1 \\ j \neq i}}^{p+1} \frac{\theta - \theta_j}{\theta_i - \theta_j} \tag{2.16}$$

Here, note that

$$T_i^{(p)}(\theta_j) = \begin{cases} 1 & \text{if} \quad i = j \\ 0 & \text{if} \quad i \neq j \end{cases}$$

[4] The internal nodes may be located at specific locations in I_n which are determined from the zeros of the orthonormal polynomials like the Jacobi polynomials. This approach can be used for developing the high-order time accurate spectral finite element schemes Hesthaven and Warburton, 2007, see.

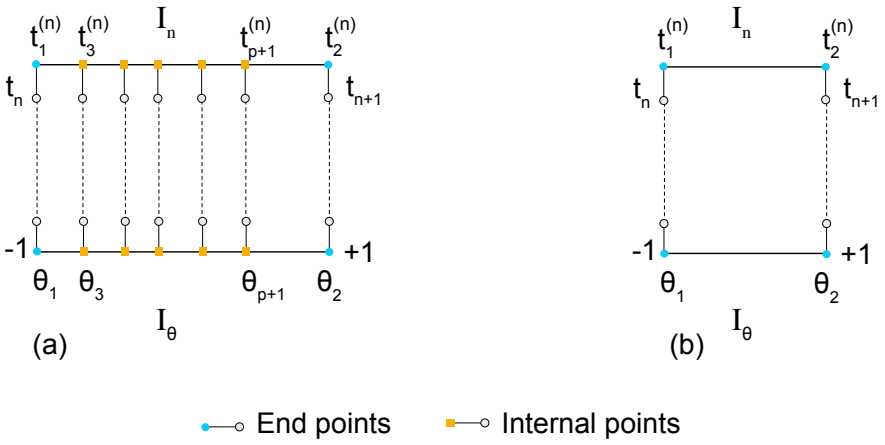

Fig. 2.3.: Conceptual diagram of (a) p-order time-finite element with $p+1$ local time nodes, (b) two node linear time-finite element.

Accordingly, the p-order local approximation for the trial function u^h reads,

$$u^h = T_1^{(p)} u_n^+ + T_2^{(p)} u_{n+1}^- + \sum_{a=3}^{p+1} T_a^{(p)} u_a^{(n)} \tag{2.17}$$

In Eq. (2.17) u_n^+ and u_{n+1}^- represent the discontinuous nodal values at times $t = (t_n + \varepsilon) \in I_n$ and $t = (t_{n+1} - \varepsilon) \in I_n$ (see also Eq. 2.4), respectively. Further, the values of u^h at the internal nodes of I_n are given by $u_a^{(n)}$, for $a = 3, \cdots, p+1$, which are well defined in the time-slab I_n. For the sake of clarity, let us denote,

$$u_1^{(n)} = u_n^+,$$

$$u_2^{(n)} = u_{n+1}^-.$$

With such convention Eq. (2.17) becomes

$$u^h = \sum_{a=1}^{p+1} T_a^{(p)} u_a^{(n)} \tag{2.18}$$

Similarly, the p-order local approximation for the test function δu^h can be given by,

$$\delta u^h = \sum_{a=1}^{p+1} T_a^{(p)} \delta u_a^{(n)} \tag{2.19}$$

Subsequently, using the above interpolations for u^h and δu^h in the weak-form given by Eq. (2.14) one can get the following discretized form. Henceforth, the use of summation symbol is avoided and Einstein summation convention is implied.

$$\delta u_a^{(n)} \left\{ \left[\int_{I_n} T_a^{(p)} \frac{dT_b^{(p)}}{dt} dt \right] u_b^{(n)} + \left[\int_{I_n} T_a^{(p)} \lambda T_b^{(p)} dt \right] u_b^{(n)} - \int_{I_n} T_a^{(p)} f\left(t\right) dt \right\} + \delta u_1^{(n)} \left(u_1^{(n)} - u_n^- \right) = 0 \tag{2.20}$$

Further, using the Kronecker delta function δ_{ab} in the last term of the above equation,

$$\delta u_1^{(n)} \left(u_1^{(n)} - u_n^- \right) = \delta u_a^{(n)} \delta_{a1} \delta_{b1} \left(u_b^{(n)} - u_n^- \right),$$

Accordingly, Eq. (2.20) becomes,

$$\delta u_a^{(n)} \left\{ \left[\int_{I_n} T_a^{(p)} \frac{dT_b^{(p)}}{dt} dt + \delta_{a1}\delta_{b1} + \int_{I_n} T_a^{(p)} \lambda T_b^{(p)} dt \right] u_b^{(n)} - \delta_{a1} u_n^- - \int_{I_n} T_a^{(p)} f\left(t\right) dt \right\} = 0 \tag{2.21}$$

Since Eq. (2.20) is true for all $\delta_a^{(n)}$, one can get the following system of $p+1$ algebraic equations.

$$[m]^{ab} u_b^{(n)} + \lambda [c]^{ab} u_b^{(n)} = \delta_{a1} u_n^- + \{J_{ext}\}^a \tag{2.22}$$

where $[m]^{ab}$ and $[c]^{ab}$ are the $(p+1) \times (p+1)$ finite element matrices, and $\{f\}^a$ is a vector of length $p+1$. The matrix-vector form of above equation is depicted by

$$[\mathbf{m}] \{\tilde{\mathbf{u}}\} + \lambda [\mathbf{c}] \{\tilde{\mathbf{u}}\} = \{\mathbf{e}_1^p\} u_n^- + \{\mathbf{J_{ext}}\} \tag{2.23}$$

The details about the terms present in Eq. (2.21) and Eq. (2.22) are given below.

$$[\mathbf{m}] := [m]^{ab} = \int_{I_n} T_a^{(p)} \frac{dT_b^{(p)}}{dt} dt + \delta_{a1}\delta_{b1} \tag{2.24}$$

$$[\mathbf{c}] := [c]^{ab} = \int_{I_n} T_a^{(p)} T_b^{(p)} dt \tag{2.25}$$

$$\{\mathbf{e}_1^p\} := \delta_{a1} = \{1, 0, \cdots, 0\} \tag{2.26}$$

$$\{\mathbf{J_{ext}}\} := \{J_{ext}\}^a = \int_{I_n} T_a^{(p)} f\left(t\right) dt \tag{2.27}$$

In this way, at the beginning of the computation (i.e., n=0) the initial condition u_0 is used to compute the right hand side of Eq. (2.23), and then the system of linear

equations is solved to obtain u_1^-. This information is then used for constructing the right hand side for the next time slab.

In the subsequent sections, the numerical analysis of the TDG/FEM for the first order ODE is discussed. Henceforth, for the sake of simplicity, only the case of linear interpolation in time (i.e., $p = 1$) is discussed.

In case of the linear interpolation in time the shape functions are given by

$$T_1(\theta) := T_1^{(1)} = \frac{1-\theta}{2} \qquad T_2(\theta) := T_2^{(1)} = \frac{1+\theta}{2}. \tag{2.28}$$

In this case, two linear equations in two unknowns u_n^+ and u_{n+1}^- can be obtained. These equations are described below in the matrix-vector form.

$$\frac{1}{2}\begin{bmatrix} 1 & 1 \\ -1 & 1 \end{bmatrix}\begin{Bmatrix} u_n^+ \\ u_{n+1}^- \end{Bmatrix} + \lambda\frac{\Delta t_n}{6}\begin{bmatrix} 2 & 1 \\ 1 & 2 \end{bmatrix}\begin{Bmatrix} u_n^+ \\ u_{n+1}^- \end{Bmatrix} = \begin{Bmatrix} u_n^- \\ 0 \end{Bmatrix} + \begin{Bmatrix} J_{ext}^1 \\ J_{ext}^2 \end{Bmatrix} \tag{2.29}$$

where J_{ext}^1 and J_{ext}^2 are given by

$$J_{ext}^1 = \int_{I_n} T_1 f\,(t)\,dt$$
$$J_{ext}^2 = \int_{I_n} T_2 f\,(t)\,dt$$

2.2.3 Stability analysis of the TDG/FEM

Let us denote the exact value of the solution at any instant t_n by $u(t_n)$ and the corresponding numerical value obtained by TDG/FEM by u_n^-. Let the error in u_n^- be denoted by:

$$e(t_n) := u_n^- - u(t_n) \tag{2.30}$$

To motivate the appropriate notion of stability for the ease under consideration, let us investigate the behavior of the homogeneous form of Eq. (2.1).[5] The exact solutions of the homogeneous ODE is given by (Hughes, 2012, Chapter 8)

$$u\,(t_n) = u_0 \mathrm{e}^{-\lambda t_n} \tag{2.31}$$

[5] Homogeneous form of Eq. (2.1) is obtained by setting $f = 0$, i.e.,

$$\frac{du}{dt} + \lambda u = 0 \quad t \in [0, T]\,, u(0) = u_0$$

At time $t = t_{n+1}$ the exact solutions can be described as,

$$u\left(t_{n+1}\right) = u\left(t_n\right) \mathrm{e}^{-\lambda \Delta t_n} \tag{2.32}$$

In Eq. (2.32) one should note that the exact solutions decay in time for $\lambda > 0$, and mathematically the solutions can be characterized by:

$$\left.\begin{array}{ll} \left|u\left(t_{n+1}\right)\right| < \left|u\left(t_n\right)\right|, & \lambda > 0 \\ u\left(t_{n+1}\right) = u\left(t_n\right), & \lambda = 0 \end{array}\right\} \tag{2.33}$$

In homogeneous case Eq. (2.29) becomes

$$\frac{1}{2}\begin{bmatrix} 1 & 1 \\ -1 & 1 \end{bmatrix}\begin{Bmatrix} u_n^+ \\ u_{n+1}^- \end{Bmatrix} + \lambda\frac{\Delta t_n}{6}\begin{bmatrix} 2 & 1 \\ 1 & 2 \end{bmatrix}\begin{Bmatrix} u_n^+ \\ u_{n+1}^- \end{Bmatrix} = \begin{Bmatrix} u_n^- \\ 0 \end{Bmatrix} \tag{2.34}$$

By eliminating u_n^+ from above equations we can get

$$u_{n+1}^- = A u_n^- \tag{2.35}$$

where,

$$A = \frac{6 - 2\Omega}{\Omega^2 + 4\Omega + 6} \tag{2.36}$$

is called the *amplification factor*, and $\Omega = \lambda \Delta t_n$.

For the stability of the TDG/FEM it is necessary that

$$\left.\begin{array}{ll} \left|u_{n+1}^-\right| < \left|u_n^-\right|, & \lambda > 0 \\ u_{n+1}^- = u_n^-, & \lambda = 0 \end{array}\right\} \tag{2.37}$$

From the definition of A (see Eq. 2.36), second condition of Eq. (2.37) is satisfied. The first condition is always satisfied if amplification factor satisfies the following,

$$|A| < 1 \tag{2.38}$$

Fig. 2.4 plots the variation of amplification factor with the dimensionless time $\Omega = \lambda \Delta t_n$, where it is evident that the TDG/FEM algorithm always satisfies the above-mentioned condition (cf. Eq. 2.38). Thus, it is proved that the TDG/FEM is an *unconditionally stable* algorithm.

2.2.4 Convergence analysis of the TDG/FEM

TDG/FEM algorithm will be called convergent if for t_n fixed, $u_n^- \to u(t_n)$ as $\Delta t \to 0$. To establish the convergence of an algorithm, two additional notion must be

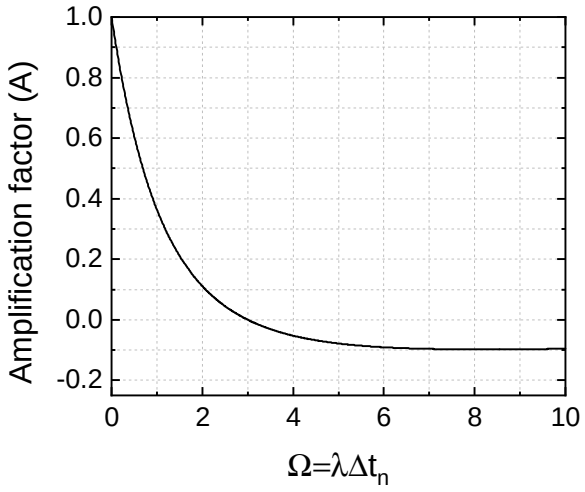

Fig. 2.4.: Amplification factor for the time-discontinuous Galerkin method for the first order ODE with linear interpolation in time.

considered: *stability* and *consistency*. In the previous section it has been shown that the TDG/FEM algorithm is unconditionally stable. Therefore, in this section, the consistency of the algorithm will be proven.

Rewriting the temporally discrete model problem described by Eq. (2.35) in the form,

$$u_{n+1}^{-} - Au_n^{-} = 0 \tag{2.39}$$

Replacing u_n^- and u_{n+1}^- with the exact values $u(t_n)$ and $u(t_{n+1})$, respectively, following expression is obtained

$$u(t_{n+1}) - Au(t_n) = \Delta t_n \cdot \tau(t_n) \tag{2.40}$$

where $\tau(t_n)$ is called the *local truncation error*.

Definition. The algorithm defined by Eq. (2.39) is called *consistent* if $|\tau(t)| \leqslant c\Delta t^k$, for all $t \in [0, T]$, where c is a constant independent of Δt, and $k > 0$. Moreover, k is called the *order of accuracy* or *rate of convergence*.

To show that TDG/FEM algorithm is consistent use Taylor expansion for $u(t_{n+1})$ about t_n,

$$u\left(t_{n+1}\right) = u\left(t_n\right) + \Delta t_n \frac{du_n}{dt} + \frac{\Delta t_n^2}{2}\frac{d^2u_n}{dt^2} + \frac{\Delta t_n^3}{6}\frac{d^3u_n}{dt^3} + O\left(\Delta t^2\right) \tag{2.41}$$

using the homogeneous form of model equation to eliminate the time derivatives in above equation one can get,

$$u\left(t_{n+1}\right) = \left(1 - \Omega + \frac{\Omega^2}{2} - \frac{\Omega^3}{6}\right) u\left(t_n\right) + O\left(\Delta t^2\right) \tag{2.42}$$

From Eq. (2.36, 2.40, and 2.42) it follows that,

$$|\tau(t)| \leqslant \frac{1}{36}\Delta t_n^3 \qquad \forall t \in [0, T] \tag{2.43}$$

This completes the proof that TDG/FEM algorithm is consistent.

Remark 2.2.1. Therefore, the TDG/FEM algorithm is consistent and unconditionally stable which also proves the convergence of the algorithm according to the Lax equivalence theorem. [6]

Remark 2.2.2. The TDG/FEM is a third order accurate algorithm for the linear interpolation in time. Moreover, the scheme can be classified as a single-step algorithm.

2.3 TDG/FEM for the second order ODE

Consider a mass-spring-dashpot system as depicted in Fig. 2.5. The governing equation of motion is described by the following second order initial value problem in time.

$$\begin{aligned} \frac{d^2u}{dt^2} + 2\zeta\omega_n\frac{du}{dt} + \omega_n^2 u = f\,(t) \quad \forall t \in [0, T] \\ u(0) = u_0 \\ \frac{du(0)}{dt} = v_0 \end{aligned} \tag{2.44}$$

where $u := u(t)$ is the unknown displacement, $f(t)$ is the external force acting on the system. Further, u_0 and v_0 are the prescribed initial values of the displacement and velocity, respectively. Damping ratio ζ and the natural frequency of vibration ω_n of the system are related to the mass m, stiffness of the spring k, and damping coefficient c by:

$$\omega_n = \sqrt{k/m}, \qquad \zeta = \frac{c}{2m\omega_n} = \frac{c}{2\sqrt{mk}} \tag{2.45}$$

Further, the TDG/FEM for solving the second order ODE can be arranged into two categories; the displacement-velocity based two-field TDG/FEM, and the single-field TDG/FEM. These strategies are discussed in the following sections.

[6] Lax equivalence theorem may be stated as *consistency and stability of an algorithm are the necessary and sufficient conditions for the convergence of an algorithm.*

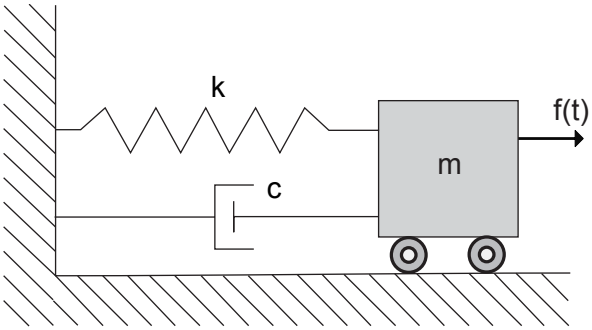

Fig. 2.5.: Schematic diagram of the mass-spring-dashpot system

2.3.1 Two-field TDG/FEM

In the two-field TDG/FEM, both the displacement (u) and the velocity (v) are independently interpolated using the piecewise polynomials. [7] The interpolation is performed such that within a time-slab I_n the solutions remain continuous, and at the end-points (i.e., t_n and t_{n+1}) the solutions are discontinuous. Accordingly, the set $\{t_1, t_2, \cdots, t_N\}$ denotes the locations in time where discontinuity in solutions occur. Thus, the displacement and velocity are the primary unknowns in the uv-TDG/FEM.

Therefore, the critical step in solving the second order initial value problem using the uv-TDG/FEM involves recasting of Eq. (2.44) into a system of two first-order ODEs. The new system is then described by

$$\frac{dv}{dt} + 2\zeta\omega_n v + \omega_n^2 u = f(t) \quad \forall t \in [0, T] \tag{2.46}$$

$$\frac{du}{dt} - v = 0 \quad \forall t \in [0, T] \tag{2.47}$$

$$u(0) = u_0, \quad v(0) = v_0 \tag{2.48}$$

Eq. (2.46) and Eq. (2.47) represent the first order ODE, and the TDG/FEM described in the previous section can be employed directly. However, note that these two equations cannot be solved independently due to the coupling between displacement and velocity.

Following the same procedure as described in the previous section (see Eq. 2.6–2.14), the weak-form of the uv-TDG/FEM can be stated as:

[7] Henceforth uv-TDG/FEM will be used to denote the two-field TDG/FEM

Weak-form. *Find* $u^h \in \Im_l^h$ *and* $v^h \in \Im_l^h$*, such that for all* $\delta u^h \in \Im_l^h$ *and* $\delta v^h \in \Im_l^h$*, and for all* $n = 0, \cdots, N-1$ *Eq.* (2.49) *holds.*

$$\begin{aligned} &\int_{I_n} \delta v^h \left(\frac{dv^h}{dt} + 2\zeta\omega_n v^h + \omega_n^2 u^h - f(t) \right) dt + \delta v^h(t_n) \left[\!\left[v^h \right]\!\right]_n \\ &+ \int_{I_n} \delta u^h \left(\frac{du^h}{dt} - v^h \right) dt + \delta u^h(t_n) \left[\!\left[u^h \right]\!\right]_n = 0 \end{aligned} \tag{2.49}$$

A careful examination of uv-TDG/FEM weak-form leads to the following remarks.

Remark 2.3.1. In the above weak-form, the presence of jump discontinuity in time for the displacement, $\left[\!\left[u^h \right]\!\right]_n$, and for the velocity, $\left[\!\left[v^h \right]\!\right]_n$, correspond to the weakly enforced initial condition for the displacement and velocity, respectively.

Remark 2.3.2. Since the selection of the test functions, δu^h and δv^h, are independent from each other Eq. (2.49) can be depicted by the combination of following two variational forms.

$$\int_{I_n} \delta v^h \left(\frac{dv^h}{dt} + 2\zeta\omega_n v^h + \omega_n^2 u^h - f(t) \right) dt + \delta v^h(t_n) \left[\!\left[v^h \right]\!\right]_n = 0 \tag{2.50}$$

$$\int_{I_n} \delta u^h \left(\frac{du^h}{dt} - v^h \right) dt + \delta u^h(t_n) \left[\!\left[u^h \right]\!\right]_n = 0 \tag{2.51}$$

From Eq. (2.51) it follows that in two-field TDG/FEM, the displacement-velocity compatibility relationship is satisfied in weak form.

Remark 2.3.3. It is of course possible to use the different order interpolation for the displacement and velocity in the above weak-form. Only equal order interpolations, however, yield useful and efficient algorithms (Hulbert, 1992).

Let us now focus on the discretization of the two-field TDG weak-form. The discretization will be performed by using the locally defined p-order test and trial functions of the form,

$$u^h = \sum_{a=1}^{p+1} T_a^{(p)} u_a^{(n)}, \qquad \delta u^h = \sum_{a=1}^{p+1} T_a^{(p)} \delta u_a^{(n)}, \qquad \forall t \in I_n \tag{2.52}$$

$$v^h = \sum_{a=1}^{p+1} T_a^{(p)} v_a^{(n)}, \qquad \delta v^h = \sum_{a=1}^{p+1} T_a^{(p)} \delta v_a^{(n)}, \qquad \forall t \in I_n \tag{2.53}$$

where $T_a^{(p)}$ are the p-order Lagrange polynomials, and given by Eq. (2.16). Besides, in above equation, following conventions have been used.

$$u_1^{(n)} = u_n^+, \qquad u_2^{(n)} = u_{n+1}^-, \qquad v_1^{(n)} = v_n^+, \qquad v_2^{(n)} = v_{n+1}^-$$

where (u_n^+, u_{n+1}^-) and (v_n^+, v_{n+1}^-) denote the discontinuous values of the displacement and velocity, respectively (cf. Eq. 2.4).

Subsequently, using the test functions and trial function in the weak-form (Eq. 2.49) to obtain the following discretized form.

$$\begin{aligned}
&\delta v_a^{(n)} \left[\int_{I_n} T_a^{(p)} \left(\frac{dT_b^{(p)}}{dt} \right) dt + \delta_{1a}\delta_{1b} \right] v_b^{(n)} + \delta v_a^{(n)} \left[2\zeta\omega_n \int_{I_n} T_a^{(p)} T_b^{(p)} dt \right] v_b^{(n)} \\
&+ \delta v_a^{(n)} \left[\omega_n^2 \int_{I_n} T_a^{(p)} T_b^{(p)} dt \right] u_b^{(n)} - \delta v_a^{(n)} \left\{ \int_{I_n} T_a^{(p)} f(t) dt \right\} - \delta v_a^{(n)} \left\{ \delta_{1a} v_n^- \right\} \\
&\delta u_a^{(n)} \left[\int_{I_n} T_a^{(p)} \frac{dT_b^{(p)}}{dt} dt + \delta_{1a}\delta_{1b} \right] u_b^{(n)} \\
&- \delta u_a^{(n)} \left[\int_{I_n} T_a^{(p)} T_b^{(p)} dt \right] v_b^{(n)} - \delta u_a^{(n)} \left\{ \delta_{1a} u_n^- \right\} = 0
\end{aligned} \tag{2.54}$$

Since Eq. (2.54) is true for all $\delta u_a^{(n)}$ and $\delta v_a^{(n)}$, one can get the following system of $2p+2$ number of algebraic equations.

$$[m]^{ab} v_b^{(n)} + 2\zeta\omega_n [c]^{ab} v_b^{(n)} + \omega_n^2 [c]^{ab} u_b^{(n)} = \{J_{ext}\}^a + \{J_0^v\}^a \tag{2.55}$$

$$[m]^{ab} u_b^{(n)} - [c]^{ab} v_b^{(n)} = \{J_0^u\}^a \tag{2.56}$$

The matrix-vector form of Eq. (2.55) and Eq. (2.56) is given by Eq. (2.57) and Eq. (2.58), respectively.

$$[\mathbf{m}] \{\tilde{\mathbf{v}}\} + 2\zeta\omega_n [\mathbf{c}] \{\tilde{\mathbf{v}}\} + \omega_n^2 [\mathbf{c}] \{\tilde{\mathbf{u}}\} = \{\mathbf{J}_{ext}\} + \{\mathbf{J}_0^v\} \tag{2.57}$$

$$[\mathbf{m}] \{\tilde{\mathbf{u}}\} - [\mathbf{c}] \{\tilde{\mathbf{v}}\} = \{\mathbf{J}_0^u\} \tag{2.58}$$

In Eqs. (2.55–2.58), the matrices $[\mathbf{m}]$, $[\mathbf{c}]$, and the vector $\{\mathbf{J}_{ext}\}$ are given by Eq. (2.24), Eq. (2.25), and Eq. (2.27), respectively. The vectors, $\{\mathbf{J}_0^v\}$ (see Eq. 2.59)

and $\{\mathbf{J}_0^u\}$ (see Eq. 2.60) correspond to the initial value of the velocity (v_n^-) and displacement (u_n^-), respectively.

$$\{\mathbf{J}_0^v\} := \{J_0^v\}^a = \delta_{1a} v_n^- \tag{2.59}$$

$$\{\mathbf{J}_0^u\} := \{J_0^u\}^a = \delta_{1a} u_n^- \tag{2.60}$$

Remark 2.3.4. In any time-slab I_n, there are $p+1$ unknowns for the velocity and $p+1$ unknowns for the displacement. Consequently, there are total $2p+2$ unknowns to be determined in each time-slab. These unknowns are computed by solving the system of $2p+2$ equations formed by Eq. (2.57) and Eq. (2.58). Besides, in Eq. (2.57–2.58), the shape of all matrices and all vectors are $(p+1)\times(p+1)$ and $(p+1)\times(1)$.

If the displacement and the velocity are linearly interpolated in time (i.e., $p=1$) using the shape function described by Eq. (2.28) then Eq. (2.57) and Eq. (2.58) becomes

$$\begin{aligned} &\frac{1}{2}\begin{bmatrix} 1 & 1 \\ -1 & 1 \end{bmatrix}\begin{Bmatrix} v_n^+ \\ v_{n+1}^- \end{Bmatrix} + \zeta\omega_n \frac{\Delta t}{3}\begin{bmatrix} 2 & 1 \\ 1 & 2 \end{bmatrix}\begin{Bmatrix} v_n^+ \\ v_{n+1}^- \end{Bmatrix} \\ &+\omega_n^2 \frac{\Delta t}{6}\begin{bmatrix} 2 & 1 \\ 1 & 2 \end{bmatrix}\begin{Bmatrix} u_n^+ \\ u_{n+1}^- \end{Bmatrix} = \begin{Bmatrix} v_n^- \\ 0 \end{Bmatrix} + \begin{Bmatrix} J_{ext}^1 \\ J_{ext}^2 \end{Bmatrix} \end{aligned} \tag{2.61}$$

$$\frac{1}{2}\begin{bmatrix} 1 & 1 \\ -1 & 1 \end{bmatrix}\begin{Bmatrix} u_n^+ \\ u_{n+1}^- \end{Bmatrix} - \frac{\Delta t_n}{6}\begin{bmatrix} 2 & 1 \\ 1 & 2 \end{bmatrix}\begin{Bmatrix} v_n^+ \\ v_{n+1}^- \end{Bmatrix} = \begin{Bmatrix} u_n^- \\ 0 \end{Bmatrix} \tag{2.62}$$

In Eq. (2.61), the expressions for J_{ext}^1 and J_{ext}^2 are identical to those given in Eq. (2.29).

2.3.2 Displacement based single-field TDG/FEM

In the displacement based single-field TDG/FEM (u-TDG/FEM) only displacement is interpolated using the piecewise polynomials. The displacement remains continuous within a time-slab I_n. However, at the end-points (i.e., t_n and t_{n+1}) displacement takes two different values, for example, u_n^+ and u_n^- at t_n. In addition, the velocity is obtained by taking the time derivative of the displacement. Thus, the velocity-displacement compatibility relationship is naturally satisfied, and Eq. (2.47) is no longer required to be solved. However, note that both displacement and velocity still remain discontinuous in time.

The weak form of the displacement based single-field TDG/FEM, which is described below (see Eq. 2.63), is obtained by considering the second order ODE (cf. Eq. 2.44).

Weak-form. *u-TDG/FEM: Find* $u^h \in \Im_l^h$ *such that for all* $\delta u^h \in \Im_l^h$*, and for all* $n = 0, \cdots, N-1$ *Eq.* (2.63) *holds.*

$$\begin{aligned}\int_{I_n} \frac{d\delta u^h}{dt}\left(\frac{d^2u^h}{dt^2} + 2\zeta\omega_n\frac{du^h}{dt} + \omega_n^2 u^h - f(t)\right)dt \\ + \frac{d\delta u^h(t_n)}{dt}\left[\!\left[\frac{du^h}{dt}\right]\!\right]_n + \delta u^h(t_n)\omega_n^2\left[\!\left[u^h\right]\!\right]_n = 0\end{aligned} \tag{2.63}$$

The above weak form is obtained by using the following intermediate results

$$\int_{I_n} \frac{d\delta u^h}{dt}\frac{d^2u^h}{dt^2}dt = \int_{I_n} \frac{d\delta u^h}{dt}\frac{d^2u^h}{dt^2}dt + \left[\frac{d\delta u^h}{dt}\left(\left(\frac{du}{dt}\right)^* - \frac{du^h}{dt}\right)\right]_{t_n}^{t_{n+1}} \tag{2.64}$$

$$\int_{I_n} \frac{d\delta u^h}{dt}\omega_n^2 u^h dt = \int_{I_n} \frac{d\delta u^h}{dt}\omega_n^2 u^h dt + \left[\delta u^h\omega_n^2\left(u^* - u^h\right)\right]_{t_n}^{t_{n+1}} \tag{2.65}$$

These intermediate results are obtained by following the procedure described in Eq. (2.7–2.9). Further, in above equations, u^* and $\left(\frac{du}{dt}\right)^*$ denote the unique representative value of displacement and its first time derivative at the end points of I_n (here, recall that at t_n and t_{n+1} both displacement and its first time derivative are discontinuous). Furthermore, by adopting the definition of representative values, which is provided in Eq. (2.10), Eq. (2.64) and Eq. (2.65) transform into

$$\int_{I_n} \frac{d\delta u^h}{dt}\frac{d^2u^h}{dt^2}dt = \int_{I_n} \frac{d\delta u^h}{dt}\frac{d^2u^h}{dt^2}dt + \frac{d\delta u^h\left(t_n\right)}{dt}\left[\!\left[\frac{du^h}{dt}\right]\!\right]_n \tag{2.66}$$

$$\int_{I_n} \frac{d\delta u^h}{dt}\omega_n^2 u^h dt = \int_{I_n} \frac{d\delta u^h}{dt}\omega_n^2 u^h dt + \delta u^h(t_n)\omega_n^2\left[\!\left[u^h\right]\!\right]_n \tag{2.67}$$

Let us now focus on the discretization of the u-TDG/FEM weak-form given in Eq. (2.63). Here, for the sake of clarity, the discretization will be performed by using the locally defined quadratic test and trial functions of the form

$$u^h = u_1^{(n)}T_1 + u_2^{(n)}T_2 + u_3^{(n)}T_3, \qquad \delta u^h = \delta u_1^{(n)}T_1 + \delta u_2^{(n)}T_2 + \delta u_3^{(n)}T_3 \tag{2.68}$$

where, T_1, T_2, and T_3 are the quadratic shape functions described as follows.

$$T_1 = \frac{1}{2}\left(\theta^2 - \theta\right), \qquad T_2 = \frac{1}{2}\left(\theta^2 + \theta\right), \qquad T_3 = 1 - \theta^2 \tag{2.69}$$

In this case, the time derivatives of the test function and trial functions are given by following expressions.

$$\frac{du^h}{dt} = \frac{2}{\Delta t_n}\left\{\frac{1}{2}\left(2\theta-1\right)u_1^{(n)} + \frac{1}{2}\left(2\theta+1\right)u_2^{(n)} - 2\theta u_3^{(n)}\right\} \tag{2.70}$$

$$\frac{d^2u^h}{dt^2} = \frac{4}{\Delta t_n^2}\left\{u_1^{(n)} + u_2^{(n)} - 2u_3^{(n)}\right\} \tag{2.71}$$

$$\frac{d\delta u^h}{dt} = \frac{2}{\Delta t_n}\left\{\frac{1}{2}\left(2\theta-1\right)\delta u_1^{(n)} + \frac{1}{2}\left(2\theta+1\right)\delta u_2^{(n)} - 2\theta\delta u_3^{(n)}\right\} \tag{2.72}$$

$$\frac{du^h\left(t_n\right)}{dt} = \frac{2}{\Delta t_n}\left\{-\frac{3}{2}u_1^{(n)} - \frac{1}{2}u_2^{(n)} + 2u_3^{(n)}\right\} \tag{2.73}$$

$$\frac{d\delta u^h\left(t_n\right)}{dt} = \frac{2}{\Delta t_n}\left\{-\frac{3}{2}\delta u_1^{(n)} - \frac{1}{2}\delta u_2^{(n)} + 2\delta u_3^{(n)}\right\} \tag{2.74}$$

Subsequently, using the above expressions in the u-TDG/FEM weak-form following system of linear equation can be obtained.

$$\begin{aligned}
&\frac{1}{\Delta t_n^2}\begin{bmatrix} 5 & -1 & -4 \\ 7 & 5 & -12 \\ -12 & -4 & 16 \end{bmatrix}\begin{Bmatrix} u_1^{(n)} \\ u_2^{(n)} \\ u_3^{(n)} \end{Bmatrix} + \frac{2\zeta\omega_n}{3\Delta t_n}\begin{bmatrix} 7 & 1 & -8 \\ 1 & 7 & -8 \\ -8 & -8 & 16 \end{bmatrix}\begin{Bmatrix} u_1^{(n)} \\ u_2^{(n)} \\ u_3^{(n)} \end{Bmatrix} \\
&+\frac{\omega_n^2}{6}\begin{bmatrix} 3 & 1 & -4 \\ -1 & 3 & 4 \\ 4 & -4 & 0 \end{bmatrix}\begin{Bmatrix} u_1^{(n)} \\ u_2^{(n)} \\ u_3^{(n)} \end{Bmatrix} = \frac{1}{\Delta t_n}\begin{Bmatrix} -3v_n^- \\ -v_n^- \\ 4v_n^- \end{Bmatrix} + \begin{Bmatrix} \omega_n^2 u_n^- \\ 0 \\ 0 \end{Bmatrix} + \begin{Bmatrix} J_{ext}^1 \\ J_{ext}^2 \\ J_{ext}^3 \end{Bmatrix}
\end{aligned} \tag{2.75}$$

where $u_1^{(n)} := u_n^+$, $u_2^{(n)} := u_{n+1}^-$, and

$$\begin{aligned}
J_{ext}^1 &= \int_{-1}^{+1}\left(\frac{2\theta-1}{2}\right)f(t)d\theta \\
J_{ext}^2 &= \int_{-1}^{+1}\left(\frac{2\theta+1}{2}\right)f(t)d\theta \\
J_{ext}^3 &= \int_{-1}^{+1}\left(-2\theta\right)f(t)d\theta
\end{aligned} \tag{2.76}$$

Remark 2.3.5. In the case of u-TDG/FEM, the order of interpolation for the displacement should be at-least two (i.e., $p = 2$). This requirement is due to the presence of second order time derivative in the weak-form (see Eq. 2.63).

Remark 2.3.6. In case of quadratic interpolation, there are total three unknowns, $u_a^{(n)}$ for $a = 1, 2, 3$, to be determined in each time-slab I_n. Besides, the number of unknowns in case of the u-TDG/FEM is less than that of uv-TDG/FEM.

2.3.3 Velocity based single-field TDG/FEM

From the displacement based single-field TDG/FEM it follows that the number of unknowns may be decreased by explicitly satisfying the displacement-velocity compatibility condition (cf. Eq. 2.47). In the u-TDG/FEM, however, the requirement of at-least quadratic time interpolation of the displacement implies that minimum three unknowns should be determined for each time-slab I_n. One of the objectives of this thesis is to further decrease the number of unknowns in a given time-slab. To achieve this goal a velocity based single-field TDG/FEM (henceforth, v-TDG/FEM) is developed.

The key idea behind the v-TDG/FEM is to treat the velocity as the only primary unknown. In I_n, the velocity is interpolated using the Lagrange polynomials of degree p; the velocity remains continuous in I_n, but discontinuity occurs at the end-points t_n, t_{n+1}. Further, a consistent time-integration of the velocity is performed as post-processing step to compute the displacement. Thus, the displacement-velocity compatibility relationship is naturally satisfied, and Eq. (2.47) is no longer required to be solved. Regarding the v-TDG/FEM, it is worth mentioning that the displacement remains continuous throughout the time domain $[0, T]$, whereas in the uv-TDG/FEM and u-TDG/FEM displacement is discontinuous at the discrete times $\{t_0, t_1, \cdots, t_N\}$.

The weak form of the v-TDG/FEM, which is described below (see Eq. 2.77), is obtained by considering the first order ODE given by Eq. (2.46).

Weak-form. *Find* $v^h \in \Im_l^h$ *such that for all* $\delta v^h \in \Im_l^h$*, and for all* $n = 0, \cdots, N-1$ *Eq.* (2.77) *holds.*

$$\int_{I_n} \delta v^h \left(\frac{dv^h}{dt} + 2\zeta\omega_n v^h + \omega_n^2 u^h - f(t) \right) dt + \delta v^h(t_n) \left[\!\left[v^h \right]\!\right]_n = 0 \tag{2.77}$$

In the above weak-form displacement is computed by using the following relationship.

$$u^h(t) = u(t_n) + \int_{t_n}^{t} v^h(\tau) d\tau \tag{2.78}$$

Similar to the previous sections, discretization of the v-TDG/FEM weak-form can be performed by employing the locally defined p-order test and trial functions for the velocity.

$$v^h = \sum_{a=1}^{p+1} T_a^{(p)} v_a^{(n)} \qquad\qquad \delta v^h = \sum_{a=1}^{p+1} T_a^{(p)} \delta v_a^{(n)} \tag{2.79}$$

where $T_a^{(p)}$ are the p-order Lagrange polynomials (see Eq. 2.16), and $v_1^{(n)} = v_n^+$, $v_2^{(n)} = v_{n+1}^-$.

Consequently, the discrete form of the displacement-velocity compatibility relationship, which is described below, can be obtained by using the above-mentioned trial functions for the velocity in the Eq. (2.78).

$$u^h(t) = u^h(t_n) + \sum_{a=1}^{p+1} \tilde{T}_a^{(p)} v_a^{(n)} \tag{2.80}$$

where

$$\tilde{T}_a^{(p)} = \frac{\Delta t_n}{2} \int_{-1}^{+1} T_a^{(p)} d\theta \tag{2.81}$$

are $p+1$ order locally defined polynomials.

Remark 2.3.7. In Eq. (2.80), by the virtue of time integration of the p-order Lagrange polynomials, the displacement are described by the $p+1$-order local piecewise polynomials. In addition, Eq. (2.80) is equivalent to the following form.

$$u^h(t) = \sum_{a=1}^{p+2} T_a^{(p+1)} u_a^{(n)} \tag{2.82}$$

where $T_a^{(p+1)}$ are the $p+1$ order Lagrange polynomials given by Eq. (2.16). Besides, $u_1^{(n)} = u_n$ and $u_2^{(n)} = u_{n+1}$ are the continuous value of the displacement at time t_n and t_{n+1}, respectively.

After using Eq. (2.79) and Eq. (2.80) in the v-TDG/FEM weak-form described by Eq. (2.77) one can obtain the following discrete form.

$$\begin{aligned} \delta v_a^{(n)} \left[\int_{I_n} T_a^{(p)} \frac{dT_b^{(p)}}{dt} dt + \delta_{1a}\delta_{1b} \right] v_b^{(n)} + \delta v_a^{(n)} \left[2\zeta\omega_n \int_{I_n} T_a^{(p)} T_b^{(p)} dt \right] v_b^{(n)} \\ + \delta v_a^{(n)} \left[\omega_n^2 \int_{I_n} T_a^{(p)} \tilde{T}_b^{(p)} dt \right] v_b^{(n)} + \delta v_a^{(n)} \left\{ \int_{I_n} T_a^{(p)} dt \right\} \omega_n^2 u_n \\ - \delta v_a^{(n)} \left\{ \int_{I_n} T_a^{(p)} f(t) dt \right\} - \delta v_a^{(n)} \left\{ \delta_{1a} v_n^- \right\} = 0 \end{aligned} \tag{2.83}$$

Subsequently, using the fact that Eq. (2.83) is true for all $\delta v_a^{(n)}$ following system $p+1$ algebraic equations in $p+1$ unknowns can be obtained.

$$[m]^{ab} v_b^{(n)} + 2\zeta\omega_n [c]^{ab} v_b^{(n)} + \omega_n^2 [k]^{ab} v_b^{(n)} = \{J_{ext}\}^a - \{J_0^u\}^a + \{J_0^v\}^a \tag{2.84}$$

The matrix-vector form of above equation is described by

$$[\mathbf{m}]\{\tilde{\mathbf{v}}\} + 2\zeta\omega_n [\mathbf{c}]\{\tilde{\mathbf{v}}\} + \omega_n^2 [\mathbf{k}]\{\tilde{\mathbf{v}}\} = \{\mathbf{J}_{ext}\} - \{\mathbf{J}_0^u\} + \{\mathbf{J}_0^v\} \tag{2.85}$$

where the matrices $[\mathbf{m}]$, $[\mathbf{c}]$, and the vector $\{\mathbf{J}_{ext}\}$ are given by Eq. (2.24), Eq. (2.25), and Eq. (2.27), respectively. The expression for the $[\mathbf{k}]$ matrix is given below.

$$[\mathbf{k}] := [k]^{ab} = \int_{I_n} T_a^{(p)} \tilde{T}_b^{(p)} dt \tag{2.86}$$

Furthermore, in Eq. (2.85), the element vectors, $\{\mathbf{J}_0^v\}$ and $\{\mathbf{J}_0^u\}$ correspond to the initial value of velocity (v_n^-) and displacement (u_n), respectively. The expressions for these vectors are presented as follows.

$$\{\mathbf{J}_0^v\} := \{J_0^v\}^a = \delta_{1a} v_n^- \tag{2.87}$$

$$\{\mathbf{J}_0^u\} := \{J_0^u\}^a = \omega_n^2 u_n \int_{I_n} T_a^{(p)} dt \tag{2.88}$$

Let us now consider the special case when velocity is linearly interpolated in time by using the trial functions of the form

$$v^h(t) = T_1 v_n^+ + T_2 v_{n+1}^- \tag{2.89}$$

where T_1 and T_2 are linear shape functions which are given in Eq. (2.28). Accordingly, Eq. (2.80) transforms into

$$u^h(t) = u_n + v_n^+ \tilde{T}_1 + v_{n+1}^- \tilde{T}_2 \tag{2.90}$$

in which,

$$\tilde{T}_1 = \frac{\Delta t_n}{2}(1 - T_1^2), \qquad \tilde{T}_2 = \frac{\Delta t_n}{2} T_2^2 \tag{2.91}$$

are the quadratic polynomials. Accordingly, Eq. (2.85) now reads,

$$\begin{aligned}&\frac{1}{2}\begin{bmatrix}1 & 1\\ -1 & 1\end{bmatrix}\begin{Bmatrix}v_n^-\\ v_{n+1}^+\end{Bmatrix}+\frac{2\zeta\omega_n\Delta t_n}{6}\begin{bmatrix}2 & 1\\ 1 & 2\end{bmatrix}\begin{Bmatrix}v_n^-\\ v_{n+1}^+\end{Bmatrix}\\ &+\frac{\omega_n^2\Delta t_n^2}{24}\begin{bmatrix}3 & 1\\ 5 & 3\end{bmatrix}\begin{Bmatrix}v_n^-\\ v_{n+1}^+\end{Bmatrix}=\begin{Bmatrix}J_{ext}^1\\ J_{ext}^2\end{Bmatrix}-\frac{\omega_n^2\Delta t_n u_n}{2}\begin{Bmatrix}1\\ 1\end{Bmatrix}+\begin{Bmatrix}v_n^-\\ 0\end{Bmatrix}\end{aligned} \tag{2.92}$$

2.4 Numerical analysis of the TDG/FEM for the second order ODE

In this section, numerical analysis of the TDG/FEM schemes, viz. uv-TDG/FEM, u-TDG/FEM, and v-TDG/FEM, for the second order ODE in time will be performed. To assess the stability characteristics and temporal accuracy of the TDG/FEM schemes classical finite difference techniques will be used Hughes, 2012, Chapter 9. In this context, it is sufficient to consider the following homogeneous and undamped form of Eq. (2.44):

$$\frac{d^2u}{dt^2}+\omega_n^2u=0,\qquad u(0)=u_(0),\qquad \frac{du(0)}{dt}=v_0,\qquad t\in[0,T] \tag{2.93}$$

2.4.1 Total energy decay characteristics of TDG/FEM

TDG/FEM schemes can be classified as the true energy-decaying scheme. The purpose of this section is to elucidate this concept. Let us return to Eq. (2.93) which represent the governing equation of a spring-mass system. Since the damping and external forces are absent in such system, the total energy (kinetic energy plus potential energy) of the system remains constant. [8]

$$T_E\left(u,v\right):=\frac{1}{2}v^2+\frac{1}{2}\omega_n^2u^2=\text{constant} \tag{2.94}$$

[8] To prove that total energy of the spring-mass system is constant, multiply Eq. (2.93) with velocity $v=\frac{du}{dt}$,

$$v\frac{dv}{dt}+\omega_n^2u\frac{du}{dt}=0$$

then

$$\frac{d}{dt}\left(\frac{1}{2}v^2\right)+\frac{d}{dt}\left(\frac{1}{2}\omega_n^2u^2\right)=0$$

or

$$\frac{d}{dt}\left(\frac{1}{2}v^2+\frac{1}{2}\omega_n^2u^2\right)=0$$

therefore,

$$\frac{1}{2}v^2+\frac{1}{2}\omega_n^2u^2=\text{constant}$$

where the first term denotes the kinetic energy per unit mass, and second term denotes the potential energy per unit mass. In addition $\omega_n^2 = k/m$ (see also Eq. 2.45).

Consider the time domain $[0, T]$ and corresponding N time-slabs; $I_n := (t_n, t_{n+1})$ for $n = 0, 1 \cdots, N-1$. Let the displacement and velocity at time $t_0 = 0$ be given by

$$u_0^+ = u_0^- = u_0,$$

and

$$v_0^+ = v_0^- = v_0,$$

respectively. Furthermore, the displacement and velocity at time $t_N = T$ be denoted by u_N^- and u_N^-, respectively.

Proposition 2.4.1. *The uv-TDG/FEM is an energy decaying time integration algorithm, in which the total energy at the end of time interval, $T_E(u_N^-, v_N^-)$, is always bounded from above by the total energy at the beginning of the time interval (i.e., $T_E(u_0, v_0)$).*

$$T_E(u_N^-, v_N^-) \leq T_E(u_0, v_0) \tag{2.95}$$

Proof. To prove the above proposition (Eq. 2.95) use $\delta v^h = v^h$ and $\delta u^h = \omega_n^2 u^h$ in the uv-TDG/FEM weak-form, which is given by Eq. (2.49), with $\zeta = 0$ and $f = 0$.

$$\int_{I_n} v^h \frac{dv^h}{dt} dt + \int_{I_n} v^h \omega_n^2 u^h dt + v_n^+ \left(v_n^+ - v_n^-\right) + \int_{I_n} \omega_n^2 u^h \frac{du^h}{dt} dt - \int_{I_n} \omega_n^2 u^h v^h dt + \omega_n^2 u_n^+ \left(u_n^+ - u_n^-\right) = 0$$

$$\Rightarrow \int_{I_n} \frac{d}{dt} \left[\frac{1}{2}\left(v^h\right)^2 + \frac{1}{2}\omega_n^2\left(u^h\right)^2\right] dt + \left(v_n^+\right)^2 - v_n^+ v_n^- + \omega_n^2\left(u_n^+\right)^2 - \omega_n^2 u_n^+ u_n^- = 0$$

$$\Rightarrow \frac{1}{2}\left(v_{n+1}^-\right)^2 + \frac{1}{2}\omega_n^2\left(u_{n+1}^-\right)^2 + \frac{1}{2}\left(v_n^+\right)^2 + \frac{1}{2}\omega_n^2\left(u_n^+\right)^2 - v_n^+ v_n^- - \omega_n^2 u_n^+ u_n^- = 0$$

$$\Rightarrow \frac{1}{2}\sum_{n=0}^{N-1}\left[\left(v_{n+1}^-\right)^2 + \left(v_n^+\right)^2 - 2v_n^+ v_n^-\right] + \frac{1}{2}\omega_n^2 \sum_{n=0}^{N-1}\left[\left(u_{n+1}^-\right)^2 + \left(u_n^+\right)^2 - 2u_n^+ u_n^-\right] = 0$$

$$\Rightarrow \frac{1}{2}\sum_{n=0}^{N-1}\left[\left(v_n^-\right)^2 + \left(v_n^+\right)^2 - 2v_n^+ v_n^-\right] + \frac{1}{2}\omega_n^2 \sum_{n=0}^{N-1}\left[\left(u_n^-\right)^2 + \left(u_n^+\right)^2 - 2u_n^+ u_n^-\right] + \frac{1}{2}\omega_n^2\left(u_N^-\right)^2 + \frac{1}{2}\left(v_N^-\right)^2 - \frac{1}{2}\omega_n^2(u_0)^2 - \frac{1}{2}(v_0)^2 = 0$$

$$\Rightarrow \frac{1}{2}\sum_{n=0}^{N-1}\left[\left[v^h\right]\right]_n^2 + \frac{1}{2}\omega_n^2 \sum_{n=0}^{N-1}\left[\left[u^h\right]\right]_n^2 + T_E\left(u_N^-, v_N^-\right) - T_E\left(u_0, v_0\right) = 0$$

$$\Rightarrow T_E\left(u_N^-, v_N^-\right) = T_E\left(u_0, v_0\right) - \frac{1}{2}\sum_{n=0}^{N-1}\left[\left[v^h\right]\right]_n^2 - \frac{1}{2}\omega_n^2 \sum_{n=0}^{N-1}\left[\left[u^h\right]\right]_n^2$$

$$\Rightarrow T_E\left(u_N^-, v_N^-\right) \leqslant T_E\left(u_0, v_0\right)$$

□

The last step in above proof follows from the fact that

$$\frac{1}{2}\sum_{n=0}^{N-1}\left[\!\left[v^h\right]\!\right]_n^2+\frac{1}{2}\omega_n^2\sum_{n=0}^{N-1}\left[\!\left[u^h\right]\!\right]_n^2\geqslant 0 \tag{2.96}$$

where the first term on the left hand side represents the kinetic energy per unit mass due to the discontinuity jump in the velocity, and the second term on the left hand side denotes the potential energy per unit mass due to the discontinuity jump in the displacement.

Proposition 2.4.2. *The u-TDG/FEM is an energy decaying time integration algorithm with*

$$T_E(u_N^-,v_N^-)\leq T_E(u_0,v_0)$$

Proof. To prove the above proposition take $\delta u^h=u^h$ and

$$v^h=\frac{du^h}{dt}$$

in the u-TDG/FEM weak-form, which is give by Eq. (2.63), with $\zeta=0$, and $f=0$.

$$\int_{I_n}v^h\frac{dv^h}{dt}dt+\int_{I_n}\omega_n^2u^h\frac{du^h}{dt}dt+v_n^+\left(v_n^+-v_n^-\right)+\omega_n^2u_n^+\left(u_n^+-u_n^-\right)=0$$

Noting that the above equation is identical to Eq. (2.96) completes the proof. □

Proposition 2.4.3. *The v-TDG/FEM is an energy decaying time integration algorithm with*

$$T_E(u_N,v_N^-)\leq T_E(u_0,v_0)$$

Proof. To prove the above proposition consider $\delta v^h=v^h$ and

$$v^h=\frac{du^h}{dt}$$

in the v-TDG/FEM weak-form, which is given by Eq. (2.77), with $\zeta=0$ and $f=0$.

$$\int_{I_n}v^h\frac{dv^h}{dt}dt++\int_{I_n}\omega_n^2u^h\frac{du^h}{dt}dt+\left(v_n^+\right)^2-v_n^+v_n^-=0$$

$$\Rightarrow \int_{I_n} \frac{d}{dt}\left[\frac{1}{2}\left(v^h\right)^2 + \frac{1}{2}\omega_n^2\left(u^h\right)^2\right] dt + \left(v_n^+\right)^2 - v_n^+ v_n^- = 0$$

$$\Rightarrow \frac{1}{2}\left(v_{n+1}^-\right)^2 - \frac{1}{2}\left(v_n^+\right)^2 + \frac{1}{2}\omega_n^2 (u_{n+1})^2 - \frac{1}{2}\omega_n^2 (u_n)^2 + \left(v_n^+\right)^2 - v_n^+ v_n^- = 0$$

$$\Rightarrow \frac{1}{2}\sum_{n=0}^{N-1}\left[\left(v_{n+1}^-\right)^2 + \left(v_n^+\right)^2 - 2v_n^+ v_n^-\right] + \frac{1}{2}\omega_n^2 \sum\left[(u_{n+1})^2 - (u_n)^2\right] = 0$$

$$\Rightarrow \frac{1}{2}\sum_{n=0}^{N-1}\left[\left[v^h\right]\right]_n^2 + \frac{1}{2}\left(v_N^-\right)^2 - \frac{1}{2}(v_0)^2 + \frac{1}{2}\omega_n^2 (u_N)^2 - \frac{1}{2}\omega_n^2 (u_0)^2 = 0$$

$$\Rightarrow T_E\left(u_N, v_N^-\right) = T_E\left(u_0, v_0\right) - \frac{1}{2}\sum_{n=0}^{N-1}\left[\left[v^h\right]\right]_n^2$$

$$\Rightarrow T_E\left(u_N, v_N^-\right) \leqslant T_E\left(u_0, v_0\right)$$

□

To assess the energy dissipation characteristics of the time-discontinuous Galerkin schemes, the spring-mass problem (see Eq. (2.93)) is solved by using the TDG/FEMs with $\omega_n = 2\pi$, $u_0 = 0$, and $v_0 = 1.0m/s$. The undamped time period T_0 of the sinusoidal motion is 1.0 second, and the total time duration is taken as $T = 50$ seconds. Fig. 2.7 plots the time history graphs of the normalized total energy [9] computed by using the TDG schemes with different time-step sizes. As anticipated, the energy dissipation in the case of uv-TDG/FEM is relatively higher than the other two schemes. In addition, the energy decay characteristics of the u-TDG/FEM and v-TDG/FEM are identical to each other. Furthermore, the dissipation of energy decreases as the time-step size decreases (see also Fig. 2.6) which indicates that the jump discontinuity in time decreases with time-step size. In fact, the subsequent sections will demonstrate that the jump discontinuity in time decreases with time-step size.

The effect of energy-dissipation can be visualized from the displacement-velocity phase diagram. For the present problem, the displacement-velocity relationship can be obtained by using the fact that the total energy of the spring-mass sysmstem is conserved.

$$\frac{1}{2}v^2 + \frac{1}{2}\omega_n^2 u^2 = T_{E0}$$

In the $u - v$ coordinate plane this equation represents an ellipse. The presence of energy dissipation in the numerical algorithm, however, decreases the total energy which in the turn decreases the radii of the ellipse. The phase diagrams for uv-

[9] Normalized total energy at any time t is defined by total energy at time t divided by initial total energy, i.e.,

$$\text{Normalized total energy} = \frac{T_E(u, v)}{T_E(u_0, v_0)}$$

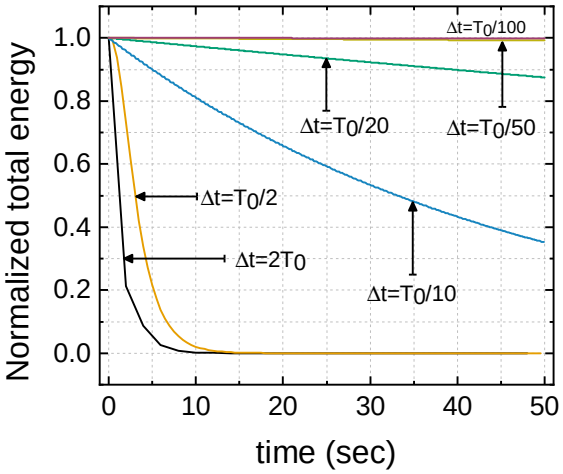

Fig. 2.6.: Spring-mass system – Time history of the normalized total energy obtained by using the v-TDG/FEM.

TDG/FEM, u-TDG/FEM, and v-TDG/FEM are given in Fig. 2.8, Fig. 2.9, and Fig. 2.10, respectively.

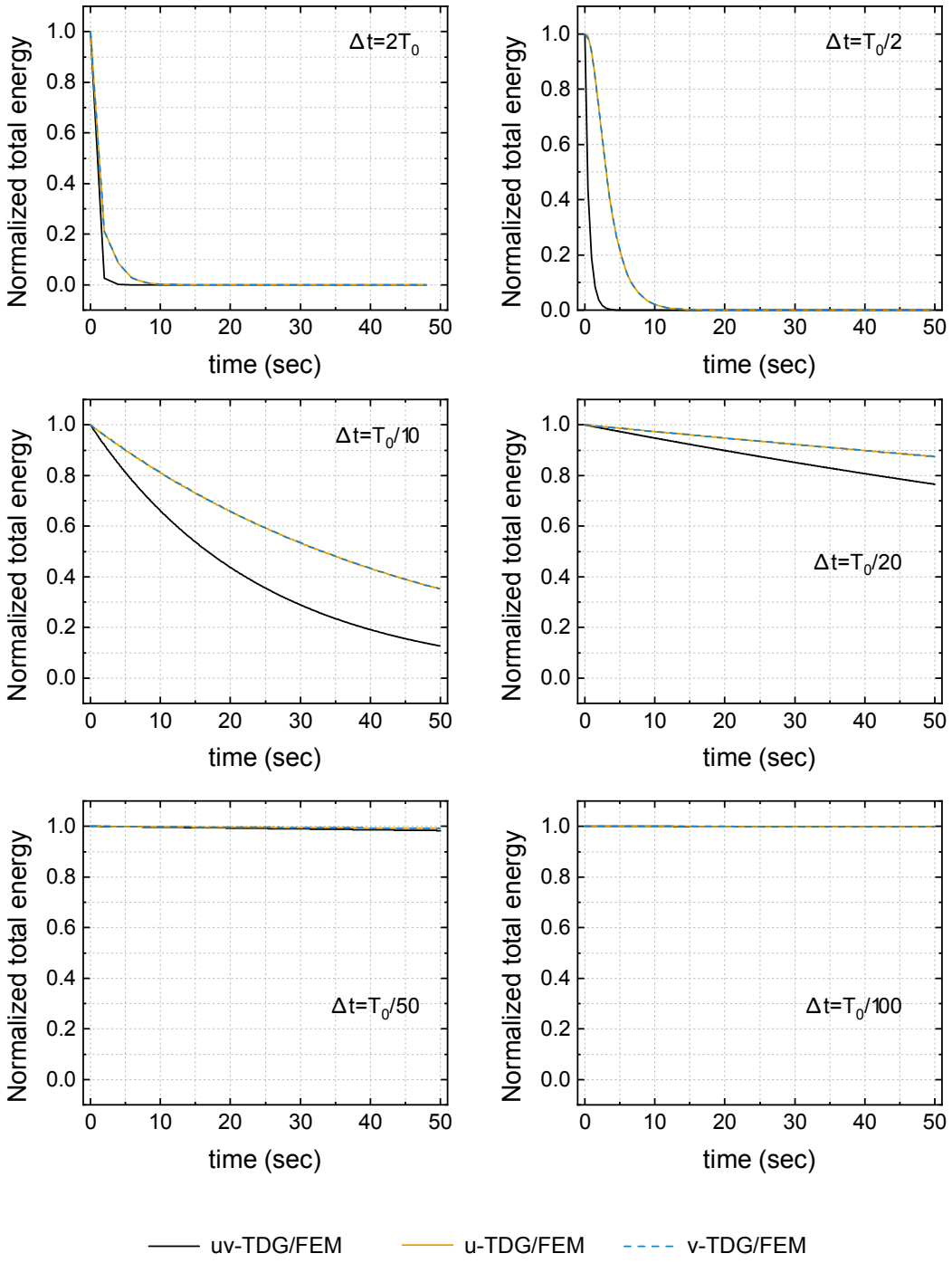

Fig. 2.7.: Spring-mass system – Time history graphs of the normalized total energy obtained by using different TDG schemes.

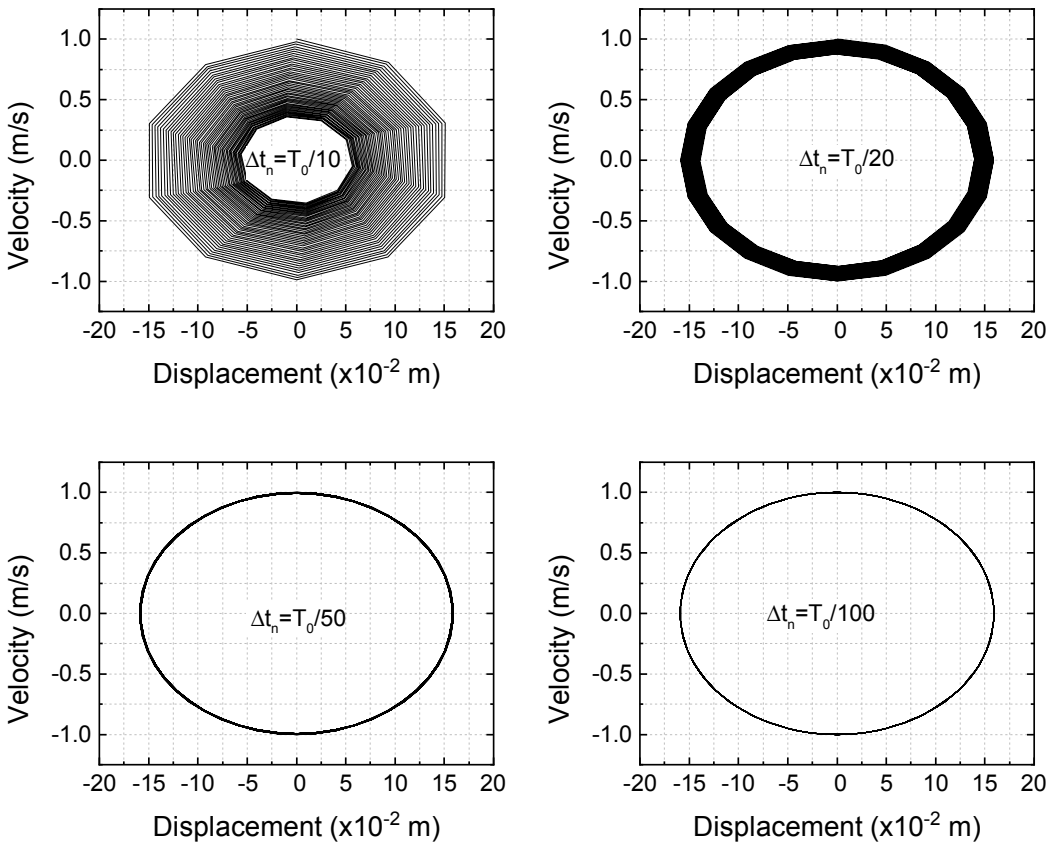

Fig. 2.8.: Spring-mass system – Phase diagram obtained by using the uv-TDG/FEM with different time-step size.

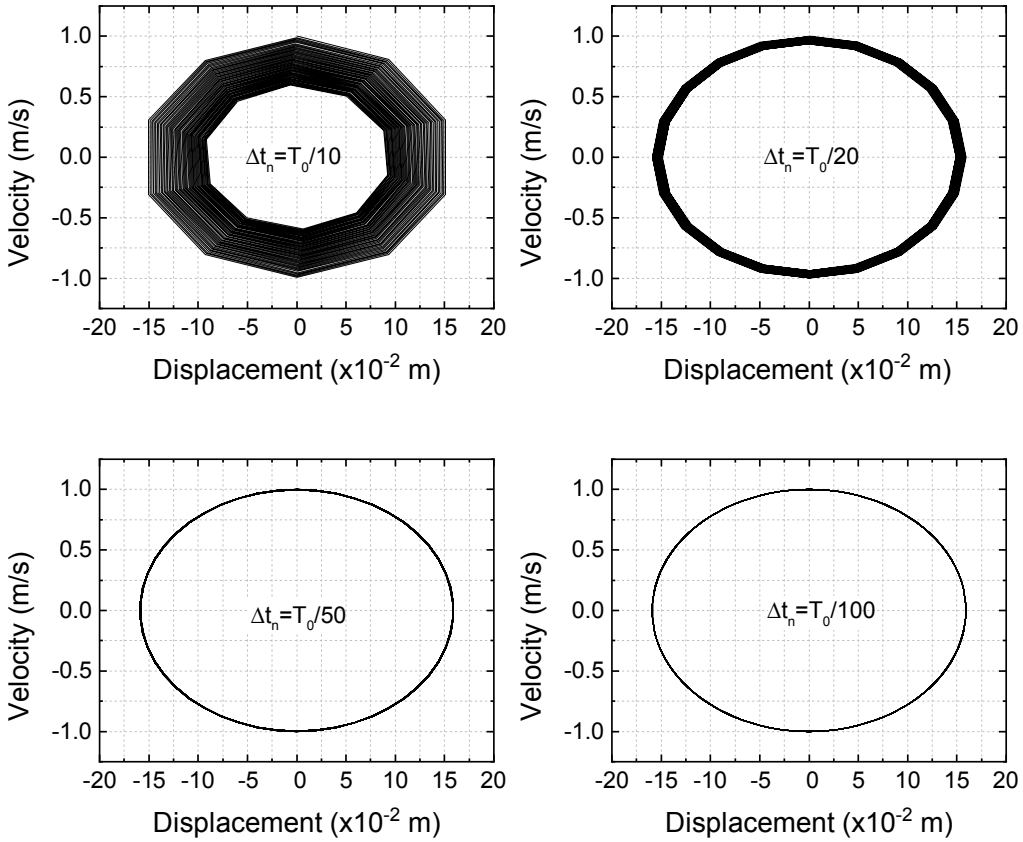

Fig. 2.9.: Spring-mass system – Phase diagram obtained by using the u-TDG/FEM with different time-step size.

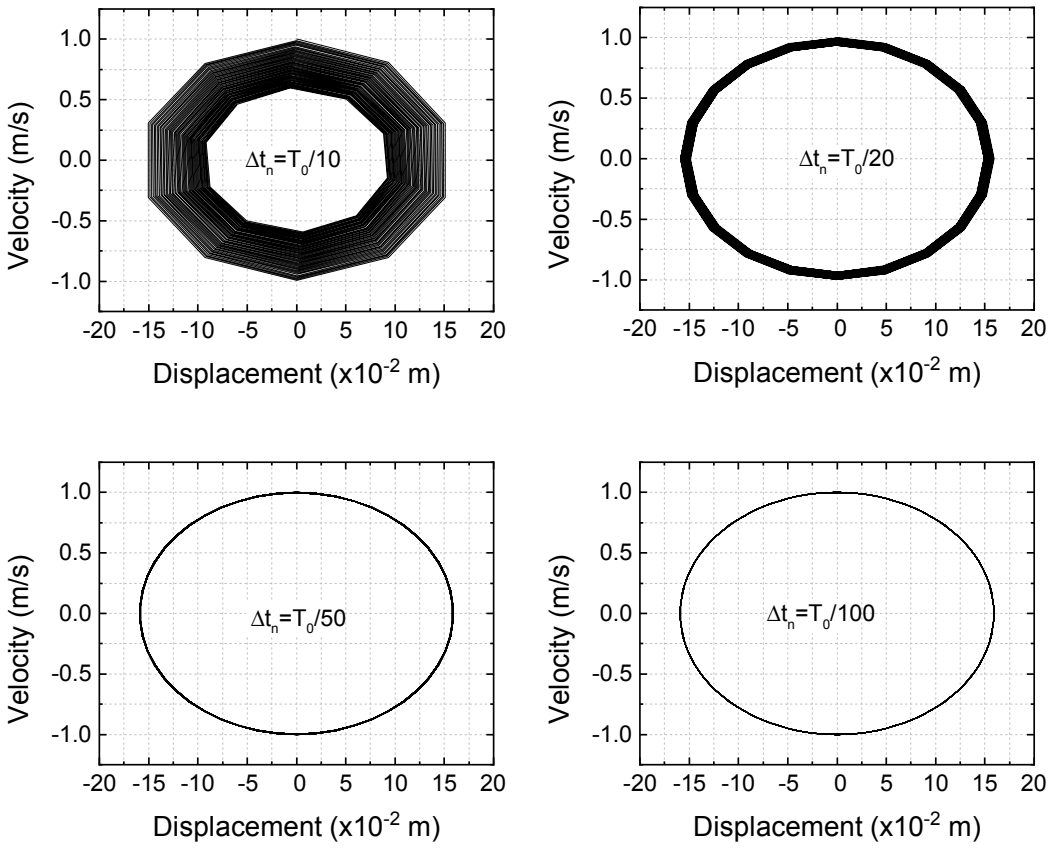

Fig. 2.10.: Spring-mass system – Phase diagram obtained by using the v-TDG/FEM with different time-step size.

2.4.2 Stability of TDG/FEM

To solve Eq. (2.93) by using the uv-TDG/FEM first order test and trial functions for both displacement and velocity have been used. In this way, the matrix-vector form, which is described below, can be obtained by setting $\zeta = 0$ and $f(t) = 0$ in Eq. (2.61).

$$\frac{1}{2}\begin{bmatrix} 1 & 1 \\ -1 & 1 \end{bmatrix}\begin{Bmatrix} v_n^+ \Delta t_n \\ v_{n+1}^- \Delta t_n \end{Bmatrix} + \frac{\Omega^2}{6}\begin{bmatrix} 2 & 1 \\ 1 & 2 \end{bmatrix}\begin{Bmatrix} u_n^+ \\ u_{n+1}^- \end{Bmatrix} = \begin{Bmatrix} v_n^- \Delta t_n \\ 0 \end{Bmatrix} \tag{2.97}$$

$$\frac{1}{2}\begin{bmatrix} 1 & 1 \\ -1 & 1 \end{bmatrix}\begin{Bmatrix} u_n^+ \\ u_{n+1}^- \end{Bmatrix} - \frac{1}{6}\begin{bmatrix} 2 & 1 \\ 1 & 2 \end{bmatrix}\begin{Bmatrix} v_n^+ \Delta t_n \\ v_{n+1}^- \Delta t_n \end{Bmatrix} = \begin{Bmatrix} u_n^- \\ 0 \end{Bmatrix} \tag{2.98}$$

By eliminating v_n^+ and u_n^+ from Eq. (2.97) and Eq. (2.98), two linear equations in v_{n+1}^- and u_{n+1}^- can be obtained. These equations are described by the following compact form.

$$\begin{Bmatrix} u_{n+1}^- \\ v_{n+1}^- \Delta t_n \end{Bmatrix} = \mathbf{A}(\Omega)\begin{Bmatrix} u_n^- \\ v_n^- \Delta t_n \end{Bmatrix} \tag{2.99}$$

In above equation, $\mathbf{A}(\Omega) \in \mathbb{R}^{2\times 2}$ is called the amplification matrix, and it depends upon $\Omega = \omega_n \Delta t_n$ (see Eq. 2.100).

$$\mathbf{A}(\Omega) = \begin{bmatrix} \frac{-14\Omega^2+36}{\Omega^4+4\Omega^2+36} & \frac{-2\Omega^2+36}{\Omega^4+4\Omega^2+36} \\ \frac{2\Omega^4-36\Omega^2}{\Omega^4+4\Omega^2+36} & \frac{-14\Omega^2+36}{\Omega^4+4\Omega^2+36} \end{bmatrix} \tag{2.100}$$

Further, to solve Eq. (2.93) by using the u-TDG/FEM quadratic test and trial functions for the displacement have been used. In this way, the matrix-vector form, which is described below, can be obtained by setting $\zeta = 0$ and $f(t) = 0$ in Eq. (2.75).

$$\begin{aligned} &\begin{bmatrix} 5 & -1 & -4 \\ 7 & 5 & -12 \\ -12 & -4 & 16 \end{bmatrix}\begin{Bmatrix} u_1^{(n)} \\ u_2^{(n)} \\ u_3^{(n)} \end{Bmatrix} + \frac{\Omega^2}{6}\begin{bmatrix} 3 & 1 & -4 \\ -1 & 3 & 4 \\ 4 & -4 & 0 \end{bmatrix}\begin{Bmatrix} u_1^{(n)} \\ u_2^{(n)} \\ u_3^{(n)} \end{Bmatrix} \\ &\qquad = \begin{Bmatrix} -3v_n^- \Delta t_n \\ -v_n^- \Delta t_n \\ 4v_n^- \Delta t_n \end{Bmatrix} + \begin{Bmatrix} \Omega^2 u_n^- \\ 0 \\ 0 \end{Bmatrix} \end{aligned} \tag{2.101}$$

Once again, it will be advantageous to recast the above system in the form given by Eq. (2.99). In the case of v-TDG/FEM the amplification matrix is given by Eq. (2.102)

$$\mathbf{A}(\Omega) = \begin{bmatrix} \frac{\Omega^4-30\Omega^2+72}{\Omega^4+6\Omega^2+72} & \frac{-6\Omega^2+72}{\Omega^4+6\Omega^2+72} \\ \frac{6\Omega^4-72x^2}{\Omega^4+6\Omega^2+72} & \frac{-30\Omega^2+72}{\Omega^4+6\Omega^2+72} \end{bmatrix} \tag{2.102}$$

Finally, to solve Eq. (2.93) by using the v-TDG/FEM linear test and trial functions for the velocity have been used. In this way, the matrix-vector form, which is described below, can be obtained by setting $\zeta = 0$ and $f(t) = 0$ in Eq. (2.92).

$$\begin{aligned} \frac{1}{2}\begin{bmatrix} 1 & 1 \\ -1 & 1 \end{bmatrix}\begin{Bmatrix} v_n^- \Delta t_n \\ v_{n+1}^+ \Delta t_n \end{Bmatrix} + \frac{\Omega^2}{24}\begin{bmatrix} 3 & 1 \\ 5 & 3 \end{bmatrix}\begin{Bmatrix} v_n^- \Delta t_n \\ v_{n+1}^+ \Delta t_n \end{Bmatrix} \\ = \begin{Bmatrix} v_n^- \Delta t_n \\ 0 \end{Bmatrix} - \begin{Bmatrix} \frac{\Omega^2 u_n}{2} \\ \frac{\Omega^2 u_n}{2} \end{Bmatrix} \end{aligned} \tag{2.103}$$

By eliminating v_n^+ from Eq. (2.103) following system of two linear equations in v_{n+1}^- and u_{n+1} can be obtained.

$$\begin{Bmatrix} u_{n+1} \\ v_{n+1}^- \Delta t_n \end{Bmatrix} = \mathbf{A}(\Omega)\begin{Bmatrix} u_n \\ v_n^- \Delta t_n \end{Bmatrix} \tag{2.104}$$

In above equation the amplification matrix is given by following expression.

$$\mathbf{A}(\Omega) = \begin{bmatrix} \frac{\Omega^4 - 30\Omega^2 + 72}{\Omega^4 + 6\Omega^2 + 72} & \frac{-6\Omega^2 + 72}{\Omega^4 + 6\Omega^2 + 72} \\ \frac{6\Omega^4 - 72\Omega^2}{\Omega^4 + 6\Omega^2 + 72} & \frac{-30\Omega^2 + 72}{\Omega^4 + 6\Omega^2 + 72} \end{bmatrix} \tag{2.105}$$

Remark 2.4.1. It is worthwhile to mention that the amplification matrix for the u-TDG/FEM and the v-TDG/FEM are identical (cf. Eq. 2.102 and Eq. 2.105). Therefore, the stability and accuracy characteristics of these two methods will be identical, and henceforth only the case of the v-TDG/FEM and uv-TDG/FEM will be discussed.

The stability of the TDG schemes is determined by the spectral properties of the amplification matrix. Let $\lambda_1(\mathbf{A})$ and $\lambda_2(\mathbf{A})$ be the eigenvalues of the amplification matrix. Accordingly, it can be shown that

$$\lambda_{1,2}(\mathbf{A}) = a_1 \pm \sqrt{a_1^2 - a_2} \tag{2.106}$$

where

$$a_1 = \frac{1}{2}(A_{11} + A_{22}), \qquad a_2 = A_{11}A_{22} - A_{12}A_{21} \tag{2.107}$$

The modulus of $\lambda_i(\mathbf{A})$ is given by

$$|\lambda_i| = \sqrt{\lambda_i \lambda_i^*} \quad \text{no sum for index i,}$$

where λ_i^* denotes the complex conjugate of λ_i. Then the spectral radius of amplification matrix is defined as

$$\rho(\mathbf{A}) = \max_{i=1,2} |\lambda_i(\mathbf{A})| \tag{2.108}$$

	uv-TDG/FEM	v-TDG/FEM
a_1	$\frac{-14\Omega^2+36}{\Omega^4+4\Omega^2+36}$	$\frac{\Omega^4-60\Omega^2+144}{2\Omega^4+12\Omega^2+144}$
a_2	$\frac{4\Omega^2+36}{\Omega^4+4\Omega^2+36}$	$\frac{6\Omega^2+72}{\Omega^4+6\Omega^2+72}$
$\lim_{\Omega\to 0}\rho(\mathbf{A})$	1	1
$\lim_{\Omega\to\infty}\rho(\mathbf{A})$	0	1

Tab. 2.1.: Amplification matrix parameters; a_1 and a_2 for the uv-TDG/FEM and v-TDG/FEM.

Accordingly, for the spectral stability of the TDG/FEM following conditions will be required Hughes, 2012, Chapter 9

(i) $\rho(A) \leq 1$

(ii) Eigenvalues of $\mathbf{A}$ of multiplicity greater than one are strictly less than one in modulus.

From Eq. (2.106), Eq. (2.107), and Table 2.1 it is easy to demonstrate that both uv-TDG/FEM and v-TDG/FEM satisfy the above-mentioned spectral stability conditions. Therefore, TDG/FEM schemes are unconditionally stable time-marching schemes.

Alternatively, for a 2×2 amplification matrix, the spectral stability can be examined by using the technique originally developed by the Hilber Hughes, 1983, for derivation. Hilber technique for the stability of the algorithm is specified in terms of the invariants of amplification matrix; a_1 and a_2. The stability region in $a_1 - a_2$ space satisfies (see also Fig. 2.11)

$$-\frac{(a_2+1)}{2} \leqslant a_1 \leqslant \frac{(a_2+1)}{2}, \qquad -1 \leqslant a_2 < 1 \tag{2.109}$$

$$-1 < a_1 < 1, \qquad a_2 = 1 \tag{2.110}$$

Fig. 2.11a and Fig. 2.11b depict the stability region corresponding to Eq. 2.109 and Eq. (2.110), respectively.

Lastly, the a_1, a_2 trajectories for the uv-TDG/FEM and v-TDG/FEM are plotted in Fig. 2.12. It can be observed that the a_1 and a_2 for the TDG/FEM are located inside the Hilber stability region, therefore, proving the unconditional stability of the uv-TDG/FEM and v-TDG/FEM.

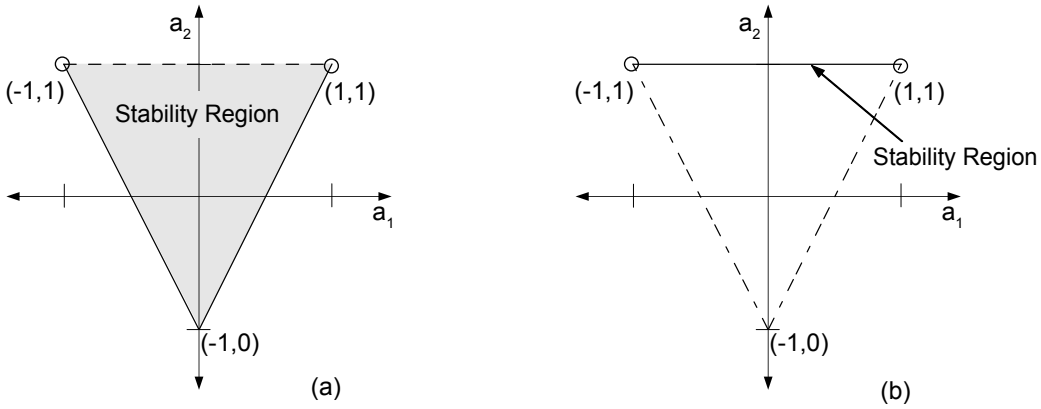

Fig. 2.11.: Spectral stability region for a 2×2 amplification matrix.

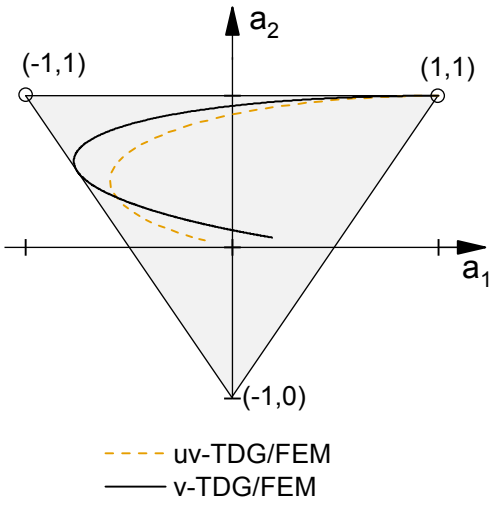

Fig. 2.12.: a_1,a_2 trajectories for the uv-TDG/FEM and v-TDG/FEM.

2.4.3 High-frequency response of TDG/FEM

Spectral radius plots are useful to observe the dissipative properties of an algorithm over the entire frequency domain (Hulbert, 1992). Moreover, High-frequency response of the spectral radius $\rho(\mathbf{A})$ provides the informations regarding the numerical stability and numerical dissipation of the spurious high-frequency components Hughes, 1983; Hughes, 2012. Fig. 2.13a depicts the frequency responses of the spectral radius for the uv-TDG/FEM and v-TDG/FEM. Furthermore, in Fig. 2.13b spectral radius of TDG schemes are plotted along with the semi-discrete algorithms. [10] Once again it can be observed that v-TDG/FEM and uv-TDG/FEM are unconditionally stable algorithms as $\rho \leq 1$.

For uv-TDG/FEM, spectral radius in the high-frequency regime (i.e., $\rho_\infty := \lim_{\Omega\to\infty} \rho$), reaches to zero, consequently, the algorithm can dissipate the spurious high-frequency response. The v-TDG/FEM, however, cannot attenuate such spurious high-frequency contents since $\rho_\infty = 1$ (see Fig. 2.13). The spectral radius for the v-TDG/FEM is lower than that of uv-TDG/FEM, therefore, the former has lower numerical dissipation than the latter. Furthermore, in lower frequency regime the spectral radius for both TDG schemes is close to one implying negligible attenuation of the small frequency content. Lastly, the points $\Omega \approx \pi$ and $\Omega \approx 3.4\pi$, at which spectral radius for the v-TDG/FEM attains its minimum value, mark the bifurcation of complex conjugate eigenvalues into distinct real eigenvalues (see Fig. 2.13a).

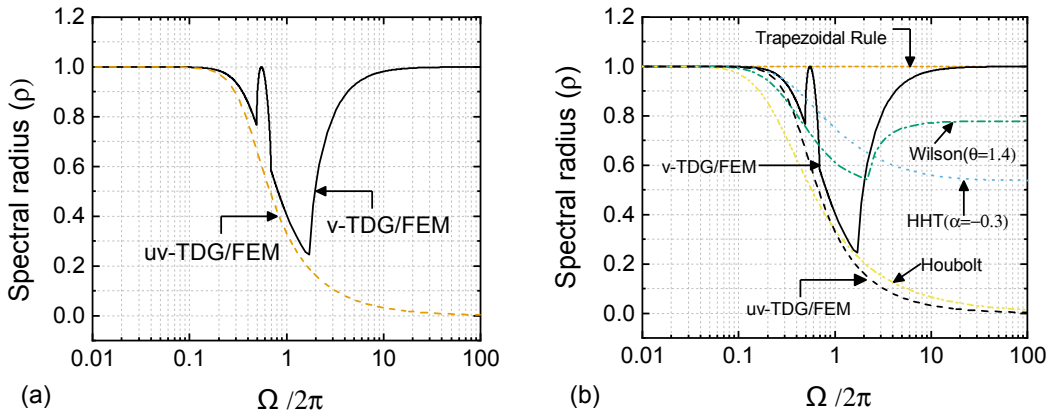

Fig. 2.13.: Frequency response of spectral radius ρ: (a) uv-TDG/FEM and v-TDG/FEM, and (b) comparison of spectral radii for TDG schemes with the semi-discrete algorithms.

[10] The term *semi-discrete algorithms* is used for collectively referencing the second order accurate implicit time-stepping algorithms viz., the trapezoidal rule (Newmark method with $\gamma = 0.5$ and $\beta = 0.25$), the Wilson-θ method with $\theta = 1.4$ Bathe and Wilson, 1976, the HHT-α method with $\alpha = -0.3$ Hilber et al., 1977, and Houbolt's method Houbolt, 1950. For details about these semi-discrete algorithms see Hughes, 1983; Hughes, 2012.

2.4.4 Accuracy of TDG/FEM

It can be shown that Eq. (2.99) and Eq. (2.104) satisfy the finite difference stencile described by Eq. (2.111) and Eq. (2.112), respectively.

$$u_{n+1}^{-} - 2a_1 u_n^{-} + a_2 u_{n-1}^{-} = 0, \qquad v_{n+1}^{-} - 2a_1 v_n^{-} + a_2 v_{n-1}^{-} = 0 \tag{2.111}$$

$$u_{n+1} - 2a_1 u_n + a_2 u_{n-1} = 0, \qquad v_{n+1}^{-} - 2a_1 v_n^{-} + a_2 v_{n-1}^{-} = 0 \tag{2.112}$$

Let $u(t)$ and $v(t)$ be the exact solutions for the displacement and velocity, respectively. Then the local truncation error $\tau(t)$ corresponding to Eq. (2.111a) and Eq. (2.112a) at any time t becomes (Hulbert, 1992)

$$u(t+\Delta t) - 2a_1 u(t) + a_2 u(t-\Delta t) = \Delta t^2 \tau\,(t) \tag{2.113}$$

Subsequently, by expanding $u(t+\Delta t)$ and $u(t-\Delta t)$ about t using the Taylor series, and then using Eq. (2.93) [11], it can be shown that both uv-TDG/FEM and v-TDG/FEM schemes are consistent, i.e.,

$$|\tau\,(t)| \leqslant c\Delta t^3 \tag{2.114}$$

with error coefficients $c = 1/36$ and $c = 1/72$ for the uv-TDG/FEM and the v-TDG/FEM, respectively. Furthermore, Eq. (2.114) proves that both TDG schemes are third order accurate in time.

Since uv-TDG/FEM and v-TDG/FEM are both consistent and stable one can use the Lax equivalence theorem to prove the convergence of the algorithms. A direct consequence of the convergence is that there exists an $\Omega_c > 0$ such that if $0 < \Omega < \Omega_c$, then the eigenvalues of amplification matrix are complex, i.e., $a_1^2 - a_2 < 0$ in Eq. (2.106), and the solution of Eq. (2.93) can be written as follows (Hughes, 1983):

$$u_n = \exp\left(-\frac{\bar{\zeta}\,\bar{\Omega} t_n}{\Delta t}\right)\left[k_1 \cos\left(\frac{\bar{\Omega} t_n}{\Delta t}\right) + k_2 \sin\left(\frac{\bar{\Omega} t_n}{\Delta t}\right)\right] \tag{2.115}$$

with

$$\bar{\Omega} = \arctan\left(\frac{\sqrt{a_2 - a_1^2}}{a_1}\right) \tag{2.116}$$

$$\bar{\zeta} = -\frac{1}{2\bar{\Omega}} \ln\,(a_2) \tag{2.117}$$

[11] Eq. (2.93) is given by following

$$\frac{d^2 u}{dt^2} + \omega_n^2 = 0$$

here, $\bar{\zeta}$ denotes the algorithmic damping ratio, $\bar{\Omega}$ is the frequency of the discrete solutions, and the coefficients k_1 and k_2 are determined by the displacement and velocity initial conditions. The relationship between the discrete frequency $\bar{\Omega}$ and discrete time period $\bar{T}$ is given by

$$\frac{\bar{\Omega}}{2\pi} = \frac{\Delta t}{\bar{T}} \tag{2.118}$$

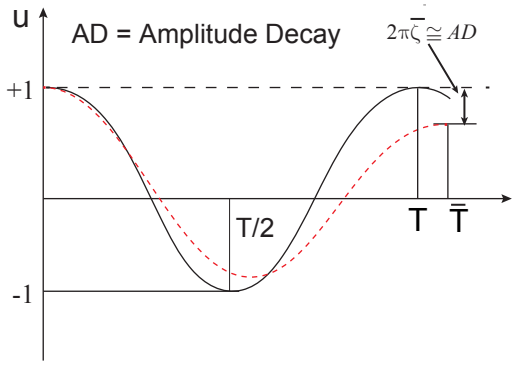

Fig. 2.14.: Illustration of the accuracy measures

Further, the numerical accuracy of a time-integration algorithm is usually measured in the lower frequency regime. Therefore, it is appropriate to use the algorithmic damping ratio $\bar{\zeta}$ and the relative frequency error $(\Omega - \bar{\Omega})/\bar{\Omega}$ as the measures of numerical dissipation and dispersion, respectively.

Numerical dissipation is the measure of amplitude decay in each cycle, while numerical dispersion measures the relative change in the time period of the wave (see Fig. 2.14). Thus, the numerical algorithms designed for long-term dynamic simulations should have little numerical dissipation and dispersion. Moreover, it is important to note that both numerical dissipation and dispersion are computed from complex eigenvalues $\lambda_{1,2}((A))$, thus, they are meaningful for the small frequency range of $0 < \Omega < \Omega_c$.

The behavior of relative frequency error for the uv-TDG/FEM, v-TDG/FEM and semi-discrete algorithms in low frequency domain is presented in Fig. 2.15. It is remarkable that the TDG schemes have very less relative frequency error compare to the semi-discrete algorithms which can be attributed to the third order accuracy of these schemes. Furthermore, relative frequency error for the v-TDG/FEM is significantly smaller than the error in uv-TDG/FEM.

Fig. 2.16 depicts the behavior of algorithm damping ratio for the uv-TDG/FEM, v-TDG/FEM and semi-discrete algorithms. The algorithmic damping for v-TDG/FEM is comparable with the HHT-α scheme, however, it is significantly smaller than the

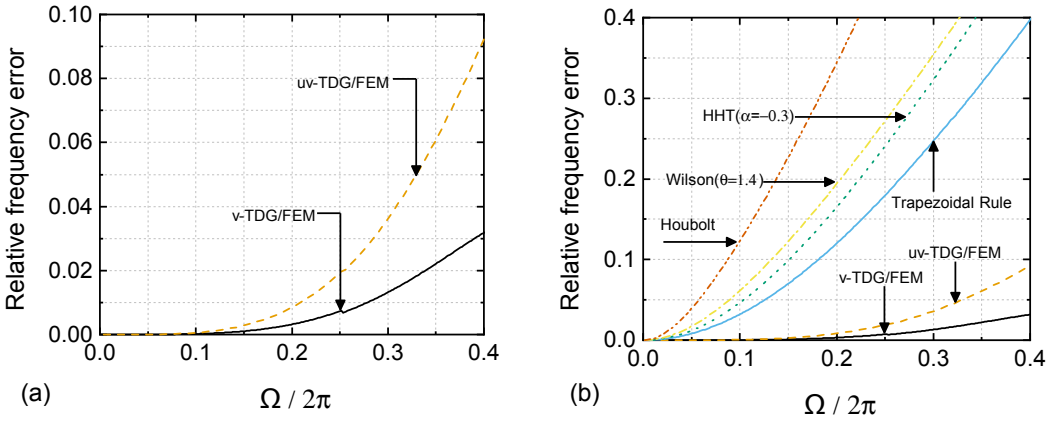

Fig. 2.15.: Relative frequency error in the low frequency domain: (a) uv-TDG/FEM and v-TDG/FEM, and (b) comparison of the relative frequency error for the TDG schemes with the semi-discrete algorithms.

uv-TDG/FEM. It is evident that the Houbolt and Wilson-θ methods are too dissipative in the low-frequency range, therefore, these algorithms are not suitable for the long-duration numerical simulations.

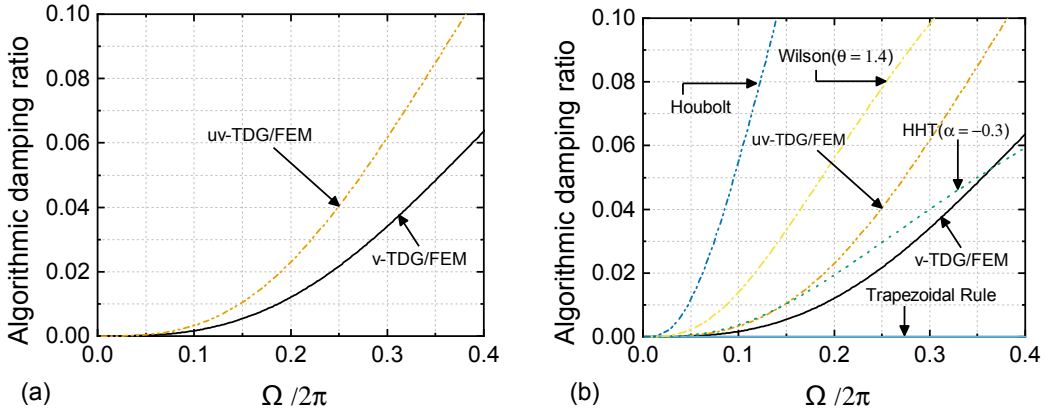

Fig. 2.16.: Algorithmic damping ratio in the low frequency domain: (a) uv-TDG/FEM and v-TDG/FEM, and (b) comparison of the algorithmic damping ratio for the TDG schemes with the semi-discrete algorithms.

Remark 2.4.2. The characteristics of the proposed v-TDG/FEM, such as very low numerical dispersion and dissipation, third-order accuracy, and unconditional stability, make v-TDG/FEM scheme suitable for long-time simulations. However, at present the only possible drawback to the v-TDG/FEM is its incapability to attenuate the spurious high-frequency components.

2.5 Continuum theory of elastodynamics

Let $\Omega \subset \mathbb{R}^{n_{sd}}$ be an open and bounded region occupied by an elastic body at time t, where n_{sd} is the number of spatial dimensions. The boundary of Ω is denoted by Γ. Let $\bar{\Omega} = \Omega \cup \Gamma$ denote the closure of Ω. Further, let indices i, j, k and l take values

from $1, \cdots, n_{sd}$, and the Einstein summation convention applies to the repeated indices i, j, k, and l only. Furthermore, consider the nonoverlapping partitions, Γ_i^g and Γ_i^h, of the boundary Γ such that

$$\Gamma = \Gamma_i^g \cup \Gamma_i^h, \qquad \Gamma_i^g \cap \Gamma_i^h = \phi, \qquad i = 1, \cdots, n_{sd}$$

The displacement, velocity, and stress field are denoted by $\mathbf{u}$, $mathbfv$, and σ, respectively. The infinitesimal strain tensor, ε, and stretching tensor, $\mathbf{d}$, are given by

$$\varepsilon := \mathbf{e}(\mathbf{u}) = \frac{1}{2}(\mathbf{u} \otimes \nabla_x) + \frac{1}{2}(\nabla_x \otimes \mathbf{u}), \quad \varepsilon_{ij} = e_{ij}(\mathbf{u}) = \frac{1}{2}\left(\frac{\partial u_i}{\partial x_j} + \frac{\partial u_j}{\partial x_i}\right) \tag{2.119}$$

$$\mathbf{d} := \mathbf{e}(\mathbf{v}) = \frac{1}{2}(\mathbf{v} \otimes \nabla_x) + \frac{1}{2}(\nabla_x \otimes \mathbf{v}), \quad d_{ij} = e_{ij}(\mathbf{v}) = \frac{1}{2}\left(\frac{\partial v_i}{\partial x_j} + \frac{\partial v_j}{\partial x_i}\right) \tag{2.120}$$

in which ε_{ij}, d_{ij}, u_i and v_i denote the Cartesian components of ε, $\mathbf{d}$, $\mathbf{u}$, and $\mathbf{v}$, respectively.

In the small strain framework, the linear elastic constitutive relationship is described as,

$$\dot{\sigma}_{ij} = C_{ijkl} d_{kl}, \qquad \sigma_{ij} = C_{ijkl} \varepsilon_{kl} \tag{2.121}$$

where $\dot{\sigma}_{ij}$ denotes the first-order time derivative of the stress field, and C_{ijkl} is the fourth-order elasticity tensor. In the case of an isotropic material, the elasticity tensor is expressed using the Lame parameters, λ, μ:

$$C_{ijkl} := \lambda \delta_{ij} \delta_{kl} + 2\mu \left(\frac{\delta_{ik}\delta_{jl} + \delta_{il}\delta_{jk}}{2}\right) \tag{2.122}$$

in which δ_{ij} represents the Kronecker-delta function. If $i = j$ then $\delta_{ij} = 1$, otherwise $\delta_{ij} = 0$.

The strong form of the initial-boundary value problem of elastodynamics can be stated as: given the functions

$$b_i : \Omega \times [0, T] \to \mathbb{R},$$

$$g_i : \Gamma_i^g \times [0, T] \to \mathbb{R},$$

$$f_i^s : \Gamma_i^h \times [0, T] \to \mathbb{R},$$

$$u_{0i} : \Omega \to \mathbb{R},$$

$$v_{0i} : \Omega \to \mathbb{R},$$

$$\rho : \Omega \to \mathbb{R},$$

find $u_i : \bar{\Omega} \times [0,T] \to \mathbb{R}$, such that

$$\rho \frac{\partial^2 u_i}{\partial t^2} - \frac{\partial \sigma_{ij}}{\partial x_j} - \rho b_i = 0, \qquad \forall (\mathbf{x}, t) \in \Omega \times (0,T) \tag{2.123}$$

$$u_i = g_i, \qquad \forall (\mathbf{x}, t) \in \Gamma_i^g \times (0,T) \tag{2.124}$$

$$\sigma_{ij} n_j = f_i^s, \qquad \forall (\mathbf{x}, t) \in \Gamma_i^h \times (0,T) \tag{2.125}$$

$$u_i(\mathbf{x}, 0) = u_{0i}, \qquad \forall \mathbf{x} \in \Omega \tag{2.126}$$

$$\frac{\partial u_i(\mathbf{x}, 0)}{\partial t} = v_{0i}, \qquad \forall \mathbf{x} \in \Omega \tag{2.127}$$

where ρ is the mass density of the elastic body, b_i is the body force density, g_i is the prescribed displacement on the Dirichlet-boundary Γ_i^g, f_i^s is the prescribed traction on the Neumann-boundary Γ_i^h, u_{0i} is the initial value of the displacement field, and v_{0i} is the initial value of the velocity field.

2.6 Time-discontinuous space-time FEM (TDG/ST/FEM) for Elastodynamics

Let Ω_h, the set of finite spatial elements $\Omega_e, e = 1, \cdots, n_{el}$, be the discretization of spatial domain Ω, where n_{el} is the total number of spatial elements in Ω_h. Furthermore, consider a non-uniform subdivision for the time domain $[0,T]$,

$$0 = t_0 < t_1 < \cdots < t_N = T$$

with

$$I_n = (t_n, t_n + 1), \quad \Delta t_n = t_{n+1} - t_n, \quad \Delta t = \max_{0 \leqslant n \leqslant N-1} \Delta t_n.$$

The space-time slab Q_n and the space-time finite element $Q_{n,e}$ are given by following expressions,

$$Q_n := \Omega_h \times I_n, \qquad Q_{n,e} := \Omega_e, \quad e = 1, \cdots, n_{el}$$

Accordingly,

$$\mathbb{Q}_h := \bigcup_{n=0}^{N-1} Q_n$$

denotes the discretization of the entire space-time domain.

In TDG/ST/FEM, the unknown fields remains continuous in the spatial domain Ω_h, and discontinuity in time occurs at times that belong to the finite set,

$$D_t := \{t_0, t_1, \ldots, t_N\}.$$

Therefore, at the discrete times $t \in D_t$ the solution have two values, and the jump discontinuity in time for some unknown scalar field $q(\mathbf{x}, t)$ at time $t_n \in D_t$ is given by Eq. (2.128)

$$[\![q(\mathbf{x})]\!]_n = q_n^+(\mathbf{x}) - q_n^-(\mathbf{x}) \tag{2.128}$$

where

$$q_n^+(\mathbf{x}) = \lim_{\varepsilon \to 0} q(\mathbf{x}, t_n + \varepsilon), \qquad q_n^-(\mathbf{x}) = \lim_{\varepsilon \to 0} q(\mathbf{x}, t_n - \varepsilon) \tag{2.129}$$

denote the right and left limits of the unknown field $q(\mathbf{x}, t)$ at time $t = t_n$, respectively.

Let us now consider $\wp_l\left(Q_{n,e}\right)$, the collection of all polynomials defined on $Q_{n,e}$ with a total degree of no more than l, and $C^0(\star)$, the space of piecewise continuous functions defined on domain $(\star)$. Consider also the following collection of functions:

$$\Im_l^h := \left\{ \mathbf{u}^h \middle| \, \mathbf{u}^h \in C^0\left(\bigcup_{n=0}^{N-1} Q_n\right)^{n_{sd}}, \mathbf{u}^h \middle| \, Q_{n,e} \in \left(\wp_l\left(Q_{n,e}\right)\right)^{n_{sd}} \right\} \tag{2.130}$$

where $\mathbf{u}^h \big| \, Q_{n,e}$ is the restriction of $\mathbf{u}^h$ to $Q_{n,e}$. Lastly, the space of the test functions for the TDG/ST/FEM is given as

$$V^h := \left\{ \mathbf{u}^h \middle| \, \mathbf{u}^h \in \Im_l^h, u_i^h = 0, \forall (\mathbf{x}, t) \in \Gamma_i^g \times I_n, \text{for } i = 1, \cdots, n_{sd} \right\} \tag{2.131}$$

In what follows, a general introduction to the two-field TDG/ST/FEM is provided, then the weak-form for the v-ST/FEM is derived by using the two-field formulation.

2.6.1 Two-field TDG/ST/FEM

In the two-field formulation, both the displacement field and velocity field are taken as primary unknowns. Accordingly, the weak form should satisfy the following conditions in the weak sense:

(i) Balance of the linear momentum, Eq. (2.123)

(ii) Essential and natural boundary conditions, Eq. (2.124) and Eq. (2.125)

(iii) Traction continuity in space;

(iv) Continuity of the velocity field in time;

$$\left[\left[\mathbf{v}^h\left(\mathbf{x}\right)\right]\right]_n = 0$$

(v) Continuity of the displacement field in time;

$$\left[\left[\mathbf{u}^h\left(\mathbf{x}\right)\right]\right]_n = 0$$

(vi) Displacement-velocity compatibility condition;

$$\frac{\partial \mathbf{u}^h}{\partial t} - \mathbf{v}^h = 0$$

Here, Conditions (i)–(iii) are always satisfied as the weak form is derived by employing the Galerkin method (Hughes, 2012). Conditions (iv) and (v) necessary due to the time-discontinuous approximation of the displacement and velocity field, respectively. Condition (vi) is due to the independent approximation of the displacement field and velocity field.

The displacement-velocity two-field weak-form for TDG/ST/FEM in its original form as presented by Hughes and Hulbert, 1988 is described as follows.

Weak-form. *Find* $\mathbf{u} \in S_u^h$ *and* $\mathbf{v} \in S_v^h$ *such that for all* $\delta\mathbf{u} \in V^h$ *and* $\delta\mathbf{v} \in V^h$*, and for all* $n = 1, \cdots, N-1$ *Eq.* (2.132) *holds.*

$$\begin{aligned}
&\int_{I_n}\int_{\Omega_h} \delta v_i \rho \frac{\partial v_i}{\partial t} d\Omega dt + \int_{\Omega_n} \delta v_i\left(\mathbf{x}, t_n^+\right) \rho [\![v_i\left(\mathbf{x}\right)]\!]_n d\Omega \\
&+ \int_{I_n}\int_{\Omega_h} \frac{\partial \delta v_i}{\partial x_j} \sigma_{ij}\left(\mathbf{x}, t\right) d\Omega dt - \int_{I_n}\int_{\Gamma_i^h} \delta v_i f_i^s ds dt \\
&- \int_{I_n}\int_{\Omega_h} \delta v_i \rho b_i d\Omega dt + \int_{I_n}\int_{\Omega_h} \frac{\partial \delta u_i}{\partial x_j} C_{ijkl} \frac{\partial}{\partial x_l}\left(\frac{\partial u_k}{\partial t} - v_k\right) d\Omega dt \\
&+ \int_{\Omega_h} \frac{\partial \delta u_i\left(\mathbf{x}, t_n\right)}{\partial x_j} C_{ijkl} \frac{\partial [\![u_k\left(\mathbf{x}\right)]\!]_n}{\partial x_l} d\Omega = 0
\end{aligned} \tag{2.132}$$

where S_u^h and S_v^h denote the collections of trial functions for the displacement field and velocity field, respectively, and given by

$$S_u^h := \left\{ \mathbf{u} | \, \mathbf{u} \in \Im_l^h, u_i = g_i, \forall \, (\mathbf{x}, t) \in \Gamma_i^g \times I_n, i = 1, \cdots, n_{sd} \right\} \tag{2.133}$$

$$S_v^h := \left\{ \mathbf{v} | \, \mathbf{v} \in \Im_l^h, v_i = \frac{\partial g_i}{\partial t}, \forall \, (\mathbf{x}, t) \in \Gamma_i^g \times I_n, i = 1, \cdots, n_{sd} \right\} \tag{2.134}$$

It is noteworthy that in the above-mentioned weak-form, Conditions (v) and (vi) are satisfied by using a strain-energy norm and Condition (iv) is satisfied by using a kinetic energy norm.

2.6.2 Velocity based TDG/ST/FEM: v-ST/FEM

In the velocity based time-discontinuous space-time finite element method (v-ST/FEM) displacement-velocity compatibility condition is strongly enforced by computing the displacement field from the consistent time-integration of the velocity field. Accordingly, displacement field remains continuous in time while velocity field still remains discontinuous at the discrete times.

The weak-form for the v-ST/FEM can be stated as:

Weak-form. *Find $\mathbf{v} \in S_v^h$ such that for all $\delta \mathbf{v} \in V^h$, and for all $n = 1, \cdots, N-1$, Eq.* (2.135) *holds.*

$$\begin{aligned} &\int_{I_n} \int_{\Omega_h} \delta v_i \rho \frac{\partial v_i}{\partial t} d\Omega dt + \int_{\Omega_n} \delta v_i \left(\mathbf{x}, t_n^+ \right) \rho v_i \left(\mathbf{x}, t_n^+ \right) d\Omega \\ &+ \int_{I_n} \int_{\Omega_h} \frac{\partial \delta v_i}{\partial x_j} \sigma_{ij} \left(\mathbf{x}, t \right) d\Omega dt - \int_{I_n} \int_{\Gamma_i^h} \delta v_i f_i^s ds dt \\ &- \int_{I_n} \int_{\Omega_h} \delta v_i \rho b_i d\Omega dt - \int_{\Omega_n} \delta v_i \left(\mathbf{x}, t_n^+ \right) \rho v_i \left(\mathbf{x}, t_n^- \right) d\Omega = 0 \end{aligned} \tag{2.135}$$

The displacement field is computed by

$$\mathbf{u} \left(\mathbf{x}, t \right) = \mathbf{u} \left(\mathbf{x}, t_n \right) + \int_{t_n}^{t} \mathbf{v} \left(\mathbf{x}, \tau \right) d\tau, \qquad \forall \, (\mathbf{x}, t) \in Q_n, \quad \forall \mathbf{v} \in S_v^h \tag{2.136}$$

In the case of hyperelastic material law, the stress is computed by first computing the displacement field (see Eq. 2.119 and Eq. 2.121b). Alternatively, if the constitutive relationship is given in the rate form (e.g., hypoelastic form) then stress field can be obtained by time integration of the rate form. In latter case, computation of displacement field can be avoided. In the realm of small strain theory, however, these

two techniques of stress recovery are equivalent, and the stress field in a space-time slab takes the form

$$\sigma_{ij}\left(\mathbf{x},t\right)=\sigma_{ij}\left(\mathbf{x},t_n\right)+C_{ijkl}\psi_{kl}\left(\mathbf{v},t\right),\qquad\forall\left(\mathbf{x},t\right)\in Q_n,\forall v\in S_v^h \tag{2.137}$$

where

$$\psi_{ij}\left(\mathbf{v},t\right)=\int_{t_n}^{t}\frac{\partial v_i}{\partial x_j}d\tau,\qquad\forall t\in I_n,\forall\mathbf{v}\in S_v^h \tag{2.138}$$

Subsequently, by substituting the expression for the stress given in Eq. (2.137) into the weak-form, Eq. (2.135), the following weak-form for v-ST/FEM is obtained;

Weak-form. *Find* $\mathbf{v}\in S_v^h$ *such that for all* $\delta\mathbf{v}\in V^h$*, and for all* $n=1,\cdots,N-1$*, Eq.* (2.139) *holds.*

$$\begin{aligned}&\int_{I_n}\int_{\Omega_h}\delta v_i\rho\frac{\partial v_i}{\partial t}d\Omega dt+\int_{\Omega_n}\delta v_i\left(\mathbf{x},t_n^+\right)\rho v_i\left(\mathbf{x},t_n^+\right)d\Omega\\&+\int_{I_n}\int_{\Omega_h}\frac{\partial\delta v_i}{\partial x_j}\sigma_{ij}\left(\mathbf{x},t_n\right)d\Omega dt+\int_{I_n}\int_{\Omega_h}\frac{\partial\delta v_i}{\partial x_j}C_{ijkl}\psi_{kl}d\Omega dt\\&-\int_{I_n}\int_{\Gamma_i^h}\delta v_i f_i^s ds dt-\int_{I_n}\int_{\Omega_h}\delta v_i\rho b_i d\Omega dt\\&-\int_{\Omega_n}\delta v_i\left(\mathbf{x},t_n^+\right)\rho v_i\left(\mathbf{x},t_n^-\right)d\Omega=0\end{aligned} \tag{2.139}$$

Remark 2.6.1. In the two-field TDG/ST/FEM, both displacement and velocity are the primary unknown. This approach usually yields a large system of linear equations which in turn increases the computation cost. In this case, special procedures are required to reduce the size of the problem. Such procedures are mainly based on the predictor-multicorrector schemes (Bonelli et al., 2002; Bonelli and Bursi, 2003; Mancuso and Ubertini, 2003; Kunthong and Thompson, 2005).

Remark 2.6.2. In v-ST/FEM, velocity field is the primary unknown, therefore, the resultant system of linear equations will be significantly smaller than the one in case of two-field TDG/ST/FEM. Accordingly, the computation cost of v-ST/FEM is lower than the two-field TDG/ST/FEM, however, the cost is still higher than the classical semi-discrete schemes.

2.6.3 Implementation of v-ST/FEM

Consider $Q_{n,e}=\Omega_e\times I_n$ denoting the space-time finite element. Let n_e be the total number of spatial nodes in the spatial finite element Ω_e. Let $v_i(\mathbf{x},t_n^+)$ and $v_i(\mathbf{x},t_{n+1}^-)$ be the spatial nodal velocities on the bottom and top faces of space-time slab Q_n, respectively (see Fig.2.17). Furthermore, time $t\in I_n$ is given by

$$t=T_1(\theta)t_n+T_2(\theta)t_{n+1},\quad\forall\theta\in[-1,1] \tag{2.140}$$

where

$$T_1(\theta) = \frac{1-\theta}{2} \qquad T_2(\theta) = \frac{1+\theta}{2} \tag{2.141}$$

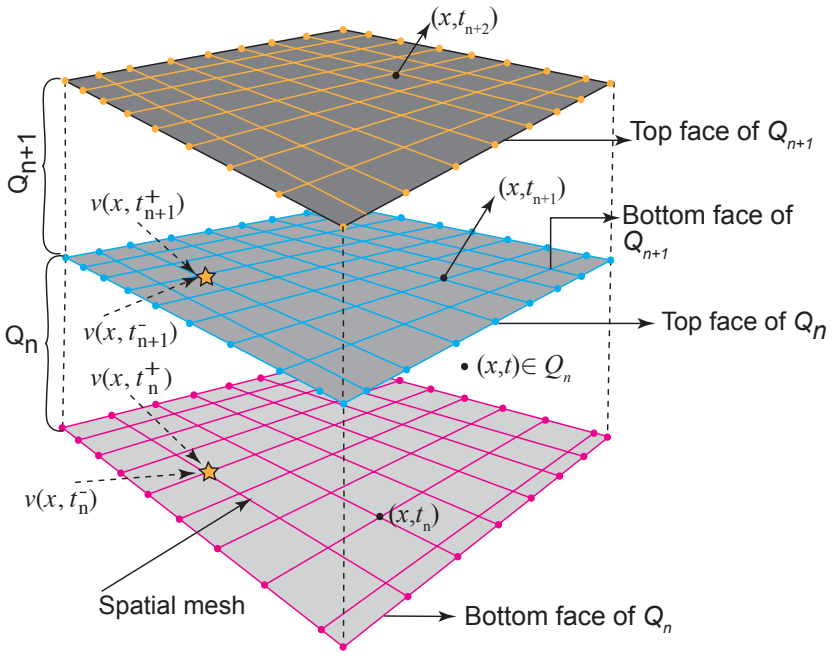

Fig. 2.17.: Schematic diagram of the space-time slabs Q_n and Q_{n+1}

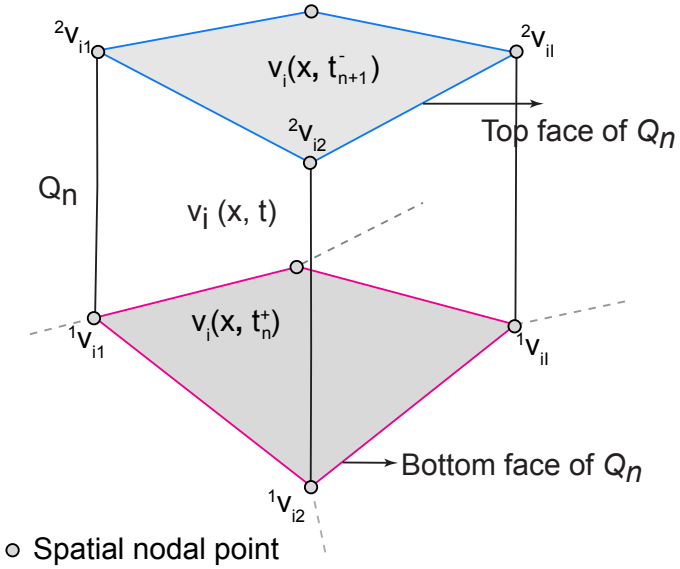

Fig. 2.18.: Schematic diagram of the space-time finite element $Q_{n,e}$

The linear trial functions for the velocity defined on $Q_{n,e}$ are give by

$$v_i(\mathbf{x},t) = {}^a v_{iI} T_a(\theta) N^I(\xi,\eta), \quad a = 1,2; \quad I = 1,\cdots,n_e \tag{2.142}$$

where ${}^{a}v_{iI}$ denotes the space-time nodal values of velocity; $a = 1$ and $a = 2$ correspond to the bottom and top face (i.e., temporal nodes) of the space-time element, and $I = 1, \cdots, n_e$ denotes the spatial node of the space-time element (see Fig. 2.18). $N^I(\xi, \eta)$ are the spatial shape functions defined on the local domain. Accordingly, $v_i(\mathbf{x}, t_n^+)$ and $v_i(\mathbf{x}, t_{n+1}^-)$ are given by Eq. (2.143) and Eq. (2.144), respectively.

$$v_i\left(\mathbf{x}, t_n^+\right) = {}^{1}v_{iI} N^I(\xi, \eta) \tag{2.143}$$

$$v_i\left(\mathbf{x}, t_{n+1}^-\right) = {}^{2}v_{iI} N^I(\xi, \eta) \tag{2.144}$$

The displacement field corresponding to the above-mentioned local interpolation for the velocity field (cf. Eq. 2.142) is obtained by using Eq. (2.136).

$$u_i(\mathbf{x}, t) = u_i(\mathbf{x}, t_n) + \tilde{T}_1(\theta)\, v_i(\mathbf{x}, t_n) + \tilde{T}_2(\theta)\, v_i(\mathbf{x}, t_{n+1}) \tag{2.145}$$

where

$$\tilde{T}_1(\theta) = \frac{\Delta t_n}{2}\left[1 - T_1^2(\theta)\right], \qquad \tilde{T}_2(\theta) = \frac{\Delta t_n}{2} T_2^2(\theta) \tag{2.146}$$

are the quadratic shape function defined on $[-1, 1]$. Subsequently, ψ_{ij} in Eq. (2.138) becomes,

$$\psi_{ij}(\mathbf{x}, t) = {}^{a}v_{iI} \tilde{T}_a \frac{\partial N^I}{\partial x_j} \tag{2.147}$$

By using the expression for psi_{ij} in Eq. (2.137) the stress σ_{ij} inside the space-time element is described as,

$$\sigma_{ij}(\mathbf{x}, t) = \sigma_{ij}(\mathbf{x}, t_n) + \tilde{T}_a C_{ijkl} \frac{\partial N^I}{\partial x_l} {}^{a}v_{kI}, \qquad \forall (\mathbf{x}, t) \in Q_{n,e} \tag{2.148}$$

Lastly, the test functions for the velocity field are desribed as

$$\delta v_i(\mathbf{x}, t) = {}^{a}\delta v_{iI} T_a(\theta)\, N^I(\xi, \eta), \quad a = 1, 2; \quad I = 1, \cdots, n_e \tag{2.149}$$

Using Eq. (2.140 – 2.149) for the space-time finite element discretization of the weak-form which is given in Eq. (2.139).

$$
\begin{aligned}
&{}^{a}\delta v_{iI}\left[\int_{I_n}\int_{\Omega_h} N^I T_a \rho \frac{\partial N^J T_b}{\partial t} d\Omega dt\right] {}^{b}v_{iJ} + {}^{a}\delta v_{iI}\left[\delta_{1a}\delta_{1b}\int_{\Omega_n} N^I \rho N^J d\Omega\right] {}^{b}v_{iJ} \\
&+ {}^{a}\delta v_{iI}\left\{\int_{I_n} T_a \int_{\Omega_h} \frac{\partial N^I}{\partial x_j}\sigma^n_{ij} d\Omega dt\right\} + {}^{a}\delta v_{iI}\left[\int_{I_n} T_a \tilde{T}_b \int_{\Omega_h} \frac{\partial N^I}{\partial x_j} C_{ijkl} \frac{\partial N^J}{\partial x_l} d\Omega dt\right] {}^{b}v_{kJ} \\
&- {}^{a}\delta v_{iI}\left\{\int_{I_n}\int_{\Gamma^h_i} T_a N^I f^s_i ds dt\right\} - {}^{a}\delta v_{iI}\left\{\int_{I_n}\int_{\Omega_h} T_a N^I \rho b_i d\Omega dt\right\} \\
&- {}^{a}\delta v_{iI}\left[\delta_{1a}\int_{\Omega_n} N^I \rho N^J d\Omega\right] v^-_{iJ} = 0
\end{aligned}
\tag{2.150}
$$

Let us now use the following notation for representing the global space-time nodal vector,

$$\{\mathbf{J}\} := \{J\}^a_i\,(I)$$

here $a = 1, 2$ corresponds to the temporal nodes, $I = 1, \cdots$ corresponds to the I^{th} spatial node, and $i = 1, 2$ corresponds to spatial components. Accordingly, $a = 1$ corresponds to the spatial nodal values of the vector defined at the bottom space-time slab (i.e., at time t^+_n). Similarly, $a = 2$ corresponds to the spatial nodal values of the vector at the top space-time slab (i.e., at time t^-_{n+1}).

A typical space-time finite element matrix will be denoted as:

$$[\mathbf{K}] := [K]^{ab}_{ij}\,(I, J)$$

where $a, b = 1, 2$ corresponds to the temporal nodes, $I = 1, \cdots, n_e$ corresponds to the spatial node, and $i, j = 1, 2$ corresponds to the spatial components.

By using these notations Eq. (2.150) can be expressed as:

$$
\{\delta v\}^a_i\,(I) \cdot \begin{pmatrix} [M]^{ab}_{ij}\,(I, J) \cdot \{v\}^b_j\,(J) + [K]^{ab}_{ij}\,(I, J) \cdot \{v\}^b_j\,(J) \\ + \{J_{\sigma^n}\}^a_i\,(I) - \{J_{ext}\}^a_i\,(I) - \{J_0\}^a_i\,(I) \end{pmatrix} = 0 \tag{2.151}
$$

Since above equation is true for all values of $\{\delta v\}^a_i$ one can obtain the following the system of linear equations:

$$
[M]^{ab}_{ij}\,(I, J) \cdot \{v\}^b_j\,(J) + [K]^{ab}_{ij}\,(I, J) \cdot \{v\}^b_j\,(J) = \{J_{ext}\}^a_i\,(I) + \{J_0\}^a_i\,(I) - \{J_{\sigma^n}\}^a_i\,(I) \tag{2.152}
$$

Matrix-vector form of above equation is given as,

$$[\mathbf{M}] \cdot \{\tilde{\mathbf{v}}\} + [\mathbf{K}] \cdot \{\tilde{\mathbf{v}}\} = \{\mathbf{J}_{ext}\} + \{\mathbf{J}_0\} - \{\mathbf{J}_{\sigma^n}\} \tag{2.153}$$

If Rayleigh damping is used to model the material damping then above equation becomes:

$$[\mathbf{M}] \cdot \{\tilde{\mathbf{v}}\} + [\mathbf{K}] \cdot \{\tilde{\mathbf{v}}\} + \alpha\,[\mathbf{M}_R] \cdot \{\tilde{\mathbf{v}}\} + \beta\,[\mathbf{K}_R] \cdot \{\tilde{\mathbf{v}}\} = \{\mathbf{J}_{ext}\} + \{\mathbf{J}_0\} - \{\mathbf{J}_{\sigma^n}\} \tag{2.154}$$

where α and β are the Rayleigh damping coefficients.

In Eq. (2.153–2.154), $[\mathbf{M}]$ denotes the space-time mass matrix, $[\mathbf{K}]$ denotes the space-time tangent stiffness matrix, $[\mathbf{M}_R]$ is the mass proportional Rayleigh damping matrix, and $[\mathbf{K}_R]$ is the stiffness proportional Rayleigh damping matrix. Furthermore, $\{\mathbf{J}_{ext}\}$ denotes the space-time nodal vectors which contains the contribution of external body force and external boundary traction, $\{\mathbf{J}_0\}$ contains the contribution of initial velocity, and $\{\mathbf{J}_\sigma^n\}$ contains the contribution of initial stress σ^n. In what follows the finite element expressions for these matrices and vectors are described.

$$[\mathbf{M}] := [M]_{ij}^{ab}(I,J) = \delta_{ij} \int_{I_n} T_a \frac{\partial T_b}{\partial t} \int_{\Omega_h} N^I \rho N^J d\Omega dt + \delta_{ij}\delta_{1a}\delta_{1b} \int_{\Omega_n} N^I \rho N^J d\Omega \tag{2.155}$$

$$[\mathbf{K}] := [K]_{ij}^{ab}(I,J) = \int_{I_n} T_a \tilde{T}_b \int_{\Omega_h} \frac{\partial N^I}{\partial x_p} C_{pijq} \frac{\partial N^J}{\partial x_q} d\Omega dt \tag{2.156}$$

$$[\mathbf{M}_R] := [M_R]_{ij}^{ab}(I,J) = \delta_{ij} \int_{I_n} T_a T_b \int_{\Omega_h} N^I N^J d\Omega dt \tag{2.157}$$

$$[\mathbf{K}_R] := [K_R]_{ij}^{ab}(I,J) = \int_{I_n} T_a T_b \int_{\Omega_h} \frac{\partial N^I}{\partial x_p} C_{pijq} \frac{\partial N^J}{\partial x_q} d\Omega dt \tag{2.158}$$

$$\{\mathbf{J}_{ext}\} := \{J_{ext}\}_i^a(I) = \int_{I_n} \int_{\Omega_h} N^I T_a \rho b_i d\Omega dt + \int_{I_n} \int_{\Gamma_i^h} N^I T_a \rho f_i^s ds dt \tag{2.159}$$

$$\{\mathbf{J}_0\} := \{J_0\}_i^a(I) = \delta_{1a}\delta_{ij} \left[\int_{\Omega_h} N^I \rho N^J d\Omega\right] \left\{{}^0v_{jJ}\right\} \tag{2.160}$$

where, $\{^0v_{jJ}\}$ denotes the initial velocity for the space-time slab Q_n, i.e., spatial nodal velocity at time t_n^-. Note that this velocity vector is known from the computation in the previous space-time slab Q_{n-1}.

$$\{\mathbf{J}_{\sigma^n}\} := \{J_{\sigma^n}\}_i^a (I) = \int_{I_n} T_a \int_{\Omega_h} \frac{\partial N^I}{\partial x_j} \sigma_{ij}^n d\Omega dt \tag{2.161}$$

where $\sigma^n := \sigma(\mathbf{x}, t_n)$ is the stress at time t_n which is usually computed from the displacement field at time t_n.

This section briefly discusses the space-time matrices and vectors, however, a detailed description about the derivation of the space-time matrices and space-time vectors can be found in Appendix A.

2.7 Numerical examples

2.7.1 Primary wave propagation in homogeneous linear elastic medium

A theoretical model of homogenous isotropic linear elastic media occupying a square domain, $\Omega = [0, L] \times [0, L]$, is considered in this section for a numerical analysis of v-ST/FEM. The governing equations of the problem are given by Eqs. (2.123–2.127). Further, it is assumed that the elastic media is subjected to the periodic boundary conditions with no external body force (i.e., $b_i = 0$ in Eq. 2.123). The initial conditions for displacement and velocity field corresponding to the Eq. (2.126) and Eq. (2.127) are given as:

$$\mathbf{u}_0 (\mathbf{x}) = \mathbf{d}_0 \cos (k\mathbf{x} \cdot \hat{\mathbf{r}}) , \qquad \mathbf{v}_0 (\mathbf{x}) = ck\mathbf{d}_0 \sin (k\mathbf{x} \cdot \hat{\mathbf{r}}) \tag{2.162}$$

where k is the wave-number, $\hat{\mathbf{r}}$ is the direction vector of the wave propagation, $\mathbf{d}_0 \in \mathbb{R}^2$ denotes the direction of the motion of particles of the medium, and c is related to the speed of the wave in the medium.

The above-mentioned initial conditions create a plane P-wave if $\hat{\mathbf{r}}$ vector is parallel to $\mathbf{d}_0$. The analytical solutions for displacement and velocity can be given by (Achenbach, 2012):

$$\mathbf{u} (\mathbf{x}, t) = \mathbf{d}_0 \cos [k (\mathbf{x} \cdot \hat{\mathbf{r}} - c_p t)] \qquad \mathbf{v} (\mathbf{x}, t) = c_p k\mathbf{d}_0 \sin [k (\mathbf{x} \cdot \hat{\mathbf{r}} - c_p t)] \tag{2.163}$$

where

$$c_p = \sqrt{\frac{\lambda + 2\mu}{\rho}}$$

is the speed of the P-wave.

L	λ	μ	ρ	k	$\mathbf{d}_0$	$\hat{\mathbf{r}}$	c_p
10.0	2.0	1.0	1.0	$\sqrt{2}\pi/5$	$[1,1]^T$	$[1,1]^T/\sqrt{2}$	2.0

Tab. 2.2.: List of constants and parameter values used for the P-wave propagation problem. All variables are dimensionless.

The values of constants and the parameters used for solving the problem are given in Table 2.2, and Fig. 2.19 depicts the physical dimensions of the problem. All variables have been made dimensionless. Letting $\mathbf{u}^h(\mathbf{x},t)$ and $\mathbf{v}^h(\mathbf{x},t)$ denote the numerical solutions computed by employing the v-ST/FEM, the error in displacement field $E_u(t_n)$ and the error in velocity field $E_v(t_n)$ are then defined as:

$$E_u(t_n) := \left\| \mathbf{u}^h(\mathbf{x},t_n) - \mathbf{u}(\mathbf{x},t_n) \right\|_2, \quad E_v(t_n) := \left\| \mathbf{v}^h(\mathbf{x},t_n^-) - \mathbf{v}(\mathbf{x},t_n) \right\|_2 \tag{2.164}$$

where $\|\cdot\|_2$ denotes the L_2 norm given by

$$\|\mathbf{u}\|_2 = \left[\int_\Omega \mathbf{u}(\mathbf{x},t) \cdot \mathbf{u}(\mathbf{x},t)\, d\Omega \right]^{1/2} \tag{2.165}$$

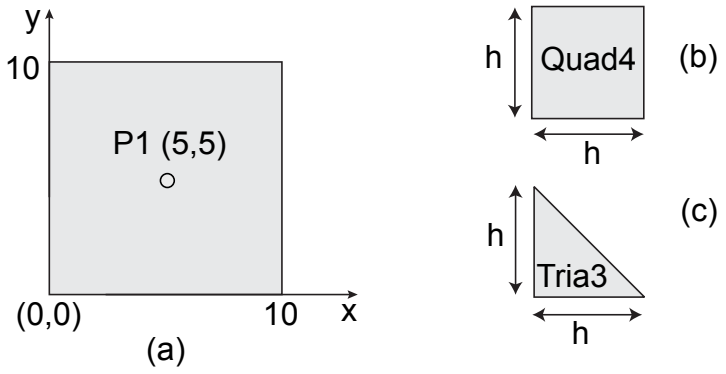

Fig. 2.19.: (a) Schematic diagram of the spatial domain for P-wave propagation problem, (b) bilinear quadrilateral element (Quad4), (c) linear triangular element (Tria3)

The numerical experiments for determining the convergence rate of the solution in the space domain are performed on two sequences of regular linear triangular (Tria3) and bilinear quadrilateral (Quad4) meshes (see Fig. 2.19), while keeping the time-step fixed $\Delta t = 0.1$ sec. Each sequence consists of four meshes with a decreasing mesh size. In Fig. 2.20, the L2 norm of the errors in the displacement and velocity fields at time $t = 1.0$ sec are given in relation to mesh spacing parameter h. Based on the convergence results, it can be stated that the v-ST/FEM formulation is

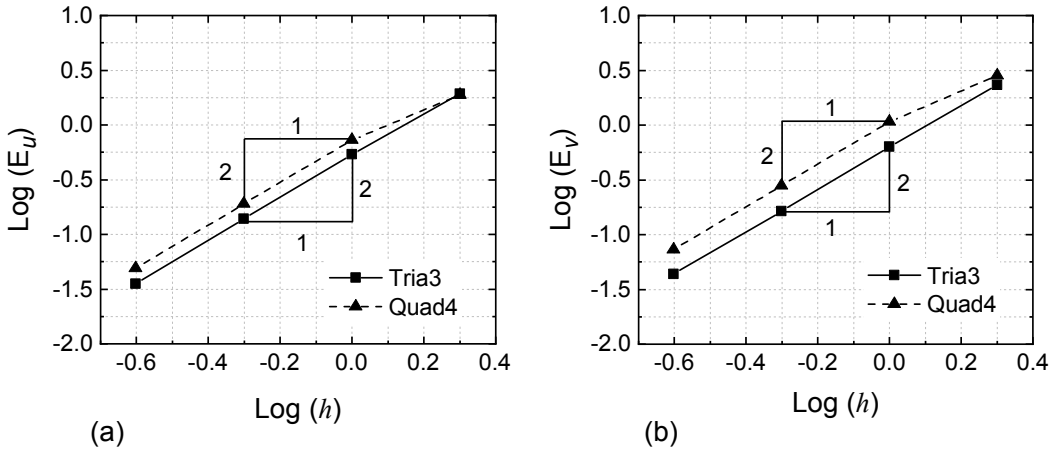

Fig. 2.20.: Rate of convergence of the solutions in space computed at time $t = 1.0$ sec: (a) displacement, and (b) velocity

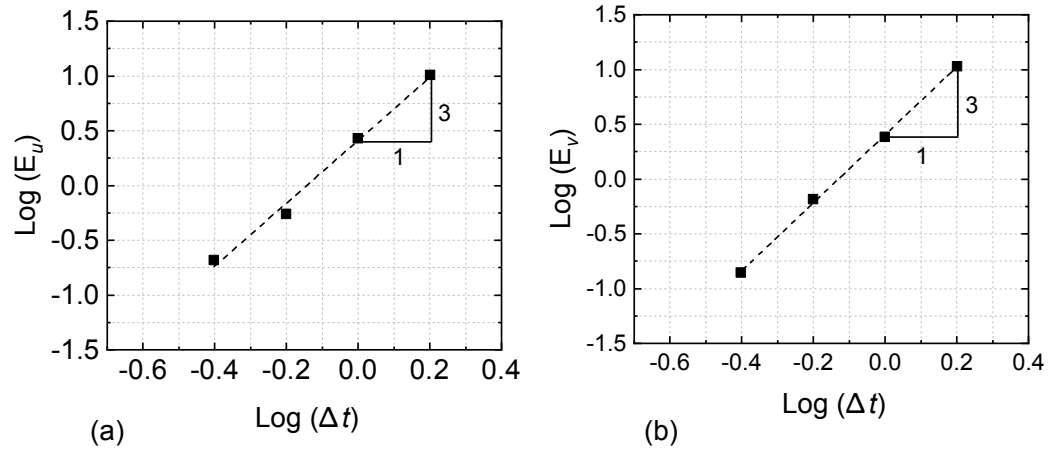

Fig. 2.21.: Rate of convergence of the solutions in time domain at time $t = 35.0$ sec: (a) displacement, and (b) velocity.

nearly second-order accurate in the space for both Quad4 and Tria3 elements. In Fig. 2.20, it is observed that the error for the triangular spatial mesh (Tria3) is less than that of the quadrilateral spatial element (Quad4) for the same mesh spacing. This can be attributed to the perfect alignment of the diagonal of the triangular elements with the characteristic lines of the wave propagation.

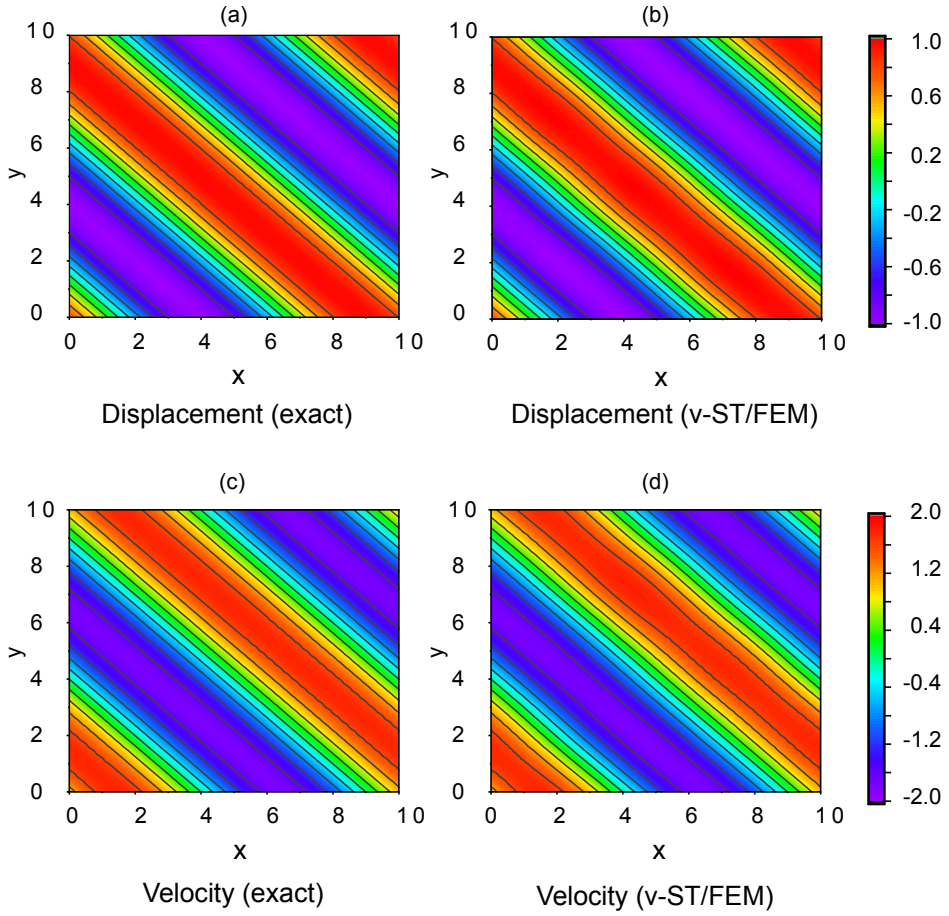

Fig. 2.22.: (a) Exact displacement (x-component) waveforms, (b) displacement (x-component) waveforms obtained by using the v-ST/FEM, (c) exact velocity (x-component) waveforms, (d) velocity (x-component) waveforms obtained by using the v-ST/FEM.

Furthermore, the convergence of the solutions (displacement and velocity) in the time domain is illustrated in Fig. 2.21. It can be seen that both displacement and velocity fields computed by the present method are third order accurate in time. Note that the results presented in Fig. 2.21 are consistent with Eq. (2.114).

Fig. 2.22 illustrates the spatial variation of the displacement and velocity fields obtained by v-ST/FEM. The results are obtained at time $t = 35$ seconds with linear triangular mesh of size $h = 0.25$ and uniform time-step of size $\Delta t = 0.1$ sec. The results advocate the ability of v-ST/FEM to maintain the high-order accuracy of the long-term solutions, especially the displacement and velocity waveforms. This can be attributed to the very low numerical dissipation and dispersion characteristics

of the present method (see also Fig. 2.15 and Fig. 2.16). To further emphasize the accuracy of the long-term solutions, the time histories of the computed displacement and velocity at the midpoint P1 (see Fig. 2.19) and the corresponding relative errors are presented in Fig. 2.23.

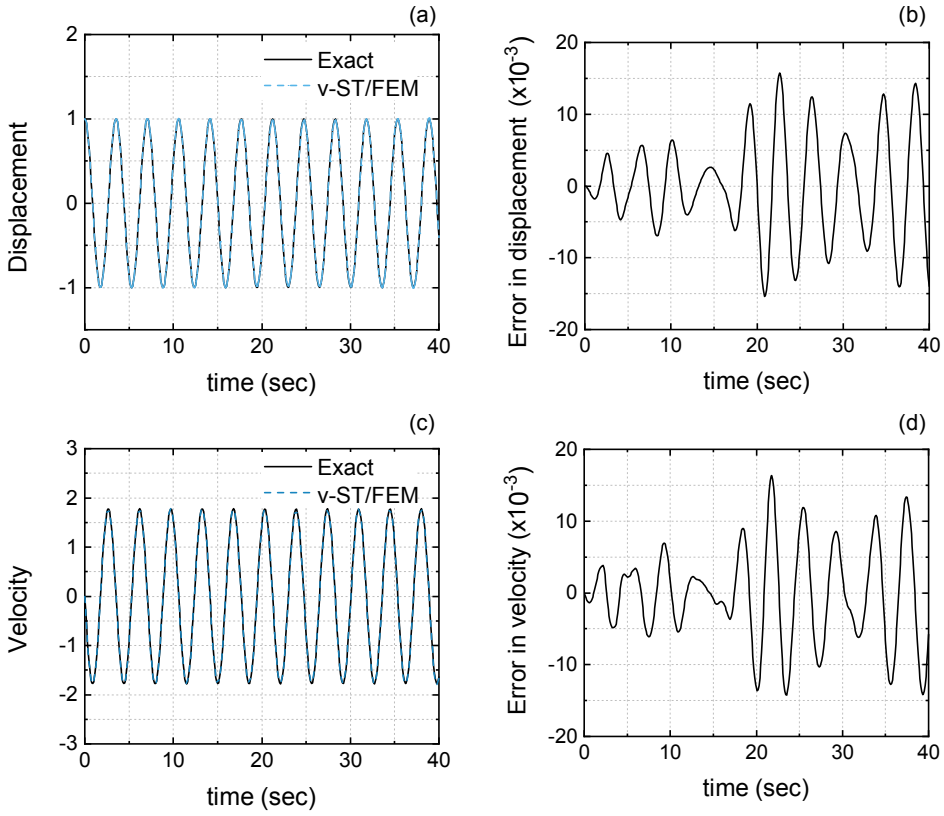

Fig. 2.23.: Temporal variation of the (a) displacement, (b) relative error in displacement, (c) velocity, and (d) relative error in velocity, at the midpoint P1 computed by using v-ST/FEM.

2.7.2 Impulsive response of a fixed-free pile

In this section, we consider a pile of length $L = 50$ m with a unit cross-section area having one fixed end and one end loaded by an axial impulsive force given by a step function, as shown in Fig. 2.24. The mass density ρ is $2500.0\ kg/m^3$ and the Young's modulus E is $1.0 \times 10^{10}\ N/m^2$. The magnitude of the implusive force is $1.0 \times 10^6\ N$. Under these circumstances, the analytical solutions for the stress and velocity fields are discontinuous in the spatial domain and given by the step functions. Furthermore, the displacements are given by the piecewise continuous linear functions (Cormeau, 1991; Li and Wiberg, 1998; Verruijt, 2009).

To solve the problem by using v-ST/FEM, uniform linear spatial elements of size $h = 0.1m$ and a uniform time-step size $\Delta t = 10^{-4}$ sec have been adopted for discretizing the space and time domain, respectively. To assess the performance of the present method, the problem is also solved with semi-discretized FEM techniques

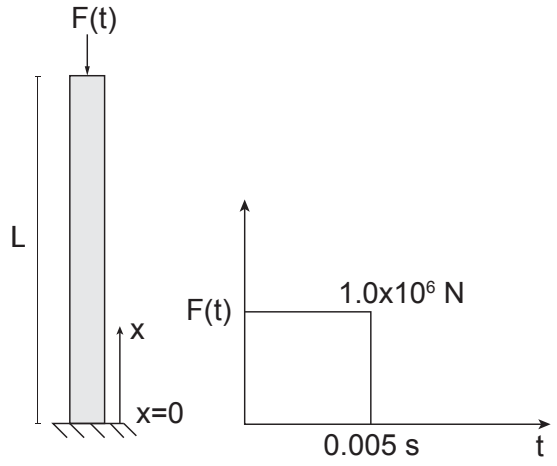

Fig. 2.24.: Geometry, boundary conditions, and impulse loading for fixed-free pile problem.

using the same mesh parameters. In the latter case, the trapezoidal rule and the HHT-α method (with $\alpha = -1/3$) have been used as the time-stepping algorithms. The results of the stress field, velocity field, and displacement field obtained by different schemes are compared in Fig. 2.25, Fig. 2.26, and Fig. 2.27, respectively.

It is observed that the solutions for the stress and velocity fields obtained by the semi-discrete algorithms contain severe oscillations. Even worse, no improvement whatsoever is obtained when refining the mesh spacing or the time-step size. Further, in the case of the Newmark-beta method, these oscillations are present in the whole spatial domain; and thus, the accuracy of the stress and velocity fields deteriorate over time (see Fig. 2.25 and Fig. 2.26). The poor performance with the Newmark-beta method is due to the absence of algorithmic damping, as discussed in previous sections. The HHT-α method improves the solutions by attenuating higher frequencies; however, the results are not satisfactory for the selected time-step size as the oscillations are still present. It is remarkable that v-ST/FEM completely localizes the oscillations in the stress and velocity fields near the point of discontinuity and yields very accurate solutions. The localization phenomenon can be attributed to the presence of jump discontinuity in the velocity field. The jump in the velocity field adds artificial viscous damping to the system, subsequently, increasing the accuracy and stabilizing the solutions (Hulbert and Hughes, 1990; Johnson, 1993). Furthermore, the presence of overshooting and undershooting around the point of discontinuity is related to the famous Gibbs phenomenon in the Fourier analysis (Olver, 2016).

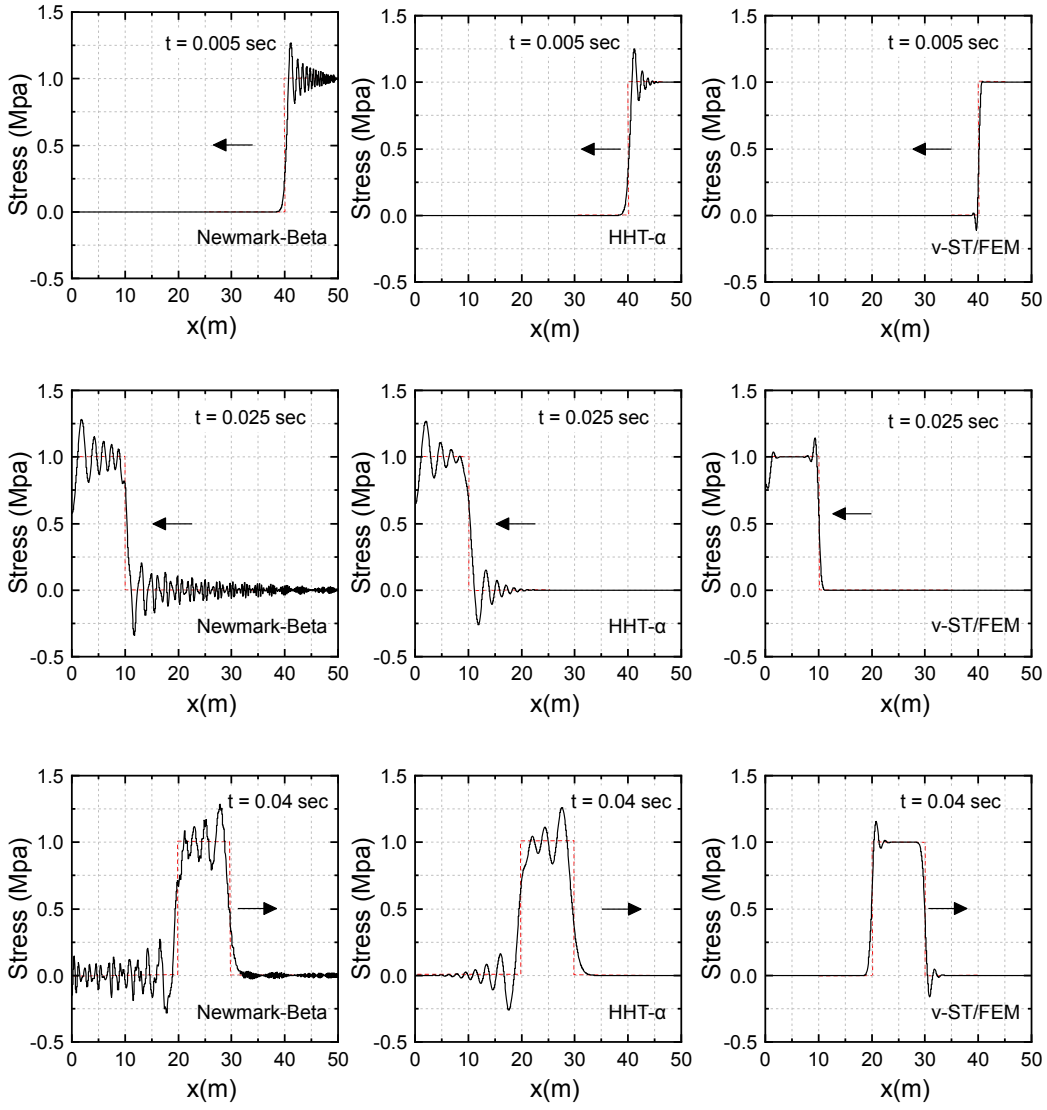

Fig. 2.25.: Stress field computed by employing the Newmark-beta method (First column), HHT-α (Second column), and v-ST/FEM (Third column) at various timesteps with linear spatial elements. Direction of wave propagation is denoted by the arrow, and dotted lines represent the analytical solutions.

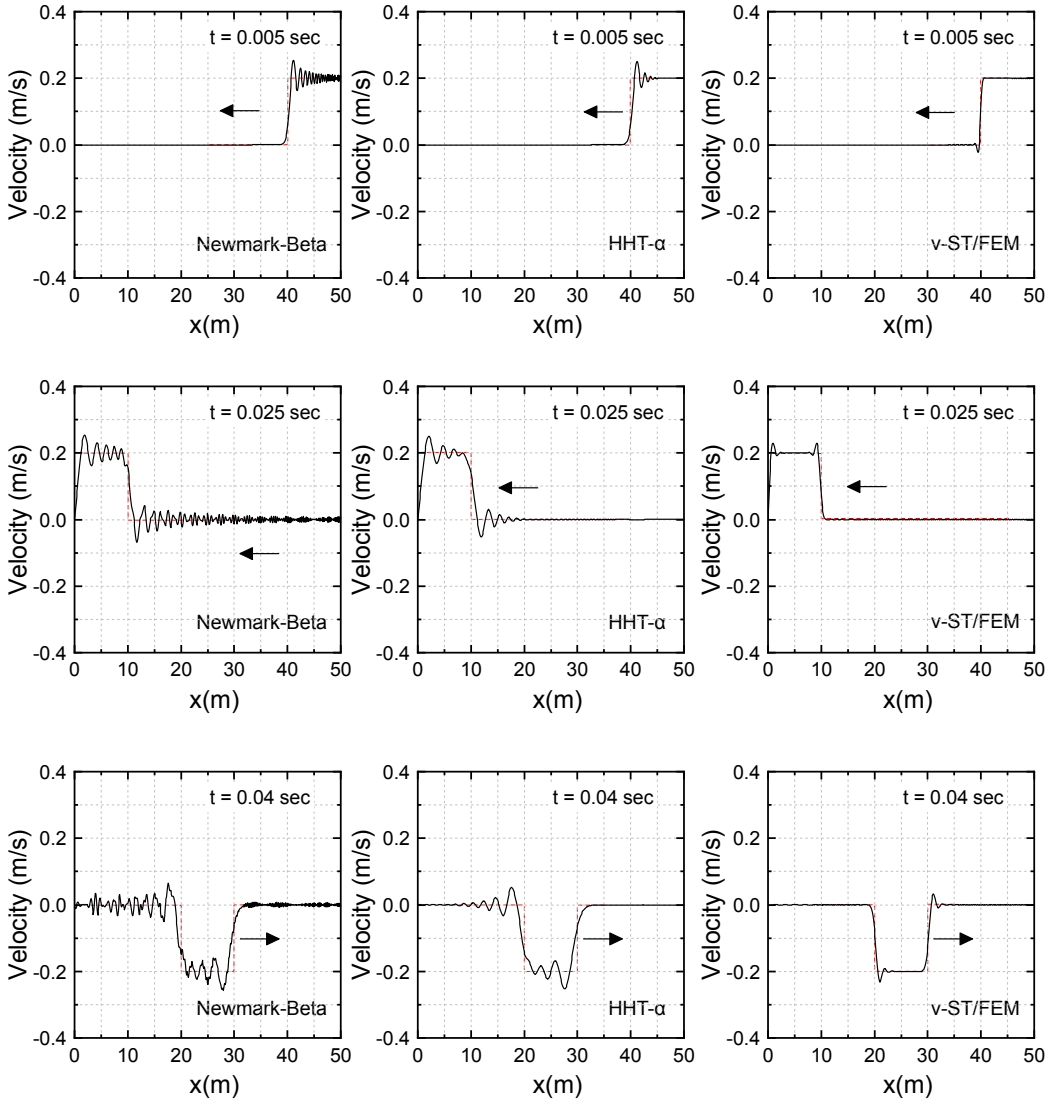

Fig. 2.26.: Velocity field computed by employing the Newmark-beta method (First column), HHT-α (Second column), and v-ST/FEM (Third column) at various time-steps with linear spatial elements. Direction of wave propagation is denoted by the arrow, and dotted lines represent the analytical solutions.

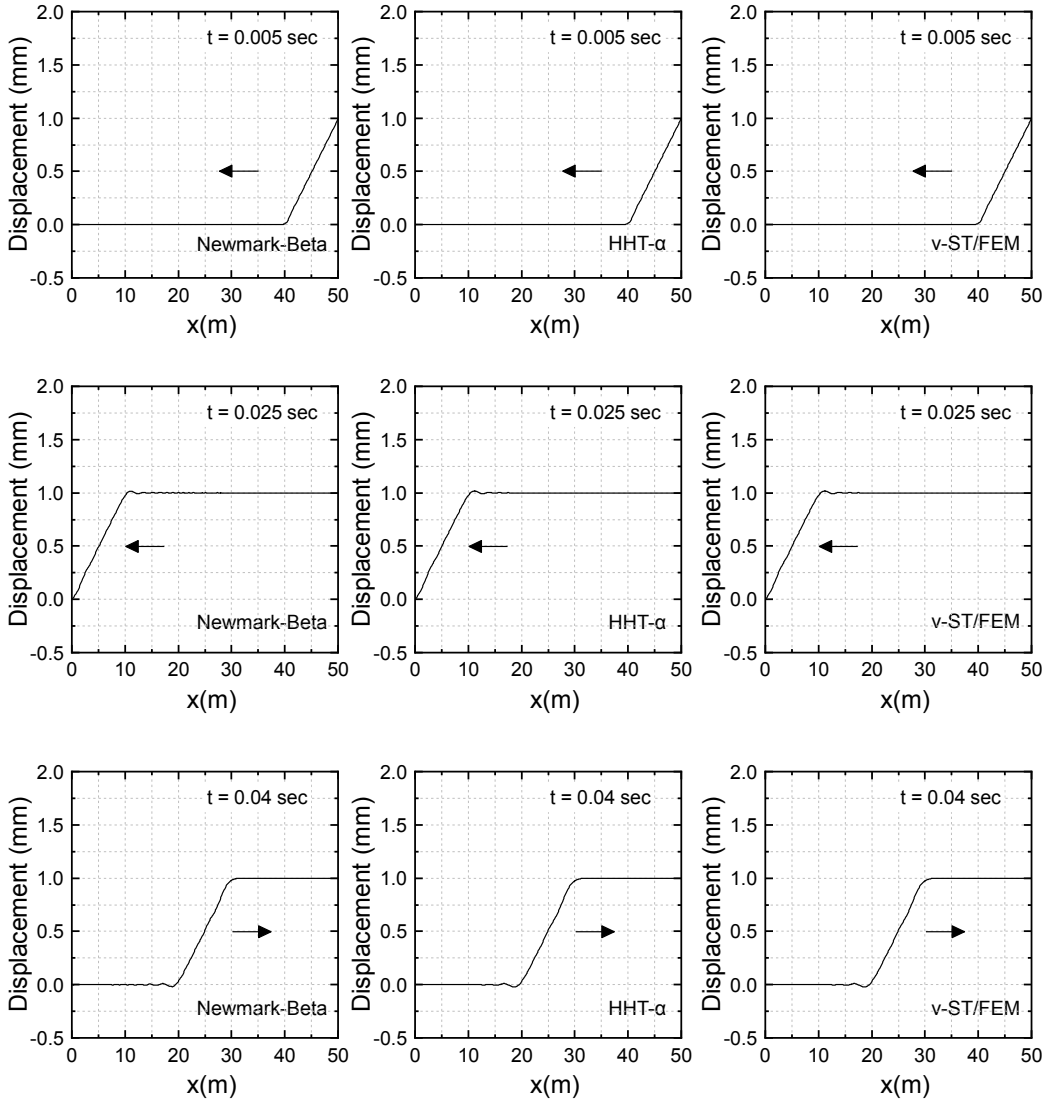

Fig. 2.27.: Displacement field computed by employing the Newmark-beta method (First column), HHT-α (Second column), and v-ST/FEM (Third column) at various timesteps with linear spatial elements. Direction of wave propagation is denoted by the arrow.

2.7.3 Dynamic plate load test (DPLT)

In this section, an attempt is made to validate v-ST/FEM by simulating the dynamic plate loading test (DPLT) using a light falling weight deflectometer (LFWD). DPLT using LFWD is a non-destructive technique for a quick assessment of the field compaction quality. In DPLT, a rigid circular loading plate of radius 0.15 m is placed on the soil surface and subjected to an impulse load generated by the falling weight from a specified height onto the plate. Subsequently, the induced soil movements are recorded and the dynamic resilience modulus of the tested material is computed by some empirical relations. A complete description of the test can be found elsewhere (Adam et al., 2009; Tawfik and El-Mossallamy, 2017).

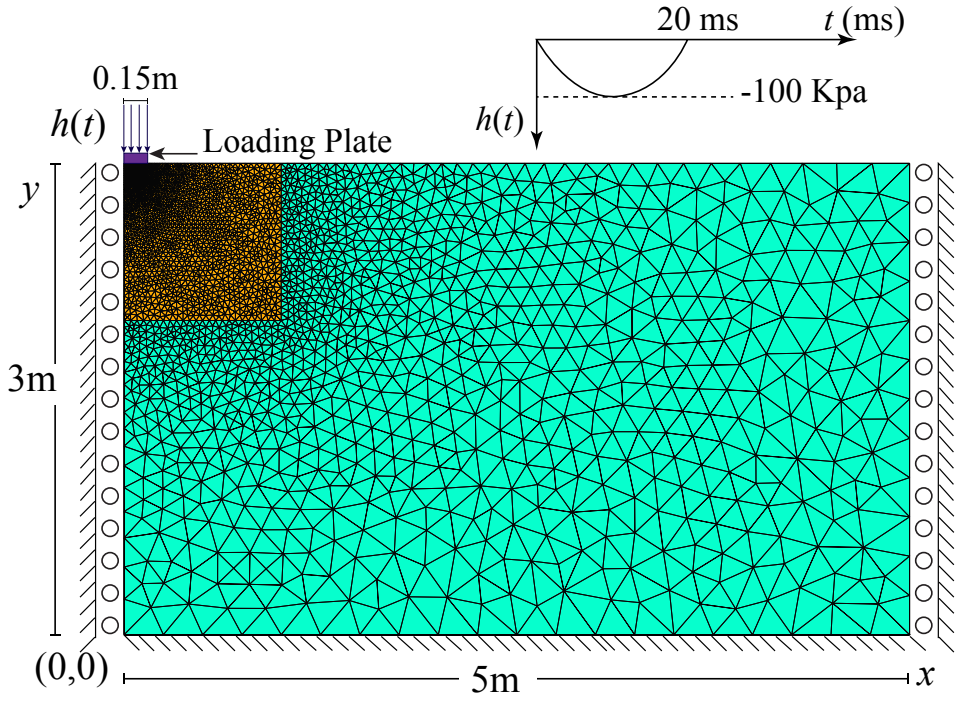

Fig. 2.28.: Geometry, boundary conditions and spatial mesh adopted for simulating DPLT using v-ST/FEM.

In the present study, DPLT is simulated by a two-dimensional axisymmetric v-ST/FEM model, where the center of the loading plate is positioned along the axis of symmetry. The geometry, boundary conditions, and spatial mesh of the finite element model are depicted in Fig. 2.28. There are 5201 linear triangular elements (Tria3) and 2688 nodes present in the spatial mesh. The impulse load due to the falling weight is modeled by using an equivalent uniform vertical stress pulse of amplitude 100 kPa

and a time duration of 20 ms (Adam et al., 2009). The stress pulse $h(t)$ acting on the loading plate is defined by a half sine wave as:

$$h(t) = -10^5 \sin(50\pi t)\,\mathrm{N/m^2}$$

The total simulation time T is set to 30 ms, and the linear time elements of size $\Delta t = 1$ ms have been adopted for discretizing the time domain. Subsequently, the results computed by the proposed method are compared with the two DPLT studies available in the literature. The first study is denoted as S1 where the in-situ LFWD test was conducted by Tawfik and El-Mossallamy, 2017, and the second study is denoted by S2 in which the numerical investigation was conducted by Adam et al., 2009 using the Boundary Element Method (BEM). In these studies (i.e., S1 and S2), the soils have different values for Young's modulus E and common values for Poisson's ratio ν and mass density ρ, as shown in Table 2.3.

Elastic parameters	Method	d_{max}	p_{max}
$E = 65$ Mpa	v-ST/FEM	0.33 mm	90.0 kPa
$\nu = 0.212$	In-situ study (S1)	0.35 mm	100 kPa
$\rho = 2000\ kg/m^3$			
$E = 32$ Mpa	v-ST/FEM	0.67 mm	90.0 kPa
$\nu = 0.212$	BEM study (S2)	0.65 mm	93.1 kPa
$\rho = 2000\ kg/m^3$			

Tab. 2.3.: List of elastic material parameters, and the results of maximum plate deflection and maximum soil-plate normal contact stress obtained by different schemes.

The results of the time histories of the vertical displacement and the velocity of the loading plate, and the soil-plate contact stress are plotted in Fig. 2.29. The maximum deflection of the plate d_{max} obtained by v-ST/FEM is about 0.33 mm and 0.67 mm corresponding to the material parameters used in the studies S1 and S2, respectively. From Table 2.3, it is evident that these computed values for d_{max} are in good agreement with those reported in studies S1 and S2. In the present study, the maximum soil-plate normal contact stress p_{max} is about 90 kPa; which lower than the values reported in studies S1 and S2 (see Table 2.3). This may be due to the use of linear triangular elements and the absence of the soil-plate interface elements in the present formulation. Furthermore, the maximum deflection of the plate occurs at time $t_d = 11$ ms, and the maximum contact stress p_{max} occurs at time $t_p = 10$ ms. The displacement contours at these time steps are depicted in Fig. 2.30, where displacements are normalized with respect to the maximum deflection of the plate.

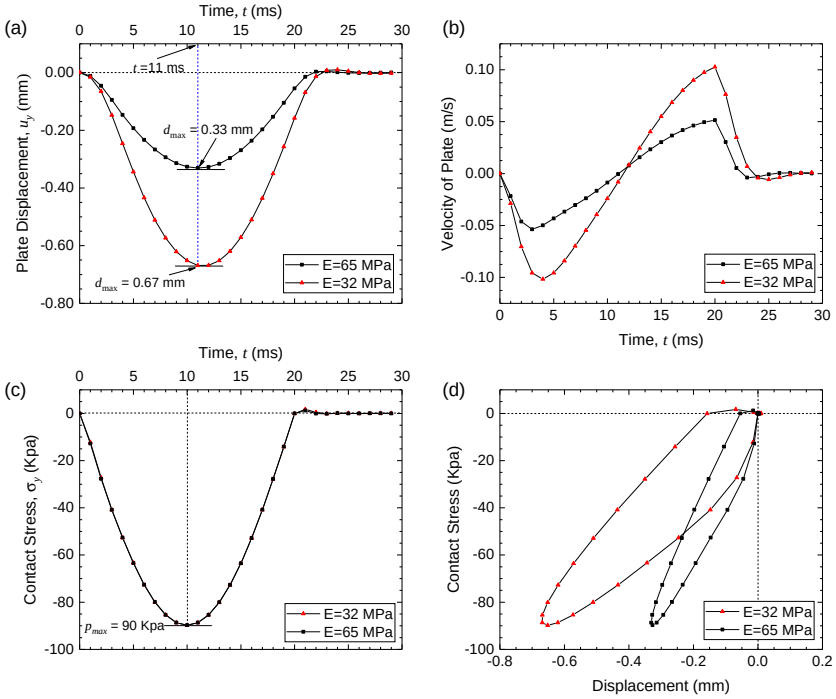

Fig. 2.29.: Temporal variation of the vertical displacement of plate (top-left), the vertical velocity of plate (top-right), and soil-plate contact stress (bottom-left), and variation of normal contact stress with the plate displacement (bottom-right) obtained by v-ST/FEM.

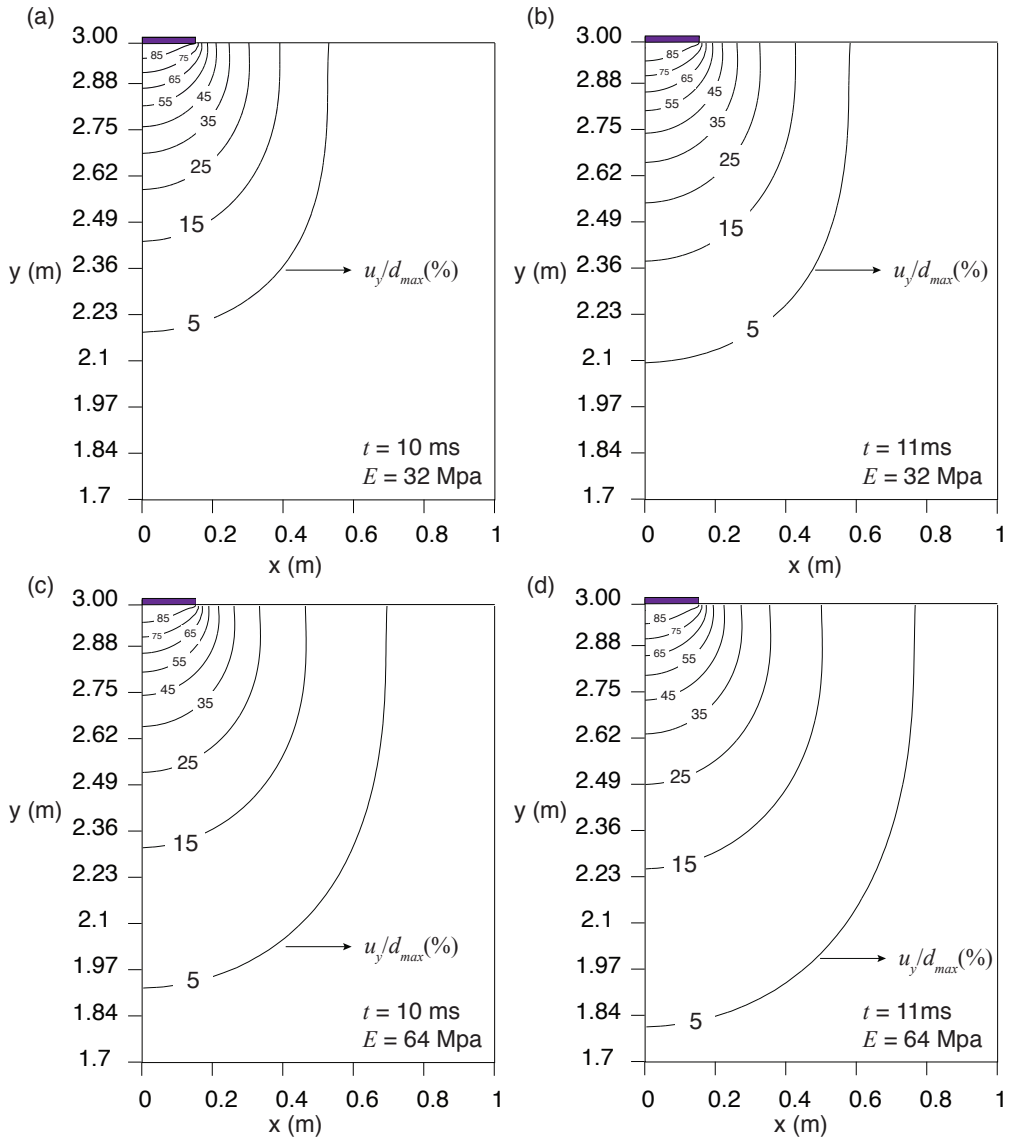

Fig. 2.30.: Normalized contours of the vertical displacements computed by v-ST/FEM at various time-steps.

2.8 Summary

In this chapter, the concept of time-discontinuous Galerkin (TDG) method is presented. The details of single-field and two-field TDG schemes, such as stability, the order of accuracy, and algorithmic damping, are discussed. Subsequently, a velocity-based single-field TDG space-time finite element method has been been developed for elastodynamics problems. The main characteristics of this method is summarized below.

(i) In v-ST/FEM velocity is the primary unknown which is discontinuous in time and continuous in space. The time-continuity of the velocity field is satisfied in a weak sense.

(ii) The displacement field is obtained by time-integration of the velocity field in a post-processing step. These displacement field are then used to compute stress-field. Both stress and displacement field remain continuous in time.

(iii) The advantage of v-ST/FEM is that it involves less number of unknowns–unlike other ST/FEM– which makes v-ST/FEM applicable to the large-scale practical problems at relatively low computational cost.

(iv) It is demonstrated that the present method is unconditionally stable and third-order accurate in time for linear interpolation of velocity in time.

(v) The numerical dissipation (amplitude decay) and dispersion (phase-delay) of v-ST/FEM is smaller than the two-field ST/FEM and semi-discrete algorithms.

(vi) In the case of a shock problem, the performance of v-ST/FEM was found to be superior to HHT-α and Newmark-beta method. v-ST/FEM is able to remove the spurious oscillations unlike HHT-α and Newmark-beta algorithms.

(vii) The numerical characteristics of the v-ST/FEM scheme, therefore, make it highly suitable for computing the response of bodies subjected to dynamic loading conditions, such as fast-moving loads, impulsive loading, long-duration seismic loading, among others.

(viii) It is shown that the proposed scheme is non-dissipative in high-frequency regime, and can attenuate only the middle band of frequencies. Therefore, the only drawback to the present methodology is that it does not include a parameter to control the numerical dissipation of the high-frequencies.

3 Elastic Wave Propagation in Unbounded Domain and Artificial Boundary Conditions

3.1 Introduction

In many fields of both engineering and physics the problems ranging from simulation of earthquake ground motion (Bao et al., 1998; Bielak et al., 2003) and dynamic soil-structure interaction (Wolf, 1985; Wolf and Hall, 1988), to electromagnetic waves (Chew, 1995), and quantum mechanics (Alonso-Mallo and Reguera, 2003) may be best represented or modeled by considering the linear wave propagation on infinite or semi-infinite unbounded domain. Such modeling is especially of interest in the design of earth-structures such as dam, tunnels, embankments, hospital and residential buildings etc. against the transient loading and vibrations caused by the high-speed trains, road-traffic, underground explosions, and more importantly earthquake motion. In these problems the finite dimensional structure dynamically interacts with the adjacent unbounded soil domain, and therefore the two domains mutually influence the dynamic responses of each other (Wolf and Song, 1996; Burman et al., 2012).

For the computation of the dynamic SSI problems, a surface called *interaction horizon* (Wolf and Song, 1996) that encloses the structure and forms the boundary of the computational domain has to be selected. The objective of these domain reduction techniques is twofold; decreasing the computation burden by reducing the size of the problem and enforcing the so called radiation condition thus prohibiting any spurious reflections at the artificial truncated boundaries (ATB). In this way, ATB simulate the effects of the far field on the dynamic response of both the structure and the near field.

The structure of the chapter is as follows. In section 2 of this chapter basic theory of wave propagation in elastic solids is given. Section 3 of this chapter reviews some of the most popular boundary conditions for solving wave propagation problems in unbounded domains. Section 4 of this chapter provides the derivation of viscous boundary condition first proposed by Lysmer and Kuhlemeyer, 1969 and discusses

its characteristics. Subsequently, in section 5 of this chapter, viscous boundary conditions are modified to allow seismic excitation to enter the computational domain.

3.2 Wave propagation in elastic solids

Linear and nonlinear dynamic response of the deformable media can be described by a wave propagation phenomenon. A deformable media subjected to a transient loading condition produces mechanical waves; as elements of the medium are deformed the disturbance is transmitted from one point in space to the next. The local mechanical disturbances of a medium is not instantaneously detected at positions that are at a distance from the region of excitation. It takes time for a disturbance to propagate from its source to other positions. In this way as the disturbance propagates through the medium it carries along amounts of energy due to motions of particles of medium about their equilibrium position.

Further, the transmission of mechanical wave depends mainly upon the deformation characteristics and inertia of the medium. As it will be seen later both stiffness and inertia of a medium tend decrease the wave speed. A rigid medium, (e.g. rocks with very high stiffness) deforms insignificantly and the mechanical disturbance travels almost instantaneously in it. Similarly, a hypothetical massless medium (i.e. no inertia) allows mechanical wave to travel without any delay. These concepts have been used widely to model the interaction between the soil/rock foundation and the earth structures such as concrete gravity dams. It is important to note that the inertia of a system first offers resistance to motion, but once the medium is in motion inertia with the resilience of the medium tends to sustain the motion (Achenbach, 2012).

3.2.1 Governing equations of motion

Consider a body $\mathfrak{B}$ occupying a regular domain $\Omega \subset \mathbb{R}^{n_{sd}}$ in the space which may be bounded or unbounded. n_{sd} is the number of spatial dimensions. Let Γ denotes the boundary of the domain, and $\bar{\Omega} = \Omega \cup \Gamma$ be the closure of Ω. Let indices i, j, k, l take values from $1, \cdots, n_{sd}$. The system of equations describing the motion of a homogeneous, isotropic, linearly elastic body consists of the Cauchy's equation of the motion, generalized Hooke's law and linearized strain-displacement relationship:

$$\frac{\partial \sigma_{ij}}{\partial x_j} + \rho b_i = \rho \frac{\partial^2 u_i}{\partial t^2} \tag{3.1}$$

$$\sigma_{ij} = \lambda \epsilon_{kk} \delta_{ij} + 2\mu \epsilon_{ij} \tag{3.2}$$

$$\epsilon_{ij} = \frac{1}{2}\left(\frac{\partial u_i}{\partial x_j} + \frac{\partial u_j}{\partial x_i}\right) \tag{3.3}$$

Here, λ and μ are the Lame's parameters. Subsequently, the displacement equation of motion Eq. (3.4) can be obtained by using Eq. (3.2) and (3.3) in Eq. (3.1)

$$\mu \frac{\partial^2 u_i}{\partial x_j^2} + (\lambda + \mu) \frac{\partial^2 u_j}{\partial x_j \partial x_i} + \rho b_i = \rho \frac{\partial^2 u_i}{\partial t^2} \tag{3.4}$$

To obtain a unique solution of the problem boundary conditions on the boundary Γ and initial state of the body must be prescribed. Some of the commonly used boundary conditions are mentioned below.

1. *Displacement boundary conditions*: Components of displacement field $u_i(\mathbf{x}, t)$ are prescribed on the boundary

$$u_i(\mathbf{x}, t) = g_i(\mathbf{x}, t) \quad on \quad \Gamma$$

2. *Traction boundary conditions*: This boundary condition relates the stress σ_{ij} to the externally applied surface force t_i using the Cauchy's formula

$$\sigma_{ij} n_j = t_i \quad on \quad \Gamma$$

3. *Mixed boundary conditions*: On a part of the boundary $\Gamma_i^g \subset \Gamma$ displacement u_i is prescribed and on the remaining part of the boundary $\Gamma_i^h \subset \Gamma$ traction boundary condition is imposed.

$$u_i(\mathbf{x}, t) = g_i(\mathbf{x}, t) \quad on \quad \Gamma_i^g$$
$$\sigma_{ij} n_j = t_i \quad on \quad \Gamma_i^h$$

with

$$\Gamma_i^g \cup \Gamma_i^h = \Gamma \quad and \quad \Gamma_i^g \cap \Gamma_i^h = \phi$$

The initial state of the body, the displacement and velocity field at time $t = 0$, must be well defined to complete the problem.

$$u_i(\mathbf{x}, 0) = u_i^0(\mathbf{x}) \quad \forall \mathbf{x} \in \bar{\Omega}$$

$$\dot{u}_i(\mathbf{x}, 0) = v_i^0(\mathbf{x}) \quad \forall \mathbf{x} \in \bar{\Omega}$$

The ordered pair $(\mathbf{u}, \sigma)$ defines the elastodynamic state on $\left(\bar{\Omega} \times T\right)$ with the displacement field $\mathbf{u}$ and the stress field σ, corresponding to given external body force density $\mathbf{b}$, the mass density $\rho \in \mathbb{R}^+$ and the Lame parameters $\lambda, \mu \in \mathbb{R}^+$, if $\mathbf{u} \in C^2(\Omega \times T) \cap C^1\left(\bar{\Omega} \times T\right)$, $\sigma \in C^1\left(\bar{\Omega} \times T\right)$ and $\mathbf{b} \in C^1\left(\bar{\Omega} \times T\right)$,and Eq. (3.1 – 3.3) is satisfied for all $(\mathbf{x}, t) \in \Omega \times T$ along with prescribed initial and boundary conditions.

3.2.2 Displacement potentials

The displacement equation of motion Eq. (3.4) couples all the displacement components $u_i(\mathbf{x}, t)$. This equation, however, can be decoupled by introducing the concept of displacement potentials (Achenbach, 2012). For brevity, Eq. (3.4) is first written in its vector form.

$$\mu \nabla^2 \mathbf{u} + (\lambda + \mu) \nabla \otimes (\nabla \cdot \mathbf{u}) + \rho \mathbf{b} = \rho \frac{\partial^2 \mathbf{u}}{\partial t^2} \tag{3.5}$$

Let $\mathbf{u} \in C^2(\Omega \times T)$ and $\mathbf{b} \in C^1(\Omega \times T)$ satisfies Eq. (3.5) for all $(\mathbf{x}, t) \in \Omega \times T$. Let the Helmholtz decomposition of the external body force density $\mathbf{b}$[1] is given by

$$\mathbf{b} = c_L^2 \nabla F + c_T^2 \nabla \times \mathbf{G} \tag{3.6}$$

Then there exists a scalar function $\phi : \Omega \times T \to \mathbb{R}$ and a vector-valued function $\boldsymbol{\psi} : \Omega \times T \to \mathbb{R}^{n_{sd}}$ such that the displacement field can be described by

$$\mathbf{u} = \nabla \phi + \nabla \times \boldsymbol{\psi} \tag{3.7}$$

Further, the displacement potential $\boldsymbol{\psi}$ usually satisfies the following constraint equation.

$$\nabla \cdot \boldsymbol{\psi} = 0 \tag{3.8}$$

[1] In Eq. (3.6) F and $\mathbf{G}$ are bounded and continuous, and are differentiable at interior points where b is continuous.

After substituting Eq. (3.6 – 3.7) into Eq. (3.5) one can obtain the following two uncoupled wave equations.

$$\nabla^2\phi + F = \frac{1}{c_L^2}\frac{\partial^2\phi}{\partial t^2} \tag{3.9}$$

and

$$\nabla^2\boldsymbol{\psi} + \mathbf{G} = \frac{1}{c_T^2}\frac{\partial^2\boldsymbol{\psi}}{\partial t^2} \tag{3.10}$$

Eq. (3.9) is a scalar wave equation and Eq. (3.10) represents wave equation in n_{sd} components of $\boldsymbol{\psi}$. The characteristic-speed c_L and c_T is given by Eq. (3.11) and (3.12), respectively.

$$c_L = \sqrt{\frac{\lambda + 2\mu}{\rho}} \tag{3.11}$$

$$c_T = \sqrt{\frac{\mu}{\rho}} \tag{3.12}$$

3.2.3 Longitudinal and transverse plane waves

Consider a plane displacement wave traveling with phase velocity c in the direction $\mathbf{p}$ is given by

$$\mathbf{u} = \mathbf{d}f\left(\mathbf{x}\cdot\mathbf{p} - ct\right) \tag{3.13}$$

where $\mathbf{d}$ is the direction of motion of the particles, $\mathbf{x}$ is the position vector of the particle in the space and the argument of $f(\cdot)$ is called the phase of the wave and given by

$$\eta = \mathbf{x}\cdot\mathbf{p} - ct \tag{3.14}$$

It is evident from Eq. (3.13) that at any given time t the plane of constant phase, i.e. $\mathbf{x}\cdot\mathbf{p} =$ constant, are normal to the direction of wave propagation. Further, the planes moves in the direction $\mathbf{p}$ with phase-velocity c.

Furthermore, the displacement given by Eq. (3.13) can satisfy the wave equation Eq. (3.4) only in two cases:

1. *Longitudinal wave*[2]: In this case the motion of particles is in the direction of the wave propagation (see Fig. 3.2) and phase-velocity is given by Eq. (3.11). Mathematically speaking,

$$\mathbf{d} = \pm\mathbf{p}; \quad c = c_L \tag{3.15}$$

[2]In literature longitudinal waves are also known as the primary-wave, a P-wave, a pressure-wave, a irrotational-wave, or a dilatation-wave

and

$$\mathbf{u} = \pm \mathbf{p} f\left(\mathbf{x} \cdot \mathbf{p} - c_L t\right) \tag{3.16}$$

2. *Transverse wave*[3]: In this case the motion of particles of media is restricted in the plane that is normal to the direction of wave propagation (see Fig. 3.2) and the phase velocity c is given by Eq. (3.12).

$$\mathbf{p} \cdot \mathbf{d} = 0; \quad c = c_T \tag{3.17}$$

The transverse waves further categorized into *SV-waves* and *SH-waves* depending upon the plane in which particle motion resides. Let's say the wave is traveling in (x_1, x_2) plane then in case of the *SV-waves* particle motion resides in the same (x_1, x_2) plane but normal to the direction of wave propagation. Therefore, $\mathbf{d}$ can be represented by

$$\mathbf{d} = \mathbf{e}_3 \times \mathbf{p} \tag{3.18}$$

However, in the case of *SH-waves* particles will move in the x_3 direction, i.e.,

$$\mathbf{d} = \mathbf{e}_3 \tag{3.19}$$

where $\mathbf{e}_3 = [0, 0, 1]^T$.

Finally, a complete classification of plane waves can be found in Fig .3.1. For clarity the plane wave propagation in unbounded elastic domain and the corresponding particle motions are depicted in Fig. 3.2.

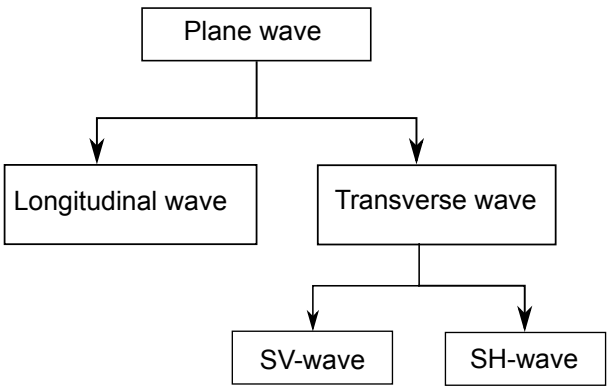

Fig. 3.1.: Classification of plane waves in unbounded elastic media

A special case of plane waves is plane harmonic waves; material points on the plane of constant phase performs harmonic motion. The studies on plane harmonic

[3] In literature transverse waves are also known as the secondary-wave, a shear-wave, a S-wave, or a distortional-wave.

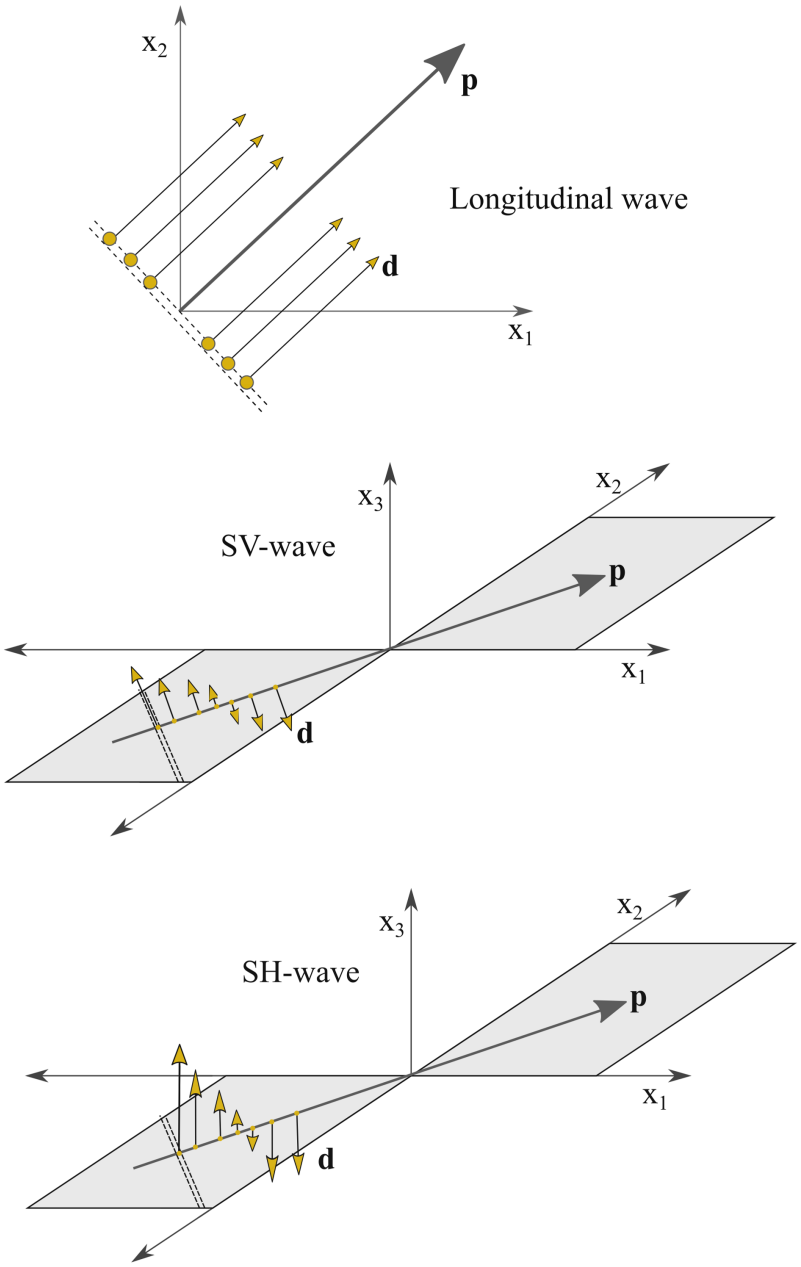

Fig. 3.2.: Schematic diagram of longitudinal and transverse wave motion in unbounded elastic media

waves in a linearly elastic medium are of interest by the virtue of the applicability of linear superimposition. By the use of Fourier series, harmonic waves can be used to describe the propagation of periodic disturbances. For plane harmonic waves Eq. (3.13) becomes

$$\mathbf{u} = A\mathbf{d}\exp\left[ik\left(\mathbf{x}\cdot\mathbf{p} - ct\right)\right] \tag{3.20}$$

where $A \in \mathbb{R}$ is the amplitude of the particle motion, $i = \sqrt{-1}$, $k = \omega c \in \mathbb{R}$ is called the wave number, $c \in \mathbb{R}$ is the phase velocity, $\omega \in \mathbb{R}$ is the circular frequency of the harmonic motion of the material points, $\mathbf{d} \in \mathbb{R}^{n_{sd}}$ is the direction of motion of particle and $\mathbf{p}$ is direction of propagation of wavefront. Since the phase velocity does not depend upon the wave number (or the wavelength), the plane harmonic waves in unbounded homogeneous, isotropic, linearly elastic media are not dispersive.

Noting Eq. (3.15) and Eq. (3.20) the longitudinal plane harmonic wave traveling in (x_1, x_2) plane in the direction $\mathbf{p} = [\sin\theta, \cos\theta, 0]$ can be described as follows

$$\mathbf{u} = A\begin{bmatrix}\sin\theta\\ \cos\theta\\ 0\end{bmatrix}\exp\left[ik\left(x_1\sin\theta_1 + x_2\cos\theta_2 - c_L t\right)\right] \tag{3.21}$$

Similarly, using Eq. (3.18) in Eq. (3.20), the *SV-wave* traveling in (x_1, x_2) plane and in the direction $\mathbf{p} = [\sin\theta, \cos\theta, 0]$ is given by

$$\mathbf{u} = A\begin{bmatrix}-\cos\theta\\ \sin\theta\\ 0\end{bmatrix}\exp\left[ik\left(x_1\sin\theta + x_2\cos\theta - c_T t\right)\right] \tag{3.22}$$

The equation of SH-wave propagating in the direction $\mathbf{p} = [\sin\theta, \cos\theta, 0]$ can be obtained by using Eq. (3.19)

$$u_3 = A\exp\left[ik\left(x_1\sin\theta + x_2\cos\theta - c_T t\right)\right] \tag{3.23}$$

For the displacement given by Eq. (3.20) the stresses generated in the elastic body are computed using the Hooke's law (see Eq. (3.2 – 3.3))

$$\sigma = ikA\left[\lambda\mathbf{d}\cdot\mathbf{p} + \mu\left(\mathbf{d}\otimes\mathbf{p} + \mathbf{p}\otimes\mathbf{d}\right)\right]\exp\left[ik\left(\mathbf{x}\cdot\mathbf{p} - ct\right)\right] \tag{3.24}$$

3.2.4 Reflection and refraction of plane waves

The presence of different materials significantly affects the systems of waves propagating through that medium. When waves reach the interface between two medium with different material properties, part of the wave is reflected and the part is

transmitted through the interface (Achenbach, 2012). The ratio of the mechanical impedances of two media completely determines the nature of the reflection and the transmission at the interface.

In such system of material discontinuity, system of plane waves — reflected and refracted waves at the interface — can be superposed to represent an incident wave. For a given incident wave, the amplitude A, the unit propagation vectors $\mathbf{p}$ and the wave numbers k of the reflected and refracted waves are computed by satisfying the continuity conditions on the displacements and stress at the interface between two media.

Consider two joined elastic half-spaces in (x_1, x_2) plane. Let $x_2 = 0$ be the interface plane between these two media. The material properties of the medium carrying the incident and reflected waves (i.e. $x_2 < 0$) are the Lame elastic constants λ and μ, velocity of longitudinal wave c_L, velocity of transverse wave c_T and the mass density ρ. Similarly, the material constants of the medium into which refraction takes place are $\lambda^B, \mu^B, c_L^B, c_T^B, \rho^B$. The superscript with a number $n = 1, 2, 3, 4$ enclosed in parenthesis is used for denoting the reflected and refracted waves. The number 0 is used for denoting the incidental wave.

***Reflection and refraction of SH-wave*:** Consider the following incidental *SH-wave* traveling in the direction $\mathbf{p} = [\sin\theta, \cos\theta, 0]$ (see Fig. 3.3).

$$u_3^{(0)} = A_0 \exp\left[ik_0 \left(x_1 \sin\theta_0 + x_2 \cos\theta_0 - c_T t\right)\right] \tag{3.25}$$

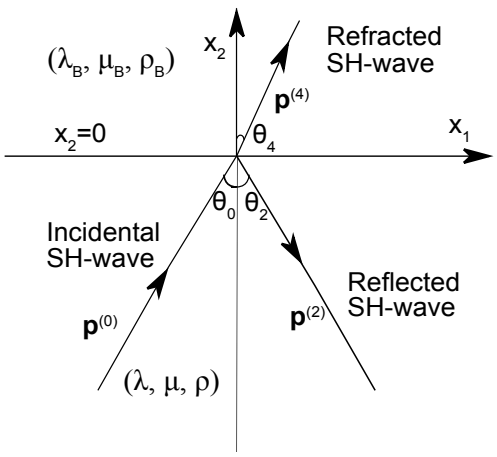

Fig. 3.3.: Reflection of SH-wave at the boundary

The reflection and refraction[4] of *SH-wave* at the interface generates the *SH-wave*. The system of waves should satisfy the continuity of the displacement and stress at

[4]The numbers 2 and 4 have been used for denoting the reflected and refracted waves, respectively.

the interface; displacement (stress) due to the incidental and reflected wave should be equal to the displacement(stress) due to the refracted wave. Accordingly, the equations of reflected and refracted wave are given by

$$u_3^{(2)} = A_2 \exp\left[ik_0\left(x_1 \sin\theta_0 + x_2 \cos\theta_0 - c_T t\right)\right] \tag{3.26}$$

$$u_3^{(4)} = A_4 \exp\left[ik_4\left(x_1 \sin\theta_4 + x_2 \cos\theta_4 - c_T^B t\right)\right] \tag{3.27}$$

where A_2, A_4, θ_4, k_4 are given by following relations

$$\frac{A_2}{A_0} = \frac{\mu \cos\theta_0 - \mu^B \left(c_T/c_T^B\right) \cos\theta_4}{\mu \cos\theta_0 + \mu^B \left(c_T/c_T^B\right) \cos\theta_4} \tag{3.28}$$

$$\frac{A_4}{A_0} = \frac{2\mu \cos\theta_0}{\mu \cos\theta_0 + \mu^B \left(c_T/c_T^B\right) \cos\theta_4} \tag{3.29}$$

$$k_4 = \frac{c_T}{c_T^B} k_0 \tag{3.30}$$

$$\sin\theta_4 = \frac{c_T^B}{c_T} \sin\theta_0 \tag{3.31}$$

The inspection of Eq. (2.25–2.31) leads to several observations:

1. The reflected wave is in phase with the incident wave and the wave-number and phase-velocity of incident and reflected wave are the same.

2. Refracted wave separates from the incident wave while moving away from the normal if $c_T^B > c_T$, and it moves towards the normal in case $c_T^B < c_T$.

3. The wave is completely transmitted (i.e. $A_2 = 0$) if

$$\mu \cos\theta_0 - \mu^B \left(c_T/c_T^B\right) \cos\theta_4 = 0 \tag{3.32}$$

   which leads to

$$\cos\theta_0 = \sqrt{\frac{1 - \left(c_T/c_T^B\right)^2}{1 - \left(\mu/\mu^B\right)^2}} \tag{3.33}$$

   Therefore, a combination of angle of incidence and material properties is possible for which no *SH-wave* is reflected.

4. If the half-space $x_2 > 0$ is vacuum (i.e., the interface is boundary of elastic half-space) then there will be no reflected waves. Further, if the boundary condition condition at $x_2 = 0$ is such that total displacement vanishes then the reflected wave will have 180° phase difference with the incident wave.

Furthermore, if the total stress at the boundary vanishes then the reflected wave is in phase with the incident wave.

***Reflection and refraction of longitudinal wave*:** As mentioned earlier, in case of longitudinal wave (or *P-wave*) material points move in the direction of wave propagation (see Eq. 3.16). The equation of incidental longitudinal wave traveling in the direction $\mathbf{p} = [\sin\theta, \cos\theta, 0]$ is given by

$$\mathbf{u}^{(0)} = \begin{bmatrix} \sin\theta_0 \\ \cos\theta_0 \\ 0 \end{bmatrix} A_0 \exp\left[ik_0\left(x_1 \sin\theta_0 + x_2 \cos\theta_0 - c_L t\right)\right] \tag{3.34}$$

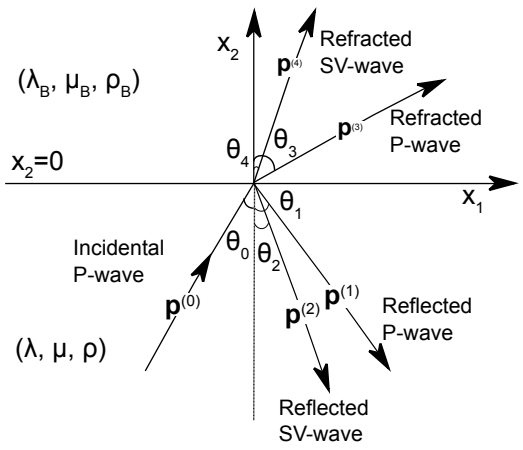

Fig. 3.4.: Reflection of longitudinal plane wave

When a *P-wave* encounters a material interface two reflected (a *P-wave* and a *SV-wave*) and two refracted waves (a *P-wave* and a *SV-wave*) are possible. The motion of system of waves is depicted in Fig. 3.4. The equation of reflected *P-wave* and *SV-wave* is given by Eq. (3.35) and Eq. (3.36), respectively.

$$\mathbf{u}^{(1)} = \begin{bmatrix} \sin\theta_1 \\ -\cos\theta_1 \\ 0 \end{bmatrix} A_1 \exp\left[ik_1\left(x_1 \sin\theta_1 - x_2 \cos\theta_1 - c_L t\right)\right] \tag{3.35}$$

$$\mathbf{u}^{(2)} = \begin{bmatrix} \cos\theta_2 \\ \sin\theta_2 \\ 0 \end{bmatrix} A_2 \exp\left[ik_2\left(x_1 \sin\theta_2 - x_2 \cos\theta_2 - c_T t\right)\right] \tag{3.36}$$

The equation of refracted *P-wave* and *SV-wave* is given by Eq. (3.37) and Eq. (3.38) respectively.

$$\mathbf{u}^{(3)} = \begin{bmatrix} \sin\theta_3 \\ \cos\theta_3 \\ 0 \end{bmatrix} A_3 \exp\left[ik_3\left(x_1\sin\theta_3 + x_2\cos\theta_3 - c_L^B t\right)\right] \tag{3.37}$$

$$\mathbf{u}^{(4)} = \begin{bmatrix} -\cos\theta_4 \\ \sin\theta_4 \\ 0 \end{bmatrix} A_4 \exp\left[ik_4\left(x_1\sin\theta_4 + x_2\cos\theta_4 - c_T^B t\right)\right] \tag{3.38}$$

This system of waves should satisfy four continuity equations at the interface; one for each $u_1, u_2, \sigma_{12}, \sigma_{22}$. In other words, total displacement (total stress) due to system of incident and reflected waves must be equal to the total displacement (total stress) due to the system of refracted waves. Accordingly, one can obtain following results for the wave-numbers and direction of wave propagation.

$$k_1 = k_0; \quad \theta_1 = \theta_0 \tag{3.39}$$

$$k_2 = k_0\frac{c_L}{c_T}; \quad \sin\theta_2 = \frac{c_T}{c_L}\sin\theta_0 \tag{3.40}$$

$$k_3 = k_0\frac{c_L}{c_L^B}; \quad \sin\theta_3 = \frac{c_L^B}{c_L}\sin\theta_0 \tag{3.41}$$

$$k_4 = k_0\frac{c_L}{c_T^B}; \quad \sin\theta_4 = \frac{c_T^B}{c_L}\sin\theta_0 \tag{3.42}$$

Subsequently, the aforementioned four continuity equations results in four linear equations for the amplitudes A_1, A_2, A_3 and A_4. In matrix form the system can be represented by

$$\mathbf{TA} = \mathbf{A}_0 \tag{3.43}$$

where

$$\mathbf{T} = \begin{bmatrix} -\sin\theta_1 & -\cos\theta_2 & \sin\theta_3 & -\cos\theta_4 \\ \cos\theta_1 & -\sin\theta_2 & \cos\theta_3 & \sin\theta_4 \\ \sin 2\theta_1 & \frac{c_L}{c_T}\cos 2\theta_2 & \frac{\mu^B}{\mu}\frac{c_L}{c_L^B}\sin 2\theta_3 & -\frac{\mu^B}{\mu}\frac{c_L}{c_T^B}\cos 2\theta_4 \\ -\left(\frac{c_L}{c_T}\right)^2\cos 2\theta_2 & \frac{c_L}{c_T}\sin 2\theta_2 & \frac{\mu^B}{\mu}\frac{c_L c^B{}_L}{\left(c_T^B\right)^2}\cos 2\theta_4 & \frac{\mu^B}{\mu}\frac{c_L}{c_T^B}\sin 2\theta_4 \end{bmatrix}$$

$$\mathbf{A} = \begin{bmatrix} A_1 & A_2 & A_3 & A_4 \end{bmatrix}^T$$

$$\mathbf{A}_0 = A_0 \begin{bmatrix} \sin\theta_0 & \cos\theta_0 & \sin 2\theta_0 & \left(\frac{c_L}{c_T}\right)^2 \cos 2\theta_2 \end{bmatrix}^T$$

In case of normal incident of *P-wave* (i.e., $\theta_0 = 0$) the reflected and refracted waves contains only a *P-wave*, i.e.

$$A_2 = A_4 = 0$$

and

$$\frac{A_1}{A_0} = \frac{\rho^B c_L^B - \rho c_L}{\rho^B c_L^B + \rho c_L} \tag{3.44}$$

$$\frac{A_3}{A_0} = \frac{2\rho c_L}{\rho^B c_L^B + \rho c_L} \tag{3.45}$$

From Eq. (3.44–3.45) it is clear that in case of normal incidence of *P-wave* the amplitude of reflected and refracted *P-wave* depends entirely on the mechanical impedance, the product of mass density and phase speed, of the two media. If both media have the same mechanical impedance then there will be no reflected wave. Further, if upper half-space has more impedance then lower half-space then the reflected *P-wave* will be out of phase with the incident wave.

In case upper half-space is vacuum – the interface becomes the boundary of elastic half-space – then there will be no refracted waves and system of reflected wave will consist a P-wave and a SV-wave. The nature of reflected waves then depends upon the boundary conditions. If the total displacement at the boundary vanishes then the reflected P-wave and SV-wave are given by Eq. (3.35) and Eq. (3.36), respectively, with amplitudes,

$$\frac{A_1}{A_0} = \frac{\cos(\theta_0 + \theta_2)}{\cos(\theta_0 - \theta_2)} \tag{3.46}$$

$$\frac{A_2}{A_0} = \frac{\sin 2\theta_0}{\cos(\theta_0 - \theta_2)} \tag{3.47}$$

If the total stress at the boundary vanishes (i.e., stress free surface) then the amplitude ratio becomes

$$\frac{A_1}{A_0} = \frac{\sin 2\theta_0 \sin 2\theta_2 - \kappa^2 \cos^2\theta_2}{\sin 2\theta_0 \sin 2\theta_2 + \kappa^2 \cos^2 2\theta_2} \tag{3.48}$$

$$\frac{A_2}{A_0} = \frac{2\kappa \sin 2\theta_0 \cos 2\theta_2}{\sin 2\theta_0 \sin 2\theta_2 + \kappa^2 \cos^2 2\theta_2} \tag{3.49}$$

From Eq. (3.48–3.49) it is observed that normal incident, $\theta_0 = 0$, and grazing incident, $\theta_0 = \pi/2$, of *P-wave* generates only a reflected *P-wave* as $A_2 = 0$. In former case the reflected *P-wave* is in the phase, and in later case reflected *P-wave* is out of phase with incident wave.

3.2.5 Surface waves

So far we have discussed the homogeneous plane harmonic waves where the amplitude of wave motion remains constant in the plane of constant phase. There exists another type of wave motion for which the amplitude changes in the plane of constant phase. Consequently, one can define the plane of constant amplitude. It turns out that the two planes are normal to each other. Moreover, the plane of constant phase moves in the direction of wave propagation, therefore, the amplitude remains constant in the wave propagation direction.

Surface waves are inhomogeneous plane waves for which amplitude of disturbance exponentially decays as one moves away from the surface. However, the amplitude of motion remains constant in the wave direction of wave propagation. From an earthquake engineering viewpoint two type of surface waves are of primary importance; *Rayleigh wave* and *Love wave*.

Consider the in-plane motion of plane waves traveling in x_1-direction in a homogeneous elastic half-space ($x_2 \leq 0$) with free surface at $x_2 = 0$. The Motion of particles as the wave passes by can be described as,

$$u_1 = \left[A_1 \exp\left(b_1 x_2\right) + A_2 \exp\left(b_2 x_2\right)\right] \exp\left[ik_R\left(x_1 - c_R t\right)\right] \tag{3.50}$$

$$u_2 = \left[-A_1 \frac{b_1}{ik_R} \exp\left(b_1 x_2\right) + A_2 \frac{ik_R}{b_2} \exp\left(b_2 x_2\right)\right] \exp\left[ik_R\left(x_1 - c_R t\right)\right] \tag{3.51}$$

where A_1, A_2 are constants to be determined, k_R and c_R are the wave number and phase-velocity of the *Rayleigh wave*, respectively. b_1 and b_2 are given by

$$b_1 = k_R \left(1 - \frac{c_R^2}{c_L^2}\right)^{1/2} \tag{3.52}$$

$$b_2 = k_R \left(1 - \frac{c_R^2}{c_T^2}\right)^{1/2} \tag{3.53}$$

Note that for b_1, b_2 are real valued if $c_R < c_T < c_L$. The mathematical expressions for A_1, A_2 and c_R are obtained by satisfying the stress free conditions (i.e. $\sigma_{22} = \sigma_{12} = 0$)

at $x_2 = 0$. Subsequently, one can obtain the following relationship between the constants A_1 and A_2

$$A_2 = -\frac{2b_1 b_2}{(k_R^2 + b_2^2)} A_1 \tag{3.54}$$

The approximate value for c_R can be given by (Achenbach, 2012)

$$c_R = \frac{0.862 + 1.14\nu}{1 + \nu} c_T \tag{3.55}$$

where ν denotes the Poission's ratio of the elastic half-space.

Using Eq. (3.54–3.55) in Eq. (3.50–3.51) following expression for displacement components can be obtained.

$$u_1 = A_1 \left[\exp(b_1 x_2) - \frac{2b_1 b_2}{k_R^2 + b_2^2} \exp(b_2 x_2) \right] \exp\left[ik_R (x_1 - c_R t)\right] \tag{3.56}$$

$$u_2 = iA_1 \left[\frac{b_1}{k_R} \exp(b_1 x_2) - \frac{2b_1 k_R}{k_R^2 + b_2^2} \exp(b_2 x_2) \right] \exp\left[ik_R (x_1 - c_R t)\right] \tag{3.57}$$

From Eq. (3.56–3.57) it can be observed that the horizontal and vertical displacement components, u_1, u_2, have a 90° phase difference; when u_1 is maximum then u_2 is zero, and vice versa. Due to 90° phase difference in u_1, u_2 the trajectories of the particles are ellipses, and particles at the free surfaces moves counter-clockwise when wave travels in positive x_1 direction. At depth $x_2 \approx 0.2\Lambda$ the direction of rotation changes (Here Λ denotes the wavelength of *Rayleigh wave*). It can be shown that at the free surface the normal displacement is about 1.5 times the tangential displacement.

It should be noted that in a homogeneous elastic half-space only *Rayleigh wave* and body waves can exist. However, *Love waves* can arise if soil layering is present. *Love waves* typically develop in shallow surface soil layers overlying layers of stiffer materials properties. They basically consists of *SH-waves* that are trapped by multiple reflection within the surface layer. Exactly like *SH-waves Love waves* propagates in the out-of-plane direction and they have no vertical components of particle motion.

3.3 Review of artificial boundary conditions

Dynamic soil-structure problems can be viewed as a wave propagation problem. Consider a structure (finite dimension) embedded in the unbounded domain of semi-infinite soil (see Fig. 3.5). The soil domain can further be divided into two regions; (i) the irregular bounded region near to the structure, and (ii) the regular unbounded

region extending to infinity. Both structure and irregular bounded region are allowed to exhibit nonlinear behaviour. However, note that the regular unbounded region must remain linear[5]. Henceforth the term *structure* will be used to denote system of irregular bounded region and structure and the term *unbounded domain* will be used for denoting the regular unbounded region. The dynamic soil-structure interaction occurs through the interface between unbounded domain and structure.

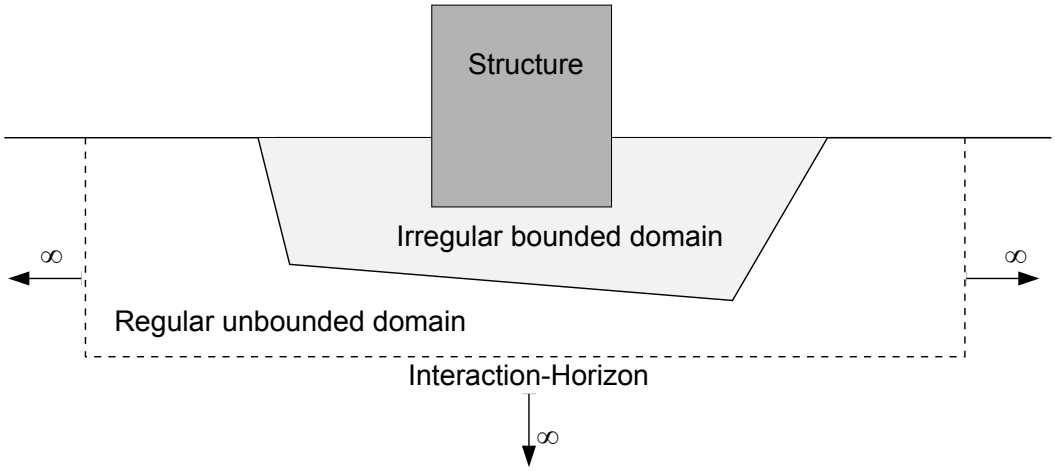

Fig. 3.5.: Schematic diagram of dynamic soil-structure interaction problem

For finite element analysis of dynamic SSI problems, a superficial surface called *interaction-horizon* that encloses the structure and forms the boundary of the computational domain has to be selected (Wolf and Song, 1996). The key issue of this approach is to impose the so called artificial boundary conditions (ABC) so that the *interaction-horizon* can model the radiation damping accurately and spurious reflections from the boundaries can be prohibited. In literature these boundary conditions have been known as *absorbing*, *non-reflecting*, *transparent*, *silent*, and *one-way* boundary conditions. Further, the use of ABC's enables one to get rid of the exterior unbounded domain from the computations.

To appreciate the radiation damping, consider a vertically propagating SV-wave in a elastic half-space with two layers of soil (see Fig. 3.6). The normal incidence of SV-wave at the interface of two layers produces reflected and refracted SV-waves. As it was shown earlier the partition of the wave depends upon the mechanical impedance of the two media. The wave reflected to lower half-space never returns to the interface due to its infinite extension in x_2-direction. This loss of energy is known as radiation damping (Kramer, 2014). Further, refracted wave approaches the free surface layered system and subsequently reflected back towards the interface. At the interface when this wave reaches again a part of energy is reflected back and a part of the energy is transmitted to the lower half-space and therefore it will be

[5] As the amplitudes of all body and surface waves decay due to geometric spreading, the nonlinearity will be limited to the irregular bounded medium

lost in the semi-infinite domain of bottom layer. This loss of energy represents again the radiation damping. One of the big challenges of dynamic finite element analysis is to model correctly this radiation damping. Further, difficulties arises due to the presence of structures (such as dam, tunnel, buildings etc.) in or on the half-space that causes multiple reflection and refraction of incoming waves.

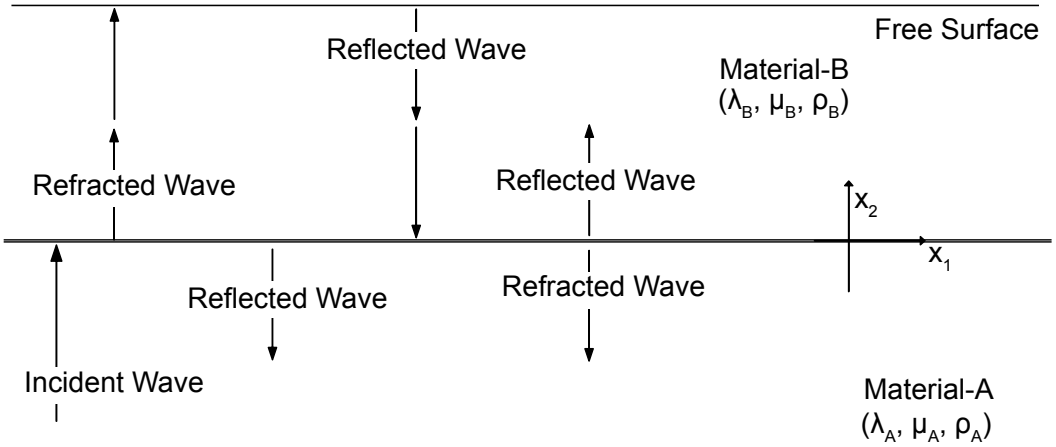

Fig. 3.6.: Schematic diagram of reflections and refractions of vertically propagating *SV-wave* in two layered elastic half-space

The minimal requirements of ABC's presented by Givoli, 1991 are; (a) the problem in truncated domain with ABC should be mathematically well posed, (b) ABC's should allow the waves that come from inside the computational domain to go out[6] and produces little spurious reflections at the artificial boundaries, (c) the solutions of truncated problem in some sense should be close enough to the original problem in unbounded domain, (d) the combination of a numerical scheme and ABC's should yield a stable numerical method, (e) ABC should be easy to implement and the cost of implementation should not be huge.

Kausel and Tassoulas in their review paper (Kausel and Tassoulas, 1981) grouped ABC's into following three categories;

1. *Elementary boundaries*: This type of boundary conditions are also known as Dirichlet, Neumann and Mixed boundary conditions. Displacements and stresses are prescribed in the case of Dirichlet and Neumann boundary condition, respectively. In case of mixed boundary conditions some components of displacement and stress are prescribed (for example roller boundary condition). Recalling that such boundary conditions act as the perfect reflector waves as no energy is absorbed or transmitted. Therefore, adoption of such boundary

[6] In some physical situations where the source is located outside the computational domain the artificial boundaries should allow the waves to come inside the computational domain.

conditions to model the unbounded domain will cause spurious reflections and spoil the accuracy of the solutions. Elementary boundaries will be adequate only under certain circumstances: (i) when the problem can be regarded as pseudo-static; frequency of excitation is below the natural frequency of a soil stratum problem, (ii) when the internal damping of the soil is sufficient to suppress the reflected wave before it return to the region of study, (iii) when the time duration of numerical simulation is shorter than the time required for a wave to return to the area of interest.

2. *Local boundaries*: The main characteristic of local boundaries is that the boundary conditions involve only spatial and temporal points in the neighbourhood of the boundary point under consideration at the time of evaluation. Further, these boundaries are based upon the physical or mathematical approximations.

3. *Consisting (nonlocal) transmitting boundaries*: These boundaries are perfect absorbers of any kind of waves impinging with arbitrary incidence. The conditions imposed by such boundaries are essentially nonlocal in nature. Most of these boundaries are frequency-dependent and thus in time domain analysis they are restricted to steady state problems.

3.3.1 Local artificial boundary conditions

The first attempt to simulate radiation with simple local boundaries was presented by Lysmer and Kuhlemeyer, 1969. These authors developed viscous boundary conditions based on physical consideration. In essence, these conditions can be interpreted as dashpots connected to the boundary points. The damping coefficient was given by the mechanical impedance of the soil to which dashpots were attached to. The derivation of this type of boundary condition is considered in the next section.

Smith, 1974 used the principle of superposition to filter out the contribution of spurious reflections from the solutions. Two solutions were obtained corresponding to the two types of boundary conditions; one in which tangential displacement and normal stresses vanishes, another in which normal displacement and tangential stresses vanishes. The reflected P-wave and S-wave corresponding to these boundary conditions have the same amplitude but they have phase difference of $180\,^{\circ}$. However, this approach is computationally not efficient, moreover this approach is limited to the linear problem only.

Engquist and Majda, 1977 and Clayton and Egquist, 1977, developed a set of time-dependent *local-ABC* of increasing order based on paraxial approximations of the

scalar and elastic wave equation. In their technique they approximated the irrational dispersion relation by a rational function to obtain the local differential operator from the nonlocal pseudodifferential operators. In this way by using rational approximations of increasing order, they obtain local boundary conditions of increasing accuracy. Further, they mentioned that a higher order paraxial approximation based on Taylor series expansions induces numerical instability. Although this difficulty can be overcome by use of Pade approximations instead of Taylor series expansions, the presence of higher order derivatives in boundary conditions greatly complicates its implementation. Another set of local boundary conditions with adjustable free parameters was proposed by Clayton and Engquist, 1980. Later, Cohen, 1980 showed that the paraxial boundary becomes unstable when Poisson's ratio exceeds 0.33. A modified version of paraxial boundary called extended-paraxial boundary and its finite element implementation was provided by Cohen and Jennings, 1983; Cohen et al., 1981. It was also shown that the performance of extended-paraxial boundary is only slightly superior to the standard-viscous boundary. Stacey, 1988 presented three new paraxial approximations superior to those presented by Clayton and Engquist while avoiding the higher order derivatives. Better finite-difference equations for internal boundaries and corners were also presented in this research.

Bayliss and Turkel, 1980 presented the sequence of local absorbing boundary conditions in spherical coordinates by employing the asymptotic expansion of the solution of scalar wave equation at large distances. The radiation conditions are given by hierarchy of differential operators B_m which annihilate the first m terms in the asymptotic expansion of the solution. The boundary conditions are given by

$$B_m u = \left[\prod_{k=1}^{m}\left(\frac{1}{c}\frac{\partial}{\partial t}+\frac{\partial}{\partial r}+\frac{2j-1}{R}\right)\right]u = 0 \tag{3.58}$$

where R is the radius of the artificial boundary. This higher order local boundary condition, like previous schemes given by other researchers, contains the higher order derivatives which makes their practical implementation near to impossible.

Higdon, 1986 considered the two-dimensional wave equation in a rectangular truncated domain Ω. In his work scalar wave equation was first discretized in space and time domain using finite difference scheme. Subsequently, some discrete boundary conditions were derived for the artificial boundary. He then presented the analytical boundary condition corresponding to the discrete one. The p-order boundary condition, for a boundary vertical boundary located at some $x > 0$, is described by the product type differential operators H_p

$$H_p u = \left[\prod_{j=1}^{p}\left(\cos\theta_j\frac{\partial}{\partial t}+c\frac{\partial}{\partial x}\right)\right]u = 0 \tag{3.59}$$

where c is some reference wave-speed and θ_j is the angle of incident and $|\theta_j| < \pi/2, \quad \forall j = 1, \cdots, p$. In literature H_p is know as *Higdon-boundary operator*, and Eq. (3.59) is called the Higdon absorbing boundary condition (Higdon ABC). The alternatively form of this boundary condition is given by

$$H_p u = \left[\prod_{j=1}^{p} \left(\frac{\partial}{\partial t} + C_j \frac{\partial}{\partial x} \right) \right] u = 0 \tag{3.60}$$

where $C_j = c/cos\theta_j; \quad C_j \geq c$ signify the phase speed in the x-direction.

Higdon ABC is perfectly absorbing for a plane wave hitting the artificial boundary at one the angles $\pm\theta_j$ for $j = 1, \cdots, p$ with speed c. Therefore, *Higdon-boundary* will appear absolutely transparent at the discrete angle of incidence $\pm\theta_1, \cdots, \pm\theta_p$. The second order Higdon ABC (i.e. $p = 2$ in Eq. (3.59)) corresponds to the linear space time interpolation of solution at the artificial boundary. Higdon also demonstrated that p-order Engquist-Majda condition is special case of Eq. (3.59) with $\theta_j = 0, \quad \forall j = 1, \cdots, p$ (for more general description see Higdon, 1986, Propostition 9.1).

Through several numerical experiments it was demonstrated that the amount of spurious reflection is not very sensitive to the choice of the θ_j (Higdon, 1987). Therefore, the fact that θ_j are not known a priori is not a major restriction for the Higdon ABC. Further, Higdon ABC is very general as they are applicable to variety of wave problems including waves in dispersive media (Higdon, 1994) and stratified media (Higdon, 1992). Moreover, the condition is exact in the sense that when the order p in Eq. (3.59) increases to infinity, it gives a global formulation. Unfortunately, the p-order Higdon ABC will contain p-order space and time derivatives. Therefore, high order conditions are impractical beyond 2nd or 3rd order from the implementation point of view. Finally, it is noteworthy that Higdon ABC is local in space and time.

Higdon, 1990; Higdon, 1991 extended the Higdon ABC for the case of elastic wave propagating in two-dimensional space. In the case of elastic waves *Higdon-boundary operator* is written by

$$H_p \mathbf{u} = \left[\prod_{j=1}^{p} \left(\beta_j \frac{\partial}{\partial t} + c_L \frac{\partial}{\partial x} \right) \right] \mathbf{u} = 0 \tag{3.61}$$

where c_L is phase-velocity of longitudinal plane wave (cf. Eq. (3.11)) and $\beta_j > 0, \forall j$ resemble to the cosine of angle of incident. The jth operator in Eq. (3.61) is perfectly absorbing for P-waves traveling at angle of incidence $\pm\cos^{-1}\beta_j$ and S-wave traveling at angle of incidence $\pm\cos^{-1}(\beta_j c_T/c_L)$. If $\beta_j \leq 1, \forall j$, then Eq. (3.61) is oriented mainly to absorb P-waves but also helps to absorb S-waves. If β_j's are are all near

the ratio $c_L/c_T > 1$ then Eq. (3.61) is oriented mainly to absorb S-waves but helps absorb P-wave. In addition, Higdon showed that Higdon ABC is stable for all values of the ratio c_L/c_T while the second order Engquist-Majda boundary conditions is unstable for large value of c_L/c_T.

Underwood and Geers, 1981 presented a local transmitting boundary condition for a structure embedded in the elastic medium problem. Their method was based on a substructure approach in which to model the effect of infinite domain *interaction-horizon* was placed at the soil-structure interface. The soil-structure interaction was approximated by first order doubly asymptotic boundary element techniques. The following relation was used for surface force vector $\{\mathbf{f}^s\}$ associated with the scattered waves

$$\{\mathbf{f}^s\} = \left[\mathbf{K}_b^0\right]\{\mathbf{u}\} + [\mathbf{C}_b^\infty]\{\mathbf{v}\} \tag{3.62}$$

where $\{\mathbf{u}\}$ and $\{\mathbf{v}\}$ is the vector of nodal displacement and velocity, respectively. From Eq. (3.62) it can be observed that in high (low frequency) limit the unbounded domain is modelled as an array of dashpots (springs). The boundary stiffness matrix $\left[\mathbf{K}_b^0\right]$ is non-symmetric and it couples all the nodes at the *interaction-horizon*, therefore, this approach is local in time but non-local in space. The method behaves poorly in intermediate range of frequency. Moreover, this approach can only absorb the waves propagating normal to the *interaction-horizon*.

Later Wolf and Song, 1995 combined the doubly asymptotic approach of Underwood and Geers, 1981 and Higdon ABC to derive the *doubly asymptotic multi-directional* (DAMD) ABC. In his approach Eq. (3.62) additionally contains the surface force vector $\{\mathbf{Q}_b^s\}$ which represents the remaining interaction forces. These forces were computed from the second-order Higdon ABC (cf. Eq. (3.59)) while replacing u with the Q. Explicit finite difference scheme was employed to calculate $\{\mathbf{Q}_b^s\}$ and then used in finite element formulation of the total dynamic system to compute the displacement and velocity field. By numerical examples, they showed that the approach is rigorous for both low and high frequency limit in all preselected angles of incidence. In addition, DAMD-ABC is highly accurate for plane waves at intermediate frequency and at other angles. The main disadvantage of this approach is that it uses explicit finite difference scheme to solve Higdon ABC which obviously makes entire scheme conditionally stable even if one uses unconditionally stable direct time integration scheme for finite element analysis. Therefore, a very small time step must be selected to ensure the overall stability. Of course one can use implicit unconditionally stable schemes but then this will increase the overall computational cost.

Following the Bayliss-Turkel conditions, Hagstrom and Hariharan, 1998 derived a sequence of local boundary conditions for isotropic problems (i.e. non-dispersive

case). In contrast to previous high-order schemes their conditions avoids the use of higher order derivatives in the normal direction and in the preferred wave propagation direction. This was made possible due to the use of auxiliary functions; the local conditions of arbitrary order are expressed recursively using auxiliary functions. This way practical use of higher order ABC is possible. However, the scheme was only applicable in the case of spherical symmetry and axial symmetry.

Collino, 1993 presented the first use of high order asymptotic boundary conditions, within finite difference framework, for two-dimensional time-dependent waves in rectangular domain. Corner compatibility conditions were also provided in their formulation. Givoli, 2001 presented a general approach to construct local arbitrary high-order boudary conditions (AHOC) with a symmetric structure and with only low order spatial and/or temporal derivatives. This enables the practical use of ABCs of arbitrarily high order.

Later, Givoli and Neta, 2003 reformulated the sequence of ABCs proposed by Higdon to obtain the arbitrary high-order local ABCs. This scheme is similar to the one proposed by Hagstrom and Hariharan, 1998 only in the sense that it eliminates the higher order derivatives by use of special auxiliary variables. In this case, however, the auxiliary variables are defined by simple recursive relations. Moreover, the formulation was presented in Cartesian coordinates for rectangular domain. The standard (C^0 continuous) finite element implementation of this scheme was presented in Givoli et al., 2003 for the case of linear inhomogeneous dispersive wave (Klein-Gordon) equation. It was shown that the scheme is stable even for equal-order nodal interpolation for all the variables. Besides, the computational effort associated with the boundary condition grows only linearly with the order of accuracy.

Joolen et al., 2005 applied the Givoli-Neta boundary conditions for exterior time-dependent wave problems in two-dimensional unbounded domain. They reported long-time instability of the method and suggested that the special compatibility conditions at the corner of rectangular domain should be include in the auxiliary-variable formulation. The corner compatibility conditions for wave equation with artificial boundary conditions were discussed by Vacus, 2005.

Following the work of Givoli and Neta, 2003, Hagstrom and Warburton, 2004 presented a new auxiliary variable formulation which includes the special corner compatibility conditions. Hangstrom and Warburton conditions can be considered as the symmetrized modification of the Givoli-Neta conditions with enhanced stability characteristics. Their formulation was also based in Cartesian coordinate system with rectangular truncated domain. In the paper they presented a finite difference formulation of their approach. The finite element implementation of Hagstrom-

Warburton formulation is presented by Givoli et al., 2006 for exterior time-dependent wave problems governed by the scalar wave equation.

Samii and Lotfi, 2012; Samii and Lotfi, 2013 implemented the Hagstrom-Warburton ABC for the dam-reservoir interaction problem using finite element methods. Hagstrom et al., 2008 employed the Hagstrom-Warburton ABC for dispersive medium for which the Klein-Gordon wave equation governs. They also extended the boundary conditions to take into account of evanescent modes. Rabinovich et al., 2011 extended the Hagstrom-Warburton ABC for time dependent elastic wave in unbounded domain and presented a variational formulation for the finite element implementation. However, their scheme suffers from long-time instability. Later, Baffet et al., 2012 suggested that the cause of this instability may be due to the use of only Higdon-type ABC for elastic wave problem. In their formulation they combined Lysmer-Kuhlemeyer type boundary operator with the Higdon-type operators. This modification leads to the long-time stability of their formulation.

Kellezi, 2000 developed a cone boundary condition for the vibration problems on the surface of a half-space where the generated waves propagates in an area that increases with depth. This boundary condition can be considered as an extension of the standard viscous boundary condition of Lysmer and Kuhlemeyer, 1969. Physically, cone boundary condition represents a series of dashpots and springs placed in the normal and tangential direction of the truncated boundary. Due to the inclusion of the additional springs, the cone boundary condition approximates the stiffness of the unbounded soil domain and therefore it eliminates the permanent movement which occurs with the viscous boundary condition at low frequencies (Kontoe et al., 2009). However, a drawback of the cone boundary is that the stiffness coefficients of the springs depend on the distance of the boundary from the source of excitation. Therefore, its use is restricted to problems with surface excitations where the distance of the boundary from the source is known.

3.4 Viscous boundary condition

Lysmer and Kuhlemeyer, 1969 first proposed the artificial boundary condition for elastic waves (henceforth known as LK-ABC). In this section LK-ABC is first derived for the case of one-dimensional longitudinal wave (P-wave) impinging normally at the boundary, then the condition is derived for the case of vertically propagating SV-wave again impinging normally at the boundary. Finally, the LK-condition is derived for plane wave impinging at some angle θ at the artificial boundary.

3.4.1 LK-ABC for normal incidence of P-wave

Consider an isotropic, homogeneous, linear elastic half-space, initially at rest, subjected to the uniform pressure $p(t)$ at the plane $x_1 = 0$ (see Fig. 3.7a). Here any plane parallel to the x_1-axis is a plane of symmetry, therefore, the displacement can be described by $\mathbf{u} = [u_1(x_1, t), 0, 0]$. Additionally, the wave-fronts are normal to x_1-axis. By using strain-displacement relationship Eq. (3.3) it can be shown that the present situation is a case of one-dimensional longitudinal strain; only non-trivial strain component is ϵ_{11}. Accordingly, the equation of motion Eq. (3.1) becomes a one-dimensional wave equation of the form

$$\frac{\partial^2 u_1}{\partial x_1^2} = \frac{1}{c_L^2}\frac{\partial^2 u_1}{\partial t^2} \tag{3.63}$$

where c_L is the phase velocity of longitudinal wave and given by Eq. (3.11). Initial conditions and boundary conditions are given by Eq. (3.64) and Eq. (3.65), respectively.

$$u_1(x_1, 0) = 0; \quad v_1(x_1, 0) = 0 \tag{3.64}$$

$$\sigma_{11}(0, t) = -p(t) \qquad p(t) = 0 \quad \textit{for} \quad t < 0 \tag{3.65}$$

The general form of solution to the wave equation Eq. (3.63) is given by

$$u_1(x_1, t) = f\left(t - \frac{x_1}{c_L}\right) + g\left(t + \frac{x_1}{c_L}\right) \tag{3.66}$$

where $f(\cdot)$ and $g(\cdot)$ denote the wave traveling positive and negative x_1-direction, respectively. Obviously, in the present case no wave will travel in the negative x_1-direction (see Achenbach, 2012, chapter 2), hence

$$u_1(x_1, t) = f\left(t - \frac{x_1}{c_L}\right) \tag{3.67}$$

Employing Eq. (3.2) and Eq. (3.67) the non-trivial components of stress tensor become

$$\sigma_{11}(x_1, t) = -\frac{(\lambda + 2\mu)}{c_L} f'\left(t - \frac{x_1}{c_L}\right) = -\rho c_L f'\left(t - \frac{x_1}{c_L}\right) \tag{3.68}$$

$$\sigma_{22}(x_1, t) = \sigma_{33} = -\frac{\lambda}{c_L} f'\left(t - \frac{x_1}{c_L}\right) \tag{3.69}$$

Futher, the velocity is given by

$$v_1(x_1, t) = f'\left(t - \frac{x_1}{c_L}\right) \tag{3.70}$$

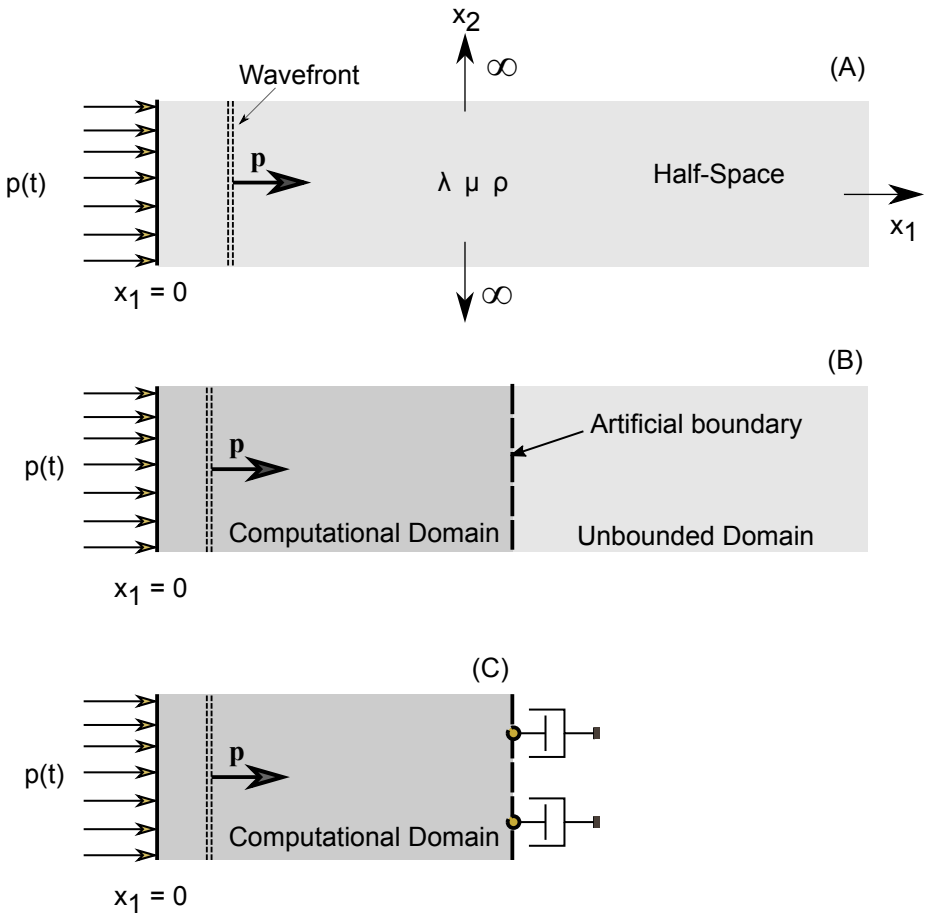

Fig. 3.7.: Illustration of (A) a half-space subjected to uniform pressure, (B) truncation of unbounded domain by introducing artificial boundary to obtain finite computational domain, (C) satisfying radiation condition by placing series of dashpots along the artificial boundary.

Noting Eq. (3.68) and Eq. (3.70) we can obtain the following relation between normal stress σ_{11} and normal velocity v_1 (here space, time coordinates are omitted for clarity of expressions).

$$\sigma_{11} = -\rho c_L v_1 \tag{3.71}$$

Eq. (3.71) is the *LK boundary condition* for the case of one-dimensional P-wave propagation. In this relation the term ρc_L is called the *mechanical impedance* of the medium. *Mechanical impedance* is the property of the medium which measures the stress that is required to generate the motion of particles (Achenbach, 2012). In simple terms, Eq. (3.71) signifies the amount of stress required to completely transfer the motion (linear momentum and energy) of a plane to the next plane. Consequently, the wave will be reflected (partially or completely) if the stress does not satisfy the above relation. Further, Eq. (3.71) is a characteristic equation of a *dashpot* with damping coefficient equal to the *mechanical impedance*. Therefore, it is possible to work with the finite computational domain by introducing the artificial boundary with boundary condition given by Eq. (3.71). In this way unbounded domain can be replaced by a series of dashpot normal to artificial boundary as depicted in Fig. 3.7c.

3.4.2 LK-ABC for normal incidence of S-wave

Fig. 3.8a illustrates the vertically propagating SV-wave in an isotropic, homogeneous, linear elastic half-space. The system is initially at rest and subjected to the uniform surface traction $s(t)$ at the plane $x_2 = 0$. In this case displacement is described by $\mathbf{u} = [u_1(x_2, t), 0, 0]$. Additionally, the wave-fronts are normal to x_2-axis. ϵ_{12} is the only non-trivial strain component (cf. Eq. (3.3)). The equation of motion is given by following one-dimensional wave equation.

$$\frac{\partial^2 u_1}{\partial x_2^2} = \frac{1}{c_T^2}\frac{\partial^2 u_1}{\partial t^2} \tag{3.72}$$

where c_T is the phase velocity of transverse wave and given by Eq. (3.12).

The general solution of Eq. (3.72) should represent a wave propagating in the x_2-direction. This solution can be described by

$$u_1\left(x_2, t\right) = f\left(t - \frac{x_2}{c_T}\right) \tag{3.73}$$

The non-trivial stress component σ_{12} and velocity v_1 are given by

$$\sigma_{12}\left(x_2, t\right) = -\rho c_T f'\left(t - \frac{x_2}{c_T}\right) \tag{3.74}$$

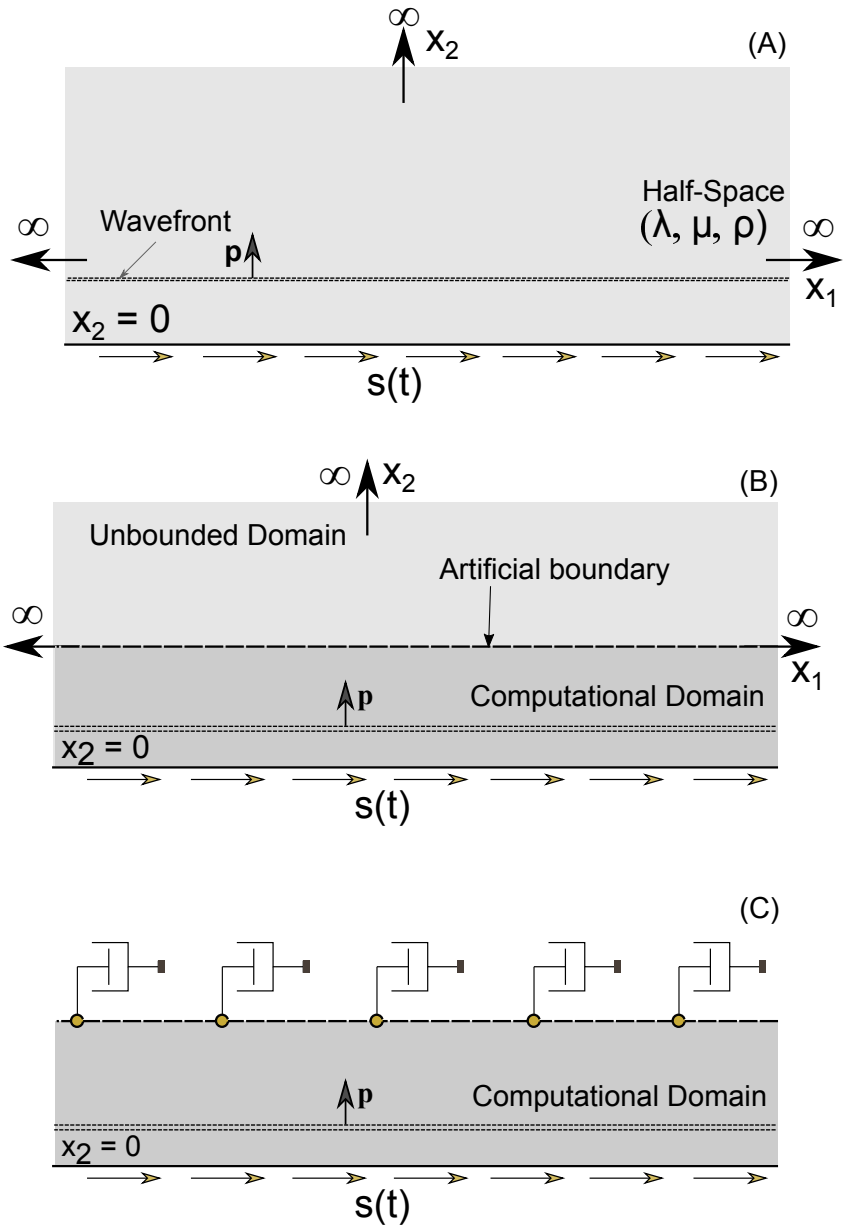

Fig. 3.8.: Schematic diagram of (A) vertically propagating SV-wave in half-space subjected to uniform surface traction, (B) truncation of unbounded domain by introducing artificial boundary to obtain finite computational domain, (C) satisfying radiation condition by placing series of dashpots along the artificial boundary.

$$v_1(x_2, t) = f'\left(t - \frac{x_2}{c_L}\right) \tag{3.75}$$

Accordingly, the following relationship between tangential stress σ_{12} and tangential velocity v_1 is self evident.

$$\sigma_{12} = -\rho c_T v_1 \tag{3.76}$$

Eq. (3.76) is the *LK boundary condition* for the case of one-dimensional S-wave propagation. In this relation the term ρc_T again denotes the *mechanical impedance* of the medium. It can observed that Eq. (3.76), analogues to Eq. (3.71), represents a *dashpot* with damping coefficient equal to ρc_T. Further, the unbounded domain can be truncated by placing an artificial boundary parallel to the x_1-axis as depicted in Fig. 3.8b. In the present case, the artificial boundary will perfectly absorb the normally impinging S-wave given Eq. (3.76) is imposed on it. Physically, the unbounded media (outside the computational domain) resembles to a situation in which an array of dashpots is placed in tangential to the truncated boundary as shown in Fig. 3.8c.

3.4.3 LK-ABC for general case of plane waves

In preceding two subsections LK-ABC is derived for the case of normal incidence of a P-wave and a S-wave. In such cases LK-ABC is exact; it perfectly absorbs the incident wave. If, however, incident wave is impinging the boundary at some angle ($\theta < \pi/2$) some amount of reflection is expected. Lysmer and Kuhlemeyer, 1969 suggested to use following absorbing boundary conditions in order to minimize such spurious reflection.

$$\sigma_n = -a\rho c_L v_n \tag{3.77}$$

$$\tau = -b\rho c_T v_s \tag{3.78}$$

where σ_n and τ are the normal and tangential stress at the boundary, respectively. Similarly, v_n and v_s are the normal and tangential velocity at the boundary, respectively. As seen earlier, this condition corresponds to a situation in which a series of dashpots are placed at the absorbing boundary in parallel and normal direction (see Fig. 3.9b).

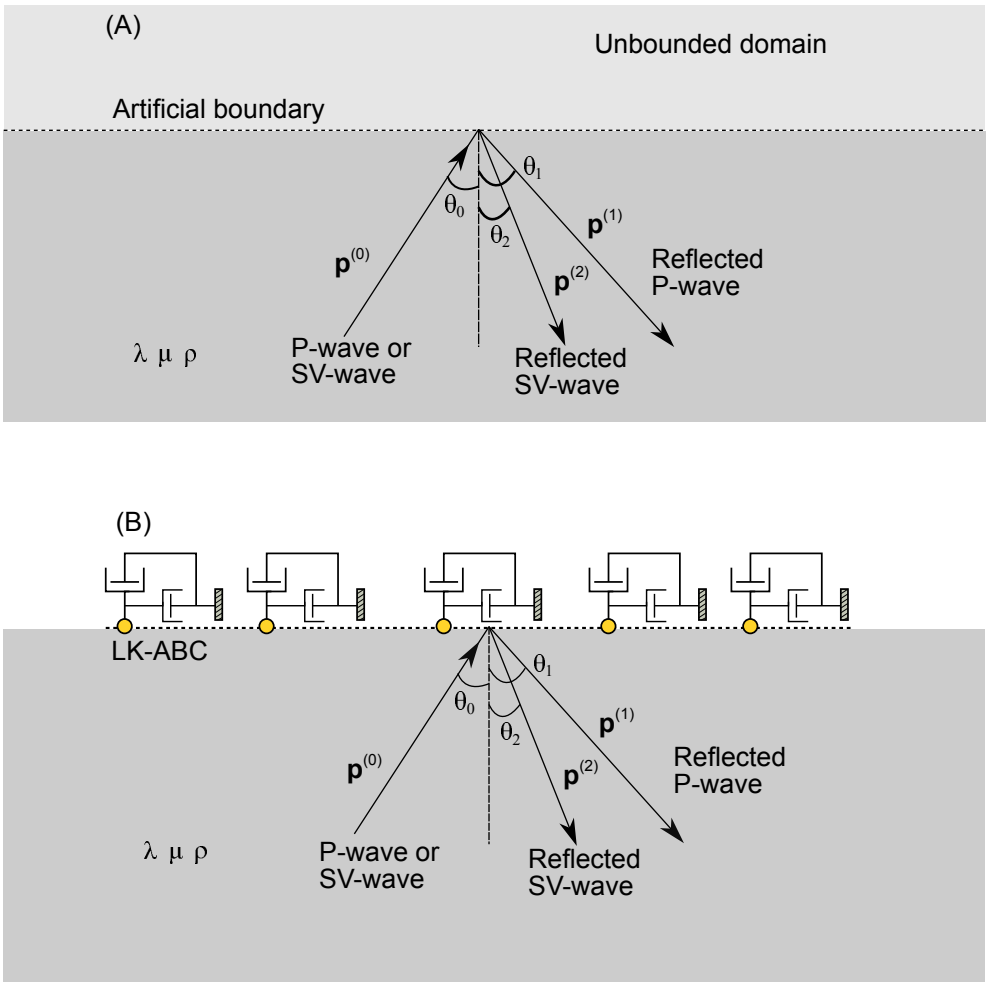

Fig. 3.9.: (A) Illustration of a plane-wave impinging at the artificial boundary at some angle θ_0, (B) Interpretation of the LK-ABC as a series of dashpots configured parallel and normal to artificial boundary.

3.4.4 Reflection of a P-wave at the LK-boundary

Fig. 3.9a shows a P-wave approaching the boundary at some angle θ_0. The wave will be reflected as a P-wave and a SV-wave (see Achenbach, 2012, chapter 5). The displacement and velocity field due to incident and reflected waves is represented by

$$\mathbf{u}^{(n)} = A_n \begin{bmatrix} d_1^{(n)} \\ d_2^{(n)} \end{bmatrix} \exp\left[ik_n\left(x_1 p_1^{(n)} + x_2 p_2^{(n)} - c_n t\right)\right] \tag{3.79}$$

$$\mathbf{v}^{(n)} = -ik_n c_n A_n \begin{bmatrix} d_1^{(n)} \\ d_2^{(n)} \end{bmatrix} \exp\left[ik_n\left(x_1 p_1^{(n)} + x_2 p_2^{(n)} - c_n t\right)\right] \tag{3.80}$$

where the unit vectors $\mathbf{d}^{(n)} = \left[d_1^{(n)}, d_2^{(n)}\right]^T$ and $\mathbf{p}^{(n)} = \left[p_1^{(n)}, p_2^{(n)}\right]^T$ denote the direction of motion of particle and wave propagation, respectively (see Table 3.1 and Fig. 3.9). The number $n = 0, 1, 2$ is used to denote the type of wave. More details about Eq. (3.79) can be found in section 3.2.3.

Wave-type	n	c_n	$\mathbf{p}^n$	$\mathbf{d}^n$
Incident P-wave	0	c_L	$(\sin\theta_0, \cos\theta_0)^T$	$(\sin\theta_0, \cos\theta_0)^T$
Reflected P-wave	1	c_L	$(\sin\theta_1, -\cos\theta_1)^T$	$(\sin\theta_1, -\cos\theta_1)^T$
Reflected SV-wave	2	c_T	$(\sin\theta_2, -\cos\theta_2)^T$	$(\cos\theta_2, \sin\theta_2)^T$

Tab. 3.1.: Parameters for the impinging P-wave, reflected P-wave and reflected SV-wave

Using Eq. (3.24), the normal stress $\sigma_n = \sigma_{22}$ and tangential stress $\tau = \sigma_{12}$ at the artificial boundary $x_2 = 0$ can be computed. These expressions are given in Table 3.2 where the variable η_n is given by

$$\eta_n = k_n\left(x_1 p_1^n - c_n t\right) \tag{3.81}$$

n	$\sigma_{22}^{(n)}$	$\sigma_{12}^{(n)}$
(0)	$ik_0 A_0\left(\lambda + 2\mu\cos^2\theta_0\right)\exp\left(i\bar{\eta}_0\right)$	$ik_0 A_0 \mu \sin 2\theta_0 \exp\left(i\bar{\eta}_0\right)$
(1)	$ik_1 A_1\left(\lambda + 2\mu\cos^2\theta_1\right)\exp\left(i\bar{\eta}_1\right)$	$-ik_1 A_1 \mu \sin 2\theta_1 \exp\left(i\bar{\eta}_1\right)$
(2)	$-ik_2 A_2 \mu \sin 2\theta_2 \exp\left(i\bar{\eta}_2\right)$	$\sigma_{12}^{(2)} = -ik_2 A_2 \mu \cos 2\theta_2 \exp\left(i\bar{\eta}_2\right)$

Tab. 3.2.: Expression for normal and tangential stress at $x_2 = 0$ due to impinging P-wave (n=0), reflected P-wave (n=1) and reflected SV-wave (n=2)

The system of incident and reflected waves should satisfy the continuity of normal and tangential stress at the truncated boundary. This condition is given by

$$\sigma_{22}^{(0)} + \sigma_{22}^{(1)} + \sigma_{22}^{(2)} = -a\rho c_L \left(v_2^{(0)} + v_2^{(1)} + v_2^{(2)} \right) \tag{3.82}$$

$$\sigma_{12}^{(0)} + \sigma_{12}^{(1)} + \sigma_{12}^{(2)} = -b\rho c_T \left(v_1^{(0)} + v_1^{(1)} + v_1^{(2)} \right) \tag{3.83}$$

Using Eq. (3.79), Eq. (3.80), Table 3.1 and Table 3.2 in above stress continuity equations one can get two linear equations in A_1 and A_2

$$A_1 \left(s^2 - 2\sin^2\theta_0 + as^2 \cos\theta_0 \right) - A_2 \left(s \sin 2\theta_2 + as \sin\theta_0 \right) = A_0 \left(as^2 \cos\theta_0 - s^2 + 2\sin^2\theta_0 \right) \tag{3.84}$$

$$A_1 \left(\sin 2\theta_0 + bs \sin\theta_0 \right) + A_2 \left(s \cos 2\theta_2 + bs \cos\theta_2 \right) = A_0 \left(\sin 2\theta_0 - bs \sin\theta_0 \right) \tag{3.85}$$

where A_1 and A_2 are the amplitude of reflected P-wave and SV-wave, respectively. Note that Eq. (3.84 – 3.85) are obtained using the following intermediate results

$$s = \frac{c_L}{c_T} \tag{3.86}$$

$$\theta_1 = \theta_0 \qquad\qquad k_1 = k_0 \tag{3.87}$$

$$\sin\theta_2 = \frac{\sin\theta_0}{s} \qquad\qquad k_2 = k_0 s \tag{3.88}$$

In order to measure the ability of LK-ABC to absorb impinging elastic waves *energy-ratio* — the ratio between the transmitted energy of the reflected waves (E_r) and the transmitted energy of the incident wave (E_i) — can be used (Lysmer and Kuhlemeyer, 1969). Consequently, a unit energy ratio denotes the perfect reflection while a zero energy ratio denotes the complete absorption of the incident wave. The time averaged stress-power[7] for impinging and reflected waves is given by

$$\left\langle \mathscr{P}^{(n)} \right\rangle = \frac{1}{2} \rho c_n \omega_n^2 A_n \tag{3.89}$$

[7] Stress-power denotes the instantaneous rate of work done by the surface traction acting on the surface element of unit area. It is given by the scalar product of surface traction and particle velocity. Moreover, it denotes the energy flux across the surface element.

where $\omega_n = k_n c_n$. The incident energy is given by

$$E_i = \left\langle \mathscr{P}^{(0)} \right\rangle \cos\theta_0 \tag{3.90}$$

Similarly, the reflected energy is

$$E_r = \left\langle \mathscr{P}^{(1)} \right\rangle \cos\theta_1 + \left\langle \mathscr{P}^{(2)} \right\rangle \cos\theta_2 \tag{3.91}$$

and the energy ratio becomes

$$\mathscr{E} := \frac{E_r}{E_i} = \left(\frac{A_1}{A_0}\right)^2 + \frac{1}{s}\frac{\cos\theta_2}{\cos\theta_0}\left(\frac{A_2}{A_0}\right)^2 \tag{3.92}$$

From Eq. (3.92) it can be observed that for a given choice of a and b the energy ratio depends only in the angle of incidence θ_0 and the Poisson's ratio ν.

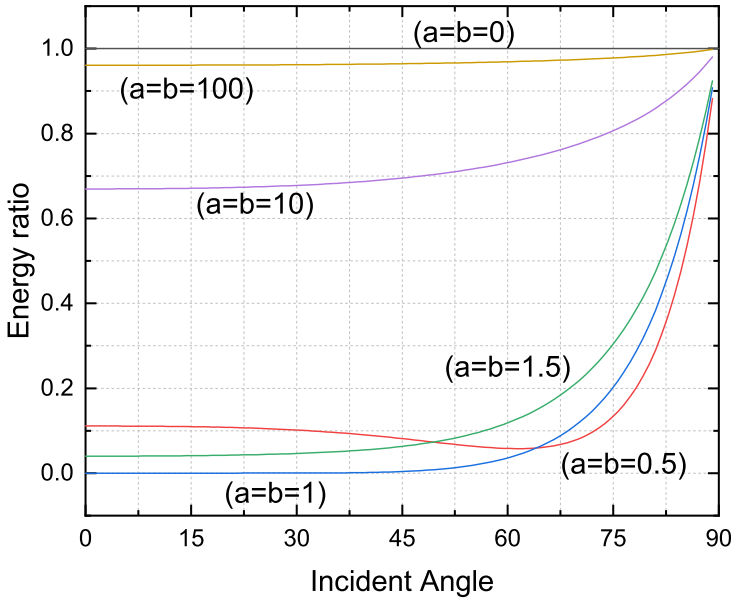

Fig. 3.10.: Effect of parameters a, b on energy ratio for incident P-wave (Poisson's ratio=0.25)

Fig. 3.10 depicts the effect of choice of free parameters a, b on the performance of LK-ABC (Poisson's ratio =0.25). It can be observed that the choice of $a = b = 1.0$ provides highly efficient LK-ABC as it gives the maximum absorption. The absorption cannot be made perfect over the whole rage of incident angles by any choice of a and b. This is further confirmed by Fig. 3.12 which present the variation of amplitudes with the angle of incidence at $a = b = 1.0$ and Poisson's ratio=0.25. Further, nearly perfect absorption is attained in the range $0 < \theta < 60°$ for $a = b = 1$. Lysmer and Kuhlemeyer, 1969 showed that the LK-ABC for $a = b = 1$ is 98.5 % effective in absorbing the impinging P-waves. Besides, Fig. 3.11 shows that LK-ABC is almost insensitive to the value of Poisson's ratio.

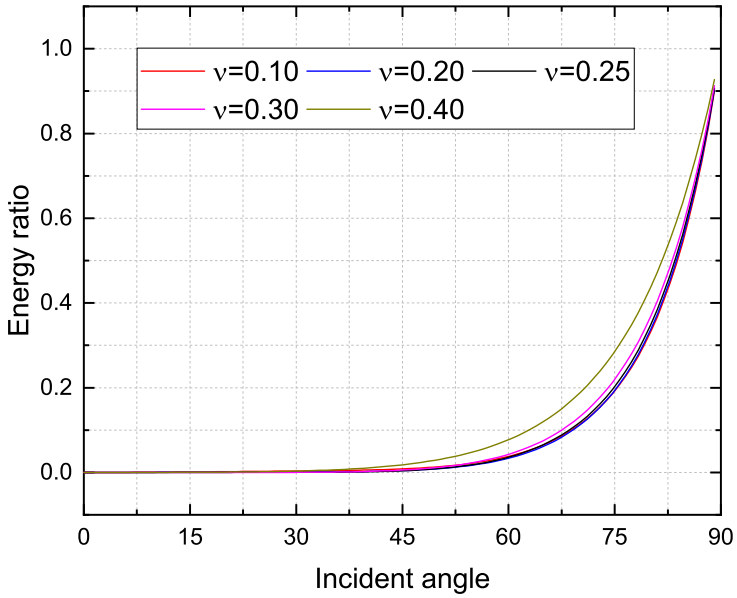

Fig. 3.11.: Effect of Poisson's ratio on energy ratio for incident P-wave ($a = b = 1.0$)

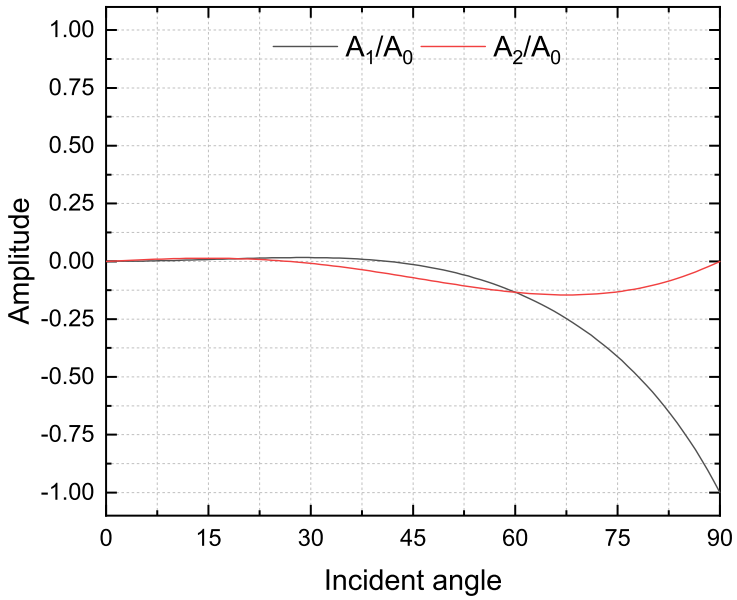

Fig. 3.12.: Variation of the normalized amplitudes A_1/A_0 and A_2/A_0 with the angle of incidence for incident P-wave (Poisson's ratio=0.25, $a = b = 1.0$)

3.4.5 Reflection of a SV-wave at the LK-boundary

Consider a SV-wave impinging the LK-boundary at an angle θ_0 with the normal as shown in Fig. 3.9a. The displacement and velocity of the incident and reflected waves is given by Eq. (3.79) and Eq. (3.80), respectively. Note that in present case the unit vector $\mathbf{d}^{(0)}$ and $\mathbf{p}^{(0)}$ in Table 3.1 are given by Eq. (3.93) and $c_0 = c_T$ while other entries related to the reflected waves remain the same.

$$\mathbf{d}^{(0)} = (-\cos\theta_0, \sin\theta_0)^T \qquad \mathbf{p}^{(0)} = (\sin\theta_0, \cos\theta_0)^T \tag{3.93}$$

In Table 3.2 the normal and tangential stress at LK-boundary due to impinging SV-wave are given by

$$\sigma_{22}^{(0)} = ik_0 A_0 \mu \sin 2\theta_0 \exp\left(i\bar{\eta}_0\right) \tag{3.94}$$

$$\sigma_{12}^{(0)} = -ik_0 A_0 \mu \cos 2\theta_0 \exp\left(i\bar{\eta}_0\right) \tag{3.95}$$

After satisfying the continuity of normal and tangential stress at LK-boundary (see Eq. 3.82 and Eq. 3.83) one can obtain the following linear equations in amplitudes A_1 and A_2.

$$A_1\left(s^2 - 2\sin^2\theta_1 + as^2\cos\theta_1\right) - A_2\left(\sin 2\theta_0 s + as^2\sin\theta_0\right) = A_0\left(as^2\sin\theta_0 - s\sin 2\theta_0\right) \tag{3.96}$$

$$A_1\left(\sin 2\theta_1 + bs\sin\theta_1\right) + A_2\left(s\cos 2\theta_0 + bs\cos\theta_0\right) = A_0\left(bs\cos\theta_0 - s\cos 2\theta_0\right) \tag{3.97}$$

Eq. (3.96) and Eq. (3.97) are obtained using the following intermediate results

$$\theta_2 = \theta_0 \qquad k_2 = k_0 \tag{3.98}$$

$$\sin\theta_1 = s\sin\theta_0 \qquad k_1 = k_0/s \tag{3.99}$$

Accordingly, the energy ratio becomes

$$\mathscr{E} := \frac{E_r}{E_i} = \left(\frac{A_2}{A_0}\right)^2 + s\frac{\cos\theta_1}{\cos\theta_0}\left(\frac{A_1}{A_0}\right)^2 \tag{3.100}$$

In case of impinging SV-wave, a special case occurs when the angle of incidence θ_0 is greater than some critical angle θ_{cr} defined by

$$\theta_{cr} = \sin^{-1}(1/s) \tag{3.101}$$

In this situation (i.e. $\theta_0 > \theta_{cr}$) Eq. (3.99a) shows that $\sin\theta_1 > 1$, consequently $\cos\theta_1$ and $\mathbf{p}^{(1)}$ (see Table 3.1) should be described by a complex number. It is noteworthy that critical angle depends only on the Poisson's ratio of the medium. Table 3.3 shows that θ_{cr} decreases with increasing Poisson's ratio. Further, amplitudes A_1 and A_2 are also given by complex numbers.

$$`A_1 = A_1^R + iA_1^I \qquad\qquad A_2 = A_2^R + iA_2^I \tag{3.102}$$

Noting these changes in Eq. (3.96) and (3.97) the system of linear equations in real and imaginary components of amplitudes takes the form

$$[\mathbf{A}]\{\mathbf{x}\} = \{\mathbf{b}\} \tag{3.103}$$

where

$$[\mathbf{T}] = \begin{bmatrix} \left(s^2 - 2\sin^2\theta_1\right) & -as^2\beta & -\left(\sin 2\theta_0 s + as^2\sin\theta_0\right) & 0 \\ as^2\beta & s^2 - 2\sin^2\theta_1 & 0 & -\left(\sin 2\theta_0 s + as^2\sin\theta_0\right) \\ bs\sin\theta_1 & -2\beta\sin\theta_1 & (s\cos 2\theta_0 + bs\cos\theta_0) & 0 \\ 2\beta\sin\theta_1 & bs\sin\theta_1 & 0 & (s\cos 2\theta_0 + bs\cos\theta_0) \end{bmatrix} \tag{3.104}$$

$$\{\mathbf{x}\} = \begin{bmatrix} A_1^R \\ A_1^I \\ A_2^R \\ A_2^I \end{bmatrix} \qquad \{\mathbf{b}\} = \begin{bmatrix} as^2\sin\theta_0 - s\sin 2\theta_0 \\ 0 \\ bs\cos\theta_0 - s\cos 2\theta_0 \\ 0 \end{bmatrix} \tag{3.105}$$

ν	θ_{cr}	ν	θ_{cr}
0.10	41.8°	0.30	32.3°
0.15	39.9°	0.35	28.7°
0.20	37.8°	0.40	24.0°
0.25	35.3°	0.45	17.5°

Tab. 3.3.: Critical angle of incidence (θ_{cr}) for different values of Poisson's ratio (ν)

The physical significance of the complex amplitudes (or $\sin\theta_1 > 1$) is that a reflected P-wave does not exist and, instead, a surface wave appears. The amplitude of the surface wave decays exponentially in the normal direction to the surface. Accordingly,

in computation of energy-ratio the energy due to surface wave should be excluded as this wave travels parallel to the surface. Eq. (3.100) now becomes

$$\mathscr{E} = \left(\frac{A_2}{A_0}\right)^2 = \left(\frac{A_2^R}{A_0}\right)^2 + \left(\frac{A_2^I}{A_0}\right)^2 \tag{3.106}$$

From Fig. 3.13 it can be observed that the choice of $a = b = 1.0$ provides highly efficient LK-ABC. Lysmer and Kuhlemeyer, 1969 showed that for $a = b = 1.0$ the LK-ABC is 95% effective in absorbing the S-waves. Fig. 3.15 depicts the variation of real and imaginary part of amplitudes with the angle of incidence at $a = b = 1.0$ and Poisson's ratio=0.25. In all cases the performance of LK-ABC decreases significantly when the angle of incidence becomes greater than the critical angle. It indicates that LK-ABC are not very efficient for the absorbing the surface waves. Further, Fig. 3.14 suggests that the performance of LK-ABC is nearly independent of the Poisson's ratio. Finally, it can be concluded that the performance of LK-ABC mainly depends upon the angle of incidence. In particular, the LK-ABC performs reasonably well when the angle of incidence is in the range $0 < \theta_0 < 60^\circ$ for $a = b = 1$.

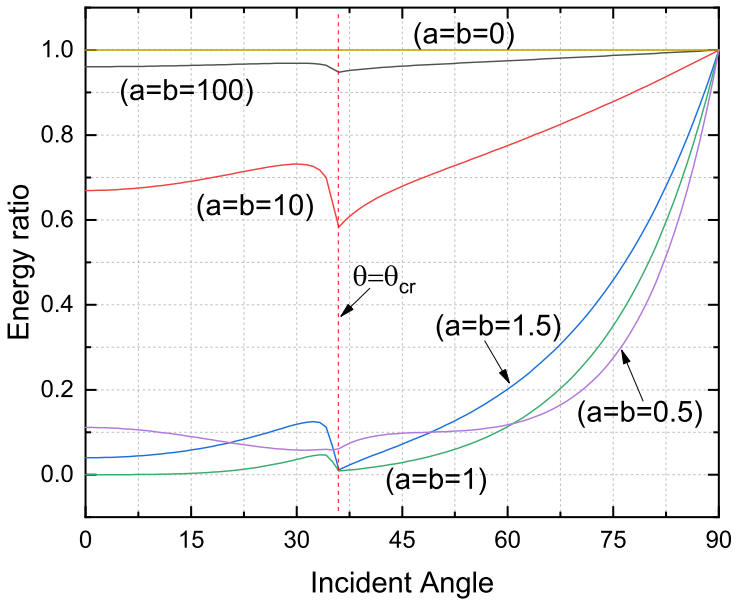

Fig. 3.13.: Effect of parameters a, b on energy ratio for incident S-wave (Poisson's ratio=0.25)

3.5 Free field response and effective seismic input

When the source of excitation is present inside the truncated computation domain, as discussed in previous section, the mechanical disturbance generates inside the domain and propagates towards the infinity through the artificial boundaries. In such cases, consequently, the dynamic response of structure does not depend upon

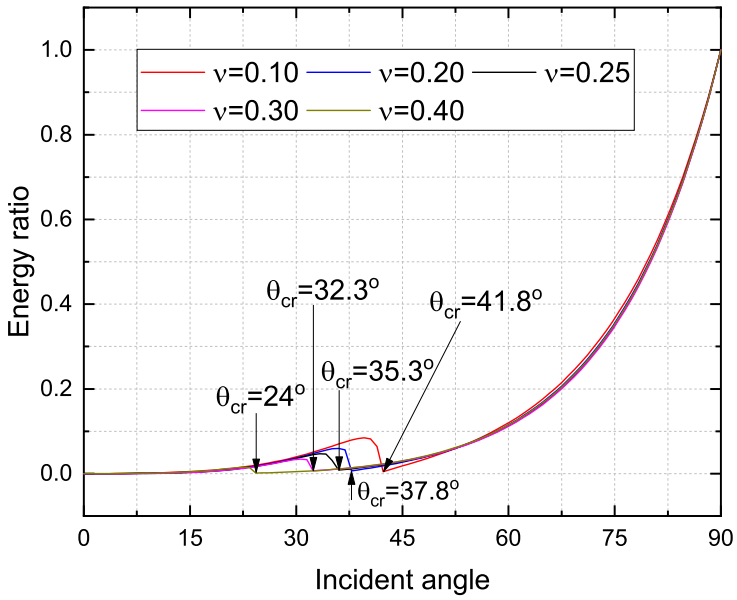

Fig. 3.14.: Effect of Poisson's ratio (ν) on energy ratio for incident S-wave ($a = b = 1.0$)

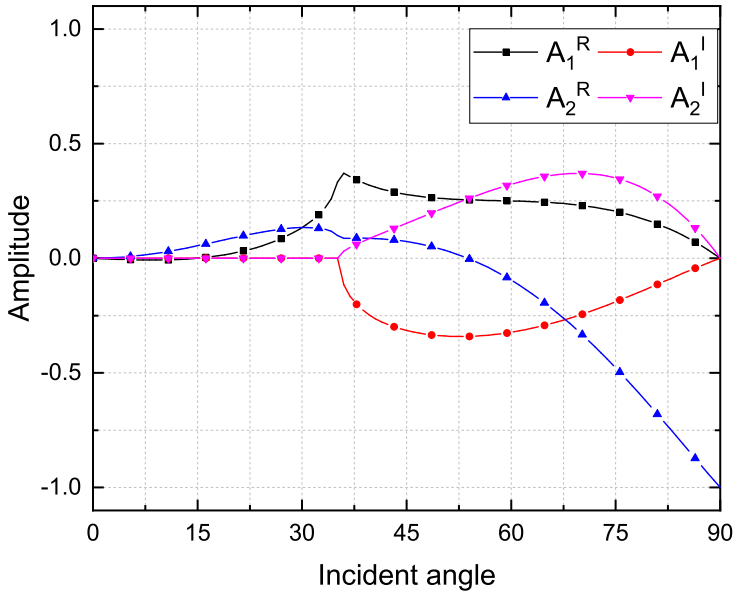

Fig. 3.15.: Variation of real and imaginary part of amplitude with angle of incidence for incident S-wave (Poisson's ratio=0.25, $a = b = 1.0$)

the response of exterior unbounded domain. Accordingly, the prescribed boundary condition on artificial boundary should satisfy the radiation damping with significant accuracy in order to simulate this one-way interaction.

In practical cases, such as earthquake excitation, blast engineering, vibrations due to high-speed railways and road-traffic among others, the source of dynamic loading may be present outside of computational domain. Consequently, the response of structure is coupled with the dynamic response of the unbounded domain. It is clear that, irrespective of the type of ABC employed to truncate the domain, the response of unbounded domain with the structure present will differ significantly from that of the free field ground motion (Bielak and Christiano, 1984). Thereby, to correctly model the dynamic SSI one has to ensure not only the absorption of the outgoing scattered wave motion using appropriate ABC but also the input of the free field ground motion into the numerical model. Unfortunately, the seismic excitation cannot be specified directly at the artificial boundaries as this would render any absorbing boundary ineffective (Løkke and Chopra, 2017). Thus it is necessary to prescribe the seismic excitation in the form of effective generalized earthquake forces.

Bielak and his coworkers (Bielak and Christiano, 1984; Bielak et al., 2003; Yoshimura et al., 2003; Cremonini et al., 1988) presented a two step procedure for an effective seismic input while treating the dynamic SSI as a scattering problem. In first step, effective seismic forces were expressed in terms of free-field tractions and displacements in unperturbed soil-medium. In second step, the effective forces are applied as input over the domain slightly bigger to contain both structure and absorbing boundary. Their method seems to be very efficient for reducing the size of computation domain as it requires to store free-field displacements only in a single layer of elements next to the soil-structure interface. Clearly, their method has the advantage of eliminating the need to transmit seismic excitation through the artificial boundary into the region of interest, in this way absorbing boundary need to only absorb the outgoing waves. However, implementation of such schemes requires a significant change in the existing finite element programs.

Alternatively, the LK-ABC can be engineered to allow sesimic excitation to enter the computation domain. Such procedures are very simple, quite effective and require little changes in the existing computer programs (Miura and Okinaka, 1989; Zienkiewicz et al., 1989; Saouma et al., 2011; Løkke and Chopra, 2017; Nielsen, 2006; Zhang et al., 2003).

Fig. 3.16a illustrates the situation where a structure (possibly with nonlinear material behaviour) embedded inside a linear elastic half-space is subjected to the earthquake excitation. The auxiliary state of the system is defined by elastic-half space without

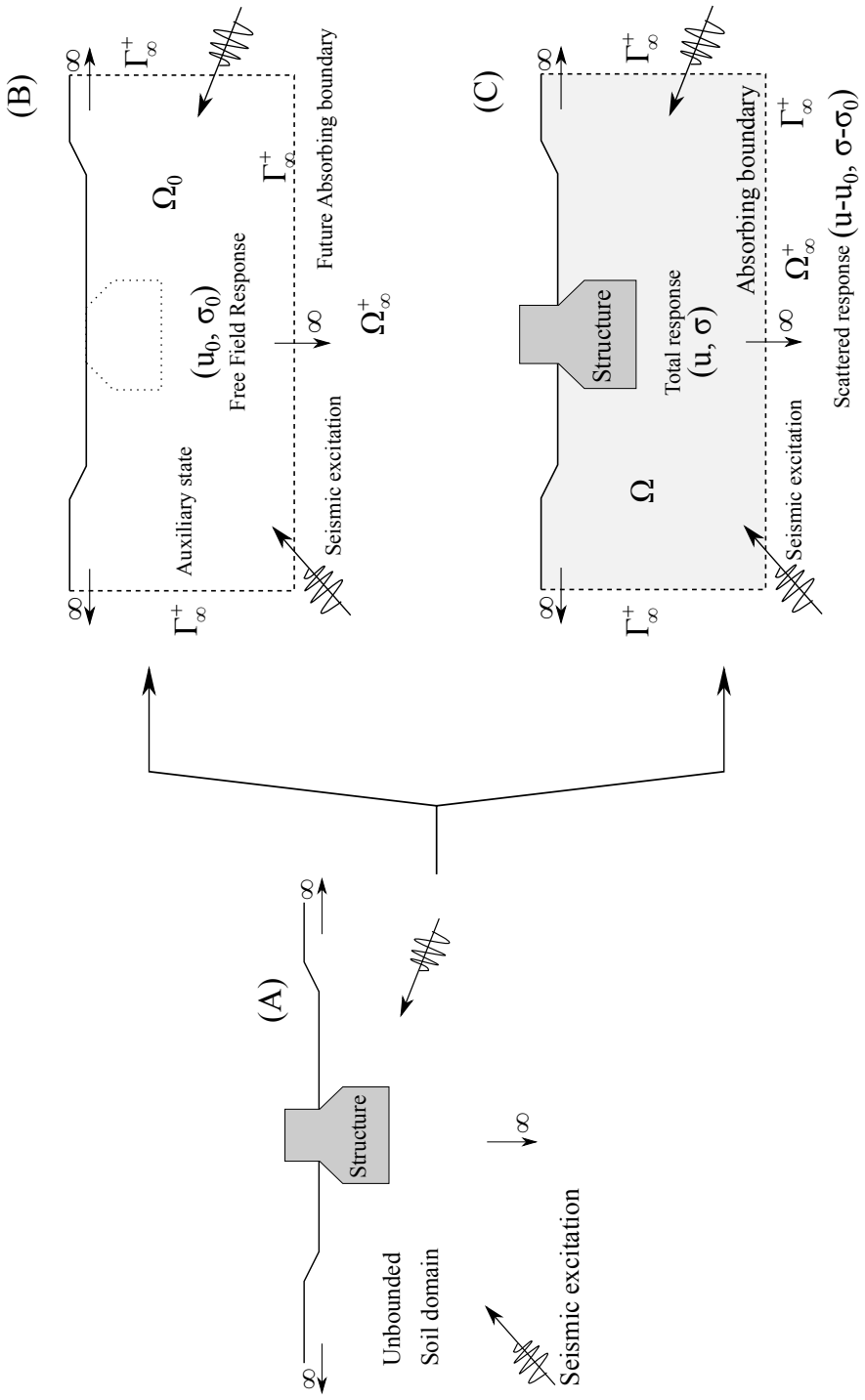

Fig. 3.16.: Illustration of soil-structure interaction as a scattering problem

the structure (see Fig. 3.16b). The term *free field* response will used for the dynamic response of the auxiliary state under seismic loading.

As described earlier in this chapter, once the wave reaches at the free surface (and/or interface between two soil layers) reflection will occur. Hence, the free field variables $(\mathbf{u}_0, \mathbf{v}_0, \sigma_0)$ contains the contribution due to both incoming and reflected waves. If some structure is embedded inside the half-space then it will perturbed the free-field response. The degree of perturbation, of course, depends upon the dynamic response of the structure itself. Clearly, the dynamic SSI can be scrutinized from the point of view of scattering problem (Bielak and Christiano, 1984; Bielak et al., 2003; Yoshimura et al., 2003; Cremonini et al., 1988; Løkke and Chopra, 2017; Basu and Chopra, 2004). In the following subsection this concept will be utilized to modify the viscous boundary condition, Eq. (3.77) and Eq. (3.78), so that LK ABC can absorb the outgoing scattered waves while allowing the energy inflow from the outer free fields.

3.5.1 Viscous boundary condition for free field input

Let Ω_0 be some fictitious finite domain of the auxiliary state which will contain the structure in the future (see Fig. 3.16). Let Γ_∞^+ denotes that part of the boundary of Ω_0 which will eventually coincide with the absorbing boundaries. Let $\mathbf{u}_0, \mathbf{v}_0, \sigma_0$ be the free field displacement, velocity and stress, respectively. Let Ω_∞^+ be the regular unbounded domain exterior to the Γ_∞^+. One should keep in mind that that the auxiliary state does not correspond to any physical state but is introduced to formulate the appropriate absorbing boundary condition. Fig. 3.16c depicts the actual computation domain Ω separated from the Ω_∞^+ through the viscous boundary Γ_∞^+. $\mathbf{u}, \mathbf{v}, \sigma$ denote the total displacement, total velocity and total stress, respectively, inside the computation domain Ω. On contrary, the variables $\tilde{\mathbf{u}}, \tilde{\mathbf{v}}, \tilde{\sigma}$ represent the scattered motion in the exterior unbounded domain Ω_∞^+. Further, the total displacement and velocity can be decomposed in terms of scattered solution and free-field solution (Bielak and Christiano, 1984).

$$\mathbf{u} = \tilde{\mathbf{u}} + \mathbf{u}_0 \qquad\qquad \mathbf{v} = \tilde{\mathbf{v}} + \mathbf{v}_0 \tag{3.107}$$

Noting the fact that the material in the vicinity of the absorbing boundary behaves linearly, the stress at the boundary can be written as

$$\sigma \cdot \mathbf{n} = \tilde{\sigma} \cdot \mathbf{n} + \sigma_0 \cdot \mathbf{n} \quad \text{on} \quad \Gamma_\infty^+ \tag{3.108}$$

where $\tilde{\sigma}$ denotes the stress corresponding to $\tilde{\mathbf{u}}$ and $\mathbf{n}$ is the unit outward normal to Γ_∞^+.

To simulate the effect of unbounded domain viscous boundary should absorb the outgoing scattered waves, accordingly Eq. (3.77) and Eq. (3.78) becomes

$$\tilde{\sigma}_n = -a\rho c_L \tilde{v}_n \tag{3.109}$$

$$\tilde{\tau} = -b\rho c_T \tilde{v}_s \tag{3.110}$$

where $\tilde{\sigma}_n$ and $\tilde{\tau}$ are the normal and tangential boundary traction and $\tilde{v}_n, \tilde{v}_s$ are the normal and tangential scattered velocity components. Finally, using Eq. (3.107) and Eq. (3.108) in the above two equation

$$\sigma_n = -a\rho c_L v_n + a\rho c_L (v_0)_n + (\sigma_0)_n \tag{3.111}$$

$$\tau = -b\rho c_T v_s + b\rho c_T (v_0)_s + \tau_0 \tag{3.112}$$

The presence of last two terms in Eq. (3.111) and Eq. (3.112) will allow the energy to flow from the exterior domain Ω_∞^+ into the computation domain Ω_0 through the viscous boundaries Γ_∞^+. At this point it is critical to note that the modified viscous boundary requires information of the free field response $(\mathbf{u}_0, \mathbf{v}_0)$ only at the absorbing boundary.

3.5.2 Effective seismic input

In order to compute the effective seismic input using Eq. (3.111) and Eq. (3.112) it is necessary to determine the free field motion $(\mathbf{u}_0, \mathbf{v}_0)$. There are various methodologies to compute $\mathbf{u}_0$. For example, if the informations about the rupture characteristics of earthquake faults, the geological material between the earthquake source and the site, and local site conditions is available then one can conduct a large-scale 3D simulation of seismic wave propagation from an earthquake source to region near the structure (Bao et al., 1998). This level of details, however, is rarely available, therefore such simulation are impractical at present.

One of the practical ways, is to define the ground motion at the some control point based on a design spectrum. Probabilistic seismic hazard analysis, artificially generated motions, recorded ground motions, among other techniques can be used to generate earthquake motions. Further, these motions can be scaled and modified to match the target spectrum in some sense (Hariri-Ardebili et al., 2016; Zhang et al., 2003). Furthermore, under the assumption of vertically propagating body waves and homogeneous or layered soil stratum, the free-field motion $\mathbf{u}_0$ at the boundary

Γ_∞^+ can be obtained by one-dimensional deconvolution of the ground motion at the control point (Schnabel, 1972; Hashash, 2009). In principle, the motion of every nodal point on Γ_∞^+ can computed usig the the deconvolution analysis, but in practice this approach may become a computational burden for a large number of elevations.

The above problem related to the deconvolution technique can be avoided under the condition that the body waves (P-wave and S-wave) due to the seismic excitation propagates in the vertical direction in an isotropic, homogeneous, elastic half space. To derive the expression for effective seismic input consider a vertically propagating SV-wave as described in Section 3.4.2. Let absorbing boundary be placed at $x_2 = 0$ where the seismic wave is entering the system. Total displacement of the particle will be

$$u_1(x_2, t) = f\left(t - \frac{x_2}{c_T}\right) + g\left(t + \frac{x_2}{c_T}\right) \tag{3.113}$$

and the velocity

$$v_1(x_2, t) = f'\left(t - \frac{x_2}{c_T}\right) + g'\left(t + \frac{x_2}{c_T}\right) \tag{3.114}$$

or

$$v_1 = v_1^I + v_1^R \tag{3.115}$$

where $v_1^I = f'(\cdot)$ and $v_1^R = g'(\cdot)$ denote incoming and outgoing velocity wave. Noting that σ_{12} is the only non-zero stress component and $\mathbf{n} = (0, -1)^T$ at the boundary $x_2 = 0$, the tangential boundary traction becomes

$$\tau = -\sigma_{12} = -\rho c_T\left(-v_1^I + v_1^R\right) \tag{3.116}$$

using Eq. (3.115) in Eq. (3.116)

$$\tau = -\rho c_T v_1 + \rho c_T 2 v_1^I \tag{3.117}$$

adopting $v_s^I = v_1^I$ and $v_s = v_1$ for the component of incoming and total velocity tangential to the boundary $x_2 = 0$, respectively.

$$\tau = -\rho c_T v_s + \rho c_T 2 v_s^I \tag{3.118}$$

Following the same procedure for the vertically propagating P-wave one can obtain

$$\sigma_n = -\rho c_L v_n + \rho c_L 2 v_n^I \tag{3.119}$$

Comparing Eq. (3.118) with Eq. (3.112) and Eq. (3.119) with Eq. (3.111) it can be seen that under the assumption of vertically propagating body waves in an isotropic, homogeneous, linear elastic-half space the equivalent forces due to seismic motion

on the bottom boundary can be described completely in terms of the incoming velocity at $x_2 = 0$. In this way the incoming velocity at the bottom can be computed through the deconvolution of the ground motion at the control point. Furthermore, from Eq. (3.118) and Eq. (3.119) it is evident that the incident velocity v^I is half of the total velocity at the free surface[8].

3.6 Summary

In this chapter, a concise presentation regarding the theory of wave propagation in an elastic solid is given. After briefly discussing the reflection and refraction of a plane harmonic waves it is shown that the problem of dynamic soil-structure interaction can be viewed as a wave-scattering phenomenon, in which the free-field response of an elastic half-space is perturbed by the existing structure. Furthermore, the chapter presents some of the most popular boundary conditions for solving wave propagation problems in the unbounded domain. In addition, the viscous boundary conditions first proposed by Lysmer and Kuhlemeyer, 1969 are derived, and a comprehensive discussion related to the numerical characteristics of the viscous boundary conditions is made. Lastly, the viscous boundary conditions are reviewed to allow seismic excitation to enter the computational domain.

[8]This result can be obtain by setting zero traction at the free surface using Eq. (3.118) and Eq. (3.119)

4 v-ST/FEM for The Dynamic Soil-Structure Interaction Problem

4.1 Introduction

The seismic behaviour of a structure is highly influenced not only by the dynamic response of the superstructure, but also by the response of the underlying soil (Kausel, 2010). The problem of dynamic soil-structure interaction (SSI) had already been studied as early as 1935 in Japan by Katsutada Sezawa and Kiyoshi Kanai who published a truly remarkable, pioneering paper on the subject (Sezawa and Kanai, 1935d; Sezawa and Kanai, 1935a; Sezawa and Kanai, 1935c; Sezawa and Kanai, 1935b). Analytical solutions for the problem of dynamic interaction between superstructure (with regular shaped foundation) and underlying isotropic, homogenous, linear elastic half-space have been presented by many researchers (Arnold et al., 1955; Bycroft, 1956; Richardson et al., 1971; Warburton et al., 1971; Luco and Contesse, 1973; Trifunac, 1972; Wong and Trifunac, 1974; Saito and Wada, 1977). However, in practice, the close form solutions are applicable only under certain circumstances, for example when the superstructure is considered as rigid and/or massless, and the shape of the foundation is circular, rectangular, or elliptical. Undoubtedly, it becomes indispensable to study the effect of soil-structure interaction for heavy structures such as concrete gravity dams.

In chapter 3, it is shown that the dynamic SSI problem can be tackled as a wave-propagation (or wave-scattering) problem in an unbounded soil domain. In order to work with the finite computational domain artificial boundaries with appropriate absorbing boundary conditions are used to truncate the unbounded soil-domain. Finite element methods (FEM) have been widely used to solve dynamic SSI problem. FEM based on frequency domain are only applicable to the linear problem, therefore, incorporation of nonlinear material behavior will be a prohibitive task for them. FEM in time domain, on the other hand, do not suffer from such limitations. Finite element methods coupled with boundary element methods (FEM-BEM) in time domain have also been developed for dynamic SSI problems (Touhei and Ohmachi, 1993; Yazdchi et al., 1999; Chuhan et al., 1995). In FEM-BEM, the domain is divided into near-field and far-field domain, subsequently, finite elements are used to model near-field while far-field is modeled by using boundary elements. FEM

equipped with the infinite elements, a natural extension of finite elements to handle unbounded domains, have been proposed to solve wave propagation in unbounded domain (Bettess, 1977; Medina and Penzien, 1982; Valliappan and Zhao, 1992; Zhao et al., 1992). In this approach, the near field is modeled by FEM and the far field is modeled by infinite elements.

In this chapter v-ST/FEM is extended to solve the problem of dynamic soil-structure interaction. The contents of this chapter are as follows. In section 4.2 governing equations of a typical soil-structure interaction problem are presented. In section 4.3, weak-form for v-ST/FEM is presented. The space-time finite element discretization of weak form is discussed in Section 4.4. Subsequently, the computer implementation of proposed method is demonstrated in section 4.5 and section 4.6. In section 4.7 v-ST/FEM method is employed for computing the seismic response of a concrete gravity dam (without reservoir). The results are then successfully compared with the semi-discrete FEM with Newmark-β method.

4.2 Statement of problem

Fig. 4.1 illustrates the computational setup for a typical two dimensional soil-structure interaction problem. The structure is allowed to exhibit nonlinear behavior and is partially (or fully) embedded in the unbounded domain. However, for clarity of v-ST/FEM formulation it will be assumed that the structure behaves linearly. The bounded and unbounded soil domain are assumed to behave linearly. In practice, the structure can represent a tunnel, a gravity dam with its foundation, a high-rise buildings, a thermal-nuclear power plant, among others.

Let Ω be the truncated computational domain that contains both the structure and the linear bounded soil domain (see Fig. 4.1). Let Γ_{∞}^{+} denotes the artificial boundary of Ω where the viscous boundary conditions are imposed. Γ_{∞}^{+} is divided into left viscous boundary Γ_{∞}^{L}, right viscous boundary Γ_{∞}^{R}, and bottom viscous boundary Γ_{∞}^{B}. Further, it is assumed that the seismic excitations are represented by vertically propagating waves and entering the computation domain Ω from the bottom viscous boundary only Γ_{∞}^{B}. Let $a_i^{in}(t)$ and $v_i^{in}(t)$, with $i = 1, 2$, denote the component of input acceleration and velocity, respectively. [1]

[1]Here, $i = 1$ and $i = 2$ denote the components along x_1-axis and x_2-axis, respectively.

The strong form of the initial-boundary value problem of elastodynamics [2] can be stated as, given the functions

$$b_i : \Omega \times [0,T] \to \mathbb{R}$$

$$g_i : \Gamma_i^g \times [0,T] \to \mathbb{R}$$

$$h_i : \Gamma_\infty^+ \cup \Gamma_i^h \times [0,T] \to \mathbb{R}$$

$$u_i^0 : \Omega \to \mathbb{R}$$

$$v_i^0 : \Omega \to \mathbb{R}$$

$$\rho : \Omega \to \mathbb{R}$$

find $u_i : \bar{\Omega} \times [0,T] \to \mathbb{R}$ such that

$$\rho \frac{\partial^2 u_i}{\partial t^2} - \frac{\partial \sigma_{ij}}{\partial x_j} - \rho b_i = 0 \quad \forall\, (\mathbf{x}, t) \in \Omega \times (0,T) \tag{4.1}$$

$$u_i(\mathbf{x},t) = g_i(\mathbf{x},t) \quad \forall (\mathbf{x},t) \in \Gamma_i^g \times (0,T) \tag{4.2}$$

$$\sigma_{ij} n_j = h_i \quad \forall (\mathbf{x},t) \in \Gamma_\infty^+ \cup \Gamma_i^h \times (0,T) \tag{4.3}$$

$$u_i(\mathbf{x},0) = u_i^0(\mathbf{x}) \quad \forall \mathbf{x} \in \Omega \tag{4.4}$$

$$\frac{\partial u_i}{\partial t}(\mathbf{x},0) = v_i^0(\mathbf{x}) \quad \forall \mathbf{x} \in \Omega \tag{4.5}$$

where ρ denotes the mass density, b_i denotes the body force, g_i is the prescribed displacement on Dirichlet-boundary Γ_i^g, h_i denotes the boundary traction, u_i^0 and v_i^0 is the initial value of the velocity field. Here $i = 1, 2$ denotes the i^{th} spatial component.

The traction boundary condition given in Eq. (4.3) can be used to classify the types of dynamic soil-structure interaction (SSI) problems. Some of the traction boundary conditions related to the dynamic SSI problem are given below.

(i) Traction condition due to the externally applied surface load on the boundary Γ_i^h (see Fig. 4.1) is given by

$$\sigma_{ij} n_j = f_i^s \quad on \quad \Gamma_i^h \tag{4.6}$$

[2] This strong form is described in Chapter 3, however, for the sake of completeness the form is repeated here.

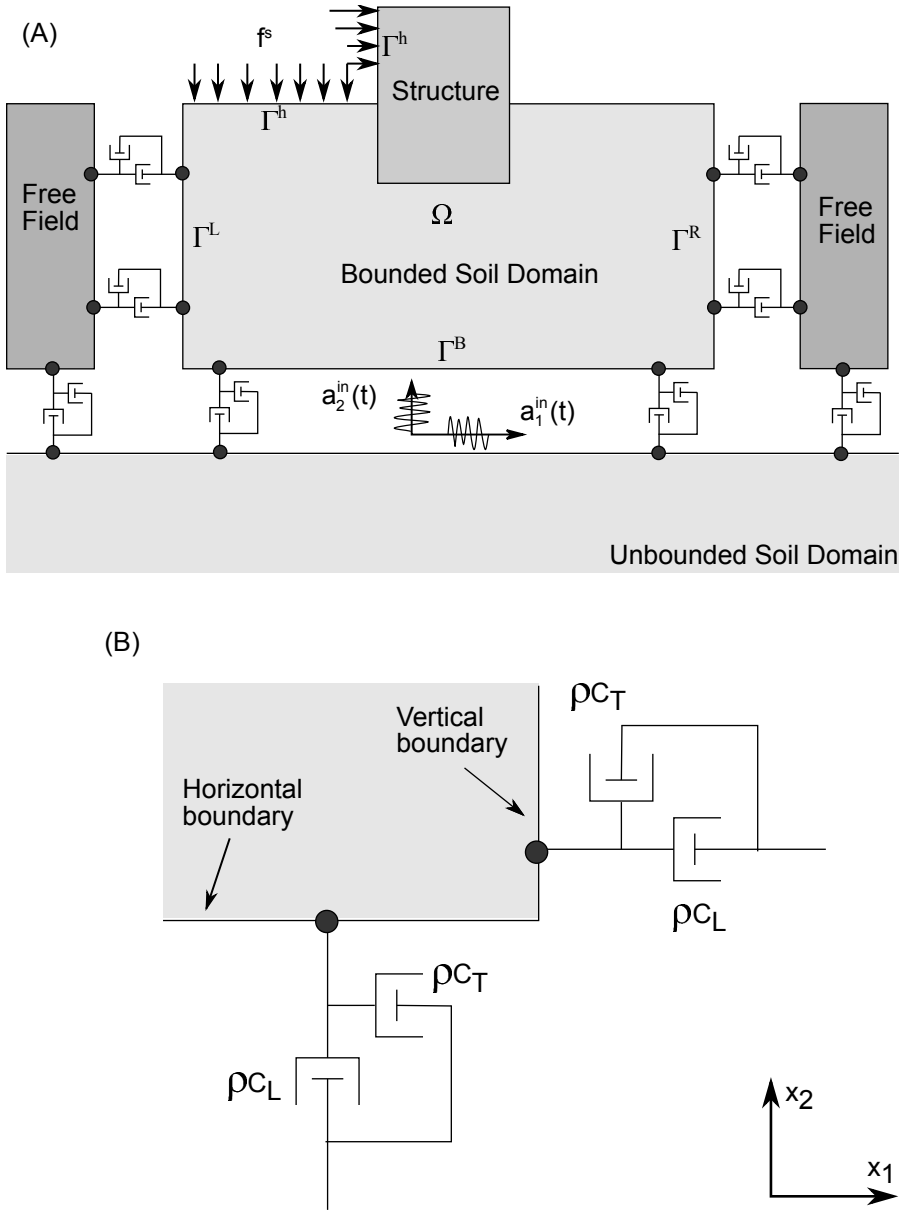

Fig. 4.1.: Schematic diagram of (A) computational setup for a general soil-structure interaction problem using modified viscous boundary condition, (B) orientation of dashpots and distribution of damping coefficients at vertical and horizontal absorbing boundary

(ii) Traction boundary conditions due to the series of dashpots arranged at the truncated absorbing (viscous) boundary Γ_∞^+ in parallel and normal direction are derived in section 3.4 (see Eq. (3.77 – 3.78) and here rewritten as,

$$\sigma_n = -\rho c_L v_n \tag{4.7}$$

$$\tau = -\rho c_T v_s \tag{4.8}$$

Recalling that in a typical two-dimensional SSI problem, the unbounded soil-domain is usually truncated by placing vertical and horizontal artificial boundaries at some distance from the area of interest. The tensor component form of viscous boundary conditions Eq. (4.7 – 4.8) for vertical boundaries Γ_∞^L and Γ_∞^R is given by

$$\sigma_{ij} n_j = -c_{ip}^v v_p \quad on \quad \Gamma_\infty^L \cup \Gamma_\infty^R \tag{4.9}$$

Similarly, viscous boundary condition on the bottom horizontal truncated boundary Γ_∞^B can be written as,

$$\sigma_{ij} n_j = -c_{ip}^h v_p \quad on \quad \Gamma_\infty^B \tag{4.10}$$

In Eq. (4.9 – 4.10), $\mathbf{c}^v$ and $\mathbf{c}^h$ denote the damping coefficients matrix for the dashpots that are placed at the vertical and horizontal truncated boundaries (see Fig. 4.1). These matrices are described as follows.

$$\mathbf{c}^v = \begin{bmatrix} \rho c_L & 0 \\ 0 & \rho c_T \end{bmatrix} \tag{4.11}$$

$$\mathbf{c}^h = \begin{bmatrix} \rho c_T & 0 \\ 0 & \rho c_L \end{bmatrix} \tag{4.12}$$

in which, c_L and c_T are the speed of longitudinal wave (P-wave) and transverse wave (S-wave) in the unbounded medium, respectively.

(iii) Traction boundary conditions for vertical artificial boundaries due to the free field motion are derived in section 3.5 (see Eq. 3.111 and Eq. 3.112), where it is shown that additional boundary terms should be included in Eq. (4.9) for viscous boundaries to allow the energy flow from far-field to the computation domain. The additional boundary terms are formulated in terms of free field motion $(\mathbf{u}^f, \mathbf{v}^f, \sigma^f)$ and given by

$$\sigma_{ij} n_j = c_{ip}^v v_p^f + \sigma_{ip}^f n_p \quad on \quad \Gamma_\infty^L \cup \Gamma_\infty^R \tag{4.13}$$

where, n_p is the p^{th} spatial component of outward normal vector at the artificial boundary, and the matrix $\mathbf{c}^h$ is same as the one given in Eq. (4.12).

(iv) Traction boundary condition at the bottom artificial boundary due to the incoming seismic waves, which allow the vertically propagating seismic waves to enter the computation, are derived in section 3.5 (see Eq. 3.118 and Eq. 3.119). The tensor component form of these boundary condition is given by

$$\sigma_{ij}^{in} n_j = 2c_{ip}^h v_p^{in} \quad on \quad \Gamma_\infty^B \tag{4.14}$$

where $\mathbf{v}^{in}$ is the incoming velocity wave.

For situations where the source of excitation resides in the computation domain the traction boundary conditions at the artificial boundary are due to the dashpots only, accordingly one can avoid Eq. (4.13) and Eq. (4.14) in the traction boundary condition. Moreover, if only Eq. (4.6) is used to impose the traction boundary condition then the problem becomes identical to the one discussed in Chapter 2 (see Section 2.5).

The final form of traction boundary conditions used in this chapter are given by

$$\sigma_{ij} n_j = f_i^s \quad on \quad \Gamma_i^h \tag{4.15}$$

$$\sigma_{ij} n_j = -c_{ip}^v v_p + c_{ip}^v v_p^f + \sigma_{ip}^f n_p \quad on \quad \Gamma_\infty^L \cup \Gamma_\infty^R \tag{4.16}$$

$$\sigma_{ij} n_j = -c_{ip}^h v_p + 2c_{ip}^h v_p^{in} \quad on \quad \Gamma_\infty^B \tag{4.17}$$

The vector form is described by

$$\sigma \cdot \mathbf{n} = \mathbf{f}^s \quad on \quad \Gamma^h \tag{4.18}$$

$$\sigma \cdot \mathbf{n} = -\mathbf{c}^v \cdot \mathbf{v} + \mathbf{c}^v \cdot \mathbf{v}^f + \sigma^f \cdot \mathbf{n} \quad on \quad \Gamma_\infty^L \cup \Gamma_\infty^R \tag{4.19}$$

$$\sigma \cdot \mathbf{n} = -\mathbf{c}^h \mathbf{v} + 2\mathbf{c}^h \cdot \mathbf{v}^{in} \quad on \quad \Gamma_\infty^B \tag{4.20}$$

4.3 v-ST/FEM formulation

Let Ω_h, the set of finite spatial elements Ω_e, $e = 1, \cdots, n_{el}$, be the discretization of spatial domain Ω, where n_{el} is the total number of spatial elements in Ω_h. Consider a non-uniform subdivision for the time domain $[0, T]$, $0 = t_0 < t_1 < \cdots < t_N = T$ with $I_n = (t_n, t_{n+1})$, $\Delta t = t_{n+1} - t_n$. The n^{th} space-time slab $Q_n = \Omega_h \times I_n$, and the space-time finite element $Q_{n,e} = \Omega_e \times I_n, e = 1, \cdots, n_{el}$.

Consider $\mathcal{P}_l(Q_{n,e})$, the collection of all polynomials defined on $Q_{n,e}$ with a total degree of no more than l, and $C^0(*)$, the space of piecewise continuous functions defined on domain $(*)$. Consider also the following collection of functions:

$$\mathfrak{F}_{l,h} := \left\{ \mathbf{u}^h \middle| \, \mathbf{u}^h \in C^0\left(\bigcup_{n=0}^{N-1} Q_n\right)^2, \mathbf{u}^h \middle| \, Q_{n,e} \in \left(\mathcal{P}_l\left(Q_{n,e}\right)\right)^2 \right\} \tag{4.21}$$

where $\mathbf{u}^h \big| \, Q_{n,e}$ is the restriction of $\mathbf{u}^h(\mathbf{x},t)$ to $Q_{n,e}$. The space of the test functions for the v-ST/FEM formulation is written as

$$V^h := \left\{ \mathbf{v}^h \middle| \, \mathbf{v}^h \in \mathfrak{F}_{l,h}, \mathbf{v}^h = 0, \forall\, (\mathbf{x},t) \in \Gamma_i^g \times I_n \right\} \tag{4.22}$$

The space of trial functions for the v-ST/FEM formulation is given by

$$S_v^h := \left\{ \mathbf{v}^h \middle| \, \mathbf{v}^h \in \mathfrak{F}_{l,h}, v_i^h = \dot{g}_i, \forall\, (\mathbf{x},t) \in \Gamma_i^g \times I_n, i = 1,2 \right\} \tag{4.23}$$

Following the procedure described in Chapter 2, and noting the traction boundary conditions Eqs. (4.15 – 4.17), the weak form for v-ST/FEM is given by; Find $\mathbf{v} \in S_v^h$ such that for all $\delta\mathbf{v} \in V^h$, and for all $n = 1, \cdots, N-1$, Eq. (4.24) holds.

$$\begin{aligned}
&\int_{I_n}\int_{\Omega_h} \delta v_i \rho \frac{\partial v_i}{\partial t} d\Omega dt + \int_{\Omega_h} \delta v_i \left(\mathbf{x}, t_n^+\right) \rho v_i \left(x, t_n^+\right) d\Omega - \int_{\Omega_h} \delta v_i \left(\mathbf{x}, t_n^+\right) \rho v_i \left(x, t_n^-\right) d\Omega \\
&- \int_{I_n}\int_{\Omega_h} \delta v_i \rho b_i d\Omega dt + \int_{I_n}\int_{\Omega_h} \frac{\partial \delta v_i}{\partial x_j} \sigma_{ij}^n d\Omega dt + \int_{I_n}\int_{\Omega_h} \frac{\partial \delta v_i}{\partial x_j} C_{ijkl} \psi_{kl} d\Omega dt \\
&- \int_{I_n}\int_{\Gamma_i^h} \delta v_i f_i^s ds dt + \int_{I_n}\int_{\Gamma_\infty^R \cup \Gamma_\infty^L} \delta v_i c_{ij}^v v_j ds dt + \int_{I_n}\int_{\Gamma_\infty^B} \delta v_i c_{ip}^h v_p ds dt \\
&- \int_{I_n}\int_{\Gamma_\infty^R \cup \Gamma_\infty^L} \delta v_i \left(c_{ij}^v v_j^f + \sigma_{ij}^f n_j\right) ds dt - \int_{I_n}\int_{\Gamma_\infty^B} \delta v_i 2 c_{ij}^h v_j^{in} ds dt = 0
\end{aligned} \tag{4.24}$$

where

$$\psi_{ij} = \int_{t_n}^{t} \frac{\partial v_i\,(\mathbf{x},\tau)}{\partial x_j} d\tau \quad \forall t \in I_n, \quad \forall \mathbf{v} \in S_v^h \tag{4.25}$$

4.4 v-ST/FEM discretization

Consider $Q_{n,e} = \Omega_e \times I_n$ denoting the space-time finite element. Let n_e be the total number of spatial nodes in Ω_e. Let $v_i(\mathbf{x}, t_n^+)$ and $v_i(\mathbf{x}, t_{n+1}^-)$ be the spatial velocities on the bottom and top faces of space-time slab Q_n, respectively (see Section 2.6). The time $t \in I_n$ is given by

$$t = T_1(\theta) t_n + T_2(\theta) t_{n+1}, \quad \forall \theta \in [-1, 1] \tag{4.26}$$

where

$$T_1(\theta) = \frac{1-\theta}{2} \qquad T_2(\theta) = \frac{1+\theta}{2} \tag{4.27}$$

The test and trial function for velocity defined on $Q_{n,e}$ are given by

$$\delta v_i(\mathbf{x},t) = {}^a\delta v_{iI} T_a(\theta) N^I(\xi,\eta) \tag{4.28}$$

$$v_i(\mathbf{x},t) = {}^a v_{iI} T_a(\theta) N^I(\xi,\eta) \tag{4.29}$$

The displacement field $\mathbf{u}(\mathbf{x},t)$ is computed by consistent integration of Eq. (4.29)

$$u_i(\mathbf{x},t) = u_i(\mathbf{x},t_n) + \tilde{T}_1(\theta) v_i(\mathbf{x},t_n) + \tilde{T}_2(\theta) v_i(\mathbf{x},t_{n+1}) \tag{4.30}$$

further, Eq. (4.25) becomes

$$\psi_{ij}(\mathbf{x},t) = \tilde{T}_1(\theta) \frac{\partial v_i}{\partial x_j}(\mathbf{x},t_n) + \tilde{T}_2(\theta) \frac{\partial v_i}{\partial x_j}(\mathbf{x},t_{n+1}) \tag{4.31}$$

where

$$\tilde{T}_1(\theta) = \frac{\Delta t_n}{2}\left[1 - T_1^2(\theta)\right] \qquad \tilde{T}_2(\theta) = \frac{\Delta t_n}{2} T_2^2(\theta) \tag{4.32}$$

In Eqs. (4.26 – 4.32), $i = 1,2$ denotes the component in x_1 and x_2 direction, $a = 1,2$ denotes the temporal node number, $I = 1,\cdots,n_e$ denotes the spatial node number, (ξ,η) are the local spatial coordinates, and $\theta \in [-1,1]$ denotes the local temporal coordinate.

Following the procedure as described in Chapter 2 for descretizing the weak form Eq. (4.24), one can obtain the following system of equation

$$\begin{aligned} &[M]_{ij}^{ab}(I,J)\{v\}_i^a(J) + [K]_{ij}^{ab}(\mathrm{I},J)\{v\}_i^a(J) + [C_\infty]_{ij}^{ab}(I,J)\{v\}_i^a(J) \\ &= \{J_{ext}\}_i^a(I) + \{J_0\}_i^a(I) - \{J_{\sigma^n}\}_i^a(I) + \{J_f\}_i^a(I) + \{J_{in}\}_i^a(I) \end{aligned} \tag{4.33}$$

the vector form

$$[\mathbf{K}_{st}]\{\tilde{\mathbf{v}}\} = \{\mathbf{J}\} \tag{4.34}$$

where

$$[\mathbf{K}_{st}] = [\mathbf{M}] + [\mathbf{K}] + [\mathbf{C}_\infty] \tag{4.35}$$

and

$$\{\mathbf{J}\} = \{\mathbf{J}_{ext}\} + \{\mathbf{J}_0\} - \{\mathbf{J}_{\sigma^n}\} + \{\mathbf{J}_f\} + \{\mathbf{J}_{in}\} \tag{4.36}$$

where the space-time nodal vector $\{\mathbf{J}_{ext}\}$ contains the contribution of external body force and external boundary traction, $\{\mathbf{J}_0\}$ contains the contribution of initial velocity,

$\{\mathbf{J}_{\sigma^n}\}$ contains the contribution of initial stress σ^n, $\{\mathbf{J}_f\}$ contains the contribution of free-field motion, $\{\mathbf{J}_{in}\}$ contains the contribution of incoming seismic velocity. In Eq. (4.34) $\{\tilde{\mathbf{v}}\}$ denotes the unknown space-time nodal values of velocity field

$$\{\tilde{\mathbf{v}}\} = \left\{ \begin{array}{c} \tilde{\mathbf{v}}^1 \\ \tilde{\mathbf{v}}^2 \end{array} \right\} \tag{4.37}$$

$$\{\tilde{\mathbf{v}}^a\} = \left\{ \begin{array}{c} \tilde{\mathbf{v}}^a_1 \\ \tilde{\mathbf{v}}^a_2 \end{array} \right\} \tag{4.38}$$

where $\{\tilde{\mathbf{v}}^1\}$ and $\{\tilde{\mathbf{v}}^2\}$ denote the space-nodal values of velocity field at time $t_n^+ = \lim_{\epsilon \to 0} (t_n + \epsilon)$ and $t_{n+1}^- = \lim_{\epsilon \to 0} (t_n - \epsilon)$, respectively, and $\left\{\tilde{\mathbf{v}}_1^{(\cdot)}\right\}$ and $\left\{\tilde{\mathbf{v}}_2^{(\cdot)}\right\}$ denote the space-nodal values of x_1 and x_2 components of velocity field. If Rayleigh damping is consider then the damping matrix,

$$[\mathbf{C}_R] = \alpha\,[\mathbf{M}_R] + \beta\,[\mathbf{K}_R] \tag{4.39}$$

where α and β are the Rayleigh damping coefficients, should be added to the space-time tangent matrix $[\mathbf{K}_{st}]$, and subsequently Eq. (4.35) becomes

$$[\mathbf{K}_{st}] = [\mathbf{M}] + [\mathbf{K}] + [\mathbf{C}_\infty] + [\mathbf{C}_R] \tag{4.40}$$

Table 4.1 and Table 4.2 succinctly provide the details about the terms present in the expression for space-time tangent matrix $[\mathbf{K}_{st}]$ and right-hand side vector $\{\mathbf{J}\}$, respectively. A detailed description about the derivation of the space-time matrices and space-time nodal vectors that are presented in this section can be found in Appendix-B.

4.5 Computation of free-field motion

In order to solve Eq. (4.34) for velocity field $\{\tilde{\mathbf{v}}\}$ contribution of the free-field motion, in the form of $\{\mathbf{J}_f\}$, should be computed at first. Noting that $\{\mathbf{J}_f\}$ involves the boundary integral over the left and right viscous boundary, only the space-time nodal values of free-field velocity $\mathbf{v}^f$ and stress σ^f defined on Γ_∞^L and Γ_∞^R should be stored. Besides, $\mathbf{v}^f$ and σ^f are computed by solving an elastodynamics problem defined for the auxiliary state as discussed in section 3.5.

Further, under following assumptions the computation of free-field response simplifies significantly.

Name	Matrix notation	Component notation	Expression
Space-time mass matrix	$[\mathbf{M}]$	$[M]_{ij}^{ab}(I,J)$	$\delta_{ij}\int_{I_n}\int_{\Omega} N^I T_a \rho \frac{\partial N^J T_b}{\partial t} dt d\Omega$ $+\delta_{ij}\delta_{1a}\delta_{1b}\int_{\Omega} N^I \rho N^J d\Omega$
Space-time tangent stiffness matrix	$[\mathbf{K}]$	$[K]_{ij}^{ab}(I,J)$	$\int_{I_n}\int_{\Omega} \frac{\partial N^I T_a}{\partial x_p} C_{pijq} \frac{\partial N^J \tilde{T}_b}{\partial x_q} d\Omega dt$
Space-time matrix due to dashpots	$[\mathbf{C}_\infty]$	$[C_\infty]_{ij}^{ab}(I,J)$	$[\mathbf{C}_{L\infty}]+[\mathbf{C}_{R\infty}]+[\mathbf{C}_{B\infty}]$
Space-time matrix due to dashpots at left boundary	$[\mathbf{C}_{L\infty}]$	$[C_{L\infty}]_{ij}^{ab}(I,J)$	$\int_{I_n}\int_{\Gamma_\infty^L} N^I T_a c_{ij}^v N^J T_b ds dt$
Space-time matrix due to dashpots at right boundary	$[\mathbf{C}_{R\infty}]$	$[C_{R\infty}]_{ij}^{ab}(I,J)$	$\int_{I_n}\int_{\Gamma_\infty^R} N^I T_a c_{ij}^v N^J T_b ds dt$
Space-time matrix due to dashpots at bottom boundary	$[\mathbf{C}_{B\infty}]$	$[C_{B\infty}]_{ij}^{ab}(I,J)$	$\int_{I_n}\int_{\Gamma_\infty^B} N^I T_a c_{ij}^h N^J T_b ds dt$
Space-time Rayleigh damping matrix	$[\mathbf{C}_R]$	$[C_R]_{ij}^{ab}(I,J)$	$\alpha[\mathbf{M}_R]+\beta[\mathbf{K}_R]$
Mass proportional space-time Rayleigh damping matrix	$[\mathbf{M}_R]$	$[M_R]_{ij}^{ab}(I,J)$	$\delta_{ij}\int_{I_n}\int_{\Omega} N^I T_a \rho N^J T_b d\Omega dt$
Stiffness proportional space-time Rayleigh damping matrix	$[\mathbf{K}_R]$	$[K_R]_{ij}^{ab}(I,J)$	$\int_{I_n}\int_{\Omega} \frac{\partial N^I T_a}{\partial x_p} C_{pijq} \frac{\partial N^J T_b}{\partial x_q} d\Omega dt$

Tab. 4.1.: Description of the space-time finite element matrices that appear in v-ST/FEM for the dynamic soil-structure problem

Term	Component notation	Expression
$\{\mathbf{J}_{ext}\}$	$\{J_{ext}\}_i^a(I)$	$\int_{I_n}\int_{\Omega} N^I T_a \rho b_i d\Omega dt + \int_{I_n}\int_{\Gamma_i^h} N^I T_a f_i^s d\Omega dt$
$\{\mathbf{J}_0\}$	$\{J_0\}_i^a(I)$	$\delta_{a1}\int_{\Omega} N^I \rho v_i^0 d\Omega$
$\{\mathbf{J}_{\sigma^n}\}$	$\{J_{\sigma^n}\}_i^a(I)$	$\int_{I_n}\int_{\Omega} \frac{\partial N^I T_a}{\partial x_j}\sigma_{ij}^n d\Omega dt$
$\{\mathbf{J}_f\}$	$\{J_f\}_i^a(I)$	$\int_{I_n}\int_{\Gamma_\infty^L} N^I T_a\left(c_{ij}^v v_j^f - \sigma_{i1}^f\right) dsdt + \int_{I_n}\int_{\Gamma_\infty^R} N^I T_a\left(c_{ij}^v v_j^f + \sigma_{i1}^f\right) dsdt$
$\{\mathbf{J}_{in}\}$	$\{J_{in}\}_i^a(I)$	$\int_{I_n}\int_{\Gamma_\infty^B} N^I T_a 2c_{ij}^h v_j^{in} dsdt$

Tab. 4.2.: Description of the space-time vectors that appear in v-ST/FEM for the dynamic soil-structure problem

1. The seismic motion is described by vertically propagating body waves (P-wave and S-wave)

2. The unbounded soil domain is represented by an isotropic, linear elastic layered half-space.

With these assumptions a multi-dimension auxiliary state problem effectively transform into a soil-column problem (Nielsen, 2006; Zienkiewicz et al., 1989; Zhang et al., 2003; Miura and Okinaka, 1989; Saouma et al., 2011) where the body waves propagate through a layered soil-column (see Fig. 4.2). The governing equation for the soil-column problem is given by Eq. (4.1) with the modified Dirichlet boundary condition (as discussed below). The top surface of the soil-column Γ_t^{sc} is a stress-free boundary. The traction boundary condition at bottom surface of soil-column,Γ_b^{sc} is due to the incoming seismic motion and the dashpots (see Fig. 4.2). The analysis of soil-column problem could be performed as follows:

1. If only horizontal component of the seismic excitation is present then free-field displacement and velocity are computed while vertical displacement of all nodes of soil-column mesh is constrained (thus allowing only the shear deformation of soil-column, see Fig. 4.2b). The Dirichlet boundary condition Eq. (4.2) becomes

$$u_2(\mathbf{x},t) = 0 \quad \forall(\mathbf{x},t) \in \Omega^{sc} \times (\mathbf{x},t) \tag{4.41}$$

The traction boundary condition on the top and bottom surface of soil-column

$$\sigma \cdot \mathbf{n} = 0 \quad \forall (\mathbf{x}, t) \in \Gamma_t^{sc} \times (\mathbf{x}, t) \tag{4.42}$$

$$\sigma \cdot \mathbf{n} = \mathbf{c}^h \cdot \left(-\mathbf{v} + 2\mathbf{v}^{in} \right) \quad \forall (\mathbf{x}, t) \in \Gamma_b^{sc} \times (\mathbf{x}, t) \tag{4.43}$$

where x_2 components of incoming seismic motion $\mathbf{v}^{in}$ is zero.

2. If only vertical component of the seismic excitation is present then the response $(\mathbf{u}^f, \mathbf{v}^f, \sigma^f)$ is computed while horizontal displacement of all nodes of soil-column mesh is constrained (thus allowing only the axial deformation of soil-column, see Fig. 4.2c). The Dirichlet boundary condition is defined as

$$u_1(\mathbf{x}, t) = 0 \quad \forall (\mathbf{x}, t) \in \Omega^{sc} \times (\mathbf{x}, t) \tag{4.44}$$

The traction boundary condition on the top and bottom surface of soil-column becomes,

$$\sigma \cdot \mathbf{n} = 0 \quad \forall (\mathbf{x}, t) \in \Gamma_t^{sc} \times (\mathbf{x}, t) \tag{4.45}$$

$$\sigma \cdot \mathbf{n} = \mathbf{c}^h \cdot \left(-\mathbf{v} + 2\mathbf{v}^{in} \right) \quad \forall (\mathbf{x}, t) \in \Gamma_b^{sc} \times (\mathbf{x}, t) \tag{4.46}$$

where x_1 components of incoming seismic motion $\mathbf{v}^{in}$ is zero.

3. If both components are present then the computation of soil-column problem should be carried out in two stages. In first stage horizontal response is computed; only the horizontal seismic motion is applied at the base of the soil-column while constraining the vertical displacement of all nodes, and problem is analyzed (see Fig. 4.2b). In second stage vertical response of soil-column is computed; only the vertical seismic motion is applied at the base of the soil-column while constraining the horizontal displacement of all nodes, and problem is analyzed (see Fig. 4.2c). Subsequently, the total response is obtained by superimposing the results of these two stages.

Following the space-time discretization procedure for the soil-column problem one can obtain the matrix-vector form

$$[\mathbf{K}_{st}^{sc}] \left\{ \tilde{\mathbf{v}}^f \right\} = \{ \mathbf{J}^{sc} \} \tag{4.47}$$

where the space-time tangent matrix is given by

$$[\mathbf{K}_{st}^{sc}] = [\mathbf{M}^{sc}] + [\mathbf{K}^{sc}] + [\mathbf{C}_{B\infty}^{sc}] + [\mathbf{C}_R^{sc}] \tag{4.48}$$

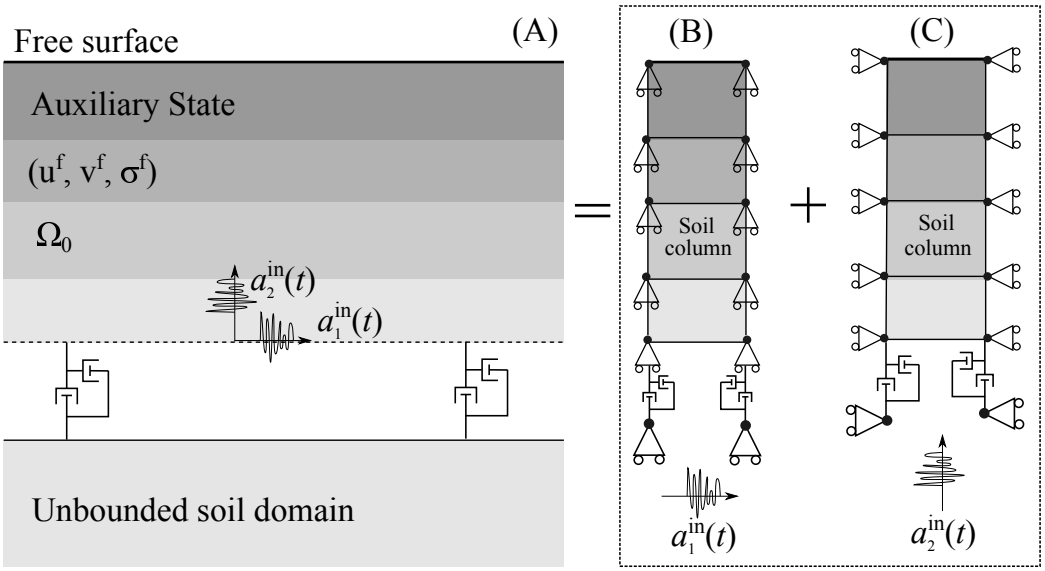

Fig. 4.2.: Modeling of a multi-dimension elastodynamics problem defined for the auxiliary state with a one-dimensional soil-column problem; (A) auxiliary state with viscous boundary placed at the bottom, (B) boundary conditions for the soil-column problem for horizontal seismic motion, (C) boundary condition for the soil-column problem for vertical seismic motion.

and the right hand side,

$$\{\mathbf{J}^{sc}\} = \{\mathbf{J}^{sc}_{ext}\} + \{\mathbf{J}^{sc}_{0}\} - \{\mathbf{J}^{sc}_{\sigma^n}\} + \{\mathbf{J}^{sc}_{in}\} \tag{4.49}$$

In Eq. (4.48), $[\mathbf{M}^{sc}]$ denotes the space-time mass matrix, $[\mathbf{K}^{sc}]$ is the space-time tangent stiffness matrix, $[\mathbf{C}^{sc}_{B\infty}]$ is the space-time dashpot matrix for the bottom viscous boundary, and $[\mathbf{C}^{sc}_{R}]$ is the space-time Rayleigh damping matrix for the soil-column. The brief description about these matrices (corresponding to the subscript used in the matrix notation) can be obtained from Table 4.1 while replacing the domain of integration appropriately. In Eq. (4.49), the space-time nodal vector $\{\mathbf{J}^{sc}_{ext}\}$ contains the contribution of external body force, $\{\mathbf{J}^{sc}_{0}\}$ contains the contribution of initial velocity, $\{\mathbf{J}^{sc}_{\sigma^n}\}$ contains the contribution of initial stress σ^n, and $\{\mathbf{J}^{sc}_{in}\}$ contains the contribution of incoming seismic velocity. Appendix-B contains a detailed presentation about the derivation and finite element computation about these space-time matrices and nodal vectors.

4.6 v-ST/FEM implementation

Eq. (4.34) and Eq. (4.47) involve unsymmetrical tangent matrix. These unsymmetrical system of linear equations are solved using GpBiCG algorithm (Zhang, 1997). The algorithm is implemented in an element by element manner thus avoiding the assembly of global tangent matrix. Further, in each time step the soil-column problem

Eq. (4.47) is solved first to compute the free field response $\left\{\tilde{\mathbf{v}}^f\right\}$. Subsequently, the space-time nodal values $\{\mathbf{J}_f\}$ in Eq. (4.36) can be computed using the expression given in Table 4.2 and Appendix-B. After computing the $\{\tilde{\mathbf{v}}\}$ the space-nodal values of displacement at time t_{n+1}, $\{\tilde{\mathbf{u}}^2\}$, is computed by

$$\left\{\tilde{\mathbf{u}}^2\right\} = \left\{\tilde{\mathbf{u}}^1\right\} + \frac{\Delta t_n}{2}\left(\left\{\tilde{\mathbf{v}}^1\right\} + \left\{\tilde{\mathbf{v}}^2\right\}\right) \tag{4.50}$$

Accordingly, the stress is computed, at element level, from the updated displacement using the isotropic linear elastic stress-strain relationship

$$\sigma_{ij} = \lambda \frac{\partial u_p}{\partial x_p}\delta_{ij} + \mu\left(\frac{\partial u_i}{\partial x_j} + \frac{\partial u_j}{\partial x_i}\right) \tag{4.51}$$

Then the updated stress is used to compute the $\{\mathbf{J}_{\sigma^n}\}$ in Eq. (4.36) for the next time-step. Eq. (4.50) and Eq. (4.51) are also utilized to update the displacement and stress for the soil-column test. The steps involved in solving the dynamic soil-structure interaction problem using the v-ST/FEM method are presented in Algorithm 1.

Algorithm 1: v-ST/FEM algorithm for soil-structure interaction problem

Initialization ;
Step-1: Get the initial value of nodal displacement ($\mathbf{u}^0$) and velocity ($\mathbf{v}^0$) ;
Step-2: Compute $[\mathbf{M}]$, $[\mathbf{K}]$, $[\mathbf{C}_R]$ for soil and structure elements;
Step-3: Compute the space-time boundary element matrices $[\mathbf{C}_{L\infty}]$, $[\mathbf{C}_{R\infty}]$, $[\mathbf{C}_{B\infty}]$ for left, right, and bottom viscous boundaries;
Step-4: Compute the space-time tangent matrix $[\mathbf{K}_{ST}]$ using element matrices from *step-2* and *step-3* according to Eq. (4.40) ;
Time Step Loop ;
for *n=0, N-1* **do**
  Step-5a: Solve soil-column problem and compute $\mathbf{u}^f, \mathbf{v}^f, \sigma^f$;
  Step-5b: Compute the $\mathbf{J}_f$;
  Step-6: Compute $\mathbf{J}_0$ using the initial velocity $\mathbf{v}^n$;
  Step-7: Compute stress σ^n using $\mathbf{u}^n$ and isotropic linear elasticity relationship ;
  Step-8: Compute $\mathbf{J}_{\sigma^n}$ using the σ^n ;
  Step-9: Compute $\mathbf{J}_{in}$ from incoming seismic motion ;
  Step-10: Compute $\mathbf{J}$ according to Eq. (4.36) ;
  Step-11: Solve

$$[\mathbf{K}_{st}]\,\mathbf{v} = \mathbf{J}$$

  using GpBiCG iterative solver algorithm;
  Step-12: Update the displacement $\mathbf{u}^n$;
  Step-13: Update the velocity $\mathbf{v}^n$;
  Step-14: Go to next time step; $n = n + 1$
end

4.7 Numerical example

In this section linear seismic analysis of concrete dam is performed by employing the v-ST/FEM algorithm. To assess the performance of v-ST/FEM for the soil-structure interaction problem (with modified viscous boundaries) the effect of reservoir will not be pursued here. Besides, the effect of reservoir will be discussed in next chapter.

Fig. 4.3 depicts a concrete gravity dam on an unbounded soil domain. The physical dimension of the dam is given in Fig. 4.4. It is assumed that the material behavior of the dam as well as the soil is given by an isotropic, homogeneous, linear elastic stress-strain relationship. For the concrete-dam, the elastic modulus $E = 28.0$ GPa, mass-density $\rho = 2347.0$ kg/m^3, and the Poisson's ratio $\nu = 0.20$. For the soil, $E = 40$ GPa, $\rho = 2551.0$ kg/m^3, and $\nu = 0.20$. Further, material damping is modeled by Rayleigh damping with $\xi = 5\%$ viscous damping specified for the soil and dam separately; the resultant values of damping coefficients α and β for the dam and soil are given in Table 4.3.

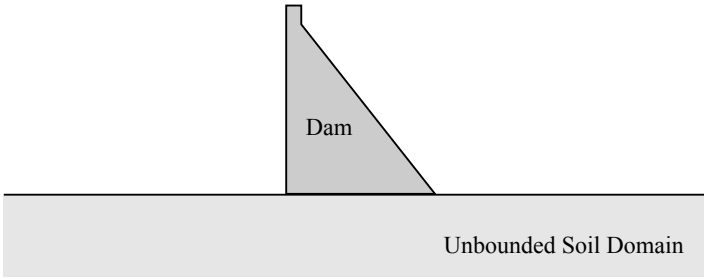

Fig. 4.3.: Numerical example for the dynamic soil structure interaction problem; concrete gravity dam on an elastic half-space

	Elastic modulus E (GPa)	Poisson's ratio ν	Mass density ρ (kg/m^3)	Rayleigh damping coefficients α	β
Dam	28.0	0.2	2347.0	4.1314	4.8×10^{-4}
Soil	40.0	0.2	2551.0	1.612	1.47×10^{-3}

Tab. 4.3.: Material parameters of the dam and soil domain

Fig. 4.7 illustrates the physical dimension and finite element mesh of the truncated computational domain (Ω). The length of soil domain in x_1-direction is nine times the length of base of the dam, and the length in x_2-direction is three times the height of the dam. The computational domain is descritised using $19,176$ number of four node quadrilateral (Quad4) elements and 453 number of three-node linear triangle (Tria3) elements (see Fig. 4.7). There are total $19,559$ number of nodes in the mesh,

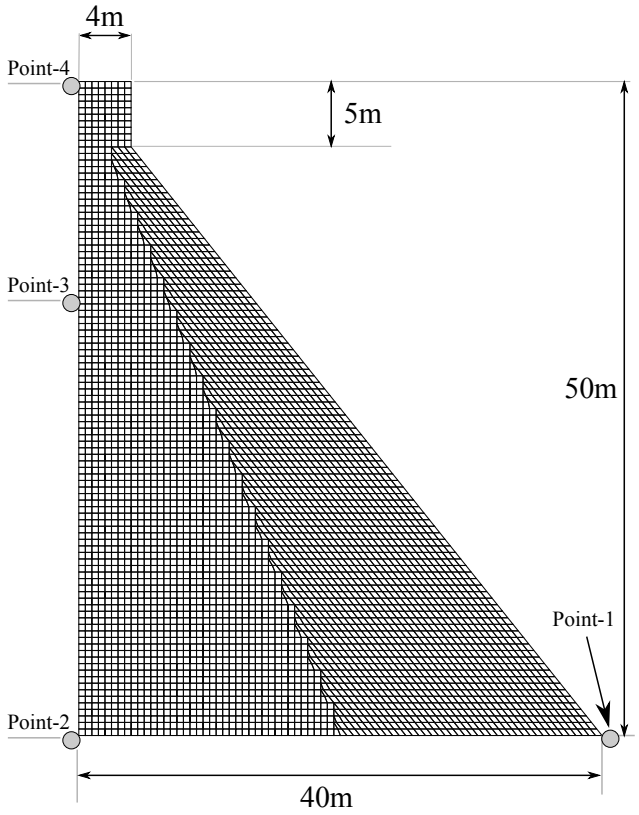

Fig. 4.4.: Physical dimension and finite element mesh detail of concrete gravity dam used for the numerical simulation

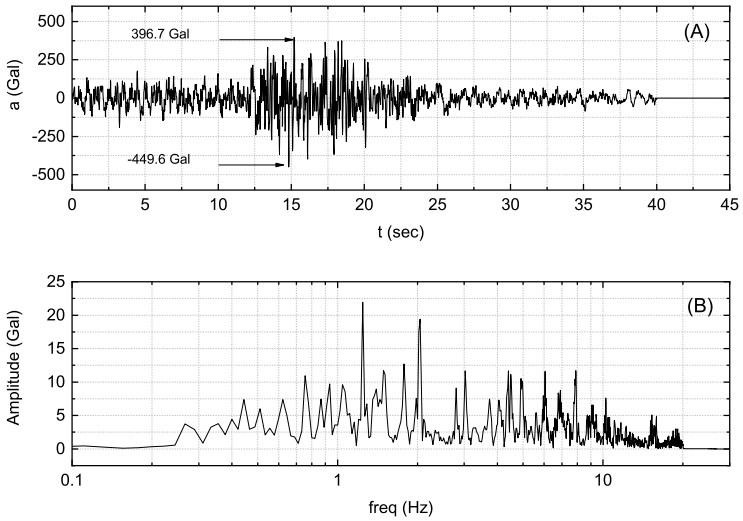

Fig. 4.5.: Horizontal component of acceleration recorded at the free-surface: (A) time history, and (B) Fourier spectrum

hence the total number of primary unknowns to be determined are $78,236$ (four times the total number of nodes).

The simulation is carried out for the horizontal seismic motion recorded at some control point on the free surface (see Fig. 4.5). Total time duration of ground motion is 45 seconds in which acceleration is set to zero after 40 seconds. Fig. 4.5a depicts the time history of the recorded acceleration; the maximum and minimum values of acceleration are 396.7 cm/s^2 and -449.6 cm/s^2, respectively. The Fourier spectrum of acceleration is depicted in Fig. 4.5b where the dominating amplitudes 21.9 cm/s^2 and 19.4 cm/s^2 occur for frequencies 1.24 Hz and 2.0 Hz, respectively. The input seismic acceleration $a_1^{in}(t)$ for the numerical simulation (see the discussion presented in section 3.5.2) is taken as half that of acceleration at the free surface.

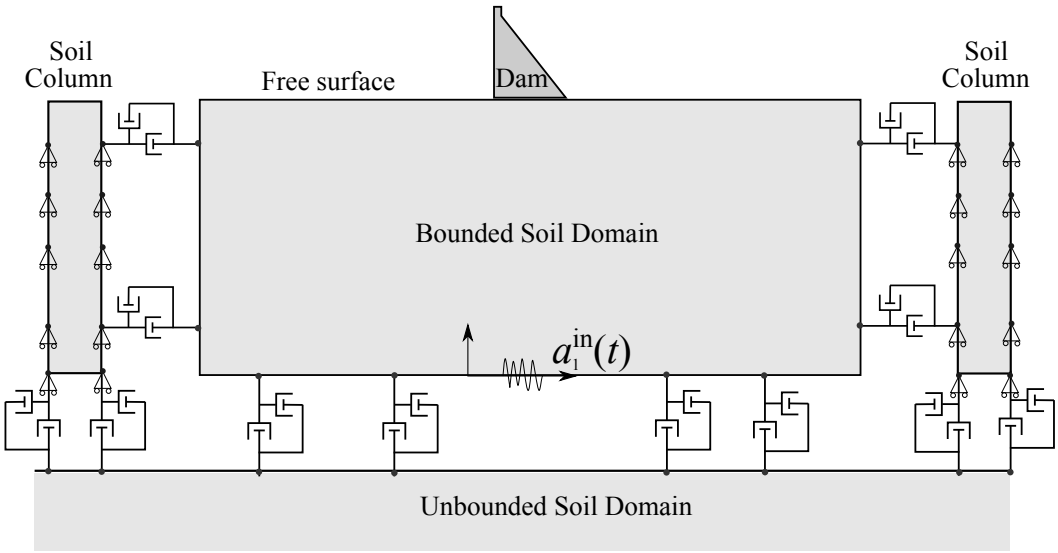

Fig. 4.6.: Physical dimension and finite element mesh detail of computational domain used for the numerical simulation

Fig. 4.6 illustrates the configuration of the components required for the computation of present problem. Dashpots are placed on the bottom and vertical boundaries of computation domain. Recall that, in this situation, only a single soil-column problem needs to be solved for determining the free-field response. In the soil-column problem vertical motion of all nodes is constrained while dashpots are placed at the bottom (see Fig. 4.6) surface only. Furthermore, material properties of the soil column (including Rayleigh damping coefficients α and β) are identical to that of soil-domain (see Table 4.3).

For the validation of v-ST/FEM, the same problem is solved using semi-discrete FEM with Newmark-β direct time integration algorithm. A uniform time-step of size $\Delta t = 0.01$ sec is adopted for both methods. In case of v-ST/FEM, the tolerance for GpBiCG (iterative linear solver) is set to $\epsilon = 1.0 \times 10^{-6}$. The observation points selected for the comparison of results are shown in Fig. 4.4. The spatial coordinates

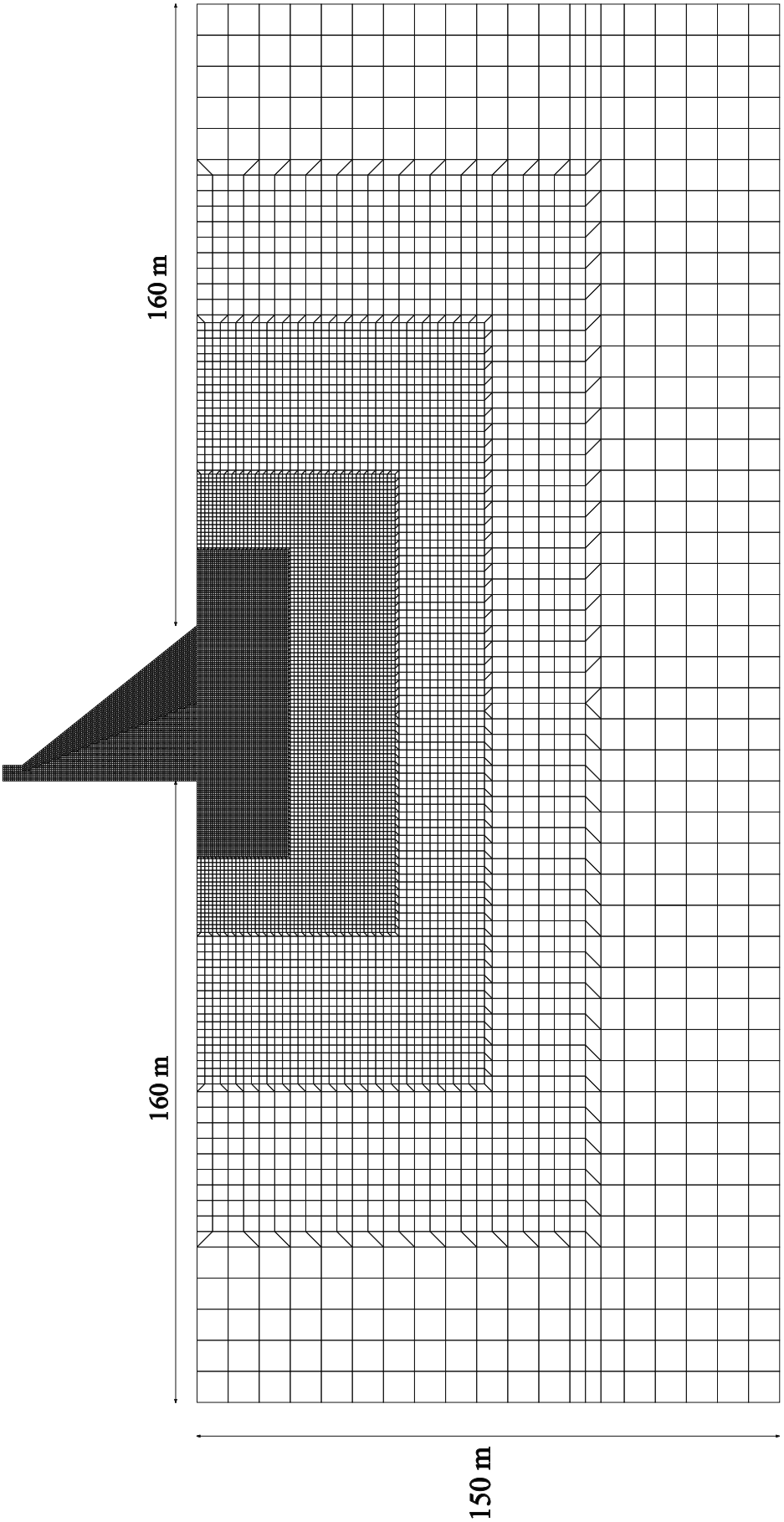

Fig. 4.7.: Physical dimension and finite element mesh detail of computational domain used for the numerical simulation

of these points are; point-1 $(40.0, 0.0)$, point-2 $(0.0, 0.0)$, point-3 $(0.0, 35.0)$, and point-4 $(0.0, 50.0)$.

Temporal variation of horizontal component of acceleration at observation points computed by employing v-ST/FEM and Newmark-β method are plotted in Figs. (4.8–4.11). In case of point-1 and point-2 the results computed by present method are almost identical to that of Newmark-β method (see Fig. 4.8 and Fig. 4.9). In case of point-3 and point-4, however, due to the algorithmic damping of v-ST/FEM the response obtained by v-ST/FEM is slightly lower than the one obtained by the Newmark-β method[3]. To further explain this point, frequency content of the acceleration response at the observation points is plotted in Fig. 4.12, where it can be seen that the dominating frequencies for point-1 and point-2 are in between 1 Hz and 2 Hz, and for point-3 and point-4 are in between 6 Hz and 8 Hz. In Chapter 2 it is shown that the v-ST/FEM has relatively large numerical damping for high-frequency content, therefore, the response of point-3 and point-4 is more damped than the response of point-1 and point-2.

In Fig. 4.13 the frequency content of horizontal acceleration obtained by v-ST/FEM is illustrated. At the base of the dam (i.e. point-1 and point-2 in Fig. 4.4) the frequency content is similar to the recorded acceleration, and the dominating frequencies are also located in between 1 Hz and 2 Hz. The high frequency content in the dynamic response of the dam starts dominating as one moves away from the base towards the crest of the dam. This is because a significant part of wave energy that enter the dam through dam-soil interface gets trapped inside the dam-region due to multiple reflections within the dam. To further understand this point, consider the boundaries of the dam, the three free surfaces of the dam (upstream face, downstream face and top surface) act as a perfect reflector. From Table 4.3 it is clear that the the mechanical impedance of the soil is more than that of dam. Therefore, when a wave, which is coming from the dam-region, impinges the dam-soil interface it partially gets reflected back into the dam-region.

4.8 Summary

This chapter extends the v-ST/FEM presented in Chapter 2 for the dynamic soil-structure interaction problems. In dynamic SSI problem, unbounded soil domain is truncated by placing artificial boundaries at some distance from the area of interest. Viscous boundary condition of Lysmer-Kuhlemeyer (Lysmer and Kuhlemeyer, 1969) is modified by introducing additional boundary terms related to the free-field response of unbounded soil domain to facilitate the energy flow from far field to com-

[3]Recall that Newmark-β method has zero algorithmic damping

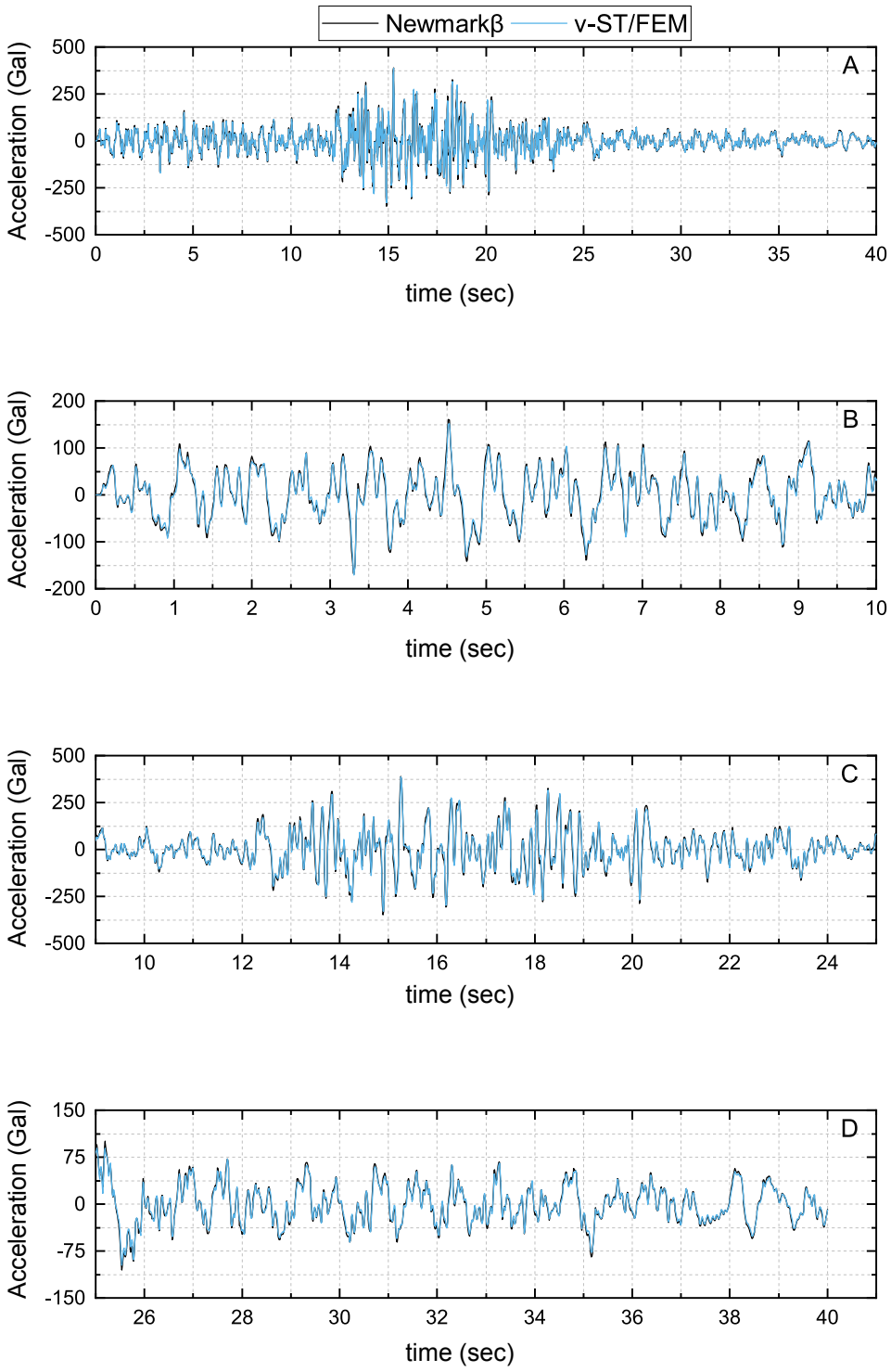

Fig. 4.8.: Comparison of horizontal component of acceleration at point-1 computed by using the v-ST/FEM and Newmark-β method

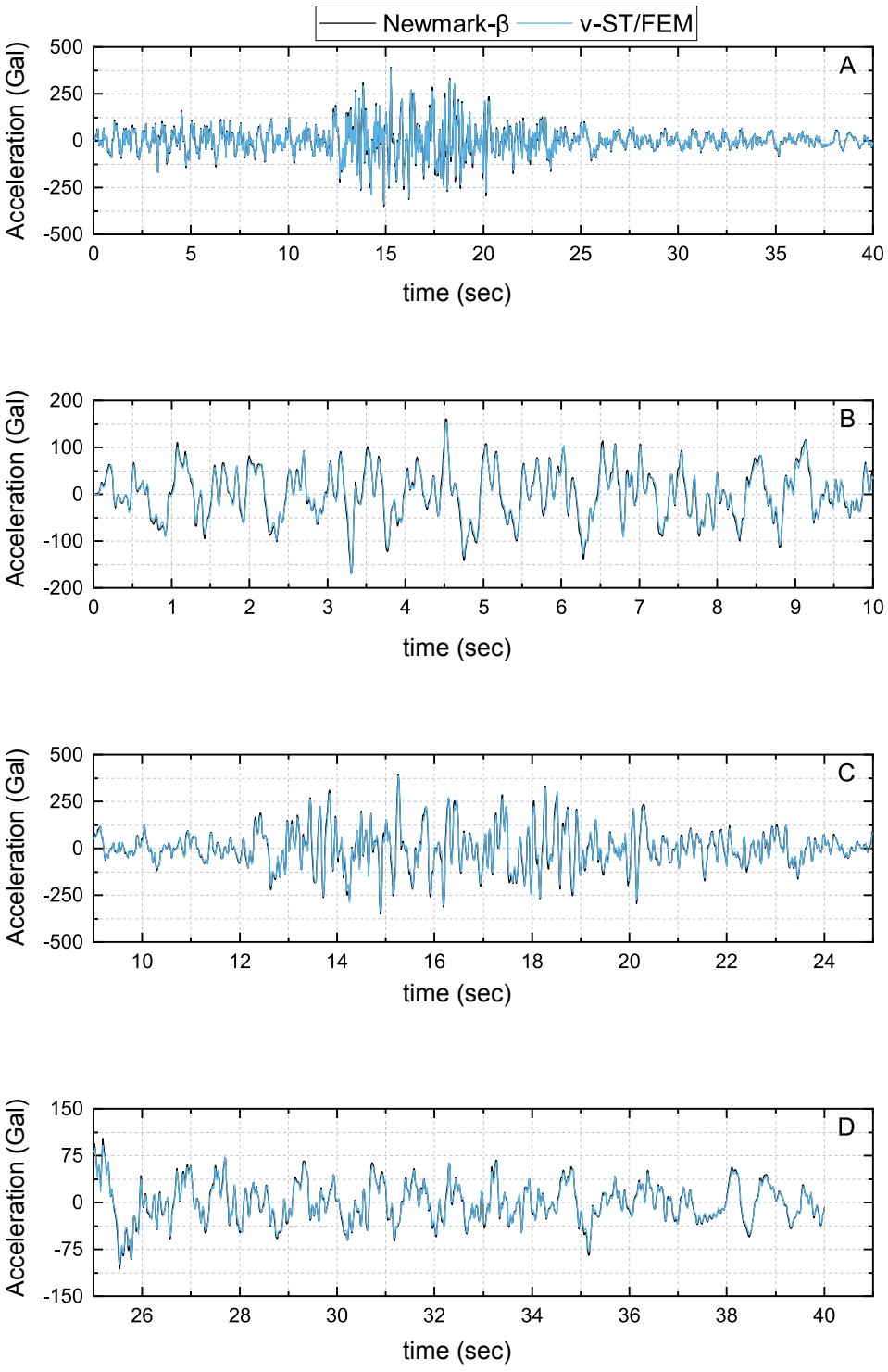

Fig. 4.9.: Comparison of horizontal component of acceleration at point-2 computed by using the v-ST/FEM and Newmark-β method

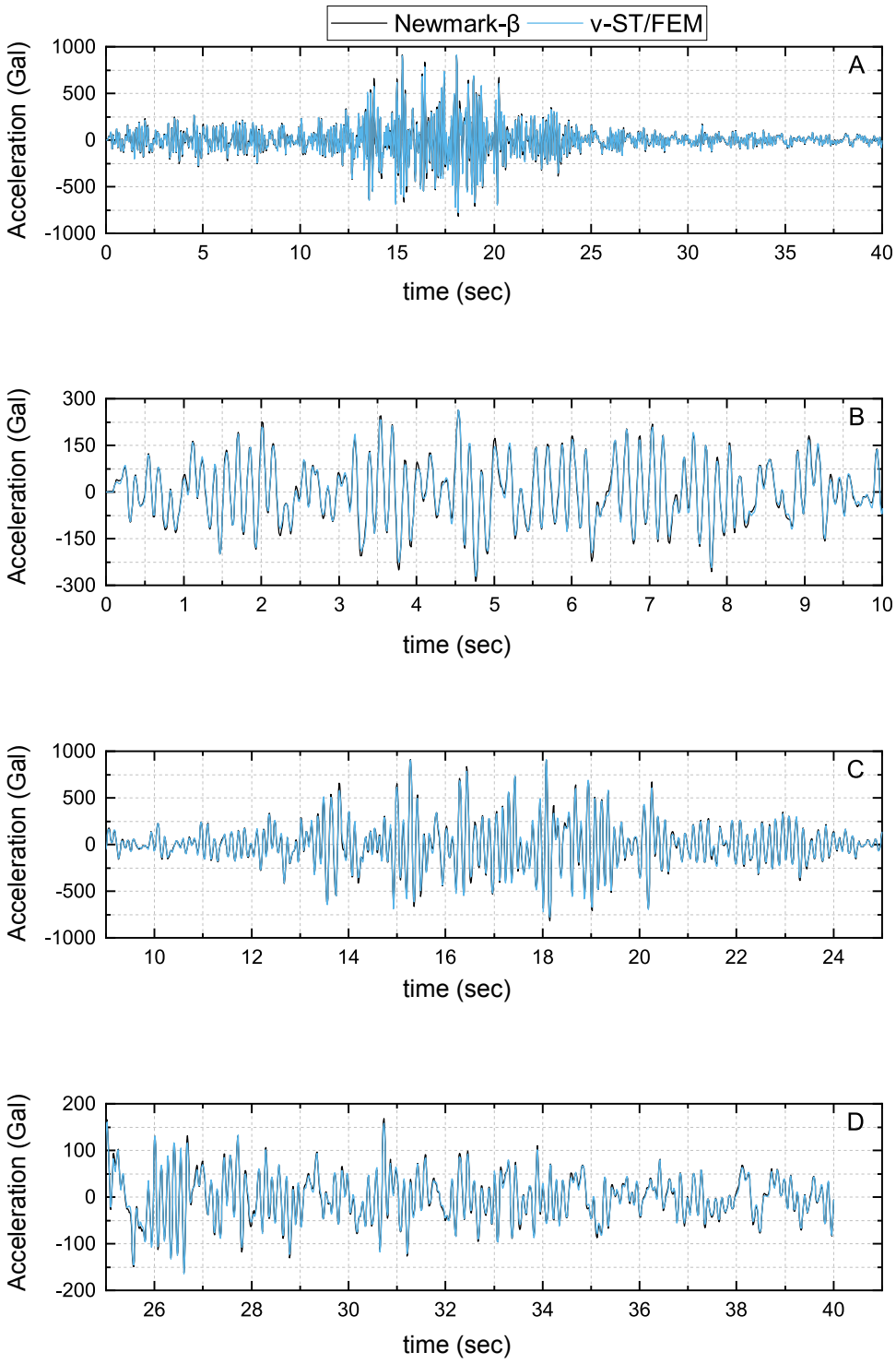

Fig. 4.10.: Comparison of horizontal component of acceleration at point-3 computed by using the v-ST/FEM and Newmark-β method

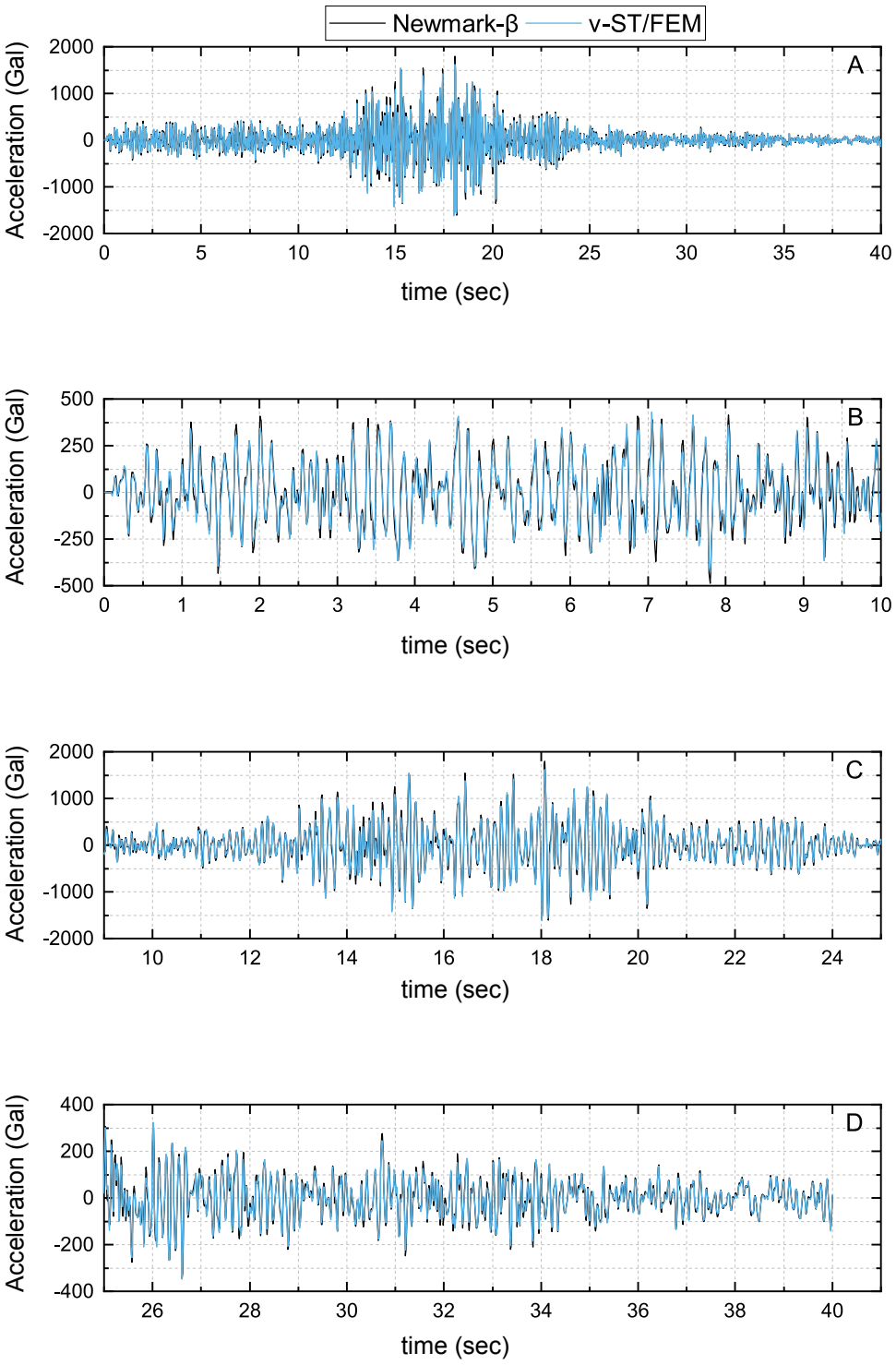

Fig. 4.11.: Comparison of horizontal component of acceleration at point-4 computed by using the v-ST/FEM and Newmark-β method

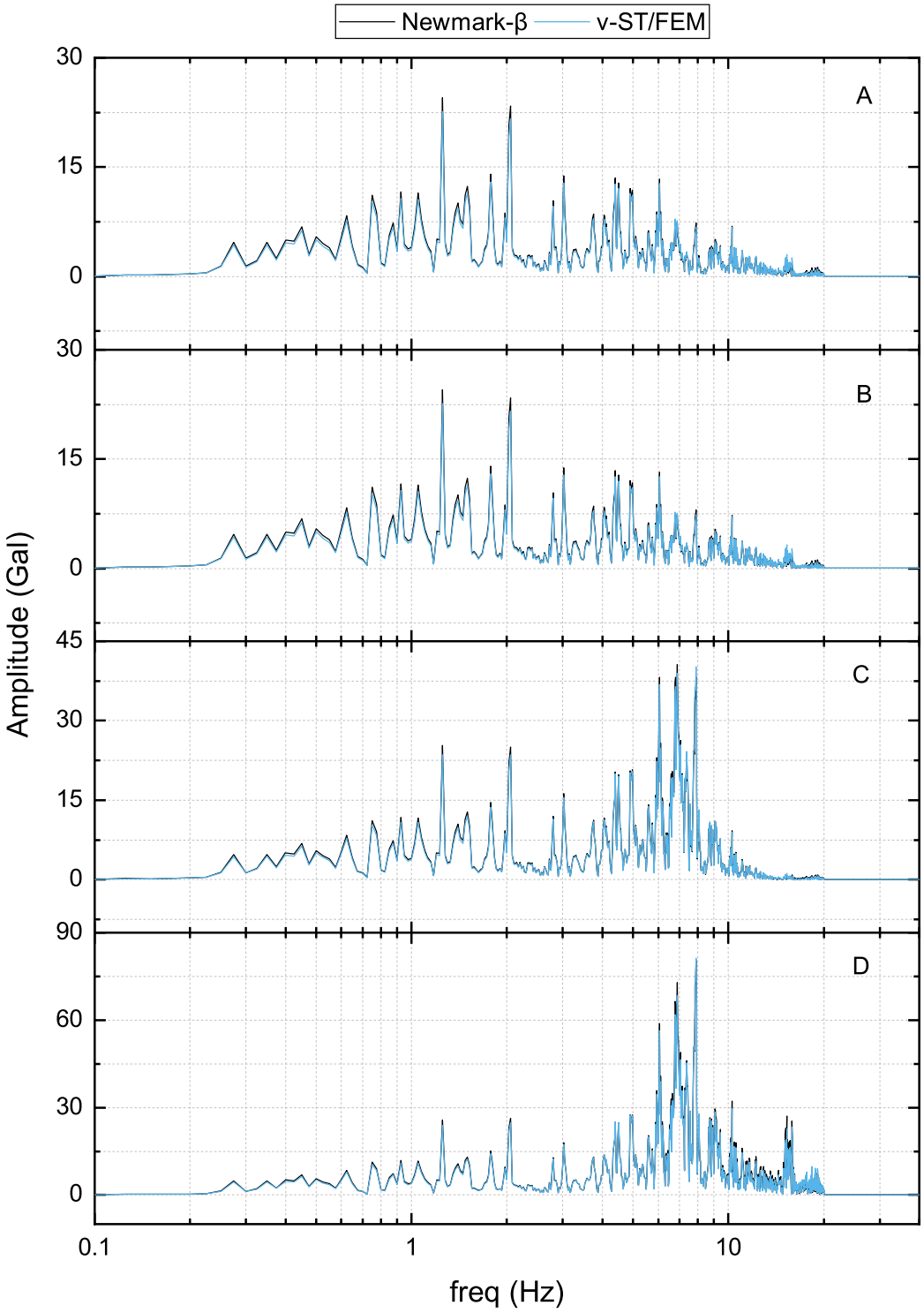

Fig. 4.12.: Comparison of Fourier spectrum of horizontal component of acceleration obtained by employing v-ST/FEM and Newmark-β; (A) Point-1, (B) Point-2, (C) Point-3, (D) Point-4

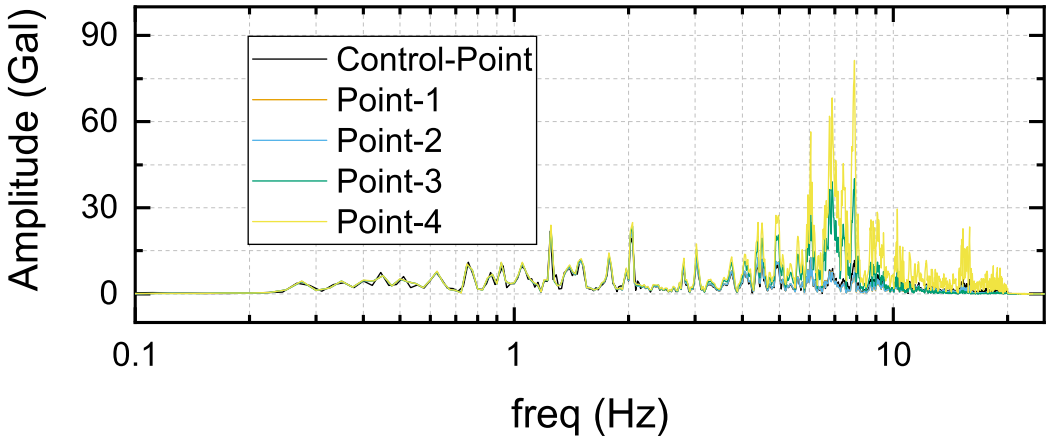

Fig. 4.13.: Fourier spectrum of horizontal component of acceleration obtained by employing v-ST/FEM for different observation points

putation domain. In the computer program, modified viscous boundary condition is treated as a combination of various traction boundary conditions; traction boundary condition due to dashpots, free-field motion, and input seismic motion. It is found that the traction boundary condition due to dashpots introduces space-time dashpot matrices $[\mathbf{C}_\infty]$ which contribute to the space-time tangent matrix. The traction boundary condition due to input seismic motion and free-field motion introduce corresponding space-time nodal vectors. Furthermore, it is shown how multiple soil-column problems can be solved (with various boundary conditions) in order to compute the free-field response. Moreover, the computation of free-field response does not depend upon the total response of soil and structure. Thanks to this weak coupling, the soil-column problem can be solved first, and then the total response of soil and structure can be computed by using this free-field response. In this way, the proposed space-time finite element formulation is applicable to a wide class of soil-structure interaction problem.

Afterwards, a dynamic dam-soil interaction problem is considered to validate the formulation and computer implementation of v-ST/FEM. In this problem, a dam (without the reservoir) resting on an elastic half-space is subjected to the horizontal component of the earthquake motion. The material damping in both dam and soil domain is modeled using the Rayleigh damping. The results obtained by proposed scheme are validated by solving the same problem using the semi-discrete FEM with classical Newmark-β method. Results obtained by two methods are compared and found to be nearly identical.

5 v-ST/FEM for The Linear Dam-Reservoir-Soil Interaction Problem

5.1 Introduction

The stability of dams during an event of earthquake is critical as failure of such a structure may have catastrophic effects on life and property. When a dam-reservoir-soil system is subjected to the earthquake-motion the hydrodynamic effects induced by the impounded water may intensify the dynamic response of the dam. In addition, the dynamic stresses in the dam depend on the dynamic coupling between the dam, the water in reservoir, and the underlying soil. It is therefore necessary to develop the numerical methods for evaluating the adequacy of a given dam-design against a particular ground motion. Seismic analysis of a dam-reservoir system can be viewed as a problem of dynamic fluid-structure interaction; the ground motion and the deformations of the upstream face of a dam will generate hydrodynamic pressure in the reservoir, and the structure deformations in turn will be affected by the distribution of hydrodynamic pressures at the upstream face. Therefore, the estimation of precise hydrodynamic forces on upstream face of the dam due to earthquakes is one of the key aspects of the analysis and design of dams. In 1933, prof. H.M. Westergaard firstly proposed a standard procedure to take into account the hydrodynamic effects on gravity dam subjected to the earthquake loading. In literature this procedure is well known as *Westergaard's added-mass* approach. Westergaard, 1933 made following assumptions in order to derive an expression for the hydrodynamic pressure exerted on upstream face of the dam.

(i) Dam was idealized as two-dimensional rigid structure with vertical upstream face.

(ii) Water in the reservoir is incompressible, and reservoir extends to infinity in the upstream direction.

(iii) The amplitudes of displacements of fluid particles are small.

(iv) The existence of surface waves at free surface of reservoir was ignored.

(v) Only horizontal ground motion in the direction perpendicular to the vertical upstream face was considered.

Under aforementioned assumptions, Prof. Westergaard posed the initial-boundary value problem, and obtained pressure solutions at upstream face of the dam. For the purpose of practical engineering use, he approximated the hydrodynamic pressure distribution at upstream face of the dam by a parabola. He observed that the hydrodynamic pressure was same as if a certain body of fluid was firmly attached to the upstream face of dam and forced to move back and forth with the dam while the remainder of the reservoir is left in active. The amount of water included was determined by equating the inertia forces of this body of water to the pressure that actually were exerted upon the faces of the dam under the same motion of the dam. Accordingly, he suggested that the hydrodynamic pressure at face of the dam could be expressed as:

$$p\left(y,t\right)=\frac{7}{8}\rho a_g\left(t\right)\sqrt{H^f\left(H^f-y\right)}$$

where y is vertical distance from the base of the dam, a_g is the horizontal ground-acceleration, H^f is the height of the reservoir, t is time, and $p(z,t)$ is the hydrodynamic pressure at height y from base of the dam applied normally to the face of the dam.

Above equation indicates that the hydrodynamic pressure is equivalent to the inertia force of a prismatic body of water of unit cross-section area and length $\frac{7}{8}\sqrt{H^f\left(H^f-y\right)}$ attached firmly to face of the dam, and moving with dam back and forth (with total acceleration a_g) in the direction normal to the face of the dam without friction. This body of the dam (*added-mass*) is confined in a volume bounded by a two-dimensional parabolic surface on the upstream side of the dam. Although the case prof. Westergaard studied was limited to rigid dams with vertical upstream face, and infinitely long reservoir, ignoring surface waves and considering only small displacements of fluid particles, this work was regarded as a milestone. Especially, the concept of added-mass, which he introduced for incompressible water reservoir, greatly simplified the analysis procedure of the response of dam considering the hydrodynamic effects during earthquakes.

In the same year, von Kármán, 1933 obtained the expression for hydrodynamic pressure force and total load on a rigid dam with a vertical upstream face by using the principle of conservation of linear momentum. These results were very close to the Westergaard results. Kotsubo, 1957; Chopra, 1967; Victoria et al., 1969 performed comprehensive analysis of hydrodynamic pressures on the vertical upstream face of a rigid dam due to horizontal as well as vertical components of ground-acceleration. Chopra, 1967 showed that significant errors are introduced by ignoring the compressibility of water, and hydrodynamic forces due to vertical

component of ground motion are much larger than those due to horizontal ground motion when the height of water in reservoir is small, however, these forces become comparable as the height of water increases. Victoria et al., 1969 found that hydrodynamic pressure due to vertical ground motion are strongly influenced by the direction of approach and the velocity of propagation of the earthquake.

Chopra, 1968; Chopra, 1970 studied the hydrodynamic interaction between a reservoir and a linear elastic dam with vertical upstream face due to horizontal ground motion. The dynamic response of the dam was approximated by its deformations in the fundamental mode. It was found that the interaction effects have considerable influence on the behavior of dam-reservoir system; the resonant period as well as earthquake response is significantly influenced by hydrodynamic interaction and compressibility of water. In addition, it was demonstrated that the compressibility of water can be ignored if the dam is flexible enough compared to the reservoir.

Furhter, the analysis of hydrodynamic pressure on the dam due to the vertical component of ground motion demands the modeling of reservoir bed. The simplest assumption is to treat the reservoir bottom as a rigid foundation, which leads to the perfect reflection of pressure waves at the reservoir bottom, and spatially uniform ground-acceleration. However, this assumption may result in unrealistically large hydrodynamic pressure at the upstream face of the dam because the reservoir-bottom condition does not allow energy dissipation in the reservoir domain. The excessive hydrodynamic pressure at vertical upstream face will cause large deformations in the dam which in turn will influence the hydrodynamic response of reservoir.

Chakrabarti and Chopra, 1973b investigated the hydrodynamic pressure and structural response of concrete gravity dam with vertical upstream face, including the dam-reservoir interaction, due to vertical component of earthquake ground motion. The response of the dam was approximated by the deformation in the fundamental mode of vibration, and the effect of flexibility of reservoir bottom was included in the analysis. It was showed the structural response to the vertical component of ground motion is significant in the presence of reservoir. This is obvious as the vertical movement of ground may increase the hydrodynamic pressure acting perpendicular to the dam face, which in turn may cause the additional deformation in the dam. The response was especially significant for low height dams in which case the response to vertical component of ground motion can be larger than the response to horizontal component of a ground motion.

Chakrabarti and Chopra, 1973a presented a general procedure for analysis of the response of gravity dams with vertical upstream face, including the hydrodynamic interaction and compressibility of water, to both horizontal and vertical components of ground motion. Their approach is based on a substructure coupling technique

in which the dam and the fluid domain are treated as separate substructure, and displacements of the dam are represented as a linear combination of the first few modes of vibration of the dam with the reservoir empty and rigid foundation.

Chwang and Housner, 1978 used von Karman's *momentum-balance* approach and Westergaard *added-mass* approach to obtain analytical solution for the hydrodynamic pressure distribution along the inclined upstream face of a rigid-dam which subjected to horizontal ground-motion. In this study they found that at any fixed point on the upstream face of dam the pressure decreases as the inclination angle (of the face of dam) decreases. However, for fixed values of inclination angle between 0 and $90\,^{\circ}$, the maximum hydrodynamic pressure occurs at the base of the dam. Further, Chwang, 1978 employed the two-dimensional potential-flow theory to obtain the exact intergral solution of the problem considered in Chwang and Housner, 1978. It was observed that for any fixed angle of inclination of upstream face of the dam the momentum-method (Chwang and Housner, 1978) (approximate theory) indicates that the maximum pressure occurs at the base of the dam, whereas the exact theory (Chwang, 1978) gives the maximum pressure at some distance above the base of the dam. However, in case of vertical upstream face of the dam both approximate theory and exact theory predicts maximum pressure at the base of the dam.

Hall and Chopra, 1982 investigated the effects of dam-fluid interaction, water compressibility, fluid-foundation interaction, reservoir shape, and extent of vertical ground motion on the dynamic response of concrete gravity dam. Fluid-foundation interaction was approximately simulated by means of an absorbing boundary condition applied at the bottom of the reservoir, while the foundation was assumed to be rigid. They reported that if the water in the reservoir is assumed as incompressible then the hydrodynamic effects are equivalent to an added mass and added load which reduce the resonant frequencies of the system and change the resonant amplitudes. In this case the dam accelerations with full reservoir are essentially independent of reservoir shape. Further, in the case where water compressibility is considered and fluid-foundation interaction is neglected the dam accelerations strongly depend on the reservoir shape. The net effect of fluid-foundation interaction is to reduce the response of dam, and the resultant dam accelerations depend much less on reservoir shape, especially for horizontal ground motion.

The reservoir bottom (or the top of bedrock foundation) in upstream direction may consist a deposition of a sediment layer of considerable depth. The effect of sedimentary layers is to partially absorb the incident hydrodynamic pressure waves and facilitate the energy dissipation in the reservoir domain. Fenves and Chopra, 1983 studied the effect of reservoir bottom absorption on the hydrodynamic pressure in reservoir and the dynamic response of concrete gravity dams. Reservoir bottom absorption effect was modeled by means of an absorbing boundary condition

applied at the bottom of reservoir allowing the partial absorption of hydrodynamic pressure waves at the reservoir bottom. The foundation underneath the dam-reservoir system was assumed to be rigid. It was concluded that the reservoir bottom absorption-effect can significantly reduce the resonant response of gravity dams to both horizontal and vertical ground motion components. This reduction in response becomes more substantial as stiffness of the dam increases. The decrease in resonant frequency of the dam due to dam-water interaction is less pronounced for a wave absorptive reservoir bottom than for a rigid reservoir bottom. The assumption of water incompressibility overestimates both resonant response and response to high excitation frequencies due to horizontal ground motion, in addition, this assumption also underestimate the importance of the response to the vertical ground motion.

Cheng, 1986 modeled the reservoir bottom as a poroelastic sediment layer of finite extent situated on top of an elastic half-space. It was showed that in case of saturated pore water the interaction between the sediment and the reservoir is negligible. Even a thin sediment layer, however, can significantly modify the reservoir response if the pore water is slightly desaturated. It was found that the resonance frequency of the system decreases and amplitude increases as the water compressibility increases. Further, it was observed that in case of highly permeable, partially saturated, and stiff sediment layer the hydrodynamic force on the rigid dam decreases significantly.

Chopra and Chakrabarti, 1981 presented a general procedure for analysis of the dynamic response of the dam-reservoir-soil (DRS) system to the horizontal and vertical components of earthquake motions. The method was based on a substructure coupling technique in which the DRS system was divided into three substructures; the dam, the reservoir with infinite length in upstream direction, and the semi-infinite viscoelastic soil domain. The displacements of the dam were expressed as a linear combination of Ritz vectors, which are selected as normal modes of an associated undamped dam-soil system.

Lotfi et al., 1987 developed a finite element procedure for the problems of dynamic interaction of dam-reservoir-soil systems. They devised a technique based on the interface elements (called the hyper-elements) for rigorous modeling of all interactions, such as reservoir-soil interaction, reservoir-dam, and dam-soil interaction. In this study they concluded that the wave reflection approach presented in (Hall and Chopra, 1982; Fenves and Chopra, 1983) to model the reservoir bottom absorption effect underestimate the response of the dam. Medina et al., 1990 rigorously model the reservoir-foundation interaction in their method of analysis, which was based on boundary element method, and found that, although the Chopra's scheme to model the sediment layer (Hall and Chopra, 1982; Fenves and Chopra, 1983) was capable of providing a reasonably accurate prediction of the response to a vertical excitation, it underestimated the peak value of crest acceleration caused by harmonic horizontal

excitation. Hatami, 1997 modified the wave reflection approach presented by the Chopra and coworkers to model the reservoir bottom absorption effects in the seismic analysis of the gravity dam. Hatami's model explicitly accounts for the thickness as well as the effects of wave attenuation in the sediment layer and reflection of waves from the underlying foundation rock. In addition, Hatami's model also utilizes the mechanical parameters of the sediment layer and the foundation rock. Unfortunately, the model is only applicable when the analysis is performed in frequency domain.

In the finite element analysis of dynamic dam-reservoir interaction problems, difficulties arise mainly because of the large extent of the fluid domain, where fluid is practically unbounded. The infinite reservoir domain is usually truncated by placing the artificial boundaries in the upstream direction at some distance from the dam. In the finite representation of such domains, a proper boundary condition must be applied at the artificial boundary to represent the effects of radiation damping. Saini et al., 1978 developed the special finite elements extending to infinity to model the large extent of reservoir. These infinite elements naturally satisfies the Sommerfeld radiation condition at the infinity. Their method of analysis was based on the substructure coupling technique in which the reservoir and the dam were handled as two substructures. The dam was discretized by using standard finite elements, which were coupled with the infinite fluid elements. This technique depend upon the frequency of vibration and, therefore, unsuitable for a time domain analysis. Sharan, 1987 proposed a simple boundary condition to model the effects of radiation damping in the analysis of hydrodynamic pressures. It was also showed that the Sommerfeld boundary condition at the truncated upstream boundary of reservoir does not truly represent the effect of radiation damping, particularly when the excitation frequency is less than the second natural frequency of the reservoir. The use of the Sommerfeld boundary condition, therefore, requires large extent of the fluid domain to be considered in the analysis. From the numerical experiments he showed that the modified damping condition is advantageous as absorbing boundary can be placed at relatively short distance from the dam as compared to distance required in case of the Sommerfeld damping condition. Yang et al., 1993; Maity and Bhattacharyya, 1999 proposed the explicit time-domain transmitting boundary condition for the analysis of dam-reservoir interactions. These boundary conditions are more accurate than Sharan's boundary conditions, however, their finite element implementation is relatively tedious. Recently, researchers (Basu and Chopra, 2004; Prempramote et al., 2009; Birk et al., 2012; Lin et al., 2012; Samii and Lotfi, 2012) have developed sophisticated procedures to model the dam-reservoir interaction problems.

Various computational techniques have been proposed in the literature to model the coupling phenomenon in dam-reservoir interaction problem. The simplest procedure being adopted is that both fluid and solid domain are coupled and solved as a

one system. Zienkiewicz and Newton, 1969; Müller, 1981 used pressure as the unknown in the fluid and displacements in the solid, but the resultant equations lead to unsymmetrical matrices. Olson and Bathe, 1985 used velocity potential and a hydrostatic pressure as unknown in each fluid region, and used displacements as unknown in the solid. The use of pressure as unknown in fluid and displacement in solid results in unsymmetrical matrices. Sandberg and Goransson, 1988 obtained a symmetrical system by using pressure and a displacement potential to describe the fluid domain. Their formulation allows the use of different nodal interpolation for pressure and displacement potential. Further, number of unknowns can be reduced by employing static condensation to the pressure field. Belytschko and Kennedy, 1976; Bathe and Hahn, 1979; Wilson and Khalvati, 1983; Chen and Taylor, 1990; Pelecanos et al., 2013 used displacements as the nodal variable in both the solid and fluid domain. However, these formulations suffer from the presence of spurious zero-energy modes unless an irrotational constraint with/without reduced integration scheme is taken into account. Bermúdez et al., 1995 also used displacement variables for both fluid and the solid domain. But they employed linear elements for the solid domain and nonconforming Raviart-Thomas elements of lower order for the fluid domain to eliminate the zero-energy modes. The advantage of the displacement-based formulation is that the fluid elements can easily be coupled to the structural elements using standard finite element assembly procedures. But the degrees of freedom for the fluid domain increase significantly.

The coupled modeled of dam-reservoir interaction problems may be achieved using the substructure techniques, in which different domains are modeled as separate computational entities amongst which interaction effects are communicated. Ghaemian and Ghobarah, 1998 presented two unconditionally stable staggered coupling schemes, in time domain, for the dam-reservoir interaction problem. The fist scheme was based on approximation of the displacement from the equation of motion in the solid domain. The second scheme was based on approximation of the pressure from the governing equation of fluid-domain. Maity and Bhattacharyya, 2003 suggested an iterative scheme in connection with the staggered solution procedure for the dam-reservoir interaction problem. More details regarding the iterative coupling techniques for dam-reservoir interaction problem can be found in literature (Park, 1980; Park, 1983; Felippa and Geers, 1988; Felippa et al., 2001; Jahromi et al., 2009; Soares and Godinho, 2014).

The objective of this chapter is to compute the seismic response of the dam-reservoir (DR) and dam-reservoir-soil (DRS) system while considering all types of dynamic interaction. The layout of this chapter is as follows. In Section 5.2 governing equations for DR and DRS system are presented. Viscous boundary conditions, which contains the contribution of free-field response of DR and DRS system, are applied at the artificial boundaries of computation domain. In Section 5.3, computation details

related to the free-field response of DR and DRS system are discussed. Section 5.4 presents the v-ST/FEM weak form for the DR and DRS system. The space-time finite element discretization of the weak form and computer implementation of v-ST/FEM formulation are given in Section 5.5 and Section 5.6, respectively. In later section, a block-iterative scheme is devised to solve the coupled equations of fluid and solid domain. InSection 5.7, various dam-reservoir interaction problems are solved to demonstrate the performance of the present approach. Lastly, for the verification of the proposed scheme, results obtained by using v-ST/FEM are compared with the results available in literature.

5.2 Statement of problem

Fig. 5.1 illustrates a dam-reservoir-soil (DRS) system that consists of following components;

1. *Structure*: the dam and irregular bounded soil domain with linear or nonlinear material behavior. In this chapter, however, for the sake of clarity of v-ST/FEM formulation the structure is assumed to behave linearly.

2. *Reservoir*: the semi-unbounded prismatic channel with linear, inviscid, irrotational, and compressible fluid. The term *fluid domain* and *reservoir* will be used interchangeably.

3. *Soil domain* : the regular unbounded soil domain which is assumed to be isotropic, homogeneous, linear elastic material. Besides, the term *soil* is used as a general expression for denoting the geological material underneath the structure and reservoir.

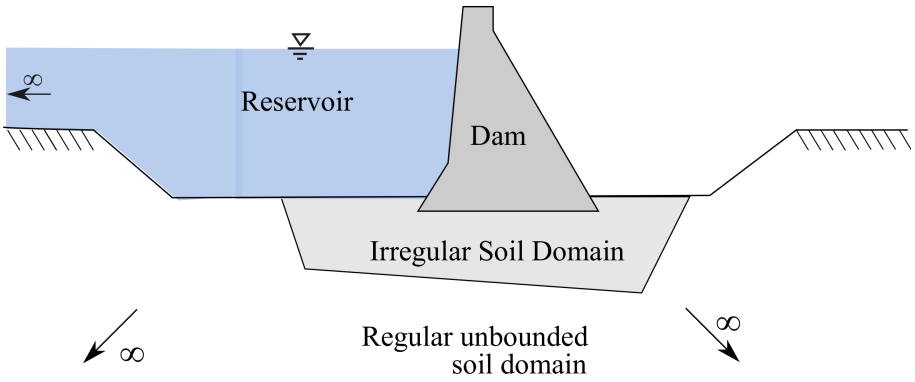

Fig. 5.1.: Schematic diagram of dam-reservoir-soil system subjected to an earthquake motion

In practice, sometimes, the structure is situated on a relatively very stiff soil. In such cases, the effect of interaction with the soil can be neglected. Subsequently, a DRS

system can simply be represented by a dam-reservoir (DR) system (see Fig. 5.2) where the dynamic interaction between structure (dam) and reservoir plays a major role. It is natural, therefore, to start with the governing equations of a DR system, and subsequently extending them to include the effect of dynamic soil-structure interaction.

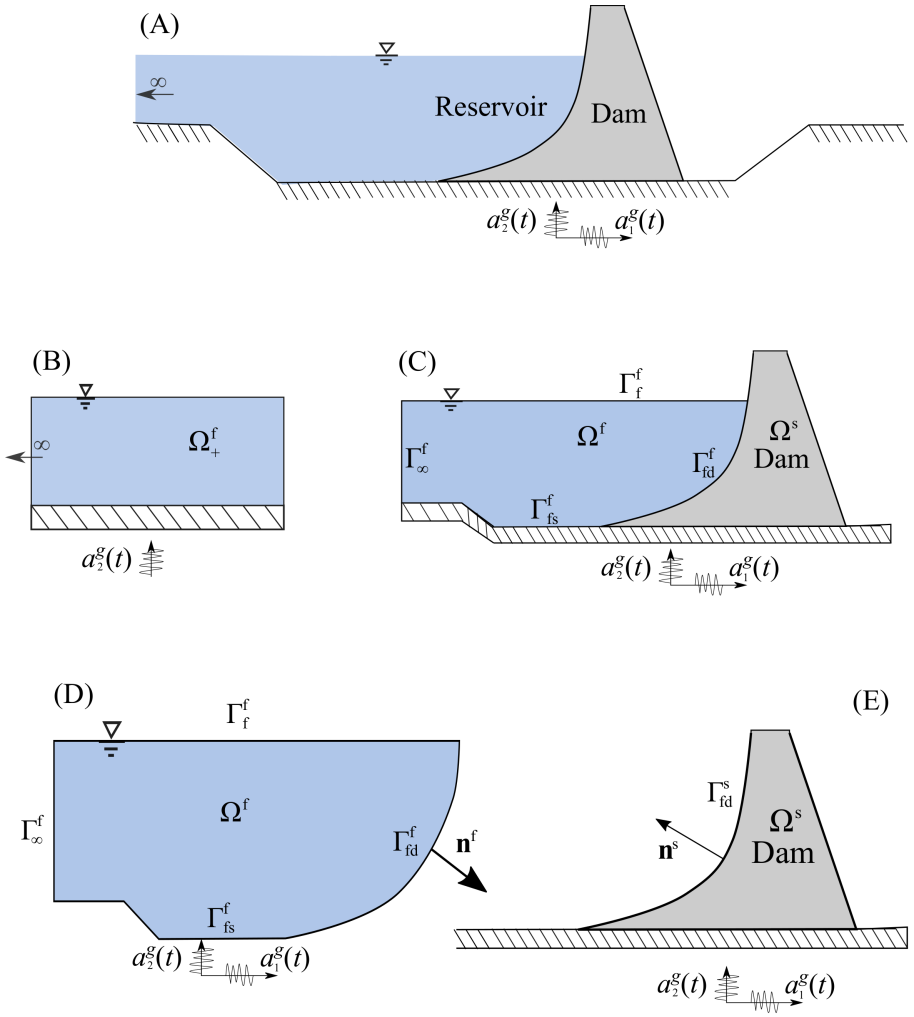

Fig. 5.2.: Illustration of different components of a dam-reservoir (DR) system on a perfectly rigid-foundation; (A) dam and a semi-infinite reservoir with impounded water subjected to ground motion, (B) auxiliary state of dam-reservoir system, (C) finite computation domain of the DR system obtained by placing an artificial boundary at the upstream end of the reservoir, (D) computation domain for fluid (reservoir), (E) computation domain for solid (dam)

5.2.1 Governing equation for dam-reservoir system

Fig. 5.2 depicts the dam-reservoir system situated on a relatively rigid ground which is subjected to the transient ground motion. The horizontal and vertical component of ground motion are denoted by $a_1^g(t)$ and $a_2^g(t)$, respectively. Note that the ground motion is assumed to be spatially-uniform. Henceforth, the superscript $(\cdot)^s$ and

$(\cdot)^f$ will be used for denoting the quantities related to the solid (dam) and fluid domain, respectively. Let Ω^f be the computation domain for fluid (i.e. reservoir) with free surface denoted by Γ_f^f and upstream artificial boundary denoted by Γ_∞^f. The fluid-soil interface (of fluid domain Ω^f) – the bottom boundary of fluid domain which is in contact with the ground – is denoted by Γ_{fs}^f. The fluid-dam interface of the fluid domain is represented by Γ_{fd}^f. Let Ω^s denote the finite computation domain for solid which, in the present case, is occupied by the dam body. The fluid-dam interface of solid domain is represented by Γ_{fd}^s. The outward unit normal vectors to the fluid and solid boundary are denoted by $\mathbf{n}^s$ and $\mathbf{n}^f$, respectively.

Neglecting the internal viscosity, and assuming the water to be linearly compressible with a small amplitudes for the displacements and velocity, the hydrodynamic pressure distribution in the reservoir is governed by the pressure wave equation (Zienkiewicz and Taylor, 2005),

$$\frac{1}{c^2}\frac{\partial^2 p}{\partial t^2} - \frac{\partial^2 p}{\partial x_i^2} = 0 \tag{5.1}$$

where $p(\vec{x}, t)$ is the hydrodynamic pressure in the water (in excess of hydrostatic pressure), and c is the speed of sound in water. Further, it is assumed that the water in the reservoir is initially at rest conditions,

$$p\left(\mathbf{x}, 0\right) = 0; \qquad \frac{\partial p\left(\mathbf{x}, 0\right)}{\partial t} = 0 \tag{5.2}$$

The hydrodynamic pressure distribution within the reservoir domain is obtained by solving Eq. (5.1) with the following boundary conditions.

1. *Boundary condition at* Γ_f^f: If the possibility of surface gravity waves at the free surface is neglected then the boundary condition on Γ_f^f becomes

$$p(x,t) = 0 \quad \forall (\mathbf{x}, t) \in \Gamma_f^f \times (0, T) \tag{5.3}$$

   If, however, one wishes to include the effect of surface-gravity waves while solving the dynamic DRI problem then the boundary condition is given by linearized surface wave condition (Zienkiewicz and Taylor, 2005)

$$\frac{\partial p}{\partial x_2} = -\frac{1}{g}\frac{\partial^2 p}{\partial t^2} \quad \forall (\mathbf{x}, t) \in \Gamma_f^f \times (0, T) \tag{5.4}$$

   where g is the acceleration due to gravity, x_2-axis is in the vertical direction, and the free surface is parallel to the x_1-axis.

In this thesis the effect of surface-gravity wave is not considered, hence, the boundary condition Eq. (5.3) will be adopted.

2. *Boundary condition at* Γ^f_∞: The upstream artificial boundary is obtained by truncating the infinite reservoir domain. In case no excitation source is present exterior to Γ^f_∞ the artificial boundary should be able to absorb the incoming waves. This is the case when vertical component of ground motion is absent. In case both horizontal and vertical component are present the vertical motion of the ground generates the free-field response which then enters the fluid domain Ω^f through the artificial boundary. Therefore, in later case the artificial boundary should only absorb the outgoing scattered pressure-waves. The absorbing boundary condition for the fluid domain is given by,

$$\nabla\left(p-p^f\right)\cdot\mathbf{n}^f=-\frac{1}{c}\frac{\partial\left(p-p^f\right)}{\partial t}\quad\forall(\mathbf{x},t)\in\Gamma^f_\infty\times(0,T)\tag{5.5}$$

where p^f is the free-field response of reservoir, and $(p-p^f)$ denotes the scattered pressure wave. Eq. (5.5) signifies that the outgoing scattered waves are traveling towards infinity and no spurious reflection of scattered waves will take place at the truncated boundary. After rearrangement of the terms in Eq. (5.5),

$$\nabla p\cdot\mathbf{n}^f=-\frac{1}{c}\frac{\partial p}{\partial t}+\nabla p^f\cdot\mathbf{n}^f+\frac{1}{c}\frac{\partial p^f}{\partial t}\quad\forall(\mathbf{x},t)\in\Gamma^f_\infty\times(0,T)$$

In Eq. 5.5 the first term corresponds to an array of dashpots (with damping coefficient equal to $1/c$) placed normal to the absorbing boundary Γ^f_f, and last two terms corresponds to the free-field response of reservoir (see Fig. 5.3). It will be shown in next section that the free-response of reservoir p^f can effectively be given by $p^f=p^f(x_2,t)$. In addition, noting that the outward normal vector $\mathbf{n}^f$ at Γ^f_∞ is $[-1,0]^T$, the second term in above equation vanishes and following traction boundary condition can be obtained

$$\nabla p\cdot\mathbf{n}^f=-\frac{1}{c}\frac{\partial p}{\partial t}+\frac{1}{c}\frac{\partial p^f}{\partial t}\quad\forall(\mathbf{x},t)\in\Gamma^f_\infty\times(0,T)\tag{5.6}$$

3. *Boundary condition at* Γ^f_{fd}: The traction boundary condition at fluid-dam interface is describe by

$$\nabla p\cdot\mathbf{n}^f=-\rho^f\frac{\partial\mathbf{v}}{\partial t}\cdot\mathbf{n}^f\quad\forall(\mathbf{x},t)\in\Gamma^f_{fd}\times(0,T)\tag{5.7}$$

where ρ^f is the mass density of water, and $\mathbf{v}$ is the total velocity of the material points of dam that belong to the interface Γ^f_{fd}.

4. *Boundary condition at* Γ_{fs}^{f}: The traction boundary condition at fluid-soil interface is describe by

$$\nabla p \cdot \mathbf{n}^f = -\rho^f \mathbf{a}^g \cdot \mathbf{n}^f - q_c \frac{\partial p}{\partial t} \quad \forall (\mathbf{x}, t) \in \Gamma_{fs}^{f} \times (0, T) \tag{5.8}$$

where $\mathbf{a}^g(t)$ is the acceleration of ground, and q_c is the damping coefficient which is the fundamental parameter characterizing the effect of reservoir bottom materials and it is given in Fenves and Chopra, 1983 as,

$$q_c = \frac{1 - \alpha_b}{c\,(1 + \alpha_b)} \tag{5.9}$$

in which α_b is the ratio of the amplitude of reflected hydrodynamic pressure wave to the amplitude of a vertically propagating pressure wave incident on the reservoir bottom. The wave reflection coefficient α_b is more physically meaningful description than q_c of the behavior of hydrodynamic pressure waves at the reservoir bottom. The wave reflection coefficient α_b may range within the limiting values of 1 and -1. For $\alpha_b = 1$ the reservoir-bottom acts as the perfect reflector for the pressure waves, and $\alpha_b = -1$ models a very soft reservoir bottom (or foundation).

The second term in Eq. (5.8) represents the modification of the vertical free-field ground acceleration due to interaction between the impounded water and the foundation medium. Due to this term the reservoir bottom also produces a damping effect representing the energy radiated through refraction (or absorption) of hydrodynamic pressure waves into the foundation medium away from the dam-water system. Accordingly, this term signifies the dynamic interaction between the reservoir water and the ground which permits partial absorption of hydrodynamic pressure waves at the reservoir bottom.

Lastly, computation domain of fluid, in the dam-reservoir system with a rigid foundation, and the aforementioned boundary conditions are illustrated in Fig. 5.3.

Let us now discuss the governing equation for the solid domain (recall that in DR-system the solid domain is occupied by dam only) which is given by,

$$\rho^s \frac{\partial v_i}{\partial t} - \frac{\partial \sigma_{ij}}{\partial x_j} - \rho^s b_i = 0 \quad \forall (\mathbf{x}, t) \in \Omega^s \times (0, T) \tag{5.10}$$

where ρ^s is the mass density of the solid domain. Further, for an isotropic, homogeneous, linear elastic material stress-strain relationship is described by

$$\sigma_{ij} = \lambda \epsilon_{kk} \delta_{ij} + 2\mu \epsilon_{ij} \tag{5.11}$$

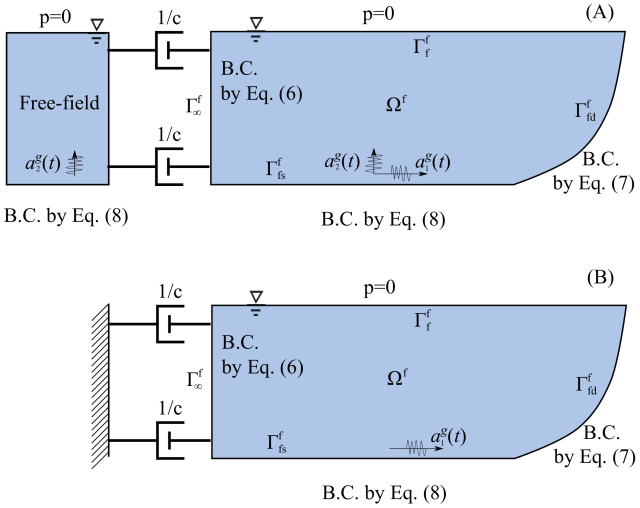

Fig. 5.3.: Computation domain of the fluid in the dam-reservoir system on rigid foundation with appropriate boundary conditions (given by equation numbers); (A) the reservoir bottom is subjected to both both horizontal and vertical components of ground motion, (B) the reservoir bottom is subjected to only horizontal component of ground motion(here B.C. stands for boundary condition)

where λ and μ are the Lame parameters, and

$$\epsilon_{ij} = \frac{1}{2}\left(\frac{\partial u_i}{\partial x_j} + \frac{\partial u_j}{\partial x_i}\right) \tag{5.12}$$

The initial conditions for the solid domain are

$$\begin{aligned} u_i\left(\mathbf{x},0\right) &= u_i^0\left(\mathbf{x}\right) \quad \forall \mathbf{x} \in \Omega^s \\ v_i\left(\mathbf{x},0\right) &= v_i^0\left(\mathbf{x}\right) \quad \forall \mathbf{x} \in \Omega^s \end{aligned} \tag{5.13}$$

and the Dirichlet boundary condition is described by

$$u_i\left(\mathbf{x},t\right) = g_i\left(\mathbf{x},t\right) \quad \forall\left(\mathbf{x},t\right) \in \Gamma_i^g \times (0,T) \tag{5.14}$$

In case of DR-system, the traction boundary condition for solid domain can be decomposed into (i) traction boundary condition due to externally applied surface loads (see Eq. 5.15), (ii) traction boundary condition due to total pressure (hydrostatic and hydrodynamic pressure) of impounded water acting on Γ_{fd}^s (see Eq. 5.16).

$$\sigma_{ij} n_j^s = f_i^s \quad \forall\left(\mathbf{x},t\right) \in \Gamma_{i,h}^s \times (0,T) \tag{5.15}$$

$$\sigma_{ij} n_j^s = -\left\{p_0(\mathbf{x}) + p(\mathbf{x},t)\right\} n_i^s \quad \forall\left(\mathbf{x},t\right) \in \Gamma_{fd}^s \times (0,T) \tag{5.16}$$

where $p_0(\mathbf{x})$ and $p(\mathbf{x},t)$ denote the hydrostatic and hydrodynamic pressure due to impounded water in the reservoir, respectively, and $\Gamma^s_{i,h}$ denotes the portion of solid-boundary on which surface loads in x_i-direction are prescribed.

Lastly, the strong form of initial-boundary value problem of dynamic interaction between dam-reservoir system situated on a perfectly rigid ground is stated in Fig. 5.4.

Given the functions;

$$b_i : \Omega^s \times [0,T] \to \mathbb{R} \qquad g_i : \Gamma^g_i \times [0,T] \to \mathbb{R} \qquad h_i : \Gamma^s_{i,h} \times [0,T] \to \mathbb{R}$$
$$u^0_i : \Omega^s \to \mathbb{R} \qquad v^0_i : \Omega^s \to \mathbb{R} \qquad \rho^s : \Omega \to \mathbb{R}$$
$$a^g_i : [0,T] \to \mathbb{R} \qquad p^f : \Gamma^f_\infty \times [0,T] \to R$$

and the constants λ, μ, c, q_c,
find $u_i : \bar{\Omega}^s \times [0,T] \to \mathbb{R}$, $v_i : \bar{\Omega}^s \times [0,T] \to \mathbb{R}$, and $p : \bar{\Omega}^f \times [0,T]$ such that

$$\frac{1}{c^2}\frac{\partial^2 p}{\partial t^2} - \frac{\partial^2 p}{\partial x_i^2} = 0 \quad \forall (\mathbf{x},t) \in \Omega^f \times (0,T)$$

$$p(x,t) = 0 \quad \forall (\mathbf{x},t) \in \Gamma^f_f \times (0,T)$$
$$\nabla p \cdot \mathbf{n}^f = -\frac{1}{c}\frac{\partial p}{\partial t} + \frac{1}{c}\frac{\partial p^f}{\partial t} \quad \forall (\mathbf{x},t) \in \Gamma^f_\infty \times (0,T)$$
$$\nabla p \cdot \mathbf{n}^f = -\rho^f \frac{\partial \mathbf{v}}{\partial t} \cdot \mathbf{n}^f \quad \forall (\mathbf{x},t) \in \Gamma^f_{fd} \times (0,T)$$
$$\nabla p \cdot \mathbf{n}^f = -\rho^f \mathbf{a}^g \cdot \mathbf{n}^f - q_c \frac{\partial p}{\partial t} \quad \forall (\mathbf{x},t) \in \Gamma^f_{fs} \times (0,T)$$

$$\frac{\partial v_i}{\partial t} - \frac{\partial \sigma_{ij}}{\partial x_j} - \rho^s b_i = 0 \quad \forall (\mathbf{x},t) \in \Omega^s \times (0,T)$$

$$\sigma_{ij} = \lambda \epsilon_{kk} \delta_{ij} + 2\mu \epsilon_{ij} \qquad \epsilon_{ij} = \frac{1}{2}\left(\frac{\partial u_i}{\partial x_j} + \frac{\partial u_j}{\partial x_i}\right)$$
$$u_i(\mathbf{x},0) = u^0_i(\mathbf{x}) \quad \forall \mathbf{x} \in \Omega^s \qquad v_i(\mathbf{x},0) = v^0_i(\mathbf{x}) \quad \forall \mathbf{x} \in \Omega^s$$

$$u_i(\mathbf{x},t) = g_i(\mathbf{x},t) \quad \forall (\mathbf{x},t) \in \Gamma^g_i \times (0,T)$$
$$\sigma_{ij} n^s_j = f^s_i \quad \forall (\mathbf{x},t) \in \Gamma^s_{i,h} \times (0,T)$$
$$\sigma_{ij} n^s_j = -\{p_0(\mathbf{x}) + p(\mathbf{x},t)\} n^s_i \quad \forall (\mathbf{x},t) \in \Gamma^s_{fd} \times (0,T)$$

Fig. 5.4.: Strong form of initial-boundary value problem of dynamic interaction between a dam and a reservoir (with impounded water) on a rigid foundation subjected to the ground motion

5.2.2 Governing equation for dam-reservoir-soil system

In case of dam-reservoir-soil system, solid domain Ω^s consists of dam and bounded soil domain, and in this chapter both are assumed to behave linearly. The governing equation for fluid domain, initially at rest, is described by the pressure-wave equation Eq. (5.1). The boundary condition at the free surface Γ_f^f, the upstream artificial boundary Γ_∞^f, and fluid-dam interface Γ_{fd}^f is given by Eq. (5.3), Eq. (5.6), and Eq. (5.7), respectively. At reservoir bottom (i.e. fluid-soil interface) the traction boundary condition becomes,

$$\nabla p \cdot \mathbf{n}^f = -\rho^f \frac{\partial \mathbf{v}}{\partial t} \cdot \mathbf{n}^f - q_c \frac{\partial p}{\partial t} \quad \forall (\mathbf{x}, t) \in \Gamma_{fs}^f \times (0, T) \tag{5.17}$$

where $\mathbf{v}$ is the velocity of material-points (of soil domain) that are positioned at the fluid-soil interface Γ_{fs}^s, and q_c is given by Eq. (5.9).

The motion of solid domain (both soil and dam) is governed by the classical elastodynamics equation presented in Eqs. (5.10–5.12). The initial conditions and the Dirichlet boundary condition are given by Eq. (5.13) and Eq. (5.14), respectively. The traction boundary condition due to the external surface loading is given in Eq. (5.15), and the traction boundary condition due to the hydrostatic pressure $p_0(\mathbf{x})$ and hydrodynamic pressure $p(\mathbf{x}, t)$ of impounded water acting on the dam-fluid interface Γ_{fd}^s and the fluid-soil interface Γ_{fs}^s is given by Eq. (5.18).

$$\sigma_{ij} n_j^s = -\left\{ p_0(\mathbf{x}) + p(\mathbf{x}, t) \right\} n_i^s \quad \forall (\mathbf{x}, t) \in \Gamma_{fd}^s \cup \Gamma_{fs}^s \times (0, T) \tag{5.18}$$

in which $\mathbf{n}^s$ is the outward normal vector to the boundary of solid domain Ω^s. Further, the traction boundary condition at the artificial boundary of truncated soil domain must be satisfied for correctly modeling the radiation-damping effect of unbounded soil domain. These boundary conditions are describe as follows.

$$\sigma_{ij} n_j^s = -c_{ip}^v v_p + c_{ip}^v v_p^f + \sigma_{ip}^f n_p^s \quad \forall (\mathbf{x}, t) \in \Gamma_\infty^L \cup \Gamma_\infty^R \times (0, T) \tag{5.19}$$

$$\sigma_{ij} n_j^s = -c_{ip}^h v_p + 2 c_{ip}^h v_p^{in} \quad \forall (\mathbf{x}, t) \in \Gamma_\infty^B \times (0, T) \tag{5.20}$$

where Γ_∞^L, Γ_∞^R, and Γ_∞^B are the left, right and bottom artificial (absorbing) boundary of truncated soil domain, respectively (see Fig. 5.5). $\mathbf{v}^f$ and σ^f are the velocity and stress due to free-field response of unbounded soil domain. $\mathbf{c}^v$ and $\mathbf{c}^h$ are the damping coefficient matrix of dashpots which are arranged at the vertical and horizontal viscous boundaries, respectively. Furthermore, the free-field response of reservoir and soil domain is obtained by solving the auxiliary state problem for the DRS system (see Fig. 5.5a). The derivation of Eq. (5.19) and Eq. (5.20) is covered in Section 3.5 (see Eq. 3.118 and Eq. (3.119)).

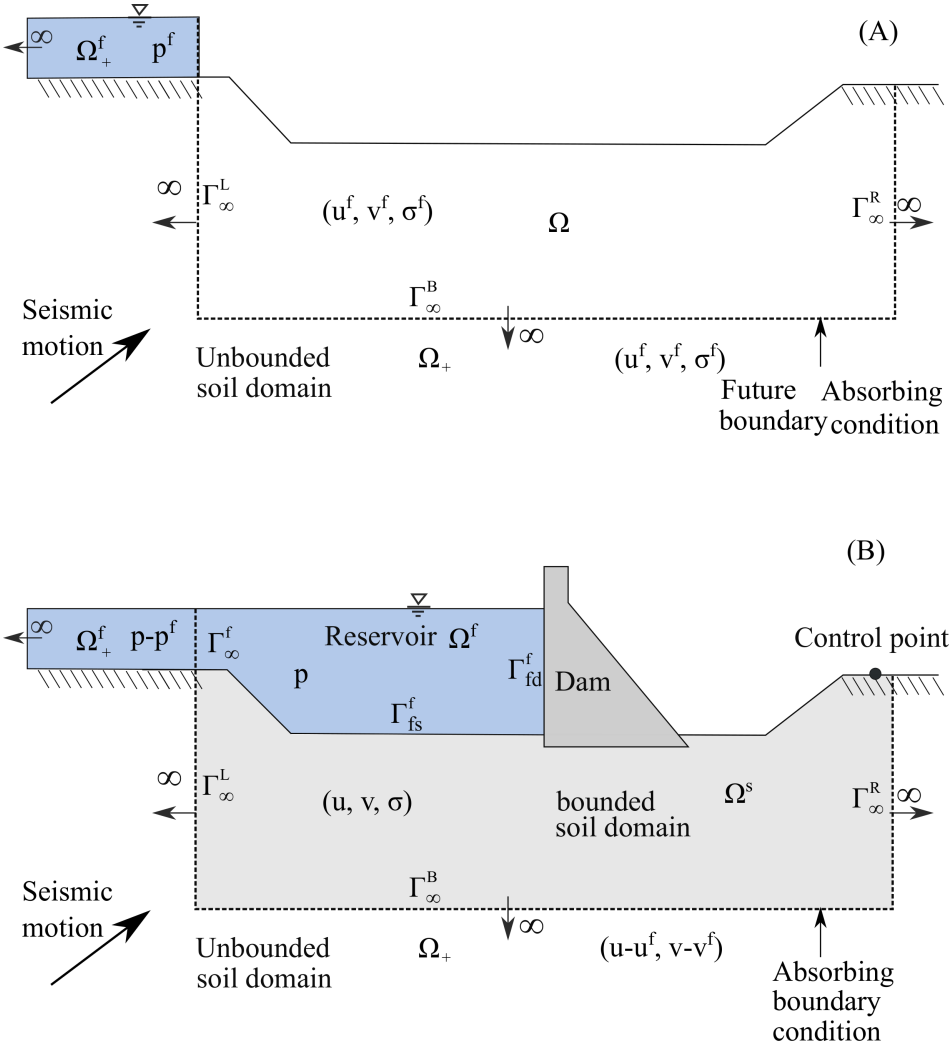

Fig. 5.5.: Illustration of dynamic dam-reservoir-soil interaction problem as a wave scattering problem, (A) auxiliary state of dam-reservoir-soil system for computing the free-field response, (B) finite computation domain of dam-reservoir-soil system and the absorbing boundaries

The strong form of initial-boundary value problem of dynamic dam-reservoir-soil interaction (DRSI) is summarized in Fig. 5.6.

Given the functions;

$$b_i : \Omega^s \times [0,T] \to \mathbb{R} \quad g_i : \Gamma_i^g \times [0,T] \to \mathbb{R} \quad h_i : \Gamma_{i,h}^s \times [0,T] \to \mathbb{R}$$
$$u_i^0 : \Omega^s \to \mathbb{R} \quad v_i^0 : \Omega^s \to \mathbb{R} \quad \rho^s : \Omega \to \mathbb{R}$$
$$v_i^{in} : [0,T] \to \mathbb{R} \quad p^f : \Gamma_\infty^f \times [0,T] \to R \quad u_i^f : \Gamma_\infty^L \cup \Gamma_\infty^R \times [0,T] \to \mathbb{R}$$

and the constants λ, μ, c, q_c, $\mathbf{c}^v$, $\mathbf{c}^h$
find $u_i : \bar{\Omega}^s \times [0,T] \to \mathbb{R}$, $v_i : \bar{\Omega}^s \times [0,T] \to \mathbb{R}$, and $p : \bar{\Omega}^f \times [0,T]$ such that

$$\frac{1}{c^2}\frac{\partial^2 p}{\partial t^2} - \frac{\partial^2 p}{\partial x_i^2} = 0 \quad \forall (\mathbf{x},t) \in \Omega^f \times (0,T)$$
$$p(x,t) = 0 \quad \forall (\mathbf{x},t) \in \Gamma_f^f \times (0,T)$$
$$\nabla p \cdot \mathbf{n}^f = -\frac{1}{c}\frac{\partial p}{\partial t} + \nabla p^f \cdot \mathbf{n}^f + \frac{1}{c}\frac{\partial p^f}{\partial t} \quad \forall (\mathbf{x},t) \in \Gamma_\infty^f \times (0,T)$$
$$\nabla p \cdot \mathbf{n}^f = -\rho^f \frac{\partial \mathbf{v}}{\partial t} \cdot \mathbf{n}^f \quad \forall (\mathbf{x},t) \in \Gamma_{fd}^f \times (0,T)$$
$$\nabla p \cdot \mathbf{n}^f = -\rho^f \frac{\partial \mathbf{v}}{\partial t} \cdot \mathbf{n}^f - q_c \frac{\partial p}{\partial t} \quad \forall (\mathbf{x},t) \in \Gamma_{fs}^f \times (0,T)$$

$$\frac{\partial v_i}{\partial t} - \frac{\partial \sigma_{ij}}{\partial x_j} - \rho^s b_i = 0 \quad \forall (\mathbf{x},t) \in \Omega^s \times (0,T)$$

$$\sigma_{ij} = \lambda \epsilon_{kk} \delta_{ij} + 2\mu \epsilon_{ij} \qquad \epsilon_{ij} = \frac{1}{2}\left(\frac{\partial u_i}{\partial x_j} + \frac{\partial u_j}{\partial x_i}\right)$$
$$u_i(\mathbf{x},0) = u_i^0(\mathbf{x}) \quad \forall \mathbf{x} \in \Omega^s \qquad v_i(\mathbf{x},0) = v_i^0(\mathbf{x}) \quad \forall \mathbf{x} \in \Omega^s$$

$$u_i(\mathbf{x},t) = g_i(\mathbf{x},t) \quad \forall (\mathbf{x},t) \in \Gamma_i^g \times (0,T)$$
$$\sigma_{ij} n_j^s = f_i^s \quad \forall (\mathbf{x},t) \in \Gamma_{i,h}^s \times (0,T)$$
$$\sigma_{ij} n_j^s = -\{p_0(\mathbf{x}) + p(\mathbf{x},t)\} n_i^s \quad \forall (\mathbf{x},t) \in \Gamma_{fd}^s \times (0,T)$$
$$\sigma_{ij} n_j^s = -c_{ip}^v v_p + c_{ip}^v v_p^f + \sigma_{ip}^f n_p^s \quad \forall (\mathbf{x},t) \in \Gamma_\infty^L \cup \Gamma_\infty^R \times (0,T)$$
$$\sigma_{ij} n_j^s = -c_{ip}^h v_p + 2c_{ip}^h v_p^{in} \quad \forall (\mathbf{x},t) \in \Gamma_\infty^B \times (0,T)$$

Fig. 5.6.: Strong form of initial-boundary value problem of dynamic dam-reservoir-soil interaction

5.3 Computation of free-field response

In order to obtain the dynamic response of dam-reservoir or dam-reservoir-soil system the free field response must be obtained by analysis of the corresponding auxiliary system.

5.3.1 Free-field response of dam-reservoir system

Fig. 5.2b illustrates the auxiliary state of a dam-reservoir system. Let Ω_+^f be the two-dimensional spatial domain occupied by the auxiliary-state. The free field response is obtained by solving pressure wave equation for the auxiliary state. Recall that the reservoir bottom is horizontal and only vertical motion of ground (reservoir-bottom) need to be considered in the analysis. In this situation the hydrodynamic pressure p^f depends upon x_2 coordinate only and satisfied the following one-dimensional wave equation,

$$\frac{1}{c^2}\frac{\partial^2 p^f}{\partial t^2} - \frac{\partial^2 p^f}{\partial x_2^2} = 0 \tag{5.21}$$

In this way the auxiliary state can be represented by a fluid-column placed adjacent to the upstream truncated boundary of reservoir (i.e. Γ_∞^f). The fluid-column is considered at the rest at $t = 0$. At the top surface of the fluid-column $p^f = 0$, and at the bottom surface following traction boundary condition should be imposed

$$\frac{\partial p^f}{\partial x_2} = \rho^f a_2^g(t) + q_c \frac{\partial p^f}{\partial t} \tag{5.22}$$

where $a_2^g(t)$ is the x_2-component of ground acceleration, and q_c is given by Eq. (5.9).

5.3.2 Free field response of dam-reservoir-soil system

Fig. 5.5a depicts the auxiliary state for dam-reservoir-soil system. The auxiliary state contains both the infinite reservoir and the soil domain, and the spatial-domain occupied by the auxiliary state is given by $\Omega \cup \Omega_+ \cup \Omega_+^f$. Accordingly, the free-field hydrodynamic pressure (p^f) and the free-field displacement (u^f) of soil domain are the primary unknowns. [1]

Theoretically speaking, the free-field response (u^f, p^f) is obtained by analysis of auxiliary dam-reservoir-soil system while considering the effects of reservoir-soil interaction in spatial domain $\Omega_+^f \cup \Omega_+$. This strategy, however, will require huge computational cost. This expensive analysis may be simplified by ignoring the coupling between the reservoir and soil in spatial domain $\Omega_+^f \cup \Omega_+$. Under this assumption, the bottom surface of reservoir domain Ω_+^f can be treated as a rigid-surface thus ignoring the effects of foundation flexibility. Subsequently, p^f can be computed by solving a fluid-column problem as discussed in the previous subsection. Further, u_f will be computed by solving the soil-column problem as discussed in Section 4.5. In this way, by ignoring the effects of secondary reservoir-soil interaction

[1] However, in order to compute the total response of the DRS system we only need the information of free-field solutions at the truncated boundaries.

in spatial domain $\Omega^f_+ \cup \Omega_+$, it is now possible to compute u^f and p^f from the the corresponding simple column problems at very low computational cost.

5.4 v-ST/FEM formulation

Let Ω^f_h, the set of finite spatial fluid-elements $\Omega^f_e, e = 1, \cdots, n^f_{el}$, be the discretization of reservoir domain Ω^f, where n^f_{el} is the total number of spatial fluid elements in Ω^f_h. Further, let Ω^s_h, the set of finite spatial solid-elements Ω^s_e, $e = 1, \cdots, n_{el}$, be the discretization of solid domain Ω^s, where n_{el} is the total number of spatial elements in Ω_h. Now, consider a non-uniform subdivision for the time domain $[0, T]$, $0 = t_0 < t_1 < \cdots < t_N = T$ with $I_n = (t_n, t_{n+1})$, $\Delta t = t_{n+1} - t_n$. The n^{th} space-time slab for fluid domain $Q^f_n = \Omega^f_h \times I_n$ and for solid domain $Q^s_n = \Omega^s_h \times I_n$, and corresponding space-time finite element for fluid domain $Q^f_{n,e} = \Omega^f_e \times I_n, e = 1, \cdots, n^f_{el}$, and for solid domain $Q^s_{n,e} = \Omega^s_e \times I_n, e = 1, \cdots, n_{el}$.

Let us now consider $\mathcal{P}_l(Q^f_{n,e})$ and $\mathcal{P}_l(Q^s_{n,e})$, the collection of all polynomials defined on $Q^f_{n,e}$ and $Q^s_{n,e}$, respectively, with a total degree of no more than l. Let the space of piecewise continuous functions defined on domain $(*)$ is given by $C^0(*)$. Consider also the following collection of functions:

$$\mathfrak{F}^f_{l,h} := \left\{ p^h \middle| \, p^h \in C^0\left(\bigcup_{n=0}^{N-1} Q^f_n\right), p^h \middle| \, Q^f_{n,e} \in \mathcal{P}_l\left(Q^f_{n,e}\right) \right\} \tag{5.23}$$

$$\mathfrak{F}^s_{l,h} := \left\{ \mathbf{u}^h \middle| \, \mathbf{u}^h \in C^0\left(\bigcup_{n=0}^{N-1} Q^s_n\right)^2, \mathbf{u}^h \middle| \, Q^s_{n,e} \in \left(\mathcal{P}_l\left(Q^s_{n,e}\right)\right)^2 \right\} \tag{5.24}$$

where $p^h \big| \, Q^f_{n,e}$ and $\mathbf{u}^h \big| \, Q^s_{n,e}$ is the restriction of $p^h(\mathbf{x}, t)$ to $Q^f_{n,e}$ and restriction of $\mathbf{u}^h(\mathbf{x}, t)$ to $Q^s_{n,e}$, respectively.

The space of the test functions for the fluid-domain is

$$\mathscr{Q}^h := \left\{ q^h \middle| \, q^h \in \mathfrak{F}^f_{l,h}, q^h = 0, \forall\, (\mathbf{x}, t) \in \Gamma^f_f \times I_n \right\} \tag{5.25}$$

and the space of trial functions is same as the space of test function, i.e.

$$S^h_p = \mathscr{Q}^h \tag{5.26}$$

The space of the test functions for the solid domain is

$$V^h := \left\{ \mathbf{v}^h \middle| \, \mathbf{v}^h \in \mathfrak{F}_{l,h}, \mathbf{v}^h = 0, \forall\, (\mathbf{x}, t) \in \Gamma^g_i \times I_n, i = 1, 2 \right\} \tag{5.27}$$

and the space of trial functions for solid domain is

$$S_v^h := \left\{ \mathbf{v}^h \middle| \, \mathbf{v}^h \in \mathfrak{F}_{l,h}, v_i^h = \dot{g}_i, \forall \left(\mathbf{x}, t\right) \in \Gamma_i^g \times I_n, i = 1, 2 \right\} \tag{5.28}$$

In order to obtain the space-time weak form of pressure-wave equation Eq. (5.1) is rewritten as

$$\frac{1}{c^2} \frac{\partial q}{\partial t} - \frac{\partial^2 p}{\partial x_i^2} = 0 \tag{5.29}$$

where $q(\mathbf{x}, t)$ is the auxiliary variable given by

$$q = \frac{\partial p}{\partial t} \tag{5.30}$$

and

$$p\left(\mathbf{x}, t\right) = p\left(\mathbf{x}, t_n\right) + \int_{t_n}^{t} q\left(\mathbf{x}, \tau\right) d\tau \quad \forall \left(\mathbf{x}, \tau\right) \in \Omega^f \times \left[t_n, t\right] \tag{5.31}$$

5.4.1 v-ST/FEM weak form for dam-reservoir system

The v-ST/FEM weak-form of strong-form presented in Fig. 5.4 can be stated as; Find $\mathbf{v} \in S_v^h$ and $q \in S_p^h$ such that for all $\delta \mathbf{v} \in V^h$, $\delta q \in \mathscr{Q}^h$, and for all $n = 1, \cdots, N-1$, Eq. (5.32) and Eq. (5.33) hold true.

$$\begin{aligned}
&\int_{I_n} \int_{\Omega_h^f} \delta q \frac{1}{c^2} \frac{\partial q}{\partial t} d\Omega dt + \int_{\Omega_h^f} \delta q\left(\mathbf{x}, t_n\right) \frac{1}{c^2} q\left(\mathbf{x}, t_n^+\right) d\Omega \\
&- \int_{\Omega_h^f} \delta q\left(\mathbf{x}, t_n\right) \frac{1}{c^2} q\left(\mathbf{x}, t_n^-\right) d\Omega \\
&+ \int_{I_n} \int_{\Omega_h^f} \frac{\partial \delta q}{\partial x_i} \frac{\partial p}{\partial x_i} d\Omega dt + \int_{I_n} \int_{\Gamma_{fd}^f} \delta q \rho^f \frac{\partial v_i}{\partial t} n_i^f ds dt \\
&+ \int_{I_n} \int_{\Gamma_{fs}^f} \delta q \rho^f a_i^g n_i^f ds dt + \int_{I_n} \int_{\Gamma_{fs}^f} \delta q \rho^f q_c q ds dt \\
&+ \int_{I_n} \int_{\Gamma_{\infty}^f} \delta q \frac{1}{c} q ds dt - \int_{I_n} \int_{\Gamma_{\infty}^f} \delta q \frac{1}{c} q^f ds dt = 0
\end{aligned} \tag{5.32}$$

$$\begin{aligned}
&\int_{I_n} \int_{\Omega_h^s} \rho^s \delta v_i \frac{\partial v_i}{\partial t} d\Omega dt + \int_{\Omega_h^s} \rho^s \delta v_i\left(\mathbf{x}, t_n^+\right) v_i\left(\mathbf{x}, t_n^+\right) d\Omega \\
&- \int_{\Omega_h^s} \rho^s \delta v_i\left(\mathbf{x}, t_n^+\right) v_i\left(x, t_n^-\right) d\Omega + \int_{I_n} \int_{\Omega_h^s} \frac{\partial \delta v_i}{\partial x_j} C_{ijkl} \psi_{kl} d\Omega dt \\
&- \int_{I_n} \int_{\Gamma_i^h} \delta v_i f_i^s ds dt - \int_{I_n} \int_{\Omega_h^s} \rho^s \delta v_i b_i d\Omega dt \\
&+ \int_{I_n} \int_{\Omega_h^s} \frac{\partial \delta v_i}{\partial x_j} \sigma_{ij}^n d\Omega dt + \int_{I_n} \int_{\Gamma_{fd}^s} \delta v_i \left(p + p_0\right) n_i^s ds dt = 0
\end{aligned} \tag{5.33}$$

In Eq. (5.32) and Eq. (5.33), n_i^f and n_i^s are the components of outward normal vector at the fluid and solid boundary, respectively. Hydrodynamic pressure p and displacements $\mathbf{u}$ are obtained by consistent integration of q and $\mathbf{v}$, respectively, and q^f is related to the the free-field hydrodynamic pressure by

$$q^f = \frac{\partial p^f}{\partial t} \tag{5.34}$$

In Eq. (5.33) C_{ijkl} and ψ_{ij} are given by

$$C_{ijkl} = \lambda \delta_{ij}\delta_{kl} + \mu\left(\delta_{ik}\delta_{jl} + \delta_{il}\delta_{jk}\right) \tag{5.35}$$

$$\psi_{ij} = \int_{t_n}^{t} \frac{\partial v_i\left(\mathbf{x},\tau\right)}{\partial x_j} d\tau \quad \forall t \in I_n, \forall \mathbf{v} \in S_v^h \tag{5.36}$$

5.4.2 v-ST/FEM weak form for dam-reservoir-soil system

The v-ST/FEM weak-form of strong-form presented in Fig. 5.6 can be stated as; Find $\mathbf{v} \in S_v^h$ and $q \in S_p^h$ such that for all $\delta\mathbf{v} \in V^h$, $\delta q \in \mathscr{Q}^h$, and for all $n = 1, \cdots, N-1$, Eq. (5.37) and Eq. (5.38) hold true.

$$\begin{aligned}
&\int_{I_n}\int_{\Omega_h^f} \delta q \frac{1}{c^2}\frac{\partial q}{\partial t} d\Omega dt + \int_{\Omega_h^f} \delta q\left(\mathbf{x}, t_n\right) \frac{1}{c^2} q\left(\mathbf{x}, t_n^+\right) d\Omega \\
&- \int_{\Omega_h^f} \delta q\left(\mathbf{x}, t_n\right) \frac{1}{c^2} q\left(\mathbf{x}, t_n^-\right) d\Omega + \int_{I_n}\int_{\Omega_h^f} \frac{\partial \delta q}{\partial x_i}\frac{\partial p}{\partial x_i} d\Omega dt \\
&+ \int_{I_n}\int_{\Gamma_{fd}^f} \delta q \rho^f \frac{\partial v_i}{\partial t} n_i^f \, ds dt + \int_{I_n}\int_{\Gamma_{fs}^f} \delta q \rho^f \frac{\partial v_i}{\partial t} n_i^f \, ds dt \\
&+ \int_{I_n}\int_{\Gamma_{fs}^f} \delta q \rho^f q_c q \, ds dt + \int_{I_n}\int_{\Gamma_\infty^f} \delta q \frac{1}{c} q \, ds dt - \int_{I_n}\int_{\Gamma_\infty^f} \delta q \frac{1}{c} q^f \, ds dt = 0
\end{aligned} \tag{5.37}$$

$$\begin{aligned}
&\int_{I_n}\int_{\Omega_h^s} \delta v_i \rho^s \frac{\partial v_i}{\partial t} d\Omega dt + \int_{\Omega_h^s} \delta v_i\left(\mathbf{x}, t_n^+\right) \rho^s v_i\left(x, t_n^+\right) d\Omega \\
&- \int_{\Omega_h^s} \delta v_i\left(\mathbf{x}, t_n^+\right) \rho^s v_i\left(x, t_n^-\right) d\Omega - \int_{I_n}\int_{\Omega_h^s} \delta v_i \rho^s b_i d\Omega dt \\
&+ \int_{I_n}\int_{\Omega_h^s} \frac{\partial \delta v_i}{\partial x_j} \sigma_{ij}^n d\Omega dt + \int_{I_n}\int_{\Omega_h^s} \frac{\partial \delta v_i}{\partial x_j} C_{ijkl}\psi_{kl} d\Omega dt \\
&- \int_{I_n}\int_{\Gamma_i^h} \delta v_i f_i^s \, ds dt + \int_{I_n}\int_{\Gamma_\infty^R \cup \Gamma_\infty^L} \delta v_i c_{ij}^v v_j \, ds dt \\
&+ \int_{I_n}\int_{\Gamma_\infty^B} \delta v_i c_{ip}^h v_p \, ds dt - \int_{I_n}\int_{\Gamma_\infty^R \cup \Gamma_\infty^L} \delta v_i \left(c_{ij}^v v_j^f + \sigma_{ij}^f n_j\right) ds dt \\
&- \int_{I_n}\int_{\Gamma_\infty^B} \delta v_i 2 c_{ij}^h v_j^{in} \, ds dt + \int_{I_n}\int_{\Gamma_{fd}^s} \delta v_i (p + p_0) n_i^s \, ds dt + \int_{I_n}\int_{\Gamma_{fb}^s} \delta v_i (p + p_0) n_i^s \, ds dt = 0
\end{aligned} \tag{5.38}$$

It is noteworthy that in Eq. (5.37) the boundary integral defined on upstream truncated boundary Γ^f_∞ corresponds to the Eq. (5.6). This equation does not include the term $\nabla p^f \cdot \mathbf{n}^f$ as the dynamic interaction of reservoir-soil is ignored while computing the free-field response (see Section 5.3.2).

5.5 Space-time finite element discretization

Let n_e and n_e^f be the total number of nodes in spatial finite element for solid and fluid domain, respectively. Let $v_i(\mathbf{x}, t_n^+)$ and $v_i(\mathbf{x}, t_{n+1}^-)$ be the spatial velocities on the bottom and top faces of space-time slab Q_n, respectively. Similarly, let $q(\mathbf{x}, t_n^+)$ and $q(\mathbf{x}, t_{n+1}^-)$ be the spatial velocities on the bottom and top faces of space-time slab Q_n^f, respectively. Linear interpolation of time $t \in I_n$ is given by

$$t = T_1(\theta)t_n + T_2(\theta)t_{n+1}, \quad \forall\theta \in [-1, 1] \tag{5.39}$$

where,

$$T_1(\theta) = \frac{1-\theta}{2} \qquad T_2(\theta) = \frac{1+\theta}{2} \tag{5.40}$$

The test and trial function for velocity defined on $Q_{n,e}$ are given by

$$\delta v_i\left(\mathbf{x}, t\right) = {}^a\delta v_{iI} T_a\left(\theta\right) N^I\left(\xi, \eta\right) \tag{5.41}$$

$$v_i\left(\mathbf{x}, t\right) = {}^a v_{iI} T_a\left(\theta\right) N^I\left(\xi, \eta\right) \tag{5.42}$$

The displacement field $\mathbf{u}(\mathbf{x}, t)$ is computed by consistent integration of Eq. (5.42)

$$u_i\left(\mathbf{x}, t\right) = u_i\left(\mathbf{x}, t_n\right) + \tilde{T}_1\left(\theta\right) v_i\left(\mathbf{x}, t_n\right) + \tilde{T}_2\left(\theta\right) v_i\left(\mathbf{x}, t_{n+1}\right) \tag{5.43}$$

further, Eq. (5.36) becomes

$$\psi_{ij}\left(\mathbf{x}, t\right) = \tilde{T}_1\left(\theta\right) \frac{\partial v_i}{\partial x_j}\left(\mathbf{x}, t_n\right) + \tilde{T}_2\left(\theta\right) \frac{\partial v_i}{\partial x_j}\left(\mathbf{x}, t_{n+1}\right) \tag{5.44}$$

where

$$\tilde{T}_1\left(\theta\right) = \frac{\Delta t_n}{2}\left[1 - T_1^2\left(\theta\right)\right] \qquad \tilde{T}_2\left(\theta\right) = \frac{\Delta t_n}{2} T_2^2\left(\theta\right) \tag{5.45}$$

The test and trial function for $q(\mathbf{x}, t)$ defined on $Q_{n,e}$ are given by

$$\delta q\left(\mathbf{x}, t\right) = {}^a\delta q_I T_a\left(\theta\right) N_f^I\left(\xi, \eta\right) \tag{5.46}$$

$$q\left(\mathbf{x},t\right) = {}^{a}q_I T_a\left(\theta\right) N_f^I\left(\xi,\eta\right) \tag{5.47}$$

Using Eq. (5.47) in Eq. (5.31) to determine the hydrodynamic pressure p,

$$p\left(\mathbf{x},t\right) = p\left(\mathbf{x},t_n\right) + \tilde{T}_1\left(\theta\right) q\left(\mathbf{x},t_n\right) + \tilde{T}_2\left(\theta\right) q\left(\mathbf{x},t_{n+1}\right) \tag{5.48}$$

In Eqs. (5.39 – 5.48), $i = 1,2$ denotes the spatial component along x_1 and x_2 direction, $a = 1,2$ denotes the temporal node number, $\theta \in [-1,1]$ denotes the local temporal coordinate, and (ξ,η) denotes the local coordinates in the spatial finite element. In Eq. (5.41–5.42) $I = 1,\cdots,n_e$, and in Eq. (5.46–5.47) $I = 1,\cdots,n_e^f$ denote the local node number of a spatial finite element for dam and reservoir, respectively. The shape function for an I^{th} spatial local node is denoted by N^I and N_f^I for solid and fluid domain, respectively.

5.5.1 v-ST/FEM discretization for dam-reservoir system

By using the space-time interpolation for $\mathbf{v}$, $\delta\mathbf{v}$, $\mathbf{u}$, ψ_{ij}, p, q, and δq in Eq. (5.32) and Eq. (5.33) one can obtain the following system of discrete equations (see Appendix-C for derivation).

$$\left[\mathbf{K}_{st}^f\right]\cdot\{\tilde{\mathbf{q}}\} + \left[\mathbf{H}_{fd}^f\right]\cdot\{\tilde{\mathbf{v}}\} = \left\{\mathbf{J}^f\right\} \tag{5.49}$$

$$\left[\mathbf{K}_{st}^s\right]\cdot\{\tilde{\mathbf{v}}\} + \left[\mathbf{H}_{fd}^s\right]\cdot\{\tilde{\mathbf{q}}\} = \{\mathbf{J}^s\} \tag{5.50}$$

where

$$\left[\mathbf{K}_{st}^f\right] = \left[\mathbf{M}^f\right] + \left[\mathbf{K}^f\right] + \left[\mathbf{C}_{fs}^f\right] + \left[\mathbf{C}_{\infty}^f\right] \tag{5.51}$$

$$\left[\mathbf{K}_{st}^s\right] = \left[\mathbf{M}^s\right] + \left[\mathbf{K}^s\right] \tag{5.52}$$

$$\left\{\mathbf{J}^f\right\} = \left\{\mathbf{J}_0^f\right\} + \left\{\mathbf{J}_f^f\right\} - \left\{\mathbf{J}_g^{fs}\right\} - \left\{\mathbf{J}_{p^n}^f\right\} \tag{5.53}$$

$$\{\mathbf{J}^s\} = \{\mathbf{J}_{ext}^s\} + \{\mathbf{J}_0^s\} - \{\mathbf{J}_{\sigma^n}^s\} - \left\{\mathbf{J}_{p^n}^{fd}\right\} - \left\{\mathbf{J}_{p_0}^{fd}\right\} \tag{5.54}$$

Further, if Rayleigh damping is used to model the material damping in solid domain then Eq. (5.52) becomes,

$$\left[\mathbf{K}_{st}^s\right] = \left[\mathbf{M}^s\right] + \left[\mathbf{K}^s\right] + \alpha\left[\mathbf{M}_R^s\right] + \beta\left[\mathbf{K}_R^s\right] \tag{5.55}$$

in which α and β are the Rayleigh damping coefficients.

Further, in Eq. (5.49) and Eq. (5.50) $\{\tilde{\mathbf{q}}\}$ is used to denote the space-time nodal values of auxiliary variable q, and $\{\tilde{\mathbf{v}}\}$ which denotes the space-time nodal values of

velocity field are the primary unknowns for the fluid and solid domain, respectively. The finite element structure of these unknown vectors are given by

$$\{\tilde{\mathbf{q}}\} = \left\{ \begin{array}{c} \tilde{\mathbf{q}}^1 \\ \tilde{\mathbf{q}}^2 \end{array} \right\} \qquad \{\tilde{\mathbf{v}}\} = \left\{ \begin{array}{c} \tilde{\mathbf{v}}^1 \\ \tilde{\mathbf{v}}^2 \end{array} \right\} \qquad \left\{\tilde{\mathbf{v}}^1\right\} = \left\{ \begin{array}{c} \tilde{\mathbf{v}}_1^1 \\ \tilde{\mathbf{v}}_2^1 \end{array} \right\} \qquad \left\{\tilde{\mathbf{v}}^2\right\} = \left\{ \begin{array}{c} \tilde{\mathbf{v}}_1^2 \\ \tilde{\mathbf{v}}_2^2 \end{array} \right\}$$

in which $\{\tilde{\mathbf{q}}^1\}$ and $\{\tilde{\mathbf{q}}^2\}$ are the space-nodal values of q at time $t = t_n^+$ (bottom space-time slab) and time $t = t_{n+1}^-$ (top space-time slab), respectively. Similarly, $\{\tilde{\mathbf{v}}^1\}$ and $\{\tilde{\mathbf{v}}^2\}$ are the space-nodal values of $\mathbf{v}$ at time $t = t_n^+$ and time $t = t_{n+1}^-$, respectively. Furthermore, $\{\tilde{\mathbf{v}}_1^a\}$ and $\{\tilde{\mathbf{v}}_2^a\}$ (for $a = 1, 2$) stand for the space-nodal values of spatial component of velocity field along x_1 and x_2 direction, respectively.

In Eq. (5.49) and Eq. (5.51), $\left[\mathbf{M}^f\right]$ denotes the space-time mass matrix for the fluid domain, $\left[\mathbf{K}^f\right]$ corresponds to the space-time diffusion matrix for fluid domain, $\left[\mathbf{C}_{fs}^f\right]$ is the space-time matrix which is related to the reservoir bottom absorption effect, $\left[\mathbf{C}_{\infty}^f\right]$ is the space-time matrix corresponding to the dashpots placed at the truncated upstream boundary of reservoir, and $\left[\mathbf{H}_{fd}^f\right]$ is the coupling matrix which relates the hydrodynamic pressure in the reservoir with the dynamic response of dam. Further, in Eq. (5.53), the space-time nodal vector $\left\{\mathbf{J}_0^f\right\}$ corresponds to the value of q at time $t = t_n$, $\left\{\mathbf{J}_f^f\right\}$ is related to the free-field hydrodynamic response of the reservoir, $\left\{\mathbf{J}_g^{fs}\right\}$ is related to the motion of underlying rigid-foundation, and $\left\{\mathbf{J}_{p^n}^f\right\}$ is related to the pressure-gradient in the reservoir at time $t = t_n$.

In Eq. (5.52) and Eq. (5.55), $[\mathbf{M}^s]$ denotes the space-time mass matrix for the solid domain, $[\mathbf{K}^s]$ is the space-time tangent stiffness matrix for the solid domain, $[\mathbf{M}_R^s]$ and $[\mathbf{K}_R^s]$ are the mass-proportional and stiffness-proportional space-time Rayleigh damping matrix, respectively, and $\left[\mathbf{H}_{fd}^s\right]$ is the coupling matrix which relates the hydrodynamic pressure in the reservoir with the dynamic response of dam. Further, in Eq. (5.53), $\{\mathbf{J}_0^s\}$ corresponds to the velocity of the dam at time $t = t_n$, $\{\mathbf{J}_{ext}^s\}$ is related to the external body force and surface acting on the dam, $\{\mathbf{J}_{\sigma^n}^s\}$ is related to the stresses in the dam at time $t = t_n$, and the vectors $\left\{\mathbf{J}_{p^n}^{fd}\right\}$ and $\left\{\mathbf{J}_{p_0}^{fd}\right\}$ correspond to the hydrodynamic pressure and hydrostatic pressure due to reservoir, respectively.

The finite element expressions of the terms present in Eqs. (5.49 – 5.55) are depicted in Table 5.1 and Table 5.2. A detailed description about the derivation of space-time matrices and space-time nodal vectors (including their finite element data-structure) is given in Appendix-C.

Matrix notation	Component notation	Expression
$[\mathbf{M}^s]$	$[M^s]_{ij}^{ab}\,(I,J)$	$\delta_{ij}\int_{I_n}\int_{\Omega_h^s} N^I T_a \rho^s \frac{\partial N^J T_b}{\partial t} dt d\Omega$ $+\delta_{ij}\delta_{1a}\delta_{1b}\int_{\Omega_h^s} N^I \rho^s N^J d\Omega$
$[\mathbf{K}^s]$	$[K^s]_{ij}^{ab}\,(I,J)$	$\int_{I_n}\int_{\Omega_h^s} \frac{\partial N^I T_a}{\partial x_p} C_{pijq} \frac{\partial N^J \tilde{T}_b}{\partial x_q} d\Omega dt$
$[\mathbf{M}_R^s]$	$[M_R^s]_{ij}^{ab}\,(I,J)$	$\delta_{ij}\int_{I_n}\int_{\Omega_h^s} N^I T_a \rho N^J T_b d\Omega dt$
$[\mathbf{K}_R^s]$	$[K_R^s]_{ij}^{ab}\,(I,J)$	$\int_{I_n}\int_{\Omega_h^s} \frac{\partial N^I T_a}{\partial x_p} C_{pijq} \frac{\partial N^J T_b}{\partial x_q} d\Omega dt$
$\left[\mathbf{M}^f\right]$	$\left[M^f\right]^{ab}\,(I,J)$	$\int_{I_n}\int_{\Omega_h^f} N_f^I T_a \frac{1}{c^2} \frac{\partial N_f^J T_b}{\partial t} dt d\Omega$ $+\delta_{1a}\delta_{1b}\int_{\Omega_h^s} N_f^I \frac{1}{c^2} N_f^J d\Omega$
$\left[\mathbf{K}^f\right]$	$\left[K^f\right]^{ab}\,(I,J)$	$\int_{I_n}\int_{\Omega_h^f} T_a \tilde{T}_b \frac{\partial N_f^I}{\partial x_i} \frac{\partial N_f^J}{\partial x_i} d\Omega dt$
$\left[\mathbf{C}_{fs}^f\right]$	$\left[C_{fs}^f\right]^{ab}\,(I,J)$	$\int_{I_n}\int_{\Gamma_{fs}^f} N_f^I T_a \rho^f q_c N_f^J T_b ds dt$
$\left[\mathbf{C}_{\infty}^f\right]$	$\left[C_{\infty}^f\right]^{ab}\,(I,J)$	$\int_{I_n}\int_{\Gamma_{\infty}^f} N_f^I T_a \frac{1}{c} N_f^J T_b ds dt$
$[\mathbf{C}_{L\infty}]$	$[C_{L\infty}]_{ij}^{ab}\,(I,J)$	$\int_{I_n}\int_{\Gamma_{\infty}^L} N^I T_a c_{ij}^v N^J T_b ds dt$
$[\mathbf{C}_{R\infty}]$	$[C_{R\infty}]_{ij}^{ab}\,(I,J)$	$\int_{I_n}\int_{\Gamma_{\infty}^R} N^I T_a c_{ij}^v N^J T_b ds dt$
$[\mathbf{C}_{B\infty}]$	$[C_{B\infty}]_{ij}^{ab}\,(I,J)$	$\int_{I_n}\int_{\Gamma_{\infty}^B} N^I T_a c_{ij}^h N^J T_b ds dt$
$\left[\mathbf{H}_{fd}^f\right]$	$\left[H_{fd}^f\right]_i^{ab}\,(I,J)$	$\int_{I_n} T_a \frac{\partial T_b}{\partial t} dt \int_{\Gamma_{fd}^f} N_f^I \rho^f N^J n_i^f ds$
$\left[\mathbf{H}_{fs}^f\right]$	$\left[H_{fs}^f\right]_i^{ab}\,(I,J)$	$\int_{I_n} T_a \frac{\partial T_b}{\partial t} dt \int_{\Gamma_{fs}^f} N_f^I \rho^f N^J n_i^f ds$
$\left[\mathbf{H}_{fd}^s\right]$	$\left[H_{fd}^s\right]_i^{ab}\,(I,J)$	$\int_{I_n} T_a \tilde{T}_b dt \int_{\Gamma_{fd}^s} N^I N_f^J n_i^s ds$
$\left[\mathbf{H}_{fs}^s\right]$	$\left[H_{fs}^s\right]_i^{ab}\,(I,J)$	$\int_{I_n} T_a \tilde{T}_b dt \int_{\Gamma_{fs}^s} N^I N_f^J n_i^s ds$

Tab. 5.1.: Description of the space-time finite element matrices used in the v-ST/FEM for the linear seismic analysis of the dam-reservoir and dam-reservoir-soil system.

Matrix notation	Component notation	Expression
$\{\mathbf{J}^s_{ext}\}$	$\{J^s_{ext}\}^a_i\,(I)$	$\int_{I_n}\int_{\Omega^s_h} N^I T_a \rho^s b_i d\Omega dt$ $+\int_{I_n}\int_{\Gamma^h_i} N^I T_a f^s_i d\Omega dt$
$\{\mathbf{J}^s_0\}$	$\{J^s_0\}^a_i\,(I)$	$\delta_{a1}\int_{\Omega^s_h} N^I \rho^s v^0_i d\Omega$
$\{\mathbf{J}^s_{\sigma^n}\}$	$\{J^s_{\sigma^n}\}^a_i\,(I)$	$\int_{I_n}\int_{\Omega^s_h} \frac{\partial N^I T_a}{\partial x_j}\sigma^n_{ij} d\Omega dt$
$\left\{\mathbf{J}^{fd}_{p^n}\right\}$	$\left\{J^{fd}_{p^n}\right\}^a_i\,(I)$	$\int_{I_n}\int_{\Gamma^s_{fd}} T_a N^I p^n n^s_i ds dt$
$\left\{\mathbf{J}^{fs}_{p^n}\right\}$	$\left\{J^{fs}_{p^n}\right\}^a_i\,(I)$	$\int_{I_n}\int_{\Gamma^s_{fs}} T_a N^I p^n n^s_i ds dt$
$\left\{\mathbf{J}^{fd}_{p_0}\right\}$	$\left\{J^{fd}_{p_0}\right\}^a_i\,(I)$	$\int_{I_n}\int_{\Gamma^s_{fd}} T_a N^I p_0 n^s_i ds dt$
$\left\{\mathbf{J}^{fs}_{p_0}\right\}$	$\left\{J^{fs}_{p_0}\right\}^a_i\,(I)$	$\int_{I_n}\int_{\Gamma^s_{fs}} T_a N^I p_0 n^s_i ds dt$
$\left\{\mathbf{J}^f_0\right\}$	$\left\{J^f_0\right\}^a\,(I)$	$\delta_{1a}\int_{\Omega^f_h} N^I_f \frac{1}{c^2} q^0 d\Omega$
$\left\{\mathbf{J}^f_f\right\}$	$\left\{J^f_f\right\}^a\,(I)$	$\int_{I_n}\int_{\Gamma^f_\infty} N^I_f T_a \frac{1}{c} q^f ds dt$
$\left\{\mathbf{J}^{fs}_g\right\}$	$\left\{J^{fs}_g\right\}^a\,(I)$	$\int_{I_n}\int_{\Gamma^f_{fs}} N^I_f T_a \rho^f a^g_i n^f_i ds dt$
$\left\{\mathbf{J}^f_{p^n}\right\}$	$\left\{J^f_{p^n}\right\}^a\,(I)$	$\int_{I_n}\int_{\Omega^f_h} T_a \frac{\partial N^I_f}{\partial x_i}\frac{\partial p^n}{\partial x_i} d\Omega dt$
$\left\{\mathbf{J}^s_f\right\}$	$\left\{J^s_f\right\}^a\,(I)$	$\int_{I_n}\int_{\Gamma^L_\infty} N^I T_a \left(c^v_{ij} v^f_j - \sigma^f_{i1}\right) ds dt$ $+\int_{I_n}\int_{\Gamma^R_\infty} N^I T_a \left(c^v_{ij} v^f_j + \sigma^f_{i1}\right) ds dt$
$\{\mathbf{J}^s_{in}\}$	$\{J^s_{in}\}^a\,(I)$	$\int_{I_n}\int_{\Gamma^B_\infty} N^I T_a 2 c^h_{ij} v^{in}_j ds dt$

Tab. 5.2.: Description of the space-time nodal vectors used in the v-ST/FEM for the linear seismic analysis of the dam-reservoir and dam-reservoir-soil system.

5.5.2 v-ST/FEM discretization for dam-reservoir-soil system

After using space-time interpolation for $\mathbf{v}$, $\delta\mathbf{v}$, $\mathbf{u}$, ψ_{ij}, p, q and δq in the weak form which is described by Eq. (5.37) and Eq. (5.38) one can obtain the following discrete form.

$$\left[\mathbf{K}_{st}^{f}\right]\cdot\{\tilde{\mathbf{q}}\}+\left[\mathbf{H}_{fd}^{f}\right]\cdot\{\tilde{\mathbf{v}}\}+\left[\mathbf{H}_{fs}^{f}\right]\cdot\{\tilde{\mathbf{v}}\}=\left\{\mathbf{J}^{f}\right\} \tag{5.56}$$

$$\left[\mathbf{K}_{st}^{s}\right]\cdot\{\tilde{\mathbf{v}}\}+\left[\mathbf{H}_{fd}^{s}\right]\cdot\{\tilde{\mathbf{q}}\}+\left[\mathbf{H}_{fs}^{s}\right]\cdot\{\tilde{\mathbf{q}}\}=\{\mathbf{J}^{s}\} \tag{5.57}$$

where

$$\left[\mathbf{K}_{st}^{f}\right]=\left[\mathbf{M}^{f}\right]+\left[\mathbf{K}^{f}\right]+\left[\mathbf{C}_{fs}^{f}\right]+\left[\mathbf{C}_{\infty}^{f}\right] \tag{5.58}$$

$$\left[\mathbf{K}_{st}^{s}\right]=\left[\mathbf{M}^{s}\right]+\left[\mathbf{K}^{s}\right]+\left[\mathbf{C}_{L\infty}\right]+\left[\mathbf{C}_{R\infty}\right]+\left[\mathbf{C}_{B\infty}\right] \tag{5.59}$$

$$\left\{\mathbf{J}^{f}\right\}=\left\{\mathbf{J}_{0}^{f}\right\}+\left\{\mathbf{J}_{f}^{f}\right\}-\left\{\mathbf{J}_{p^{n}}^{f}\right\} \tag{5.60}$$

$$\begin{aligned}\{\mathbf{J}^{s}\}=\{\mathbf{J}_{ext}^{s}\}+\{\mathbf{J}_{0}^{s}\}-\{\mathbf{J}_{\sigma^{n}}^{s}\}+\left\{\mathbf{J}_{f}^{s}\right\}+\{\mathbf{J}_{in}^{s}\}\\-\left\{\mathbf{J}_{p^{n}}^{fd}\right\}-\left\{\mathbf{J}_{p^{n}}^{fs}\right\}-\left\{\mathbf{J}_{p_{0}}^{fd}\right\}-\left\{\mathbf{J}_{p_{0}}^{fs}\right\}\end{aligned} \tag{5.61}$$

Further, if Rayleigh damping is employed to model the material damping then Eq. (5.59) becomes

$$\left[\mathbf{K}_{st}^{s}\right]=\left[\mathbf{M}^{s}\right]+\left[\mathbf{K}^{s}\right]+\alpha\left[\mathbf{M}_{R}^{s}\right]+\beta\left[\mathbf{K}_{R}^{s}\right]+\left[\mathbf{C}_{L\infty}\right]+\left[\mathbf{C}_{R\infty}\right]+\left[\mathbf{C}_{B\infty}\right] \tag{5.62}$$

where α and β are the Rayleigh damping coefficients.

In Eq. (5.57), $\left[\mathbf{H}_{fd}^{f}\right]$ is the coupling matrix which relates the hydrodynamic pressure in the reservoir with the dynamic response of dam, and $\left[\mathbf{H}_{fs}^{f}\right]$ is the coupling matrix which relates the hydrodynamic pressure in the reservoir with the dynamic response of soil domain. In Eq. (5.58), $\left[\mathbf{M}^{f}\right]$ denotes the space-time mass matrix for the fluid domain, $\left[\mathbf{K}^{f}\right]$ corresponds to the space-time diffusion matrix for fluid domain, $\left[\mathbf{C}_{fs}^{f}\right]$ is the space-time matrix which is related to the reservoir bottom absorption effect, and $\left[\mathbf{C}_{\infty}^{f}\right]$ is the space-time matrix corresponding to the dashpots placed at the truncated upstream boundary of reservoir. Further, in Eq. (5.60), the space-time nodal vector $\left\{\mathbf{J}_{0}^{f}\right\}$ corresponds to the value of q at time $t=t_{n}$, $\left\{\mathbf{J}_{f}^{f}\right\}$ is related to the free-field hydrodynamic response of the reservoir, and $\left\{\mathbf{J}_{p^{n}}^{f}\right\}$ is related to the pressure-gradient in the reservoir at time $t=t_{n}$.

In Eq. (5.56), $\left[\mathbf{H}^s_{fd}\right]$ is the coupling matrix which relates the hydrodynamic pressure in the reservoir with the dynamic response of dam, and $\left[\mathbf{H}^s_{fs}\right]$ is the coupling matrix which relates the hydrodynamic pressure in the reservoir with the dynamic response of soil domain. In Eq. (5.59) and Eq. (5.63), $[\mathbf{M}^s]$ denotes the space-time mass matrix for the solid domain, $[\mathbf{K}^s]$ is the space-time tangent stiffness matrix for the solid domain, $[\mathbf{M}^s_R]$ and $[\mathbf{K}^s_R]$ are the mass-proportional and stiffness-proportional space-time Rayleigh damping matrix, respectively, $[\mathbf{C}_{L\infty}]$, $[\mathbf{C}_{R\infty}]$ and $[\mathbf{C}_{B\infty}]$ are the space-time damping matrices due to dashpots placed at the left, right and bottom side of the truncated soil-domain. Further, in Eq. (5.61), $\{\mathbf{J}^s_0\}$ corresponds to the velocity of the solid domain at time $t = t_n$, $\{\mathbf{J}^s_{ext}\}$ is related to the external body force and surface acting on the solid domain, $\{\mathbf{J}^s_{\sigma^n}\}$ is related to the stresses in the solid domain at time $t = t_n$, and the vectors $\left\{\mathbf{J}^{fd}_{p^n}\right\}$, $\left\{\mathbf{J}^{fs}_{p^n}\right\}$ correspond to the hydrodynamic pressure in the reservoir acting over Γ^s_{fd} and Γ^s_{fs}, respectively. $\left\{\mathbf{J}^{fd}_{p_0}\right\}$ and $\left\{\mathbf{J}^{fs}_{p_0}\right\}$ correspond to the hydrostatic pressure in the reservoir acting over Γ^s_{fd} and Γ^s_{fs}, respectively.

The finite element expressions of the terms present in Eqs. (5.56 – 5.62) are depicted in Table 5.1 and Table 5.2. A detailed description about the derivation of space-time matrices and space-time nodal vectors (including their finite element data-structure) is given in Appendix-D.

5.6 v-ST/FEM implementation

In case of dam-reservoir system, if rigid-ground motion contains the vertical movement then free-field hydrodynamic pressure p^f should be computed first in order to compute the total hydrodynamic pressure in the reservoir. The free-field response of reservoir is computed by solving a one-dimensional wave equation (cf. Eq. 5.21) with appropriate boundary conditions (cf. Eq. 5.22). Similarly, in case of dam-reservoir-soil system, the free-field response of soil-domain $(\mathbf{u}^f, \mathbf{v}^f, \sigma^f)$ and free-field response of reservoir (p^f, q^f) is needed to compute the total response of dam-reservoir-soil system. Recalling that soil-column problem should be solved for determining the free-field response of soil-domain. The detailed description about the soil-column problem is presented in Section 4.5. Once again, the free-field response of reservoir is computed by solving a one-dimensional wave equation as discussed in Section 5.3.

In a given time step (i.e., $I_n = (t_n, t_{n+1})$), once the space-time nodal values of $(\mathbf{u}^f, \mathbf{v}^f, \sigma^f)$ on $\Gamma^L_\infty \cup \Gamma^R_\infty \cup \Gamma^B_\infty$ and (p^f, q^f) on Γ^f_∞ are determined the total response of reservoir (in the form of primary unknown q), and the total velocity field for the solid-domain $\mathbf{v}$ can be computed by solving the linear system of coupled-equations;

Eq. (5.49, 5.50) for the dam-reservoir (DR) system, and Eq. (5.56, 5.57) for the dam-reservoir-soil (DRS) system. Here it is important to note that the primary unknowns to be determined are q and $\mathbf{v}$. Further, it is possible to solve the coupled-equations simultaneously, however, this implementation strategy is undesirable as the number of unknowns increases drastically. Therefore, a block-iterative algorithm is devised to solve the system of coupled-equations given by Eq. (5.49, 5.50) or Eq. (5.56, 5.57) iteratively. In this strategy the solution of the coupled system can be obtained by solving the two systems (fluid domain and solid domain) separately with interaction effects enforced by iteration. The major advantage of this approach is that coupled field problems can be handled in a sequential manner. The structure of block-iterative algorithm is explicated as follows.

Without the loss of generality let's write Eq. (5.49, 5.50) and Eq. (5.56, 5.57) in the following form

$$\left[\mathbf{K}_{st}^{f}\right] \cdot \{\tilde{\mathbf{q}}\} + \left[\mathbf{H}^{f}\right] \cdot \{\tilde{\mathbf{v}}\} = \left\{\mathbf{J}^{f}\right\} \tag{5.63}$$

$$[\mathbf{K}_{st}^{s}] \cdot \{\tilde{\mathbf{v}}\} + [\mathbf{H}^{s}] \cdot \{\tilde{\mathbf{q}}\} = \{\mathbf{J}^{s}\} \tag{5.64}$$

where

$$\left[\mathbf{H}^{f}\right] = \left[\mathbf{H}_{fd}^{f}\right] \qquad [\mathbf{H}^{s}] = \left[\mathbf{H}_{fd}^{s}\right] \tag{5.65}$$

in the case of dam-reservoir system, and

$$\left[\mathbf{H}^{f}\right] = \left[\mathbf{H}_{fd}^{f}\right] + \left[\mathbf{H}_{fs}^{f}\right] \qquad [\mathbf{H}^{s}] = \left[\mathbf{H}_{fd}^{s}\right] + \left[\mathbf{H}_{fs}^{s}\right] \tag{5.66}$$

in the case of dam-reservoir-dam system.

Consider a time step corresponding to $I_n = (t_n, t_{n+1})$, and iteration number k. Let the space-time nodal values of q and $\mathbf{v}$ in k^{th} iteration be denoted by $\{\tilde{\mathbf{q}}\}^{(k)}$ and $\{\tilde{\mathbf{v}}\}^{(k)}$, respectively. The block-iterative algorithm for solving the Eq. (5.63) and Eq. (5.64) can be described as

$$[\mathbf{K}_{st}^{s}] \cdot \{\tilde{\mathbf{v}}\}^{(k)} = \{\mathbf{J}^{s}\} - [\mathbf{H}^{s}] \cdot \{\tilde{\mathbf{q}}\}^{(k-1)} \tag{5.67}$$

$$\left[\mathbf{K}_{st}^{f}\right] \cdot \{\tilde{\mathbf{q}}\}^{(k)} = \left\{\mathbf{J}^{f}\right\} - \left[\mathbf{H}^{f}\right] \cdot \{\tilde{\mathbf{v}}\}^{(k)} \tag{5.68}$$

The proposed block-iterative scheme can be viewed as a two-stage iterative algorithm in which the analysis is carried out for each field (q and $\mathbf{v}$) and interaction effect is accommodated by updating the variables of the fields in the respective coupling terms. In first-stage, see Eq. (5.67), $\{\tilde{\mathbf{q}}\}^{(k-1)}$ is utilized to compute the velocity field $\{\tilde{\mathbf{v}}\}^{(k-1)}$ in the solid-domain. At this stage, one can start by setting q to be zero,

Algorithm 2: v-ST/FEM algorithm with block-iterative scheme for solving the problem of dynamic interaction of dam-reservoir (DR) and dam-reservoir-soil (DRS) system

Initialization ;

Step-1: Get the initial value of nodal displacement $\{\tilde{\mathbf{u}}^0\}$, and velocity $\{\tilde{\mathbf{v}}^0\}$, set $\{\tilde{\mathbf{p}}^0\} = 0$, and $\{\tilde{\mathbf{q}}^0\} = 0$;

Step-2: Compute space-time tangent matrices for fluid and solid domain $[\mathbf{K}^s_{st}]$ and $\left[\mathbf{K}^f_{st}\right]$;

Step-3: Compute coupling matrices for solid and fluid domain $[\mathbf{H}^s]$ and $\left[\mathbf{H}^f\right]$;

Time Step Loop ;

for *n=0, N-1* **do**

- *Step-4*: Solve soil-column problem and compute $\mathbf{u}^f, \mathbf{v}^f, \sigma^f$. Compute the $\mathbf{J}^s_f$ (DRS only);
- *Step-5*: Compute $\mathbf{J}^s_{ext}$;
- *Step-6*: Compute $\mathbf{J}^s_0$ using $\{\tilde{\mathbf{v}}^0\}$;
- *Step-7*: Compute stress σ^n using $\{\tilde{\mathbf{u}}^0\}$, and then compute $\mathbf{J}^s_{\sigma^n}$ using the σ^n ;
- *Step-8*: Compute $\mathbf{J}^s_{in}$ from incoming seismic motion (DRS only);
- *Step-9*: Compute $\mathbf{J}^{fd}_{p^n}$ using $\{\tilde{\mathbf{p}}^0\}$;
- *Step-10*: Compute $\mathbf{J}^{fs}_{p^n}$ using $\{\tilde{\mathbf{p}}^0\}$ (DRS only);
- *Step-11*: Compute $\mathbf{J}^f_0$ using the initial nodal values of $\{\tilde{\mathbf{q}}^0\}$;
- *Step-12*: Solve fluid-column problem and compute p^f, q^f, then compute $\mathbf{J}^f_f$ using q^f ;
- *Step-13*: Compute $\mathbf{J}^f_{p^n}$ using $\{\tilde{\mathbf{p}}^0\}$;
- *Step-14*: Compute $\mathbf{J}^f_g$ using the rigid-ground motion $\mathbf{a}^g(t)$ (DR only);
- *Step-15*: Set $\{\tilde{\mathbf{v}}\} = 0$, $\{\tilde{\mathbf{q}}\} = 0$;
- **Block-Iteration Loop** ;
- **for** *k=0, maxIter* **do**
  - *Step-16*: Compute the space time nodal vector given by $[\mathbf{H}^s]\{\tilde{\mathbf{q}}\}$;
  - *Step-17*: Compute $\{\tilde{\mathbf{v}}\}$ by solving $[\mathbf{K}^s_{st}]\{\tilde{\mathbf{v}}\} = \{\mathbf{J}^s\} - [\mathbf{H}^s]\{\tilde{\mathbf{q}}\}$;
  - *Step-18*: Compute the space time nodal vector given by $\left[\mathbf{H}^f\right]\{\tilde{\mathbf{v}}\}$;
  - *Step-19*: Compute $\{\tilde{\mathbf{v}}\}$ by solving $\left[\mathbf{K}^f_{st}\right]\{\tilde{\mathbf{q}}\} = \left\{\mathbf{J}^f\right\} - \left[\mathbf{H}^f\right]\{\tilde{\mathbf{v}}\}$;
  - *Step-20*: Check the convergence;
  - **if** *Converged* **then**
    - Update $\{\tilde{\mathbf{u}}^0\}$, $\{\tilde{\mathbf{v}}^0\}$, $\{\tilde{\mathbf{p}}^0\}$, $\{\tilde{\mathbf{q}}^0\}$ and Go to next time step
  - **else**
    - Go to Step-16
  - **end**
- **end**

end

that is $\{\tilde{\mathbf{q}}\}^{(0)} = \mathbf{0}$. After computing the trial value of velocity field $\{\tilde{\mathbf{v}}\}^{(k)}$, the trial displacement of solid domain at time $t = t_{n+1}$ is computed by using the relation given in Eq. (5.43).

$$\left\{\tilde{\mathbf{u}}^2\right\}^{(k)} = \left\{\tilde{\mathbf{u}}^1\right\} + \frac{\Delta t_n}{2}\left(\left\{\tilde{\mathbf{v}}^1\right\}^{(k)} + \left\{\tilde{\mathbf{v}}^2\right\}^{(k)}\right) \tag{5.69}$$

where $\{\tilde{\mathbf{u}}^1\}$ denotes the space-nodal values of displacement field at time $t = t_n$, and $\{\tilde{\mathbf{u}}^1\}^{(k)}$ denotes the trial space-nodal values of displacement field at time $t = t_{n+1}$.

In second-stage, see Eq. (5.68), the velocity field $\{\tilde{\mathbf{v}}\}^{(k)}$ is used for computing the $\{\tilde{\mathbf{q}}\}^{(k)}$. Subsequently, the space-nodal values of hydrodynamic-pressure at time $t = t_{n+1}$ is computed by employing the Eq. (5.48).

$$\left\{\tilde{\mathbf{p}}^2\right\}^{(k)} = \left\{\tilde{\mathbf{p}}^1\right\} + \frac{\Delta t_n}{2}\left(\left\{\tilde{\mathbf{q}}^1\right\}^{(k)} + \left\{\tilde{\mathbf{q}}^2\right\}^{(k)}\right) \tag{5.70}$$

where $\{\tilde{\mathbf{p}}^1\}$ denotes the space-nodal values of hydrodynamic pressure in reservoir at time $t = t_n$, and $\{\tilde{\mathbf{p}}^2\}$ denotes the trial space-nodal values of pressure field at time $t = t_{n+1}$.

In each iteration step, after computing trial values of q and $\mathbf{v}$, convergence of sequences formed by the trial space-time nodal values $\{\tilde{\mathbf{q}}\}^{(k)}$ and $\{\tilde{\mathbf{v}}\}^{(k)}$ should be checked. In present study following convergence criterion has been adopted

$$\left\|\{\tilde{\mathbf{q}}\}^{(k)}\right\| - \left\|\{\tilde{\mathbf{q}}\}^{(k-1)}\right\| \leqslant \epsilon_q \left\|\{\tilde{\mathbf{q}}\}^{(0)}\right\| \tag{5.71}$$

$$\left\|\{\tilde{\mathbf{v}}\}^{(k)}\right\| - \left\|\{\tilde{\mathbf{v}}\}^{(k-1)}\right\| \leqslant \epsilon_v \left\|\{\tilde{\mathbf{v}}\}^{(0)}\right\| \tag{5.72}$$

in which ϵ_q and ϵ_v denote the tolerance for convergence in q and $\mathbf{v}$, respectively. $\|\cdot\|$ denotes Euclidean norm of space-time vectors. Note that Eq. (5.71) and Eq. (5.72) define the local convergence criterion for the sequence $\{\tilde{\mathbf{q}}\}^{(k)}$ and $\{\tilde{\mathbf{v}}\}^{(k)}$, respectively. The global convergence is defined when both Eq. (5.71) and Eq. (5.72) are true. In this way, for any given time-step, iterations are performed until global convergence is achieved.

Note that in Eq. (5.67) and Eq. (5.68) the space-time nodal vectors $\{\mathbf{J}^s\}$ and $\left\{\mathbf{J}^f\right\}$, and the space-time matrices $[\mathbf{K}^s_{st}]$, $\left[\mathbf{K}^f_{st}\right]$, $[\mathbf{H}^s]$ and $\left[\mathbf{H}^f\right]$ remain fixed during the iteration in a given time-step. Therefore, aforesaid space-time vectors and matrices only need to be computed once in the beginning of the iteration for a given time-step. Further, if a uniform time-step size $\Delta t_n = \Delta t, \forall n = 0, N-1$ is employed then the space-time matrices need to be computed only once for all the time-step. Furthermore, the space-time tangent matrix $[\mathbf{K}^s_{st}]$ in Eq. (5.67) and $\left[\mathbf{K}^f_{st}\right]$ in Eq. (5.68) yield unsymmetrical system of linear equations. These linear

equations are solved by using GpBiCG algorithm (Zhang, 1997). The algorithm is implemented in an element by element manner thus avoiding the assembly of global space-time tangent matrix. Lastly, the complete procedure to solve the problem of dynamic interaction of dam-reservoir system and dam-reservoir-soil system is given in Algorithm 2.

5.7 Numerical examples

In this section, three types of dam-reservoir interaction problems are solved to demonstrate the performance of the present approach. The first problem is related to the dynamic interaction between a reservoir and a vertical faced rigid dam. The second problem is related to the dynamic interaction between a reservoir and a vertical faced deformable dam. In aforementioned problems, the foundation underneath the dam-reservoir system is taken to be rigid. For the verification of the proposed scheme results obtained by using v-ST/FEM are compared with the available results in the literature. Lastly, linear seismic analysis of the concrete gravity dam including the hydrodynamic effects of the reservoir is performed by using the v-ST/FEM.

5.7.1 Vertical faced rigid dam

Fig. 5.7 depicts a vertical faced rigid dam and a reservoir of constant height extending up to infinity in upstream direction. The height of the dam and reservoir, H, is 180 m, and the width of the dam, W, is 15 m. The reservoir domain is truncated by placing an absorbing boundary at a distance L from the dam in the upstream direction. The dam is subjected to a ramp acceleration in negative x_1 direction as shown in Fig. 5.8, where $a_0 = 1\ m/s^2$ is the maximum ramp acceleration. The speed of acoustic wave in water is $c = 1439$ m/s, and water is assumed to be inviscid and compressible with a mass density of 1000 kg/m^3. The wave reflection coefficient α_b for reservoir bottom is taken as 1 (i.e. reservoir bottom acts as a perfect reflector for the pressure waves). In order to model a rigid-dam the elastic modulus of dam is set to a very high value $E = 2.2 \times 10^{17}$, the Poisson's ratio and mass density for dam is taken as $\nu = 0$ and $\rho^s = 2600\ kg/m^3$, respectively.

The finite element model of the present problem uses four-node quadrilateral elements (Quad4) to discretize both fluid and solid domain. All simulations are performed with a uniform time step size $\Delta t = 0.01$ sec for total time duration of 5 seconds. In block iterative algorithm, tolerance for q and $\mathbf{v}$ is set to 0.01%. The resultant unsymmetrical system of linear equation is solved using the GpBiCG algorithm with tolerance value 1.0×10^{-6}. Further, in order to evaluated the effectiveness

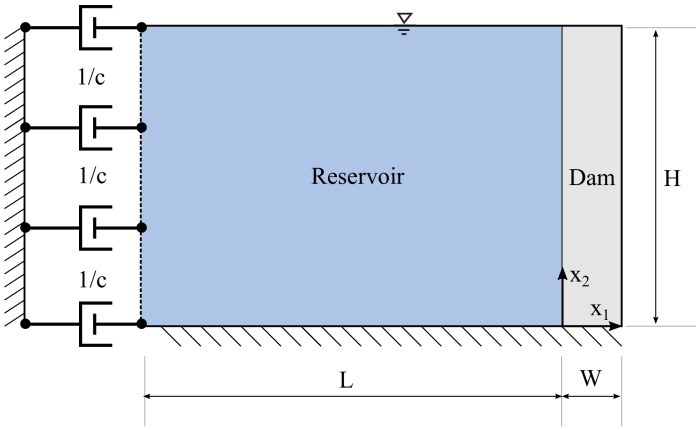

Fig. 5.7.: Geometry of computation domain for vertical faced dam and rectangular reservoir

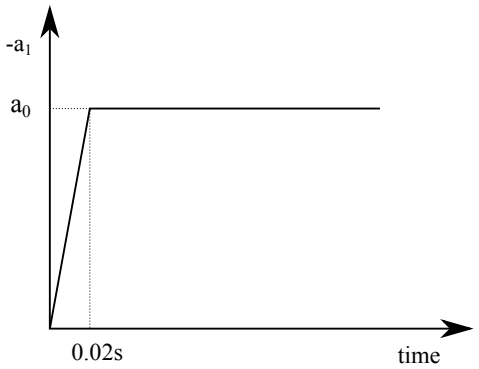

Fig. 5.8.: Ramp acceleration

of the viscous (or Sommerfeld) boundary condition (cf. Eq. 5.6) at the upstream truncated boundary of reservoir, numerical simulations are performed for four cases corresponding to the different length of reservoir; $L = 3H$, $L = 4H$, $L = 5H$, and $L = 7H$ (where $H = 180$m is the height of water in reservoir). Fig. 5.9 shows the finite element mesh of dam and reservoir used in the numerical simulations. Note that the finite element mesh for vertical faced dam remains identical in all cases corresponding to different L/H values.

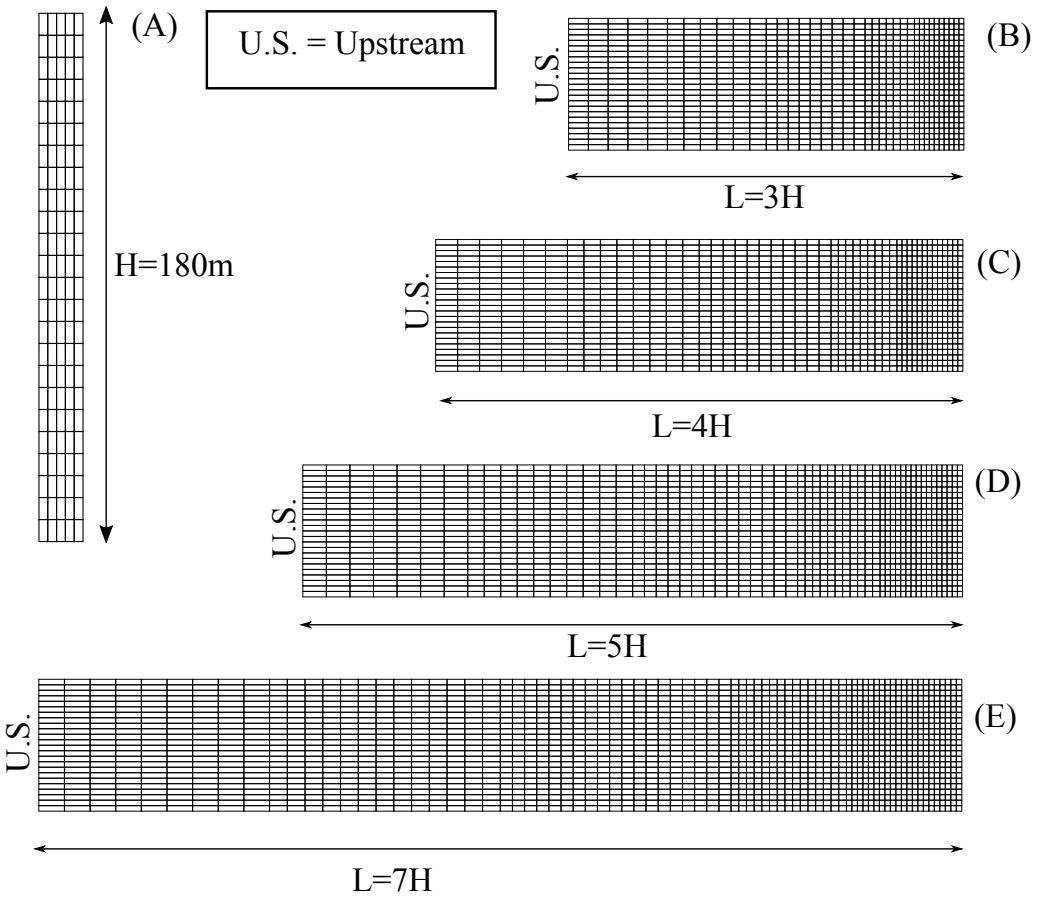

Fig. 5.9.: Finite element meshes for vertical faced dam and reservoir system: (A) mesh for vertical faced dam of height $H = 180$ m, (B) mesh for reservoir of length $L = 3H$, (C) mesh for reservoir of length $L = 4H$, (D) mesh for reservoir of length $L = 5H$, and (E) mesh for reservoir of length $L = 7H$

The analytical solution for hydrodynamic pressures on a rigid dam with a vertical upstream face due to rectangular reservoir under general horizontal ground acceleration is given by Tsai et al., 1990,

$$p\left(x_1, x_2, t\right) = \frac{-2\rho^w c}{H}\left\{\sum_{k=1}^{\infty}\frac{\left(-1\right)^k \cos\left(\lambda_k x_2\right)}{\lambda_k}\int_0^t a_1\left(\tau\right) J_0\left[\lambda_k c\left(t-\tau\right)\right] d\tau\right\} \tag{5.73}$$

where $\lambda_k = (2k-1)\pi/2H$ is the k^{th} wavelength, H is the height of the fluid and $J_0(\cdot)$ is the Bessel function of first kind. $a_1(t)$ is the horizontal ground acceleration (see Fig. 5.8), c is the speed of sound in water, ρ^w is the mass density of water. x_1

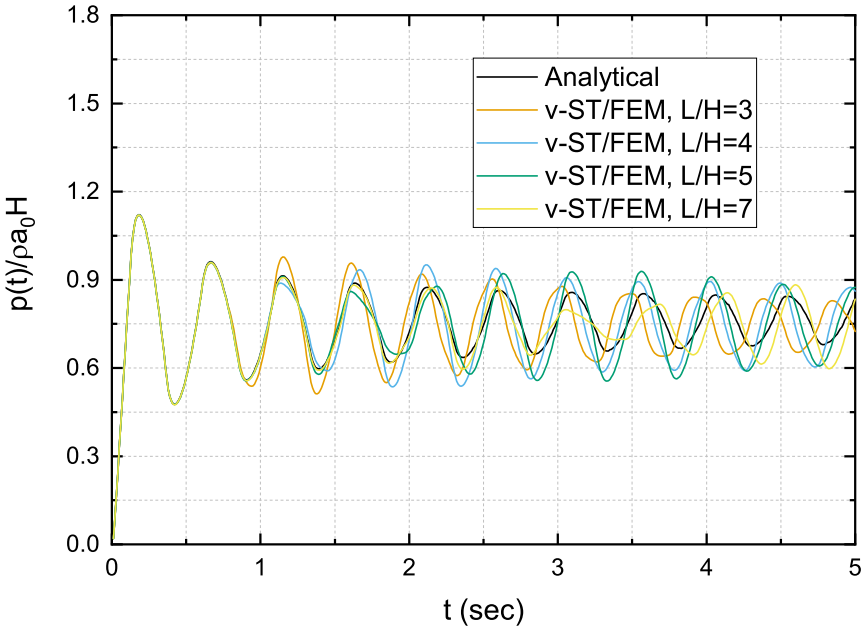

Fig. 5.10.: Hydrodynamic pressure obtained by v-ST/FEM approach at the base of rigid dam due to ramp acceleration for different values of reservoir length (L)

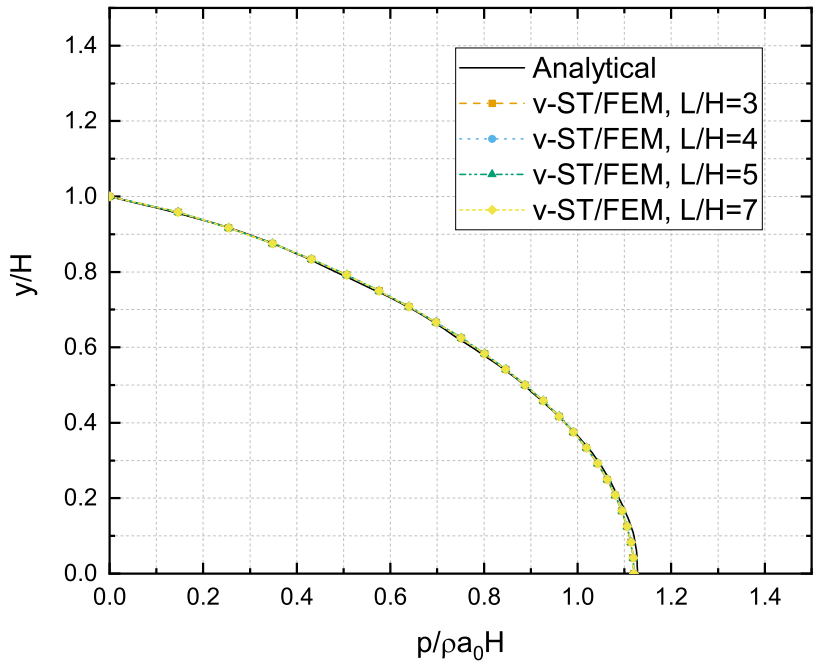

Fig. 5.11.: Distribution of the maximum value of hydrodynamic pressure computed by v-ST/FEM approach on the upstream vertical face of the rigid dam due to ramp acceleration

and x_2 are the spatial coordinates along horizontal and vertical direction; $x_1 = 0$ corresponds to the vertical face the dam, and $x_2 = 0$ correspond to the base of dam and reservoir.

The hydrodynamic pressure at the base of the rigid dam obtained by employing v-ST/FEM formulation, for different values of L/H, are compared with the analytical results. Fig. 5.10 shows the time history of the *normalized hydrodynamic pressures* [2] at the base of the dam for different values of the reservoir lengths. It can be observed that as the length of the reservoir increases the difference between computed and analytical solution decreases. In 5.10, it is remarkable that the peak value of hydrodynamic pressure is attained during the first cycle of pressure wave, and in all cases the first cycle of hydrodynamic pressure wave is predicted correctly. In addition, for smaller values of L/H the increase in the amplitude of the pressure fluctuations and shortening of time period occurs much earlier than that for large values of L/H.

Fig. 5.11 compares the distribution of the maximum hydrodynamic pressure on the upstream face of the rigid-dam for all L/H values with the analytical solution. Interestingly, in all cases the distribution of maximum hydrodynamic pressure on the vertical face of rigid-dam is in good agreement with the the analytical result. This is because the maximum pressure at any point on the face of the dam occurs during the first half cycle of pressure wave, and from Fig. 5.10 it can be seen that, for all values of L/H ratio, the computed peak hydrodynamic pressure is nearly same as the analytical result.

Fig. 5.12 and 5.13 compare the hydrodynamic pressures computed by v-ST/FEM approach at the base of the rigid dam for $L/H = 3$ and $L/H = 7$ with both the analytical solution given by Eq. (5.73) and the finite element solution obtained by Pelecanos et al., 2013. It can be observed that results obtained from present approach are nearly identical to the finite element results of Pelecanos et al., 2013, which implies that the discrepancy between the analytical solutions and the computed results is mainly due to the viscous boundary condition given by Eq. (5.6).

Lastly, the hydrodynamic pressure fields in the reservoir of length, $L = 3H$, $L = 5H$, and $L = 7H$, computed by using v-ST/FEM approach at time $t = 0.19$s and $t = 1.6$s are given in Fig. 5.14 and Fig. 5.15, respectively. At time $t = 0.19$s, the spatial variation of pressure field in the reservoir of different lengths is almost identical. At time $t = 1.6$s, however, the hydrodynamic pressure in the reservoir of smaller length is more than the hydrodynamic pressure in reservoir of the larger length. This is because, the viscous boundary condition (cf. Eq. (5.6)), especially in case of

[2] Normalized hydrodynamic pressure is given by the ratio of hydrodynamic pressure $p(t)$ to the $\rho^w a_0 H$, where a_0 is the maximum value of ramp acceleration

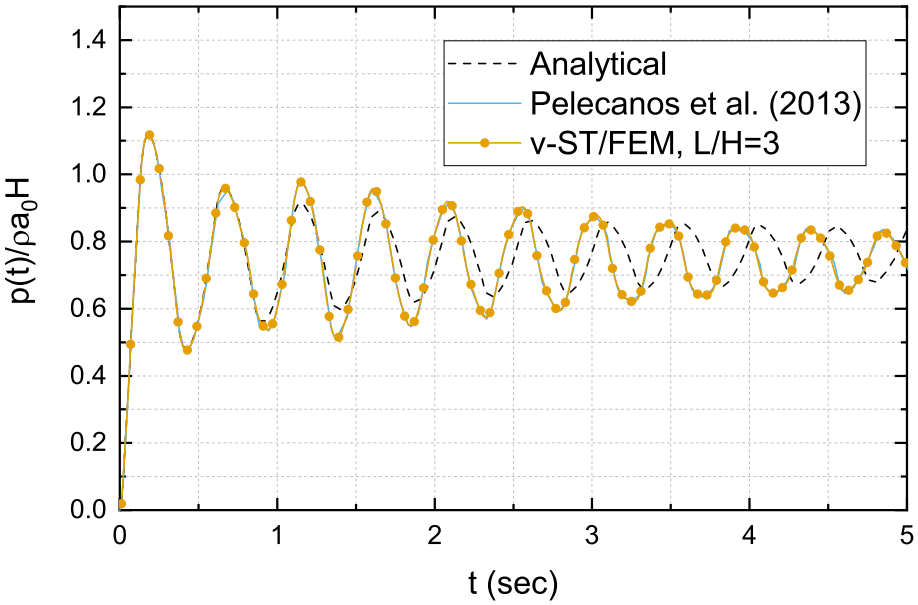

Fig. 5.12.: Comparison of hydrodynamic pressure at the base of rigid dam due to ramp acceleration for $L/H = 3$ with the analytical solution of Tsai et al., 1990 and the finite element solution of Pelecanos et al., 2013.

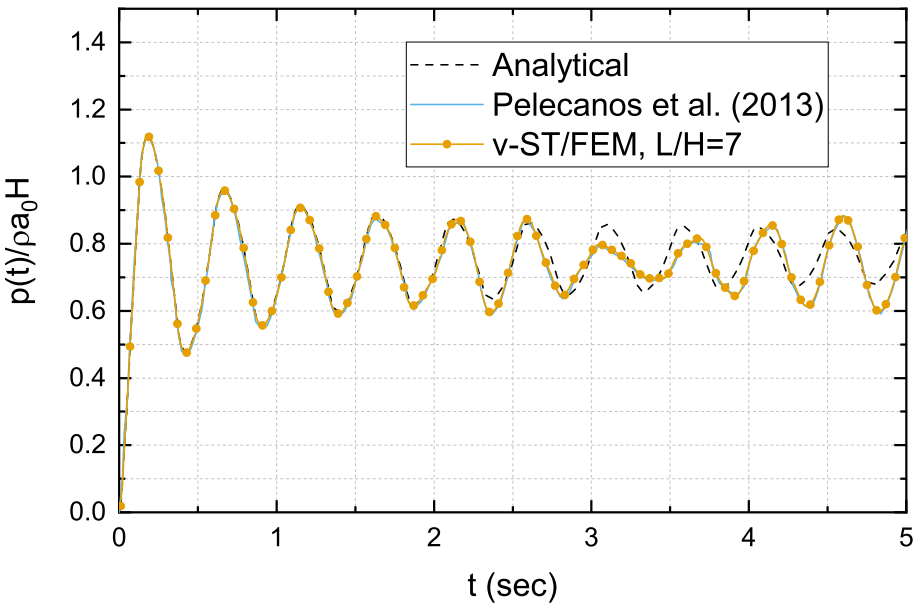

Fig. 5.13.: Comparison of hydrodynamic pressure at the base of rigid dam due to ramp acceleration for $L/H = 7$ with the analytical solution of Tsai et al., 1990 and the finite element solution of Pelecanos et al., 2013.

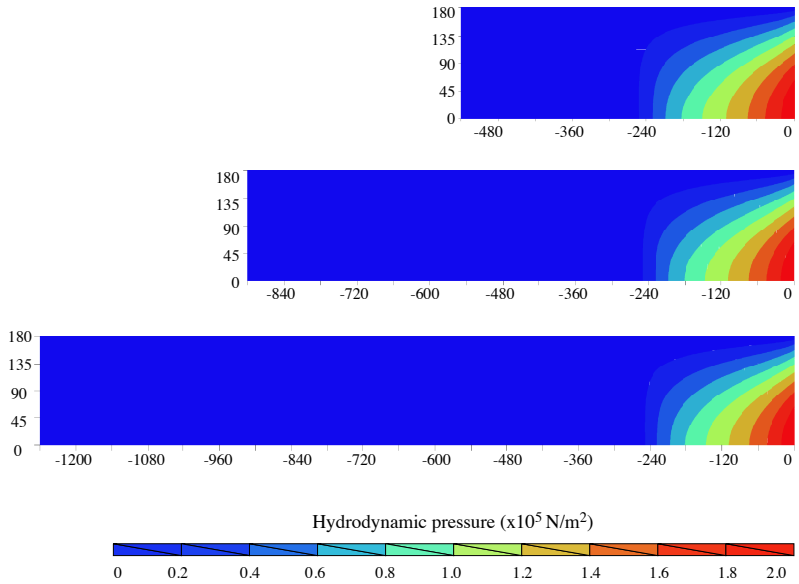

Fig. 5.14.: Hydrodynamic pressure field in the reservoir of length, $L = 3H$ (top), $L = 5H$ (middle), $L = 7H$ (bottom), computed by using v-ST/FEM at time $t = 0.19$ seconds due to ramp acceleration

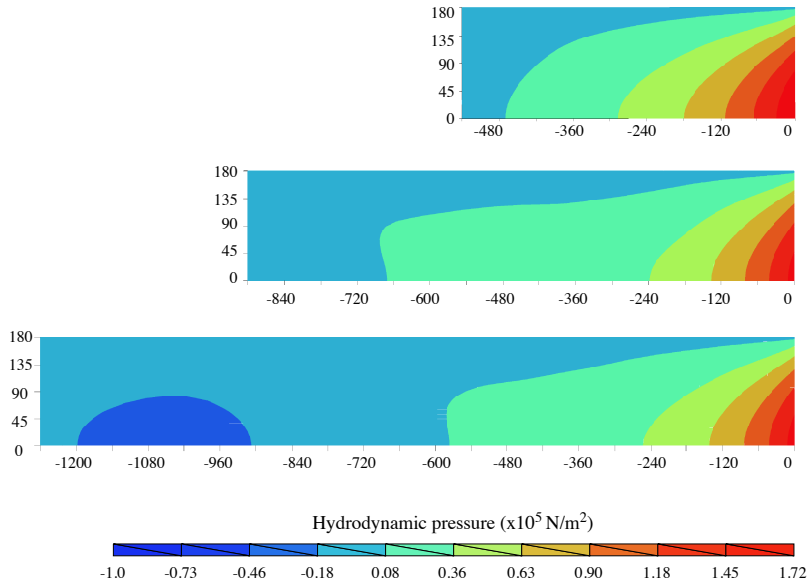

Fig. 5.15.: Hydrodynamic pressure field in the reservoir of length, $L = 3H$ (top), $L = 5H$ (middle), $L = 7H$ (bottom), computed by using v-ST/FEM at time $t = 1.60$ seconds due to ramp acceleration

small-length reservoir, is inadequate for perfectly absorbing the impinging pressure waves. Consequently, some fraction of incident energy will be reflected back into the truncated reservoir domain, which in turn will amplify the hydrodynamic pressure waves in the truncated reservoir domain.

5.7.2 Vertical faced flexible dam

A vertical faced flexible dam and a reservoir (see Fig. 5.7) of constant height extending to infinity in upstream direction is analyzed under horizontal component of earthquake motion . The height of the dam and reservoir, H, is 180 m, and the width of the dam is 15 m. The reservoir domain is truncated by placing an absorbing boundary at a distance $L = 900$ m from the dam in the upstream direction. The horizontal component of earthquake motion is selected as north-south component of El Centro (1940) ground motion and is depicted in Fig. 5.16, where g denotes the acceleration due to gravity. The speed of acoustic wave in water is $c = 1439$ m/s, and the water is assumed to be inviscid and compressible with a mass density of 1000 kg/m^3. The wave reflection coefficient α_b for reservoir bottom is taken as unity (i.e. reservoir bottom acts as a perfect reflector for the pressure waves). The foundation underlying the dam and reservoir is assumed to be rigid. The elastic modulus, Poisson's ratio, and mass density of dam is given by $E = 3.43 \times 10^{11}$ N/m^2, $\nu = 0.0$, and $\rho^s = 2400$ kg/m^3, respectively.

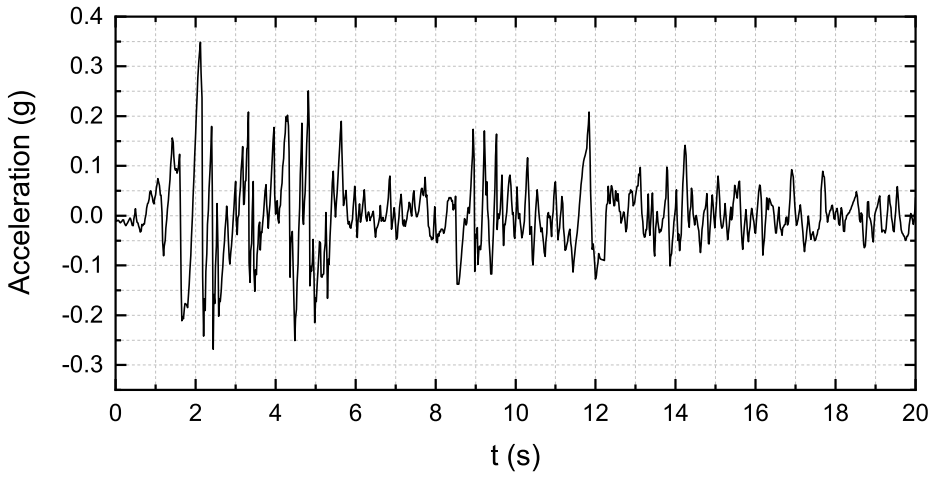

Fig. 5.16.: Time history of north-south component of El Centro (1940) ground motion

The spatial domain of dam and reservoir are discretized by using four-node quadrilateral elements (see Fig. 5.9a and Fig. 5.9d). A uniform time step size $\Delta t = 0.02$ s is used to discretized the time domain. The simulation is performed for total time duration of 5 seconds. In block iterative algorithm, tolerance for q and $\mathbf{v}$ are set to 0.01%. The resultant unsymmetrical system of linear equation is solved by using the GpBiCG algorithm with tolerance value of 1.0×10^{-6}.

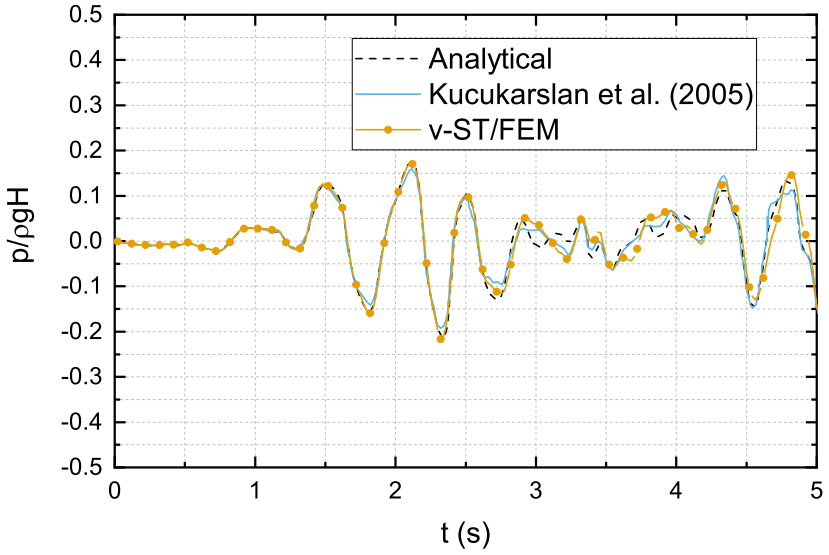

Fig. 5.17.: Comparison of hydrodynamic pressure at the base of vertical faced flexible dam subjected to 1940 El Centro ground motion (horizontal component only) with the analytical solution of Lee and Tsai, 1991 and the finite element solution of Küçükarslan et al., 2005.

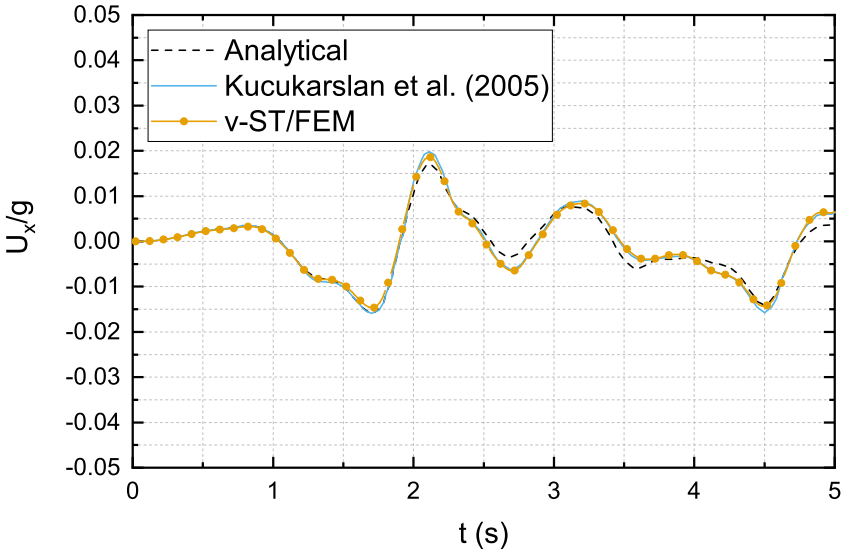

Fig. 5.18.: Comparison of relative horizontal-displacement at top of vertical faced flexible dam subjected to 1940 El Centro ground motion (horizontal component only) with the analytical solution of Lee and Tsai, 1991 and the finite element solution of Küçükarslan et al., 2005.

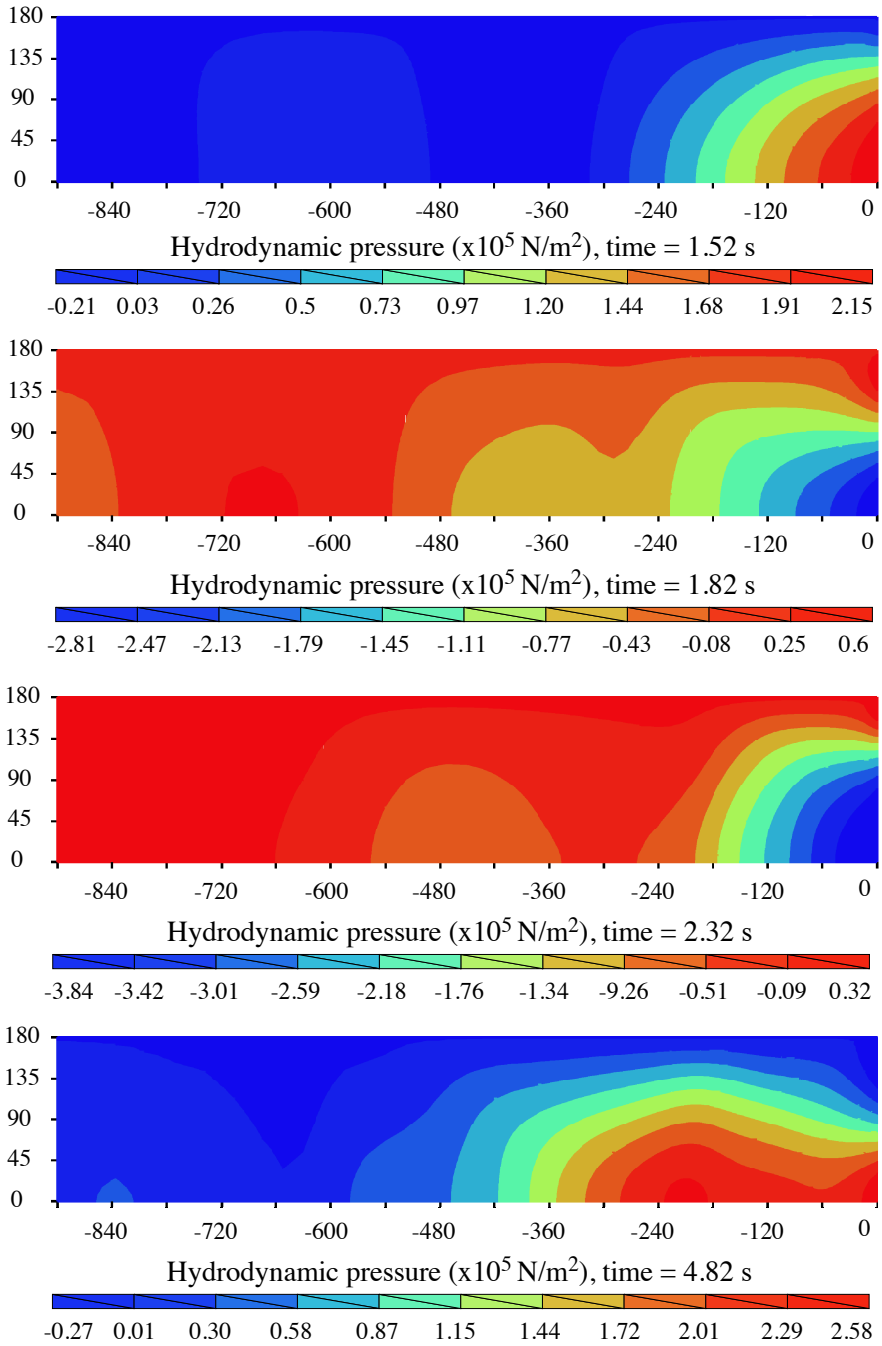

Fig. 5.19.: Hydrodynamic pressure field in the reservoir computed by using v-ST/FEM approach at different times (from top to bottom), $t = 1.52$ s, $t = 1.82$ s, $t = 2.32$ s, and $t = 4.82$ s, due to 1940 El Centro ground motion

The analytical solutions of the present problem are given by Lee and Tsai, 1991, and Küçükarslan et al., 2005 analyze the same problem by using a finite element procedure. Fig. 5.17 successfully compares the *normalized hydrodynamic pressure*[3] computed by using the v-ST/FEM at the base of the vertical faced flexible dam with both the analytical solutions of Lee and Tsai, 1991 and the finite element solutions of Küçükarslan et al., 2005.

Fig. 5.18 successfully compares the *normalized horizontal displacement*[4] at top of vertical dam with both the analytical solutions of Lee and Tsai, 1991 and the finite element solutions of Küçükarslan et al., 2005. The hydrodynamic pressure fields in the reservoir computed by using v-ST/FEM approach at different times $t = 1.52$ s, $t = 1.82$ s, $t = 2.32$ s, and $t = 1.52$ s are depicted in Fig. 5.19, where it can be observed that the absolute maximum value of hydrodynamic pressure always occurs at the base of vertical faced dam.

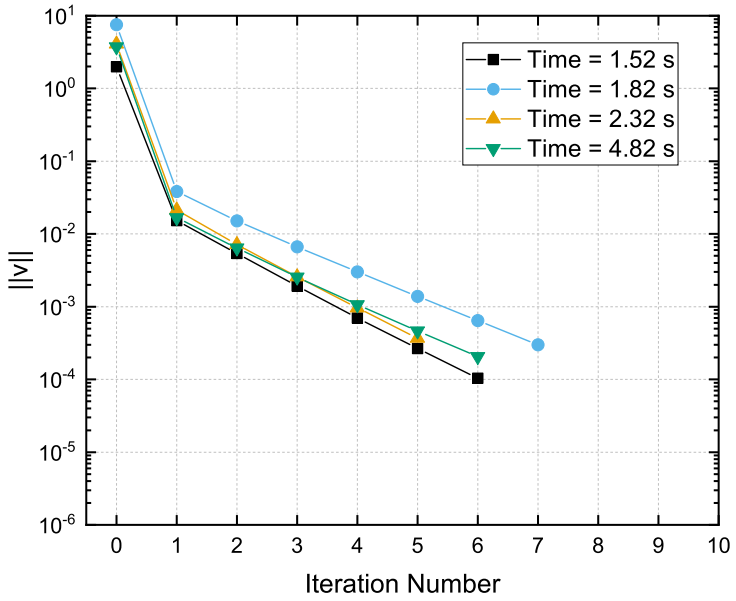

Fig. 5.20.: Convergence of v-ST/FEM method using the block-iterative scheme for vertical faced flexible dam problem: convergence history of velocity field $\mathbf{v}$ at various time steps

Let us discuss now the Convergence of v-ST/FEM method using the block-iterative scheme. The convergence histories of velocity field $\mathbf{v}$ and the auxiliary variable q at various time steps are plotted in Fig 5.20 and Fig 5.21, respectively. The convergence histories of the solutions in Fig 5.20 and suggest that the global convergence of the proposed scheme is mainly controlled by the local convergence in the velocity field. Further, the total number of iterations required to attain the global convergence (i.e. convergence in both $\mathbf{v}$ and q) in a given time-step approximately varies between 5

[3]Normalized hydrodynamic pressure is defined as the ratio of hydrodynamic pressure $p(t)$ to the hydrostatic pressure at the of the vertical faced dam $p_0 = \rho^w g H$

[4]Normalized horizontal displacement denotes the ratio of relative horizontal displacement u_x to the acceleration due to gravity g.

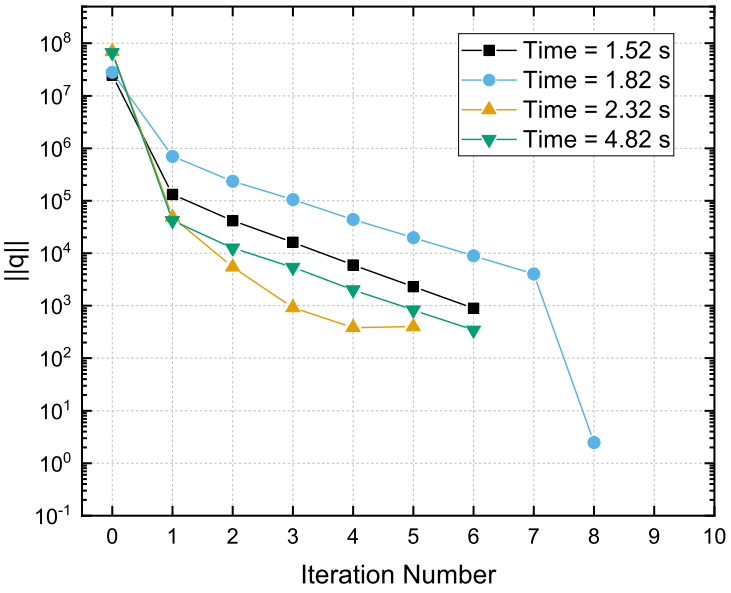

Fig. 5.21.: Convergence of v-ST/FEM method using the block-iterative scheme for vertical faced flexible dam problem: convergence history of auxiliary field variable q at various time steps

to 10 iterations. The convergence tolerance in velocity field and q has been set to 0.01% to obtain the results presented in this section, although it is worthwhile to mention that almost the same accuracy is obtained with a tolerance of 0.1%, which reduces the number of iteration almost by 50%, making this approach much more cost-effective.

5.7.3 Concrete gravity dam

In this section the dynamic response of a concrete gravity dam subjected to the horizontal component of earthquake motion is computed by using the v-ST/FEM approach. Numerical simulations are performed for following two situations,

(i) *Dam-reservoir system* (DR): In this case, the unbounded soil domain underneath the dam-reservoir system is assumed to be rigid, therefore neglecting the interaction between dam-reservoir system and the underlying foundation. The dam-reservoir interaction is modeled by the discretizing the dam and reservoir domain using finite elements.

(ii) *Dam-reservoir-soil system* (DRS): In this case, all interactions of dam-reservoir-soil system are considered. The fluid domain and unbounded soil domain are truncated by using the viscous boundaries.

The physical dimensions of the dam and reservoir are given in Fig. 5.22. The height of the vertical upstream face of the dam is 50 m, and the width of the base is 40 m. The spatial domain of dam is discretized by using 658 number of three-node triangular (Tria3) finite elements (see Fig. 5.23). Further, it is assumed that the depth of water in the reservoir, H^f, remains constant at value 44 m. The computation domain for the semi-infinite reservoir is obtained by placing a viscous boundary at a distance of 200 m from the dam in the upstream direction. Finite element mesh of the reservoir consists of 1144 number of four-node rectangular (Quad4) finite elements (see Fig. 5.23). Similarly, the unbounded soil domain is truncated by using the horizontal and vertical viscous boundaries; the length of the soil domain in x_1 and x_2 direction is 440 m and 150 m, respectively. Finite element mesh of the soil domain which contains 6448 number of four-node rectangular finite elements is depicted in Fig. 5.23. In finite element modeling of unbounded soil domain, the free field responses of the soil domain are obtained by using the soil-columns (with constrained vertical motion) placed next to the vertical artificial boundaries, and the effective seismic input is described in terms of traction boundary condition at the bottom truncated boundary.

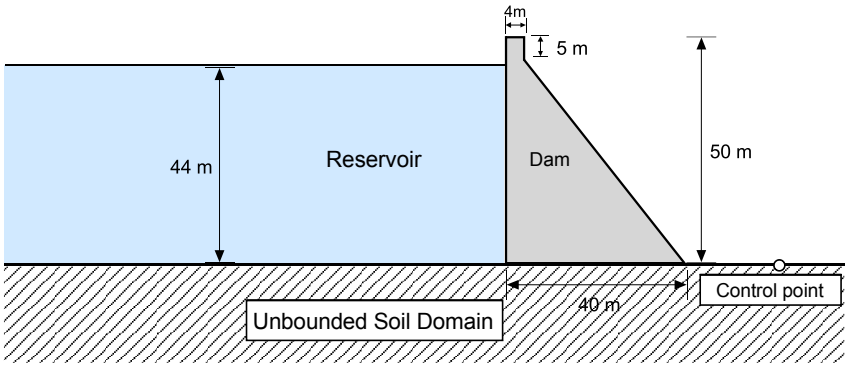

Fig. 5.22.: Physical dimensions of the concrete gravity dam and reservoir

It is assumed that the material behavior of dam as well as the soil is given by an isotropic, homogenous, linear elastic stress-strain relationship. For the concrete-dam, the elastic modulus $E = 28.0$ GPa, mass-density $\rho = 2347.0$ kg/m ^{3}, and the Poisson's ratio $\nu = 0.20$. For the soil, $E = 40.0$ GPa, $\rho = 2551.0$ kg/m ^{3}, and $\nu = 0.20$. Further, material damping is modeled by Rayleigh damping with $\xi = 5\%$ viscous damping specified for the soil and dam separately. The resultant values of damping coefficients (α, β) for the dam and soil are given by $(4.1314, 4.8 \times 10^{-4})$ and $(1.612, 1.47 \times 10^{-3})$, respectively. The speed of acoustic wave in water is $c = 1439$ m/s, and the water is assumed to be inviscid and compressible with a mass density of 1000 kg/m^3. The wave reflection coefficient α_b for reservoir bottom is taken as unity (i.e., reservoir bottom acts as a perfect reflector for the pressure waves).

The simulations are carried out for the horizontal component of the earthquake motion recorded at some control point on the free surface (see Fig. 5.22). Total

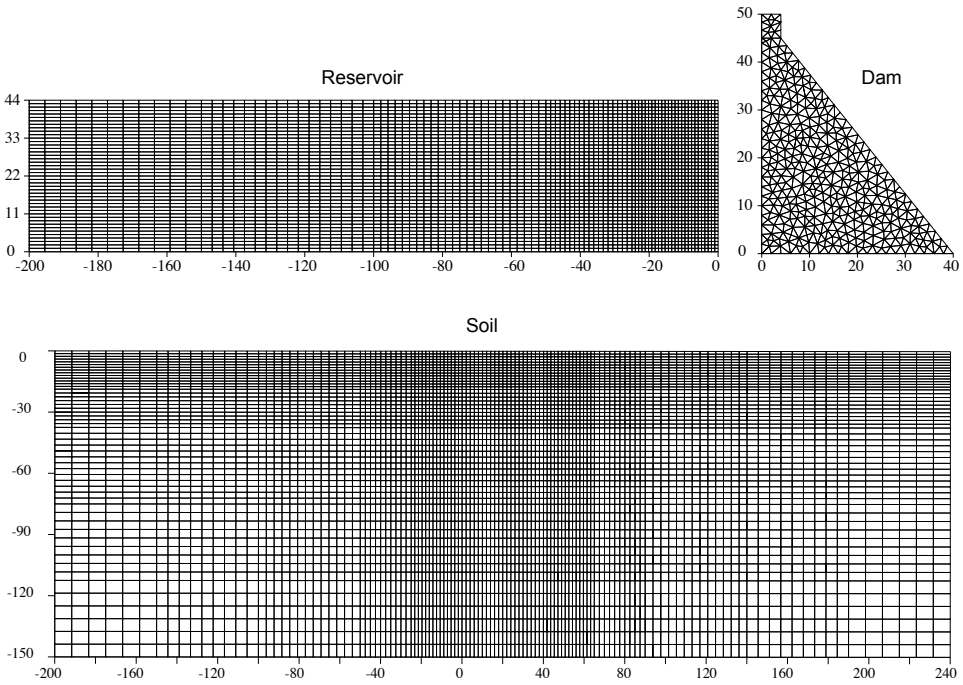

Fig. 5.23.: Finite element mesh of reservoir-domain (top-left), dam-domain (top-right), and soil-domain (bottom)

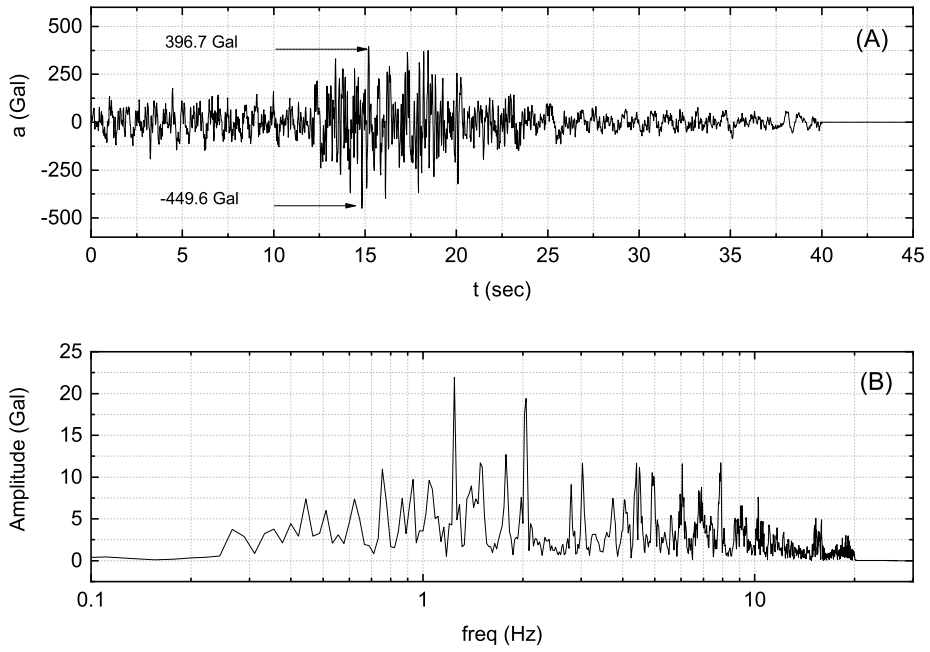

Fig. 5.24.: Horizontal component of ground motion recorded at the free-surface: (A) time history, and (B) Fourier spectrum

time duration of ground motion is 45 seconds in which acceleration is set to zero after 40 seconds. Fig. 5.24a depicts the time history of the earthquake motion; the maximum and minimum values of acceleration are 396.7 cm/s^2 and -449.6 cm/s^2, respectively. The Fourier spectrum of acceleration is plotted in Fig. 5.24b; the dominating dominating amplitudes 21.9 cm/s^2 and 19.4 cm/s^2 occur at frequencies 1.24 Hz and 2.0 Hz, respectively. It is worthwhile to mention that in the case of dam-reservoir system (DR), the earthquake motion plotted in Fig. 5.22 is directly used as a boundary condition at the base of concrete-dam. On the other hand, for numerical simulation of DS and DRS the input seismic acceleration is taken as half that of acceleration at the free surface.

All numerical simulations are performed with a uniform time step size $\Delta t = 0.01$ s for total time duration of 40 seconds. The initial value of displacement and stress field is obtained by solving corresponding static problem. The convergence tolerance for q and $\mathbf{v}$ in block iterative algorithm are set to 0.01%. The resultant unsymmetrical system of linear equation is solved by using the GpBiCG algorithm with tolerance value of 1.0×10^{-6}.

Let us now focus on the effect of interaction between dam-reservoir system (with impounded water) and the underlying soil-domain on the response of dam to horizontal component of the earthquake motion. For this purpose the results obtained in the case of DR (where the underlying soil is modeled as rigid foundation) and DRS (in which underlying soil is modeled as flexible foundation) are compared.

The acceleration response at the crest of the concrete-dam (Node-2) obtained in the case of DR and DRS is plotted in Fig. 5.25. The acceleration response obtained in case of DRS is significantly lower than the one obtained in case of DR. In case of DRS the absolute maximum value of horizontal and vertical component of acceleration is 1489.89 Gal and 597.47 Gal, respectively, whereas for DR these values correspond to 3897.10 Gal and 1274.65 Gal, respectively. Fourier spectrum of the acceleration response at the crest of the dam reveals that for DRS there is significant decay in the amplitudes, and the entire spectrum shifts towards the lower frequencies indicating the elongation of time period in acceleration time history (see Fig. 5.25c and Fig. 5.25d).

The effect of neglecting the interaction between dam-reservoir system and the underlying soil on the hydrodynamic pressure at the base of the concrete-dam is illustrated in Fig. 5.26. It can be observed that the assumption of rigid foundation leads to an amplification of hydrodynamic pressure at upstream face of the concrete dam. The reservoir-soil interaction also alter the hydrodynamic pressure distribution in the reservoir domain as shown in Fig. 5.27.

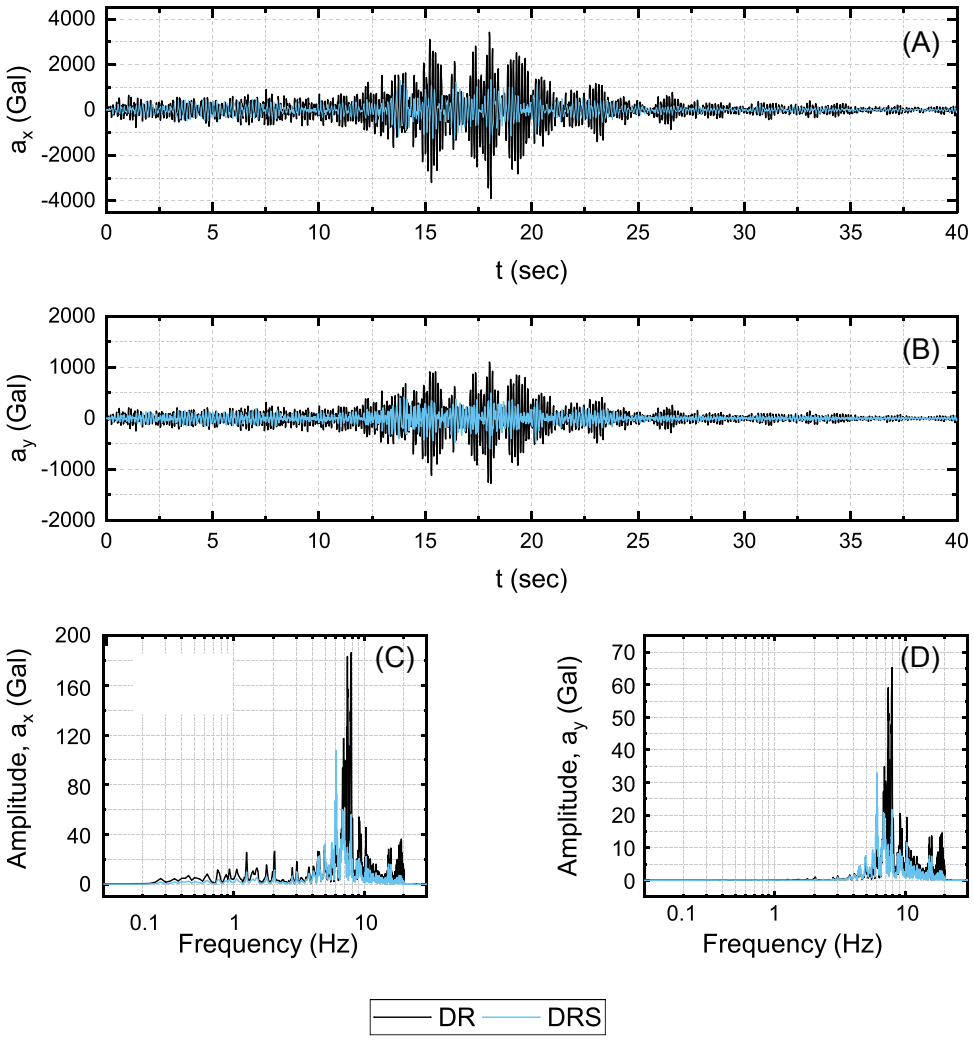

Fig. 5.25.: Acceleration response at the crest of the concrete-dam (Node-2) to horizontal component of earthquake motion for the case of dam-reservoir (DR) and dam-reservoir-soil (DRS) system. In DR underlying foundation is rigid, and in DRS the foundation is flexible; (A) time history of horizontal component of acceleration, (B) time history of vertical component of acceleration, (C) Fourier spectrum of horizontal component of acceleration, (D) Fourier spectrum of vertical component of acceleration

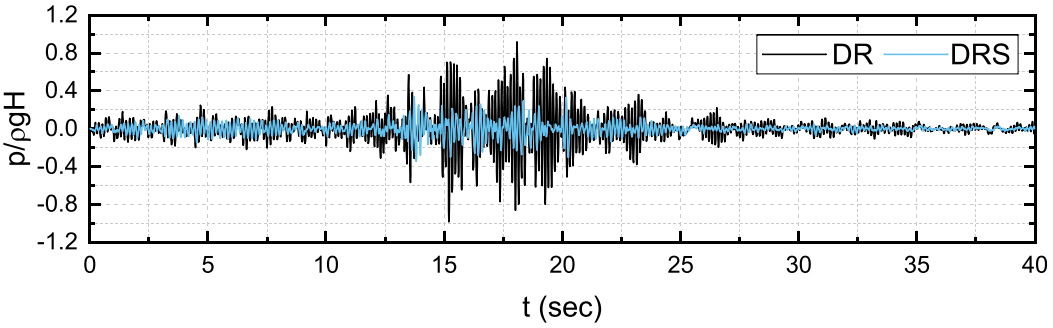

Fig. 5.26.: Time history of hydrodynamic pressure at the base of the dam subjected to horizontal component of earthquake motion for the case of dam-reservoir (DR) and dam-reservoir-soil (DRS) system. In DR underlying foundation is rigid, and in DRS the foundation is flexible

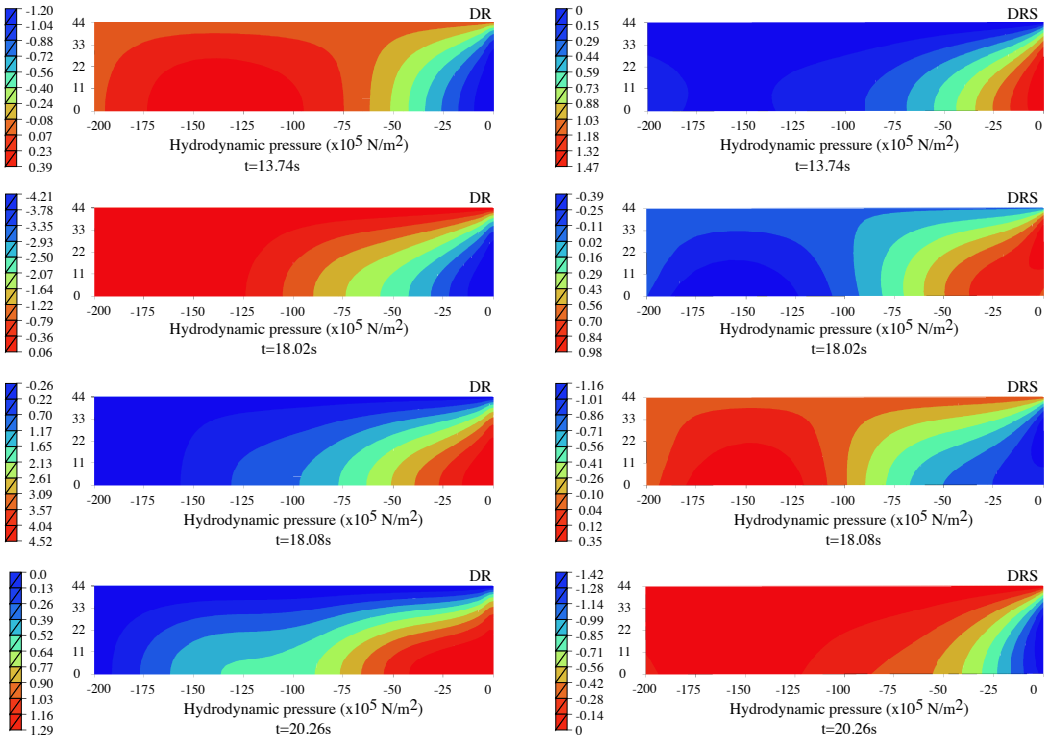

Fig. 5.27.: Hydrodynamic pressure distribution in the reservoir at different times due to horizontal component of earthquake motion for the case of dam-reservoir (DR) and dam-reservoir-soil (DRS) system. In DR underlying foundation is rigid, and in DRS the foundation is flexible

The temporal variation of the maximum and minimum principal stress, σ_1 and σ_2 respectively, at the base of the dam (which corresponds to the Gauss point of triangular Element-A), which is given in see Fig. 5.28, indicates that the incomprehension of the dynamic interaction between underlying soil and structure may cause large compressive and tensile stresses in the dam. In Fig. 5.28, the peak value of σ_1 and σ_2 for DRS is given by 2.24 MPa and -3.09 MPa, respectively, whereas for DR these values are given by 6.08 MPa and -5.97 MPa, respectively. In both cases, tensile stress at the base of the dam may exceed the ultimate tensile strength of the concrete, which may cause cracking in the concrete-dam. Further, the stress distribution inside the dam obtained in the case of DR and DRS differs significantly from each other as shown in Fig. 5.29. In both cases, however, large tensile stresses develop near the heel of the dam and at the downstream inclined face of the dam.

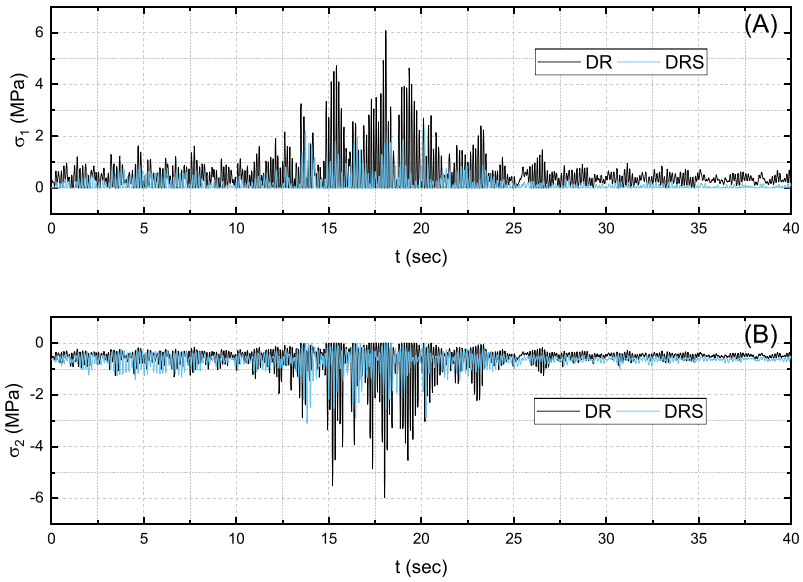

Fig. 5.28.: Time history of maximum (A) and minimum (B) principal stress at the base of the dam (Element-A) subjected to horizontal component of earthquake motion for the case of dam-reservoir (DR) and dam-reservoir-soil (DRS) system. In DR underlying foundation is rigid, and in DRS the foundation is flexible

Based on the results obtained in this section, it may be concluded that interactions between the dam-reservoir and the underlying soil significantly decay the response of concrete-dam reservoir system to the horizontal component of the ground motion. This is because for DR radiation of energy can occur only through the upstream artificial truncated boundary of the reservoir domain, and the pressure and displacement waves impinging the rigid-foundation are completely reflected back into the dam-reservoir domain, which is responsible for the amplification of the response. On the other hand, in case of DRS the flexible foundation provides additional mechanisms for the radiation of energy through the soil strata, which in turn reduces the overall response of the dam-reservoir system.

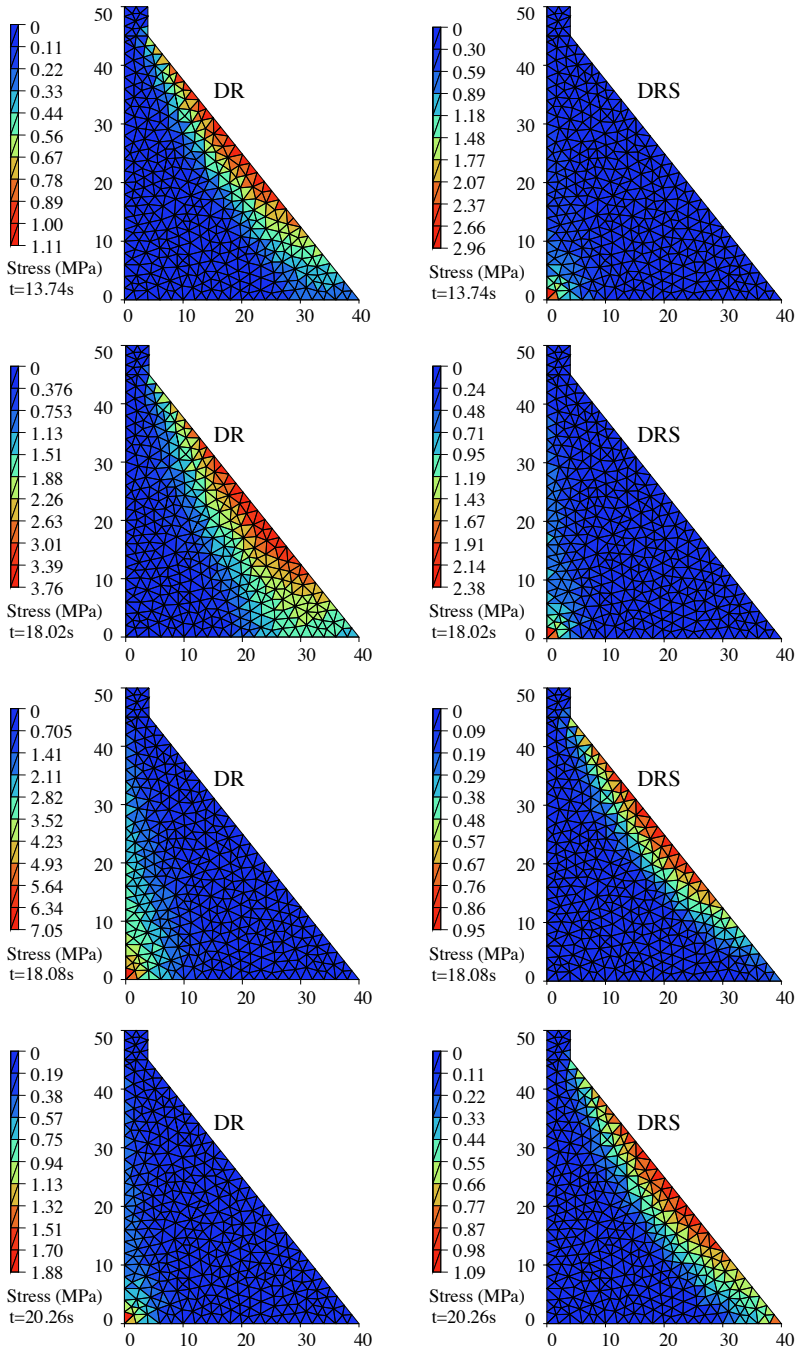

Fig. 5.29.: Spatial distribution of maximum principal stress σ_1 in the concrete dam subjected to horizontal component of earthquake motion for the case of dam-reservoir (DR) and dam-reservoir-soil (DRS) system. In DR underlying foundation is rigid, and in DRS the foundation is flexible

5.8 Summary

This chapter discusses the problem of dynamic interaction in a dam-reservoir-soil system subjected to the earthquake motion. Both dam and the underlying soil domain is assumed to be linearly elastic, and material damping can be modeled by Rayleigh damping. The water in the reservoir is assumed to be inviscid, linearly compressible with a small amplitudes for the displacements and velocity. Therefore, the hydrodynamic pressure in the reservoir is modeled by the pressure wave equation. Viscous boundary conditions are employed to truncate the semi-infinite domain of reservoir and underlying soil-domain. The space-time finite element formulation for coupled problem is described in terms of velocity field in the solid domain and the auxiliary variable q for the fluid domain, which denotes the first order time derivative of the hydrodynamic pressure field. Subsequently, a system of linearly coupled equations is obtained by the space-time finite element discretization of the weak form. The resultant system of linear equations is solved for the space-time nodal values of unknown fields q and $\mathbf{v}$ by using a two stage block-iterative scheme. Due to this scheme the size of the coupled-problem significantly decreases but at the cost of around 5 to 10 iterations per time steps. In each iteration step, first, a system of linear equations (which corresponds to the solid domain) is solved to compute the trial values of velocity field, and then the space-time nodal values of auxiliary variable q are computed by solving another system of linear equations (which corresponds to the fluid domain). The numerical performance of the proposed scheme is demonstrated by solving different types dam-reservoir interaction problems. The results obtained by the proposed scheme are successfully compared with results available in the literature.

Lastly, the response of a concrete gravity dam and reservoir with impounded water to the horizontal component of the earthquake motion is analyzed by using v-ST/FEM. Numerical simulations are performed for two cases; (i) DR, in which the interactions between the dam-reservoir and the underlying soil are ignored by assuming the ground to be perfectly rigid, (ii) DRS, in which the underlying soil domain is modeled as an isotropic, homogenous, linear elastic half space. Material damping in both dam and underlying soil domain is modeled by using Rayleigh damping. It is found that the dynamic interactions with the underlying deformable soil domain can significantly dampen the response of the dam-reservoir to the horizontal component of earthquake motion. The comparison of Fourier spectrum of acceleration response obtained for these two cases reveals an elongation of time period for DRS. In both cases, significant tensile stresses develop near the heel and at the downstream inclined face of the dam. The tensile and compressible stresses in the dam are much higher in case of DR than DRS. However, in both cases the tensile stress may exceed the ultimate tensile strength of the concrete which may cause cracking in the dam.

Therefore, a nonlinear analysis of concrete gravity dam and reservoir system should be performed to evaluate the safety and performance of a specific dam design.

6 v-ST/FEM for The Nonlinear Dam-Reservoir Interaction Problem

6.1 Introduction

In previous chapters linear dynamic problems are solved by using v-ST/FEM. In Chapter 5, linear dynamic analysis of gravity dam subjected to the earthquake ground motion show that the large tensile stresses may develop in dam which can exceed the tensile strength of the mass concrete. In such cases, a linear analysis is no longer valid since tensile cracks will form and propagates in the concrete, affecting the vibration properties an dynamic response of the dam. Consequently, cracking based on seismic actions in dams is an important factor in the safety evaluation of gravity dams and it may cause catastrophic consequences such as loss of life and property if the dam fails.

Extensive research has been performed over the last 25 years into the fracture behavior of concrete. A tensile-strength-based crack propagation analysis is generally considered unreliable due to the mesh-dependent response prediction (Bažant, 1987). Non-linear behavior in the fracture process zone (FPZ), which is significantly large for the concrete normally used in dams, is neglected in the conventional linear elastic fracture mechanics (LEFM) models. Under very slowly applied loads and also under impulsive loads, concrete fracture behavior seems to be adequately predicted by the LEFM models (Bhattacharjee and Leger, 1993). In the intermediate range, from short-term static loading to seismic-induced strain rates, non-linear fracture mechanics (NLFM) models considering the strain softening behavior in the FPZ appear to be more appropriate.

Continuum mechanics approaches to represent the tensile crack propagation are computationally very attractive for applications in complex structural analysis when the crack profiles are not known a priori. General drawbacks of the conventional smeared crack analysis model, such as the mesh-sensitive response prediction and the stress-locking in finite elements, can largely be overcome using the energy conserving co-axial rotating crack model (CRCM), which is an improved NLFM model (Bhattacharjee and Leger, 1993).

Bhattacharjee and Leger, 1993 investigated the dynamic fracture response of Koyna dam by using the CRCM concrete model. In the analysis of this dam, the foundation was assumed to be rigid, and the dynamic interaction of dam-reservoir system was modeled by the Westergaard added mass technique. The response results of the dam indicated that cracks formed at the base and at the upper portion near the change in downstream slope for the Koyna earthquake records. Lee and Fenves, 1998 also obtained similar solutions for Koyna dam under the same boundary and loading conditions by using a plastic-damage concrete model which includes tension and compression strain softening effects. They studied in detail tension damage in the dam and noted that damage in compression is less important in comparison with damage in tension for dams. In another paper, Cervera et al., 1995 developed an isotropic damage model for the seismic evaluation of concrete gravity and arch dams. This model accounts for the different behavior of concrete in tension and compression by splitting the stress tensor into tensile and compressive components, each with its own damage surface and evolution law. The seismic analyses of their selected gravity dam which resembles very closely Koyna dam, including dam-reservoir-foundation interactions, subjected to artificially generated earthquakes of different intensities indicated tension damage in the dam, but no compression damage occurred. The formed tension damage was seen at the upper portion of the dam. In the lights of these investigations, the tension cracks have only important influence on the seismic response of concrete gravity dams. Therefore, tension cracking is only considered in the present study.

In this chapter, v-ST/FEM is employed for the problems involving dynamic response of solids and structures with nonlinear stress-strain relationships. The structure of the present chapter is described as follows. Section 6.2 defines the problem of dynamic interaction between the concrete gravity dam and reservoir, in which a generalized nonlinear stress-strain relationship is used to describe the material behavior of concrete in the dam. The space-time weak form the model problem is described in Section 6.3, and its space-time finite element discretization is explained in Section 6.4. It is shown that the nonlinearity is caused by only the presence of stress term in the v-ST/FEM weak form. Subsequently, two v-ST/FEM schemes are proposed for the time integration of the space-time nodal vectors and matrices comprising the stress term. Section 6.5 then presents a block-iterative scheme to enforce the coupling between the solid and fluid domain. In Section 6.6, a co-axially rotating crack model (CRCM) with exponential strain softening rule is used to model the fracture of the concrete. Afterwards, to evaluate the numerical performance of the v-ST/FEM schemes dynamic fracture analyses of the concrete dam are performed in Section 6.7 and Section 6.8. The former section ignores the hydrodynamic coupling between the dam and reservoir while the latter section includes the coupling between dam and reservoir.

6.2 Statement of problem

Fig. 5.2 depicts the dam-reservoir system situated on a relatively rigid ground which is subjected to the spatially uniform transient ground motion. The horizontal and vertical component of ground motion are denoted by $a_1^g(t)$ and $a_2^g(t)$, respectively. Henceforth, the superscript $(\cdot)^s$ and $(\cdot)^f$ will be used for denoting the quantities related to the solid (dam) and fluid domain, respectively. Let Ω^f be the computation domain of reservoir which is enclosed by a free surface Γ_f^f, an upstream artificial boundary Γ_∞^f, a fluid-soil interface Γ_{fs}^f, and a fluid-dam interface Γ_{fd}^f. Accordingly, the boundary of the fluid domain can be described by

$$\Gamma^f = \Gamma_f^f \cup \Gamma_\infty^f \cup \Gamma_{fs}^f \cup \Gamma_{fd}^f \tag{6.1}$$

Let Ω^s be the computation domain of dam, Γ_{fd}^s be the fluid-dam interface of dam, and Γ_{ds}^s be the base of the dam. The outward unit normal vectors to the fluid and solid boundary are denoted by $\mathbf{n}^s$ and $\mathbf{n}^f$, respectively, and

$$\mathbf{n}^s + \mathbf{n}^f = \mathbf{0} \tag{6.2}$$

Since the ground underneath the dam, which is in spatially uniform motion, is assumed to be perfectly-rigid it is advantageous to describe the motion of the dam relative to the ground. Let $\mathbf{u}$ and $\mathbf{v}$ be the relative displacements and relative velocities of the dam, respectively, and ρ^s be the mass-density of the dam. The governing equation of motion for the dam becomes,

$$\rho^s \frac{\partial v_i}{\partial t} - \frac{\partial \sigma_{ij}}{\partial x_j} = \rho^s \left(b_i - a_i^g\right) \quad \forall (\mathbf{x}, t) \in \Omega^s \times (0, T) \tag{6.3}$$

where b_i is the external body force density, and $-\rho^s \mathbf{a}^g(t)$ is the pseudo force acting on the dam due to the accelerating frame of reference. The above equation can be derived from the Eq. (5.10) while noting that the spatial gradient of ground motion is zero.

The initial conditions for the dam are given by,

$$\begin{aligned} u_i(\mathbf{x}, 0) &= u_i^0(\mathbf{x}) \quad \forall \mathbf{x} \in \Omega^s \\ v_i(\mathbf{x}, 0) &= v_i^0(\mathbf{x}) \quad \forall \mathbf{x} \in \Omega^s \end{aligned} \tag{6.4}$$

and the boundary condition,

$$u_i(\mathbf{x}, t) = 0 \quad \forall (\mathbf{x}, t) \in \Gamma_s^{ds} \times (0, T) \tag{6.5}$$

characterizes the rigid-base boundary condition for the dam at Γ_{ds}^s.

The traction boundary condition for the dam can be divided into two components; (i) traction boundary condition due to the external surface loads acting on Γ_h^s (see Eq. 6.6), (ii) traction boundary condition due to total pressure (hydrostatic and hydrodynamic pressure) of impounded water acting on Γ_{fd}^s (see Eq. 6.7).

$$\sigma \cdot \mathbf{n}^s = \mathbf{h} \quad \forall (\mathbf{x}, t) \in \Gamma_h^s \times (0, T) \tag{6.6}$$

$$\sigma \cdot \mathbf{n}^s = -p_0 (\mathbf{x}) \mathbf{n}^s - p (\mathbf{x}, t) \mathbf{n}^s \quad \forall (\mathbf{x}, t) \in \Gamma_{fd}^s \times (0, T) \tag{6.7}$$

If it is assumed that the strains in the dam body are small enough so that the problem remains geometrically linear then the nonlinear stress-strain relationship for the dam can be described by rate-form,

$$\frac{\partial \sigma}{\partial t} = \mathbf{C} : \mathbf{d} \qquad \text{or} \qquad \frac{\partial \sigma_{ij}}{\partial t} = \mathbf{C}_{ijkl} : \mathbf{d}_{kl} \tag{6.8}$$

where $\mathbf{C}$ denotes a fourth order tangent modulus tensor which may depends upon the small-strain tensor ϵ, stretching tensor $\mathbf{d}$, and/or some internal variables (Hashiguchi, 2014). Expression for small-strain tensor and stretching tensor is given below,

$$\epsilon_{ij} = \frac{1}{2} \left(\frac{\partial u_i}{\partial x_j} + \frac{\partial u_j}{\partial x_i} \right) \tag{6.9}$$

$$d_{ij} = \frac{1}{2} \left(\frac{\partial v_i}{\partial x_j} + \frac{\partial v_j}{\partial x_i} \right) \tag{6.10}$$

Let us now focus on the governing equations for the impounded water in the reservoir. Assuming the impounded water in the reservoir to be inviscid, linearly compressible with a small amplitudes for the displacements and velocity, the initial-boundary value problem for the fluid domain can be described as follows (Zienkiewicz and Taylor, 2005).

$$\frac{1}{c^2} \frac{\partial^2 p}{\partial t^2} - \frac{\partial^2 p}{\partial x_i^2} = 0 \quad \text{in} \quad \forall (\mathbf{x}, t) \in \Omega^f \times (0, T) \tag{6.11}$$

$$p (\mathbf{x}, 0) = 0 \quad \forall \mathbf{x} \in \Omega^f \tag{6.12}$$

$$\frac{\partial p (\mathbf{x}, 0)}{\partial t} = 0 \quad \forall \mathbf{x} \in \Omega^f \tag{6.13}$$

$$p(x, t) = 0 \quad \forall (\mathbf{x}, t) \in \Gamma_f^f \times (0, T) \tag{6.14}$$

$$\nabla p \cdot \mathbf{n}^f = -\frac{1}{c}\frac{\partial p}{\partial t} + \frac{1}{c}\frac{\partial p^f}{\partial t} \quad \forall(\mathbf{x},t) \in \Gamma^f_\infty \times (0,T) \tag{6.15}$$

$$\nabla p \cdot \mathbf{n}^f = -\rho^f \frac{\partial \mathbf{v}}{\partial t} \cdot \mathbf{n}^f - \rho^f \mathbf{a}^g \cdot \mathbf{n}^f \quad \forall(\mathbf{x},t) \in \Gamma^f_{fd} \times (0,T) \tag{6.16}$$

$$\nabla p \cdot \mathbf{n}^f = -\rho^f \mathbf{a}^g \cdot \mathbf{n}^f - q_c \frac{\partial p}{\partial t} \quad \forall(\mathbf{x},t) \in \Gamma^f_{fs} \times (0,T) \tag{6.17}$$

where $p(\vec{x},t)$ is the hydrodynamic pressure in the water (in excess of hydrostatic pressure), c is the speed of sound in water, p^f is the free-field hydrodynamic pressure in the reservoir, $\mathbf{a}^g(t)$ is the spatially uniform ground motion, ρ^f is the mass density of the water. In Eq. (6.16), $\mathbf{v}$ denotes the relative velocity of the dam with respect to the base of the dam. In Eq. (6.17), q_c is the damping coefficient which is the fundamental parameter characterizing the effect of reservoir bottom materials and it is given in Fenves and Chopra, 1983 as,

$$q_c = \frac{1-\alpha_b}{c\,(1+\alpha_b)} \tag{6.18}$$

in which, α_b is the ratio of the amplitude of reflected hydrodynamic pressure wave to the amplitude of a vertically propagating pressure wave incident on the reservoir bottom. More information about the boundary conditions Eq. (6.14–6.18) can be found in section 5.2.

Note that the governing equation for the fluid domain, which is given by Eq. (6.11), remains linear for both p and $\mathbf{v}$. This equation is identical to the one presented in the last chapter (see section 5.2.1). The governing equation for the solid domain (i.e. dam), which is given by Eq. (6.3), is nonlinear due to the nonlinear stress-strain relationship. However, this equation is linear in hydrodynamic pressure acting on the dam-fluid interface (see boundary condition given by Eq. 6.7). The linearity of Eq. (6.3) in p and Eq. (6.11) in $\mathbf{v}$ implies the linear coupling between fluid and solid domain.

6.3 v-ST/FEM formulation

Let Ω^f_h, the set of finite spatial fluid-elements $\Omega^f_e, e = 1, \cdots, n^f_{el}$, be the discretization of reservoir domain Ω^f, where n^f_{el} is the total number of spatial fluid elements in Ω^f_h. Further, let Ω^s_h, the set of finite spatial solid-elements Ω^s_e, $e = 1, \cdots, n_{el}$, be the discretization of solid domain Ω^s, where n_{el} is the total number of spatial elements in Ω_h. Now, consider a non-uniform subdivision for the time domain $[0,T]$, $0 = t_0 < t_1 < \cdots < t_N = T$ with $I_n = (t_n, t_{n+1})$, $\Delta t = t_{n+1} - t_n$. The n^{th} space-time slab for fluid domain $Q^f_n = \Omega^f_h \times I_n$ and for solid domain $Q^s_n = \Omega^s_h \times I_n$, and corresponding

space-time finite element for fluid domain $Q^f_{n,e} = \Omega^f_e \times I_n, e = 1, \cdots, n^f_{el}$, and for solid domain $Q^s_{n,e} = \Omega^s_e \times I_n, e = 1, \cdots, n_{el}$.

Consider $\mathscr{P}_l(Q^f_{n,e})$ and $\mathscr{P}_l(Q^s_{n,e})$, the collection of all polynomials defined on $Q^f_{n,e}$ and $Q^s_{n,e}$, respectively, with a total degree of no more than l. Let the space of piecewise continuous functions defined on domain $(*)$ is given by $C^0(*)$. Consider also the following collection of functions:

$$\mathfrak{F}^f_{l,h} := \left\{ p^h \middle| \, p^h \in C^0\left(\bigcup_{n=0}^{N-1} Q^f_n\right), p^h \middle| \, Q^f_{n,e} \in \mathcal{P}_l\left(Q^f_{n,e}\right) \right\} \tag{6.19}$$

$$\mathfrak{F}^s_{l,h} := \left\{ \mathbf{u}^h \middle| \, \mathbf{u}^h \in C^0\left(\bigcup_{n=0}^{N-1} Q^s_n\right)^2, \mathbf{u}^h \middle| \, Q^s_{n,e} \in \left(\mathcal{P}_l\left(Q^s_{n,e}\right)\right)^2 \right\} \tag{6.20}$$

where $p^h \Big| \, Q^f_{n,e}$ and $\mathbf{u}^h \Big| \, Q^s_{n,e}$ is the restriction of $p^h(\mathbf{x}, t)$ to $Q^f_{n,e}$ and restriction of $\mathbf{u}^h(\mathbf{x}, t)$ to $Q^s_{n,e}$, respectively. The space of the test functions for the fluid-domain is

$$\mathscr{Q}^h := \left\{ q^h \middle| \, q^h \in \mathfrak{F}^f_{l,h}, q^h = 0, \forall\, (\mathbf{x}, t) \in \Gamma^f_f \times I_n \right\} \tag{6.21}$$

and the space of trial functions is same as the space of test function, i.e.

$$S^h_p = \mathscr{Q}^h \tag{6.22}$$

The space of the test functions for the solid domain is

$$V^h := \left\{ \mathbf{v}^h \middle| \, \mathbf{v}^h \in \mathfrak{F}_{l,h}, \mathbf{v}^h = 0, \forall\, (\mathbf{x}, t) \in \Gamma^s_{ds} \times I_n, i = 1, 2 \right\} \tag{6.23}$$

and the space of trial functions for solid domain is same as the space of test function, i.e.

$$S^h_v = V^h \tag{6.24}$$

In order to obtain the space-time weak form of pressure-wave equation Eq. (6.11) is rewritten as

$$\frac{1}{c^2}\frac{\partial q}{\partial t} - \frac{\partial^2 p}{\partial x_i^2} = 0 \tag{6.25}$$

where $q(\mathbf{x}, t)$ is an auxiliary variable given by

$$q = \frac{\partial p}{\partial t} \tag{6.26}$$

and

$$p\,(\mathbf{x}, t) = p\,(\mathbf{x}, t_n) + \int_{t_n}^{t} q\,(\mathbf{x}, \tau)\, d\tau \quad \forall\, (\mathbf{x}, \tau) \in \Omega^f \times [t_n, t] \tag{6.27}$$

The v-ST/FEM weak-form for Eq. (6.25) and Eq. (6.3) can be stated as; Find $\mathbf{v} \in S_v^h$ and $q \in S_p^h$ such that for all $\delta\mathbf{v} \in V^h$, $\delta q \in \mathscr{Q}^h$, and for all $n = 1, \cdots, N-1$, Eq. (6.28) and Eq. (6.29) hold true.

$$
\begin{aligned}
&\int_{I_n}\int_{\Omega_h^f} \delta q \frac{1}{c^2}\frac{\partial q}{\partial t} d\Omega dt + \int_{\Omega_h^f} \delta q\left(\mathbf{x}, t_n\right) \frac{1}{c^2} q\left(\mathbf{x}, t_n^+\right) d\Omega \\
&- \int_{\Omega_h^f} \delta q\left(\mathbf{x}, t_n\right) \frac{1}{c^2} q\left(\mathbf{x}, t_n^-\right) d\Omega + \int_{I_n}\int_{\Omega_h^f} \frac{\partial \delta q}{\partial x_i}\frac{\partial p}{\partial x_i} d\Omega dt \\
&+ \int_{I_n}\int_{\Gamma_{fd}^f} \delta q \rho^f \frac{\partial v_i}{\partial t} n_i^f ds dt + \int_{I_n}\int_{\Gamma_{fd}^f} \delta q \rho^f a_i^g n_i^f ds dt \\
&+ \int_{I_n}\int_{\Gamma_{fs}^f} \delta q \rho^f a_i^g n_i^f ds dt + \int_{I_n}\int_{\Gamma_{fs}^f} \delta q \rho^f q_c q ds dt \\
&+ \int_{I_n}\int_{\Gamma_{\infty}^f} \delta q \frac{1}{c} q ds dt - \int_{I_n}\int_{\Gamma_{\infty}^f} \delta q \frac{1}{c} q^f ds dt = 0
\end{aligned}
\tag{6.28}
$$

$$
\begin{aligned}
&\int_{I_n}\int_{\Omega_h^s} \rho^s \delta v_i \frac{\partial v_i}{\partial t} d\Omega dt + \int_{\Omega_h^s} \rho^s \delta v_i\left(\mathbf{x}, t_n^+\right) v_i\left(\mathbf{x}, t_n^+\right) d\Omega \\
&- \int_{\Omega_h^s} \rho^s \delta v_i\left(\mathbf{x}, t_n^+\right) v_i\left(x, t_n^-\right) d\Omega + \int_{I_n}\int_{\Omega_h^s} \frac{\partial \delta v_i}{\partial x_j}\sigma_{ij} d\Omega dt \\
&- \int_{I_n}\int_{\Gamma_i^h} \delta v_i f_i^s ds dt - \int_{I_n}\int_{\Omega_h^s} \rho^s \delta v_i\left(b_i - a_i^g\right) d\Omega dt \\
&+ \int_{I_n}\int_{\Gamma_{fd}^s} \delta v_i p_0 n_i^s ds dt + \int_{I_n}\int_{\Gamma_{fd}^s} \delta v_i p n_i^s ds dt = 0
\end{aligned}
\tag{6.29}
$$

In Eq. (6.28) and Eq. (6.29), n_i^f and n_i^s are the components of outward normal vector at the fluid and solid boundary, respectively (see also Eq. 6.2). Hydrodynamic pressure p and displacements $\mathbf{u}$ are obtained by consistent integration of q and $\mathbf{v}$, respectively, and q^f is related to the the free-field hydrodynamic pressure by

$$
q^f = \frac{\partial p^f}{\partial t} \tag{6.30}
$$

More information regarding the free-field response of reservoir, that is p^f and q^f, can be found in the section 5.3.

6.4 Space-time finite element discretization

Let n_e and n_e^f be the total number of nodes in spatial finite element for solid and fluid domain, respectively. Let $v_i(\mathbf{x}, t_n^+)$ and $v_i(\mathbf{x}, t_{n+1}^-)$ be the spatial velocities on the bottom and top faces of space-time slab Q_n, respectively. Similarly, let $q(\mathbf{x}, t_n^+)$

and $q(\mathbf{x}, t_{n+1}^{-})$ be the spatial velocities on the bottom and top faces of space-time slab Q_n^f, respectively. Considering linear interpolation of time $t \in I_n$,

$$t(\theta) = T_1(\theta)t_n + T_2(\theta)t_{n+1}, \quad \forall\theta \in [-1, 1] \tag{6.31}$$

where,

$$T_1(\theta) = \frac{1-\theta}{2} \qquad T_2(\theta) = \frac{1+\theta}{2} \tag{6.32}$$

The test function and trial function for velocity field defined on $Q_{n,e}$ are given by

$$\delta v_i(\mathbf{x}, t) = {}^a\delta v_{iI} T_a(\theta) N^I(\xi, \eta) \tag{6.33}$$

$$v_i(\mathbf{x}, t) = {}^a v_{iI} T_a(\theta) N^I(\xi, \eta) \tag{6.34}$$

The displacements of dam $\mathbf{u}(\mathbf{x}, t)$ are given by Eq. (6.32) which are obtained by time integration of Eq. (6.34) while using Eq. (6.32).

$$u_i(\mathbf{x}, t) = u_i(\mathbf{x}, t_n) + \tilde{T}_1(\theta) v_i(\mathbf{x}, t_n) + \tilde{T}_2(\theta) v_i(\mathbf{x}, t_{n+1}) \tag{6.35}$$

in which,

$$\tilde{T}_1(\theta) = \frac{\Delta t_n}{2}\left[1 - T_1^2(\theta)\right] \qquad \tilde{T}_2(\theta) = \frac{\Delta t_n}{2} T_2^2(\theta) \tag{6.36}$$

The test and trial function for $q(\mathbf{x}, t)$ defined on $Q_{n,e}$ are given by

$$\delta q(\mathbf{x}, t) = {}^a\delta q_I T_a(\theta) N_f^I(\xi, \eta) \tag{6.37}$$

$$q(\mathbf{x}, t) = {}^a q_I T_a(\theta) N_f^I(\xi, \eta) \tag{6.38}$$

The hydrodynamic pressure p due to impounded water in the reservoir is given by Eq. (6.39) which is obtained by time integration of Eq. (6.38) while using the expression for T_1 and T_2 given in Eq. (6.32).

$$p(\mathbf{x}, t) = p(\mathbf{x}, t_n) + \tilde{T}_1(\theta) q(\mathbf{x}, t_n) + \tilde{T}_2(\theta) q(\mathbf{x}, t_{n+1}) \tag{6.39}$$

In Eqs. (6.31 – 6.39), $i = 1, 2$ denotes the spatial component along x_1 and x_2 direction, $a = 1, 2$ denotes the temporal node number, $\theta \in [-1, 1]$ denotes the local temporal coordinate, and (ξ, η) denotes the local coordinates in a spatial finite element. In Eq. (6.33–6.34) $I = 1, \cdots, n_e$, and in Eq. (6.37–6.38) $I = 1, \cdots, n_e^f$ denote the local node number of a spatial finite element for dam and reservoir, respectively. The shape function for an I^{th} spatial local node is denoted by N^I and N_f^I for solid and fluid domain, respectively.

The weak form described in Eq. (6.28) and Eq. (6.29) are now discretized by using the aforementioned space-time finite element interpolation for $\delta\mathbf{v}$, $\mathbf{v}$, δq, and q. Accordingly, the space-time matrix-vector forms of the resultant system of discretized equations can be described by Eq. (6.40) and Eq. (6.41), where former corresponds to the solid domain and latter corresponds to the fluid domain.

$$[\mathbf{M}^s]\{\tilde{\mathbf{v}}\} + \left[\mathbf{H}_{fd}^s\right] \cdot \{\tilde{\mathbf{q}}\} + \{\mathbf{J}_\sigma^s\} - \{\mathbf{J}_0^s\} + \left\{\mathbf{J}_g^s\right\} - \{\mathbf{J}_{ext}^s\} + \left\{\mathbf{J}_{p_0}^{fd}\right\} + \left\{\mathbf{J}_{p^n}^{fd}\right\} = \mathbf{0} \tag{6.40}$$

$$\begin{aligned}\left[\mathbf{M}^f\right] \cdot \{\tilde{\mathbf{q}}\} + \left[\mathbf{K}^f\right] \cdot \{\tilde{\mathbf{q}}\} + \left[\mathbf{C}_{fs}^f\right] \cdot \{\tilde{\mathbf{q}}\} + \left[\mathbf{C}_\infty^f\right] \cdot \{\tilde{\mathbf{q}}\} + \left[\mathbf{H}_{fd}^f\right] \cdot \{\tilde{\mathbf{v}}\} \\ - \left\{\mathbf{J}_0^f\right\} - \left\{\mathbf{J}_f^f\right\} + \left\{\mathbf{J}_g^{fd}\right\} + \left\{\mathbf{J}_g^{fs}\right\} + \left\{\mathbf{J}_{p^n}^f\right\} = \mathbf{0}\end{aligned} \tag{6.41}$$

Further, if Rayleigh damping is used to model the material damping in solid domain then Eq. (6.40) becomes,

$$\begin{aligned}&[\mathbf{M}^s]\{\tilde{\mathbf{v}}\} + \alpha\,[\mathbf{M}_R^s]\{\tilde{\mathbf{v}}\} + \beta\,[\mathbf{K}_R^s]\{\tilde{\mathbf{v}}\} + \left[\mathbf{H}_{fd}^s\right] \cdot \{\tilde{\mathbf{q}}\} \\ &+ \{\mathbf{J}_\sigma^s\} - \{\mathbf{J}_0^s\} + \left\{\mathbf{J}_g^s\right\} - \{\mathbf{J}_{ext}^s\} + \left\{\mathbf{J}_{p_0}^{fd}\right\} + \left\{\mathbf{J}_{p^n}^{fd}\right\} = \mathbf{0}\end{aligned} \tag{6.42}$$

in which α and β are the Rayleigh damping coefficients.

In Eqs. (6.40–6.42), $[\cdot]$ and $\{\cdot\}$ represent the space-time matrix and space-time nodal vector, respectively. $\{\tilde{\mathbf{q}}\}$ is used to denote the space-time nodal values of auxiliary variable q, and $\{\tilde{\mathbf{v}}\}$ which denotes the space-time nodal values of velocity field are the primary unknowns to be determined for the fluid and solid domain, respectively. The finite element structure of these unknown vectors are given by

$$\{\tilde{\mathbf{q}}\} = \begin{Bmatrix} \tilde{\mathbf{q}}^1 \\ \tilde{\mathbf{q}}^2 \end{Bmatrix} \quad \{\tilde{\mathbf{v}}\} = \begin{Bmatrix} \tilde{\mathbf{v}}^1 \\ \tilde{\mathbf{v}}^2 \end{Bmatrix} \quad \left\{\tilde{\mathbf{v}}^1\right\} = \begin{Bmatrix} \tilde{\mathbf{v}}_1^1 \\ \tilde{\mathbf{v}}_2^1 \end{Bmatrix} \quad \left\{\tilde{\mathbf{v}}^2\right\} = \begin{Bmatrix} \tilde{\mathbf{v}}_1^2 \\ \tilde{\mathbf{v}}_2^2 \end{Bmatrix}$$

in which $\{\tilde{\mathbf{q}}^1\}$ and $\{\tilde{\mathbf{q}}^2\}$ are the space-nodal values of q at time $t = t_n^+$ (bottom space-time slab) and time $t = t_{n+1}^-$ (top space-time slab), respectively. Similarly, $\{\tilde{\mathbf{v}}^1\}$ and $\{\tilde{\mathbf{v}}^2\}$ are the space-nodal values of $\mathbf{v}$ at time $t = t_n^+$ and time $t = t_{n+1}^-$,

respectively. Furthermore, $\{\tilde{\mathbf{v}}_1^a\}$ and $\{\tilde{\mathbf{v}}_2^a\}$ (for $a = 1, 2$) stand for the space-nodal values of spatial component of velocity field along x_1 and x_2 direction, respectively.

In Eq. (6.41), $\left[\mathbf{M}^f\right]$ denotes the space-time mass matrix for the fluid domain, $\left[\mathbf{K}^f\right]$ denotes the space-time diffusion matrix for fluid domain, $\left[\mathbf{C}_{fs}^f\right]$ is the space-time matrix which corresponds to the reservoir bottom absorption effect, $\left[\mathbf{C}_{\infty}^f\right]$ is the space-time matrix corresponding to the dashpots placed at the truncated upstream boundary of reservoir, and $\left[\mathbf{H}_{fd}^f\right]$ is the coupling matrix which relates the hydrodynamic pressure in the reservoir with the dynamic response of dam. Further, in Eq. (6.41), the space-time nodal vector $\left\{\mathbf{J}_0^f\right\}$ corresponds to the value of q at time $t = t_n$, $\left\{\mathbf{J}_f^f\right\}$ is related to the free-field hydrodynamic response of the reservoir, $\left\{\mathbf{J}_g^{fs}\right\}$ and $\left\{\mathbf{J}_g^{fd}\right\}$ are related to the motion of underlying rigid-foundation, and $\left\{\mathbf{J}_{p^n}^f\right\}$ is related to the pressure-gradient in the reservoir at time $t = t_n$.

In Eq. (6.40) and Eq. (6.42), $[\mathbf{M}^s]$ denotes the space-time mass matrix for the solid domain, $[\mathbf{M}_R^s]$ and $[\mathbf{K}_R^s]$ are the mass-proportional and stiffness-proportional space-time Rayleigh damping matrix, respectively, and $\left[\mathbf{H}_{fd}^s\right]$ is the coupling matrix which relates the hydrodynamic pressure in the reservoir to the dynamic response of the dam. Furthermore, in Eq. (6.40) and Eq. (6.42), $\{\mathbf{J}_\sigma^s\}$ is related to the stresses in the dam, $\{\mathbf{J}_0^s\}$ corresponds to the velocity of the dam at time $t = t_n$, $\left\{\mathbf{J}_g^s\right\}$ is related to the motion of underlying rigid-ground, $\{\mathbf{J}_{ext}^s\}$ is related to the external body force and surface acting on the dam, and the vectors $\left\{\mathbf{J}_{p^n}^{fd}\right\}$ and $\left\{\mathbf{J}_{p_0}^{fd}\right\}$ correspond to the hydrodynamic pressure and hydrostatic pressure due to reservoir acting at fluid-dam interface Γ_{fd}^s.

Lastly, the finite element expressions of the terms present in Eqs. (6.40 – 6.42) are depicted in Table 6.1 and Table 6.2. A detailed description about the derivation of space-time matrices and space-time nodal vectors (including their finite element data-structure) is given in Appendix-E.

6.5 Implementation of v-ST/FEM formulation

The finite element discretized equations for fluid domain, Eq. (6.41), and solid domain, Eq. 6.42, constructs a system of coupled equations. The coupling between dam (solid-domain) and reservoir (fluid-domain) takes place through the soil-dam interface Γ_{fd}^s; the motion of the dam influences the hydrodynamic pressure in the reservoir which in turn modifies the response of dam. In addition, the nature of interfacial coupling between the dam and reservoir is linear; Eq. (6.41) (for fluid domain) is linear in both $\mathbf{v}$, and Eq. (6.42) is linear in q.

Matrix notation	Component notation	Expression
$[\mathbf{M}^s]$	$[M^s]_{ij}^{ab}\,(I,J)$	$\delta_{ij}\int_{I_n}\int_{\Omega_h^s} N^I T_a \rho^s \frac{\partial N^J T_b}{\partial t} dt d\Omega$ $+\delta_{ij}\delta_{1a}\delta_{1b}\int_{\Omega_h^s} N^I \rho^s N^J d\Omega$
$[\mathbf{M}_R^s]$	$[M_R^s]_{ij}^{ab}\,(I,J)$	$\delta_{ij}\int_{I_n}\int_{\Omega_h^s} N^I T_a \rho N^J T_b d\Omega dt$
$\left[\mathbf{M}^f\right]$	$\left[M^f\right]^{ab}(I,J)$	$\int_{I_n}\int_{\Omega_h^f} N_f^I T_a \frac{1}{c^2}\frac{\partial N_f^J T_b}{\partial t} dt d\Omega$ $+\delta_{1a}\delta_{1b}\int_{\Omega_h^s} N_f^I \frac{1}{c^2} N_f^J d\Omega$
$[\mathbf{K}_R^s]$	$[K_R^s]_{ij}^{ab}\,(I,J)$	$\int_{I_n}\int_{\Omega_h^s} \frac{\partial N^I T_a}{\partial x_p} C_{pijq} \frac{\partial N^J T_b}{\partial x_q} d\Omega dt$
$\left[\mathbf{K}^f\right]$	$\left[K^f\right]^{ab}(I,J)$	$\int_{I_n}\int_{\Omega_h^f} T_a \tilde{T}_b \frac{\partial N_f^I}{\partial x_i}\frac{\partial N_f^J}{\partial x_i} d\Omega dt$
$\left[\mathbf{C}_{fs}^f\right]$	$\left[C_{fs}^f\right]^{ab}(I,J)$	$\int_{I_n}\int_{\Gamma_{fs}^f} N_f^I T_a \rho^f q_c N_f^J T_b ds dt$
$\left[\mathbf{C}_{\infty}^f\right]$	$\left[C_{\infty}^f\right]^{ab}(I,J)$	$\int_{I_n}\int_{\Gamma_{\infty}^f} N_f^I T_a \frac{1}{c} N_f^J T_b ds dt$
$\left[\mathbf{H}_{fd}^f\right]$	$\left[H_{fd}^f\right]_i^{ab}(I,J)$	$\int_{I_n} T_a \frac{\partial T_b}{\partial t} dt \int_{\Gamma_{fd}^f} N_f^I \rho^f N^J n_i^f ds$
$\left[\mathbf{H}_{fd}^s\right]$	$\left[H_{fd}^s\right]_i^{ab}(I,J)$	$\int_{I_n} T_a \tilde{T}_b dt \int_{\Gamma_{fd}^s} N^I N_f^J n_i^s ds$

Tab. 6.1.: Description of the space-time finite element matrices used in the v-ST/FEM for the nonlinear dynamic analysis of the dam-reservoir sysmtem.

Matrix notation	Component notation	Expression
$\{\mathbf{J}^s_{ext}\}$	$\{J^s_{ext}\}^a_i\,(I)$	$\int_{I_n}\int_{\Omega^s_h} N^I T_a \rho^s b_i d\Omega dt$ $+\int_{I_n}\int_{\Gamma^h_i} N^I T_a f^s_i d\Omega dt$
$\{\mathbf{J}^s_0\}$	$\{J^s_0\}^a_i\,(I)$	$\delta_{a1}\int_{\Omega^s_h} N^I \rho^s v^0_i d\Omega$
$\{\mathbf{J}^s_\sigma\}$	$\{J^s_\sigma\}^a_i\,(I)$	$\int_{I_n}\int_{\Omega^s_h} \frac{\partial N^I T_a}{\partial x_j}\sigma_{ij} d\Omega dt$
$\left\{\mathbf{J}^{fd}_{p^n}\right\}$	$\left\{J^{fd}_{p^n}\right\}^a_i\,(I)$	$\int_{I_n}\int_{\Gamma^s_{fd}} T_a N^I p^n n^s_i ds dt$
$\left\{\mathbf{J}^{fd}_{p_0}\right\}$	$\left\{J^{fd}_{p_0}\right\}^a_i\,(I)$	$\int_{I_n}\int_{\Gamma^s_{fd}} T_a N^I p_0 n^s_i ds dt$
$\left\{\mathbf{J}^s_g\right\}$	$\left\{J^s_g\right\}^a\,(I)$	$\int_{I_n}\int_{\Omega^s_h} N^I T_a \rho^s a^g_i d\Omega dt$
$\left\{\mathbf{J}^f_0\right\}$	$\left\{J^f_0\right\}^a\,(I)$	$\delta_{1a}\int_{\Omega^f_h} N^I_f \frac{1}{c^2} q^0 d\Omega$
$\left\{\mathbf{J}^f_f\right\}$	$\left\{J^f_f\right\}^a\,(I)$	$\int_{I_n}\int_{\Gamma^f_\infty} N^I_f T_a \frac{1}{c} q^f ds dt$
$\left\{\mathbf{J}^{fd}_g\right\}$	$\left\{J^{fd}_g\right\}^a\,(I)$	$\int_{I_n}\int_{\Gamma^f_{fd}} N^I_f T_a \rho^f a^g_i n^f_i ds dt$
$\left\{\mathbf{J}^{fs}_g\right\}$	$\left\{J^{fs}_g\right\}^a\,(I)$	$\int_{I_n}\int_{\Gamma^f_{fs}} N^I_f T_a \rho^f a^g_i n^f_i ds dt$
$\left\{\mathbf{J}^f_{p^n}\right\}$	$\left\{J^f_{p^n}\right\}^a\,(I)$	$\int_{I_n}\int_{\Omega^f_h} T_a \frac{\partial N^I_f}{\partial x_i}\frac{\partial p^n}{\partial x_i} d\Omega dt$

Tab. 6.2.: Description of the space-time vectors used in the v-ST/FEM for the nonlinear dynamic analysis of dam-reservoir system.

Further, Eq. (6.41) and Eq. (6.42) individually constitute a system of linear and nonlinear algebraic equations, respectively. Moreover, the nonlinearity of Eq. (6.42), and the system of coupled equations, only comes from the nonlinear stress-strain relationship of the dam. The space-time nodal vector $\{\mathbf{J}_{\sigma}^{s}\}$ in Eq. (6.42) is the one which contains the stress term, and finite element expression for this term is given by [1]

$$\{\mathbf{J}_{\sigma}^{s}\} := \{J_{\sigma}^{s}\}_{i}^{a}(I) = \int_{I_n} T_a \left(\int_{\Omega_h^s} \frac{\partial N^I}{\partial x_j} \sigma_{ij} d\Omega \right) dt \tag{6.43}$$

In Eq. (6.43), the term enclosed inside the parentheses denotes the spatial-nodal value of the internal force vector $\mathbf{f_{int}}$, which is often used in the semi-discrete finite element analysis. For the sake of clarity, let us recast $\{\mathbf{J}_{\sigma}^{s}\}$ in terms of internal force vector $\{\mathbf{f}_{\text{int}}\}$ as,

$$\{J_{\sigma}^{s}\}_{i}^{a}(I) = \int_{I_n} T_a f_{\text{int}}(i, I)\, dt \tag{6.44}$$

where

$$f_{\text{int}}(i, I) = \int_{\Omega_h^s} \frac{\partial N^I}{\partial x_j} \sigma_{ij} d\Omega \tag{6.45}$$

denotes the nodal value of i^{th} spatial component of the internal force vector at time $t \in I_n$.

In a finite element computer program, integration over the spatial domain of a finite element is computed by using the Gaussian quadrature rules. [2] Similarly, the integration in time domain given in Eq. (6.44) can be performed by using the Gaussian quadrature rules. In former case, the choice of a particular quadrature rule for numerical integration depends upon the topology of the spatial finite element.

In the context of numerical integration in time domain one can notice that the topological structure of a time finite element is essentially same as the topological structure of the one-dimensional spatial finite element. Therefore, by using a finite set of quadrature points, $\{\theta^1, \cdots, \theta^{n_{ipt}}\}$, and corresponding weights, $\{w_t^1, \cdots, {w_t}^{n_{ipt}}\}$, for numerical integration of Eq. (6.44),

$$\{J_{\sigma}^{s}\}_{i}^{a}(I) \approx \frac{\Delta t_n}{2} \sum_{\alpha=1}^{n_{ipt}} T_a^{\alpha} f_{\text{int}}^{\alpha}(i, I)\, w_t^{\alpha} \tag{6.46}$$

[1] In Eq. (6.43), $i = 1, 2$ denotes the spatial component, $a = 1, 2$ denotes the temporal node, $I = 1, \cdots, n_e^s$ denotes the local spatial node, accordingly $\{J_{\sigma}^{s}\}_{i}^{a}(I)$ corresponds to the value of i^{th} spatial component of the vector $\{\mathbf{J}_{\sigma}^{s}\}$ defined at I^{th} local spatial node and a^{th} temporal node of a local space-time finite element.

[2] In a typical numerical integration method based on quadrature rules, the integrand is evaluated a finite set of points called the *integration points* and a weighted sum of these values is used to approximate the integral. The choice of integration points and weights depends upon the specific method used and the accuracy required from the approximation.

where n_{ipt} is the total number of integration points, T_a^α for $a = 1, 2$ are obtained by using θ^α in Eq. (6.32), and $f_{int}^\alpha(i, I)$ is given by

$$f_{\text{int}}^{\alpha}(i, I) = \int_{\Omega_h^s} \frac{\partial N^I}{\partial x_j} \sigma_{ij}^{\alpha} d\Omega \tag{6.47}$$

in which $\sigma_{ij}^\alpha := \sigma(\mathbf{x}, \theta^\alpha)$ is the stress at any spatial point $\mathbf{x} \in \Omega_h^s$ and time $t^\alpha = t(\theta^\alpha) \in I_n$ (cf. Eq. 6.31).

	Gauss-Legendre Quadrature		Gauss-Lobatto Quadrature	
Number of points (n)	Quadrature points (θ)	Weights (w)	Quadrature points (θ)	Weights (w)
1	0	2		
2	$\pm\frac{1}{\sqrt{3}}$	1		
3	0	$\frac{8}{9}$	0	$\frac{4}{3}$
	$\pm\sqrt{\frac{3}{5}}$	$\frac{5}{9}$	± 1	$\frac{1}{3}$
4	$\pm\sqrt{\frac{3}{7} - \frac{2}{7}\sqrt{\frac{6}{5}}}$	$\frac{18+\sqrt{30}}{36}$	$\pm\sqrt{\frac{1}{5}}$	$\frac{5}{6}$
	$\pm\sqrt{\frac{3}{7} + \frac{2}{7}\sqrt{\frac{6}{5}}}$	$\frac{18-\sqrt{30}}{36}$	± 1	$\frac{1}{6}$

Tab. 6.3.: Low order Gauss-Legendre and Gauss-Lobatto quadrature rules.

The numerical integration of Eq. (6.47) is performed by using the finite number of quadrature points, $\{(\xi^1, \eta^1), \cdots, (\xi^{n_{ips}}, \eta^{n_{ips}})\}$ defined in the parent domain, and corresponding weights, $\left\{w_s^1, \cdots, w_s^{n_{ips}}\right\}$.

$$f_{\text{int}}^{\alpha}(i, I) \approx \sum_{\beta=1}^{n_{ips}} w^\beta J^\beta \frac{\partial N^I}{\partial x_j}\bigg|_\beta \sigma_{ij}^{\alpha}\Big|_\beta \tag{6.48}$$

where J^β denotes the determinant of the Jacobian matrix of mapping between the parent element and physical element, and $\sigma_{ij}^{\alpha}\big|_\beta$ denotes the value of stress evaluated at α-integration point of the time domain, and β-integration point of the space domain (i.e., value at the space-time quadrature point).

Although various type of quadrature rules are available for numerical integration in Eq. (6.46), within finite element framework the choice of Gauss-Legendre and Gauss-Lobatto quadrature rules seems to be advantageous. Table 6.3 presents some low-order Gauss-Legendre and Gauss-Lobatto quadrature rules for computing the integration over the interval $[-1, 1]$. It is worthwhile to mention that most of the finite element programs demand information of the Gauss-Legendre quadrature rules to perform integration over the spatial domain of a line element, a quadrangle,

brick element, among others. From the view point of Eq. (6.46), Gauss-Legendre rules, however, appear to be inconvenient since the end points of the domain $[-1,1]$ are not included in the Gauss-Legendre quadrature points. Therefore, stresses already computed at time $t=t_n$ cannot be used in Eq. (6.46), moreover, additional computations must be performed in case information about the stress at time $t=t_{n+1}$ is required. The Gauss-Lobatto quadrature rules, on the other hand, always comprise the end points of the domain $[-1,1]$. It should also be note that n Gauss-Lobatto quadrature points are only accurate for polynomials up to degree $2n-3$, whereas n number of Gauss-Legendre quadrature points yields an exact result for polynomial of degree $2n-1$ or less.

Let us now focus on the total number of temporal quadrature points required in Eq. (6.46). The linear interpolation of velocity in time (see Eq. 6.34) makes the displacement and strain quadratic in time (see Eq. 6.35 and Eq. 6.9). In accordance with Eqs (6.8,6.10,6.34), it is safe to assume a quadratic variation of the stress in time interval I_n which will make the integrand in Eq. (6.44) third order in time. Therefore, it is sufficient to use the two-point Gauss-Legendre rule or the three-point Gauss-Lobatto rule in Eq. (6.46) (see Table 6.3).

The two-point Gauss-Legendre form of Eq. (6.46) can be obtained by using the quadratures points $\left\{-\frac{1}{\sqrt{3}},\frac{1}{\sqrt{3}}\right\}$, and the corresponding weights $\{1,1\}$. The results are presented below.

$$\begin{aligned}\{J_\sigma^s\}_i^{a=1}(I)&=\frac{\Delta t_n}{2}\left\{0.211f_{\text{int}}^1(i,I)+0.789f_{\text{int}}^2(i,I)\right\}\\ \{J_\sigma^s\}_i^{a=2}(I)&=\frac{\Delta t_n}{2}\left\{0.789f_{\text{int}}^1(i,I)+0.211f_{\text{int}}^2(i,I)\right\}\end{aligned}\tag{6.49}$$

where $f_{\text{int}}^1(i,I)$ and $f_{\text{int}}^2(i,I)$ correspond to the stress evaluated at time $t_1=0.211t_n+0.789t_{n+1}$ and $t_2=0.789t_n+0.211t_{n+1}$, respectively.

The three-point Gauss-Lobatto form of Eq. (6.46) is obtained by using the quadratures points $\{-1,0,1\}$, and the corresponding weights $\left\{\frac{1}{3},\frac{4}{3},\frac{1}{3}\right\}$. The results are presented below.

$$\begin{aligned}\{J_\sigma^s\}_i^{a=1}(I)&=\frac{\Delta t_n}{6}f_{\text{int}}^0(i,I)+\frac{\Delta t_n}{3}f_{\text{int}}^1(i,I)\\ \{J_\sigma^s\}_i^{a=2}(I)&=\frac{\Delta t_n}{6}\left\{2f_{\text{int}}^1(i,I)+f_{\text{int}}^2(i,I)\right\}\end{aligned}\tag{6.50}$$

where $f_{\text{int}}^0(i,I)$, $f_{\text{int}}^1(i,I)$ and $f_{\text{int}}^2(i,I)$ correspond to the stress evaluated at time $t_0=t_n$, $t_1=0.5(t_n+t_{n+1})$ and $t_2=t_{n+1}$, respectively.

The generalized form of Eq. (**??**) and Eq. (**??**) can be described as,

$$\{J_\sigma^s\}_i^a(I) = \frac{\Delta t_n}{2}\left\{A_a f_{\text{int}}^0(i,I) + B_a f_{\text{int}}^1(i,I) + C_a f_{\text{int}}^2(i,I)\right\} \tag{6.51}$$

where the $A_a, B_a, C_a, \quad$ for $\quad a = 1,2$ are constant values associated with the two-point Gauss-Legendre form and three-point Gauss-Lobatto form, and $f_{\text{int}}^0(i,I)$, $f_{\text{int}}^1(i,I)$ and $f_{\text{int}}^2(i,I)$ correspond to the stress evaluated at time $t = t^n$, $t = t^1$ and $t = t^2$, respectively. The values of A_a, B_a, C_a are listed in Table 6.4.

	A_1	A_2	B_1	B_2	C_1	C_2
Two-point Gauss-Legendre rule	0	0	$\frac{\sqrt{3}-1}{2\sqrt{3}}$	$\frac{\sqrt{3}+1}{2\sqrt{3}}$	$\frac{\sqrt{3}+1}{2\sqrt{3}}$	$\frac{\sqrt{3}-1}{2\sqrt{3}}$
Three-point Gauss-Lobatto rule	$\frac{1}{3}$	0	$\frac{2}{3}$	$\frac{2}{3}$	0	$\frac{1}{3}$

Tab. 6.4.: Numerical values of the coefficients in Eq. (6.51)

The matrix vector form

$$\{\mathbf{J}_\sigma^s\} = \{\mathbf{J}_{\sigma^0}^s\} + \{\mathbf{J}_{\sigma^1}^s\} + \{\mathbf{J}_{\sigma^2}^s\} \tag{6.52}$$

where,

$$\{\mathbf{J}_{\sigma^0}^s\} := \{J_{\sigma^0}^s\}_i^a(I) = \frac{\Delta t_n}{2} A_a f_{\text{int}}^0(i,I) \tag{6.53}$$

$$\{\mathbf{J}_{\sigma^1}^s\} := \{J_{\sigma^0}^s\}_i^a(I) = \frac{\Delta t_n}{2} B_a f_{\text{int}}^1(i,I) \tag{6.54}$$

$$\{\mathbf{J}_{\sigma^2}^s\} := \{J_{\sigma^0}^s\}_i^a(I) = \frac{\Delta t_n}{2} C_a f_{\text{int}}^2(i,I) \tag{6.55}$$

Using Eq. (6.52) in Eq. (6.42), and rearranging the terms in (6.41), the system of coupled equations can be recast into the following.

$$\begin{aligned}\{\mathbf{R}^s\} := \{\mathbf{J}_0^s\} - \left\{\mathbf{J}_g^s\right\} + \{\mathbf{J}_{ext}^s\} - \left\{\mathbf{J}_{p_0}^{fd}\right\} - \left\{\mathbf{J}_{p^n}^{fd}\right\} - \{\mathbf{J}_{\sigma^0}^s\} \\ - \left[\mathbf{H}_{fd}^s\right]\cdot\{\tilde{\mathbf{q}}\} - \{\mathbf{J}_{\sigma^1}^s\} - \{\mathbf{J}_{\sigma^2}^s\} - [\mathbf{M}^s]\{\tilde{\mathbf{v}}\} \\ -\alpha[\mathbf{M}_R^s]\{\tilde{\mathbf{v}}\} - \beta[\mathbf{K}_R^s]\{\tilde{\mathbf{v}}\} = \mathbf{0}\end{aligned} \tag{6.56}$$

$$\left[\mathbf{K}_{st}^f\right]\{\tilde{\mathbf{q}}\} = \left\{\mathbf{J}^f\right\} - \left[\mathbf{H}_{fd}^f\right]\{\tilde{\mathbf{v}}\} \tag{6.57}$$

where, $\{\mathbf{R}^s\}$ corresponds to the residual of Eq. (6.42), and

$$\left[\mathbf{K}^f_{st}\right] = \left[\mathbf{M}^f\right] + \left[\mathbf{K}^f\right] + \left[\mathbf{C}^f_{fs}\right] + \left[\mathbf{C}^f_{\infty}\right] \tag{6.58}$$

$$\left\{\mathbf{J}^f\right\} = \left\{\mathbf{J}^f_0\right\} + \left\{\mathbf{J}^f_f\right\} - \left\{\mathbf{J}^{fd}_g\right\} - \left\{\mathbf{J}^{fs}_g\right\} - \left\{\mathbf{J}^f_{p^n}\right\} \tag{6.59}$$

6.5.1 Block-iterative scheme

The algorithm for the direct solution of the coupled problem defined by Eq. (6.56) and Eq. (6.57) can be chosen from among the variety of linearization schemes available for the solution of nonlinear problems. However, this implementation strategy may become undesirable as the number of unknowns increases. In this section, a block-iterative scheme is devised to solve the coupled problem. The scheme can be characterized as a partitioned method in which Eq. (6.56) and Eq. (6.57) are solved separately while the nonlinearity and coupling of the problem are dealt within a single iterative loop.

Consider a time step corresponding to $I_n = (t_n, t_{n+1})$, and iteration number k. Let the space-time nodal values of q and $\mathbf{v}$ in k^{th} iteration be denoted by $\{\tilde{\mathbf{q}}\}^{(k)}$ and $\{\tilde{\mathbf{v}}\}^{(k)}$, respectively. Noting $\{\tilde{\mathbf{q}}\}^{(k)}$ and $\{\tilde{\mathbf{v}}\}^{(k)}$ in Eq. (6.57) the residual vector can be decomposed in two parts; $\left\{\mathbf{J}^s_{fixed}\right\}$ which remains fixed during the iteration and $\{\mathbf{J}^s_{iter}\}^{(k)}$ which needs to be updated during each iteration.

$$\{\mathbf{R}^s\}^{(k)} = \left\{\mathbf{J}^s_{fixed}\right\} - \{\mathbf{J}^s_{iter}\}^{(k)} \tag{6.60}$$

where

$$\left\{\mathbf{J}^s_{fixed}\right\} = \{\mathbf{J}^s_0\} - \left\{\mathbf{J}^s_g\right\} + \{\mathbf{J}^s_{ext}\} - \left\{\mathbf{J}^{fd}_{p_0}\right\} - \left\{\mathbf{J}^{fd}_{p^n}\right\} - \{\mathbf{J}^s_{\sigma^0}\} \tag{6.61}$$

$$\begin{aligned}\{\mathbf{J}^s_{iter}\}^{(k)} = \left[\mathbf{H}^s_{fd}\right] \cdot \{\tilde{\mathbf{q}}\}^{(k)} + [\mathbf{M}^s]\{\tilde{\mathbf{v}}\}^{(k)} + \alpha\,[\mathbf{M}^s_R]\{\tilde{\mathbf{v}}\}^{(k)} \\ + \beta[\mathbf{K}^s_R]^{(k)}\{\tilde{\mathbf{v}}\}^{(k)} + \{\mathbf{J}^s_{\sigma^1}\}^{(k)} + \{\mathbf{J}^s_{\sigma^2}\}^{(k)}\end{aligned} \tag{6.62}$$

In a k^{th} iteration, Eq. (6.60) is linearized with respect to the space-time nodal velocities $\{\tilde{\mathbf{v}}\}$ while keeping $\{\tilde{\mathbf{q}}\}$ fixed to obtain

$$[\mathbf{K}^s_{st}]^{(k-1)}\{\Delta\tilde{\mathbf{v}}\}^{(k)} = \{\mathbf{R}^s\}^{(k-1)} \tag{6.63}$$

in which, $[\mathbf{K}^s_{st}]^{(k-1)}$ is the space-time tangent matrix for the solid domain which can be evaluated by using $\{\tilde{\mathbf{v}}\}^{(k-1)}$. In similarity with $\{\mathbf{R}^s\}^{(k)}$ (see Eq. **??**), $[\mathbf{K}^s_{st}]^{(k-1)}$ can be divided into a fixed part and an iterative part as shown below.

$$[\mathbf{K}^s_{st}]^{(k-1)} = \left[\mathbf{K}^s_{fixed}\right] + [\mathbf{K}^s_{iter}]^{(k-1)} \tag{6.64}$$

where

$$\left[\mathbf{K}^s_{fixed}\right] = [\mathbf{M}^s] + \alpha\,[\mathbf{M}^s_R] \tag{6.65}$$

$$[\mathbf{K}^s_{iter}]^{(k-1)} = \beta[\mathbf{K}^s_R]^{(k-1)} + [\mathbf{K}^s_{\sigma^1}]^{(k-1)} + [\mathbf{K}^s_{\sigma^2}]^{(k-1)} \tag{6.66}$$

where $[\mathbf{K}^s_R]^{(k-1)}$ denotes the stiffness proportional Rayleigh damping matrix, $\left[\mathbf{K}^s_{\sigma^1}\right]^{(k-1)}$ and $\left[\mathbf{K}^s_{\sigma^2}\right]^{(k-1)}$ corresponds to the linearization of Eq. (6.54) and Eq. (6.55), respectively. The detailed description about the derivation of these space-time matrices is included in Appendix E.

Once the incremental-velocity vector $\{\Delta\tilde{\mathbf{v}}\}^{(k)}$ is being computed from Eq. (6.63) the velocity vector can be updated using

$$\{\tilde{\mathbf{v}}\}^{(k)} = \{\tilde{\mathbf{v}}\}^{(k-1)} + \{\Delta\tilde{\mathbf{v}}\}^{(k)} \tag{6.67}$$

The updated space-time nodal values of velocity are then used for predicting the $\{\tilde{\mathbf{q}}\}^{(k)}$ by solving the following equation in fluid-domain.

$$\left[\mathbf{K}^f_{st}\right]\{\tilde{\mathbf{q}}\}^{(k)} = \left\{\mathbf{J}^f\right\} - \left[\mathbf{H}^f_{fd}\right]\{\tilde{\mathbf{v}}\}^{(k)} \tag{6.68}$$

At the end of an iteration the displacements in the solid domain and hydrodynamic pressures in the fluid domain are updated by using Eq. (6.35) and (6.39), respectively. The strains in solid domain are also computed using the updated values of displacement field which are subsequently used for calculating the stress and material tangent tensor C_{ijkl} from the stress-strain relationship. The stresses and material tangent modulus are then used for computing the residual vector (see Eq. 6.60) and the space-time tangent matrix in Eq. (6.64) and Eq. (6.66). Finally, the convergence in solutions is checked by computing the Euclidian norm of residual vector $\left\|\{\mathbf{R}^s\}^{(k)}\right\|$ and incremental-velocity vector $\left\|\{\Delta\tilde{\mathbf{v}}\}^{(k)}\right\|$ and using the following convergence criterion.

$$\left\|\{\mathbf{R}^s\}^{(k)}\right\| \leqslant \epsilon_R \left\|\{\mathbf{R}^s\}^{(0)}\right\| \tag{6.69}$$

$$\left\|\{\Delta\tilde{\mathbf{v}}\}^{(k)}\right\| \leqslant \epsilon_v \left\|\{\Delta\tilde{\mathbf{v}}\}^{(0)}\right\| \tag{6.70}$$

where ϵ_R and ϵ_v are the tolerance for convergence in residual vector and velocity field, respectively. The iterations are stopped incase Eq. (6.69) and/or Eq. (6.70) are satisfied by the trial solutions.

In Eq. (6.63) and Eq. (6.68) the space-time nodal vectors $\left\{\mathbf{J}^f\right\}$ and $\left\{\mathbf{J}^s_{fixed}\right\}$, and the space-time matrices $\left[\mathbf{K}^s_{fixed}\right]$, $\left[\mathbf{H}^s_{fd}\right]$, $\left[\mathbf{H}^f_{fd}\right]$, and $\left[\mathbf{K}^f_{st}\right]$ remain fixed during the iteration in a given time step. Accordingly, these space-time vectors and matrices only need to be computed once in the beginning of the iteration in a given time step. In this context, if a uniform time-step size $\Delta t_n = \Delta t, \forall n = 0, \cdots, N-1$ is employed then the aforementioned space-time matrices need to be computed only once for all the time. Furthermore, the space-time tangent matrix $[\mathbf{K}^s_{st}]$ in Eq. (6.63) and $\left[\mathbf{K}^f_{st}\right]$ in Eq. (6.68) yield unsymmetrical system of linear equations. These linear equations can be solved by using GpBiCG algorithm (Zhang, 1997). The algorithm should be implemented in an element by element manner for avoiding the assembly of global space-time tangent matrix. Lastly, the complete procedure to solve Eq. (6.63) and Eq. (6.68) with the block-iterative scheme as discussed in this section is summarized in Algorithm 3.

The presentation of v-ST/FEM formulation and its implementation procedure made so far is applicable to a wide class of nonlinear material behavior such as elasto-plasticity, elasto-visco-plasticity, damage-model, nonlinear cyclic models for soils, among others. Moreover, if the hydrodynamic pressure related terms are ignored in governing equations of the solid domain (both partial differential equations and space-time finite element discretization), then the present model-problem transforms into a problem of analyzing the dynamic response of solids with nonlinear stress-strain relationship to the transient loading. To demonstrated the performance of v-ST/FEM the Coaxially-Rotating-Crack-Model (CRCM) will be used to model the concrete material in the dam since the major nonlinearities of typical concrete structures are often caused by cracking. The theoretical and computational aspects of the CRCM model are discussed in the next section.

6.6 A nonlinear smeared crack model for concrete material

Materials such as concrete, mortar, and rocks have very less tensile strength (about 10 percent) than compressive strength and exhibit a quasi-brittle behavior. Tensile fracture in concrete like materials involves progressive micro-cracking, tortuous debonding and other processes of internal damage which eventually coalesce into a macro-cracks. Accordingly, a mass concrete when subjected to the tensile loading undergo strain softening before leading to a complete loss of strength. Fig. 6.1

Algorithm 3: v-ST/FEM algorithm with block-iterative scheme to solve a system of nonlinear-linear coupled equations

Initialization ;

Step-1: Solve a static problem and get the initial displacement $\{\tilde{\mathbf{u}}^0\}$, and stress in the solid-domain, and set $\{\tilde{\mathbf{v}}^0\} = 0$, $\{\tilde{\mathbf{p}}^0\} = 0$, and $\{\tilde{\mathbf{q}}^0\} = 0$;

Start Time Step Loop ;

for *n=0, N-1* **do**

- *Step-2*: Compute and store the fixed space-time tangent matrices for fluid-domain by using Eq. (6.58) and solid-domain by using Eq. (6.65);
- *Step-3*: Compute and store the coupling matrices for solid-domain $\left[\mathbf{H}^s_{fd}\right]$ and fluid-domain $\left[\mathbf{H}^f_{fd}\right]$;
- *Step-4*: Compute and store $\left\{\mathbf{J}^s_{fixed}\right\}$ by using Eq. (6.61);
- *Step-5*: Compute and store $\left\{\mathbf{J}^f\right\}$ by using Eq. (6.59);
- *Step-6*: Set $\{\tilde{\mathbf{v}}\}^{(k)} = 0$ and $\{\tilde{\mathbf{q}}\}^{(k)} = 0$ for $k = 0$;
- **Start Block-Iteration Loop** ;
- **for** *k=1, maxIter* **do**
  - *Step-7*: Compute displacements at time t^1 and t^2 from $\{\tilde{\mathbf{v}}\}^{(k-1)}$ by using Eq. (6.35), and also calculate strains;
  - *Step-8*: Obtain trial stress σ^1 and σ^2 from constitutive model, and use them to compute $\{\mathbf{J}^s_{\sigma^1}\}^{(k-1)}$, $\{\mathbf{J}^s_{\sigma^2}\}^{(k-1)}$ and $[\mathbf{K}^s_{iter}]^{(k-1)}$;
  - *Step-9*: Compute $\{\mathbf{J}^s_{iter}\}^{(k)}$ and assemble the residual $\{\mathbf{R}^s\}^{(k)}$, then solve Eq. (6.63) and update velocity $\{\tilde{\mathbf{v}}\}^{(k)}$ by using Eq. (6.67);
  - *Step-10*: Update the right hand side of Eq. (6.68) by using $\{\tilde{\mathbf{v}}\}^{(k)}$ and $\left\{\mathbf{J}^f\right\}$, and obtain $\left\{\mathbf{q}^f\right\}^{(k)}$;
  - *Step-11*: Check the convergence;
  - **if** *Converged* **then**
    - Update $\{\tilde{\mathbf{u}}^0\}$, $\{\tilde{\mathbf{v}}^0\}$, $\{\tilde{\mathbf{p}}^0\}$, $\{\tilde{\mathbf{q}}^0\}$, and stresses in the solid domain;
    - Go to next time step
  - **else**
    - Go to Step-7
  - **end**
- **end**

end

shows a typical stress-strain relationship for mass concrete from uniaxial tension test obtained by Brühwiler, 1990. At the beginning, a linear relationship between stress and strain exists until the elastic limit is reached. Once the elastic limit is crossed, micro-cracks develop within the mass concrete, which results in nonlinearity in the curve up to the ultimate tensile strength σ_t. The post-peak behavior starts with the strain-softening due to growth of micro-cracks in the weakest cross-section of the specimen which then coalescence into a crack: a geometrical discontinuity that separates the material. Therefore, the stress-strain relationship for the concrete like materials can be divided into two regime: (i) pre-softening regime and (ii) softening regime.

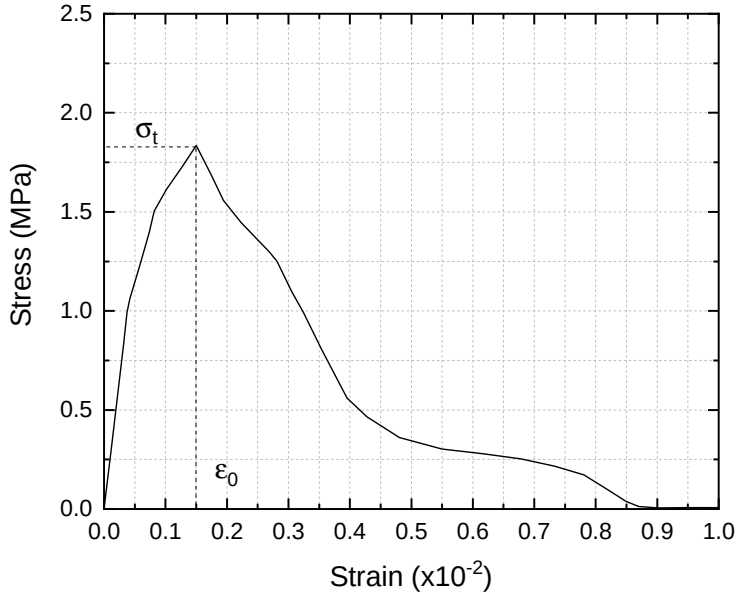

Fig. 6.1.: Typical stress-strain curve for mass concrete from simple tension test after (Brühwiler, 1990)

In what follows the co-axially rotating crack model (CRCM)[3] which is defined by (i) the pre-softening material behavior, (ii) the criterion for crack initiation, (iii) the fracture energy conservation, and (iv) the growth, closing and reopening of cracks, and v-ST/FEM implementation of this constitutive model are presented.

6.6.1 Pre-softening behavior

The stress-strain relationship at a material point is given by

$$\{\sigma\} = [\mathbf{C}] \cdot \{\varepsilon\} \tag{6.71}$$

[3]The CRCM model was first proposed by Bhattacharjee and Leger, 1993 and recently modified by Calayir and Karaton, 2005b

where $[\mathbf{C}]$, $\{\sigma\} = [\sigma_{11}, \sigma_{22}, \sigma_{12}]$ and $\{\varepsilon\} = [\varepsilon_{11}, \varepsilon_{22}, 2\varepsilon_{12}]$ denotes Voigt-form of the constitutive matrix, stress tensor and strain tensor, respectively. In pre-softening case since there are no cracks developed in concrete, the standard elastic plane stress-strain matrix for an isotropic material is used. Then, the matrix $[\mathbf{C}]$ is given by

$$[\mathbf{C}] = \frac{E_0}{1-\nu^2} \begin{bmatrix} 1 & \nu & 0 \\ \nu & 1 & 0 \\ 0 & 0 & \frac{1-\nu}{2} \end{bmatrix} \tag{6.72}$$

where ν is the Poisson's ratio, and E_0 is the modulus of elasticity.

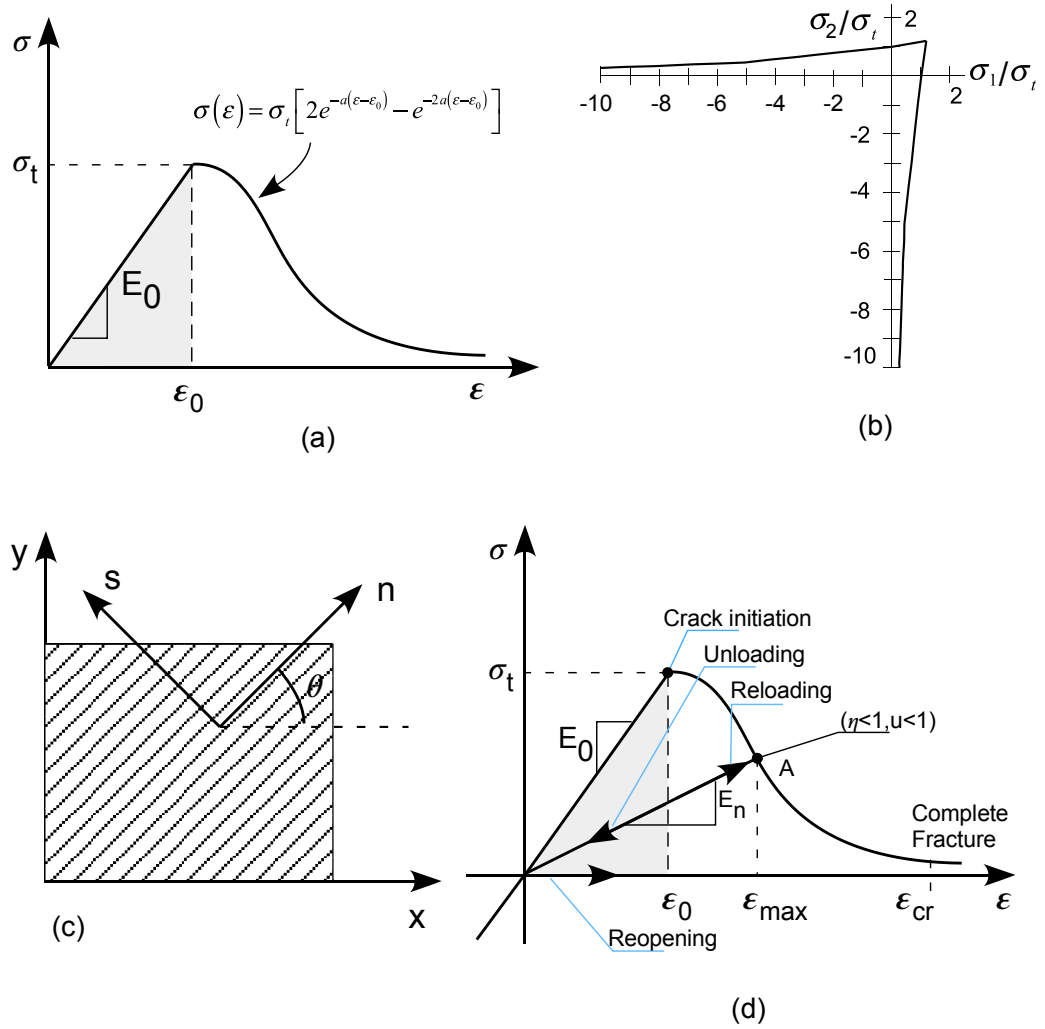

Fig. 6.2.: Constitutive modeling for nonlinear smeared crack analysis. (a) Idealized stress-strain curve for concrete; (b) biaxial stress effect in the strain softening initiation; (c) local axis system; (d) closing and reopening of cracks.

6.6.2 Crack initiation criterion

The stress-strain relationship for concrete becomes non-linear near the peak strength as shown in Fig. 6.2a. In the post-peak strain softening phase, coalescence of the

micro-cracks causes a gradual reduction of the stress resistance. The area under the uniaxial stress-strain curve up to the peak, defined in Eq. (6.71), is taken as the index for softening initiation:

$$U_0 = \frac{1}{2}\sigma_t \varepsilon_0 = \frac{\sigma_t^2}{2E_0} \tag{6.73}$$

where σ_t is the uniaxial tensile strength of mass concrete, ε_0 is the corresponding strain threshold, E_0 is the modulus of elasticity. In the plane-stress finite element analyses, the crack initiation criterion is given by (Bhattacharjee and Leger, 1993; Calayir and Karaton, 2005b)

$$\frac{1}{2}\sigma_1 \varepsilon_1 \geq U_0 \tag{6.74}$$

where σ_1 and ε_1 are the maximum principal stress and strain, respectively. In above equation the term $(\sigma_1 \varepsilon_1/2)$ denotes the tensile strain energy density. Accordingly, the biaxial effect in the crack initiation criterion may be given by

$$\sigma_1 \geq \frac{\sigma_t^2}{E_0 \varepsilon_1} \quad \text{or} \quad \frac{\sigma_1}{\sigma_t} \geq \sqrt{\frac{\sigma_1}{E_0 \varepsilon_1}} \tag{6.75}$$

This equation represents a biaxial failure envelope which is illustrated in Fig. 6.2b It can be observed that strain softening occurs for tension-tension and tension-compression stress states due to tension cracking, however, no cracks develop under compression-compression stress state.

6.6.3 Strain softening model for concrete and fracture energy conservation

Bhattacharjee and Leger, 1993 used a linear strain softening relationship; the tensile resistance of concrete is assumed to decrease linearly from the pre-softening undamaged state to the fully damaged state of zero tensile resistance. Recently, numerous researchers have shown that it is more realistic to assume a strain softening curve with a steep initial decline followed by an extended tail (Kurumatani et al., 2016; Geers et al., 2000; Jirasek and Grassl, 2008; Giry et al., 2011; Peerlings et al., 1998; Calayir and Karaton, 2005b). According to Calayir and Karaton, 2005b, the post-peak strain softening behavior of concrete can be modeled by using following exponential strain softening relationship (see also Fig. 6.2a)

$$\sigma(\varepsilon) = \begin{cases} E_0 \varepsilon, & \varepsilon \leqslant \varepsilon_0 \\ \sigma_t \left[2e^{-a(\varepsilon - \varepsilon_0)} - e^{-2a(\varepsilon - \varepsilon_0)} \right], & \varepsilon_0 < \varepsilon < \varepsilon_{cr} \\ 0, & \varepsilon \geqslant \varepsilon_{cr} \end{cases} \tag{6.76}$$

where ε_{cr} denotes the maximum strain that may not be exceeded during strain softening, and is consistent with the study carried out by Bažant, 1987. The value of ε_{cr} can be calculated when its corresponding stress given is equal to $\delta_{cr}\sigma_t$. Thus, $\sigma = \delta_{cr}\sigma_t$ in Eq. (6.76b) one can expressed ε as

$$\varepsilon_{cr} = \varepsilon_0 + \frac{1}{a}\ln\left(\frac{1+\sqrt{1-\delta_{cr}}}{\delta_{cr}}\right) \tag{6.77}$$

In this study $\delta_{cr} = 0.02$, therefore, ε_{cr} is given by

$$\varepsilon_{cr} = \varepsilon_0 + \frac{4.6}{a} \tag{6.78}$$

In Eqs. (6.76,6.77, 6.78) a is a dimensionless parameter which is related to the slope of the softening curve. The parameter a should be adjusted such that the energy dissipation for a unit area of crack plane propagation is conserved. Let the fracture energy[4] be denoted by G_f. In the energy balance approach it is assumed that the fracture energy G_f will be absorbed due to formation of a unit area of crack surface. When the crack propagates a certain amount of stored energy is released, and the crack can only propagates when the released energy is equal to or greater than the absorbed energy (Hillerborg et al., 1976). The limiting value of a can be obtained b,

$$\int_0^\infty \sigma d\varepsilon := \int_0^{\varepsilon_0} \sigma d\varepsilon + \int_{\varepsilon_0}^\infty \sigma d\varepsilon = \frac{G_f}{l_{ch}} \tag{6.79}$$

Now, use of the stress-strain relationship as given by Eq. (6.76) in above equation will yield following expression for a.

$$a = \frac{3}{\varepsilon_o\left(\frac{2G_f}{l_{ch}\sigma_t\varepsilon_o} - 1\right)} \geqslant 0 \tag{6.80}$$

In Eq. (6.79) and Eq. (6.80), l_{ch} is a geometrical constant which is introduced as a measure of the length of fracture processing zone in mass concrete. In two-dimensional finite element analyses, l_{ch} can be calculated by using the relations given below (Kurumatani et al., 2016),

$$\begin{aligned} \text{Triangular element:} l_{ch} &= \sqrt{2A_e} \\ \text{Quadrilateral element:} l_{ch} &= \sqrt{A_e} \end{aligned} \tag{6.81}$$

in which A_e denotes the area of a two-dimensional finite element.

[4]The fracture energy is defined as the energy per unit area required to form a fracture surface

6.6.4 Constitutive relationship during softening

After the softening initiation, a smeared band of micro-cracks is assumed to appear in the direction normal to the principal the tensile stress. The axes of principal stresses rotates during the cracking. In a co-axially rotating crack model (CRCM), the axes of principal stress and strain are allowed to rotate during or after cracking while assuming stress and strain to be coaxial (Rots, 1991; Bhattacharjee and Leger, 1993; Calayir and Karaton, 2005). The material reference axis system, referred to as the local axis system, is aligned with the principal strain directions (direction $n-s$ in Fig. 6.2c). The constitutive matrix relating the local stresses to local strains is defined as

$$[\mathbf{C}_{ns}] = \frac{E_0}{1-\eta\nu^2}\begin{bmatrix} \eta & \nu\eta & 0 \\ \eta\nu & 1 & 0 \\ 0 & 0 & \mu\frac{1-\eta\nu^2}{2(1+\nu)} \end{bmatrix}; \quad \eta = \frac{E_n}{E_0} \tag{6.82}$$

where $\eta \in [0,1]$ is the ratio of the softened elastic modulus (E_n) in the direction normal to the fracture plane to the initial isotropic elastic modulus (E_0), thus η denotes the damaged state of the material; $\eta = 1$ implies undamaged state and $\eta = 0$ implies a fully damaged state. In this equation, μ is the shear resistance factor defined for the CRCM as follows:

$$\mu = \frac{1+\nu}{1-\eta\nu^2}\left(\frac{\eta\varepsilon_n - \varepsilon_s}{\varepsilon_n - \varepsilon_s} - \eta\nu\right), \qquad \mu \in [0,1] \tag{6.83}$$

where ε_n is the maximum principal strain, $\varepsilon_s = \max(\varepsilon_1, \varepsilon_2)$, which is in normal direction to the fracture plane, and ε_s is the minimum principal strain , $\varepsilon_s = \min(\varepsilon_1, \varepsilon_2)$, which in the direction parallel to the fracture plane (i.e., smeared band of micro-cracks).

It is important to note that in Eq. (6.82) constitutive matrix $[\mathbf{C}_{ns}]$ is defined in the local axis system ($n-s$ direction in Fig. 6.2c). However, in a finite element computation this matrix is transformed to the global $x-y$ coordinate directions, $[\mathbf{C}_{global}]$, by using

$$[\mathbf{C}_{global}] = [\mathbf{R}]^T [\mathbf{C}_{ns}] [\mathbf{R}] \tag{6.84}$$

where

$$[\mathbf{R}] = \begin{bmatrix} \cos^2\theta & \sin^2\theta & \sin\theta\cos\theta \\ \sin^2\theta & \cos^2\theta & -\sin\theta\cos\theta \\ -2\sin\theta\cos\theta & 2\sin\theta\cos\theta & \cos^2\theta - \sin^2\theta \end{bmatrix} \tag{6.85}$$

in which θ is the angle between the n-axis and x-axis as shown in Fig. 6.2c.

With increasing strain softening, the damaged elastic modulus E_n (see Fig. 6.2d), and therefore the parameters η and μ decrease gradually and may eventually reach zero values after complete fracture ($\varepsilon_n > \varepsilon_{cr}$). The damaged state constitutive

matrix given in Eq. (6.82) is updated as the parameters η and μ change their values, and these changes are also reflected in the global constitutive matrix (see Eq. 6.84). In addition, the change in global constitutive matrix $[\mathbf{C}_{global}]$ is also caused by a rotation of the local axis system, which is always kept aligned with the directions of principal strains to keep the principal stresses and strains coaxial. The CRCM is very effective in alleviating the stress locking which is usually observed in fixed crack models (Rots, 1991).

6.6.5 Closing and reopening of cracks

During the unloading/reloading, when the strain, ε_n, is less than the previously attained maximum value, ε_{max} (see Fig. 6.2d), the secant modulus, E_n and therefore η, do not change; however, the parameter μ changes during this process. During unloading the shear reduction factor, μ, gradually increases with the reduction of ε_n. The damaged state elastic modulus in the normal direction, E_n (which may have reached a zero value), is replaced by the undamaged initial value, E_0, if the parameter μ is greater than a threshold value μ_c. In this study $\mu_c = 0.95$ is considered. In subsequent loading steps, when $\varepsilon_n > 0$, the value μ is determined by using the damaged value η to determine the reopening of cracks. If μ becomes less than μ_c, the element behavior is determined by either reloading or the reopening path depending on the final state attained in previous tensile cycles. The appropriate value of the damage modulus, E_n, is reused in Eq. (6.82) at that state.

In what follows an informal explanation regarding the the physical significance of CRCM during the unloading/reloading process is presented. Imagine the smeared band of micro-cracks developed inside the test-specimen subjected to dynamic loading. In addition, assume that the material is partially damaged (this state is described by point-A in Fig. 6.2d). At this stage, strength of the material has degraded in both normal and tangential directions to the plane. In CRCM this corresponds to the $\eta < 1.0$ and $\mu < 1.0$, where the former and later are related to the strength reduction in normal and tangential directions, respectively. At this stage, if loading continues then η and μ will keep decreasing denoting the strength reduction in smeared band due to growth of cracks. In case of unloading, the normal strain ε_n decreases and cracks start closing, accordingly the shear resistance factor, μ, starts to increase compare to its value at point-A in Fig. 6.2d. This signifies the gain of strength in tangential direction to the damaged plane due to the partial closing of cracks. During unloading, as long as the cracks are still opened (i.e. $\mu < \mu_c$), the strength in the normal direction remains same as that of point-A. In CRCM, this behavior is simulated by keeping E_n and η fixed to their values at point point-A as long as the condition $\mu < \mu_c$ is satisfied. The condition $\mu \geq \mu_c$ depicts the state of fully closed cracks. In this situation material regains its undamaged initial

compressible strength. In addition to $\mu \geq \mu_c$, one should also check the value of η since $\eta < 1$ and $eta = 1$ refer to the damaged and undamaged state, respectively. During reloading, partially or fully closed cracks reopen, and the condition $\mu < \mu_c$ is satisfied. The element behavior is determined by either reloading or the reopening path depending on the final state attained in previous tensile cycles. The appropriate values, η, μ, and E_n should be used in Eq. (6.82) to compute the constitutive matrix.

6.6.6 Finite element implementation

In the finite element implementation of CRCM strains are computed at each integration point and the average of Gaussian point strains is taken as representative of the behavior of the element as a whole (Bhattacharjee and Leger, 1993; Calayir and Karaton, 2005b). In space-time finite element procedures there are two different ways to compute the average strains: (i) average of space-time integration point strains in a space-time element, (ii) average of space-integration point strains in spatial-element at a given time instant. Henceforth, the term space-time averaged strain and space averaged strain will be used for the average strain obtained from the former and later procedures, respectively. The steps involved in implementation of CRCM are given below.

Step-1: Compute the space-time averaged strain or space averaged strain as follows

$$\varepsilon_{st}^{avg} = \frac{1}{n_{ipt} n_{ips}} \sum_{\alpha=1}^{n_{ipt}} \sum_{\beta=1}^{n_{ips}} \varepsilon_{\beta}^{\alpha}$$

$$\varepsilon_{s}^{avg} = \frac{1}{n_{ips}} \sum_{\beta=1}^{n_{ips}} \varepsilon_{\beta}^{\alpha}$$

where ε_{st}^{avg} denotes the space-time averaged strain, ε_{s}^{avg} denotes the space averaged strain, $\varepsilon_{\beta}^{\alpha}$ is the strain defined at space-time integration point, n_{ipt}, n_{ips} are the total number of integration points for space and time domain, respectively.

Step-2: Compute the principal strains (ε_n, ε_s) and principal direction θ of averaged strain tensor;

Step-3: Check loading condition;

If($\varepsilon_n \geq \varepsilon_{max}$) Then
  $\varepsilon = \varepsilon_n$; Loading $= .True.$
Else
  $\varepsilon = \varepsilon_{max}$; Loading $= .False.$
End If

Step-4: Check damaged state of material and compute η;

If($\varepsilon \geq \varepsilon_0$) Then
  Damaged $= .True.$
  If($\varepsilon \geq \varepsilon_{cr}$) Then
    $\eta = 0.0$;
  Else
    $\eta = \frac{\varepsilon_0}{\varepsilon}\left[2e^{-a(\varepsilon-\varepsilon_0)} - e^{-2a(\varepsilon-\varepsilon_0)}\right]$
    (see Eq. 6.80)
  End If
Else
  Damaged $= .True.$; $\eta = 1.0; \mu = 1.0$
End If

Step-5: Check the crack-closing condition

If($\mu \geq 0.95$ .and. Damaged .and. .Not. Loading) Then
  $\eta = 1.0$
End If

Step-6: Compute the local constitutive matrix by using η and μ in Eq. (6.82), and then compute global constitutive matrix by transformation of local constitutive matrix (see Eq. 6.84).

Step-7: Compute stress by using

$$\left\{\sigma_\alpha^\beta\right\} = [\mathbf{C}_{global}]\left\{\varepsilon_\alpha^\beta\right\}$$

where $\left\{\sigma_{\alpha}^{\beta}\right\}$ and $\left\{\varepsilon_{\alpha}^{\beta}\right\}$ are the vector of stress and strain components in Voigt-notation corresponding to a space-time integration point.

6.7 Dynamic response of the nonlinear dam without hydrodynamic effects

Koyna concrete gravity dam, which is extensively analyzed in several previous studies (Bhattacharjee and Leger, 1993; Calayir and Karaton, 2005b; Calayir and Karaton, 2005a; Cervera et al., 1995; Omidi et al., 2013; Ghrib and Tinawi, 1995), is selected for numerical application. This dam is one of the few concrete dams that have experienced a destructive earthquake. The earthquake of December 11, 1967, with maximum and minimum acceleration around 0.5g, caused significant structural damage of the dam, including horizontal cracks on the upstream and down streams faces of a number of number of non-overflow monoliths around the elevation at which the slope of downstream face changes abruptly.

In this section, the nonlinear dynamic fracture analysis of Koyna concrete gravity dam which is subjected to both horizontal and vertical components of earthquake motion is performed. The physical dimensions and finite element mesh of the tallest section of the dam are illustrated in Fig. 6.3. The dam is 103 m tall and 70 m wide at the base. The height of water in the reservoir is taken to be 90.5 m and the upstream face of the dam is assumed to be straight and vertical. The dam is subjected to the self-weight and hydrostatic pressure loads to determine the pre-seismic state.

Further, the concrete material in the dam is modeled by using the co-axially rotating crack model (CRCM) which is described in the previous section. The material parameters for the concrete dam are selected as follows: The elastic modulus (E) is 31027 MPa, the Poisson's ratio (ν) is 0.2, the mass density (ρ) is 2643 Kg/m^3, the ultimate tensile strength (σ_t) is 1.5 MPa and the fracture energy (G_f) is 150 N/m. Dynamic loading affects the concrete material parameters. Elastic modulus of concrete is generally considered to be less sensitive to strain rate than the tensile strength and fracture energy Bhattacharjee and Leger, 1993. Due to strain rate effects, the tensile strength and the fracture energy are increased by 20% approximately, leading to the values of 1.8 MPa and 180 N/m. Further, damping in the concrete dam is modeled by Rayleigh damping with critical damping ratio of 5% in the fundamental vibration mode of the dam alone with no cracking. The resultant values of damping coefficients are $\alpha = 0.0026$ and $\beta = 0.9676$.

Numerical simulations are carried out for the horizontal and vertical components of the Koyna accelerogram (Fig. 6.4) without considering the hydrodynamic in-

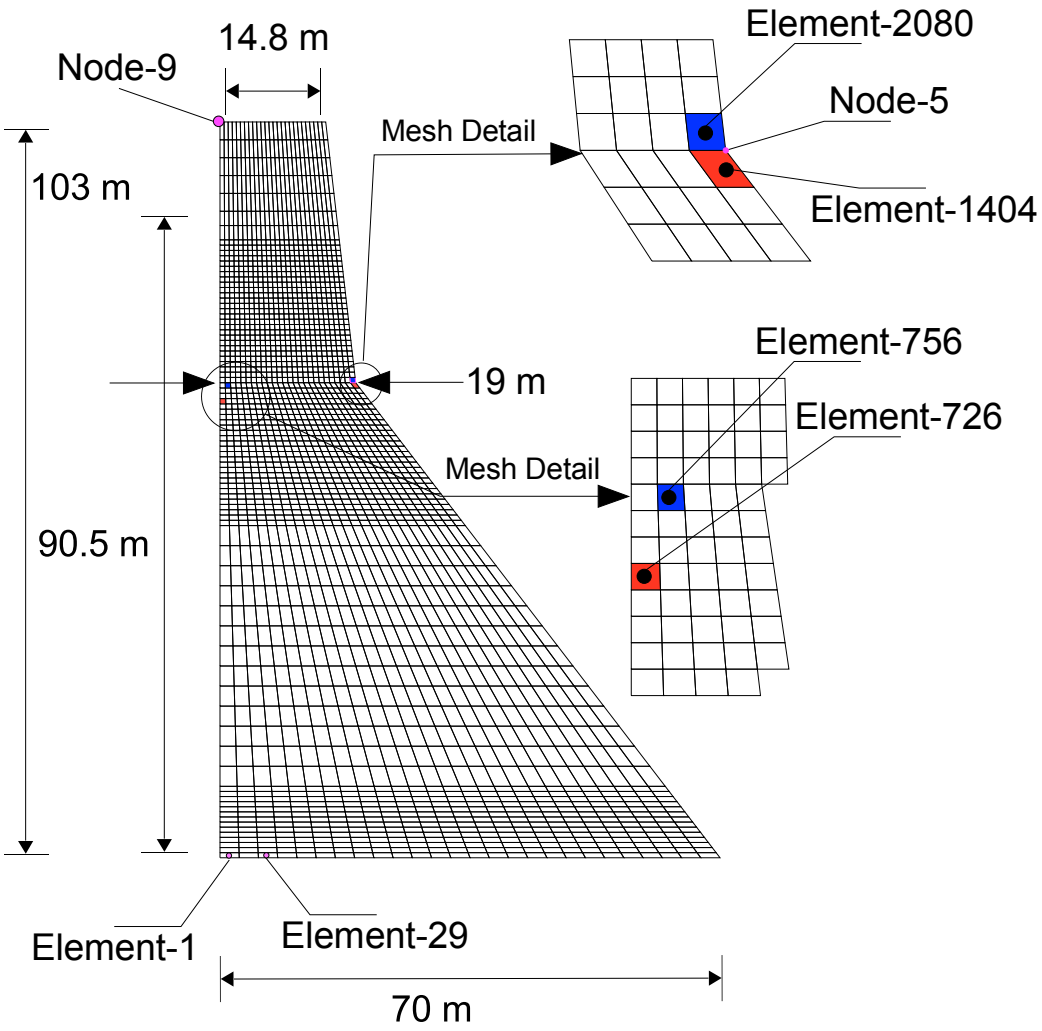

Fig. 6.3.: Physical dimensions and finite element mesh of the Koyna dam.

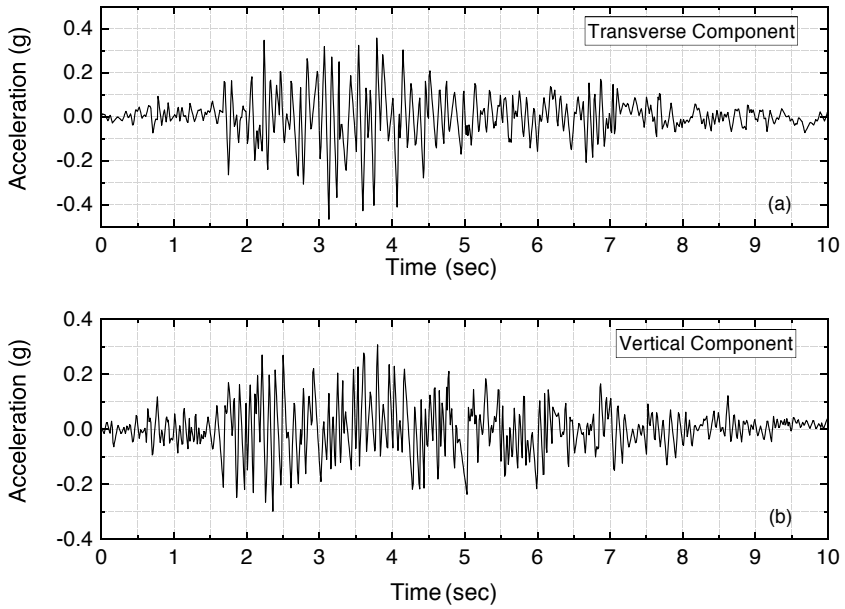

Fig. 6.4.: The Koyna-1967 earthquake ground motion: (a) Transverse component, and (b) vertical component

teractions between the dam and reservoir [5]. A uniform time step size $\Delta t = 0.01$ s is adopted for time integration, and the resultant unsymmetrical system of linear equations is solved by using the GpBiCG algorithm with tolerance value of 1.0×10^{-6}. In this section, dynamic response of the dam is computed by using following three different v-ST/FEM schemes:

(i) *v-ST/FEM-1*, which represents the v-ST/FEM with a three-point Gauss-Lobatto integration rule for computing Eq.(6.43) and Eq.(6.46) (see also Eq. 6.50). In finite element implementation of CRCM, average of spatial-integration point strains is taken as representative of the behavior of the spatial-element as a whole.

(ii) *v-ST/FEM-2*, which represents the v-ST/FEM with a two-point Gauss-Legendre integration rule for computing Eq.(6.43) and Eq.(6.46) (see also Eq. 6.49). In finite element implementation of CRCM, average of spatial-integration point strains is taken as representative of the behavior of the spatial-element as a whole.

(iii) *v-ST/FEM-3*, which represents the v-ST/FEM with a two-point Gauss-Legendre integration rule for computing Eq.(6.43) and Eq.(6.46) (see also Eq. 6.49). In finite element implementation of CRCM, average of space-time integration point strains is taken as representative of the behavior of the space-time element as a whole.

[5] Hydrodynamic interactions between the dam and reservoir are included in Section 6.8

The contents of this section are as follows. In Section 6.7.1, *v-ST/FEM-1* is employed to compute the nonlinear response of the Koyna dam. Subsequently, the nonlinear response of the dam is compared with the linear response to examine the effects of cracking in the concrete material. The last two subsections then assess the performances of these v-ST/FEM schemes.

6.7.1 Results for *v-ST/FEM-1* scheme

This section examines the cracking effects of the concrete material on the seismic response of the concrete dam. In linear analysis isotropic, homogeneous, linear elastic stress-strain relationship is used for the concrete whereas for nonlinear analysis material behavior is modeled by CRCM. *v-ST/FEM-1* with tolerance in residual and velocity set to 1.0×10^{-3} (see Eq. 6.69 and Eq. 6.70) is employed to compute the nonlinear response of the Koyna dam.

Fig. 6.6 and Fig. 6.8 show the time history graphs of the horizontal and vertical components of the displacement, velocity, and acceleration at node-9 [6] and node-5 [7] of the dam, respectively. Due to the infinite rigidity of the foundation, a stress concentration induces a crack at the base of the dam. At time $t = 1.89$ sec, the heel of the dam (element-1 in Fig. 6.3) softens completely (i.e., $\eta \approx 0$) which corresponds to the case of complete fracture of that element, subsequently, the crack propagates horizontally in the downstream direction along the base of the dam. The cracks at the base of the dam then extend to an approximate distance of 13 m from the heel of the dam. During the upstream movement of the dam around $t = 2.94$ sec element-2080 in the dam starts softening. The crack, however, does not propagate instantaneously since more elements at the base of the dam continue softening. The spatial distribution of CRCM parameter η, which indicates the strength reduction of the material in the direction normal to the fractured plane, at time $t = 2.73$ sec is depicted in Fig. 6.11a, and the corresponding deformed configuration of the dam is plotted in Fig. 6.12a.

During the upstream movement of the dam, around time $t = 3.91$ sec, a fully opened crack appears in the element-2080 which subsequently propagates in the horizontal direction towards the downstream face of the dam. This process forms a localized band of cracked elements in the neck-area of the dam which can be seen from the deformed configuration of the dam given in Fig. 6.12b. Fig. 6.11b depicts the spatial distribution of the CRCM parameter, η, at time $t = 3.91$ sec, where it is noteworthy that due to the upstream movement of the dam cracks at the base are

[6] Node-9 corresponds to the crest of the dam see Fig. 6.3

[7] Node-5 corresponds to the point at the downstream face of the dam where discontinuity in the slope of the downstream face occurs as shown in Fig. 6.3

closed. The continued upstream movement of the dam causes the cracks in the neck-area of the dam to propagate in the downward direction towards the upstream face of the dam (see Fig. 6.11c and Fig. 6.12c). Subsequently, the downstream movement of the dam causes new cracks at the base and the upstream face of the dam. In addition during this time, the band of cracks near the element-2080 starts to close. Accordingly, the elements in this regime momentarily gain their original compressive strength (see Fig. 6.10). Spatial distribution of the CRCM parameter, η, and deformed configuration of the dam at time $t = 4.15$ sec are presented in Fig. 6.11d and Fig. 6.12d depict, respectively.

The maximum displacement at node-9 of the dam in the upstream direction occurs at time $t = 4.35$ sec as depicted in Fig. 6.6. At this instant, the spatial distribution of the CRCM parameter, η, and the corresponding deformed configuration of the dam are illustrated in Fig. 6.11e and Fig. 6.12e, respectively. The maximum horizontal and vertical displacement of the node-9, which occurs at time $t = 4.55$ sec as depicted in Fig. 6.6, corresponds to the situation where element-726 at the upstream face of the dam undergoes a complete strain-softening. This is confirmed by the deformed configuration of the dam at time $t = 4.55$ given in Fig. 6.12f. The spatial distribution of the parameter η, which is given in Fig. 6.11f, shows the localization of a crack band meeting the downstream crack profile in the dam interior. At this time, the cracks near the downstream face close as the dam swings towards the downstream direction. Accordingly, the maximum compressive principal stresses inside the element-2080 of the dam achieve a peak value of 9 MPa around this time (see Fig. 6.10). At this instant the entire neck of the dam is damaged, and the subsequent motion of the cracked dam is dominated by rigid-body rocking of the upper portion of the dam.

From the time-history graphs of displacement, velocity and acceleration plotted in Fig. 6.6 (at node-9) and Fig. 6.8 (at node-5) it is evident that the vibration period of the dam increases due to crack propagation in the dam. This effect is clearly visible in the corresponding Fourier spectrums presented in Fig. 6.7 and Fig. 6.9, where the cracking in concrete dam shifts the spectrum towards the lower frequency regime.

The time history graphs of the maximum tensile and compressive principal stresses occurred in the element-1, element-726, and element-2080 are plotted in Fig. 6.10. [8] The maximum tensile principal stresses for the linear case take larger peak values while the maximum peak values of those for the nonlinear case are about the tensile strength of the concrete. In Fig. 6.10 it is visible that the tensile strength of an element is completely removed after the cracking. The maximum compressive

[8] Element-1 is located at the base of the dam, element-726 is located at upstream face of the dam, and element-2080 is located at the downstream face of the dam where the discontinuity in the slope occurs as shown in Fig. 6.3

principal stresses for linear case also generally take larger peak values than those for nonlinear case. However, in situations where a crack closes completely (i.e., $\mu \geq 0.95$), peak values of the maximum compressive principal stresses in nonlinear case are slightly more than the peak values of those for the linear case (see Fig. 6.10). Lastly, the evolution of CRCM parameter η in selected elements of the Koyna dam is depicted in Fig. 6.5.

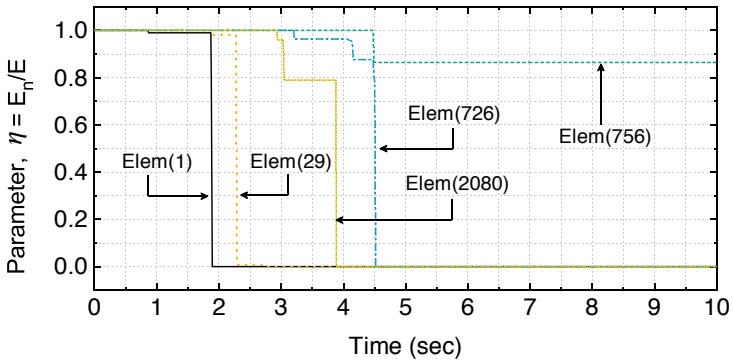

Fig. 6.5.: Evolution of the CRCM parameter, $\eta = E_n/E_0$, for some elements of the Koyna dam obtained by using the *v-ST/FEM-1* without considering the hydrodynamic effects of the reservoir.

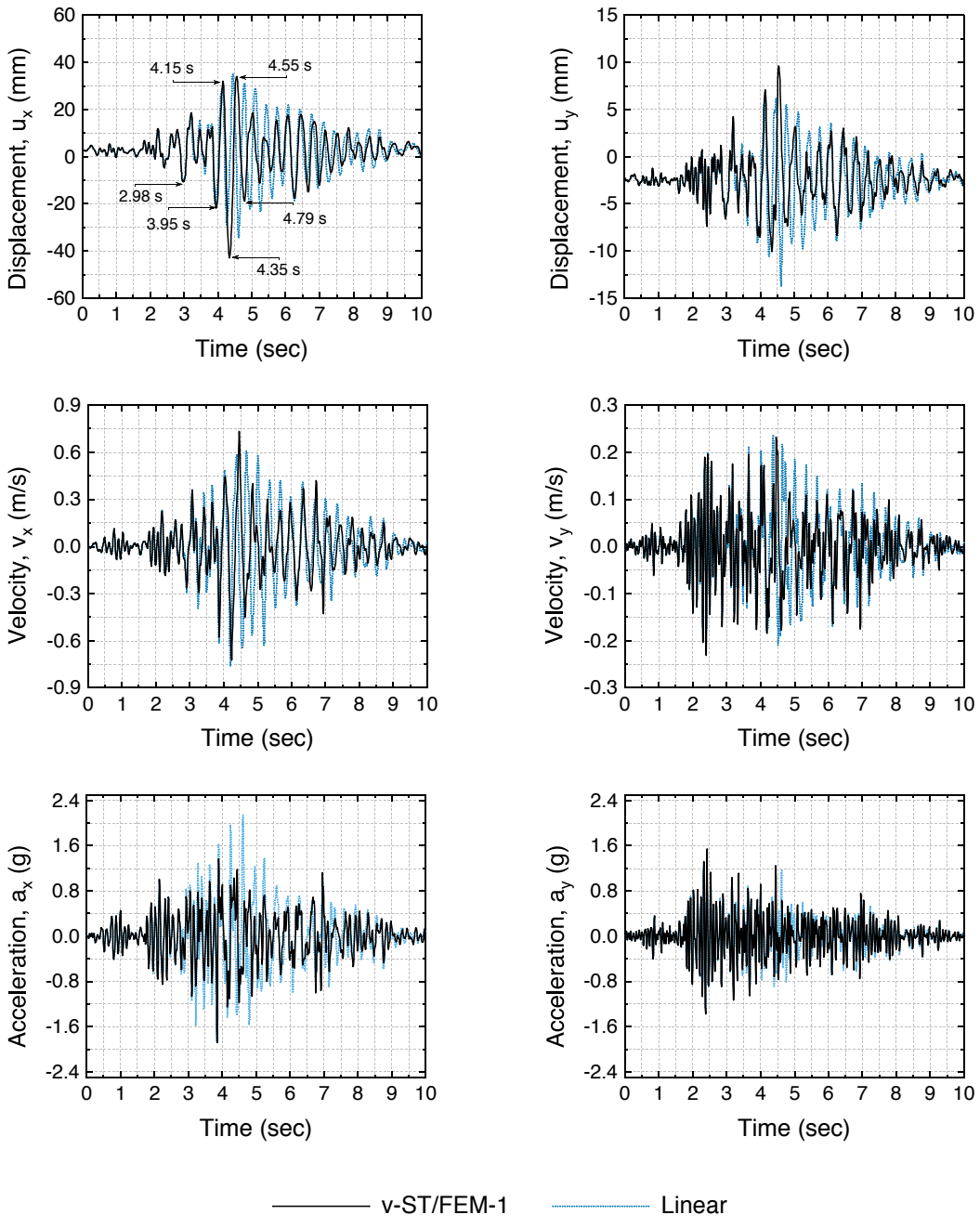

Fig. 6.6.: Time history graphs of the displacement, velocity and acceleration at the crest of the Koyna dam (node-9) computed by using *v-ST/FEM-1* without considering the hydrodynamic effects of the reservoir.

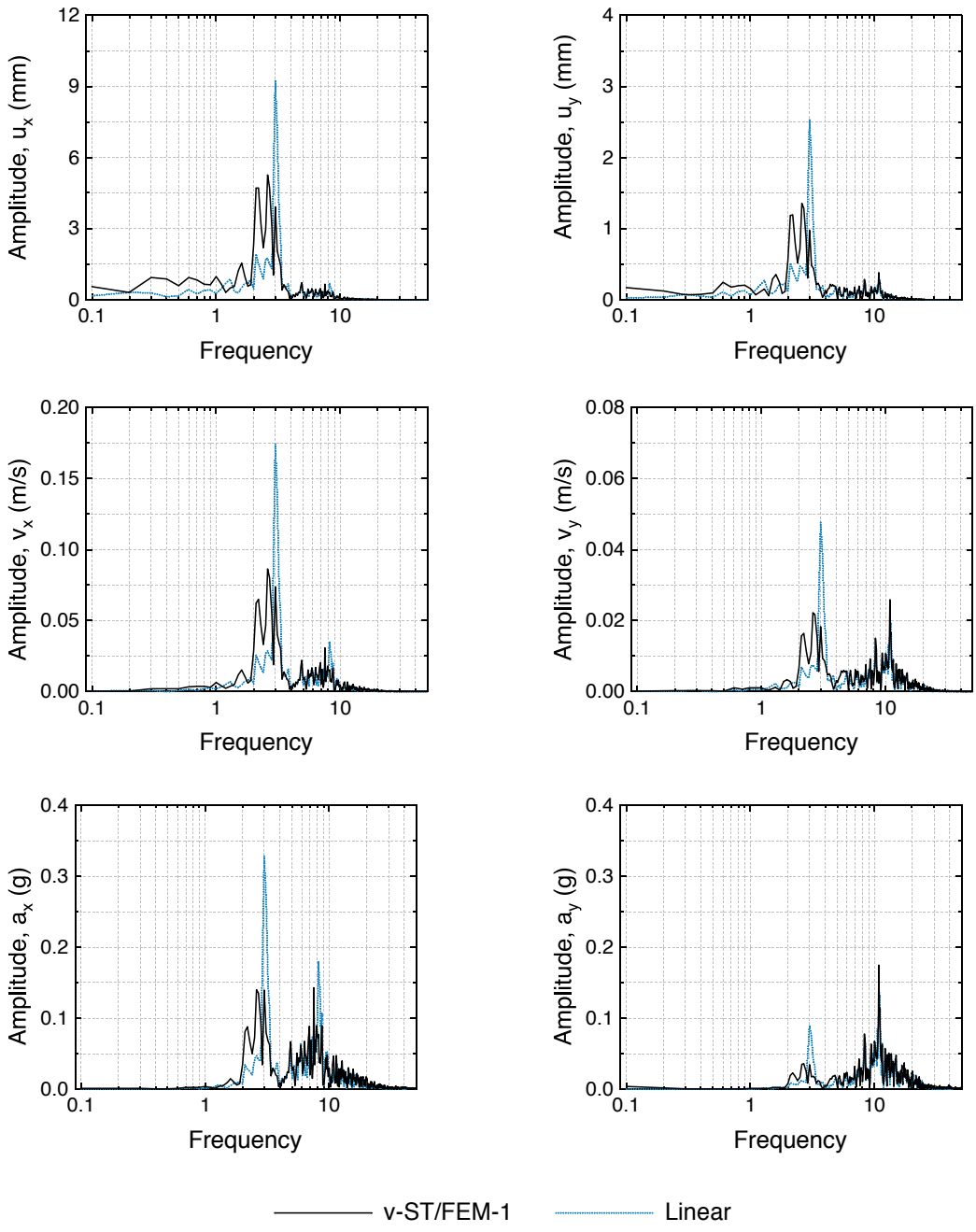

Fig. 6.7.: Fourier spectrum of the displacement, velocity and acceleration at the crest of the Koyna dam (node-9) computed by using *v-ST/FEM-1* without considering the hydrodynamic effects of the reservoir.

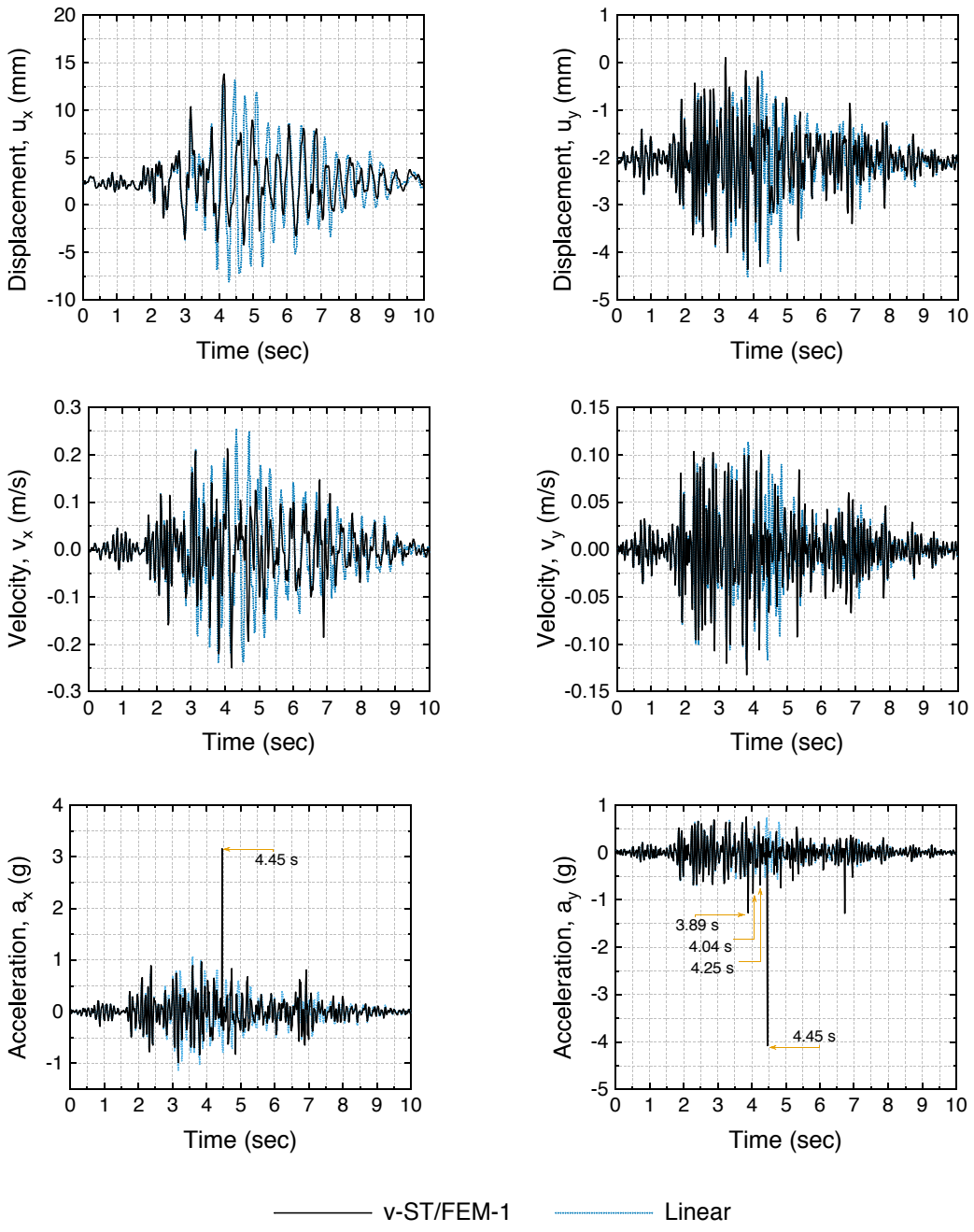

Fig. 6.8.: Time history graphs of the displacement, velocity and acceleration at node-9 of the Koyna dam computed by using *v-ST/FEM-1* without considering the hydrodynamic effects of the reservoir.

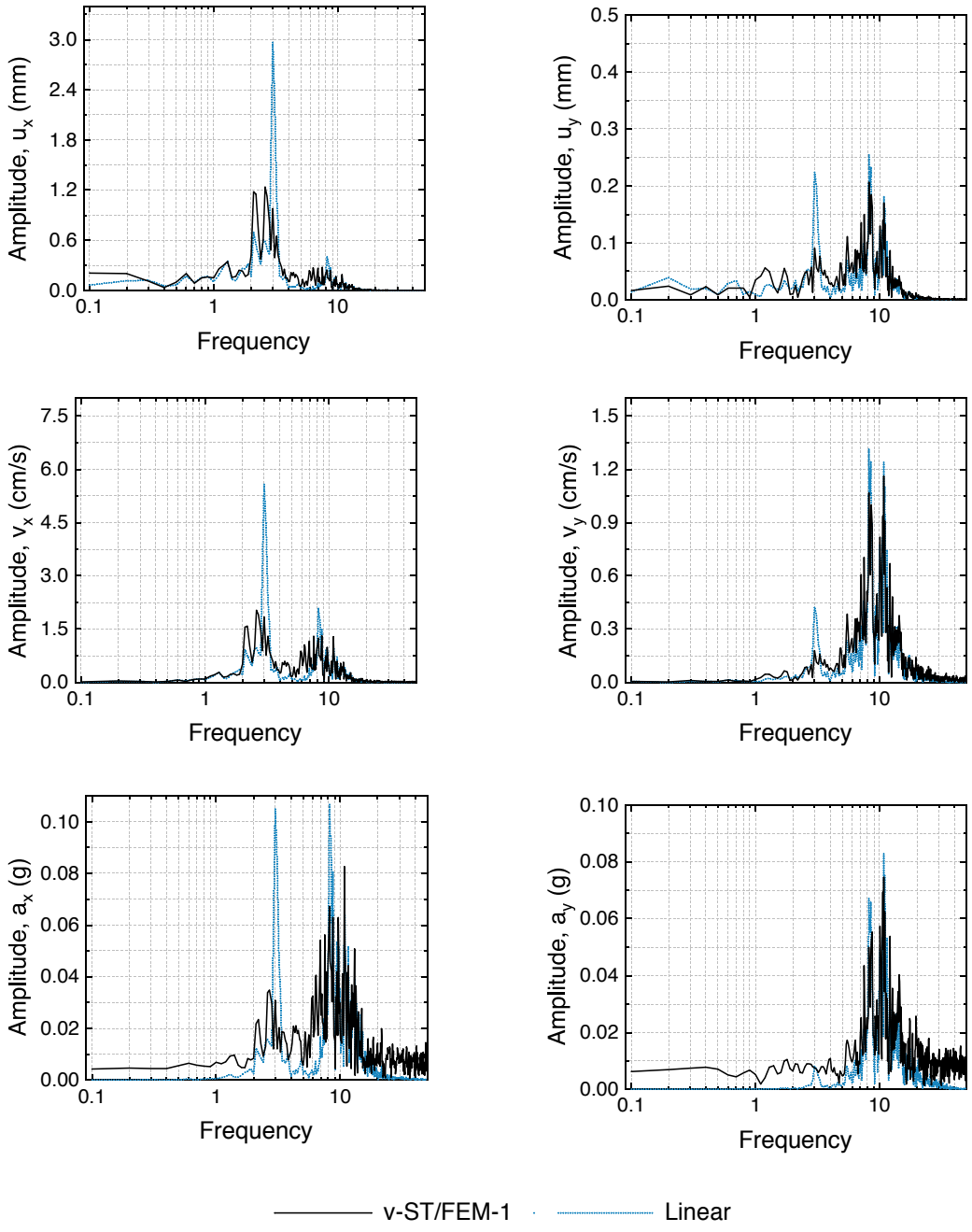

Fig. 6.9.: Fourier spectrum of the displacement, velocity and acceleration at node-9 of the Koyna dam computed by using *v-ST/FEM-1* without considering the hydrodynamic effects of the reservoir.

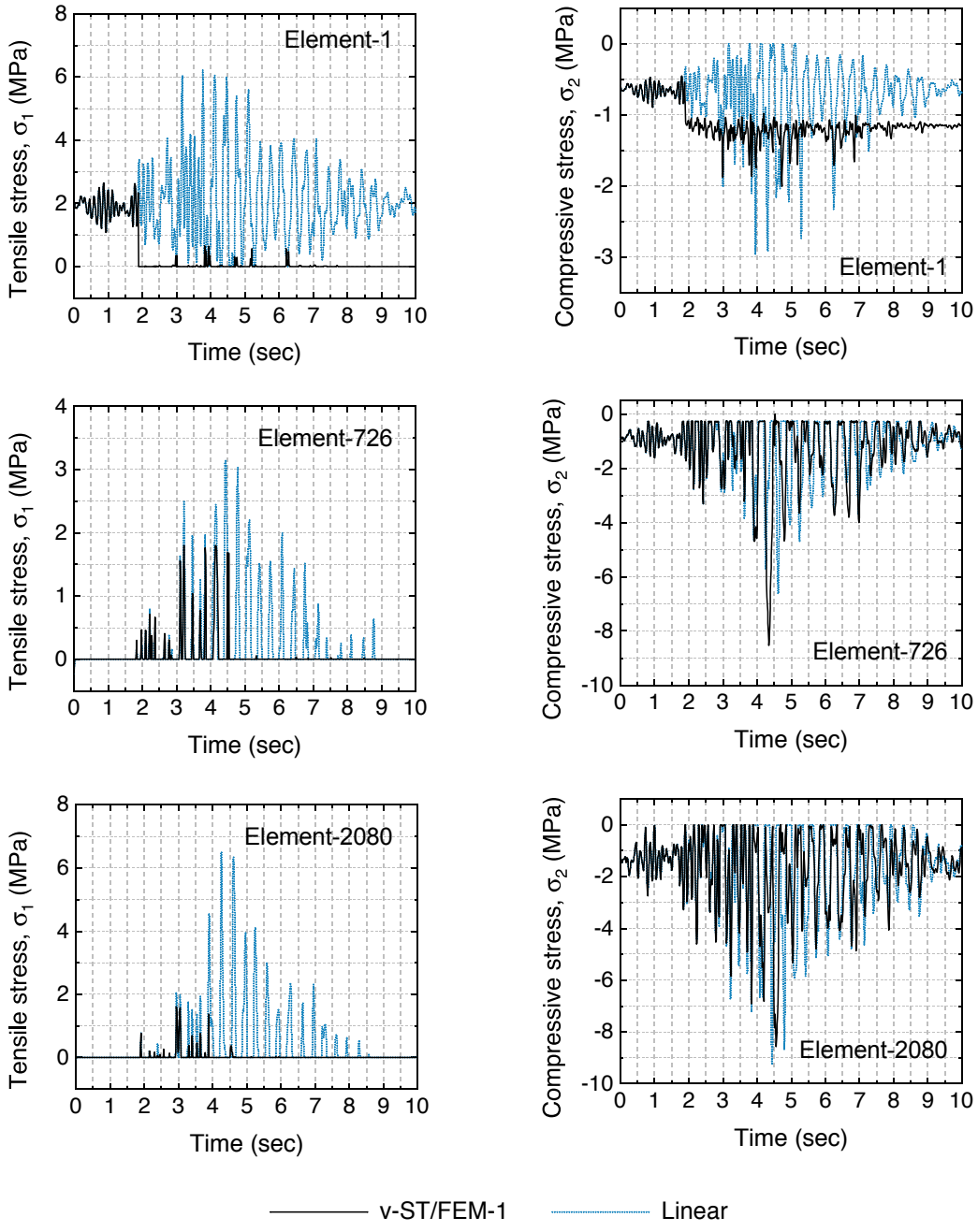

Fig. 6.10.: Time history graphs of the maximum tensile principal stresses, σ_1 on the left hand side, and maximum compressive principal stresses, σ_2 on the right hand side, inside the selected elements of the Koyna dam computed by using *v-ST/FEM-1* without considering the hydrodynamic effects of the reservoir.

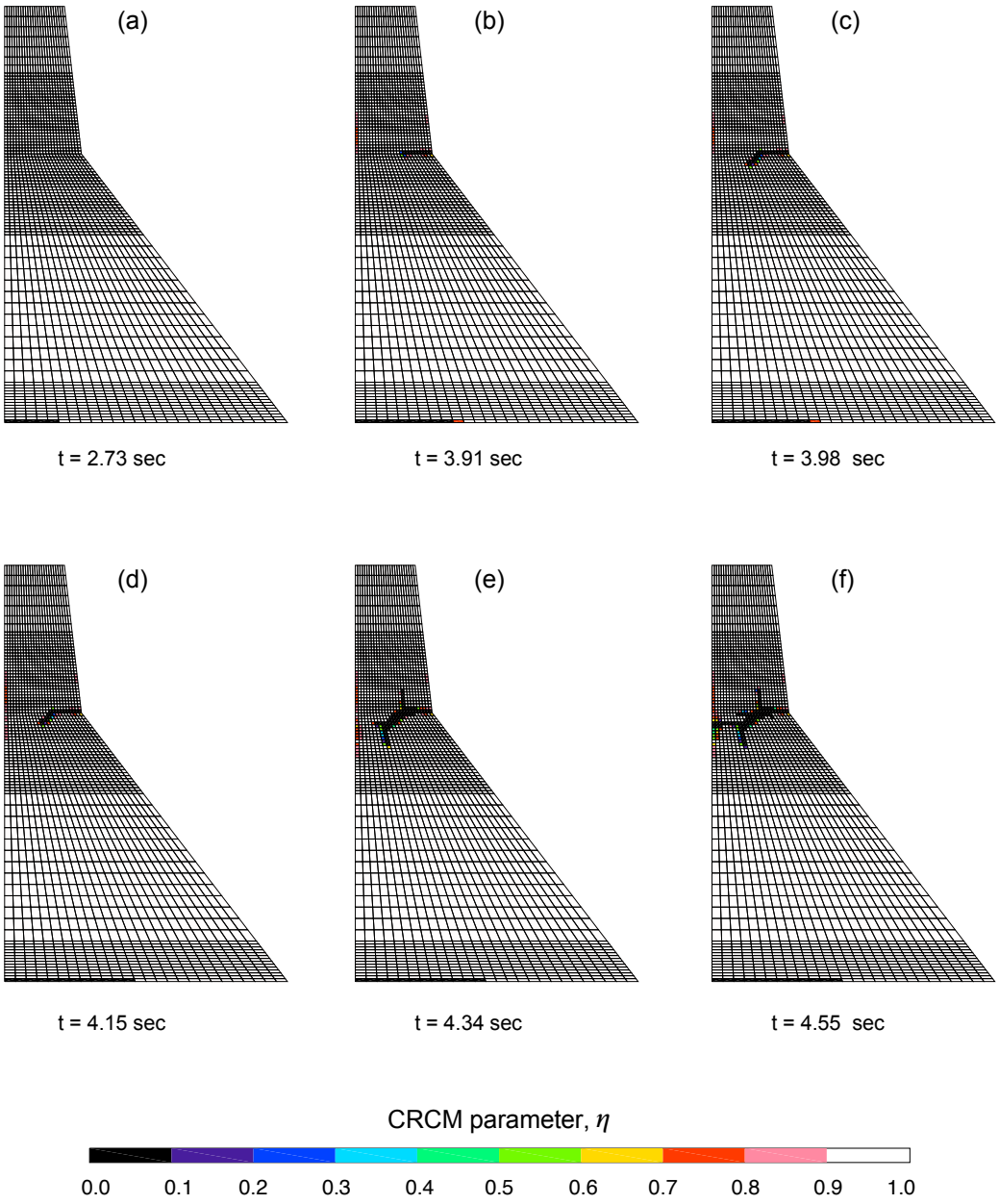

Fig. 6.11.: Spatial distribution of the CRCM parameter, $\eta = E_n/E_0$ in Koyna dam at selected times computed by using the *v-ST/FEM-1* without considering the hydrodynamic effects of the reservoir.

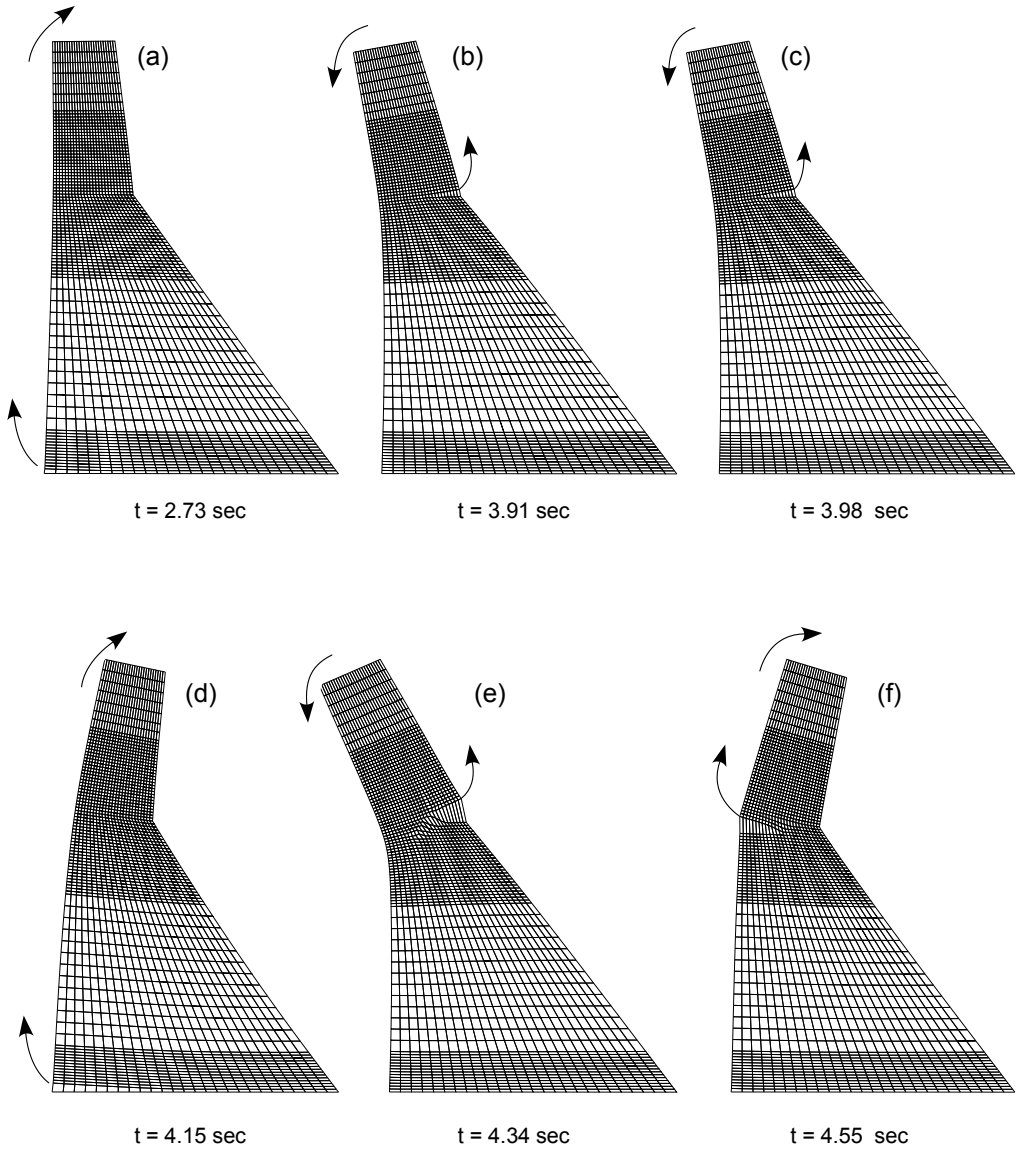

Fig. 6.12.: Amplified deformed configuration of the Koyna dam at selected times computed by using the *v-ST/FEM-1* without considering the hydrodynamic effects of the reservoir.

6.7.2 Results for *v-ST/FEM-2* scheme

In this section, the nonlinear dynamic response of the Koyna dam is computed by using the *v-ST/FEM-2* with the tolerance in residual and velocity is set to 1.0×10^{-3}. The analysis terminates at about 6.8 sec because of an energy balance error during the rigid body rocking of the upper part of the dam body. Fig. 6.14 and Fig. 6.15 compare the temporal variation of the displacement, velocity and acceleration at node-9 and node-5 of the dam obtained by employing *v-ST/FEM-1* and *v-ST/FEM-2*. The results obtained by using *v-ST/FEM-2* are nearly identical to those obtained by using the *v-ST/FEM-1*. The spatial distribution of the CRCM parameter η and the deformed configuration of the dam at selected times are given in Fig. 6.16 and Fig. 6.17, respectively, which is nearly identical to those obtained in case of $v - ST/FEM - 1$ (see Fig. 6.11 and Fig. 6.12. The evolutions of CRCM parameter η in element-726 and element-2080 obtained by using *v-ST/FEM-1* and *v-ST/FEM-2* are plotted in Fig. 6.13 which further confirm that these two schemes predict the event of cracking nearly at the same time.

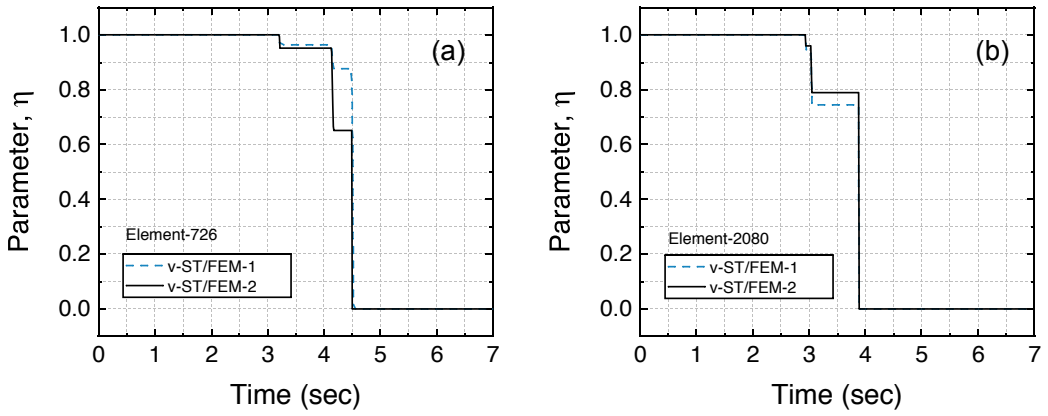

Fig. 6.13.: Comparison of the CRCM parameter, $\eta = E_n/E_0$, in (a) element-726 and (b) element-2080 of the Koyna-dam obtained by using *v-ST/FEM-1* and *v-ST/FEM-2* schemes.

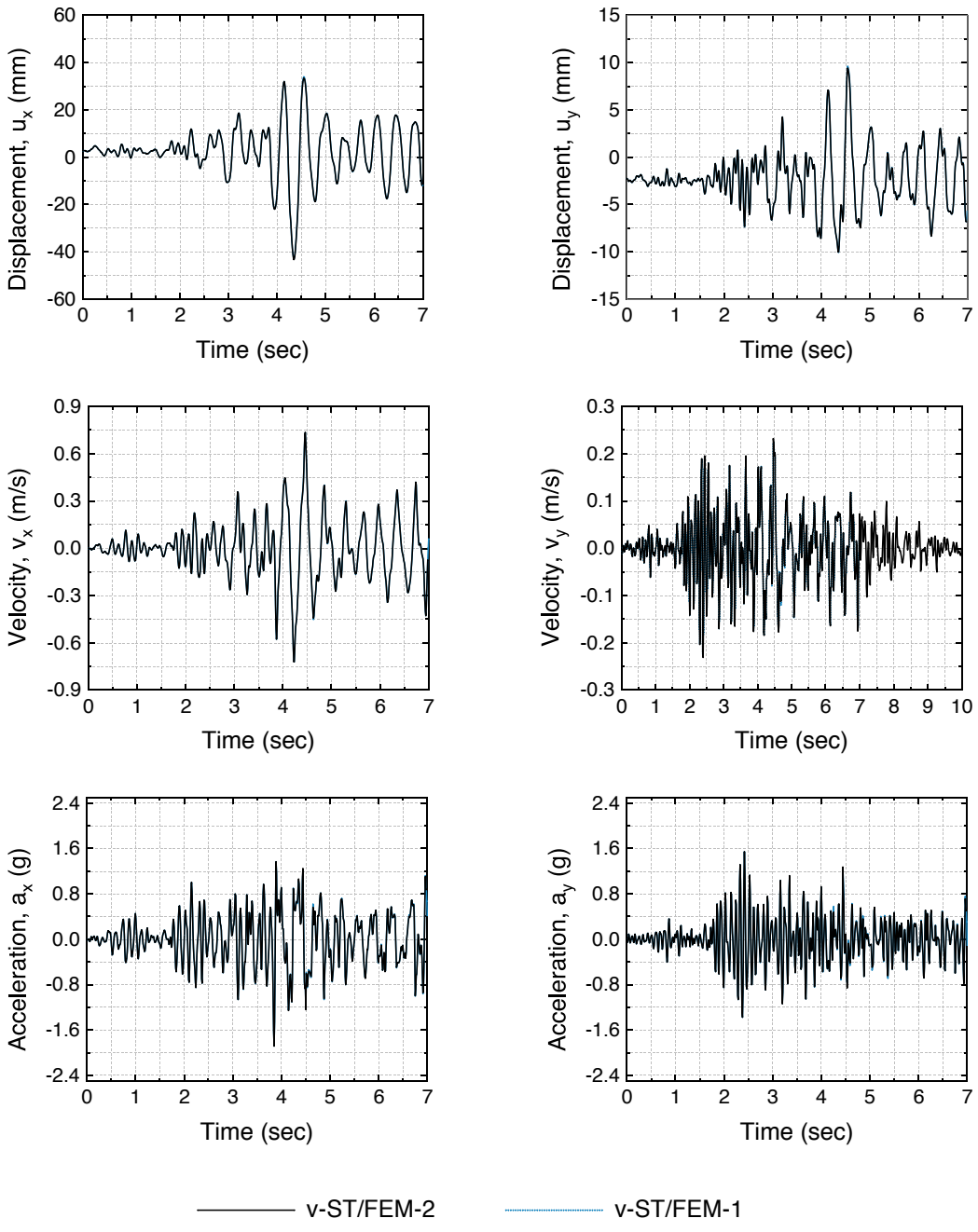

Fig. 6.14.: Comparison of the displacement, velocity and acceleration responses at node-9 of the Koyna-dam computed by using the *v-ST/FEM-1* and *v-ST/FEM-2* without considering the hydrodynamic effects of the reservoir.

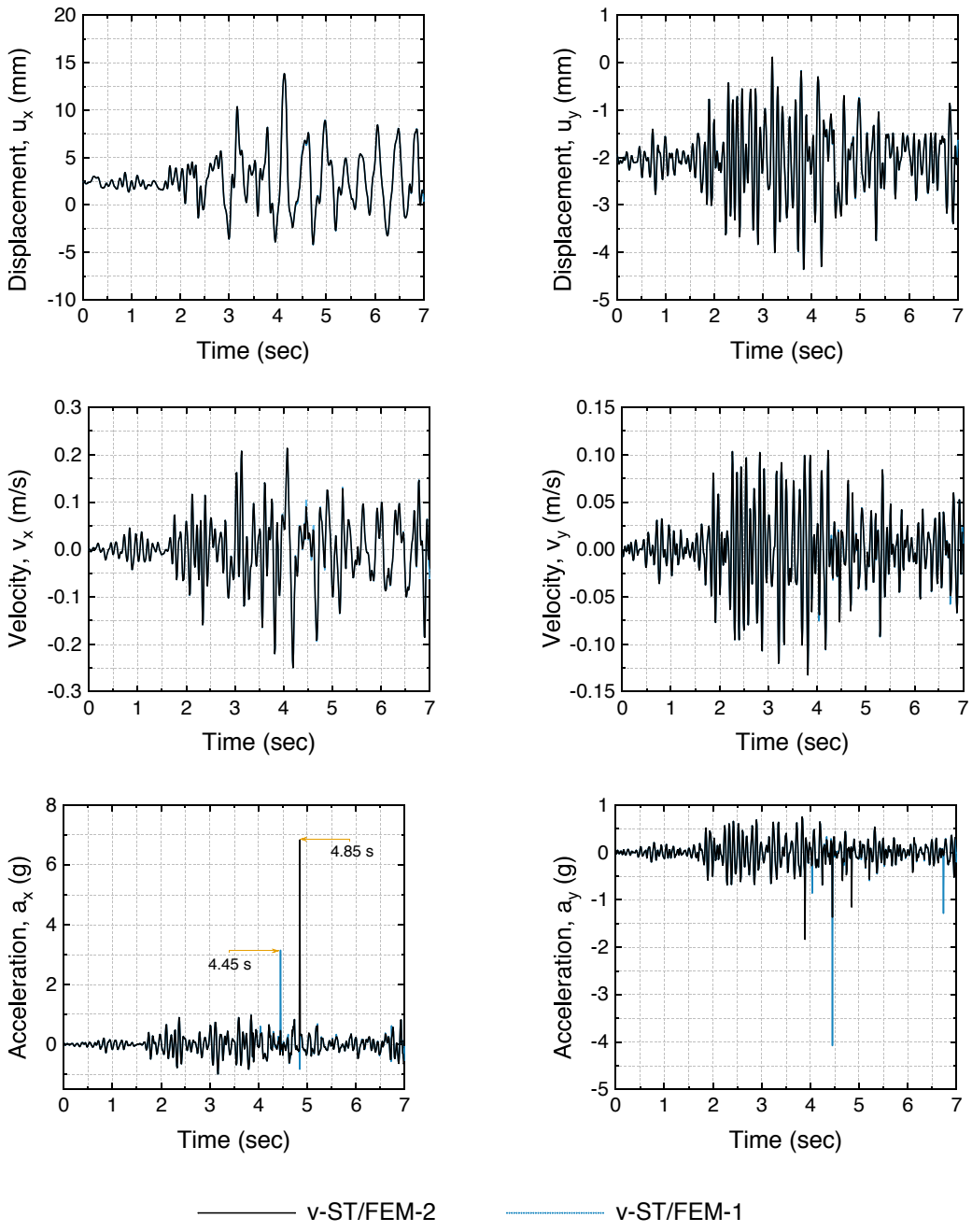

Fig. 6.15.: Comparison of the displacement, velocity and acceleration responses at node-5 of the Koyna-dam computed by using the *v-ST/FEM-1* and *v-ST/FEM-2* without considering the hydrodynamic effects of the reservoir.

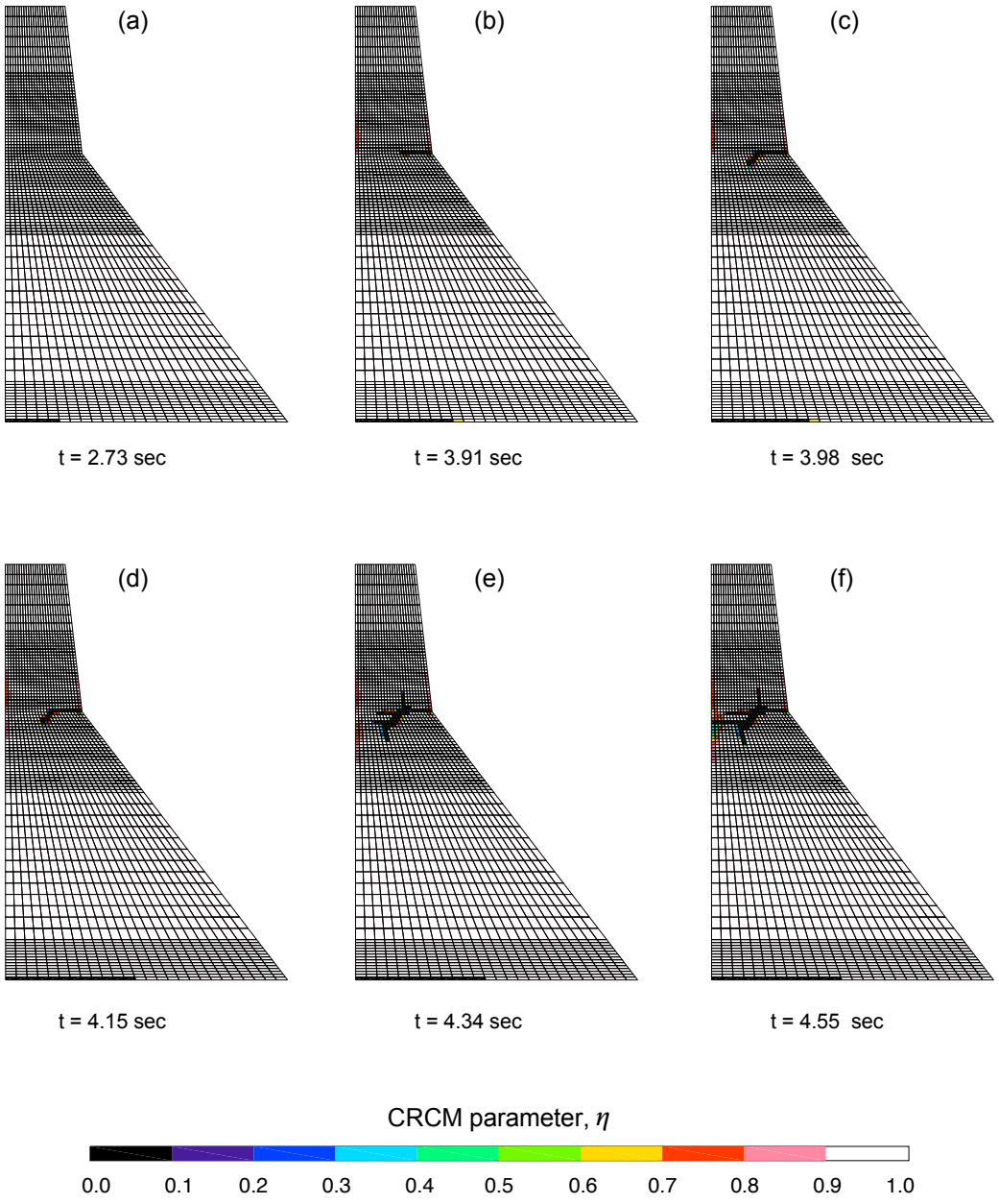

Fig. 6.16.: Spatial distribution of the CRCM parameter, $\eta = E_n/E_0$ in Koyna dam at selected times computed by using the *ν-ST/FEM-2* without considering the hydrodynamic effects of the reservoir.

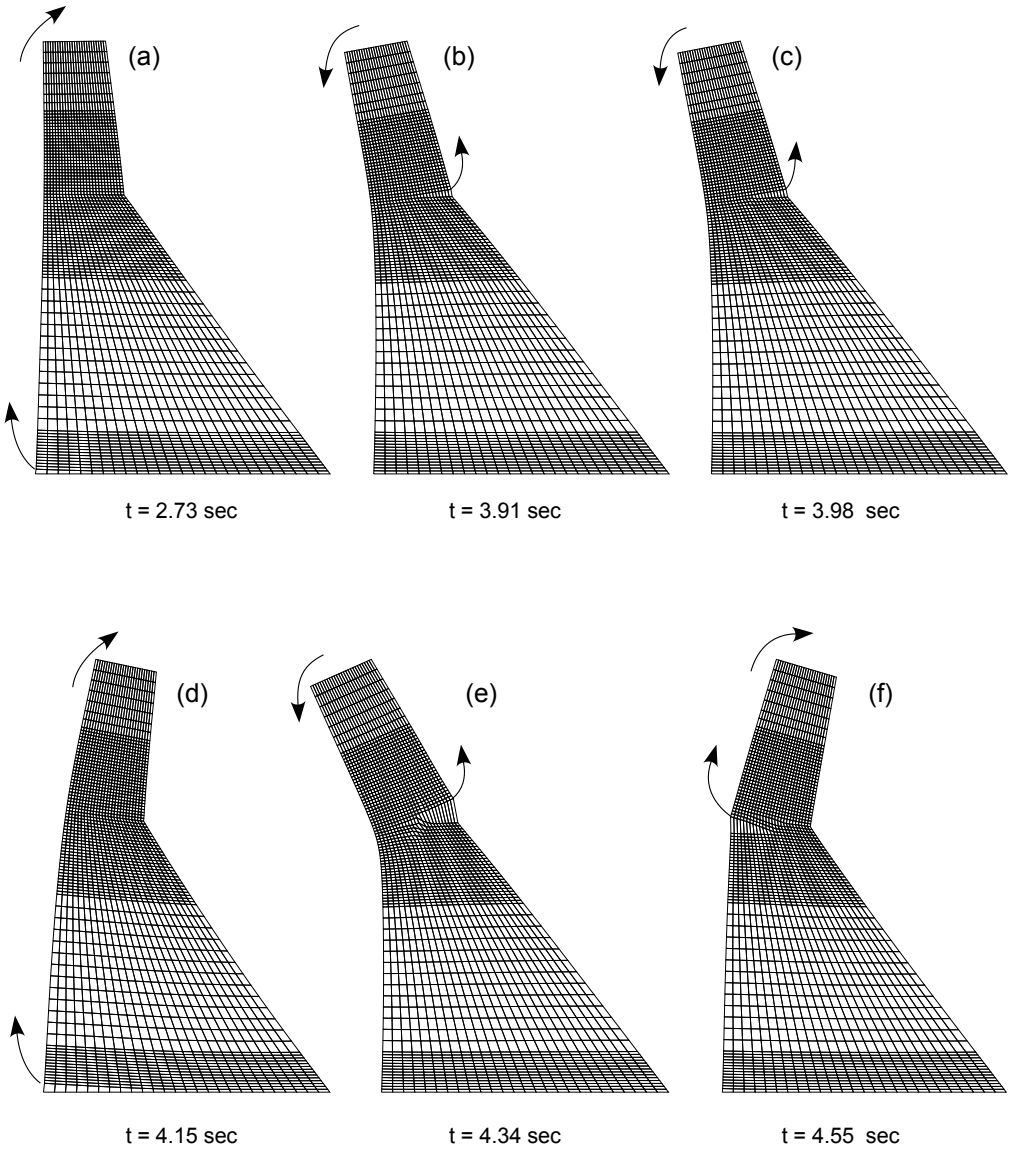

Fig. 6.17.: Amplified deformed configuration of the Koyna dam at selected times computed by using the *v-ST/FEM-2* without considering the hydrodynamic effects of the reservoir.

6.7.3 Results for *v-ST/FEM-3* scheme

In this section, the nonlinear dynamic response of the Koyna dam is computed by using the *v-ST/FEM-3* with the tolerance in residual and velocity is set to 1.0×10^{-2}. Unlike *v-ST/FEM-2* this scheme could converge for all the time steps. Fig. 6.19 and Fig. 6.20 compare the displacements, velocity, and acceleration time history at node-9 and node-5 obtained by using *v-ST/FEM-3* with those obtained by *v-ST/FEM-1* and *v-ST/FEM-2*.

The spatial distribution of the CRCM parameter (Fig. 6.21), η, and the corresponding deformed configuration (Fig. 6.22) of the dam obtained by using *v-ST/FEM-3* are consistent with those obtained by using other v-ST/FEM schemes. Evolution of the CRCM parameter, η, in different v-ST/FEM schemes is plotted in Fig. 6.18 which confirms that the events of cracking predicted by the proposed schemes are nearly identical with the each other.

Furthermore, it should be noted that in case of *v-ST/FEM-3* the dynamic response is obtained at relatively low tolerance value. It is remarkable that the numerical solutions obtained by using the *v-ST/FEM-3* at low tolerance are nearly identical to those obtained by using the *v-ST/FEM-1* and *v-ST/FEM-2* at relatively high tolerance. In addition, the use of space-time averaged strains as representative of the behavior of the space-time element as a whole significantly improves the convergence of the numerical scheme.

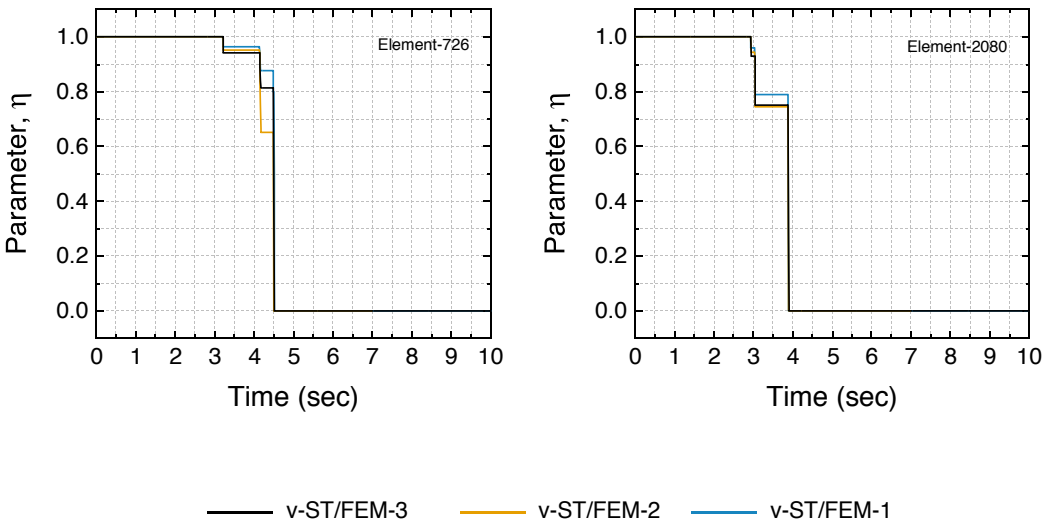

Fig. 6.18.: Comparison of the CRCM parameter, $\eta = E_n/E_0$, in (a) element-726 and (b) element-2080 of the Koyna-dam obtained by using the *v-ST/FEM-1*, *v-ST/FEM-2* and *v-ST/FEM-3*.

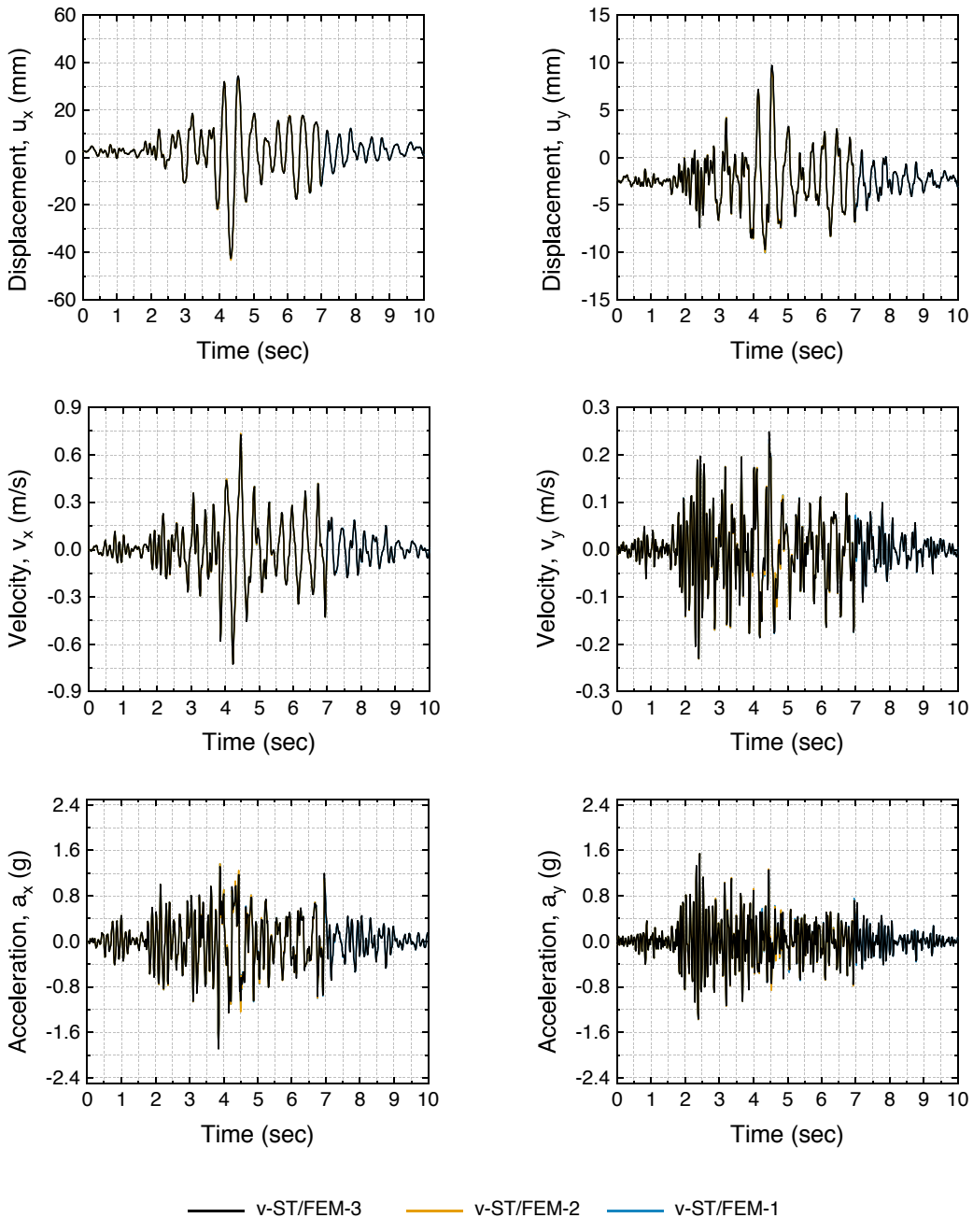

Fig. 6.19.: Comparison of the displacement, velocity and acceleration responses at node-9 of the Koyna-dam computed by using the *v-ST/FEM-1*, *v-ST/FEM-2* and *v-ST/FEM-3* without considering the hydrodynamic effects of the reservoir.

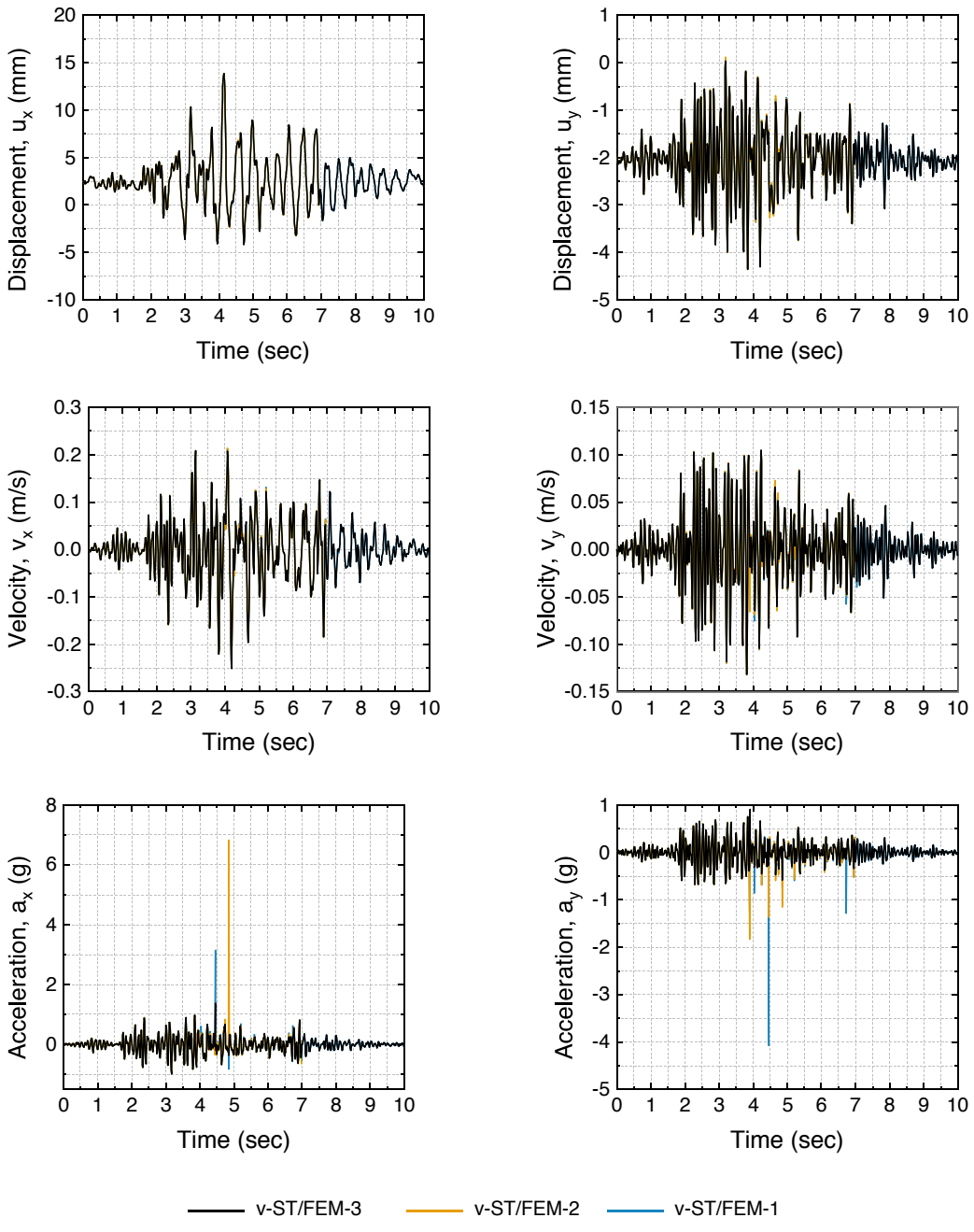

Fig. 6.20.: Comparison of the displacement, velocity and acceleration responses at node-5 of the Koyna-dam computed by using the *v-ST/FEM-1*, *v-ST/FEM-2* and *v-ST/FEM-3* without considering the hydrodynamic effects of the reservoir.

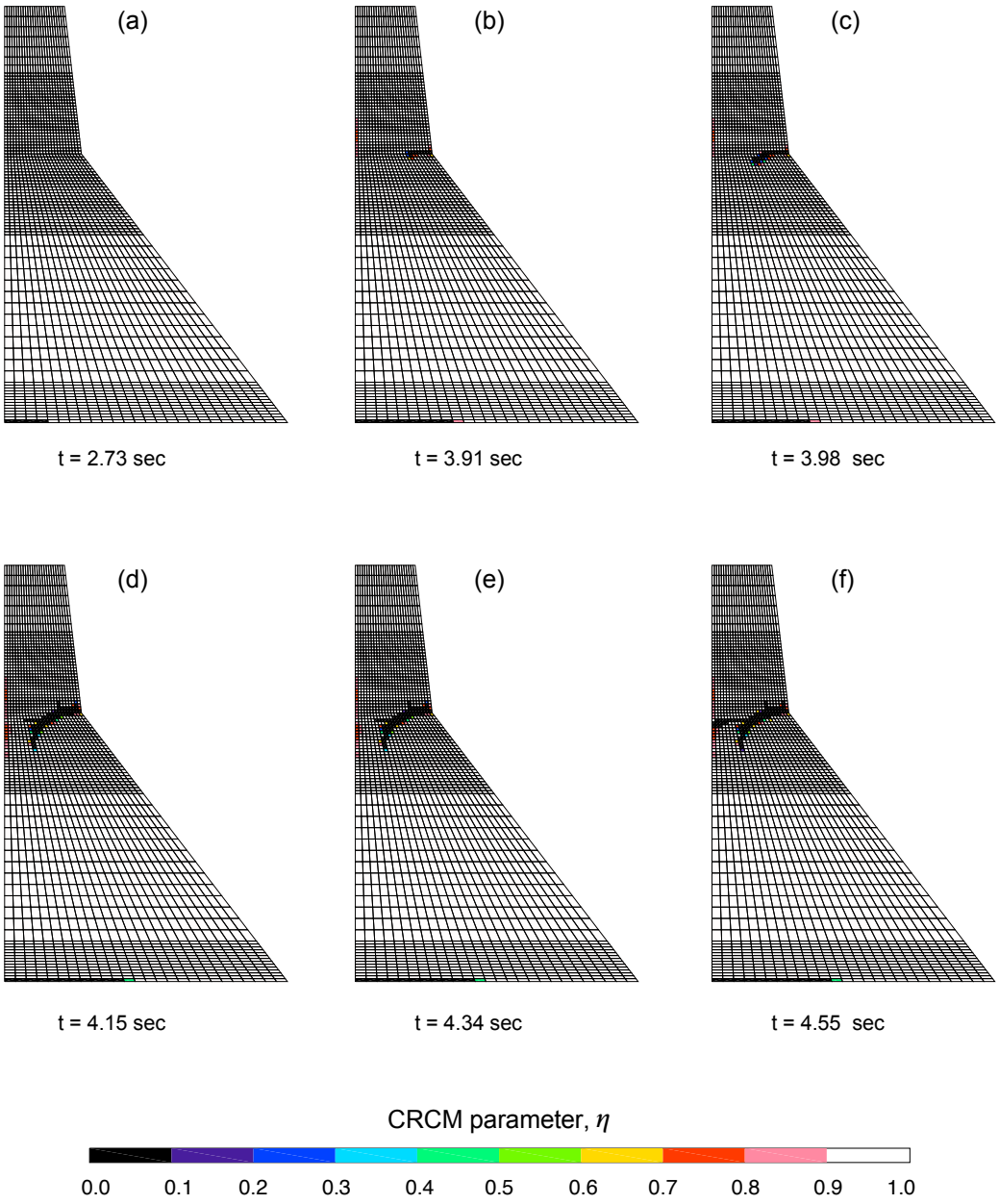

Fig. 6.21.: Spatial distribution of the CRCM parameter, $\eta = E_n/E_0$ in Koyna dam at selected times computed by using the *v-ST/FEM-3* without considering the hydrodynamic effects of the reservoir.

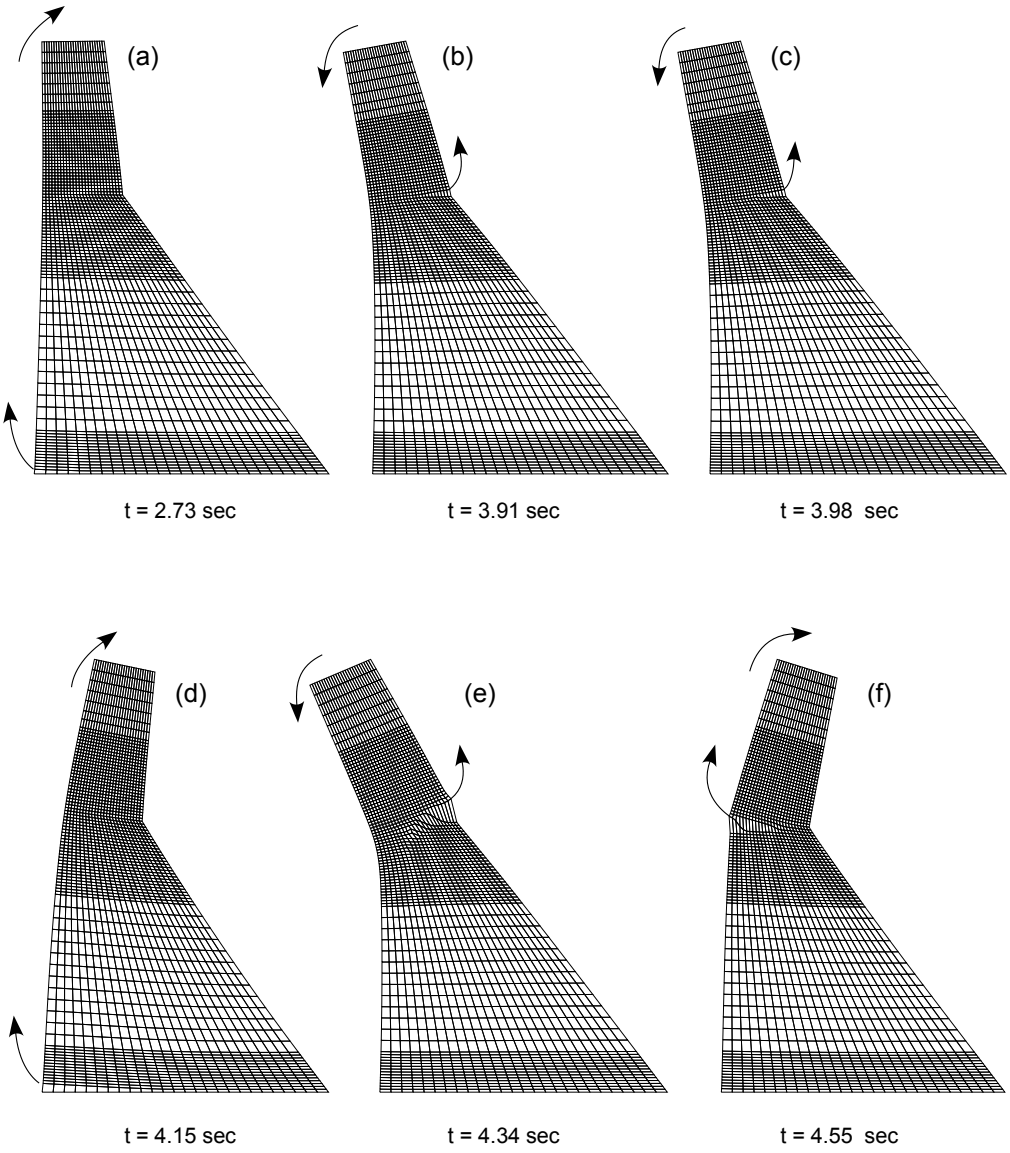

Fig. 6.22.: Amplified deformed configuration of the Koyna dam at selected times computed by using the *v-ST/FEM-3* without considering the hydrodynamic effects of the reservoir.

6.8 Dynamic response of nonlinear dam including hydrodynamic effects

In this section, the nonlinear dynamic fracture analysis of Koyna concrete gravity dam subjected to the earthquake motion is performed including the dynamic interactions between the dam and reservoir. The physical dimensions, finite element mesh and the material properties of the concrete dam are identical to the those presented in the previous section. The height of water in the reservoir, H_f, is assumed to be constant at a value of 90.5 m. Reservoir domain is truncated by placing a viscous boundary at a distance of 412 m, which is four times the height of the concrete dam, from the dam in the upstream direction. Fig. 6.23 depicts the finite element mesh of the reservoir used for the numerical simulations. The speed of acoustic wave in water is 1439 m/s, and the mass density of the water is 1000 kg/m^3. The wave reflection coefficient α_b for reservoir bottom is taken as unity (i.e., reservoir bottom acts as a perfect reflector for the hydrodynamic pressure waves).

Numerical simulations are carried out for the horizontal and vertical components of the Koyna accelerograms plotted in Fig. 6.4. The dam-reservoir interactions are modeled by solving the system of coupled equations using the v-ST/FEM and the block-iterative scheme presented in this chapter. For time integration a uniform time step size $\Delta t = 0.01$ sec is adopted, and GpBiCG algorithm with tolerance value of 1.0×10^{-6} is used to solve the resultant unsymmetrical system of linear equations. In Section 6.8.1, *v-ST/FEM-1* is employed to compute the nonlinear response of the dam-reservoir (DR) system. Subsequently, the nonlinear response of the DR system is compared with the linear response to examine the effects of cracking in the concrete material. Section 6.8.2 then compare the performances of *v-ST/FEM-1* and *v-ST/FEM-3* schemes.

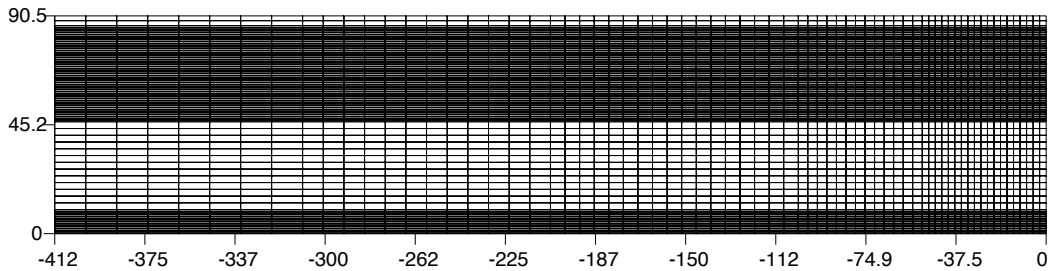

Fig. 6.23.: Finite element mesh for the reservoir domain.

6.8.1 Results for *v-ST/FEM-1* scheme

This section examines the cracking effects of the concrete material on the seismic response of the concrete dam. In linear analysis isotropic, homogeneous, linear elastic stress-strain relationship is used for the concrete whereas for nonlinear analysis material behavior is modeled by CRCM. *v-ST/FEM-1* with tolerance in residual and velocity set to 1.0×10^{-3} (see Eq. 6.69 and Eq. 6.70) is employed to compute the nonlinear response of the Koyna dam.

Fig. 6.25 and Fig. 6.27 show the time history graphs of the horizontal and vertical components of the displacement, velocity, and acceleration at node-9 and node-5 of the dam, respectively. Around time $t = 1.82$ sec, element-1 near the heel of the dam (see Fig. 6.3) softens completely (i.e., $\eta \approx 0$). Due to the infinite rigidity of the foundation during the downstream motion of the dam, the cracks propagate in the downstream direction along the base of the dam. At time $t = 2.30$ sec the cracks at the base of the dam extend to an approximate distance of 17 m from the heel of the dam.

During the upstream movement of the dam, around time $t = 2.46$ sec, significant strain softening occurs (i.e., $\eta \approx 0$) in element-1404 located near the discontinuity in the slope of the downstream face (see Fig. 6.24). The crack quickly propagates in the horizontal direction towards the downstream face of the dam. Thus a localized band of cracked elements forms in the neck-area of the dam. Both the deformed configuration of the dam given in Fig. 6.31a and the spatial distribution of the CRCM parameter, η, given in Fig. 6.30a confirms this. In the later figure, it is noteworthy that due to the upstream movement of the dam cracks at the base are closed. Subsequently, the downstream movement of the dam causes severe cracks at the upstream face. At time $t = 2.70$ sec the crack profile and the corresponding deformed configuration of the dam are given in Fig. 6.30b and 6.31b, respectively. During this time, the cracks near the vicinity of element-1404 start closing. Therefore, elements in this regime momentarily gain their original compressible strength (see Fig. 6.29). The maximum displacement at node-9 of the dam in the upstream direction occurs at time $t = 4.00$ sec as shown in Fig. 6.25. Consequently, during this time, vertical displacement at node-5 of the dam achieves a peak value (see Fig. 6.27) which corresponds to the maximum opening state of the crack at the downstream face. At this instant, the spatial distribution of the CRCM parameter, η, and the corresponding deformed configuration of the dam are illustrated in Fig. 6.30d and Fig. 6.11d, respectively. Note that the cracks at the upstream face are in the closed state due to the upstream motion of the dam. However, these closed cracks open again when the dam swings back in the downstream direction leading to a maximum displacement of the node-9 in both horizontal and vertical directions (see Fig. 6.25).

The spatial distribution of the CRCM parameter, η, and the corresponding deformed configuration of the dam at time $t = 4.17$ are given in Fig. 6.30e and Fig. 6.31e, respectively. The cracks at the downstream face are in the closed state due to the downstream motion of the dam. Accordingly, the maximum compressive principal stress inside the element-1404 of the dam achieve a peak value of 10 MPa around this time (see Fig. 6.29). At this instant the entire neck of the dam is damaged, and the subsequent motion of the cracked dam is dominated by rigid-body rocking of the upper portion of the dam.

From the time-history graphs of displacement, velocity and acceleration plotted in Fig. 6.25 (at node-9) and Fig. 6.27 (at node-5) it is evident that the vibration period of the dam increases due to crack propagation in the dam. This effect is clearly visible in the corresponding Fourier spectrums presented in Fig. 6.26 and Fig. 6.28, where the cracking in concrete dam shifts the spectrum towards the lower frequency regime.

The time history graphs of the maximum tensile and compressive principal stresses occurred in the element-1 and element-1404 are plotted in Fig. 6.29. [9] The maximum tensile principal stresses for the linear case take larger peak values while the maximum peak values of those for the nonlinear case are about the tensile strength of the concrete. In Fig. 6.29 it is visible that the tensile strength of an element is completely removed after the cracking. The maximum compressive principal stresses for linear case also generally take larger peak values than those for nonlinear case. However, in situations where a crack closes completely (i.e., $\mu \geq 0.95$), peak values of the maximum compressive principal stresses in nonlinear case are slightly more than the peak values of those for the linear case (see Fig. 6.29). Lastly, the evolution of the CRCM parameter, η, in selected elements of the Koyna dam is depicted in Fig. 6.24.

[9] Element-1 is located at the base of the dam, and and element-1404 is located at the downstream face of the dam where the discontinuity in the slope occurs as shown in Fig. 6.3

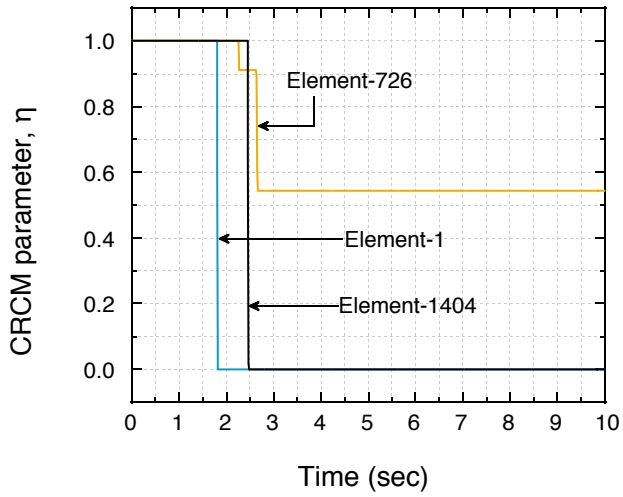

Fig. 6.24.: Evolution of the CRCM parameter, $\eta = E_n/E_0$, for some elements of the Koyna dam obtained by using the *ν-ST/FEM-1* including the hydrodynamic effects of the reservoir.

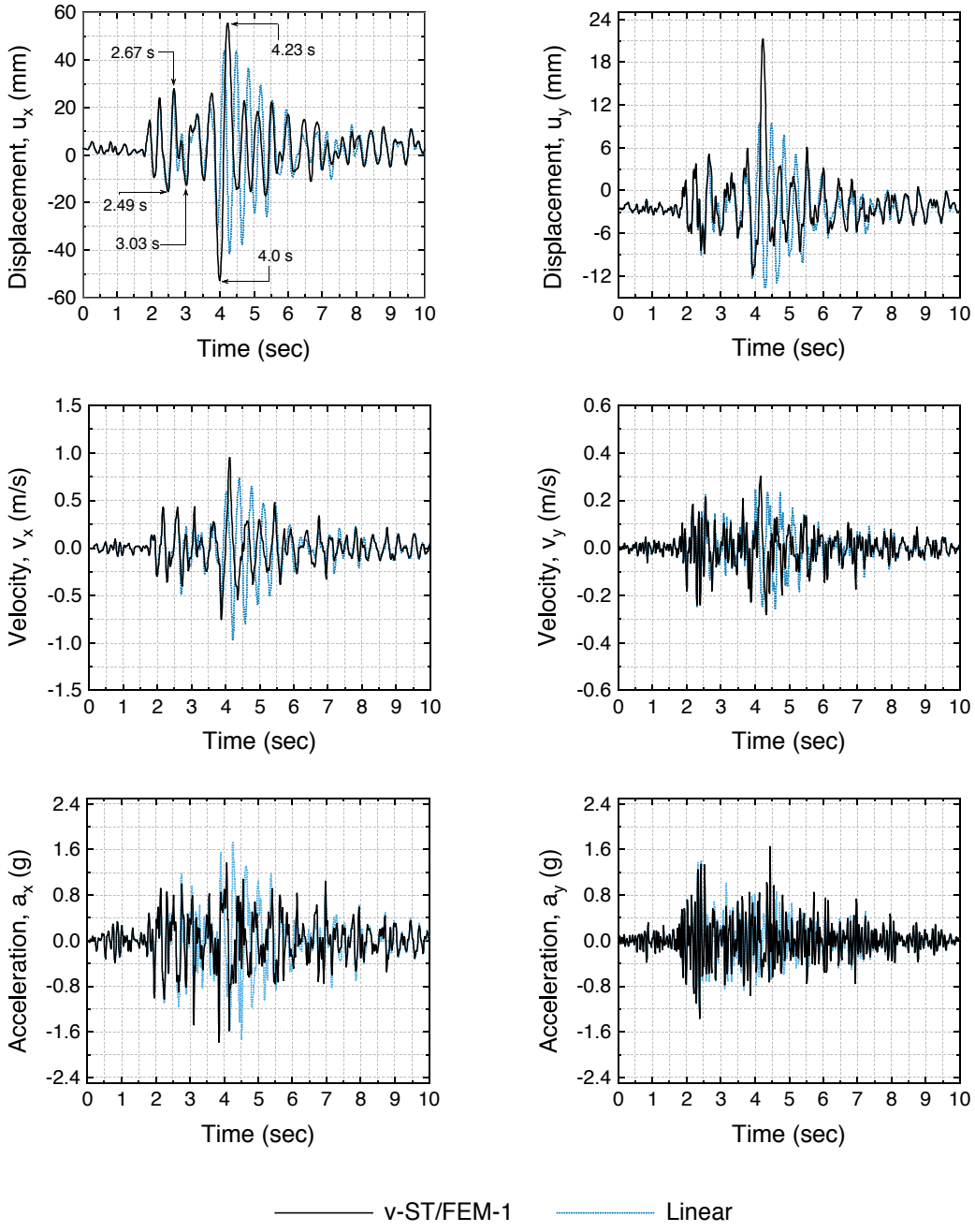

Fig. 6.25.: Time history graphs of the displacement, velocity and acceleration at node-9 of the Koyna dam computed by using the *v-ST/FEM-1* including the hydrodynamic effects of the reservoir.

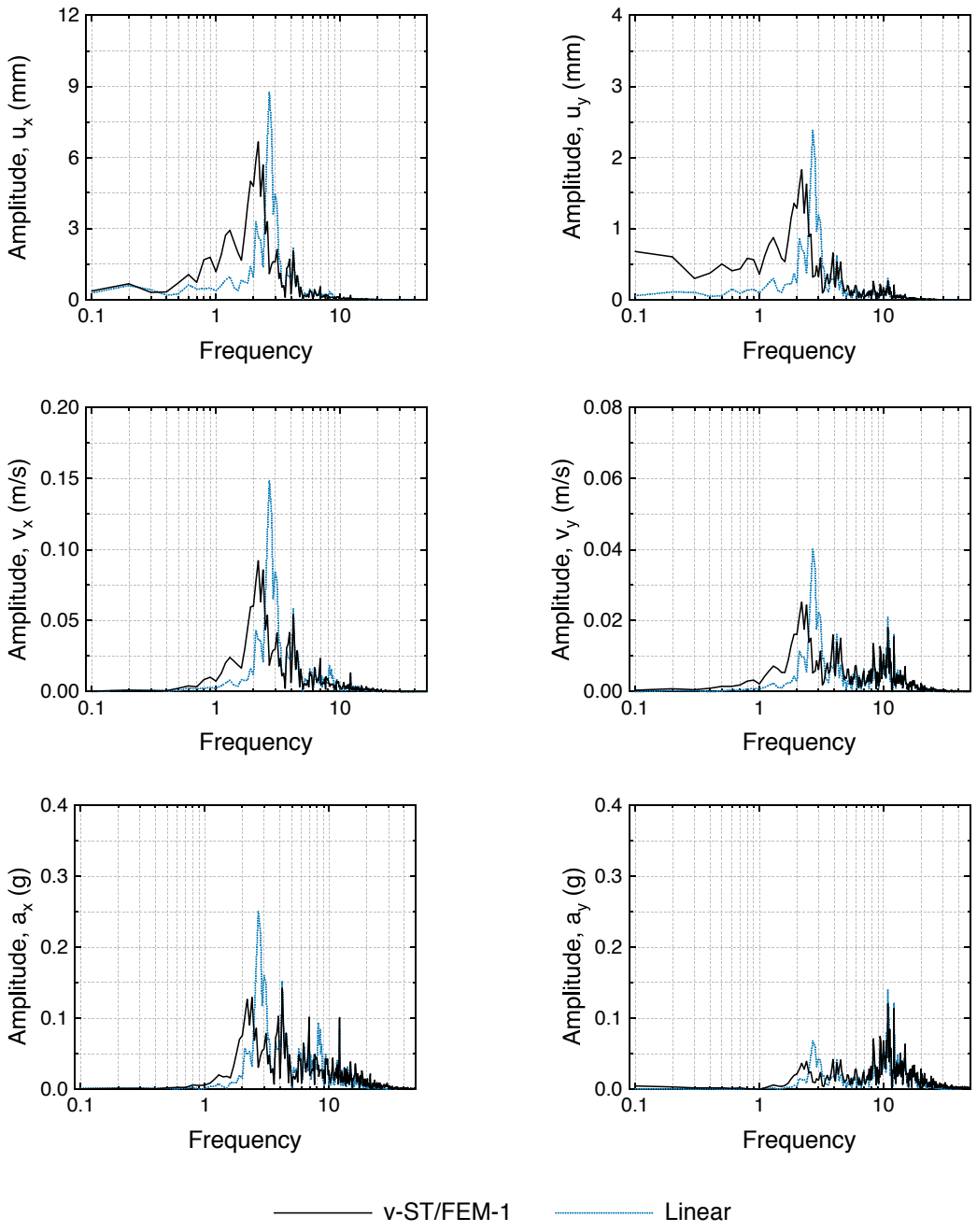

Fig. 6.26.: Fourier spectrum of the displacement, velocity and acceleration at node-9 of the Koyna dam computed by using the *v-ST/FEM-1* including the hydrodynamic effects of the reservoir.

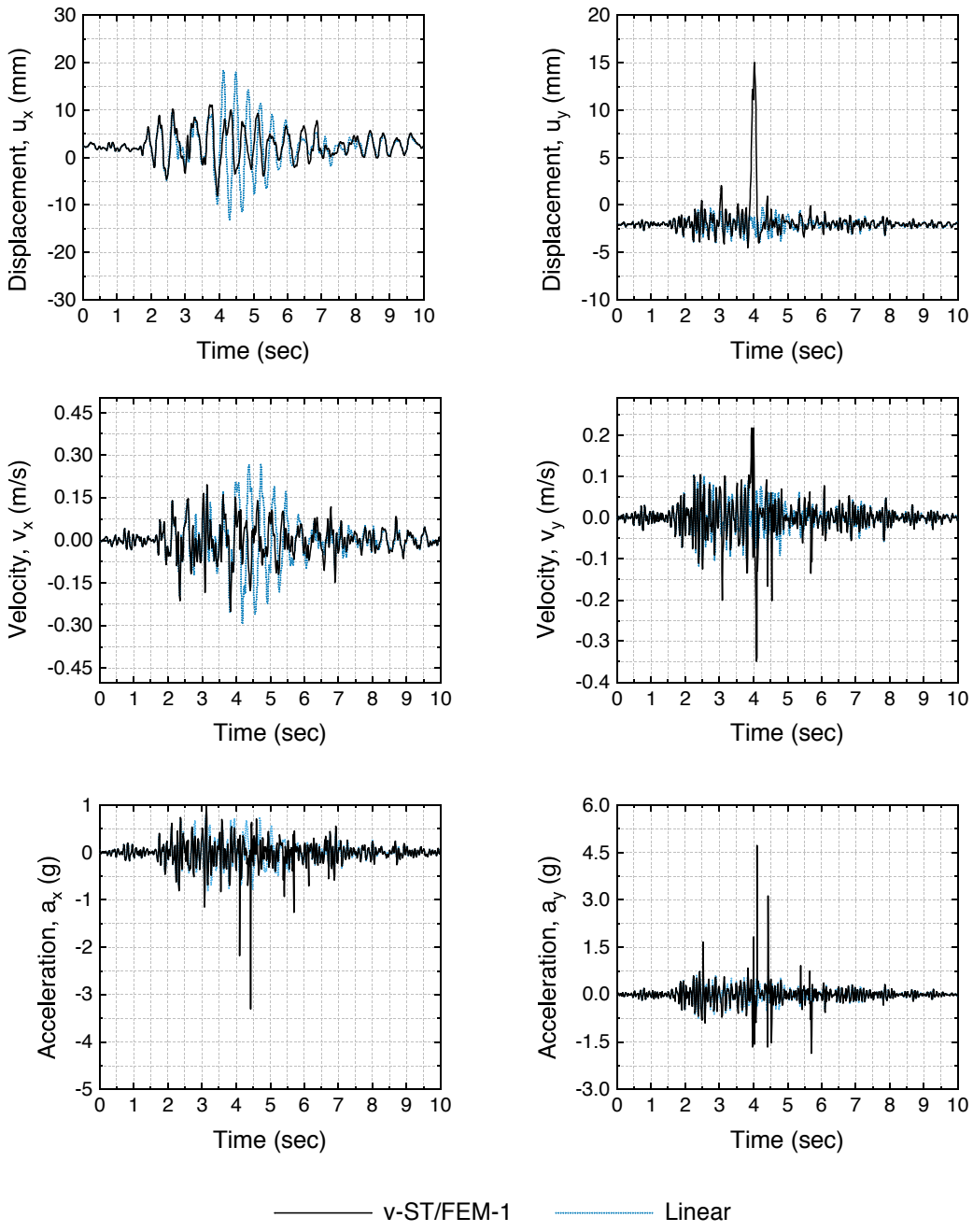

Fig. 6.27.: Time history graphs of the displacement, velocity and acceleration at node-5 of the Koyna dam computed by using *v-ST/FEM-1* including the hydrodynamic effects of the reservoir.

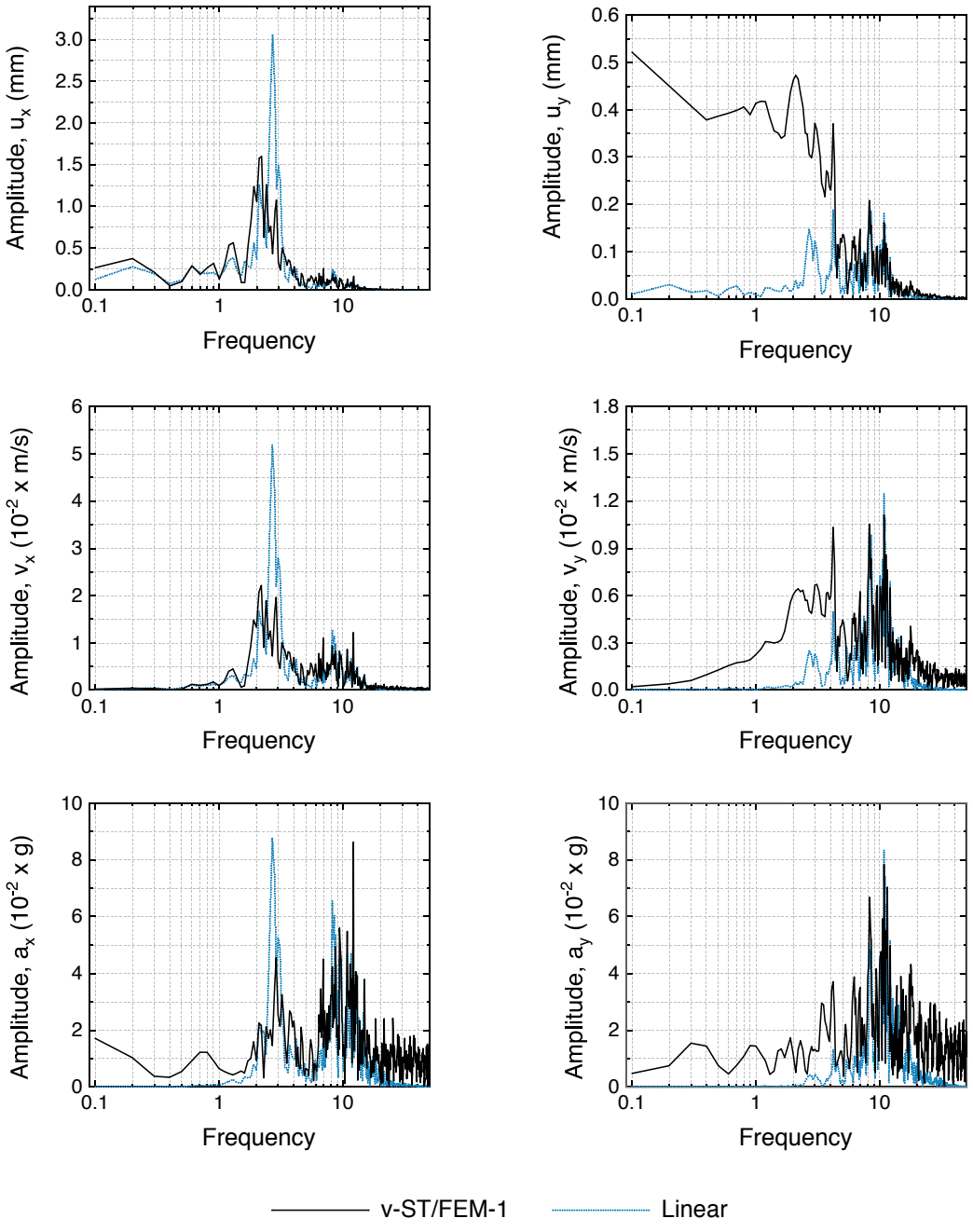

Fig. 6.28.: Fourier spectrum of the displacement, velocity and acceleration at node-5 of the Koyna dam computed by using *v-ST/FEM-1* including the hydrodynamic effects of the reservoir.

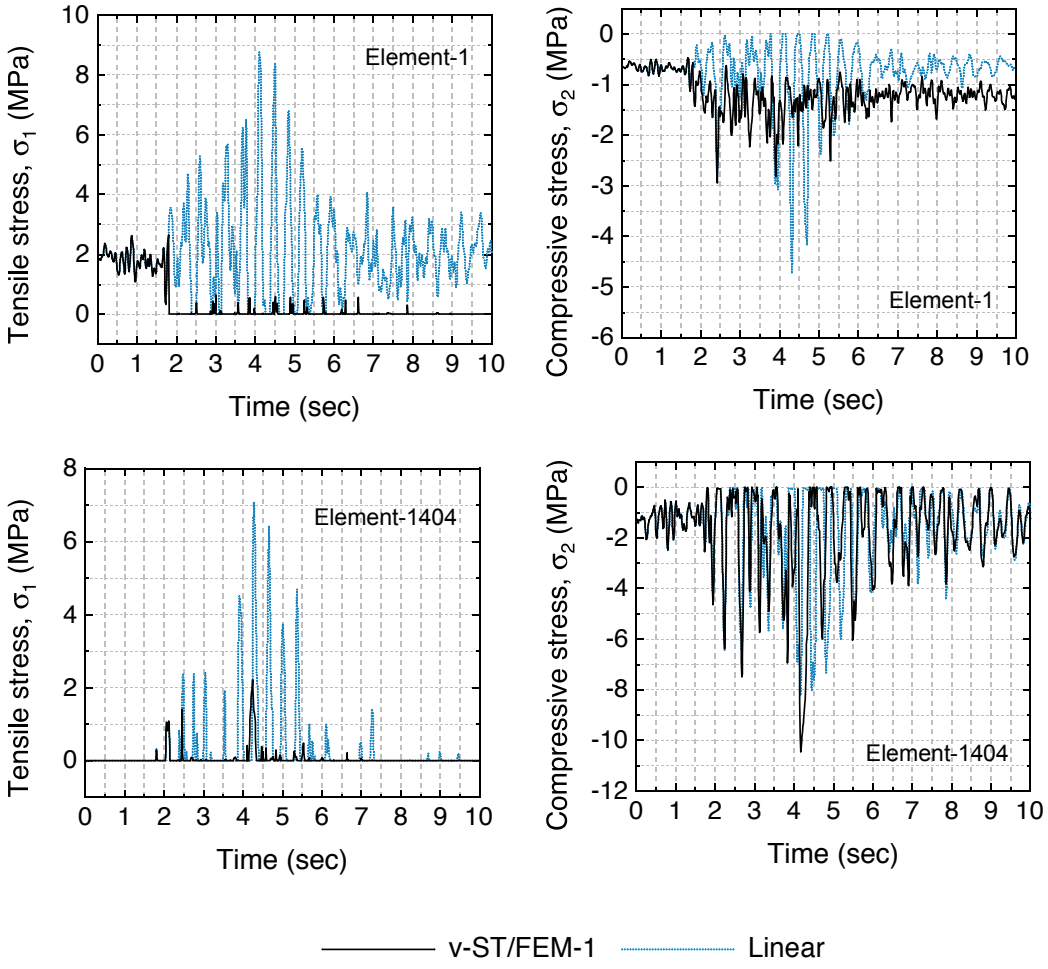

Fig. 6.29.: Time history graphs of the maximum tensile principal stresses, σ_1 on the left hand side, and maximum compressive principal stresses, σ_2 on the right hand side, inside the selected elements of the Koyna-dam computed by using the *v-ST/FEM-1* including the hydrodynamic effects of the reservoir.

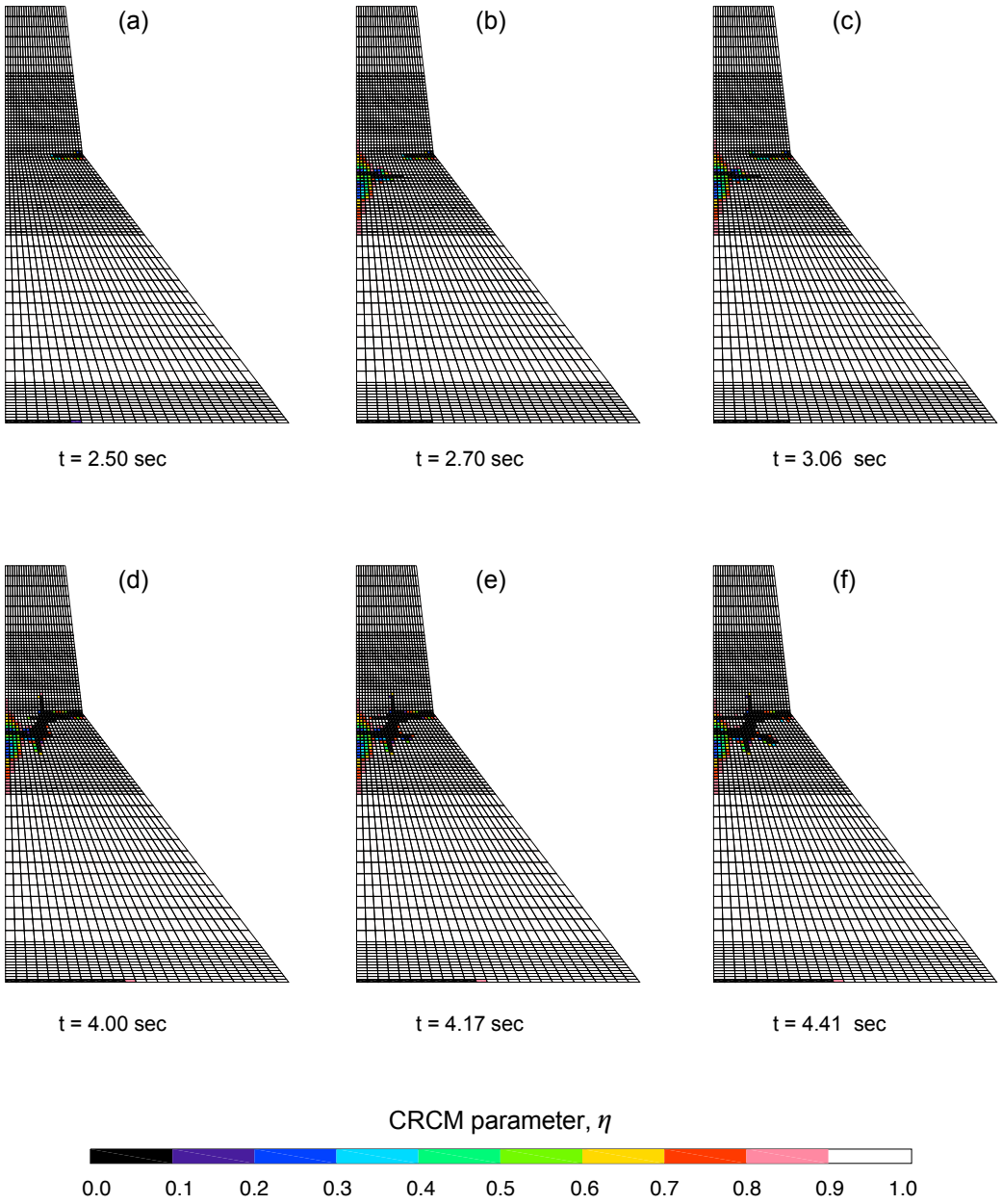

Fig. 6.30.: Spatial distribution of the CRCM parameter, η, in the Koyna dam at selected times computed by using the *ν-ST/FEM-1* including the hydrodynamic effects of the reservoir.

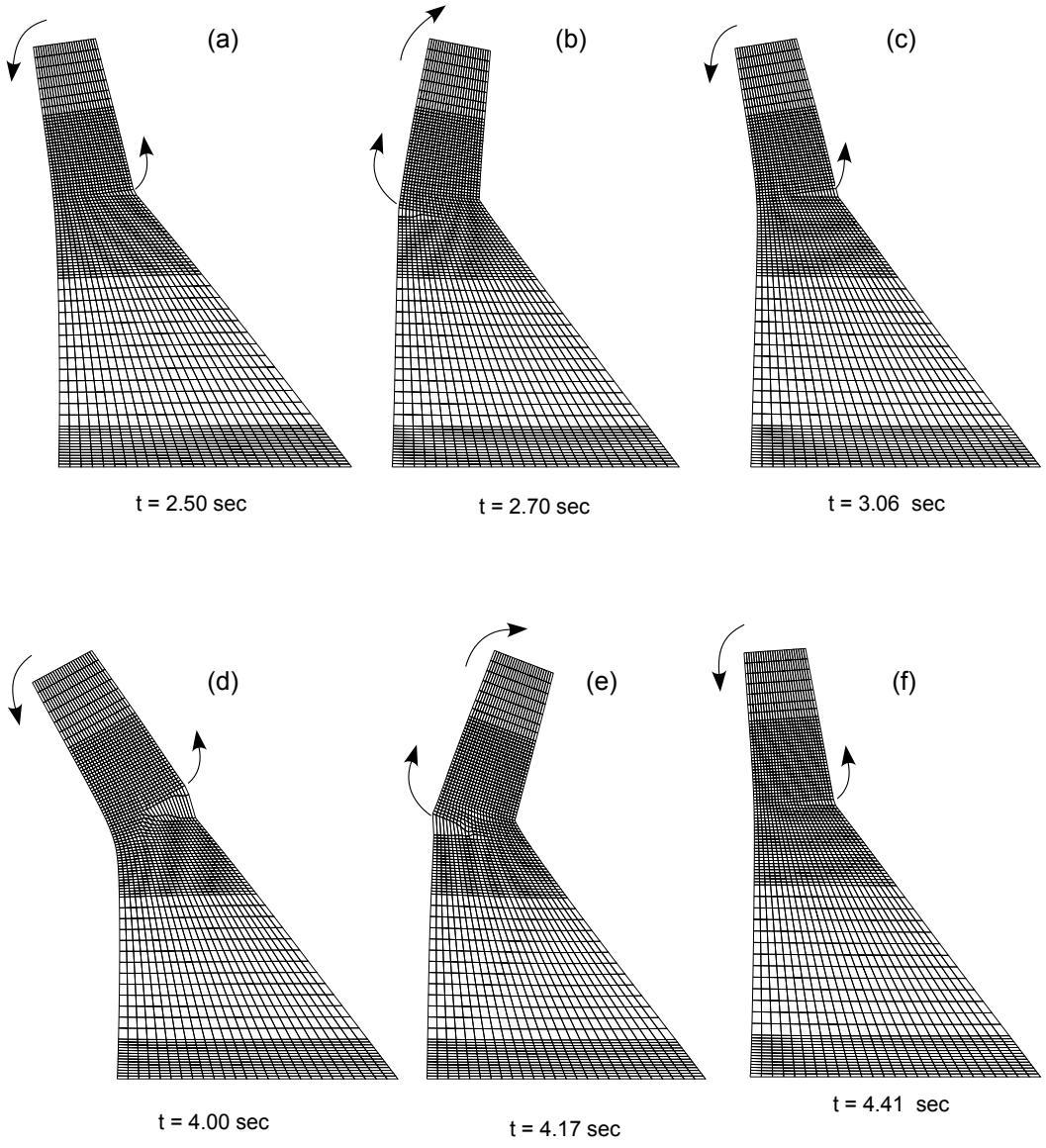

Fig. 6.31.: Amplified deformed configuration of the Koyna dam at selected times computed by using the *v-ST/FEM-1* including the hydrodynamic effects of the reservoir.

6.8.2 Results for *v-ST/FEM-3* scheme

In this section, the nonlinear dynamic response of the Koyna dam is computed by using the *v-ST/FEM-3* with the tolerance in residual and velocity 1.0×10^{-2}. Fig. 6.32 and Fig. 6.33 successfully compare the numerical solutions at node-9 and node-5 obtained by using the *v-ST/FEM-1* and *v-ST/FEM-3*. Spatial distribution of the CRCM parameter, η, and the deformed configuration of the dam are given in Fig. 6.34 and Fig. 6.35, respectively. The events of cracking predicted by the both schemes are nearly identical with the each other. Note that *v-ST/FEM-3* results are obtained at relatively low tolerance value compare to the *v-ST/FEM-1*. It is remarkable that the numerical solutions obtained by using the *v-ST/FEM-3* at low tolerance are nearly identical to those obtained by using the *v-ST/FEM-1*. In addition, the use of space-time averaged strains as representative of the behavior of the space-time element as a whole significantly improves the convergence of the numerical scheme.

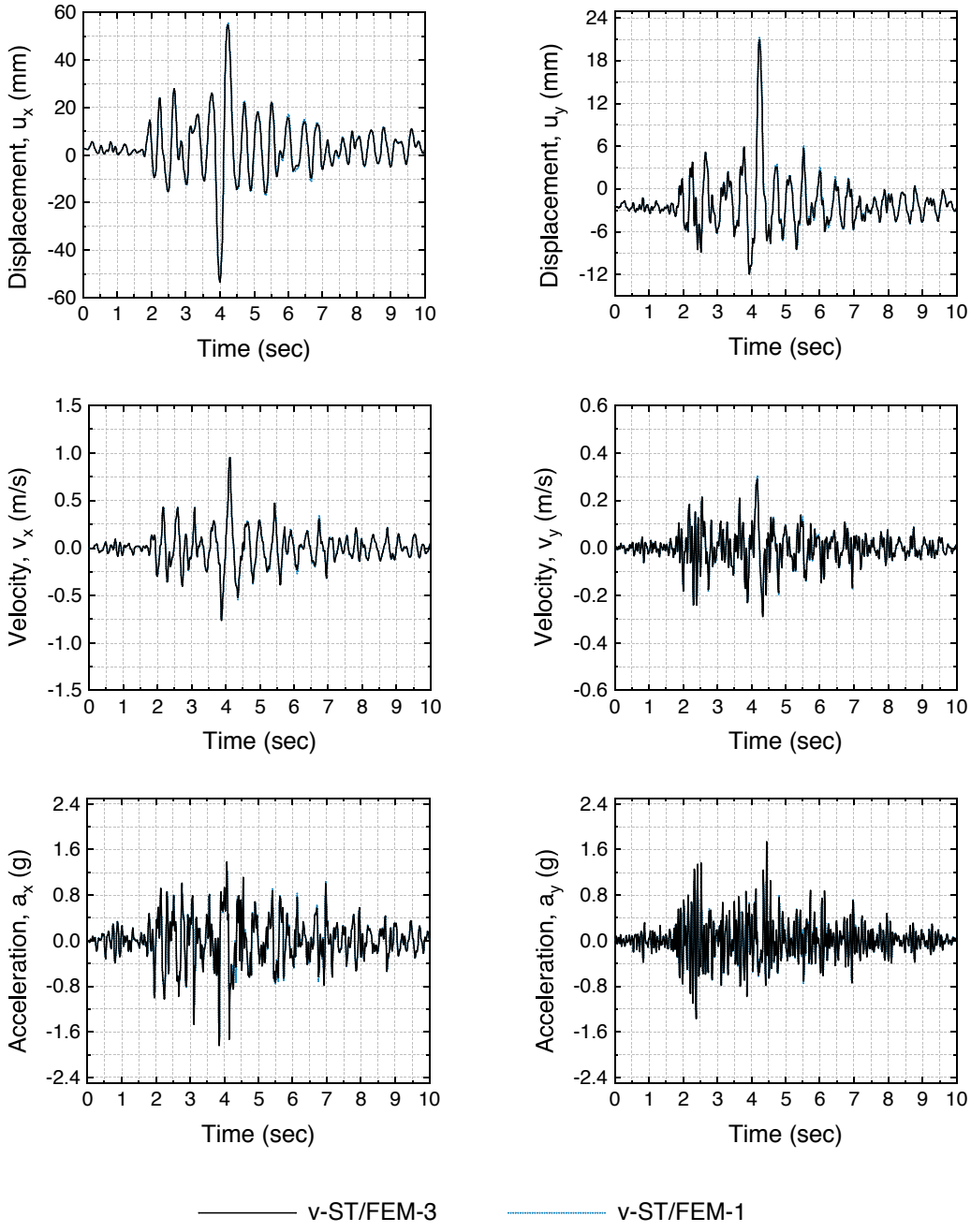

Fig. 6.32.: Comparison of the displacement, velocity and acceleration responses at node-9 of the Koyna dam computed by using the *v-ST/FEM-1* and *v-ST/FEM-3* including the hydrodynamic effects of the reservoir.

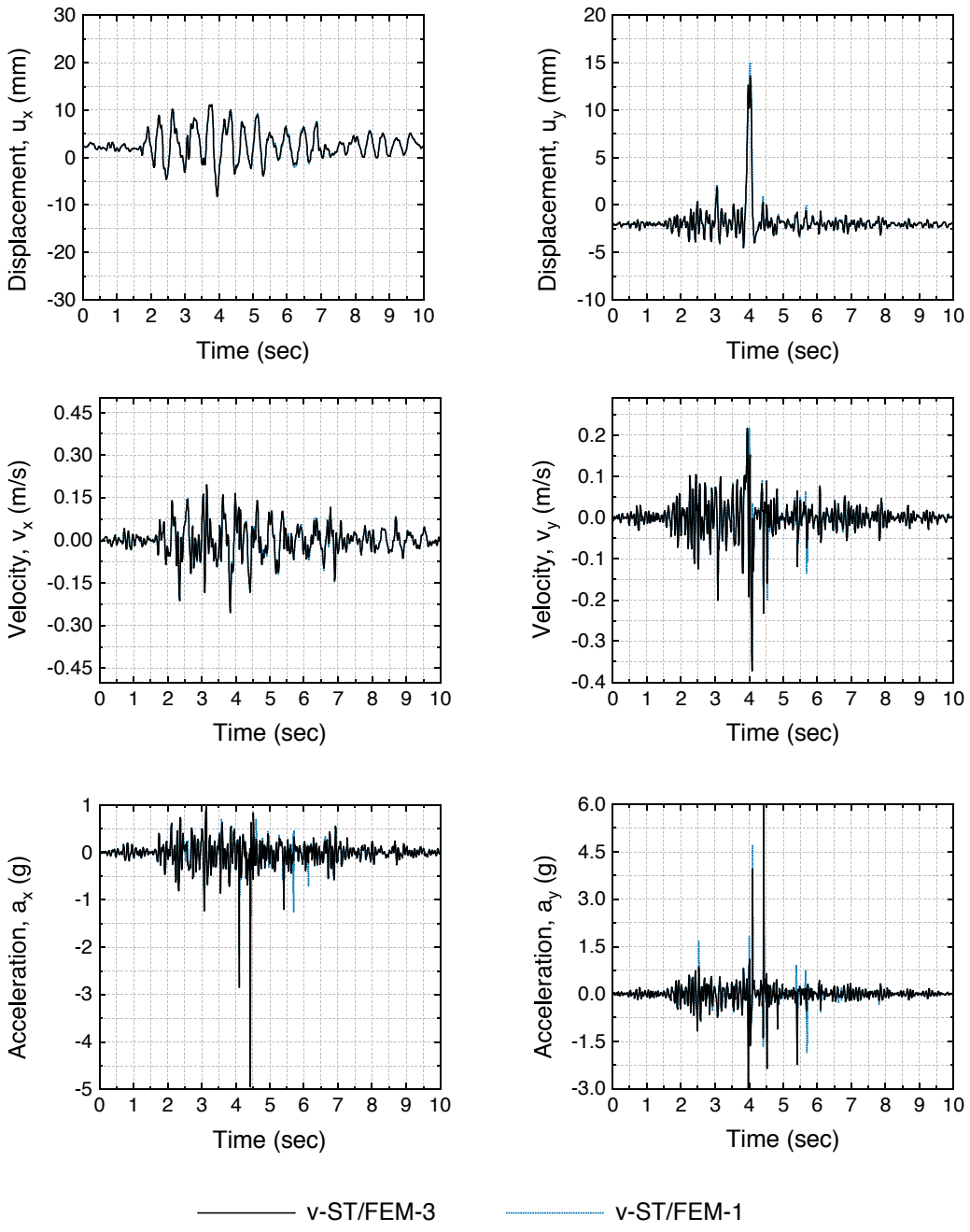

Fig. 6.33.: Comparison of the displacement, velocity and acceleration responses at node-5 of the Koyna dam computed by using the *v-ST/FEM-1* and *v-ST/FEM-3* including the hydrodynamic effects of the reservoir.

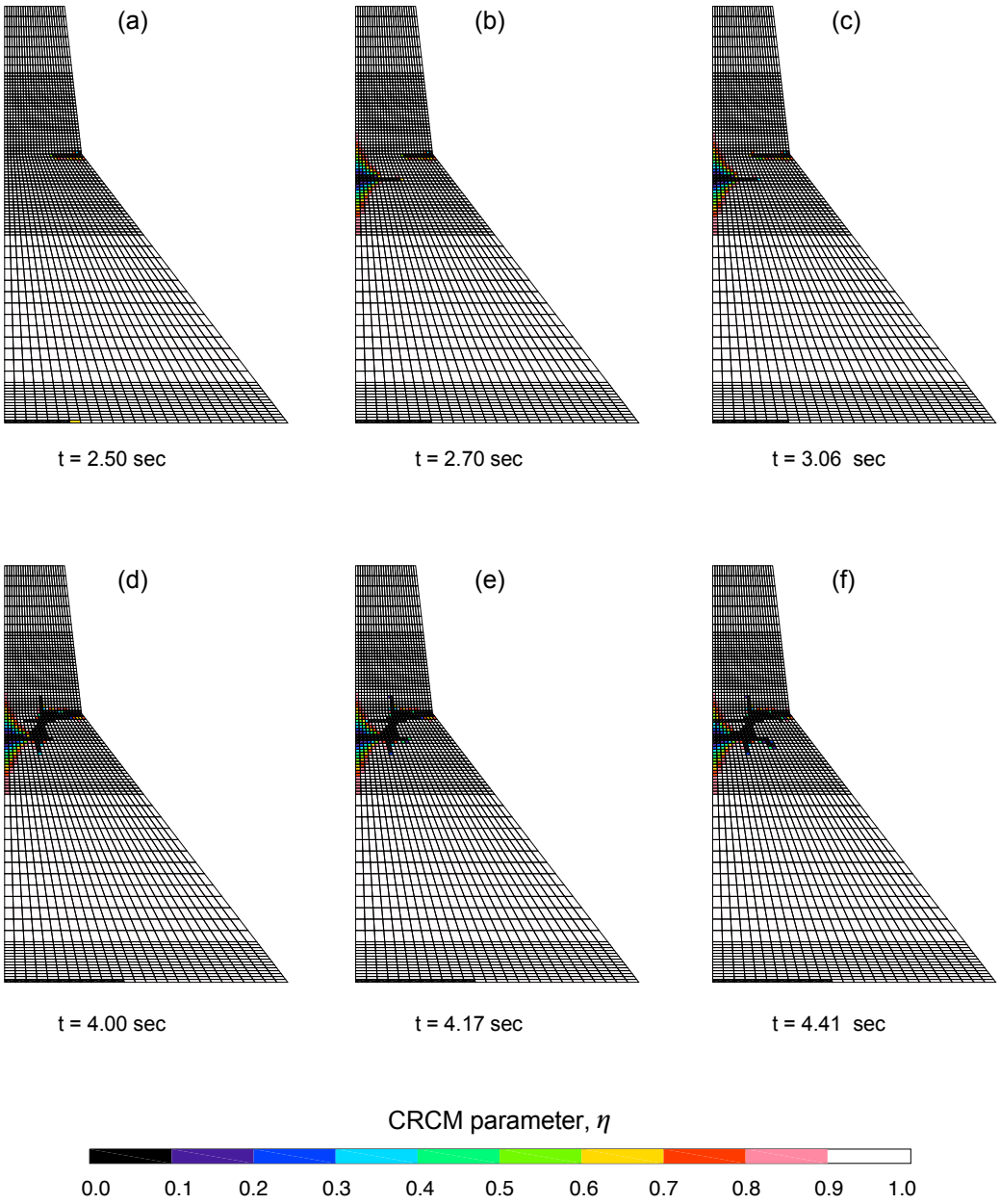

Fig. 6.34.: Spatial distribution of the CRCM parameter, $\eta = E_n/E_0$ in Koyna dam at selected times computed by using the *v-ST/FEM-3* including the hydrodynamic effects of the reservoir.

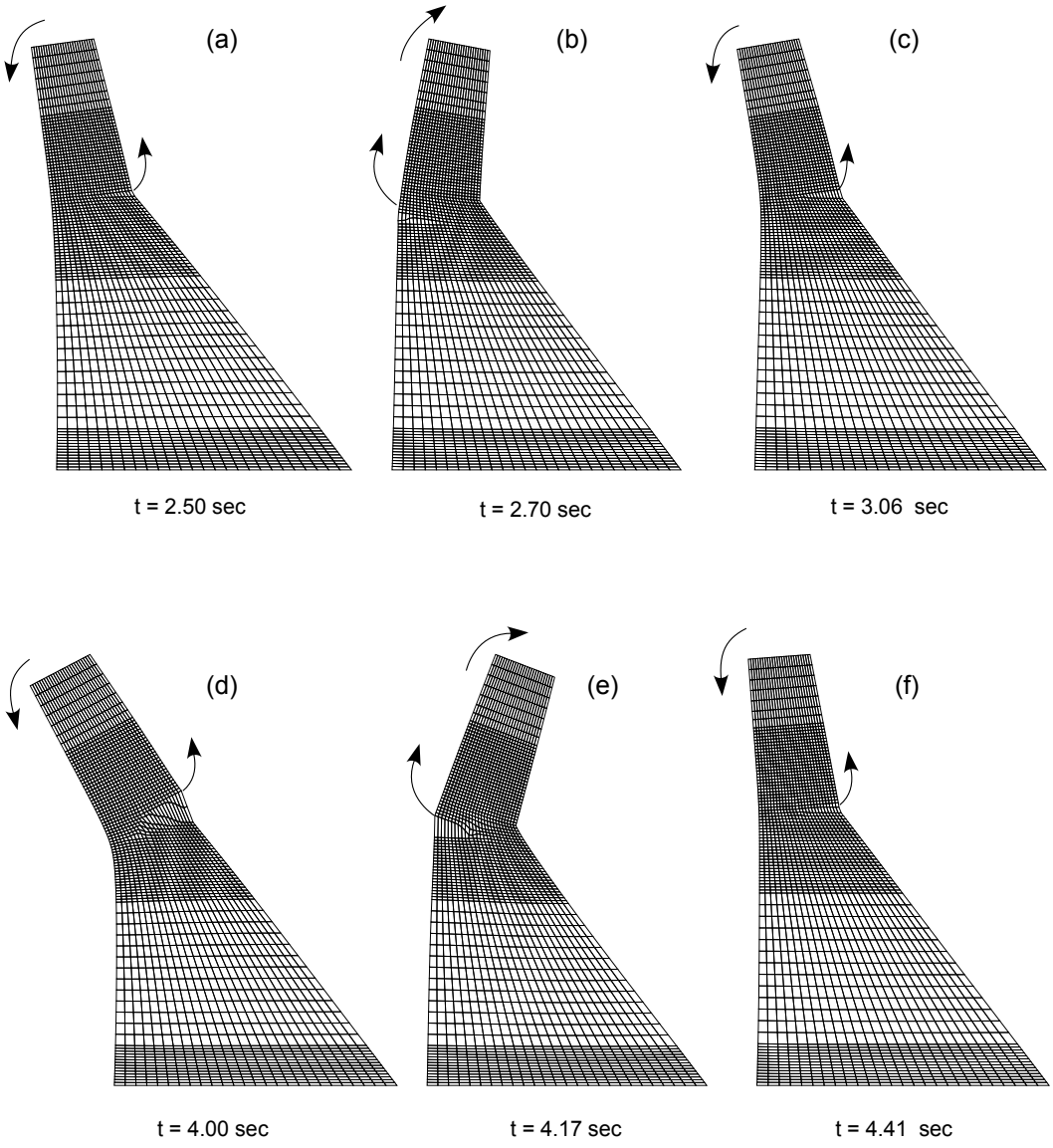

Fig. 6.35.: Amplified deformed configuration of the Koyna dam at selected times computed by using the *v-ST/FEM-3* including the hydrodynamic effects of the reservoir.

6.9 Summary

The chapter presents space-time finite element formulations for the problems involving dynamic response of solids and structures with nonlinear stress-strain relationships. The problem of dynamic interaction between the concrete gravity dam and reservoir is taken as a model problem, in which a generalized nonlinear stress-strain relationship is used to describe the material behavior of concrete in the dam. The foundation underneath the dam-reservoir (DR) system is assumed to be perfectly rigid. The governing equations describing the dynamic interaction between dam and reservoir constitute a system of linear-nonlinear coupled equations, in which linear equations govern the reservoir domain and nonlinear equations govern the solid domain. Subsequently, v-ST/FEM weak form is derived and then discretized by using the space-time finite elements. Accordingly, an unsymmetrical system of linear-nonlinear algebraic equations describes the discrete form of the v-ST/FEM weak form. A block-iterative scheme is devised to enforce the coupling between the solid and fluid domain. In each iteration of v-ST/FEM with the block-iterative scheme, the linearized equations of the solid domain are first solved to compute the increments in the velocity field. Subsequently, the total velocities are corrected and then used for computing the trial values of hydrodynamic pressures in the reservoir by solving the linear equation for the reservoir domain. Iterations are performed until the convergence in the solutions is achieved. In each iteration of the proposed scheme, therefore, linear equations for the solid and fluid domain are solved, separately, which significantly decreases the computation cost.

In the present problem, nonlinearity is caused by only the presence of stress term in the v-ST/FEM weak form. Accordingly, two v-ST/FEM schemes are proposed for the time integration of the space-time nodal vectors and matrices comprising the stress term. The first scheme uses the three-point Gauss-Lobatto quadrature rule for time-integration, whereas the second scheme uses the two-point Gauss-Legendre quadrature rule. Further, the Gauss-Lobatto quadrature rules include the endpoints of the time interval, while the latter approach includes the points only located inside the time interval.

Subsequently, to evaluate the numerical performance of the v-ST/FEM schemes dynamic fracture analyses of the concrete dam are performed. Numerical simulations are performed for following two cases: the first case ignores the coupling between the dam and reservoir, and the second case includes the coupling between dam and reservoir. In the former case, hydrodynamic pressures are set to zero in the discretized equations of the solid domain, consequently, block-iterative scheme reduces to the Newton method.

A co-axially rotating crack model (CRCM) with exponential strain softening rule is employed to model the fracture of the concrete. Finite element implementation of the CRCM requires the average of integration point strains to determine the cracking behavior of the element as a whole. In v-ST/FEM, one can opt the average of either spatial integration point strains or the space-time integration point strains. Accordingly, three v-ST/FEM schemes are devised for the dynamic fracture analysis of the concrete dam: *v-ST/FEM-1* corresponds to the three-point Gauss-Lobatto rule and the spatially averaged strains, *v-ST/FEM-2* corresponds to the two-point Gauss-Legendre rule and the spatially averaged strains, and *v-ST/FEM-3* corresponds to the two-point Gauss-Legendre rule and the space-time averaged strains.

Numerical simulations presented in this chapter confirms that all v-ST/FEM schemes are consistent with each other. All schemes can successfully simulate the crack propagation in the concrete dam during the earthquake loading. Dynamic fracture analysis of concrete dam involves the rapid change of the stiffness of the dam due to the crack opening-closing-reopening cycles. The results indicates that *v-ST/FEM-1* is the most robust algorithm among the three v-ST/FEM schemes discussed here. Further, total number of iteration increases at the instant of crack closing and smaller time steps may be required to achieve the convergence. During the crack opening and reopening, however, number of iterations are relatively low which can be attributed to the high order accuracy of the v-ST/FEM schemes.

7 Concluding Remarks

This dissertation uses the time-discontinuous Galerkin finite element method to develop a high-order accurate time integration scheme, which is termed as the v-ST/FEM, for the dynamic problems in geotechnical and structural engineering. In v-ST/FEM, the shape functions depend upon both the space and the time domain unlike the classical semi-discrete finite element approaches where shape functions depend only on the space domain. The central ideas in v-ST/FEM is to use the time-discontinuous interpolation for the velocity field and to develop a weak-form of the linear-momentum balance equation which is defined on the space-time domain. The space-time weak-form is designed to satisfy the continuity of the velocity field in time in the weak sense, which in turn allows the natural introduction of the initial conditions. Furthermore, both the displacement and stress fields in the v-ST/FEM are secondary unknowns, and are computed in a post processing steps. The numerical performance of the v-ST/FEM is then demonstrated by solving several practical engineering problems involving both the linear and nonlinear dynamics behavior of the structures.

In what follows the content of foregoing chapters are summarized.

In Chapter 2, the working principles of the time-discontinuous Galerkin finite element method (TDG/FEM) are described by using a first order ordinary differential equation (ODE). This ODE resembles to the uncoupled modal equations of the linear parabolic partial differential equations (PDE), and involves only a single unknown. The ideas related to the time-discontinuous interpolation and jump discontinuity in time are then explained. It is proved that TDG/FEM is an unconditional stable algorithm, moreover, it is shown that the algorithm is third order accurate for linear interpolation in time.

Subsequently, the concept of discontinuous interpolation in time is extended to a second order ODE in time which involves displacement and velocity as the unknowns. Here, the second order ODE represents the uncoupled modal equation of a viscoelastic media. Three types of TDG schemes are proposed for solving the second order ODE; uv-TDG/FEM, u-TDG/FEM, and v-TDG/FEM. In uv-TDG/FEM, an independent time-discontinuous interpolation is performed for both the displacement and velocity. In u-TDG/FEM, time-discontinuous approximation is used only for the displacement,

and velocity is computed by taking the first order time derivative of the displacement. In v-TDG/FEM, however, time-discontinuous approximation is employed only for velocity, and the displacement is obtained by time-integration of the velocity. It is shown that the u-TDG/FEM and v-TDG/FEM are mathematically equivalent but computationally different. Both uv-TDG/FEM and v-TDG/FEM are unconditional stable algorithms, and have third order accuracy in time for the linear interpolation. However, the former approach produces a larger system of linear equations compare to the one in latter approach.

The framework of v-TDG/FEM is then extended to devise the velocity-based time-discontinuous space-time finite element method (v-ST/FEM) for a multidimensional elastodynamics problem. In v-ST/FEM, space-time nodal values of the velocity field are the main unknowns, and displacement field is obtained through a time-integration post-processing step. In this way, the present methodology can greatly reduce the size of the resulting linear system to be solved in each time step. Several numerical tests are performed to demonstrate the efficiency and the applicability of the v-ST/FEM. Furthermore, it is proven that the present method is unconditionally stable and third-order accurate in time. In addition, the proposed scheme is found to be non-dissipative in both low and high-frequency regimes and to attenuate only the middle band of frequencies. Moreover, v-ST/FEM induces negligible numerical dispersion into the system, and hence, produces negligible phase delay. In the case of a shock problem, the performance of v-ST/FEM was found to be superior to both HHT-α and Newmark-beta method.

In Chapter 3, a concise presentation regarding the theory of wave propagation in an elastic solid is given. After briefly discussing the reflection and refraction of a plane harmonic waves it is shown that the problem of dynamic soil-structure interaction (SSI) can be viewed as a wave-scattering phenomenon, in which the free-field response of an elastic half-space is perturbed by the existing structure. In dynamic SSI problem, unbounded soil domain is truncated by placing artificial boundaries at some distance from the area of interest. Accordingly, the chapter presents some of the most popular boundary conditions for solving wave propagation problems in the unbounded domain. In addition, the viscous boundary conditions first proposed by Lysmer and Kuhlemeyer, 1969 are derived, and a comprehensive discussion related to the numerical characteristics of the viscous boundary conditions is made. Later in this chapter, viscous boundary condition of Lysmer-Kuhlemeyer is modified by introducing additional boundary terms related to the free-field response of unbounded soil domain to facilitate the energy flow from far field to computation domain.

In Chapter 4, v-ST/FEM method is used to solve the problem of dynamic soil-structure interaction. In this context, finite element modeling of the unbounded

soil domain is performed by placing modified viscous boundaries at some distance from the existing structure. In the computer program, these boundary conditions are treated as a combination of various traction boundary conditions; traction boundary condition due to dashpots, free-field motion, and input seismic motion. It is found that the traction boundary condition due to dashpots introduces space-time dashpot matrices which contribute to the space-time tangent matrix. The traction boundary condition due to input seismic motion and free-field motion introduce corresponding space-time nodal vectors. Furthermore, a procedure involving solutions to the soil-column problems is presented for obtaining the free-field response. It is noticed that the computation of the free-field response does not depend upon the total response of soil and structure. Due to this weak coupling, the soil-column problem is solved first, and then the total response of soil and structure is computed by using this free-field response. Afterwards, a dynamic dam-soil interaction problem is considered to validate the formulation and computer implementation of v-ST/FEM. The results obtained by proposed scheme are validated by solving the same problem using the semi-discrete FEM with classical Newmark-β method. Results obtained by two methods are compared and found to be nearly identical.

In Chapter 5, v-ST/FEM is used to compute the seismic response of the dam-reservoir (DR) and dam-reservoir-soil (DRS) system while considering all types of dynamic interaction. Both dam and the underlying soil domain is assumed to be linearly elastic, and material damping is modeled by Rayleigh damping. The water in the reservoir is assumed to be inviscid, linearly compressible with a small amplitudes for the displacements and velocity. Thus, the hydrodynamic pressure in the reservoir is given by the pressure wave equation. In the finite element modeling, viscous boundary conditions are used to truncate the semi-infinite domain of reservoir and underlying soil-domain.

The space-time finite element formulation for coupled problem is then described in terms of velocity field for the solid domain and the auxiliary variable q for the fluid domain. Here q denotes the first order time derivative of the hydrodynamic pressure field. The space-time discretization of the governing equations leads to a system of linearly coupled equations. A two-stage block-iterative scheme is then developed to solve the resultant system of linear equations for the space-time nodal values of unknown fields q and $\mathbf{v}$. Due to the block-iterative scheme the size of the coupled-problem significantly decreases but at the cost of around 5 to 10 iterations per time steps.

In each iteration step, first, a system of linear equations (which corresponds to the solid domain) is solved to compute the trial values of velocity field, and then the space-time nodal values of auxiliary variable q are computed by solving another system of linear equations (which corresponds to the fluid domain). The numerical

performance of the proposed scheme is demonstrated by solving different types dam-reservoir interaction problems. The results obtained by the proposed scheme are successfully compared with results available in the literature.

Afterwards, in this chapter, the response of a concrete gravity dam and reservoir with impounded water to the horizontal component of the earthquake motion is analyzed by using the v-ST/FEM. Numerical simulations are performed for two cases: (i) DR, in which the interactions between the dam-reservoir and the underlying soil are ignored by assuming the ground to be perfectly rigid, and (ii) DRS, in which the underlying soil domain is modeled as an isotropic, homogenous, linear elastic half space. It is found that the dynamic interactions with the underlying deformable soil domain can significantly dampen the response of the dam-reservoir to the horizontal component of earthquake motion. The comparison of Fourier spectrum of acceleration response obtained for these two cases reveals an elongation of time period for DRS. In both cases, significant tensile stresses develop near the heel and at the downstream inclined face of the dam.

In Chapter 6, v-ST/FEM is employed for the problems involving dynamic response of solids and structures with nonlinear stress-strain relationships. The problem of dynamic interaction between the concrete gravity dam and reservoir is taken as a model problem, in which a generalized nonlinear stress-strain relationship is used to describe the material behavior of concrete in the dam. The foundation underneath the dam-reservoir (DR) system is assumed to be perfectly rigid. The governing equations describing the dynamic interaction between dam and reservoir constitute a system of linear-nonlinear coupled equations, in which linear equations govern the reservoir domain and nonlinear equations govern the solid domain. A block-iterative scheme is used to enforce the coupling between the solid and fluid domain. In each iteration of v-ST/FEM with the block-iterative scheme, the linearized equations of the solid domain are first solved to compute the increments in the velocity field. Subsequently, the total velocities are corrected and then used for computing the trial values of hydrodynamic pressures in the reservoir by solving the linear equation for the reservoir domain. In each iteration of the proposed scheme, therefore, linear equations for the solid and fluid domain are solved, separately, which significantly decreases the computation cost.

In this chapter, nonlinearity is caused by only the presence of stress term in the v-ST/FEM weak form. Accordingly, two v-ST/FEM schemes are proposed for the time integration of the space-time nodal vectors and matrices comprising the stress term. The first scheme uses the three-point Gauss-Lobatto quadrature rule for time-integration, whereas the second scheme uses the two-point Gauss-Legendre quadrature rule. Further, the Gauss-Lobatto quadrature rules include the endpoints

of the time interval, while the latter approach includes the points only located inside the time interval.

Subsequently, to evaluate the numerical performance of the v-ST/FEM schemes dynamic fracture analyses of the concrete dam are performed. Numerical simulations are performed for following two cases: the first case ignores the coupling between the dam and reservoir, and the second case includes the coupling between dam and reservoir. A co-axially rotating crack model (CRCM) with exponential strain softening rule is employed to model the fracture of the concrete. Finite element implementation of the CRCM requires the average of integration point strains to determine the cracking behavior of the element as a whole. In v-ST/FEM, one can opt the average of either spatial integration point strains or the space-time integration point strains. Accordingly, three v-ST/FEM schemes are devised for the dynamic fracture analysis of the concrete dam: *v-ST/FEM-1* corresponds to the three-point Gauss-Lobatto rule and the spatially averaged strains, *v-ST/FEM-2* corresponds to the two-point Gauss-Legendre rule and the spatially averaged strains, and *v-ST/FEM-3* corresponds to the two-point Gauss-Legendre rule and the space-time averaged strains.

Numerical simulations presented in this chapter confirms that all v-ST/FEM schemes are consistent with each other. All schemes can successfully simulate the crack propagation in the concrete dam during the earthquake loading. Dynamic fracture analysis of concrete dam involves the rapid change of the stiffness of the dam due to the crack opening-closing-reopening cycles. The results indicates that *v-ST/FEM-1* is the most robust algorithm among the three v-ST/FEM schemes discussed here. Further, total number of iteration increases at the instant of crack closing and smaller time steps may be required to achieve the convergence. During the crack opening and reopening, however, number of iterations are relatively low which can be attributed to the high order accuracy of the v-ST/FEM schemes.

In conclusion, v-ST/FEM is an effective technique for solving both the linear and nonlinear dynamic problems due to following reasons

(i) The main drawback of time-discontinuous space-time finite element schemes is that such schemes results in large number of unknowns which preclude their application to the large scale practical problems due to high computation-cost and memory-storage requirements. The advantage of v-ST/FEM is that it involves less number of unknowns–unlike other ST/FEM–which makes v-ST/FEM applicable to the large-scale practical problems at relatively low computation cost. The problem of memory-storage can be solved by using the iterative linear solvers (e.g., GpBiCG) within element-by-element framework.

(ii) The scheme is third order accurate in the time for the linear interpolation in time. Besides, the technique developed in this thesis can be used to formulate the arbitrary high-order time accurate schemes by adopting the higher order time-interpolation for the velocity field.

(iii) v-ST/FEM is an unconditionally stable time integration algorithm. In addition, the proposed method forms a true energy decaying scheme which implies that the v-ST/FEM will remain unconditionally stable even for the nonlinear problems.

(iv) It is well established that the time-discontinuous Galerkin method can effectively solve the problems which are governed by the hyperbolic PDE (e.g., Conservation laws) or by the parabolic PDE (e.g., Heat diffusion equation). Since the foundation of v-ST/FEM is based on the time-discontinuous Galerkin methods, the proposed scheme provides a stable and high-order accurate framework for solving different types of dynamic problems.

By using the present research as a basis, we now consider how this study may be extended.

(i) The major limitation of v-ST/FEM for structural dynamics problems is that it can not attenuate the spurious high-frequency components. Further efforts should be made for including a parameter to control the numerical dissipation of the high-frequency components. In this context, research may focus on the selection of an appropriate combination of the test and trial functions for the velocity field.

(ii) In nonlinear problems, the effect of quadrature points (the total number of quadrature points and the type of quadrature points) for the time-integration of space-time nodal vector comprising the stress term should be studied further.

(iii) In this thesis, geometrical nonlinear problems have not been discussed. However, it is belived that v-ST/FEM may be an effective approach for solving large deformation dynamic problems. In such problems, one can use v-ST/FEM while working with Lagrangian mesh.

(iv) In addition, incorporation of the moving mesh framework with v-ST/FEM is natural since the shape functions in v-ST/FEM are defined in terms of space-time coordinates. In this case, the governing equations should be recast into their Eulerian forms.

A

Space-Time Finite Element Matrices and Vectors for Elastodynamics Problem

In Section 2.6 following v-ST/FEM weak-form for elastodynamics problem was presented (see Eq. 2.139),

$$\begin{aligned}
&\int_{I_n}\int_{\Omega_h}\delta v_i\rho\frac{\partial v_i}{\partial t}d\Omega dt+\int_{\Omega_h}\delta v_i\left(\mathbf{x},t_n^+\right)\rho v_i\left(x,t_n^+\right)d\Omega\\
&-\int_{\Omega_h}\delta v_i\left(\mathbf{x},t_n^+\right)\rho v_i\left(x,t_n^-\right)d\Omega+\int_{I_n}\int_{\Omega_h}\frac{\partial\delta v_i}{\partial x_j}C_{ijkl}\psi_{kl}d\Omega dt\\
&-\int_{I_n}\int_{\Gamma_i^h}\delta v_i f_i^s dsdt-\int_{I_n}\int_{\Omega_h}\delta v_i\rho b_i d\Omega dt\\
&+\int_{I_n}\int_{\Omega_h}\frac{\partial\delta v_i}{\partial x_j}\sigma_{ij}^n d\Omega dt=0
\end{aligned}\tag{A.1}$$

In above equation using the space-time interpolation for v_i and δv_i, given in Eq. (2.142) and Eq.(2.149), respectively.

$$\begin{aligned}
&\{\delta v\}_i^a(I)\cdot[M]_{ij}^{ab}(I,J)\cdot\{v\}_j^a(J)+\{\delta v\}_i^a(I)\cdot[K]_{ij}^{ab}(I,J)\cdot\{v\}_j^a(J)\\
&-\{\delta v\}_i^a(I)\cdot\{J_{ext}\}_i^a(I)-\{\delta v\}_i^a(I)\cdot\{J_0\}_i^a(I)\\
&+\{\delta v\}_i^a(I)\cdot\{J_{\sigma^n}\}_i^a(I)=0
\end{aligned}\tag{A.2}$$

Noting that the above equation is true for all values of $\{\delta v\}_i^a(I)$, hence

$$\begin{aligned}
&[M]_{ij}^{ab}(I,J)\cdot\{v\}_j^a(J)+[K]_{ij}^{ab}(I,J)\cdot\{v\}_j^a(J)\\
&-\{J_{ext}\}_i^a(I)-\{J_0\}_i^a(I)+\{J_{\sigma^n}\}_i^a(I)=0
\end{aligned}$$

or

$$\begin{aligned}
&[M]_{ij}^{ab}(I,J)\cdot\{v\}_j^a(J)+[K]_{ij}^{ab}(I,J)\cdot\{v\}_j^a(J)\\
&=\{J_{ext}\}_i^a(I)+\{J_0\}_i^a(I)-\{J_{\sigma^n}\}_i^a(I)
\end{aligned}\tag{A.3}$$

The matrix-vector form of Eq. (A.3) is

$$[\mathbf{M}]\cdot\{\tilde{\mathbf{v}}\}+[\mathbf{K}]\cdot\{\tilde{\mathbf{v}}\}=\{\mathbf{J}_{ext}\}+\{\mathbf{J}_0\}-\{\mathbf{J}_{\sigma^n}\}\tag{A.4}$$

If Rayleigh damping is employed to model the material damping then Eq. (A.4) becomes

$$\begin{aligned}&[\mathbf{M}]\cdot\{\tilde{\mathbf{v}}\}+[\mathbf{K}]\cdot\{\tilde{\mathbf{v}}\}+\alpha\,[\mathbf{M}_R]\cdot\{\tilde{\mathbf{v}}\}+\beta\,[\mathbf{K}_R]\cdot\{\tilde{\mathbf{v}}\}\\&=\{\mathbf{J}_{ext}\}+\{\mathbf{J}_0\}-\{\mathbf{J}_{\sigma^n}\}\end{aligned}\tag{A.5}$$

Description of the space-time matrices and space-time nodal vectors that appear in the above mentioned equations is given as follows.

In Eq. (A.4) and Eq. (A.5), $[\mathbf{M}]$ (in component form $[M]_{ij}^{ab}(I,J)$) is the space-time mass matrix.

$$\begin{aligned}[M]_{ij}^{ab}(I,J)=\delta_{ij}\int_{I_n}\int_{\Omega}N^I T_a\rho\frac{\partial N^J T_b}{\partial t}d\Omega dt\\+\delta_{ij}\delta_{1a}\delta_{1b}\int_{\Omega}N^I\rho N^J d\Omega\end{aligned}\tag{A.6}$$

or

$$\begin{aligned}[M]_{ij}^{ab}(I,J)=\delta_{ij}\int_{I_n}T_a\frac{\partial T_b}{\partial t}dt\int_{\Omega}N^I\rho N^J d\Omega\\+\delta_{ij}\delta_{1a}\delta_{1b}\int_{\Omega}N^I\rho N^J d\Omega\end{aligned}\tag{A.7}$$

where δ_{ij} is the Dirac-delta function. In above equation using the expression for $T_1(\theta)$ and $T_2(\theta)$ given in Eq. (2.141) one can obtain the following.

$$[\mathbf{M}]=\frac{1}{2}\begin{bmatrix}\mathbf{M}^{\Omega} & \mathbf{M}^{\Omega}\\ -\mathbf{M}^{\Omega} & \mathbf{M}^{\Omega}\end{bmatrix}\tag{A.8}$$

where

$$\left[\mathbf{M}^{\Omega}\right]=\begin{bmatrix}\mathbf{m} & 0\\ 0 & \mathbf{m}\end{bmatrix}\tag{A.9}$$

in which

$$m(I,J)=\int_{\Omega}N^I\rho N^J d\Omega\tag{A.10}$$

In Eq. (A.4) and Eq. (A.5), $[\mathbf{K}]$ (or $[K]_{ij}^{ab}$) is the space-time tangent stiffness matrix.

$$[K]_{ij}^{ab}(I,J)=\int_{I_n}\int_{\Omega}\frac{\partial N^I T_a}{\partial x_p}C_{pijq}\frac{\partial N^J\tilde{T}_b}{\partial x_q}d\Omega dt\tag{A.11}$$

or

$$[K]_{ij}^{ab}(I,J)=\int_{I_n}T_a\tilde{T}_b dt\int_{\Omega}\frac{\partial N^I}{\partial x_p}C_{pijq}\frac{\partial N^J}{\partial x_q}d\Omega\tag{A.12}$$

In above equation, using the expression for $T_a(\theta)$ and $\tilde{T}_a(\theta)$ as given in Eq. (2.141) and Eq. (2.146), respectively.

$$[\mathbf{K}] = \frac{\Delta t_n^2}{24} \begin{bmatrix} 3\mathbf{K}^\Omega & \mathbf{K}^\Omega \\ 5\mathbf{K}^\Omega & 3\mathbf{K}^\Omega \end{bmatrix} \tag{A.13}$$

where

$$\left[\mathbf{K}^\Omega\right] = \begin{bmatrix} \mathbf{k}_{11} & \mathbf{k}_{12} \\ \mathbf{k}_{21} & \mathbf{k}_{22} \end{bmatrix} \tag{A.14}$$

in which

$$k_{ij}\,(I,J) = \int_\Omega \frac{\partial N^I}{\partial x_p} C_{pijq} \frac{\partial N^J}{\partial x_q} d\Omega \tag{A.15}$$

In Eq. (A.5), $[\mathbf{M}_R]$ is the mass proportional space-time Rayleigh damping matrix.

$$[M_R]_{ij}^{ab}\,(I,J) = \delta_{ij} \int_{I_n} \int_\Omega N^I T_a \rho N^J T_b d\Omega dt \tag{A.16}$$

or

$$[M_R]_{ij}^{ab}\,(I,J) = \delta_{ij} \int_{I_n} T_a T_b dt \int_\Omega N^I \rho N^J d\Omega \tag{A.17}$$

In above equation using the expression for $T_1(\theta)$ and $T_2(\theta)$ as given in Eq. (2.141).

$$[\mathbf{M}_R] = \frac{\Delta t_n}{6} \begin{bmatrix} 2\mathbf{M}^\Omega & \mathbf{M}^\Omega \\ \mathbf{M}^\Omega & 2\mathbf{M}^\Omega \end{bmatrix} \tag{A.18}$$

where $\mathbf{M}^\Omega$ is given by Eq. (A.9).

In Eq. (A.5), $[\mathbf{K}_R]$ is the stiffness proportional space-time Rayleigh damping matrix.

$$[K_R]_{ij}^{ab}\,(I,J) = \int_{I_n} \int_\Omega \frac{\partial N^I T_a}{\partial x_p} C_{pijq} \frac{\partial N^J T_b}{\partial x_q} d\Omega dt \tag{A.19}$$

or

$$[K_R]_{ij}^{ab}\,(I,J) = \int_{I_n} T_a T_b dt \int_\Omega \frac{\partial N^I}{\partial x_p} C_{pijq} \frac{\partial N^J}{\partial x_q} d\Omega \tag{A.20}$$

In above equation using the expression for $T_1(\theta)$ and $T_2(\theta)$ given in Eq. (2.141).

$$[\mathbf{K}_R] = \frac{\Delta t_n}{6} \begin{bmatrix} 2\mathbf{K}^\Omega & \mathbf{K}^\Omega \\ \mathbf{K}^\Omega & 2\mathbf{K}^\Omega \end{bmatrix} \tag{A.21}$$

where $\mathbf{K}^\Omega$ is given by Eq. (A.14).

In Eq. (A.4) and Eq. (A.5), $\{\mathbf{J}_{ext}\}$ (or $\{J_{ext}\}_i^a(I)$) is the space-time nodal vector which contains the contribution of external body force $\mathbf{b}$ and surface force $\mathbf{f}^s$.

$$\{J_{ext}\}_i^a(I) = \int_{I_n}\int_{\Omega} N^I T_a \rho b_i d\Omega dt + \int_{I_n}\int_{\Gamma_i^h} N^I T_a f_i^s ds dt \tag{A.22}$$

The space-time data-structure of $\{\mathbf{J}_{ext}\}$ is given by

$$\{\mathbf{J}_{ext}\} = \begin{Bmatrix} \mathbf{J}_{ext}^1 \\ \mathbf{J}_{ext}^2 \end{Bmatrix} \tag{A.23}$$

where $\{\mathbf{J}_{ext}^1\}$ and $\{\mathbf{J}_{ext}^2\}$ correspond to the space-nodal values at the bottom and top space-time slab. These vectors are arranged in terms of x_1 and x_2 spatial components as,

$$\left\{\mathbf{J}_{ext}^1\right\} = \begin{Bmatrix} \mathbf{J}_{ext,1}^1 \\ \mathbf{J}_{ext,2}^1 \end{Bmatrix} \quad \left\{\mathbf{J}_{ext}^2\right\} = \begin{Bmatrix} \mathbf{J}_{ext,1}^2 \\ \mathbf{J}_{ext,2}^2 \end{Bmatrix} \tag{A.24}$$

where $\left\{\mathbf{J}_{ext,1}^a\right\}$ and $\left\{\mathbf{J}_{ext,1}^a\right\}$ denote the space-nodal values of x_1 and x_2 components, respectively (here $a = 1$ corresponds to the bottom space-time slab and $a = 2$ corresponds to the top space-time slab).

$$\begin{aligned} J_{ext,1}^1(I) &= \int_{I_n}\int_{\Omega} N^I T_1 \rho b_1 d\Omega dt + \int_{I_n}\int_{\Gamma_1^h} N^I T_1 f_1^s ds dt \\ J_{ext,2}^1(I) &= \int_{I_n}\int_{\Omega} N^I T_1 \rho b_2 d\Omega dt + \int_{I_n}\int_{\Gamma_2^h} N^I T_1 f_2^s ds dt \end{aligned} \tag{A.25}$$

$$\begin{aligned} J_{ext,1}^2(I) &= \int_{I_n}\int_{\Omega} N^I T_2 \rho b_1 d\Omega dt + \int_{I_n}\int_{\Gamma_1^h} N^I T_2 f_1^s ds dt \\ J_{ext,2}^2(I) &= \int_{I_n}\int_{\Omega} N^I T_2 \rho b_2 d\Omega dt + \int_{I_n}\int_{\Gamma_2^h} N^I T_2 f_2^s ds dt \end{aligned} \tag{A.26}$$

In Eq. (A.4) and Eq. (A.5), $\{\mathbf{J}_0\}$ is the space-time vector which contains the contribution of initial velocity ${}^0\mathbf{v}$.

$$\{J_0\}_i^a(I) = \delta_{a1}\delta_{ij}\left(\int_{\Omega} N^I \rho N^J d\Omega\right)\left\{{}^0v_{jJ}\right\} \tag{A.27}$$

The space-time data-structure of $\{\mathbf{J}_0\}$ is given by

$$\{\mathbf{J}_0\} = \begin{Bmatrix} \mathbf{J}_0^{\Omega} \\ \mathbf{0} \end{Bmatrix} \tag{A.28}$$

where

$$\left\{\mathbf{J}_0^{\Omega}\right\} = \left[\mathbf{M}^{\Omega}\right] \cdot \left\{\tilde{\mathbf{v}}^0\right\} \tag{A.29}$$

where $\left[\mathbf{M}^{\Omega}\right]$ is given by Eq. (A.9), and $\{\tilde{\mathbf{v}}^0\}$ is space-nodal values of velocity at the last time step.

In Eq. (A.4) and Eq. (A.5), $\{\mathbf{J}_{\sigma^n}\}$ is the space-time vector that contains the contribution of initial stress σ^n.

$$\{J_{\sigma^n}\}_i^a(I) = \int_{I_n}\int_{\Omega} \frac{\partial N^I T_a}{\partial x_j}\sigma_{ij}^n d\Omega dt$$

or

$$\{J_{\sigma^n}\}_i^a(I) = \int_{I_n} T_a dt \int_{\Omega} \frac{\partial N^I}{\partial x_j}\sigma_{ij}^n d\Omega \tag{A.30}$$

The space-time data-structure of $\{\mathbf{J}_{\sigma^n}\}$ is given by

$$\{\mathbf{J}_{\sigma^n}\} = \frac{\Delta t_n}{2}\begin{Bmatrix} \mathbf{f}_{\text{int}} \\ \mathbf{f}_{\text{int}} \end{Bmatrix} \tag{A.31}$$

where $\mathbf{f}_{\text{int}}$ represent the space nodal values of internal-force. This vectors is further arranged in terms of x_1 and x_2 spatial components as,

$$\{\mathbf{f}_{\text{int}}\} = \begin{Bmatrix} \mathbf{f}_1^{\text{int}} \\ \mathbf{f}_2^{\text{int}} \end{Bmatrix} \tag{A.32}$$

in which $\mathbf{f}_1^{\text{int}}$ and $\mathbf{f}_1^{\text{int}}$ denote the space-nodal values of x_1 and x_2 components, respectively.

$$f_1^{\text{int}}(I) = \int_{\Omega} \frac{\partial N^I}{\partial x_j}\sigma_{j1}^n d\Omega \quad f_2^{\text{int}}(I) = \int_{\Omega} \frac{\partial N^I}{\partial x_j}\sigma_{j2}^n d\Omega \tag{A.33}$$

B

Space-Time Finite Element Matrices and Vectors for Dynamic Soil-Structure Interaction Problem

In section 4.3 of chapter 4 following v-ST/FEM weak form for dynamic soil-structure interaction problem was derived,

$$\begin{aligned}
&\int_{I_n}\int_{\Omega_h}\delta v_i\rho\frac{\partial v_i}{\partial t}d\Omega dt+\int_{\Omega_h}\delta v_i\left(\mathbf{x},t_n^+\right)\rho v_i\left(x,t_n^+\right)d\Omega\\
&-\int_{\Omega_h}\delta v_i\left(\mathbf{x},t_n^+\right)\rho v_i\left(x,t_n^-\right)d\Omega-\int_{I_n}\int_{\Omega_h}\delta v_i\rho b_i d\Omega dt\\
&+\int_{I_n}\int_{\Omega_h}\frac{\partial\delta v_i}{\partial x_j}\sigma_{ij}^n d\Omega dt+\int_{I_n}\int_{\Omega_h}\frac{\partial\delta v_i}{\partial x_j}C_{ijkl}\psi_{kl}d\Omega dt-\int_{I_n}\int_{\Gamma_i^h}\delta v_i f_i^s dsdt\\
&+\int_{I_n}\int_{\Gamma_\infty^R\cup\Gamma_\infty^L}\delta v_i c_{ij}^v v_j dsdt+\int_{I_n}\int_{\Gamma_\infty^B}\delta v_i c_{ip}^h v_p dsdt\\
&-\int_{I_n}\int_{\Gamma_\infty^R\cup\Gamma_\infty^L}\delta v_i\left(c_{ij}^v v_j^f+\sigma_{ij}^f n_j\right)dsdt-\int_{I_n}\int_{\Gamma_\infty^B}\delta v_i 2c_{ij}^h v_j^{in}dsdt=0
\end{aligned}\tag{B.1}$$

In above equation using the space-time interpolation for v_i and δv_i that is given by Eq. (4.28) and Eq. (4.29) , respectively, (see section 4.4)

$$\begin{aligned}
&\{\delta v\}_i^a(I)\cdot[M]_{ij}^{ab}(I,J)\cdot\{v\}_j^b(J)+\{\delta v\}_i^a(I)\cdot[K]_{ij}^{ab}(I,J)\cdot\{v\}_j^b(J)\\
&+\{\delta v\}_i^a(I)\cdot[C_{L\infty}]_{ij}^{ab}(I,J)\cdot\{v\}_j^b(J)+\{\delta v\}_i^a(I)\cdot[C_{R\infty}]_{ij}^{ab}(I,J)\cdot\{v\}_j^b(J)\\
&+\{\delta v\}_i^a(I)\cdot[C_{B\infty}]_{ij}^{ab}(I,J)\cdot\{v\}_j^b(J)-\{\delta v\}_i^a(I)\cdot\{J_{ext}\}_i^a(I)\\
&-\{\delta v\}_i^a(I)\cdot\{J_0\}_i^a(I)+\{\delta v\}_i^a(I)\cdot\{J_{\sigma^n}\}_i^a(I)\\
&-\{\delta v\}_i^a(I)\cdot\{J_f\}_i^a(I)-\{\delta v\}_i^a(I)\cdot\{J_{in}\}_i^a(I)=0
\end{aligned}\tag{B.2}$$

Noting that the above equation is true for all values of $\{\delta v\}_i^a(I)$, hence

$$\begin{aligned}
&[M]_{ij}^{ab}(I,J)\cdot\{v\}_j^b(J)+[K]_{ij}^{ab}(I,J)\cdot\{v\}_j^b(J)+[C_{L\infty}]_{ij}^{ab}(I,J)\cdot\{v\}_j^b(J)\\
&+[C_{R\infty}]_{ij}^{ab}(I,J)\cdot\{v\}_j^b(J)+[C_{B\infty}]_{ij}^{ab}(I,J)\cdot\{v\}_j^b(J)\\
&-\{J_{ext}\}_i^a(I)-\{J_0\}_i^a(I)+\{J_{\sigma^n}\}_i^a(I)-\{J_f\}_i^a(I)-\{J_{in}\}_i^a(I)=0
\end{aligned}$$

or

$$
\begin{aligned}
&[M]_{ij}^{ab}(I,J)\cdot\{v\}_j^b(J)+[K]_{ij}^{ab}(I,J)\cdot\{v\}_j^b(J)+[C_{L\infty}]_{ij}^{ab}(I,J)\cdot\{v\}_j^b(J)\\
&+[C_{R\infty}]_{ij}^{ab}(I,J)\cdot\{v\}_j^b(J)+[C_{B\infty}]_{ij}^{ab}(I,J)\cdot\{v\}_j^b(J)\\
&=\{J_{ext}\}_i^a(I)+\{J_0\}_i^a(I)-\{J_{\sigma^n}\}_i^a(I)+\{J_f\}_i^a(I)+\{J_{in}\}_i^a(I)
\end{aligned}
\tag{B.3}
$$

The matrix-vector form of Eq. (B.3) is

$$
\begin{aligned}
&[\mathbf{M}]\cdot\{\tilde{\mathbf{v}}\}+[\mathbf{K}]\cdot\{\tilde{\mathbf{v}}\}+[\mathbf{C}_{L\infty}]\cdot\{\tilde{\mathbf{v}}\}+[\mathbf{C}_{R\infty}]\cdot\{\tilde{\mathbf{v}}\}+[\mathbf{C}_{B\infty}]\cdot\{\tilde{\mathbf{v}}\}\\
&=\{\mathbf{J}_{ext}\}+\{\mathbf{J}_0\}-\{\mathbf{J}_{\sigma^n}\}+\{\mathbf{J}_f\}+\{\mathbf{J}_{in}\}
\end{aligned}
\tag{B.4}
$$

If Rayleigh damping is adopted to model the material damping then Eq. (B.4) becomes the following.

$$
\begin{aligned}
&[\mathbf{M}]\cdot\{\tilde{\mathbf{v}}\}+[\mathbf{K}]\cdot\{\tilde{\mathbf{v}}\}+[\mathbf{C}_{L\infty}]\cdot\{\tilde{\mathbf{v}}\}+[\mathbf{C}_{R\infty}]\cdot\{\tilde{\mathbf{v}}\}+[\mathbf{C}_{B\infty}]\cdot\{\tilde{\mathbf{v}}\}\\
&+\alpha[\mathbf{M}_R]\cdot\{\tilde{\mathbf{v}}\}+\beta[\mathbf{K}_R]\cdot\{\tilde{\mathbf{v}}\}=\{\mathbf{J}_{ext}\}+\{\mathbf{J}_0\}-\{\mathbf{J}_{\sigma^n}\}+\{\mathbf{J}_f\}+\{\mathbf{J}_{in}\}
\end{aligned}
\tag{B.5}
$$

Description of the space-time matrices and space-time nodal vectors that appear in the above mentioned equations is given as follows.

In Eq. (B.4) and Eq. (B.5), $[\mathbf{M}]$ is the space-time mass matrix which is identical to the one given by Eq. (A.6). $[\mathbf{K}]$ is the space-time tangent matrix given and its expression is given by Eq. (A.11). $[\mathbf{M}_R]$ is the mass proportional space-time Rayleigh damping matrix given by Eq. (A.16), and $[\mathbf{K}_R]$ is the stiffness proportional space-time Rayleigh damping matrix given by Eq. (A.19).

In Eq. (B.4) and Eq. (B.5), $[\mathbf{C}_{L\infty}]$ is the space-time matrix due to the dashpots placed at the left-side truncated (or absorbing) boundary.

$$
[C_{L\infty}]_{ij}^{ab}(I,J)=\int_{I_n}\int_{\Gamma_\infty^L}N^I T_a c_{ij}^v N^J T_b ds dt \tag{B.6}
$$

or

$$
[C_{L\infty}]_{ij}^{ab}(I,J)=\int_{I_n}T_a T_b dt\int_{\Gamma_\infty^L}N^I c_{ij}^v N^J ds \tag{B.7}
$$

In above equation using the expression for $T_1(\theta)$ and $T_2(\theta)$ given in Eq. (4.27) (see section 4.4)

$$
[\mathbf{C}_{L\infty}]=\frac{\Delta t_n}{6}\begin{bmatrix}2\mathbf{C}_{L\infty}^{\Gamma} & \mathbf{C}_{L\infty}^{\Gamma}\\ \mathbf{C}_{L\infty}^{\Gamma} & 2\mathbf{C}_{L\infty}^{\Gamma}\end{bmatrix} \tag{B.8}
$$

where the matrix $\left[\mathbf{C}_{L\infty}^{\Gamma}\right]$ is evaluated on the spatial domain of left-side truncated boundary Γ_∞^L and given by

$$
\left[\mathbf{C}_{L\infty}^{\Gamma}\right]=\begin{bmatrix}\mathbf{c}_{11}^{L\infty} & \mathbf{0}\\ \mathbf{0} & \mathbf{c}_{22}^{L\infty}\end{bmatrix} \tag{B.9}
$$

in which

$$c_{11}^{L\infty}(I,J) = \int_{\Gamma_\infty^L} N^I \rho c_L N^J ds \tag{B.10}$$

$$c_{22}^{L\infty}(I,J) = \int_{\Gamma_\infty^L} N^I \rho c_T N^J ds \tag{B.11}$$

where c_L and c_T denote the speed of P-wave and S-wave in the elastic medium.

In Eq. (B.4) and Eq. (B.5), $[\mathbf{C}_{R\infty}]$ is the space-time matrix due to the dashpots placed at the right-side truncated (or absorbing) boundary.

$$[C_{R\infty}]_{ij}^{ab}(I,J) = \int_{I_n}\int_{\Gamma_\infty^R} N^I T_a c_{ij}^v N^J T_b ds dt \tag{B.12}$$

or

$$[C_{R\infty}]_{ij}^{ab}(I,J) = \int_{I_n} T_a T_b dt \int_{\Gamma_\infty^R} N^I c_{ij}^v N^J ds \tag{B.13}$$

In above equation using the expression for $T_1(\theta)$ and $T_2(\theta)$ given in Eq. (4.27) (see section 4.4)

$$[\mathbf{C}_{R\infty}] = \frac{\Delta t_n}{6}\begin{bmatrix} 2\mathbf{C}_{R\infty}^{\Gamma} & \mathbf{C}_{R\infty}^{\Gamma} \\ \mathbf{C}_{R\infty}^{\Gamma} & 2\mathbf{C}_{R\infty}^{\Gamma} \end{bmatrix} \tag{B.14}$$

where the matrix $\left[\mathbf{C}_{R\infty}^{\Gamma}\right]$ is evaluated on the spatial domain of right-side truncated boundary Γ_∞^R and given by

$$\left[\mathbf{C}_{R\infty}^{\Gamma}\right] = \begin{bmatrix} \mathbf{c}_{11}^{R\infty} & \mathbf{0} \\ \mathbf{0} & \mathbf{c}_{22}^{R\infty} \end{bmatrix} \tag{B.15}$$

in which

$$c_{11}^{R\infty}(I,J) = \int_{\Gamma_\infty^R} N^I \rho c_L N^J ds \tag{B.16}$$

$$c_{22}^{R\infty}(I,J) = \int_{\Gamma_\infty^R} N^I \rho c_T N^J ds \tag{B.17}$$

where c_L and c_T denote the speed of P-wave and S-wave in the elastic medium.

In Eq. (B.4) and Eq. (B.5), $[\mathbf{C}_{B\infty}]$ is the space-time matrix due to the dashpots placed at the bottom truncated (or absorbing) boundary.

$$[C_{B\infty}]_{ij}^{ab}(I,J) = \int_{I_n}\int_{\Gamma_\infty^B} N^I T_a c_{ij}^h N^J T_b ds dt \tag{B.18}$$

or

$$[C_{B\infty}]_{ij}^{ab}(I,J) = \int_{I_n} T_a T_b dt \int_{\Gamma_\infty^B} N^I c_{ij}^h N^J ds \tag{B.19}$$

In above equation using the expression for $T_1(\theta)$ and $T_2(\theta)$ given in Eq. (4.27) (see section 4.4)

$$[\mathbf{C}_{B\infty}] = \frac{\Delta t_n}{6}\begin{bmatrix} 2\mathbf{C}^{\Gamma}_{B\infty} & \mathbf{C}^{\Gamma}_{B\infty} \\ \mathbf{C}^{\Gamma}_{B\infty} & 2\mathbf{C}^{\Gamma}_{B\infty} \end{bmatrix} \tag{B.20}$$

where the matrix $\left[\mathbf{C}^{\Gamma}_{B\infty}\right]$ is evaluated on the spatial domain of bottom truncated boundary Γ^B_∞ and given by

$$\left[\mathbf{C}^{\Gamma}_{B\infty}\right] = \begin{bmatrix} \mathbf{c}^{B\infty}_{11} & \mathbf{0} \\ \mathbf{0} & \mathbf{c}^{B\infty}_{22} \end{bmatrix} \tag{B.21}$$

in which

$$c^{B\infty}_{11}(I,J) = \int_{\Gamma^B_\infty} N^I \rho c_T N^J ds \tag{B.22}$$

$$c^{B\infty}_{22}(I,J) = \int_{\Gamma^B_\infty} N^I \rho c_L N^J ds \tag{B.23}$$

where c_L and c_T denote the speed of P-wave and S-wave in the elastic medium.

In Eq. (B.4) and Eq. (B.5), $\{\mathbf{J}_{ext}\}$ is the space-time nodal vector that contains the contribution of external body force $\mathbf{b}$ and surface force $\mathbf{f}^s$ (see Eq. (A.22)). $\{\mathbf{J}_0\}$ is the space-time nodal vector that contains the contribution of initial velocity, and is given by Eq. (A.27). $\{\mathbf{J}_{\sigma^n}\}$ is the space-time nodal vector that contains the contribution of initial stress (σ^n), and is given by Eq. (A.30).

In Eq. (B.4) and Eq. (B.5), $\{\mathbf{J}_f\}$ is the space-time nodal vector that contains the contribution of free-field response of soil-domain.

$$\begin{aligned} \{J_f\}^a_i(I) = &\int_{I_n}\int_{\Gamma^L_\infty} N^I T_a\left(c^v_{ij}v^f_j - \sigma^f_{i1}\right) dsdt \\ &+ \int_{I_n}\int_{\Gamma^R_\infty} N^I T_a\left(c^v_{ij}v^f_j + \sigma^f_{i1}\right) dsdt \end{aligned} \tag{B.24}$$

The space-time data-structure of $\{\mathbf{J}_f\}$ is given by

$$\{\mathbf{J}_f\} = \begin{Bmatrix} \mathbf{J}^1_f \\ \mathbf{J}^2_f \end{Bmatrix} \tag{B.25}$$

where $\left\{\mathbf{J}^1_f\right\}$ and $\left\{\mathbf{J}^2_f\right\}$ correspond to the space-nodal values at the bottom and top space-time slab. These vectors are further arranged in terms of x_1 and x_2 spatial components as,

$$\left\{\mathbf{J}^1_f\right\} = \begin{Bmatrix} \mathbf{J}^1_{f,1} \\ \mathbf{J}^1_{f,2} \end{Bmatrix} \quad \left\{\mathbf{J}^2_f\right\} = \begin{Bmatrix} \mathbf{J}^2_{f,1} \\ \mathbf{J}^2_{f,2} \end{Bmatrix} \tag{B.26}$$

where $\left\{\mathbf{J}^a_{f,1}\right\}$ and $\left\{\mathbf{J}^a_{f,2}\right\}$ denote the space-nodal values of x_1 and x_2 components, respectively (here $a = 1$ and $a = 2$ correspond to the bottom and top space-time slab).

$$\begin{aligned} J^1_{f,1}(I) = &\int_{I_n}\int_{\Gamma^L_\infty} N^I T_1 \left(\rho c_L v^f_1 - \sigma^f_{11}\right) dsdt \\ &+ \int_{I_n}\int_{\Gamma^R_\infty} N^I T_1 \left(\rho c_L v^f_1 + \sigma^f_{11}\right) dsdt \end{aligned} \tag{B.27}$$

$$\begin{aligned} J^1_{f,2}(I) = &\int_{I_n}\int_{\Gamma^L_\infty} N^I T_1 \left(\rho c_T v^f_2 - \sigma^f_{21}\right) dsdt \\ &+ \int_{I_n}\int_{\Gamma^R_\infty} N^I T_1 \left(\rho c_T v^f_2 + \sigma^f_{21}\right) dsdt \end{aligned} \tag{B.28}$$

$$\begin{aligned} J^2_{f,1}(I) = &\int_{I_n}\int_{\Gamma^L_\infty} N^I T_2 \left(\rho c_L v^f_1 - \sigma^f_{11}\right) dsdt \\ &+ \int_{I_n}\int_{\Gamma^R_\infty} N^I T_2 \left(\rho c_L v^f_1 + \sigma^f_{11}\right) dsdt \end{aligned} \tag{B.29}$$

$$\begin{aligned} J^2_{f,2}(I) = &\int_{I_n}\int_{\Gamma^L_\infty} N^I T_2 \left(\rho c_T v^f_2 - \sigma^f_{21}\right) dsdt \\ &+ \int_{I_n}\int_{\Gamma^R_\infty} N^I T_2 \left(\rho c_T v^f_2 + \sigma^f_{21}\right) dsdt \end{aligned} \tag{B.30}$$

In Eq. (B.4) and Eq. (B.5), $\{\mathbf{J}_{in}\}$ is the space-time nodal vector that contains the contribution of input seismic motion.

$$\{J_{in}\}^a_i(I) = \int_{I_n}\int_{\Gamma^B_\infty} N^I T_a 2c^h_{ij} v^{in}_j dsdt \tag{B.31}$$

The space-time data-structure of $\{\mathbf{J}_{in}\}$ is given by

$$\{\mathbf{J}_{in}\} = \left\{ \begin{array}{c} \mathbf{J}^1_{in} \\ \mathbf{J}^2_{in} \end{array} \right\} \tag{B.32}$$

where $\{\mathbf{J}^1_{in}\}$ and $\{\mathbf{J}^2_{in}\}$ correspond to the space-nodal values at bottom and top space-time slab. These vectors are further arranged in terms of x_1 and x_2 spatial components as,

$$\left\{\mathbf{J}^1_{in}\right\} = \left\{ \begin{array}{c} \mathbf{J}^1_{in,1} \\ \mathbf{J}^1_{in,2} \end{array} \right\} \quad \left\{\mathbf{J}^2_{in}\right\} = \left\{ \begin{array}{c} \mathbf{J}^2_{in,1} \\ \mathbf{J}^2_{in,2} \end{array} \right\} \tag{B.33}$$

where $\left\{\mathbf{J}^a_{in,1}\right\}$ and $\left\{\mathbf{J}^a_{in,2}\right\}$ denote the space-nodal values of x_1 and x_2 components, respectively (here $a = 1$ and $a = 2$ correspond to the bottom and top space-time slab).

$$J^1_{in,1}(I) = \int_{I_n}\int_{\Gamma^B_\infty} N^I T_1 2\rho c_T v_1^{in} ds dt \tag{B.34}$$

$$J^1_{in,2}(I) = \int_{I_n}\int_{\Gamma^B_\infty} N^I T_1 2\rho c_L v_2^{in} ds dt \tag{B.35}$$

$$J^2_{in,1}(I) = \int_{I_n}\int_{\Gamma^B_\infty} N^I T_2 2\rho c_T v_1^{in} ds dt \tag{B.36}$$

$$J^2_{in,2}(I) = \int_{I_n}\int_{\Gamma^B_\infty} N^I T_2 2\rho c_L v_2^{in} ds dt \tag{B.37}$$

C

Space-Time Finite Element Matrices and Vectors for Dam-Reservoir Interaction Problem

Section 5.4.1 describes the following v-ST/FEM weak form for the dynamic interaction between dam and reservoir subjected to the horizontal and verticle components of the ground motion.

$$
\begin{aligned}
&\int_{I_n}\int_{\Omega_h^f}\delta q\frac{1}{c^2}\frac{\partial q}{\partial t}d\Omega dt+\int_{\Omega_h^f}\delta q\left(\mathbf{x},t_n\right)\frac{1}{c^2}q\left(\mathbf{x},t_n^+\right)d\Omega\\
&-\int_{\Omega_h^f}\delta q\left(\mathbf{x},t_n\right)\frac{1}{c^2}q\left(\mathbf{x},t_n^-\right)d\Omega+\int_{I_n}\int_{\Omega_h^f}\frac{\partial\delta q}{\partial x_i}\frac{\partial p}{\partial x_i}d\Omega dt\\
&+\int_{I_n}\int_{\Gamma_{fd}^f}\delta q\rho^f\frac{\partial v_i}{\partial t}n_i^f dsdt+\int_{I_n}\int_{\Gamma_{fs}^f}\delta q\rho^f a_i^g n_i^f dsdt\\
&+\int_{I_n}\int_{\Gamma_{fs}^f}\delta q\rho^f q_c q dsdt+\int_{I_n}\int_{\Gamma_\infty^f}\delta q\frac{1}{c}qdsdt\\
&-\int_{I_n}\int_{\Gamma_\infty^f}\delta q\frac{1}{c}q^f dsdt=0
\end{aligned}
\tag{C.1}
$$

$$
\begin{aligned}
&\int_{I_n}\int_{\Omega_h^s}\rho^s\delta v_i\frac{\partial v_i}{\partial t}d\Omega dt+\int_{\Omega_h^s}\rho^s\delta v_i\left(\mathbf{x},t_n^+\right)v_i\left(x,t_n^+\right)d\Omega\\
&-\int_{\Omega_h^s}\rho^s\delta v_i\left(\mathbf{x},t_n^+\right)v_i\left(x,t_n^-\right)d\Omega+\int_{I_n}\int_{\Omega_h^s}\frac{\partial\delta v_i}{\partial x_j}C_{ijkl}\psi_{kl}d\Omega dt\\
&-\int_{I_n}\int_{\Gamma_i^h}\delta v_i f_i^s dsdt-\int_{I_n}\int_{\Omega_h^s}\rho^s\delta v_i b_i d\Omega dt\\
&+\int_{I_n}\int_{\Omega_h^s}\frac{\partial\delta v_i}{\partial x_j}\sigma_{ij}^n d\Omega dt+\int_{I_n}\int_{\Gamma_{fd}^s}\delta v_i p n_i^s dsdt\\
&+\int_{I_n}\int_{\Gamma_{fd}^s}\delta v_i p_0 n_i^s dsdt=0
\end{aligned}
\tag{C.2}
$$

In Eq. (C.1) and Eq. (C.2) by using the space-time interpolation for $\delta\mathbf{v}$, $\mathbf{v}$, δq, and q given by Eq. (5.41), Eq. (5.42), Eq. (5.46), and Eq. (5.47), respectively, one can obtain the following discrete form of v-ST/FEM weak form.

$$\begin{aligned}
&\{\delta q\}^a(I)\cdot\left[M^f\right]^{ab}(I,J)\cdot\{q\}^b(J)+\{\delta q\}^a(I)\cdot\left[K^f\right]^{ab}(I,J)\cdot\{q\}^b(J)\\
&+\{\delta q\}^a(I)\cdot\left[C^f_{fs}\right]^{ab}(I,J)\cdot\{q\}^b(J)+\{\delta q\}^a(I)\cdot\left[C^f_{\infty}\right]^{ab}(I,J)\cdot\{q\}^b(J)\\
&+\{\delta q\}^a(I)\cdot\left[H^f_{fd}\right]^{ab}_i(I,J)\cdot\{v\}^b_i(J)-\{\delta q\}^a(I)\cdot\left\{J^f_0\right\}^a(I)\\
&-\{\delta q\}^a(I)\cdot\left\{J^f_f\right\}^a(I)+\{\delta q\}^a(I)\cdot\left\{J^{fs}_g\right\}^a(I)\\
&+\{\delta q\}^a(I)\cdot\left\{J^f_{p^n}\right\}^a(I)=0
\end{aligned}\tag{C.3}$$

$$\begin{aligned}
&\{\delta v\}^a_i(I)\cdot[M^s]^{ab}_{ij}(I,J)\cdot\{v\}^b_j(J)+\{\delta v\}^a_i(I)\cdot[K^s]^{ab}_{ij}(I,J)\cdot\{v\}^b_j(J)\\
&-\{\delta v\}^a_i(I)\cdot\{J^s_{ext}\}^a_i(I)-\{\delta v\}^a_i(I)\cdot\{J^s_0\}^a_i(I)+\{\delta v\}^a_i(I)\cdot\{J^s_{\sigma^n}\}^a_i(I)\\
&+\{\delta v\}^a_i(I)\cdot\left[H^s_{fd}\right]^{ab}_i(I,J)\cdot\{q\}^b(J)+\{\delta v\}^a_i(I)\cdot\left\{J^{fd}_{p^n}\right\}^a_i(I)\\
&+\{\delta v\}^a_i(I)\cdot\left\{J^{fd}_{p_0}\right\}^a_i(I)=0
\end{aligned}\tag{C.4}$$

Since Eq. (C.3) and Eq. (C.4) are true for all values of $\{\delta v\}^a_i(I)$ and $\{\delta q\}^a(I)$, the discrete weak form will produce following system of algebraic equations.

$$\begin{aligned}
&\left[M^f\right]^{ab}(I,J)\cdot\{q\}^b(J)+\left[K^f\right]^{ab}(I,J)\cdot\{q\}^b(J)\\
&+\left[C^f_{fs}\right]^{ab}(I,J)\cdot\{q\}^b(J)+\left[C^f_{\infty}\right]^{ab}(I,J)\cdot\{q\}^b(J)\\
&+\left[H^f_{fd}\right]^{ab}_i(I,J)\cdot\{v\}^b_i(J)-\left\{J^f_0\right\}^a(I)\\
&-\left\{J^f_f\right\}^a(I)+\left\{J^{fs}_g\right\}^a(I)+\left\{J^f_{p^n}\right\}^a(I)=0
\end{aligned}\tag{C.5}$$

$$\begin{aligned}
&[M^s]^{ab}_{ij}(I,J)\cdot\{v\}^b_j(J)+[K^s]^{ab}_{ij}(I,J)\cdot\{v\}^b_j(J)\\
&+\left[H^s_{fd}\right]^{ab}_i(I,J)\cdot\{q\}^b(J)-\{J^s_{ext}\}^a_i(I)-\{J^s_0\}^a_i(I)\\
&+\{J^s_{\sigma^n}\}^a_i(I)+\left\{J^{fd}_{p^n}\right\}^a_i(I)+\left\{J^{fd}_{p_0}\right\}^a_i(I)=0
\end{aligned}\tag{C.6}$$

The matrix-vector form of Eq. (C.5) and Eq. (C.6) is given by

$$\begin{aligned}
\left[\mathbf{M}^f\right]\cdot\{\tilde{\mathbf{q}}\}+\left[\mathbf{K}^f\right]\cdot\{\tilde{\mathbf{q}}\}+\left[\mathbf{C}^f_{fs}\right]\cdot\{\tilde{\mathbf{q}}\}+\left[\mathbf{C}^f_{\infty}\right]\cdot\{\tilde{\mathbf{q}}\}+\left[\mathbf{H}^f_{fd}\right]\cdot\{\tilde{\mathbf{v}}\}\\
=\left\{\mathbf{J}^f_0\right\}+\left\{\mathbf{J}^f_f\right\}-\left\{\mathbf{J}^{fs}_g\right\}-\left\{\mathbf{J}^f_{p^n}\right\}
\end{aligned}\tag{C.7}$$

$$
\begin{aligned}
&[\mathbf{M}^s]\{\tilde{\mathbf{v}}\} + [\mathbf{K}^s]\cdot\{\tilde{\mathbf{v}}\} + \left[\mathbf{H}^s_{fd}\right]\cdot\{\tilde{\mathbf{q}}\} \\
&= \{\mathbf{J}^s_{ext}\} + \{\mathbf{J}^s_0\} - \{\mathbf{J}^s_{\sigma^n}\} - \left\{\mathbf{J}^{fd}_{p^n}\right\} - \left\{\mathbf{J}^{fd}_{p_0}\right\}
\end{aligned}
\tag{C.8}
$$

If Rayleigh damping is employed to model the material damping in the solid domain then Eq. (C.8) is given by

$$
\begin{aligned}
&[\mathbf{M}^s]\cdot\{\tilde{\mathbf{v}}\} + [\mathbf{K}^s]\cdot\{\tilde{\mathbf{v}}\} + \alpha\,[\mathbf{M}^s_R]\cdot\{\tilde{\mathbf{v}}\} + \beta\,[\mathbf{K}^s_R]\cdot\{\tilde{\mathbf{v}}\} \\
&+ \left[\mathbf{H}^s_{fd}\right]\cdot\{\tilde{\mathbf{q}}\} = \{\mathbf{J}^s_{ext}\} + \{\mathbf{J}^s_0\} - \{\mathbf{J}^s_{\sigma^n}\} - \left\{\mathbf{J}^{fd}_{p^n}\right\} - \left\{\mathbf{J}^{fd}_{p_0}\right\}
\end{aligned}
\tag{C.9}
$$

In Eq. (C.7), $\left[\mathbf{M}^f\right]$ (or $\left[M^f\right]^{ab}(I,J)$) is space-time mass matrix for the fluid domain.

$$
\left[M^f\right]^{ab}(I,J) = \int_{I_n}\int_{\Omega^f_h} N^I_f T_a \frac{1}{c^2}\frac{\partial N^J_f T_b}{\partial t} d\Omega dt + \delta_{1a}\delta_{1b}\int_{\Omega^f_h} N^I_f \frac{1}{c^2} N^J_f d\Omega \tag{C.10}
$$

or

$$
\begin{aligned}
\left[M^f\right]^{ab}(I,J) = &\int_{I_n} T_a \frac{\partial T_b}{\partial t} dt \int_{\Omega^f_h} N^I_f \frac{1}{c^2} N^J_f d\Omega \\
&+ \delta_{1a}\delta_{1b}\int_{\Omega^f_h} N^I_f N^J_f d\Omega
\end{aligned}
\tag{C.11}
$$

In above equation using the expression for $T_1(\theta)$ and $T_2(\theta)$ given in Eq. (5.40),

$$
\left[\mathbf{M}^f\right] = \frac{1}{2}\begin{bmatrix} \mathbf{m}^f & \mathbf{m}^f \\ -\mathbf{m}^f & \mathbf{m}^f \end{bmatrix} \tag{C.12}
$$

where

$$
m^f(I,J) = \int_{\Omega^f_h} N^I_f \frac{1}{c^2} N^J_f d\Omega \tag{C.13}
$$

In Eq. (C.7), $\left[\mathbf{K}^f\right]$ (or $\left[K^f\right]^{ab}(I,J)$) is the space-time diffusion matrix for the fluid domain. In order to derive the expression for diffusion matrix following relation between p and q should be used,

$$
p(\mathbf{x},t) = p(\mathbf{x},t_n) + \tilde{T}_1(\theta)\,q(\mathbf{x},t_n) + \tilde{T}_2(\theta)\,q(\mathbf{x},t_{n+1}) \tag{C.14}
$$

where $q(\mathbf{x},t_n)$ and $q(\mathbf{x},t_n)$ are the values of q at bottom and top space-time slab, respectively. The expression for $\tilde{T}_1$ and $\tilde{T}_2$ are given in Eq. (5.45),

$$
\left[K^f\right]^{ab}(I,J) = \int_{I_n}\int_{\Omega^f_h} T_a \tilde{T}_b \frac{\partial N^I_f}{\partial x_i}\frac{\partial N^J_f}{\partial x_i} d\Omega dt \tag{C.15}
$$

or

$$\left[K^f\right]^{ab}(I,J) = \int_{I_n} T_a \tilde{T}_b dt \int_{\Omega_h^f} \frac{\partial N_f^I}{\partial x_i}\frac{\partial N_f^J}{\partial x_i} d\Omega \tag{C.16}$$

In above equation using the expression for $T_a(\theta)$ and $\tilde{T}_a(\theta)$ presented in Eq. (5.40) and Eq. (5.45), respectively.

$$\left[\mathbf{K}^f\right] = \frac{\Delta t_n^2}{24}\begin{bmatrix} 3\mathbf{k}^f & \mathbf{k}^f \\ 5\mathbf{k}^f & 3\mathbf{k}^f \end{bmatrix} \tag{C.17}$$

$$k^f(I,J) = \int_{\Omega_h^f} \frac{\partial N_f^I}{\partial x_i}\frac{\partial N_f^J}{\partial x_i} d\Omega \tag{C.18}$$

In Eq. (C.7), $\left[\mathbf{C}_{fs}^f\right]$ is the space-time matrix that correspond to the reservoir bottom absorption.

$$\left[C_{fs}^f\right]^{ab}(I,J) = \int_{I_n}\int_{\Gamma_{fs}^f} N_f^I T_a \rho^f q_c N_f^J T_b ds dt \tag{C.19}$$

or

$$\left[C_{fs}^f\right]^{ab}(I,J) = \int_{I_n} T_a T_b dt \int_{\Gamma_{fs}^f} N_f^I \rho^f q_c N_f^J ds \tag{C.20}$$

In above equation using the expression for $T_1(\theta)$ and $T_2(\theta)$ given in Eq. (5.40)

$$\left[\mathbf{C}_{fs}^f\right] = \frac{\Delta t_n}{6}\begin{bmatrix} 2\mathbf{c}_{fs}^f & \mathbf{c}_{fs}^f \\ \mathbf{c}_{fs}^f & 2\mathbf{c}_{fs}^f \end{bmatrix} \tag{C.21}$$

where

$$c_{fs}^f(I,J) = \int_{\Gamma_{fs}^f} N_f^I \rho^f q_c N_f^J ds \tag{C.22}$$

In Eq. (C.7), $\left[\mathbf{C}_{\infty}^f\right]$ is the space-time matrix that correspond to the dashpots placed at the truncated upstream boundary of reservoir.

$$\left[C_{\infty}^f\right]^{ab}(I,J) = \int_{I_n}\int_{\Gamma_{\infty}^f} N_f^I T_a \frac{1}{c} N_f^J T_b ds dt \tag{C.23}$$

or

$$\left[C_{\infty}^f\right]^{ab}(I,J) = \int_{I_n} T_a T_b dt \int_{\Gamma_{\infty}^f} N_f^I \frac{1}{c} N_f^J ds \tag{C.24}$$

using the expression for $T_1(\theta)$ and $T_2(\theta)$ presented in Eq. (5.40)

$$\left[\mathbf{C}_{\infty}^f\right] = \frac{\Delta t_n}{6}\begin{bmatrix} 2\mathbf{c}_{\infty}^f & \mathbf{c}_{\infty}^f \\ \mathbf{c}_{\infty}^f & 2\mathbf{c}_{\infty}^f \end{bmatrix} \tag{C.25}$$

where

$$c_{\infty}^f(I,J) = \int_{\Gamma_{\infty}^f} N_f^I \frac{1}{c} N_f^J ds \tag{C.26}$$

In Eq. (C.7), $\left[\mathbf{H}_{fd}^{f}\right]$ is the space-time matrix which couples the hydrodynamic response of reservoir and the dynamic response of the dam. Note that the reservoir dynamically interacts with the dam at the dam-reservoir interface. The space-time nodal vector for fluid domain that contains the contribution of the motion of dam is denoted by $\left\{\mathbf{J}_{fd}^{f}\right\}$, and it is given by

$$\left\{J_{fd}^{f}\right\}^{a}(I)=\int_{I_n}\int_{\Gamma_{fd}^{f}} N_f^I T_a \rho^f \frac{\partial v_i}{\partial t} n_i^f ds dt \tag{C.27}$$

In above equation using the space-time interpolation for velocity $\mathbf{v}$ as presented in Eq. (5.42)

$$\left\{J_{fd}^{f}\right\}^{a}(I)=\left(\int_{I_n}\int_{\Gamma_{fd}^{f}} N_f^I T_a \rho^f \frac{\partial N^J T_b}{\partial t} n_i^f ds dt\right)\cdot\{v\}_i^b(J) \tag{C.28}$$

or

$$\left\{J_{fd}^{f}\right\}^{a}(I)=\left(\int_{I_n} T_a \frac{\partial T_b}{\partial t} dt \int_{\Gamma_{fd}^{f}} N_f^I \rho^f N^J n_i^f ds\right)\{v\}_i^b(J) \tag{C.29}$$

The matrix-vector form of above equation is

$$\left\{\mathbf{J}_{fd}^{f}\right\}=\left[\mathbf{H}_{fd}^{f}\right]\{\tilde{\mathbf{v}}\} \tag{C.30}$$

where

$$\left[H_{fd}^{f}\right]_i^{ab}(I,J)=\int_{I_n} T_a \frac{\partial T_b}{\partial t} dt \int_{\Gamma_{fd}^{f}} N_f^I \rho^f N^J n_i^f ds \tag{C.31}$$

In above equation using the expression for $T_1(\theta)$ and $T_2(\theta)$ as presented in Eq. (5.40)

$$\left[\mathbf{H}_{fd}^{f}\right]=\frac{1}{2}\begin{bmatrix} -\mathbf{H}_{fd}^{\Gamma} & \mathbf{H}_{fd}^{\Gamma} \\ -\mathbf{H}_{fd}^{\Gamma} & \mathbf{H}_{fd}^{\Gamma}\end{bmatrix} \tag{C.32}$$

where the matrix $\mathbf{H}_{fd}^{\Gamma}$ is evaluated at the fluid-dam interface Γ_{fd}^{f}, and given by

$$\left[\mathbf{H}_{fd}^{\Gamma}\right]=\begin{bmatrix} \mathbf{h}_{11}^{fd} & \mathbf{0} \\ \mathbf{0} & \mathbf{h}_{22}^{fd}\end{bmatrix} \tag{C.33}$$

in which,

$$h_{11}^{fd}(\mathrm{I},J)=\int_{\Gamma_{fd}^{f}} N_f^I \rho^f N^J n_1^f ds \tag{C.34}$$

$$h_{22}^{fd}(\mathrm{I},J)=\int_{\Gamma_{fd}^{f}} N_f^I \rho^f N^J n_2^f ds \tag{C.35}$$

In Eq. (C.7), $\left\{\mathbf{J}_0^f\right\}$ is the space-time nodal vector that contain the contribution of the initial value of $\{\tilde{\mathbf{q}}^0\}$.

$$\left\{J_0^f\right\}^a(I) = \left(\delta_{1a}\int_{\Omega_h^f} N_f^I \frac{1}{c^2} N_f^J d\Omega\right)\,{}^0q_J \tag{C.36}$$

the space-time structure of $\left\{\mathbf{J}_0^f\right\}$ is given by

$$\left\{\mathbf{J}_0^f\right\} = \left\{\begin{array}{c}\mathbf{J}_0^\Omega\\ 0\end{array}\right\} \tag{C.37}$$

where

$$\left\{\mathbf{J}_0^\Omega\right\} = \left[\mathbf{m}^f\right]\left\{\tilde{\mathbf{q}}^0\right\} \tag{C.38}$$

in which the matrix $\left[\mathbf{m}^f\right]$ is given by Eq. (C.13).

In Eq. (C.7), $\left\{\mathbf{J}_f^f\right\}$ is the space-time nodal vector that contain the contribution of the free-field hydrodynamic pressure.

$$\left\{J_f^f\right\}^a(I) = \left(\int_{I_n}\int_{\Gamma_\infty^f} N_f^I T_a \frac{1}{c} N_f^J T_b ds dt\right)\cdot\left\{q^f\right\}^b(J) \tag{C.39}$$

the matrix vector form of above equation is

$$\left\{J_f^f\right\}^a(I) = \left[C_\infty^f\right]^{ab}(I,J)\cdot\left\{q^f\right\}^b(J) \tag{C.40}$$

or

$$\left\{\mathbf{J}_f^f\right\} = \left[\mathbf{C}_\infty^f\right]\left\{\tilde{\mathbf{q}}^f\right\} \tag{C.41}$$

where the matrix $\left[\mathbf{C}_\infty^f\right]$ is same as given by Eq. (C.23).

In Eq. (C.7), $\left\{\mathbf{J}_g^{fs}\right\}$ is the space-time nodal vector that contain the contribution of the rigid-ground motion.

$$\left\{J_g^{fs}\right\}^a(I) = \int_{I_n}\int_{\Gamma_{fs}^f} N_f^I T_a \rho^f a_i^g n_i^f ds dt \tag{C.42}$$

the space-time data structure of $\left\{\mathbf{J}_g^{fs}\right\}$ is given by

$$\left\{\mathbf{J}_g^{fs}\right\} = \left\{\begin{array}{c}\mathbf{J}_{g,fs}^1\\ \mathbf{J}_{g,fs}^2\end{array}\right\} \tag{C.43}$$

where $\left\{\mathbf{J}^1_{g,fs}\right\}$ and $\left\{\mathbf{J}^2_{g,fs}\right\}$ correspond to the space-nodal values at the bottom and top space-time slab. These vectors are defined at the reservoir-ground interface Γ^f_{fs}.

$$J^1_{g,fs}(I) = \int_{I_n}\int_{\Gamma^f_{fs}} N^I_f T_1 \rho^f a^g_i n^f_i \, dsdt \tag{C.44}$$

$$J^2_{g,fs}(I) = \int_{I_n}\int_{\Gamma^f_{fs}} N^I_f T_2 \rho^f a^g_i n^f_i \, dsdt \tag{C.45}$$

In Eq. (C.7), $\left\{\mathbf{J}^f_{p^n}\right\}$ is the space-time vector that contains the contribution of pressure gradient at time $t = t_n$.

$$\left\{J^f_{p_n}\right\}^a(I) = \int_{I_n}\int_{\Omega^f_h} T_a \frac{\partial N^I_f}{\partial x_i}\frac{\partial p^n}{\partial x_i} d\Omega dt \tag{C.46}$$

or

$$\left\{J^f_{p^n}\right\}^a(I) = \int_{I_n} T_a dt \int_{\Omega^f_h} \frac{\partial N^I_f}{\partial x_i}\frac{\partial p^n}{\partial x_i} d\Omega \tag{C.47}$$

In above equation using the expression for $T_1(\theta)$ and $T_2(\theta)$ as presented in the Eq. (5.40)

$$\left\{\mathbf{J}^f_{p^n}\right\} = \frac{\Delta t_n}{2}\begin{Bmatrix} \mathbf{J}^\Omega_{p^n} \\ \mathbf{J}^\Omega_{p^n} \end{Bmatrix} \tag{C.48}$$

where

$$J^\Omega_{p^n}(I) = \int_{\Omega^f_h} \frac{\partial N^I_f}{\partial x_i}\frac{\partial p^n}{\partial x_i} d\Omega \tag{C.49}$$

In Eq. (C.8) and Eq. (C.9), $[\mathbf{M}^s]$ is the space-time mass matrix for solid-domain and given by Eq. (A.6). $[\mathbf{K}^s]$ is the space-time stiffness matrix for solid-domain and given by Eq. (A.11). $[\mathbf{M}^s_R]$ is the mass-proportional space-time Rayleigh damping matrix and given by Eq. (A.16). $[\mathbf{K}^s_R]$ is the stiffness-proportional space-time Rayleigh damping matrix and given by Eq. (A.19).

In Eq. (C.8) and Eq. (C.9), $\left[\mathbf{H}^s_{fd}\right]$ is the space-time matrix that couples the hydrodynamic response of reservoir and the dynamic response of the dam. Note that the dam dynamically interacts with the reservoir at the dam-reservoir interface. The space-time nodal vector for solid domain that contain the contribution of hydrodynamic pressure is denoted by $\left\{\mathbf{J}^s_{fd}\right\}$, and it is given by

$$\left\{J^s_{fd}\right\}^a_i(I) = \int_{I_n}\int_{\Gamma^s_{fd}} N^I T_a p n^s_i dsdt + \int_{I_n}\int_{\Gamma^s_{fd}} N^I T_a p_0 n^s_i dsdt \tag{C.50}$$

In above equation by using the space-time interpolation for the pressure (cf. Eq. (C.14)) as presented in Eq. (5.48)

$$\begin{aligned}\left\{J_{fd}^{s}\right\}_{i}^{a}(I) &= \int_{I_n}\int_{\Gamma_{fd}^{s}} N^I T_a p^n n_i^s ds dt \\ &+ \int_{I_n}\int_{\Gamma_{fd}^{s}} N^I T_a p_0 n_i^s ds dt \\ &+ \int_{I_n}\int_{\Gamma_{fd}^{s}} N^I T_a \tilde{T}_b N_f^J n_i^s ds dt \{q\}^b (J)\end{aligned} \tag{C.51}$$

or

$$\begin{aligned}\left\{J_{fd}^{s}\right\}_{i}^{a}(I) &= \int_{I_n} T_a dt \int_{\Gamma_{fd}^{s}} N^I p^n n_i^s ds \\ &+ \int_{I_n} T_a dt \int_{\Gamma_{fd}^{s}} N^I p_0 n_i^s ds \\ &+ \int_{I_n} T_a \tilde{T}_b dt \int_{\Gamma_{fd}^{s}} N^I N_f^J n_i^s ds \{q\}^b (J)\end{aligned} \tag{C.52}$$

In above equation using the expression for $T_a(\theta)$ and $\tilde{T}_a(\theta)$ as presented in Eq. (5.40) and Eq. (5.45), respectively, following matrix-vector form can be obtained.

$$\left\{\mathbf{J}_{fd}^{s}\right\} = \left\{\mathbf{J}_{p_0}^{fd}\right\} + \left\{\mathbf{J}_{p^n}^{fd}\right\} + \left[\mathbf{H}_{fd}^{s}\right] \cdot \{\tilde{\mathbf{q}}\} \tag{C.53}$$

where

$$\left\{\mathbf{J}_{p^n}^{fd}\right\} = \frac{\Delta t_n}{2}\begin{Bmatrix}\mathbf{f}_{p}^{fd}\\ \mathbf{f}_{p}^{fd}\end{Bmatrix} \qquad \left\{\mathbf{J}_{p_0}^{fd}\right\} = \frac{\Delta t_n}{2}\begin{Bmatrix}\mathbf{f}_{p_0}^{fd}\\ \mathbf{f}_{p_0}^{fd}\end{Bmatrix} \tag{C.54}$$

in which

$$\left\{\mathbf{f}_{p}^{fd}\right\} = \begin{Bmatrix}\mathbf{f}_{p,1}^{fd}\\ \mathbf{f}_{p,2}^{fd}\end{Bmatrix} \qquad \left\{\mathbf{f}_{p}^{fd}\right\} = \begin{Bmatrix}\mathbf{f}_{p_0,1}^{fd}\\ \mathbf{f}_{p_0,2}^{fd}\end{Bmatrix} \tag{C.55}$$

$$f_{p,1}^{fd}(I) = \int_{\Gamma_{fd}^{s}} N^I p^n n_1^s ds \qquad f_{p,2}^{fd}(I) = \int_{\Gamma_{fd}^{s}} N^I p^n n_2^s ds \tag{C.56}$$

$$f_{p_0,1}^{fd}(I) = \int_{\Gamma_{fd}^{s}} N^I p_0 n_1^s ds \qquad f_{p_0,2}^{fd}(I) = \int_{\Gamma_{fd}^{s}} N^I p_0 n_2^s ds \tag{C.57}$$

and

$$\left[H_{fd}^{s}\right]_{i}^{ab}(I,J) = \int_{I_n} T_a \tilde{T}_b dt \int_{\Gamma_{fd}^{s}} N^I N_f^J n_i^s ds \tag{C.58}$$

The space-time data-structure of $\left[\mathbf{H}^s_{fd}\right]$ is given below,

$$\left[\mathbf{H}^s_{fd}\right] = \frac{\Delta t_n^2}{24}\begin{bmatrix} 3\mathbf{H}^{\Gamma}_{fd} & \mathbf{H}^{\Gamma}_{fd} \\ 5\mathbf{H}^{\Gamma}_{fd} & 3\mathbf{H}^{\Gamma}_{fd} \end{bmatrix} \tag{C.59}$$

where

$$\left[\mathbf{H}^{\Gamma}_{fd}\right] = \begin{bmatrix} \mathbf{h}^{fd}_{11} & \mathbf{0} \\ \mathbf{0} & \mathbf{h}^{fd}_{22} \end{bmatrix} \tag{C.60}$$

in which,

$$h^{fd}_{11}(I,J) = \int_{\Gamma^s_{fd}} N^I N^J_f n^s_1 ds \qquad h^{fd}_{22}(I,J) = \int_{\Gamma^s_{fd}} N^I N^J_f n^s_2 ds \tag{C.61}$$

In Eq. (C.8) and Eq. (C.9), $\{\mathbf{J}^s_{ext}\}$ is the space-time nodal vector that contains the contribution of external body force $\mathbf{b}$ and surface force $\mathbf{f}^s$. It is given by Eq. (A.22). $\{\mathbf{J}^s_0\}$ is the space-time nodal vector that contains the contribution of initial velocity. It is given by Eq. (A.27). $\{\mathbf{J}^s_{\sigma^n}\}$ is the space-time nodal vector that contains the contribution of initial stress σ^n. It is given by Eq. (A.30).

D

Space-Time Finite Element Matrices and Vectors for Dam-Reservoir-Soil Interaction Problems

Section 5.4.2 describes the following v-ST/FEM weak form for the dynamic dam-reservoir-soil interaction problem.

$$
\begin{aligned}
&\int_{I_n}\int_{\Omega_h^f}\delta q\frac{1}{c^2}\frac{\partial q}{\partial t}d\Omega dt+\int_{\Omega_h^f}\delta q\left(\mathbf{x},t_n\right)\frac{1}{c^2}q\left(\mathbf{x},t_n^+\right)d\Omega\\
&-\int_{\Omega_h^f}\delta q\left(\mathbf{x},t_n\right)\frac{1}{c^2}q\left(\mathbf{x},t_n^-\right)d\Omega+\int_{I_n}\int_{\Omega_h^f}\frac{\partial\delta q}{\partial x_i}\frac{\partial p}{\partial x_i}d\Omega dt\\
&+\int_{I_n}\int_{\Gamma_{fd}^f}\delta q\rho^f\frac{\partial v_i}{\partial t}n_i^f dsdt+\int_{I_n}\int_{\Gamma_{fs}^f}\delta q\rho^f\frac{\partial v_i}{\partial t}n_i^f dsdt\\
&+\int_{I_n}\int_{\Gamma_{fs}^f}\delta q\rho^f q_c q dsdt+\int_{I_n}\int_{\Gamma_\infty^f}\delta q\frac{1}{c}q dsdt\\
&-\int_{I_n}\int_{\Gamma_\infty^f}\delta q\frac{1}{c}q^f dsdt=0
\end{aligned}
\tag{D.1}
$$

$$
\begin{aligned}
&\int_{I_n}\int_{\Omega_h^s}\delta v_i\rho^s\frac{\partial v_i}{\partial t}d\Omega dt+\int_{\Omega_h^s}\delta v_i\left(\mathbf{x},t_n^+\right)\rho^s v_i\left(x,t_n^+\right)d\Omega\\
&-\int_{\Omega_h^s}\delta v_i\left(\mathbf{x},t_n^+\right)\rho^s v_i\left(x,t_n^-\right)d\Omega-\int_{I_n}\int_{\Omega_h^s}\delta v_i\rho^s b_i d\Omega dt\\
&+\int_{I_n}\int_{\Omega_h^s}\frac{\partial\delta v_i}{\partial x_j}\sigma_{ij}^n d\Omega dt+\int_{I_n}\int_{\Omega_h^s}\frac{\partial\delta v_i}{\partial x_j}C_{ijkl}\psi_{kl}d\Omega dt\\
&-\int_{I_n}\int_{\Gamma_i^h}\delta v_i f_i^s dsdt+\int_{I_n}\int_{\Gamma_\infty^R\cup\Gamma_\infty^L}\delta v_i c_{ij}^v v_j dsdt\\
&+\int_{I_n}\int_{\Gamma_\infty^B}\delta v_i c_{ip}^h v_p dsdt-\int_{I_n}\int_{\Gamma_\infty^R\cup\Gamma_\infty^L}\delta v_i\left(c_{ij}^v v_j^f+\sigma_{ij}^f n_j\right)dsdt\\
&-\int_{I_n}\int_{\Gamma_\infty^B}\delta v_i 2c_{ij}^h v_j^{in}dsdt+\int_{I_n}\int_{\Gamma_{fd}^s}\delta v_i(p+p_0)n_i^s dsdt\\
&+\int_{I_n}\int_{\Gamma_{fb}^s}\delta v_i(p+p_0)n_i^s dsdt=0
\end{aligned}
\tag{D.2}
$$

In Eq. (D.1) and Eq. (D.2) using the space-time interpolation for $\delta\mathbf{v}$, $\mathbf{v}$, δq, and q given in Eq. (5.41), Eq. (5.42), Eq. (5.46), Eq. (5.47), respectively, one can obtain the following discrete form of v-ST/FEM weak form.

$$
\begin{aligned}
&\{\delta q\}^a(I)\cdot\left[M^f\right]^{ab}(I,J)\cdot\{q\}^b(J)+\{\delta q\}^a(I)\cdot\left[K^f\right]^{ab}(I,J)\cdot\{q\}^b(J)\\
&+\{\delta q\}^a(I)\cdot\left[C^f_{fs}\right]^{ab}(I,J)\cdot\{q\}^b(J)+\{\delta q\}^a(I)\cdot\left[H^f_{fs}\right]^{ab}_i(I,J)\cdot\{v\}^b_i(J)\\
&+\{\delta q\}^a(I)\cdot\left[H^f_{fd}\right]^{ab}_i(I,J)\cdot\{v\}^b_i(J)+\{\delta q\}^a(I)\cdot\left[C^f_{\infty}\right]^{ab}(I,J)\cdot\{q\}^b(J)\\
&-\{\delta q\}^a(I)\cdot\left\{J^f_0\right\}^a(I)-\{\delta q\}^a(I)\cdot\left\{J^f_f\right\}^a(I)\\
&+\{\delta q\}^a(I)\cdot\left\{J^f_{p^n}\right\}^a(I)=0
\end{aligned}
\tag{D.3}
$$

$$
\begin{aligned}
&\{\delta v\}^a_i(I)\cdot[M^s]^{ab}_{ij}(I,J)\cdot\{v\}^b_j(J)+\{\delta v\}^a_i(I)\cdot[K^s]^{ab}_{ij}(I,J)\cdot\{v\}^b_j(J)\\
&+\{\delta v\}^a_i(I)\cdot[C_{L\infty}]^{ab}_{ij}(I,J)\cdot\{v\}^b_j(J)+\{\delta v\}^a_i(I)\cdot[C_{R\infty}]^{ab}_{ij}(I,J)\cdot\{v\}^b_j(J)\\
&+\{\delta v\}^a_i(I)\cdot[C_{B\infty}]^{ab}_{ij}(I,J)\cdot\{v\}^b_j(J)-\{\delta v\}^a_i(I)\cdot\{J^s_{ext}\}^a_i(I)\\
&-\{\delta v\}^a_i(I)\cdot\{J^s_0\}^a_i(I)+\{\delta v\}^a_i(I)\cdot\{J^s_{\sigma^n}\}^a_i(I)-\{\delta v\}^a_i(I)\cdot\left\{J^s_f\right\}^a_i(I)\\
&-\{\delta v\}^a_i(I)\cdot\{J^s_{in}\}^a_i(I)+\{\delta v\}^a_i(I)\cdot\left[H^s_{fd}\right]^{ab}_i(I,J)\cdot\{q\}^b(J)\\
&+\{\delta v\}^a_i(I)\cdot\left[H^s_{fs}\right]^{ab}_i(I,J)\cdot\{q\}^b(J)\\
&+\{\delta v\}^a_i(I)\cdot\left\{J^{fd}_{p^n}\right\}^a_i(I)+\{\delta v\}^a_i(I)\cdot\left\{J^{fs}_{p^n}\right\}^a_i(I)\\
&+\{\delta v\}^a_i(I)\cdot\left\{J^{fd}_{p_0}\right\}^a_i(I)+\{\delta v\}^a_i(I)\cdot\left\{J^{fs}_{p_0}\right\}^a_i(I)=0
\end{aligned}
\tag{D.4}
$$

Since Eq. (D.3) and Eq. (D.4) are true for all values of $\{\delta v\}^a_i(I)$ and $\{\delta q\}^a(I)$, the discrete weak form will produce following system of algebraic equations.

$$
\begin{aligned}
&\left[M^f\right]^{ab}(I,J)\cdot\{q\}^b(J)+\left[K^f\right]^{ab}(I,J)\cdot\{q\}^b(J)\\
&+\left[C^f_{fs}\right]^{ab}(I,J)\cdot\{q\}^b(J)+\left[H^f_{fs}\right]^{ab}_i(I,J)\cdot\{v\}^b_i(J)\\
&+\left[H^f_{fd}\right]^{ab}_i(I,J)\cdot\{v\}^b_i(J)+\left[C^f_{\infty}\right]^{ab}(I,J)\cdot\{q\}^b(J)\\
&-\left\{J^f_0\right\}^a(I)-\left\{J^f_f\right\}^a(I)+\left\{J^f_{p^n}\right\}^a(I)=0
\end{aligned}
\tag{D.5}
$$

$$
\begin{aligned}
&[M^s]_{ij}^{ab}(I,J)\cdot\{v\}_j^b(J)+[K^s]_{ij}^{ab}(I,J)\cdot\{v\}_j^b(J)\\
&+[C_{L\infty}]_{ij}^{ab}(I,J)\cdot\{v\}_j^b(J)+[C_{R\infty}]_{ij}^{ab}(I,J)\cdot\{v\}_j^b(J)\\
&+[C_{B\infty}]_{ij}^{ab}(I,J)\cdot\{v\}_j^b(J)-\{J_{ext}^s\}_i^a(I)\\
&-\{J_0^s\}_i^a(I)+\{J_{\sigma^n}^s\}_i^a(I)-\left\{J_f^s\right\}_i^a(I)-\{J_{in}^s\}_i^a(I)\\
&+\left[H_{fd}^s\right]_i^{ab}(I,J)\cdot\{q\}^b(J)+\left[H_{fs}^s\right]_i^{ab}(I,J)\cdot\{q\}^b(J)\\
&+\left\{J_{p^n}^{fd}\right\}_i^a(I)+\left\{J_{p^n}^{fs}\right\}_i^a(I)\\
&+\left\{J_{p_0}^{fd}\right\}_i^a(I)+\left\{J_{p_0}^{fs}\right\}_i^a(I)=0
\end{aligned}
\tag{D.6}
$$

The matrix-vector form of Eq. (D.5) and Eq. (D.6) is given by

$$
\begin{aligned}
&\left[\mathbf{M}^f\right]\cdot\{\tilde{\mathbf{q}}\}+\left[\mathbf{K}^f\right]\cdot\{\tilde{\mathbf{q}}\}+\left[\mathbf{C}_{fs}^f\right]\cdot\{\tilde{\mathbf{q}}\}+\left[\mathbf{H}_{fs}^f\right]\cdot\{\tilde{\mathbf{v}}\}+\left[\mathbf{H}_{fd}^f\right]\cdot\{\tilde{\mathbf{v}}\}\\
&+\left[\mathbf{C}_{\infty}^f\right]\cdot\{\tilde{\mathbf{q}}\}=\left\{\mathbf{J}_0^f\right\}+\left\{\mathbf{J}_f^f\right\}-\left\{\mathbf{J}_{p^n}^f\right\}
\end{aligned}
\tag{D.7}
$$

$$
\begin{aligned}
&[\mathbf{M}^s]\cdot\{\tilde{\mathbf{v}}\}+[\mathbf{K}^s]\cdot\{\tilde{\mathbf{v}}\}+[\mathbf{C}_{L\infty}]\cdot\{\tilde{\mathbf{v}}\}+[\mathbf{C}_{R\infty}]\cdot\{\tilde{\mathbf{v}}\}+[\mathbf{C}_{B\infty}]\cdot\{\tilde{\mathbf{v}}\}\\
&+\left[\mathbf{H}_{fd}^s\right]\cdot\{\tilde{\mathbf{q}}\}+\left[\mathbf{H}_{fs}^s\right]\cdot\{\tilde{\mathbf{q}}\}\\
&=\{\mathbf{J}_{ext}^s\}+\{\mathbf{J}_0^s\}-\{\mathbf{J}_{\sigma^n}^s\}+\left\{\mathbf{J}_f^s\right\}+\{\mathbf{J}_{in}^s\}\\
&-\left\{\mathbf{J}_{p^n}^{fd}\right\}-\left\{\mathbf{J}_{p^n}^{fs}\right\}-\left\{\mathbf{J}_{p_0}^{fd}\right\}-\left\{\mathbf{J}_{p_0}^{fs}\right\}
\end{aligned}
\tag{D.8}
$$

If Rayleigh damping is considered for modelling the material damping in solid domain then Eq. (D.8) is given by

$$
\begin{aligned}
&[\mathbf{M}^s]\cdot\{\tilde{\mathbf{v}}\}+[\mathbf{K}^s]\cdot\{\tilde{\mathbf{v}}\}+\alpha\,[\mathbf{M}_R^s]\cdot\{\tilde{\mathbf{v}}\}+\beta\,[\mathbf{K}_R^s]\cdot\{\tilde{\mathbf{v}}\}\\
&+[\mathbf{C}_{L\infty}]\cdot\{\tilde{\mathbf{v}}\}+[\mathbf{C}_{R\infty}]\cdot\{\tilde{\mathbf{v}}\}+[\mathbf{C}_{B\infty}]\cdot\{\tilde{\mathbf{v}}\}+\left[\mathbf{H}_{fd}^s\right]\cdot\{\tilde{\mathbf{q}}\}+\left[\mathbf{H}_{fs}^s\right]\cdot\{\tilde{\mathbf{q}}\}\\
&=\{\mathbf{J}_{ext}^s\}+\{\mathbf{J}_0^s\}-\{\mathbf{J}_{\sigma^n}^s\}+\left\{\mathbf{J}_f^s\right\}+\{\mathbf{J}_{in}^s\}\\
&-\left\{\mathbf{J}_{p^n}^{fd}\right\}-\left\{\mathbf{J}_{p^n}^{fs}\right\}-\left\{\mathbf{J}_{p_0}^{fd}\right\}-\left\{\mathbf{J}_{p_0}^{fs}\right\}
\end{aligned}
\tag{D.9}
$$

Description of the space-time matrices and space-time nodal vectors that appear in Eq. (D.7), Eq. (D.8), and Eq. (D.9) is given as follows.

In Eq. (D.7), $\left[\mathbf{M}^f\right]$ is space-time mass matrix for the fluid domain, and it is given by Eq. (C.10). $\left[\mathbf{K}^f\right]$ is space-time diffusion matrix for the fluid domain, and it is given by Eq. (C.14). $\left[\mathbf{C}_{fs}^f\right]$ is the space-time matrix that corresponds to the reservoir-bottom absorption, and it is given by Eq. (C.19). $\left[\mathbf{C}_{\infty}^f\right]$ is space-time matrix that corresponds to the dashpots placed at the truncated upstream boundary of reservoir, and it is given by Eq. (C.23). $\left[\mathbf{H}_{fd}^f\right]$ is the space-time matrix that

couples the hydrodynamic respone of reservoir and the dynamic response of the dam, and it is given by Eq. (C.31).

In Eq. (D.7), $\left[\mathbf{H}_{fs}^{f}\right]$ is the space-time matrix that couples the hydrodynamic respone of reservoir and the dynamic response of the soil. Note that the reservoir dynamically interacts with the soil at the fluid-dam interface. The space-time nodal vector for fluid domain that contains the contribution of the motion of soil is denoted by $\left\{\mathbf{J}_{fd}^{f}\right\}$, and it is given by

$$\left\{J_{fs}^{f}\right\}^{a}(I)=\int_{I_n}\int_{\Gamma_{fs}^{f}} N_f^I T_a \rho^f \frac{\partial v_i}{\partial t} n_i^f \, ds dt \tag{D.10}$$

in above equation using the space-time interpolation for velocity $\mathbf{v}$ as presented in Eq. (5.42)

$$\left\{J_{fs}^{f}\right\}^{a}(I)=\left(\int_{I_n}\int_{\Gamma_{fs}^{f}} N_f^I T_a \rho^f \frac{\partial N^J T_b}{\partial t} n_i^f \, ds dt\right)\cdot\{v\}_i^b(J) \tag{D.11}$$

or

$$\left\{J_{fs}^{f}\right\}^{a}(I)=\left(\int_{I_n} T_a \frac{\partial T_b}{\partial t} dt \int_{\Gamma_{fs}^{f}} N_f^I \rho^f N^J n_i^f \, ds\right)\{v\}_i^b(J) \tag{D.12}$$

The matrix-vector form of above equation is given by

$$\left\{\mathbf{J}_{fs}^{f}\right\}=\left[\mathbf{H}_{fs}^{f}\right]\{\tilde{\mathbf{v}}\} \tag{D.13}$$

where

$$\left[H_{fs}^{f}\right]_i^{ab}(I,J)=\int_{I_n} T_a \frac{\partial T_b}{\partial t} dt \int_{\Gamma_{fs}^{f}} N_f^I \rho^f N^J n_i^f \, ds \tag{D.14}$$

In above equation using the expression for $T_1(\theta)$ and $T_2(\theta)$ as presented in Eq. (5.40)

$$\left[\mathbf{H}_{fd}^{f}\right]=\frac{1}{2}\begin{bmatrix} -\mathbf{H}_{fd}^{\Gamma} & \mathbf{H}_{fd}^{\Gamma} \\ -\mathbf{H}_{fd}^{\Gamma} & \mathbf{H}_{fd}^{\Gamma} \end{bmatrix} \tag{D.15}$$

where the matrix $\mathbf{H}_{fs}^{\Gamma}$ is evaluated at the fluid-soil interface Γ_{fs}^{f}, and given by

$$\left[\mathbf{H}_{fs}^{\Gamma}\right]=\begin{bmatrix} \mathbf{h}_{11}^{fs} & \mathbf{0} \\ \mathbf{0} & \mathbf{h}_{22}^{fs} \end{bmatrix} \tag{D.16}$$

in which,

$$h_{11}^{fs}(\mathrm{I},J)=\int_{\Gamma_{fs}^{f}} N_f^I \rho^f N^J n_1^f \, ds \tag{D.17}$$

$$h_{22}^{fs}(\mathrm{I},J)=\int_{\Gamma_{fs}^{f}} N_f^I \rho^f N^J n_2^f \, ds \tag{D.18}$$

In Eq. (D.7), $\left\{\mathbf{J}_0^f\right\}$ is the space-time nodal vector that contain the contribution of the initial value of q, and it is given by Eq. (C.36). $\left\{\mathbf{J}_f^f\right\}$ is the space-time nodal vector that contain the contribution of the free-field hydrodynamic pressure, and it is given by Eq. (C.39). $\left\{\mathbf{J}_{p^n}^f\right\}$ is the space-time nodal vector that contain the contribution of pressure gradient at time $t = t_n$, and it is given by Eq. (C.46).

In Eq. (D.8) and Eq. (D.9), $[\mathbf{M}^s]$ is the space-time mass matrix for the solid domain, and it is given by Eq. (A.6). $[\mathbf{K}^s]$ is the space-time tangent stiffness matrix for the solid domain, and it is given by Eq. (A.11). $[\mathbf{M}_R^s]$ is the mass-proportional space-time Rayleigh damping matrix for the solid domain, and it is given by Eq. (A.16). $[\mathbf{K}_R^s]$ is the stiffness-proportional space-time Rayleigh damping matrix for the solid domain, and it is given by Eq. (A.19). $[\mathbf{C}_{L\infty}]$ is the space-time matrix due to the dashpots placed at the left-side truncated boundary, and it is given by Eq. (B.6). $[\mathbf{C}_{R\infty}]$ is the space-time matrix due to the dashpots placed at the right-side truncated boundary, and it is given by Eq. (B.12). $[\mathbf{C}_{B\infty}]$ is the space-time matrix due to the dashpots placed at the bottom truncated boundary, and it is given by Eq. (B.18). $\left[\mathbf{H}_{fd}^s\right]$ is the space-time matrix that couples the hydrodynamic response of reservoir and the dynamic response of the dam, and it is given by Eq. (C.58).

In Eq. (D.8) and Eq. (D.9), $\left[\mathbf{H}_{fs}^s\right]$ is the space-time matrix that couples the hydrodynamic response of reservoir and the dynamic response of the soil. Note that the soil-domain dynamically interacts with the reservoir at the soil-reservoir interface. The space-time nodal vector for solid domain that contain the contribution of hydrodynamic pressure is denoted by $\left\{\mathbf{J}_{fs}^s\right\}$, and it is given by

$$\left\{J_{fs}^s\right\}_i^a(I) = \int_{I_n}\int_{\Gamma_{fs}^s} N^I T_a p n_i^s ds dt \tag{D.19}$$

In above equation using space-time interpolation for the pressure (cf. Eq. (C.14)) as presented in Eq. (5.48)

$$\left\{J_{fs}^s\right\}_i^a(I) = \int_{I_n}\int_{\Gamma_{fs}^s} N^I T_a p^n n_i^s ds dt + \int_{I_n}\int_{\Gamma_{fs}^s} N^I T_a p_0 n_i^s ds dt + \int_{I_n}\int_{\Gamma_{fs}^s} N^I T_a \tilde{T}_b N_f^J n_i^s ds dt \{q\}^b(J) \tag{D.20}$$

or

$$\begin{aligned}\left\{J_{fs}^{s}\right\}_{i}^{a}(I) &= \int_{I_n} T_a dt \int_{\Gamma_{fs}^{s}} N^I p^n n_i^s ds \\ &+ \int_{I_n} T_a dt \int_{\Gamma_{fs}^{s}} N^I p_0 n_i^s ds \\ &+ \int_{I_n} T_a \tilde{T}_b dt \int_{\Gamma_{fs}^{s}} N^I N_f^J n_i^s ds \{q\}^b (J)\end{aligned} \tag{D.21}$$

Now using the expression for $T_a(\theta)$ and $\tilde{T}_a(\theta)$ as presented in Eq. (5.40) and Eq. (5.45), respectively, following matrix-vector form can be obtained.

$$\left\{\mathbf{J}_{fs}^{s}\right\} = \left\{\mathbf{J}_{p_0}^{fs}\right\} + \left\{\mathbf{J}_{p^n}^{fs}\right\} + \left[\mathbf{H}_{fs}^{s}\right] \cdot \{\tilde{\mathbf{q}}\} \tag{D.22}$$

where

$$\left\{\mathbf{J}_{p^n}^{fs}\right\} = \frac{\Delta t_n}{2} \begin{Bmatrix} \mathbf{f}_p^{fs} \\ \mathbf{f}_p^{fs} \end{Bmatrix} \tag{D.23}$$

in which

$$\left\{\mathbf{f}_{p}^{fs}\right\} = \begin{Bmatrix} \mathbf{f}_{p,1}^{fs} \\ \mathbf{f}_{p,2}^{fs} \end{Bmatrix} \tag{D.24}$$

$$f_{p,1}^{fs}(I) = \int_{\Gamma_{fs}^{s}} N^I p^n n_1^s ds \qquad f_{p,2}^{fs}(I) = \int_{\Gamma_{fs}^{s}} N^I p^n n_2^s ds \tag{D.25}$$

and

$$\left[H_{fs}^{s}\right]_{i}^{ab}(I,J) = \int_{I_n} T_a \tilde{T}_b dt \int_{\Gamma_{fs}^{s}} N^I N_f^J n_i^s ds \tag{D.26}$$

The space-time data-structure of $\left[\mathbf{H}_{fs}^{s}\right]$ is given below,

$$\left[\mathbf{H}_{fs}^{s}\right] = \frac{\Delta t_n^2}{24} \begin{bmatrix} 3\mathbf{H}_{fs}^{\Gamma} & \mathbf{H}_{fs}^{\Gamma} \\ 5\mathbf{H}_{fs}^{\Gamma} & 3\mathbf{H}_{fs}^{\Gamma} \end{bmatrix} \tag{D.27}$$

where

$$\left[\mathbf{H}_{fs}^{\Gamma}\right] = \begin{bmatrix} \mathbf{h}_{11}^{fs} & \mathbf{0} \\ \mathbf{0} & \mathbf{h}_{22}^{fs} \end{bmatrix} \tag{D.28}$$

in which,

$$h_{11}^{fs}(I,J) = \int_{\Gamma_{fs}^{s}} N^I N_f^J n_1^s ds \qquad h_{22}^{fs}(I,J) = \int_{\Gamma_{fs}^{s}} N^I N_f^J n_2^s ds \tag{D.29}$$

In Eq. (D.8) and Eq. (D.9), $\{\mathbf{J}_{ext}^{s}\}$ is the space-time nodal vector that contains the contribution of external body force $\mathbf{b}$ and surface force $\mathbf{f}^s$, and it is given by Eq. (A.23). $\{\mathbf{J}_{0}^{s}\}$ is the space-time nodal vector that contains the contribution of initial

velocity, and it is given by Eq. (A.27). $\{\mathbf{J}^s_{\sigma^n}\}$ is the space-time nodal vector that contains the contribution of initial stress σ^n, and it is given by Eq. (A.30). $\left\{\mathbf{J}^s_f\right\}$ is the space-time nodal vector that contains the contribution of free-field response of soil-domain, and it is given by Eq. (B.24). $\{\mathbf{J}^s_{in}\}$ is the space-time nodal vector that contains the contribution of input seismic motion, and it is given by Eq. (B.31).

E

Space-Time Finite Element Matrices and Vectors for Nonlinear Dam-Reservoir Interaction Problems

Section 6.3 presents the following v-ST/FEM weak form for the nonlinear dynamic analysis of the dam-reservoir system subjected to the horizontal and vertical ground motion.

$$
\begin{aligned}
&\int_{I_n}\int_{\Omega_h^f}\delta q\frac{1}{c^2}\frac{\partial q}{\partial t}d\Omega dt+\int_{\Omega_h^f}\delta q\left(\mathbf{x},t_n\right)\frac{1}{c^2}q\left(\mathbf{x},t_n^+\right)d\Omega\\
&-\int_{\Omega_h^f}\delta q\left(\mathbf{x},t_n\right)\frac{1}{c^2}q\left(\mathbf{x},t_n^-\right)d\Omega+\int_{I_n}\int_{\Omega_h^f}\frac{\partial\delta q}{\partial x_i}\frac{\partial p}{\partial x_i}d\Omega dt\\
&+\int_{I_n}\int_{\Gamma_{fd}^f}\delta q\rho^f\frac{\partial v_i}{\partial t}n_i^f dsdt+\int_{I_n}\int_{\Gamma_{fd}^f}\delta q\rho^f a_i^g n_i^f dsdt\\
&+\int_{I_n}\int_{\Gamma_{fs}^f}\delta q\rho^f a_i^g n_i^f dsdt+\int_{I_n}\int_{\Gamma_{fs}^f}\delta q\rho^f q_c q dsdt\\
&+\int_{I_n}\int_{\Gamma_{\infty}^f}\delta q\frac{1}{c}qdsdt-\int_{I_n}\int_{\Gamma_{\infty}^f}\delta q\frac{1}{c}q^f dsdt=0
\end{aligned}
\tag{E.1}
$$

$$
\begin{aligned}
&\int_{I_n}\int_{\Omega_h^s}\rho^s\delta v_i\frac{\partial v_i}{\partial t}d\Omega dt+\int_{\Omega_h^s}\rho^s\delta v_i\left(\mathbf{x},t_n^+\right)v_i\left(\mathbf{x},t_n^+\right)d\Omega\\
&-\int_{\Omega_h^s}\rho^s\delta v_i\left(\mathbf{x},t_n^+\right)v_i\left(x,t_n^-\right)d\Omega+\int_{I_n}\int_{\Omega_h^s}\frac{\partial\delta v_i}{\partial x_j}\sigma_{ij}d\Omega dt\\
&-\int_{I_n}\int_{\Gamma_i^h}\delta v_i f_i^s dsdt-\int_{I_n}\int_{\Omega_h^s}\rho^s\delta v_i\left(b_i-a_i^g\right)d\Omega dt\\
&+\int_{I_n}\int_{\Gamma_{fd}^s}\delta v_i p_0 n_i^s dsdt+\int_{I_n}\int_{\Gamma_{fd}^s}\delta v_i p n_i^s dsdt=0
\end{aligned}
\tag{E.2}
$$

In Eq. (E.1) and Eq. (E.2) using the space-time finite element approximations for $\delta\mathbf{v}$, $\mathbf{v}$, δq, and q given in Eq. (6.33), Eq. (6.34), Eq. (6.37), and Eq. (6.38), respectively, one can obtain the following discrete form of the v-ST/FEM.

$$
\begin{aligned}
&\{\delta v\}_i^a(I)\cdot[M^s]_{ij}^{ab}(I,J)\cdot\{v\}_j^b(J)+\{\delta v\}_i^a(I)\cdot\left[H_{fd}^s\right]_i^{ab}(I,J)\cdot\{v\}_j^b(J)\\
&+\{\delta v\}_i^a(I)\cdot\{J_\sigma^s\}_i^a(I)-\{\delta v\}_i^a(I)\cdot\{J_0^s\}_i^a(I)+\{\delta v\}_i^a(I)\cdot\left\{J_g^s\right\}_i^a(I)\\
&-\{\delta v\}_i^a(I)\cdot\{J_{ext}^s\}_i^a(I)+\{\delta v\}_i^a(I)\cdot\left\{J_{p_0}^{fd}\right\}_i^a(I)\\
&+\{\delta v\}_i^a(I)\cdot\left\{J_{p^n}^{fd}\right\}_i^a(I)=0
\end{aligned}
\tag{E.3}
$$

$$
\begin{aligned}
&\{\delta q\}^a(I)\cdot\left[M^f\right]^{ab}(I,J)\cdot\{q\}^b(J)+\{\delta q\}^a(I)\cdot\left[K^f\right]^{ab}(I,J)\cdot\{q\}^b(J)\\
&+\{\delta q\}^a(I)\cdot\left[C_{fs}^f\right]^{ab}(I,J)\cdot\{q\}^b(J)+\{\delta q\}^a(I)\cdot\left[C_\infty^f\right]^{ab}(I,J)\cdot\{q\}^b(J)\\
&+\{\delta q\}^a(I)\cdot\left[H_{fd}^f\right]_i^{ab}(I,J)\cdot\{v\}_i^b(J)-\{\delta q\}^a(I)\cdot\left\{J_0^f\right\}^a(I)\\
&-\{\delta q\}^a(I)\cdot\left\{J_f^f\right\}^a(I)+\{\delta q\}^a(I)\cdot\left\{J_g^{fd}\right\}^a(I)\\
&+\{\delta q\}^a(I)\cdot\left\{J_g^{fs}\right\}^a(I)\\
&+\{\delta q\}^a(I)\cdot\left\{J_{p^n}^f\right\}^a(I)=0
\end{aligned}
\tag{E.4}
$$

Since Eq. (E.3) and Eq. (E.4) are true for all values of $\{\delta v\}_i^a$ and $\{\delta q\}^a$, , the discrete weak form will produce following system of algebraic equations.

$$
\begin{aligned}
&[M^s]_{ij}^{ab}(I,J)\cdot\{v\}_j^b(J)+\left[H_{fd}^s\right]_i^{ab}(I,J)\cdot\{v\}_j^b(J)+\{J_\sigma^s\}_i^a(I)\\
&-\{J_0^s\}_i^a(I)+\left\{J_g^s\right\}_i^a(I)-\{J_{ext}^s\}_i^a(I)\\
&+\left\{J_{p_0}^{fd}\right\}_i^a(I)+\left\{J_{p^n}^{fd}\right\}_i^a(I)=0
\end{aligned}
\tag{E.5}
$$

$$
\begin{aligned}
&\left[M^f\right]^{ab}(I,J)\cdot\{q\}^b(J)+\left[K^f\right]^{ab}(I,J)\cdot\{q\}^b(J)+\left[C_{fs}^f\right]^{ab}(I,J)\cdot\{q\}^b(J)\\
&+\left[C_\infty^f\right]^{ab}(I,J)\cdot\{q\}^b(J)+\left[H_{fd}^f\right]_i^{ab}(I,J)\cdot\{v\}_i^b(J)-\left\{J_0^f\right\}^a(I)\\
&-\left\{J_f^f\right\}^a(I)+\left\{J_g^{fd}\right\}^a(I)+\left\{J_g^{fs}\right\}^a(I)+\left\{J_{p^n}^f\right\}^a(I)=0
\end{aligned}
\tag{E.6}
$$

The matrix-vector form of Eq. (E.5) and Eq. (E.6) can be depicted by

$$
\begin{aligned}
&[\mathbf{M}^s]\{\tilde{\mathbf{v}}\}+\left[\mathbf{H}_{fd}^s\right]\cdot\{\tilde{\mathbf{q}}\}+\{\mathbf{J}_\sigma^s\}-\{\mathbf{J}_0^s\}+\left\{\mathbf{J}_g^s\right\}\\
&-\{\mathbf{J}_{ext}^s\}+\left\{\mathbf{J}_{p_0}^{fd}\right\}+\left\{\mathbf{J}_{p^n}^{fd}\right\}=\mathbf{0}
\end{aligned}
\tag{E.7}
$$

$$\begin{aligned}&\left[\mathbf{M}^f\right]\cdot\{\tilde{\mathbf{q}}\}+\left[\mathbf{K}^f\right]\cdot\{\tilde{\mathbf{q}}\}+\left[\mathbf{C}^f_{fs}\right]\cdot\{\tilde{\mathbf{q}}\}+\left[\mathbf{C}^f_{\infty}\right]\cdot\{\tilde{\mathbf{q}}\}+\left[\mathbf{H}^f_{fd}\right]\cdot\{\tilde{\mathbf{v}}\}\\&-\left\{\mathbf{J}^f_0\right\}-\left\{\mathbf{J}^f_f\right\}+\left\{\mathbf{J}^{fd}_g\right\}+\left\{\mathbf{J}^{fs}_g\right\}+\left\{\mathbf{J}^f_{p^n}\right\}=\mathbf{0}\end{aligned}\tag{E.8}$$

If the Rayleigh damping is used to model the material damping in the solid domain then Eq. (E.7) becomes

$$\begin{aligned}&\left[\mathbf{M}^s\right]\{\tilde{\mathbf{v}}\}+\alpha\left[\mathbf{M}^s_R\right]\{\tilde{\mathbf{v}}\}+\beta\left[\mathbf{K}^s_R\right]\{\tilde{\mathbf{v}}\}+\left[\mathbf{H}^s_{fd}\right]\cdot\{\tilde{\mathbf{q}}\}\\&+\{\mathbf{J}^s_\sigma\}-\{\mathbf{J}^s_0\}+\left\{\mathbf{J}^s_g\right\}-\{\mathbf{J}^s_{ext}\}+\left\{\mathbf{J}^{fd}_{p_0}\right\}+\left\{\mathbf{J}^{fd}_{p^n}\right\}=\mathbf{0}\end{aligned}\tag{E.9}$$

In Eq. (E.8), the space-time finite element matrices and space-time nodal vectors for fluid domain are identical to those presented in Appendix C (see Eq. C.7). In Eq. (E.7) and Eq. (E.9), the space-time mass matrix, $[\mathbf{M}^s]$ and the mass proportional Rayleigh damping matrix, $[\mathbf{M}^s_R]$, are given in Eq. (A.6) and Eq. (A.16), respectively. The space-time nodal vectors, $\{\mathbf{J}^s_0\}$ and $\{\mathbf{J}^s_{ext}\}$ are given by Eq. (A.27) and Eq. (A.22), respectively. Nodal vectors $\left\{\mathbf{J}^{fd}_{p_0}\right\}$ and $\left\{\mathbf{J}^{fd}_{p^n}\right\}$ contains the contribution of the hydrostatic and hydrodynamic pressures, respectively. These vectors are described in Appendix C (see Eq. C.54).

The space-time nodal vector $\left\{\mathbf{J}^s_g\right\}$ in Eq. (E.7) and Eq. (E.9) corresponds to the motion of the perfectly rigid foundation underneath the dam-reservoir system. Finite element expression for this term is given below.

$$\left\{J^s_g\right\}^a_i(I)=\int_{I_n}\int_{\Omega^s_h}N^I T_a\rho^s a^g_i d\Omega dt\tag{E.10}$$

The stiffness proportional tangent stiffness matrix $[\mathbf{K}^s_R]$ is given by

$$[K^s_R]^{ab}_{ij}(I,J)=\int_{I_n}\int_{\Omega^s_h}\frac{\partial N^I T_a}{\partial x_p}C_{pijq}\frac{\partial N^J T_b}{\partial x_q}d\Omega dt\tag{E.11}$$

where C_{ijkl} denotes the material tangent matrix for the nonlinear stress-strain relationship. Recasting the above equation in following,

$$[K^s_R]^{ab}_{ij}(I,J)=\int_{I_n}T_aT_bk_{ij}(I,J)dt\tag{E.12}$$

where

$$k_{ij}(I,J)=\int_{\Omega^s_h}\frac{\partial N^I}{\partial x_p}C_{pijq}\frac{\partial N^J}{\partial x_q}d\Omega\tag{E.13}$$

denotes the tangent stiffness matrix which is identical to the one presented in the Eq. (A.15).

It is noteworhty that the stiffness tangent matrix in above equation changes with time due to the nonlinear stress-strain relationship. Therefore, Eq. (E.11) should be computed by using the numerical integration techniques. By using a finite set of quadrature points, $\{\theta^1, \cdots, \theta^{n_{ipt}}\}$, and corresponding weights, $\left\{w_t^1, \cdots, w_t^{n_{ipt}}\right\}$, for numerical integration of the Eq. (E.11),

$$[K_R^s]_{ij}^{ab}(I,J) = \frac{\Delta t}{2} \sum_{\alpha=1}^{n_{ipt}} T_a^\alpha T_b^\alpha k_{ij}^\alpha (I,J)\, w_t^\alpha \tag{E.14}$$

where k_{ij}^α is tangent stiffness matrix corresponding to C_{ijkl}^α which is computed at some time $t^\alpha \in I_n$.

For three-point Gauss-Lobatto rule the quadrature points and the corresponding weights are given by $\{-1, 0, 1\}$ and $\left\{\frac{1}{3}, \frac{4}{3}, \frac{1}{3}\right\}$, respectively. If this rule is used in above equation then,

$$[\mathbf{K}_R^s] = \frac{\Delta t}{6} \begin{bmatrix} \mathbf{K}_0^\Omega + \mathbf{K}_1^\Omega & \mathbf{K}_1^\Omega \\ \mathbf{K}_1^\Omega & \mathbf{K}_1^\Omega + \mathbf{K}_2^\Omega \end{bmatrix} \tag{E.15}$$

where $\mathbf{K}_0^\Omega$, $\mathbf{K}_1^\Omega$ and $\mathbf{K}_2^\Omega$ are tangent stiffness matrices defined at the time $t = t_n$, $t = (t_n + t_{n+1})/2$, and $t = t_{n+1}$, respectively. The finite element structure of tangent stiffness matrix is discusses in Appendix A (see Eq. A.14).

For two-point Gauss-Legendre rule the quadrature points and the corresponding weights are given by $\{-1/3, 1/3\}$ and $\{1, 1\}$, respectively. If this rule is used in Eq. (E.14), then

$$\begin{aligned} [\mathbf{K}_R^s] = &\frac{\Delta t}{24} \begin{bmatrix} \left(1+\sqrt{3}\right)^2 \mathbf{K}_1^\Omega & 2\mathbf{K}_1^\Omega \\ 2\mathbf{K}_1^\Omega & \left(1-\sqrt{3}\right)^2 \mathbf{K}_1^\Omega \end{bmatrix} \\ &+ \frac{\Delta t}{24} \begin{bmatrix} \left(1-\sqrt{3}\right)^2 \mathbf{K}_2^\Omega & 2\mathbf{K}_2^\Omega \\ 2\mathbf{K}_2^\Omega & \left(1+\sqrt{3}\right)^2 \mathbf{K}_2^\Omega \end{bmatrix} \end{aligned} \tag{E.16}$$

where $\mathbf{K}_1^\Omega$ and $\mathbf{K}_1^\Omega$ are the tangent stiffness matrices computed at the time $t = t_1$ and $t = t_2$, respectively. The expressions for t_1 and t_2 are given below.

$$t_1 = \frac{t_n\left(\sqrt{3}+1\right) + t_{n+1}\left(\sqrt{3}-1\right)}{2\sqrt{3}} \tag{E.17}$$

$$t_2 = \frac{t_n\left(\sqrt{3}-1\right) + t_{n+1}\left(\sqrt{3}+1\right)}{2\sqrt{3}} \tag{E.18}$$

In Eq. (E.7) and Eq. (E.9) the space-time nodal vector $\{\mathbf{J}^s_\sigma\}$ corresponds to the internal stresses in the solid domain. The space-time finite element structure is given below

$$\{\mathbf{J}^s_\sigma\} = \left\{ \begin{array}{c} \mathbf{J}^1_\sigma \\ \mathbf{J}^2_\sigma \end{array} \right\} \tag{E.19}$$

where $\{\mathbf{J}^1_\sigma\}$ and $\{\mathbf{J}^2_\sigma\}$ correspond to the spatial nodal values at the bottom and top space-time slab. In Section 6.5, a three-point Gauss-Lobatto rule is used to compute this term to obtain following expression (see Eq. 6.50, Eq. 6.52).

$$\left\{\mathbf{J}^1_\sigma\right\} = \frac{\Delta t}{6}\left\{\mathbf{f}^0_{\text{int}}\right\} + \frac{\Delta t}{3}\left\{\mathbf{f}^1_{\text{int}}\right\} \tag{E.20}$$

$$\left\{\mathbf{J}^2_\sigma\right\} = \frac{\Delta t}{3}\left\{\mathbf{f}^1_{\text{int}}\right\} + \frac{\Delta t}{6}\left\{\mathbf{f}^2_{\text{int}}\right\} \tag{E.21}$$

where $\mathbf{f}^0_{\text{int}}$, $\mathbf{f}^1_{\text{int}}$, and $\mathbf{f}^2_{\text{int}}$ denote the internal force vectors computed at time $t_1 = t_n$, $t_2 = (t_n + t_{n+1})/2$, and $t_3 = t_{n+1}$, respectively. The finite element expressions for these terms are given below.

$$\left\{\mathbf{f}^0_{\text{int}}\right\} := f^0_{\text{int}}(i,I) = \int_{\Omega^s_h} \frac{\partial N^I}{\partial x_j}\sigma^0_{ij} d\Omega \tag{E.22}$$

$$\left\{\mathbf{f}^1_{\text{int}}\right\} := f^1_{\text{int}}(i,I) = \int_{\Omega^s_h} \frac{\partial N^I}{\partial x_j}\sigma^1_{ij} d\Omega \tag{E.23}$$

$$\left\{\mathbf{f}^2_{\text{int}}\right\} := f^2_{\text{int}}(i,I) = \int_{\Omega^s_h} \frac{\partial N^I}{\partial x_j}\sigma^2_{ij} d\Omega \tag{E.24}$$

In Eqs. (E.22 – E.24), σ^0, σ^1, and σ^2 are stresses computed at the times t_1, t_2, and t_3, respectively. It should be noted that the σ^0 and $\{\mathbf{f}^0_{\text{int}}\}$ are already known from the previous time step, therefore, linearization of Eq. (E.22) will vanish. Linearization of Eq. (E.23) and Eq. (E.24) will yield following tangent stiffness matrices.

$$\left\{\Delta\mathbf{f}^1_{\text{int}}\right\} = \left[\mathbf{K}^\Omega_1\right]\{\Delta\tilde{\mathbf{u}}\}_{t=t_1} \tag{E.25}$$

$$\left\{\Delta \mathbf{f}_{\text{int}}^{2}\right\} = \left[\mathbf{K}_{2}^{\Omega}\right] \{\Delta \tilde{\mathbf{u}}\}_{t=t_2} \tag{E.26}$$

where $\{\Delta \tilde{\mathbf{u}}\}_{t=t_1}$ and $\{\Delta \tilde{\mathbf{u}}\}_{t=t_2}$ denote the displacement-increments at time t_1 and t_2, respectively, and the tangent stiffness matrices $\mathbf{K}_{1}^{\Omega}$ and $\mathbf{K}_{2}^{\Omega}$ are indentical to those given in Eq. (E.15).

In v-ST/FEM, $\{\Delta \tilde{\mathbf{u}}\}_{t=t_1}$ and $\{\Delta \tilde{\mathbf{u}}\}_{t=t_2}$ should be recast in terms of the velocity increments. Further, in Section 6.4, the displacements at time $t \in I_n$ are given by following equation (see Eq. 6.35)

$$\{\tilde{\mathbf{u}}\}_{t} = \{\tilde{\mathbf{u}}\}_{t=t_n} + \tilde{T}_1(\theta) \left\{\tilde{\mathbf{v}}^{1}\right\} + \tilde{T}_2(\theta) \left\{\tilde{\mathbf{v}}^{2}\right\} \tag{E.27}$$

where $\tilde{T}_1(\theta)$ and $\tilde{T}_2(\theta)$ are given in Eq. (6.36). Here, $\{\tilde{\mathbf{v}}^1\}$ and $\{\tilde{\mathbf{v}}^2\}$ are the unknown velocity vectors at the bottom and top space-time slab, respectively. In above equation, $\{\tilde{\mathbf{u}}\}_{t=t_1}$ and $\{\tilde{\mathbf{u}}\}_{t=t_2}$ correspond to the $\theta = 0.0$ and $\theta = 1.0$, respectively. Therefore,

$$\{\tilde{\mathbf{u}}\}_{t=t_1} = \{\tilde{\mathbf{u}}\}_{t=t_n} + \frac{3\Delta t_n}{8} \left\{\tilde{\mathbf{v}}^{1}\right\} + \frac{\Delta t_n}{8} \left\{\tilde{\mathbf{v}}^{2}\right\} \tag{E.28}$$

$$\{\tilde{\mathbf{u}}\}_{t=t_2} = \{\tilde{\mathbf{u}}\}_{t=t_n} + \frac{\Delta t_n}{2} \left\{\tilde{\mathbf{v}}^{1}\right\} + \frac{\Delta t_n}{2} \left\{\tilde{\mathbf{v}}^{2}\right\} \tag{E.29}$$

Accordingly, one can obtain the following relatioship between displacement increaments and velocity increaments.

$$\{\Delta \tilde{\mathbf{u}}\}_{t=t_1} = \frac{3\Delta t_n}{8} \left\{\Delta \tilde{\mathbf{v}}^{1}\right\} + \frac{\Delta t_n}{8} \left\{\Delta \tilde{\mathbf{v}}^{2}\right\} \tag{E.30}$$

$$\{\Delta \tilde{\mathbf{u}}\}_{t=t_2} = \frac{\Delta t_n}{2} \left\{\Delta \tilde{\mathbf{v}}^{1}\right\} + \frac{\Delta t_n}{2} \left\{\Delta \tilde{\mathbf{v}}^{2}\right\} \tag{E.31}$$

Using Eq. (E.30) in Eq. (E.27) and Eq. (E.31) in Eq. (E.26) the space-time tangent stiffness matrix corresponding to the three-point Gauss-Lobatto rule can be described as

$$\{\Delta \mathbf{J}_{\sigma}^{s}\} := \begin{Bmatrix} \Delta \mathbf{J}_{\sigma}^{1} \\ \Delta \mathbf{J}_{\sigma}^{2} \end{Bmatrix} = [\mathbf{K}_{\sigma^1}^{s}] \begin{Bmatrix} \Delta \tilde{\mathbf{v}}^{1} \\ \Delta \tilde{\mathbf{v}}^{2} \end{Bmatrix} + [\mathbf{K}_{\sigma^2}^{s}] \begin{Bmatrix} \Delta \tilde{\mathbf{v}}^{1} \\ \Delta \tilde{\mathbf{v}}^{2} \end{Bmatrix} \tag{E.32}$$

in which

$$[\mathbf{K}_{\sigma^1}^{s}] = \frac{\Delta t_n^2}{24} \begin{bmatrix} 3\left[\mathbf{K}_{1}^{\Omega}\right] & \left[\mathbf{K}_{1}^{\Omega}\right] \\ 3\left[\mathbf{K}_{1}^{\Omega}\right] & \left[\mathbf{K}_{1}^{\Omega}\right] \end{bmatrix} \tag{E.33}$$

$$[\mathbf{K}_{\sigma^2}^{s}] = \frac{\Delta t_n^2}{12} \begin{bmatrix} \mathbf{0} & \mathbf{0} \\ \left[\mathbf{K}_{2}^{\Omega}\right] & \left[\mathbf{K}_{2}^{\Omega}\right] \end{bmatrix} \tag{E.34}$$

Lastly, a similar process can be followed to compute the space-time tangent matrix in case of the two-point Gauss-Legendre quadrature rule.

Bibliography

Achenbach, Jan D. (2012). *Wave propagation in elastic solids*. Vol. 16. Elsevier, p. 425 (cit. on pp. 56, 72, 74, 79, 85, 94, 96, 100).

Adam, Christoph, Dietmar Adam, Fritz Kopf, and Ivan Paulmichl (2009). „Computational validation of static and dynamic plate load testing". In: *Acta Geotechnica* 4.1, pp. 35–55 (cit. on pp. 65, 66).

Aharoni, D. and P. Bar-Yoseph (1992). „Mixed finite element formulations in the time domain for solution of dynamic problems". In: *Computational Mechanics* 9.5, pp. 359–374 (cit. on p. 7).

Alonso-Mallo, Isaias and Nuria Reguera (2003). „Discrete absorbing boundary conditions for Schrödinger-type equations. construction and error analysis". In: *SIAM Journal on numerical Analysis* 41.5, pp. 1824–1850 (cit. on p. 71).

Anandarajah, A (1993). „Dynamic analysis of axially-loaded footings in time domain". In: *Soils and foundations* 33.1, pp. 40–54 (cit. on p. 5).

Argyris, J.H. and D.W. Scharpf (1969). „Finite elements in time and space". In: *Nuclear Engineering and Design* 10.4, pp. 456 –464 (cit. on p. 6).

Arnold, R.N., G.N. Bycroft, and G.B. Warburton (1955). „Forced vibrations of a body on an infinite elastic solid". In: *ASME J. Appl. Mech* 77, pp. 391–401 (cit. on p. 115).

Baffet, Daniel, Jacobo Bielak, Dan Givoli, Thomas Hagstrom, and Daniel Rabinovich (2012). „Long-time stable high-order absorbing boundary conditions for elastodynamics". In: *Computer Methods in Applied Mechanics and Engineering* 241-244, pp. 20–37 (cit. on p. 93).

Bailey, C. D. (1980). „The Galerkin formulation and the Hamilton-Ritz formulation: A comparison". In: *Acta Mechanica* 36.1, pp. 63–70 (cit. on p. 6).

Bailey, CD (1982). „Hamilton's principle and the calculus of variations". In: *Acta Mechanica* 44.1-2, pp. 49–57 (cit. on p. 6).

Bailey, Cecil D. (1975). „A new look at Hamilton's principle". In: *Foundations of Physics* 5.3, pp. 433–451 (cit. on p. 6).

Bajer, C. and C. Bohatier (1995). „The soft way method and the velocity formulation". In: *Computers & Structures* 55.6, pp. 1015 –1025 (cit. on p. 7).

Bajer, Czesław I. (1987). „Notes on the stability of non-rectangular space-time finite elements". In: *International Journal for Numerical Methods in Engineering* 24.9, pp. 1721–1739 (cit. on p. 7).

Bao, Hesheng, Jacobo Bielak, Omar Ghattas, et al. (1998). „Large-scale simulation of elastic wave propagation in heterogeneous media on parallel computers“. In: *Computer Methods in Applied Mechanics and Engineering* 152.1-2, pp. 85–102 (cit. on pp. 71, 111).

Baruch, M and R Riff (1984). „Stability of time finite elements“. In: *AIAA journal* 22.8, pp. 1171–1173 (cit. on p. 6).

Baruch, Menahem and Richard Riff (1982). „Hamilton's principle, Hamilton's law-6 to the n power correct formulations“. In: *AIAA Journal* 20.5, pp. 687–692 (cit. on p. 6).

Basu, Ushnish and Anil K Chopra (2004). „Perfectly matched layers for transient elastodynamics of unbounded domains“. In: *International Journal for Numerical Methods in Engineering* 59.8, pp. 1039–1074 (cit. on pp. 110, 146).

Bathe, K. J. and W. F. Hahn (1979). „On transient analysis of fluid-structure systems“. In: *Computers & Structures* 10.1-2, pp. 383–391 (cit. on p. 147).

Bathe, Klaus-Jürgen and Edward L Wilson (1976). *Numerical methods in finite element analysis*. Prentice-Hall (cit. on pp. 2, 6, 42).

Bayliss, Alvin and Eli Turkel (1980). „Radiation boundary conditions for wave-like equations“. In: *Communications on Pure and Applied Mathematics* 33.6, pp. 707–725 (cit. on p. 89).

Bažant, Zdeněk P (1987). „Snapback instability at crack ligament tearing and its implication for fracture micromechanics“. In: *Cement and Concrete Research* 17.6, pp. 951–967 (cit. on pp. 193, 216).

Belytschko, T. B. and J. M. Kennedy (1976). „A fluid-structure finite element method for the analysis of reactor safety problems“. In: *Nuclear Engineering and Design* 38.1, pp. 71–81 (cit. on p. 147).

Bermúdez, A., R. Durán, M. A. Muschietti, R. Rodríguez, and J. Solomin (1995). „Finite element vibration analysis of fluid–solid systems without spurious modes“. In: *SIAM Journal on Numerical Analysis* 32.4, pp. 1280–1295 (cit. on p. 147).

Bettess, P. (1977). „Infinite elements“. In: *International Journal for numerical methods in engineering* 11.1, pp. 53–64 (cit. on p. 116).

Bhattacharjee, SS and P Leger (1993). „Seismic cracking and energy dissipation in concrete gravity dams“. In: *Earthquake Engineering & Structural Dynamics* 22.11, pp. 991–1007 (cit. on pp. 193, 194, 213, 215, 219, 221).

Bielak, Jacobo and Paul Christiano (1984). „On the effective seismic input for non-linear soil-structure interaction systems“. In: *Earthquake Engineering & Structural Dynamics* 12.1, pp. 107–119 (cit. on pp. 108, 110).

Bielak, Jacobo, Kostas Loukakis, Yoshiaki Hisada, and Chiaki Yoshimura (2003). „Domain reduction method for three-dimensional earthquake modeling in localized regions, Part I: Theory“. In: *Bulletin of the Seismological Society of America* 93.2, pp. 817–824 (cit. on pp. 71, 108, 110).

Birk, C., S. Prempramote, and C. Song (2012). „An improved continued-fraction-based high-order transmitting boundary for time-domain analyses in unbounded domains“. In: *International journal for numerical methods in engineering* 89.3, pp. 269–298 (cit. on p. 146).

Bonelli, A and OS Bursi (2003). „Iterative solutions for implicit time discontinuous Galerkin methods applied to non-linear elastodynamics“. In: *Computational mechanics* 30.5-6, pp. 487–498 (cit. on p. 51).

Bonelli, A, OS Bursi, and M Mancuso (2002). „Explicit predictor–multicorrector time discontinuous Galerkin methods for non-linear dynamics“. In: *Journal of Sound and Vibration* 256.4, pp. 695–724 (cit. on p. 51).

Bonnerot, R and P Jamet (1979). „A third order accurate discontinuous finite element method for the one-dimensional Stefan problem“. In: *Journal of Computational Physics* 32.2, pp. 145–167 (cit. on p. 7).

Borri, M. (1986). „Helicopter rotor dynamics by finite element time approximation“. In: *Computers & Mathematics with Applications* 12.1, Part A, pp. 149 –160 (cit. on p. 6).

Borri, M. and C. Bottasso (1993). „A general framework for interpreting time finite element formulations“. In: *Computational Mechanics* 13.3, pp. 133–142 (cit. on p. 7).

Borri, M., G.L. Ghiringhelli, M. Lanz, P. Mantegazza, and T. Merlini (1985). „Dynamic response of mechanical systems by a weak Hamiltonian formulation“. In: *Computers & Structures* 20.1-3, pp. 495–508 (cit. on p. 6).

Borri, M., F. Mello, and S. N. Atluri (1990). „Variational approaches for dynamics and time-finite-elements: numerical studies“. In: *Computational Mechanics* 7.1, pp. 49–76 (cit. on p. 7).

– (1991). „Primal and mixed forms of Hamiltons's principle for constrained rigid body systems: numerical studies“. In: *Computational Mechanics* 7.3, pp. 205–220 (cit. on p. 7).

Brühwiler, E (1990). „Fracture of mass concreete under simulated seismic action“. In: *Dam Engineering* 1.EPFL-ARTICLE-181083, pp. 153–176 (cit. on p. 213).

Burman, A, Parsuram Nayak, P Agrawal, and Damodar Maity (2012). „Coupled gravity dam–foundation analysis using a simplified direct method of soil–structure interaction“. In: *Soil Dynamics and Earthquake Engineering* 34.1, pp. 62–68 (cit. on p. 71).

Bycroft, G.N. (1956). „Forced vibrations of a rigid circular plate on a semi-infinite elastic space and on an elastic stratum“. In: *Phil. Trans. R. Soc. Lond. A* 248.948, pp. 327–368 (cit. on p. 115).

Calayir, Yusuf and Muhammet Karaton (2005a). „A continuum damage concrete model for earthquake analysis of concrete gravity dam–reservoir systems“. In: *Soil Dynamics and Earthquake Engineering* 25.11, pp. 857–869 (cit. on p. 221).

– (2005b). „Seismic fracture analysis of concrete gravity dams including dam–reservoir interaction“. In: *Computers & structures* 83.19-20, pp. 1595–1606 (cit. on pp. 213, 215, 219, 221).

Cervera, Miguel, Javier Oliver, and Rui Faria (1995). „Seismic evaluation of concrete dams via continuum damage models“. In: *Earthquake engineering & structural dynamics* 24.9, pp. 1225–1245 (cit. on pp. 194, 221).

Chai, Gary W, Rudi van Staden, and Yew-Chaye Loo (2014). „In situ assessment of pavement subgrade using Falling Weight Deflectometer“. In: *Journal of Testing and Evaluation* 43.1, pp. 140–148 (cit. on p. 5).

Chakrabarti, P. and A. K. Chopra (1973a). „Earthquake analysis of gravity dams including hydrodynamic interaction“. In: *Earthquake Engineering & Structural Dynamics* 2.2, pp. 143–160 (cit. on p. 143).

– (1973b). „Hydrodynamic pressures and response of gravity dams to vertical earthquake component“. In: *Earthquake Engineering & Structural Dynamics* 1.4, pp. 325–335 (cit. on p. 143).

Chen, H. C. and R. L. Taylor (1990). „Vibration analysis of fluid–solid systems using a finite element displacement formulation“. In: *International Journal for Numerical Methods in Engineering* 29.4, pp. 683–698 (cit. on p. 147).

Chen, Zhiyun, Holger Steeb, and Stefan Diebels (2006). „A time-discontinuous Galerkin method for the dynamical analysis of porous media“. In: *International journal for numerical and analytical methods in geomechanics* 30.11, pp. 1113–1134 (cit. on p. 12).

Cheng, A. H. D. (1986). „Effect of sediment on earthquake-induced reservoir hydrodynamic response“. In: *Journal of engineering mechanics* 112.7, pp. 654–665 (cit. on p. 145).

Chew, Weng Cho (1995). *Waves and fields in inhomogeneous media*. IEEE press (cit. on p. 71).

Chien, C-C and T-Y Wu (2000). „An improved predictor/multi-corrector algorithm for a time-discontinuous Galerkin finite element method in structural dynamics“. In: *Computational Mechanics* 25.5, pp. 430–437 (cit. on p. 7).

Chopra, A. K. (1967). „Hydrodynamic pressures on dams during earthquakes“. In: *Journal of the Engineering Mechanics Division* 93.6, pp. 205–224 (cit. on p. 142).

– (1968). „Earthquake behavior of reservoir-dam systems“. In: *Journal of the Engineering Mechanics Division* 94.6, pp. 1475–1500 (cit. on p. 143).

– (1970). „Earthquake response of concrete gravity dams“. In: *Journal of the Engineering Mechanics Division* 96.4, pp. 443–454 (cit. on p. 143).

Chopra, A. K. and P. Chakrabarti (1981). „Earthquake analysis of concrete gravity dams including dam-water-foundation rock interaction“. In: *Earthquake Engineering & Structural Dynamics* 9.4, pp. 363–383 (cit. on p. 145).

Chua, KH, T Balendra, and KW Lo (1992). „Groundborne vibrations due to trains in tunnels“. In: *Earthquake engineering & structural dynamics* 21.5, pp. 445–460 (cit. on pp. 1, 5).

Chuhan, Z., J. Feng, and O.A. Pekau (1995). „Time domain procedure of FE-BE-IBE coupling for seismic interaction of arch dams and canyons“. In: *Earthquake engineering & structural dynamics* 24.12, pp. 1651–1666 (cit. on p. 115).

Chwang, A. T. (1978). „Hydrodynamic pressures on sloping dams during earthquakes. Part 2. Exact theory“. In: *Journal of Fluid Mechanics* 87.2, pp. 343–348 (cit. on p. 144).

Chwang, A. T. and G. W. Housner (1978). „Hydrodynamic pressures on sloping dams during earthquakes. Part 1. Momentum method“. In: *Journal of Fluid Mechanics* 87.2, pp. 335–341 (cit. on p. 144).

Clayton, R. W. and B. Egquist (1977). „Absorbing boundary conditions for acoustic and elastic wave equations.“ In: *Bulletin of the Seismological Society of America* 67, pp. 1529–1540. (Cit. on p. 88).

Clayton, Robert W and Bjtjrn Engquist (1980). „Absorbing boundary conditions for wave-equation“. In: *Geophysics* 45.5, pp. 895–904 (cit. on p. 89).

Clemente, Paolo and Dario Rinaldis (1998). „Protection of a monumental building against traffic-induced vibrations“. In: *Soil Dynamics and Earthquake Engineering* 17.5, pp. 289–296 (cit. on pp. 1, 5).

Clouteau, Didier, Geert Degrande, and Geert Lombaert (2001). „Numerical modelling of traffic induced vibrations“. In: *Meccanica* 36.4, pp. 401–420 (cit. on pp. 1, 5).

Cockburn, Bernardo (2003). „Discontinuous galerkin methods“. In: *ZAMM-Journal of Applied Mathematics and Mechanics/Zeitschrift für Angewandte Mathematik und Mechanik* 83.11, pp. 731–754 (cit. on p. 12).

Cohen, M (1980). „Silent boundary methods for transient wave analysis“. PhD thesis. California Institute of Technology (cit. on p. 89).

Cohen, M. and P. C. Jennings (1983). „Silent boundary methods for transient Analysis“. In: *Computational methods for transient analysis*. Vol. 1. Amsterdam, North-Holland(Computational Methods in Mechanics., pp. 301 –360 (cit. on p. 89).

Cohen, M.F., T.J.R. Hughes, and P.C. Jennings (1981). „Comparison of paraxial and viscous silent boundary methods in finite element analysis“. In: *American Society of Mechanical Engineers, Applied Mechanics Division, AMD*. Vol. 44 (cit. on p. 89).

Collino, Francis (1993). „High order absorbing boundary conditions for wave propagation models. Straight line boundary and corner cases“. In: *Second International Conference on Mathematical and Numerical Aspects of Wave Propagation (Newark, DE, 1993)*. SIAM Philadelphia, PA, pp. 161–171 (cit. on p. 92).

Cormeau, I (1991). „The Taylor impact test problem revisiting the standard 2-node rod finite element“. In: *The finite element method in the 1990's*. Springer, pp. 225–233 (cit. on p. 60).

Cremonini, Marco G, Paul Christiano, and Jacobo Bielak (1988). „Implementation of effective seismic input for soil-structure interaction systems“. In: *Earthquake engineering & structural dynamics* 16.4, pp. 615–625 (cit. on pp. 108, 110).

Dahlquist, Germund G (1963). „A special stability problem for linear multistep methods“. In: *BIT Numerical Mathematics* 3.1, pp. 27–43 (cit. on pp. 2, 6).

Delfour, M, W Hager, and F Trochu (1981). „Discontinuous Galerkin methods for ordinary differential equations“. In: *Mathematics of Computation* 36.154, pp. 455–473 (cit. on p. 7).

Ditzel, Auke, Gerard Herman, and PAUL HÖLSCHER (2001). „Elastic waves generated by high-speed trains“. In: *Journal of Computational Acoustics* 9.03, pp. 833–840 (cit. on pp. 1, 5).

Elbagalati, Omar, Mostafa Elseifi, Kevin Gaspard, and Zhongjie Zhang (2018). „Development of the pavement structural health index based on falling weight deflectometer testing“. In: *International Journal of Pavement Engineering* 19.1, pp. 1–8 (cit. on p. 5).

Engquist, Bjorn and Andrew Majda (1977). „Absorbing Boundary Conditions for the Numerical Simulation of Waves“. In: *Mathematics of Computation* 31.139, p. 629 (cit. on p. 88).

Eriksson, Kenneth, Claes Johnson, and Vidar Thomée (1985). „Time discretization of parabolic problems by the discontinuous Galerkin method“. In: *ESAIM: Mathematical Modelling and Numerical Analysis* 19.4, pp. 611–643 (cit. on p. 12).

Fan, SC, TC Fung, and G Sheng (1997). „A comprehensive unified set of single-step algorithms with controllable dissipation for dynamics Part II. Algorithms and analysis“. In: *Computer methods in applied mechanics and engineering* 145.1-2, pp. 99–107 (cit. on p. 7).

Felippa, C. A. and T. L. Geers (1988). „Partitioned analysis for coupled mechanical systems“. In: *Engineering Computations* 5.2, pp. 123–133 (cit. on p. 147).

Felippa, C. A., K. C. Park, and C. Farhat (2001). „Partitioned analysis of coupled mechanical systems“. In: *Computer methods in applied mechanics and engineering* 190.24-25, pp. 3247–3270 (cit. on p. 147).

Fenves, G. and A. K. Chopra (1983). „Effects of reservoir bottom absorption on earthquake response of concrete gravity dams“. In: *Earthquake engineering & structural dynamics* 11.6, pp. 809–829 (cit. on pp. 144, 145, 152, 197).

Fried, I (1969). „Finite-element analysis of time-dependent phenomena.“ In: *AIAA Journal* 7.6, pp. 1170–1173 (cit. on p. 6).

Fung, T.C. (1999). „On the Accuracy of Galerkin Methods in the Time Domain“. In: *Journal of Vibration and Control* 5.2, pp. 155–174 (cit. on p. 7).

Fung, TC and AYT Leung (1996). „On the accuracy of discontinuous Galerkin methods in the time domain“. In: *Modal Analysis* 2.2, pp. 193–217 (cit. on p. 7).

Geers, MGD, R De Borst, and RHJ Peerlings (2000). „Damage and crack modeling in single-edge and double-edge notched concrete beams“. In: *Engineering Fracture Mechanics* 65.2-3, pp. 247–261 (cit. on p. 215).

Gellert, Menachem (1978). „A new algorithm for integration of dynamic systems“. In: *Computers & Structures* 9.4, pp. 401–408 (cit. on p. 6).

Geradin, M (1974). „On the variational method in the direct integration of the transient structural response“. In: *Journal of Sound Vibration* 34, pp. 479–487 (cit. on p. 6).

Ghaemian, M. and A. Ghobarah (1998). „Staggered solution schemes for dam–reservoir interaction“. In: *Journal of fluids and structures* 12.7, pp. 933–948 (cit. on p. 147).

Ghrib, Faouzi and Rene Tinawi (1995). „An application of damage mechanics for seismic analysis of concrete gravity dams“. In: *Earthquake Engineering & Structural Dynamics* 24.2, pp. 157–173 (cit. on p. 221).

Giry, Cédric, Frédéric Dufour, and Jacky Mazars (2011). „Stress-based nonlocal damage model“. In: *International Journal of Solids and Structures* 48.25-26, pp. 3431–3443 (cit. on p. 215).

Givoli, D. (1991). „Non-Reflecting Boundary Conditions“. In: *Journal of Computational Physics* 94.1, pp. 1–29 (cit. on p. 87).

Givoli, Dan (2001). „High-Order Nonreflecting Boundary Conditions without High-Order Derivatives“. In: *Journal of Computational Physics* 170.2, pp. 849–870 (cit. on p. 92).

Givoli, Dan and Beny Neta (2003). „High-order non-reflecting boundary scheme for time-dependent waves“. In: *Journal of Computational Physics* 186.1, pp. 24–26 (cit. on p. 92).

Givoli, Dan, Beny Neta, and Igor Patlashenko (2003). „Finite element analysis of time-dependent semi-infinite wave-guides with high-order boundary treatment“. In: *International Journal for Numerical Methods in Engineering* 58.13, pp. 1955–1983 (cit. on p. 92).

Givoli, Dan, Thomas Hagstrom, and Igor Patlashenko (2006). „Finite element formulation with high-order absorbing boundary conditions for time-dependent waves“. In: *Computer Methods in Applied Mechanics and Engineering* 195.29-32, pp. 3666–3690 (cit. on p. 93).

Goktepe, A Burak, Emine Agar, and A Hilmi Lav (2006). „Advances in backcalculating the mechanical properties of flexible pavements“. In: *Advances in engineering software* 37.7, pp. 421–431 (cit. on p. 5).

Hagstrom, T. and S.I. Hariharan (1998). „A formulation of asymptotic and exact boundary conditions using local operators“. In: *Applied Numerical Mathematics* 27.4, pp. 403–416 (cit. on pp. 91, 92).

Hagstrom, Thomas and Timothy Warburton (2004). „A new auxiliary variable formulation of high-order local radiation boundary conditions: Corner compatibility conditions and extensions to first-order systems“. In: *Wave Motion* 39.4, pp. 327–338 (cit. on p. 92).

Hagstrom, Thomas, Assaf Mar-Or, and Dan Givoli (2008). „High-order local absorbing conditions for the wave equation: Extensions and improvements“. In: *Journal of Computational Physics* 227.6, pp. 3322–3357 (cit. on p. 93).

Hall, J. F. and A. K. Chopra (1982). „Hydrodynamic effects in the dynamic response of concrete gravity dams“. In: *Earthquake Engineering & Structural Dynamics* 10.2, pp. 333–345 (cit. on pp. 144, 145).

Hariri-Ardebili, M. A., S. M. Seyed-Kolbadi, and M. R. Kianoush (2016). „FEM-based parametric analysis of a typical gravity dam considering input excitation mechanism“. In: *Soil Dynamics and Earthquake Engineering* 84, pp. 22–43 (cit. on p. 111).

Hashash, Y. M. A. (2009). „DeepSoil USER MANUAL and TUTORIAL“. In: *University of Illinois, Urbana, IL, USA* 57 (cit. on p. 112).

Hashiguchi, Koichi (2014). *Elastoplasticity theory*. Springer (cit. on p. 196).

Hatami, K. (1997). „Effect of reservoir bottom on earthquake response of concrete dams“. In: *Soil Dynamics and Earthquake Engineering* 16.7-8, pp. 407–415 (cit. on p. 146).

Hesthaven, Jan S and Tim Warburton (2007). *Nodal discontinuous Galerkin methods: algorithms, analysis, and applications*. Springer Science & Business Media (cit. on pp. 12, 13).

Higdon, R. L. (1991). „Absorbing boundary conditions for elastic waves“. In: *Geophysics* 56.2, p. 231 (cit. on p. 90).

Higdon, Robert L. (1986). „Absorbing boundary conditions for difference approximations to the multidimensional wave equation“. In: *Mathematics of Computation* 47.176, pp. 437–437 (cit. on pp. 89, 90).

– (1987). „Numerical absorbing boundary conditions for the wave equation“. In: *Mathematics of Computation* 49.179, pp. 65–65 (cit. on p. 90).

Higdon, Robert L (1990). „Radiation Boundary Conditions for Elastic Wave Propagation“. In: *SIAM Journal on Numerical Analysis* 27.4, pp. 831–869 (cit. on p. 90).

Higdon, Robert L. (1992). „Absorbing boundary conditions for acoustic and elastic waves in stratified media“. In: *Journal of Computational Physics* 101.2, pp. 386–418 (cit. on p. 90).

– (1994). „Radiation Boundary Conditions for Dispersive Waves“. In: *SIAM Journal on Numerical Analysis* 31.1, pp. 64–100 (cit. on p. 90).

Hilber, Hans M, Thomas JR Hughes, and Robert L Taylor (1977). „Improved numerical dissipation for time integration algorithms in structural dynamics“. In: *Earthquake Engineering & Structural Dynamics* 5.3, pp. 283–292 (cit. on pp. 2, 6, 42).

Hillerborg, Arne, Mats Modéer, and P-E Petersson (1976). „Analysis of crack formation and crack growth in concrete by means of fracture mechanics and finite elements“. In: *Cement and concrete research* 6.6, pp. 773–781 (cit. on p. 216).

Houbolt, John C. (1950). „A recurrence matrix solution for the dynamic response of elastic aircraft“. In: *Journal of the Aeronautical Sciences* 17.9, pp. 540–550 (cit. on pp. 2, 6, 42).

Howard, GF and JET Penny (1978). „The accuracy and stability of time domain finite element solutions“. In: *Journal of Sound and Vibration* 61.4, pp. 585–595 (cit. on p. 6).

Hughes, Thomas JR (1983). „Analysis of transient algorithms with particular reference to stability behavior“. In: *Computational methods for transient analysis(A 84-29160 12-64). Amsterdam, North-Holland, 1983,* pp. 67–155 (cit. on pp. 2, 6, 40, 42, 43).

– (2012). *The finite element method: linear static and dynamic finite element analysis*. Courier Corporation (cit. on pp. 16, 29, 40, 42, 49).

Hughes, Thomas JR and Gregory M Hulbert (1988). „Space-time finite element methods for elastodynamics: formulations and error estimates“. In: *Computer methods in applied mechanics and engineering* 66.3, pp. 339–363 (cit. on pp. 7, 49).

Hulbert, Gregory M (1992). „Time finite element methods for structural dynamics“. In: *International Journal for Numerical Methods in Engineering* 33.2, pp. 307–331 (cit. on pp. 7, 21, 42, 43).

Hulbert, Gregory M and Thomas JR Hughes (1990). „Space-time finite element methods for second-order hyperbolic equations“. In: *Computer methods in applied mechanics and engineering* 84.3, pp. 327–348 (cit. on p. 61).

Hung, Hsiao-Hui, Jenny Kuo, and Yeong-Bin Yang (2001). „Reduction of train-induced vibrations on adjacent buildings“. In: *Structural Engineering and Mechanics* 11.5, pp. 503–518 (cit. on p. 5).

Jahromi, H. Z., B. A. Izzuddin, and L. Zdravkovic (2009). „A domain decomposition approach for coupled modelling of nonlinear soil–structure interaction“. In: *Computer Methods in Applied Mechanics and Engineering* 198.33-36, pp. 2738–2749 (cit. on p. 147).

Jamet, Pierre (1978). „Galerkin-type approximations which are discontinuous in time for parabolic equations in a variable domain“. In: *SIAM Journal on Numerical Analysis* 15.5, pp. 912–928 (cit. on p. 7).

Jirasek, Milan and Peter Grassl (2008). „Evaluation of directional mesh bias in concrete fracture simulations using continuum damage models“. In: *Engineering Fracture Mechanics* 75.8, pp. 1921–1943 (cit. on p. 215).

Johnson, Claes (1993). „Discontinuous Galerkin finite element methods for second order hyperbolic problems“. In: *Computer Methods in Applied Mechanics and Engineering* 107.1-2, pp. 117–129 (cit. on p. 61).

Johnson, Claes and Juhani Pitkäranta (1986). „An analysis of the discontinuous Galerkin method for a scalar hyperbolic equation“. In: *Mathematics of computation* 46.173, pp. 1–26 (cit. on p. 7).

Joolen, Vince J., Beny Neta, and Dan Givoli (2005). „High-order Higdon-like boundary conditions for exterior transient wave problems“. In: *International Journal for Numerical Methods in Engineering* 63.7, pp. 1041–1068 (cit. on p. 92).

Ju, Shen Haw (2007). „Finite element analysis of structure-borne vibration from high-speed train“. In: *Soil dynamics and earthquake engineering* 27.3, pp. 259–273 (cit. on p. 5).

– (2009). „Finite element investigation of traffic induced vibrations“. In: *Journal of Sound and Vibration* 321.3-5, pp. 837–853 (cit. on p. 5).

Ju, Shen-Haw and Hung-Ta Lin (2004). „Analysis of train-induced vibrations and vibration reduction schemes above and below critical Rayleigh speeds by finite element method“. In: *Soil Dynamics and Earthquake Engineering* 24.12, pp. 993–1002 (cit. on p. 5).

Ju, Shen-Haw, Hung-Ta Lin, Chung-Cheng Hsueh, and Shin-Lin Wang (2006). „A simple finite element model for vibration analyses induced by moving vehicles“. In: *International journal for numerical methods in engineering* 68.12, pp. 1232–1256 (cit. on p. 5).

Kármán, T. von (1933). „Discussion of water pressures on dams during earthquakes“. In: *Trans. ASCE* 98, pp. 434–436 (cit. on p. 142).

Kausel, E. (2010). „Early history of soil-structure interaction“. In: *Soil Dynamics and Earthquake Engineering* 30.9, pp. 822–832 (cit. on p. 115).

Kausel, Eduardo and John L Tassoulas (1981). „Transmitting boundaries: a closed-form comparison“. In: *Bulletin of the seismological society of America* 71.1, pp. 143–159 (cit. on p. 87).

Kellezi, L (2000). „Local transmitting boundaries for transient elastic analysis“. In: *Soil dynamics and earthquake engineering* 19.7, pp. 533–547 (cit. on p. 93).

Khoshnoudian, F and Isam Shahrour (2002). „Numerical analysis of the seismic behavior of tunnels constructed in liquefiable soils“. In: *Soils and foundations* 42.6, pp. 1–8 (cit. on p. 5).

Kimura, Makoto and Feng Zhang (2000). „Seismic evaluations of pile foundations with three different methods based on three-dimensional elasto-plastic finite element analysis“. In: *Soils and Foundations* 40.5, pp. 113–132 (cit. on p. 5).

Kontoe, Stavroula, Lidija Zdravkovic, and David M Potts (2009). „An assessment of the domain reduction method as an advanced boundary condition and some pitfalls in the use of conventional absorbing boundaries“. In: *International journal for numerical and analytical methods in geomechanics* 33.3, pp. 309–330 (cit. on p. 93).

Kotsubo, S. (1957). „Dynamic water pressure on dams due to irregular earthquakes“. In: *Transactions of the Japan Society of Civil Engineers* 1957.47, pp. 38–45 (cit. on p. 142).

Kramer, S.L. (2014). *Geotechnical Earthquake Engineering*. Always learning. Pearson (cit. on p. 86).

Krylov, Victor V (1996). „Vibrational impact of high-speed trains. I. Effect of track dynamics“. In: *The Journal of the Acoustical Society of America* 100.5, pp. 3121–3134 (cit. on pp. 1, 5).

Küçükarslan, S., S. B. Coşkun, and B. Taşkın (2005). „Transient analysis of dam–reservoir interaction including the reservoir bottom effects“. In: *Journal of Fluids and Structures* 20.8, pp. 1073–1084 (cit. on pp. 180, 182).

Kunthong, Prapot and Lonny L Thompson (2005). „An efficient solver for the high-order accurate time-discontinuous Galerkin (TDG) method for second-order hyperbolic systems". In: *Finite Elements in Analysis and Design* 41.7-8, pp. 729–762 (cit. on p. 51).

Kurumatani, Mao, Kenjiro Terada, Junji Kato, Takashi Kyoya, and Kazuo Kashiyama (2016). „An isotropic damage model based on fracture mechanics for concrete". In: *Engineering Fracture Mechanics* 155, pp. 49–66 (cit. on pp. 215, 216).

Kuwano, Jiro, Kenji Ishihara, Hiroshi Haya, and Futoshi Izu (1991). „Analysis on permanent deformation of embankments caused by earthquakes". In: *Soils and foundations* 31.3, pp. 97–110 (cit. on p. 5).

Lasaint, Pierre and Pierre-Arnaud Raviart (1974). „On a finite element method for solving the neutron transport equation". In: *Mathematical aspects of finite elements in partial differential equations*. Elsevier, pp. 89–123 (cit. on p. 7).

Lee, G. C. and C. S. Tsai (1991). „Time-domain analyses of dam-reservoir system. I: Exact solution". In: *Journal of engineering mechanics* 117.9, pp. 1990–2006 (cit. on pp. 180, 182).

Lee, Jeeho and Gregory L Fenves (1998). „A plastic-damage concrete model for earthquake analysis of dams". In: *Earthquake engineering & structural dynamics* 27.9, pp. 937–956 (cit. on p. 194).

Li, Qiang and Keizo Ugai (1998). „Comparative study on static and dynamic sliding behaviors of slopes based on small and large deformation theories". In: *Soils and foundations* 38.3, pp. 201–207 (cit. on p. 5).

Li, XD and N-E Wiberg (1998). „Implementation and adaptivity of a space-time finite element method for structural dynamics". In: *Computer Methods in Applied Mechanics and Engineering* 156.1-4, pp. 211–229 (cit. on pp. 7, 60).

Lin, G., Y. Wang, and Z. Hu (2012). „An efficient approach for frequency-domain and time-domain hydrodynamic analysis of dam–reservoir systems". In: *Earthquake Engineering & Structural Dynamics* 41.13, pp. 1725–1749 (cit. on p. 146).

Loizos, Andreas and A Scarpas (2005). „Verification of falling weight deflectometer back-analysis using a dynamic finite elements simulation". In: *International Journal of Pavement Engineering* 6.2, pp. 115–123 (cit. on p. 5).

Løkke, Arnkjell and Anil K. Chopra (2017). „Direct finite element method for nonlinear analysis of semi-unbounded dam–water–foundation rock systems". In: *Earthquake Engineering and Structural Dynamics* 46.8, pp. 1267–1285 (cit. on pp. 108, 110).

Lotfi, V., J. M. Roesset, and J. L. Tassoulas (1987). „A technique for the analysis of the response of dams to earthquakes". In: *Earthquake engineering & structural dynamics* 15.4, pp. 463–489 (cit. on p. 145).

Luco, J. E. and L. Contesse (1973). „Dynamic structure-soil-structure interaction". In: *Bulletin of the Seismological Society of America* 63.4, pp. 1289–1303 (cit. on p. 115).

Lysmer, John and Roger L Kuhlemeyer (1969). „Finite dynamic model for infinite media". In: *Journal of the Engineering Mechanics Division* 95.4, pp. 859–878 (cit. on pp. 71, 88, 93, 98, 101, 102, 106, 113, 133, 264).

M. Borri, M. Lam and P. Mantegazzat (1985). „Comment on "Time Finite Element Discretization of Hamilton's Law of Varying Action"“. In: *AIAA Journal* 23.9, pp. 1457–1458 (cit. on p. 6).

Maeda, Setsuo, Miyuki Morioka, Yoshiharu Yonekawa, Kazuo Kanada, and Yukio Takahashi (1998). „Experimental Studies of Subjective Response to Road Traffic-Induced Building Vibration.“ In: *Industrial Health* 36.2, pp. 112–119 (cit. on pp. 1, 5).

Maina, JW, H Yokota, DA Mfinanga, and S Masuda (2000). „Prediction of Pavement Deterioration Based on FWD Results“. In: *Nondestructive Testing of Pavements and Backcalculation of Moduli* 3, pp. 95–109 (cit. on p. 5).

Maity, D. and S. K. Bhattacharyya (1999). „Time-domain analysis of infinite reservoir by finite element method using a novel far-boundary condition“. In: *Finite Elements in Analysis and Design* 32.2, pp. 85–96 (cit. on p. 146).

– (2003). „A parametric study on fluid–structure interaction problems“. In: *Journal of Sound and Vibration* 263.4, pp. 917–935 (cit. on p. 147).

Mancuso, Massimo and Francesco Ubertini (2003). „An efficient integration procedure for linear dynamics based on a time discontinuous Galerkin formulation“. In: *Computational Mechanics* 32.3, pp. 154–168 (cit. on pp. 7, 51).

– (2006). „An efficient time discontinuous Galerkin procedure for non-linear structural dynamics“. In: *Computer Methods in Applied Mechanics and Engineering* 195.44-47, pp. 6391–6406 (cit. on p. 7).

Medina, F. and J. Penzien (1982). „Infinite elements for elastodynamics“. In: *Earthquake Engineering & Structural Dynamics* 10.5, pp. 699–709 (cit. on p. 116).

Medina, F., J. Dominguez, and J. L. Tassoulas (1990). „Response of dams to earthquakes including effects of sediments“. In: *Journal of structural Engineering* 116.11, pp. 3108–3121 (cit. on p. 145).

Mello, F.J., M. Borri, and S.N. Atluri (1990). „Time finite element methods for large rotational dynamics of multibody systems“. In: *Computers & Structures* 37.2. Special Issue: Computational Technology for Flight Vehicles, pp. 231 –240 (cit. on p. 7).

Miura, F. and H. Okinaka (1989). „Dynamic analysis method for 3-D soil-structure interaction systems with the viscous boundary based on the principle of virtual work.“ In: *Doboku Gakkai Ronbunshu* 1989.404, pp. 395–404 (cit. on pp. 108, 125).

Müller, W. C. (1981). „Simplified analysis of linear fluid-structure interaction“. In: *International Journal for Numerical Methods in Engineering* 17.1, pp. 113–121 (cit. on p. 147).

Murakami, Akira, Akihiko Wakai, and Kazunori Fujisawa (2010). „Numerical methods“. In: *Soils and Foundations* 50.6, pp. 877–892 (cit. on p. 5).

Nazarian, S and KM Boddapati (1995). „Pavement-falling weight deflectometer interaction using dynamic finite-element analysis“. In: *Transportation Research Record* 1482, p. 33 (cit. on p. 5).

Newmark, Nathan M (1959). „A method of computation for structural dynamics“. In: *Journal of the engineering mechanics division* 85.3, pp. 67–94 (cit. on pp. 2, 6).

Nielsen, A. H. (2006). „Absorbing Boundary Conditions for Seismic Analysis in ABAQUS“. In: *2006 ABAQUS Users' Conference*, pp. 359–376 (cit. on pp. 108, 125).

Olson, L. G. and K. J. Bathe (1985). „Analysis of fluid-structure interactions. A direct symmetric coupled formulation based on the fluid velocity potential“. In: *Computers & Structures* 21.1-2, pp. 21–32 (cit. on p. 147).

Olver, Peter J (2016). *Introduction to partial differential equations*. Springer (cit. on p. 61).

Omidi, Omid, Somasundaram Valliappan, and Vahid Lotfi (2013). „Seismic cracking of concrete gravity dams by plastic–damage model using different damping mechanisms“. In: *Finite Elements in Analysis and Design* 63, pp. 80–97 (cit. on p. 221).

Park, K. C. (1980). „Partitioned transient analysis procedures for coupled-field problems: stability analysis“. In: *Journal of Applied Mechanics* 47.2, pp. 370–376 (cit. on p. 147).

– (1983). „Stabilization of partitioned solution procedure for pore fluid-soil interaction analysis“. In: *International Journal for Numerical Methods in Engineering* 19.11, pp. 1669–1673 (cit. on p. 147).

Peerlings, RHJ, R De Borst, WAM Brekelmans, and MGD Geers (1998). „Gradient-enhanced damage modelling of concrete fracture“. In: *Mechanics of Cohesive-frictional Materials: An International Journal on Experiments, Modelling and Computation of Materials and Structures* 3.4, pp. 323–342 (cit. on p. 215).

Pelecanos, L., S. Kontoe, and L. Zdravković (2013). „Numerical modelling of hydrodynamic pressures on dams“. In: *Computers and Geotechnics* 53, pp. 68–82 (cit. on pp. 147, 176, 177).

Picoux, Benoit, A El Ayadi, and Christophe Petit (2009). „Dynamic response of a flexible pavement submitted by impulsive loading“. In: *Soil Dynamics and Earthquake Engineering* 29.5, pp. 845–854 (cit. on p. 5).

Prempramote, S., C. Song, F. Tin-Loi, and G. Lin (2009). „High-order doubly asymptotic open boundaries for scalar wave equation“. In: *International Journal for Numerical Methods in Engineering* 79.3, pp. 340–374 (cit. on p. 146).

Rabinovich, Daniel, Dan Givoli, Jacobo Bielak, and Thomas Hagstrom (2011). „A finite element scheme with a high order absorbing boundary condition for elastodynamics“. In: *Computer Methods in Applied Mechanics and Engineering* 200.23-24, pp. 2048–2066 (cit. on p. 93).

Reed, William H and TR Hill (1973). *Triangular mesh methods for the neutron transport equation*. Tech. rep. Los Alamos Scientific Lab., N. Mex.(USA) (cit. on p. 7).

Richardson, J.D., J.J. Webster, and G.B. Warburton (1971). „The response on the surface of an elastic half-space near to a harmonically excited mass“. In: *Journal of Sound and Vibration* 14.3, pp. 307–316 (cit. on p. 115).

Riff, Richard and Menahem Baruch (1984). „Time finite element discretization of Hamilton's law of varying action“. In: *AIAA journal* 22.9, pp. 1310–1318 (cit. on p. 6).

Rots, Jan G (1991). „Smeared and discrete representations of localized fracture“. In: *Current Trends in Concrete Fracture Research*. Springer, pp. 45–59 (cit. on p. 218).

Ruge, P. (1996). „Hybrid time-finite-elements with time-step-adaption by discontinuity control“. In: *Computational Mechanics* 17.6, pp. 392–397 (cit. on p. 7).

Saini, S. S., P. Bettess, and O. C. Zienkiewicz (1978). „Coupled hydrodynamic response of concrete gravity dams using finite and infinite elements“. In: *Earthquake Engineering & Structural Dynamics* 6.4, pp. 363–374 (cit. on p. 146).

Saito, H. and H. Wada (1977). „Forced vibrations of a mass connected to an elastic half-space by an elastic rod or a spring“. In: *Journal of Sound and Vibration* 50.4, pp. 519–532 (cit. on p. 115).

Samii, Ali and Vahid Lotfi (2012). „Application of H-W boundary condition in damr-eservoir interaction problem“. In: *Finite Elements in Analysis and Design* 50, pp. 86–97 (cit. on pp. 93, 146).

– (2013). „A high-order based boundary condition for dynamic analysis of infinite reservoirs“. In: *Computers & Structures* 120, pp. 65–76 (cit. on p. 93).

Sandberg, G. and P. Goransson (1988). „A symmetric finite element formulation for acoustic fluid-structure interaction analysis“. In: *Journal of Sound Vibration* 123, pp. 507–515 (cit. on p. 147).

Saouma, V., F. Miura, G. Lebon, and Y. Yagome (2011). „A simplified 3D model for soil-structure interaction with radiation damping and free field input“. In: *Bulletin of Earthquake Engineering* 9.5, pp. 1387–1402 (cit. on pp. 108, 125).

Schnabel, Per B (1972). „SHAKE a computer program for earthquake response analysis of horizontally layered sites“. In: *EERC Report, Univ. of California, Berkeley* (cit. on p. 112).

Sezawa, K. and K. Kanai (1935a). „Discontinuity in Dispersion Curves of Rayleigh-Waves“. In: *Proceedings of the Imperial Academy* 11.1, pp. 13–14 (cit. on p. 115).

– (1935b). „Energy dissipation in seismic vibration of a framed structure“. In: *bulletin of the earthquake research institute, Japan* 13, pp. 698–714 (cit. on p. 115).

– (1935c). „Energy dissipation in seismic vibrations of actual buildings“. In: *Bull. Earthq. Res. Inst* 13, pp. 925–941 (cit. on p. 115).

– (1935d). „M₂ Seismic Waves“. In: *Proceedings of the Imperial Academy* 11.3, pp. 96–98 (cit. on p. 115).

Sharan, S. K. (1987). „Time-domain analysis of infinite fluid vibration“. In: *International Journal for Numerical Methods in Engineering* 24.5, pp. 945–958 (cit. on p. 146).

Simkins, T. E. (1981). „Finite Elements for Initial Value Problems in Dynamics“. In: *AIAA Journal* 19.10, pp. 1357–1362 (cit. on p. 6).

Smith, Warwick D. (1974). „A nonreflecting plane boundary for wave propagation problems“. In: *Journal of Computational Physics* 15.4, pp. 492–503 (cit. on p. 88).

Soares, D. and L. Godinho (2014). „An overview of recent advances in the iterative analysis of coupled models for wave propagation“. In: *Journal of Applied Mathematics* 2014 (cit. on p. 147).

Sorek, S and J.J Blech (1982). „Finite-element technique for solving problems formulated by Hamilton's principle“. In: *Computers & Structures* 15.5, pp. 533 –541 (cit. on p. 6).

Stacey, Richard (1988). „Improved transparent boundary formulations for the elastic-wave equation“. In: *Bulletin of the Seismological Society of America* 78.6, pp. 2089–2097 (cit. on p. 89).

Takemiya, Hirokazu (2003). „Simulation of track–ground vibrations due to a high-speed train: the case of X-2000 at Ledsgard“. In: *Journal of Sound and Vibration* 261.3, pp. 503–526 (cit. on pp. 1, 5).

Tamma, Kumar K., Jason Har, Xiangmin Zhou, Masao Shimada, and Andrew Hoitink (2011). „An Overview and Recent Advances in Vector and Scalar Formalisms: Space/Time Discretizations in Computational Dynamics—A Unified Approach“. In: *Archives of Computational Methods in Engineering* 18.2, pp. 119–283 (cit. on p. 7).

Tawfik, Mohamed M and Yasser M El-Mossallamy (2017). „Application of the finite element method for investigating the dynamic plate loading test“. In: *Ain Shams Engineering Journal* 8.1, pp. 39–49 (cit. on pp. 65, 66).

Touhei, T. and T. Ohmachi (1993). „A FE–BE method for dynamic analysis of dam–foundation–reservoir systems in the time domain“. In: *Earthquake engineering & structural dynamics* 22.3, pp. 195–209 (cit. on p. 115).

Trifunac, M.D. (1972). „Interaction of a shear wall with the soil for incident plane SH waves“. In: *Bulletin of the Seismological Society of America* 62.1, pp. 63–83 (cit. on p. 115).

Tsai, C. S., G. C. Lee, and R. L. Ketter (1990). „A semi-analytical method for time-domain analyses of dam–reservoir interactions“. In: *International Journal for Numerical Methods in Engineering* 29.5, pp. 913–933 (cit. on pp. 174, 177).

Underwood, Philip and T. L. Geers (1981). „Doubly asymptotic, boundary-element analysis of dynamic soil-structure interaction“. In: *International Journal of Solids and Structures* 17.7, pp. 687–697 (cit. on p. 91).

Vacus, Olivier (2005). „Mathematical analysis of absorbing boundary conditions for the wave equation: the corner problem“. In: *Mathematics of Computation* 74.249, pp. 177–200 (cit. on p. 92).

Valliappan, S. and C. Zhao (1992). „Dynamic response of concrete gravity dams including dam–water–foundation interaction“. In: *International journal for numerical and analytical methods in geomechanics* 16.2, pp. 79–99 (cit. on p. 116).

Verruijt, Arnold (2009). *An introduction to soil dynamics*. Vol. 24. Springer Science & Business Media (cit. on p. 60).

Victoria, A. F., I. Herrera, and C. Lozano (1969). „Hydrodynamic Pressures Generated by Vertical Earthquake Component“. In: *Fourth World Conference on Earthquake Engineering* (cit. on pp. 142, 143).

Warburton, G.B., J.D. Richardson, and J.J. Webster (1971). „Forced vibrations of two masses on an elastic half space“. In: *Journal of Applied Mechanics* 38.1, pp. 148–156 (cit. on p. 115).

Westergaard, H. M. (1933). „Water pressures on dams during earthquakes“. In: *Trans. ASCE* 95, pp. 418–433 (cit. on p. 141).

Wilson, E. L. and M. Khalvati (1983). „Finite elements for the dynamic analysis of fluid-solid systems“. In: *International Journal for Numerical Methods in Engineering* 19.11, pp. 1657–1668 (cit. on p. 147).

Wolf, J and William Hall (1988). *Soil-structure-interaction analysis in time domain*. A Division of Simon & Schuster (cit. on p. 71).

Wolf, John (1985). *Dynamic soil-structure interaction*. Prentice Hall, Inc. (cit. on p. 71).

Wolf, John P. and Chongmin Song (1995). „Doubly asymptotic multi-directional transmitting boundary for dynamic unbounded medium-structure-interaction analysis“. In: *Earthquake Engineering & Structural Dynamics* 24.2, pp. 175–188 (cit. on p. 91).

Wolf, John P and Chongmin Song (1996). *Finite-element modelling of unbounded media*. Wiley Chichester (cit. on pp. 71, 86).

Wong, H.L. and M.D. Trifunac (1974). „Interaction of a shear wall with the soil for incident plane SH waves: elliptical rigid foundation“. In: *Bulletin of the Seismological Society of America* 64.6, pp. 1825–1842 (cit. on p. 115).

Yang, R., C. S. Tsai, and G. C. Lee (1993). „Explicit time-domain transmitting boundary for dam-reservoir interaction analysis“. In: *International journal for numerical methods in engineering* 36.11, pp. 1789–1804 (cit. on p. 146).

Yazdchi, M., N. Khalili, and S. Valliappan (1999). „Dynamic soil–structure interaction analysis via coupled finite-element–boundary-element method“. In: *Soil Dynamics and Earthquake Engineering* 18.7, pp. 499–517 (cit. on p. 115).

Yoshimura, Chiaki, Jacobo Bielak, Yoshiaki Hisada, and Antonio Fernández (2003). „Domain reduction method for three-dimensional earthquake modeling in localized regions, part II: Verification and applications“. In: *Bulletin of the Seismological Society of America* 93.2, pp. 825–840 (cit. on pp. 108, 110).

Zhang, S.L. (1997). „GPBi-CG: Generalized Product-type Methods Based on Bi-CG for Solving Nonsymmetric Linear Systems“. In: *SIAM Journal on Scientific Computing* 18.2, pp. 537–551 (cit. on pp. 127, 172, 211).

Zhang, Yuyi, Zhaohui Yang, Jacobo Bielak, Joel P. Conte, and Ahmed Elgamal (2003). „Treatment of Seismic Input and Boundary Conditions in Nonlinear Seismic Analysis of a Bridge Ground System“. In: *Proceedings of the 16th ASCE Engineering Mechanics Conference*, pp. 1–11 (cit. on pp. 108, 111, 125).

Zhao, C., S. Valliappan, and Y.C. Wang (1992). „A numerical model for wave scattering problems in infinite media due to p-and sv-wave incidences“. In: *International Journal for Numerical Methods in Engineering* 33.8, pp. 1661–1682 (cit. on p. 116).

Zienkiewicz, O. C. and R. E. Newton (1969). „Coupled vibrations of a structure submerged in a compressible fluid“. In: *Proc. of Symposium on Finite Element Techniques held at the University of Stuttgart* (cit. on p. 147).

Zienkiewicz, O. C. and R. L. Taylor (2005). *The finite element method for solid and structural mechanics*. Elsevier (cit. on pp. 150, 196).

Zienkiewicz, OC, N Bicanic, and FQ Shen (1989). „Earthquake Input Definition and the Trasmitting Boundary Conditions“. In: *Advances in computational nonlinear mechanics*. Springer, pp. 109–138 (cit. on pp. 108, 125).